AD-A278 373

VOLUME 322

High Temperature Silicides and Refractory Alloys

DISTRIBUTION STATEMENT A
Approved for public release;
Distribution Unlimited

EDITORS
C.L. Briant
J.J. Petrovic
B.P. Bewlay
A.K. Vasudevan
H.A. Lipsitt

94-12196

DTIC
ELECTE
APR 21 1994
S B L

High Temperature Silicides and Refractory Alloys

Accession For	
NTIS GRA&I	☑
DTIC TAB	☐
Unannounced	☐
Justification	
By	
Distribution/	
Availability Codes	
Dist	Avail and/or Special
A-1	

MATERIALS RESEARCH SOCIETY SYMPOSIUM PROCEEDINGS VOLUME 322

High Temperature Silicides and Refractory Alloys

Symposium held November 29–December 2, 1993, Boston, Massachusetts, U.S.A.

EDITORS:

C.L. Briant
General Electric Company
Schenectady, New York, U.S.A.

J.J. Petrovic
Los Alamos National Laboratory
Los Alamos, New Mexico, U.S.A.

B.P. Bewlay
General Electric Company
Schenectady, New York, U.S.A.

A.K. Vasudevan
Office of Naval Research
Arlington, Virginia, U.S.A.

H.A. Lipsitt
Wright State University
Dayton, Ohio, U.S.A.

MRS
MATERIALS RESEARCH SOCIETY
Pittsburgh, Pennsylvania

DTIC QUALITY INSPECTED 8

This work relates to Department of Navy Grant Number N00014-1-93-0741 issued by the Office of Naval Research. The United States Government has a royalty-free license throughout the world in all copyrightable material contained herein.

Single article reprints from this publication are available through
University Microfilms Inc., 300 North Zeeb Road, Ann Arbor, Michigan 48106

CODEN: MRSPDH

Copyright 1994 by Materials Research Society.
All rights reserved.

This book has been registered with Copyright Clearance Center, Inc. For further information, please contact the Copyright Clearance Center, Salem, Massachusetts.

Published by:

Materials Research Society
9800 McKnight Road
Pittsburgh, Pennsylvania 15237
Telephone (412) 367-3003
Fax (412) 367-4373

Library of Congress Cataloging in Publication Data

Materials Research Society. Meeting (1993: Boston, Mass.)
High temperature silicides and refractory alloys: symposium held
1993 Fall MRS Meeting, November 29-December 3, 1993, Boston,
Massachusetts, U.S.A./editors, C.L. Briant, J.J. Petrovic, B.P. Bewlay,
A.K. Vasudevan, H.A. Lipsitt
p. cm.-(Materials Research Society symposium proceedings; v. 322)
Includes bibliographical references and index.
ISBN 1-55899-221-9
1. Heat resistant alloys--Congresses. 2. Silicides--Congresses.
I. Briant, C.L. II. Petrovic, J.J. III. Bewlay, B.P. IV. Vasudevan, A.K.
V. Lipsitt, H.A. VI. Materials Research Society. VII. Title.
VIII. Series: Materials Research Society symposium proceedings: v. 322.

TA418.26.M33 1993
620.1'89304217--dc20

94-5806
CIP

Manufactured in the United States of America

Contents

PREFACE xi

ACKNOWLEDGMENTS xiii

MATERIALS RESEARCH SOCIETY SYMPOSIUM PROCEEDINGS xiv

PART I: SILICIDE MICROSTRUCTURES AND DEFORMATION

OVERVIEW OF HIGH TEMPERATURE STRUCTURAL SILICIDES 3
J.J. Petrovic and A.K. Vasudevan

*PLASTIC BEHAVIOR AND DEFORMATION STRUCTURE OF SILICIDE SINGLE CRYSTALS WITH TRANSITION METALS AT HIGH TEMPERATURES 9
Y. Umakoshi, T. Nakashima, T. Nakano, and E. Yanagisawa

THE TEMPERATURE AND STRAIN RATE DEPENDENCE OF THE FLOW STRESS IN $MoSi_2$ SINGLE CRYSTALS 21
S.A. Maloy, T.E. Mitchell, John J. Petrovic, A.H. Heuer, and J.J. Lewandowski

CHARACTERIZATION OF STRUCTURE AND MECHANICAL PROPERTIES OF $MoSi_2$-SiC NANOLAYER COMPOSITES 27
H. Kung, T.R. Jervis, J-P. Hirvonen, M. Nastasi, and T.E. Mitchell

SYNTHESIS AND PROPERTIES OF *IN-SITU* $MoSi_2$/SiC COMPOSITES 33
S. Jayashankar, S.E. Riddle, and M.J. Kaufman

THE EFFECT OF DEFORMATION AND REINFORCEMENT PARTICLES ON THE GRAIN GROWTH BEHAVIOR OF $MoSi_2$ 41
Ajoy Basu and Amit Ghosh

$C11_b$-C40 TRANSFORMATION-INDUCED 1/4<111> FAULTS IN $MoSi_2$ 49
B.K. Kad, K.S. Vecchio, B.P. Bewlay, and R.J. Asaro

PART II: SILICIDE SYNTHESIS AND PROCESSING

*IN-SITU PROCESSING OF $MoSi_2$-BASE COMPOSITES 59
N. Patibandla, W.B. Hillig, M.R. Ramakrishnan, D.E. Alman, and N.S. Stoloff

*VACUUM PLASMA SPRAY FORMING OF HIGH TEMPERATURE SILICIDES 71
S. Sampath and H. Herman

FABRICATION AND TESTING OF PLASMA-SPRAY FORMED $MoSi_2$ AND $MoSi_2$ COMPOSITE TUBES 81
R.G. Castro, J.R. Hellmann, A.E. Segall, and D.L. Shelleman

*THE APPLICATION OF REACTIVE HOT COMPACTION AND IN-SITU COATING TECHNIQUES TO INTERMETALLIC MATRIX COMPOSITES 87
H. Doty, M. Somerday, and R. Abbaschian

*Invited Paper

SINTERING OF $MoSi_2$ 107
J.J. Petrovic and J.S. Idasetima

COMBUSTION SYNTHESIS OF $MoSi_2$ AND $MoSi_2$-COMPOSITES 113
K. Monroe, S. Govindarajan, J.J. Moore, B. Mishra,
D.L. Olson, and J. Disam

COMBUSTION SYNTHESIS OF MOLYBDENUM DISILICIDE
AND ITS COMPOSITES 119
Seetharama C. Deevi

SYNTHESIS AND CHARACTERIZATION OF METAL SILICIDE/
SILICON CARBIDE COMPOSITES BY LOW TEMPERATURE SOLID-
STATE REACTIONS 127
D. Zeng, M.J. Hampden-Smith, and L.-M. Wang

SYNTHESIS OF HIGH-TEMPERATURE SILICIDES VIA RAPID
SOLID-STATE METATHESIS 133
Richard M. Jacubinas and Richard B. Kaner

SYNTHESIS AND PROPERTIES OF $MoSi_2$/SiC PROCESSED BY
LOW PRESSURE PLASMA CO-INJECTION AND DEPOSITION 139
D.E. Lawrynowicz, J. Wolfenstine, S. Nutt,
E.J. Lavernia, D.E. Bailey, and A. Sickinger

THERMO-CHEMICAL SYNTHESIS OF NANOSTRUCTURED CHROMIUM
SILICIDE/SILICON CARBIDE AND MOLYBDENUM SILICIDE/
SILICON CARBIDE COMPOSITE POWDERS 149
Ping Luo, Peter R. Strutt, and Kenneth E. Gonsalves

PART III: SILICIDE MECHANICAL BEHAVIOR AND PROBLEMS

*A REVIEW OF CREEP OF SILICIDES AND COMPOSITES 157
K. Sadananda and C.R. Feng

*PLASTICITY ENHANCEMENT PROCESSES IN $MoSi_2$-BASE
MATERIALS 175
R. Gibala, H. Chang, and C.M. Czarnik

FILM SOFTENING EFFECTS OF ZrO_2 ON $MoSi_2$ 185
C.M. Czarnik, R. Gibala, M. Nastasi, and J.D. Garrett

STRENGTH AND TOUGHNESS OF SILICIDE MATRIX MATERIALS
CONSOLIDATED BY HOT ISOSTATIC PRESSING 191
R. Suryanarayanan, S.M.L. Sastry, and K.L. Jerina

CREEP BEHAVIOR OF $MoSi_2$SiC COMPOSITES 197
Darryl P. Butt, Stuart A. Maloy, H. Kung,
David A. Korzekwa, and John J. Petrovic

CREEP RUPTURE OF $MoSi_2$/SiC_p COMPOSITES 203
Jonathan D. French, Sheldon M. Wiederhorn, and
John J. Petrovic

MICROCRACKING, STRAIN RATE AND LARGE STRAIN
DEFORMATION EFFECTS IN MOLYBDENUM DISILICIDE 209
D.A. Hardwick and P.L. Martin

THE EFFECT OF GRAIN SIZE AND SiC PARTICULATES ON
THE STRENGTH AND DUCTILITY OF $MoSi_2$ 215
Amit K. Ghosh and Ajoy Basu

*Invited Paper

PLASTICITY OF $MoSi_2$ BELOW 900°C 223
H. Chang and R. Gibala

BRITTLE COMPOSITES MODELING: COMPARISONS WITH $MoSi_2/ZrO_2$ 229
S.P. Chen, R. LeSar, and A.D. Rollett

DESIGN AND SYNTHESIZE OF NEW TERNARY ZIRCONIUM SILICIDE INTERMETALLIC COMPOUNDS WITH THE 16H CRYSTAL STRUCTURE 235
Yukinori Ikarashi and Kozo Ishizaki

PART IV: SILICIDE OXIDATION AND PROPERTIES

*HIGH TEMPERATURE OXIDATION BEHAVIOR OF STRUCTURAL SILICIDES 243
C.E. Ramberg, P. Beatrice, K. Kurokawa, and W.L. Worrell

CYCLIC OXIDATION RESISTANCE OF $MoSi_2$/20v% Nb COMPOSITES 255
D.E. Alman and N.S. Stoloff

THERMAL FATIGUE OF $MoSi_2$ AND A $MoSi_2$-10 vol% TiC COMPOSITE 261
M.T. Kush, J.W. Holmes, and R. Gibala

SURFACE OXIDATION MECHANISMS OF MOLYBDENUM DISILICIDE IN HIGH-TEMPERATURE COMBUSTION ENVIRONMENTS 267
Wen-Yi Lin and Robert F. Speyer

ELECTROCHEMICAL PROTECTION OF MOLYBDENUM AND MOLYBDENUM DISILICIDE IN MOLTEN SODA-LIME-SILICATE GLASS ENVIRONMENT 273
S. Kamakshi Sundaram and Robert F. Speyer

MICROSTRUCTURE AND MECHANICAL PROPERTIES OF NITRIDED MOLYBDENUM SILICIDE COATINGS 279
J-P. Hirvonen, I. Suni, H. Kattelus, R. Lappalainen, P. Torri, H. Kung, T.R. Jervis, and M. Nastasi

HIGH TEMPERATURE SILICIDE THIN-FILM THERMOCOUPLES 285
Kenneth G. Kreider

MICROSTRUCTURAL EVOLUTION IN COMPOSITIONALLY TAILORED $MoSi_2$/SiC COMPOSITES 291
S.E. Riddle, S. Jayashankar, and M.J. Kaufman

FABRICATION AND CHARACTERIZATION OF A FUNCTIONALLY GRADIENT Mo-$MoSi_2$ COMPOSITE 297
Gaurav Agarwal, Wen-yi Lin, and Robert F. Speyer

PART V: RECENT ADVANCES IN REFRACTORY ALLOYS AND PROCESSING

THE PROPERTIES AND USES OF REFRACTORY METALS AND THEIR ALLOYS 305
C.L. Briant

*RECENT ADVANCES AND DEVELOPMENTS IN REFRACTORY ALLOYS 315
T.G. Nieh and J. Wadsworth

*Invited Paper

*DEVELOPMENT OF HIGH-STRENGTH FABRICABLE TANTALUM-BASE ALLOYS 329
R.W. Buckman, Jr.

*POWDER PROCESSING OF REFRACTORY METALS AND ALLOYS 341
Randall W. German

*DIRECTIONAL SOLIDIFICATION OF REFRACTORY INTERMETALLICS: SINGLE CRYSTALS AND COMPOSITES 353
David P. Pope, Dilip M. Shah, William Romanow, and Mark Huntley

*MECHANICAL WORKING OF REFRACTORY ALLOYS PRODUCED BY MELTING PROCESSES 363
John R. Hughes

EFFECT OF DEFORMATION PROCESSING ON MECHANICAL PROPERTIES OF Nb-10 a/o Si IN-SITU COMPOSITE 377
I. Weiss, M. Thirukkonda, and R. Srinivasan

EFFECT OF COOLING RATE ON THE TENSILE YIELD STRENGTH AND DUCTILITY OF B2 COMPOUND IN Nb-40at.% Ti-15at.%Al ALLOY 387
D.-H. Hou and H.L. Fraser

PART VI: REFRACTORY ALLOYS: PHYSICAL AND MECHANICAL METALLURGY

*REFRACTORY AND SILICIDE LAVES PHASES 395
James D. Livingston

INFLUENCE OF TUNGSTEN ALLOYING ADDITIONS ON THE MECHANICAL PROPERTIES AND TEXTURE OF TANTALUM 407
G.T. Gray III, S.R. Bingert, S.I. Wright, and S.R. Chen

EFFECT OF INTERMETALLIC COMPOUNDS ON THE PROPERTIES OF TANTALUM 413
P. Kumar, C.E. Mosheim, and C.A. Michaluk

*TERNARY $MoSi_2$ COMPOUNDS FOR HIGH TEMPERATURE STRUCTURAL APPLICATIONS 423
S. Chin, D.L. Anton, and A.F. Giamei

MOLYBDENUM-RHENIUM DISILICIDE ALLOYS 431
D.L. Davidson and A. Bose

INVESTIGATION OF B2 AND RELATED PHASES IN Ti-MODIFIED Nb-Al ALLOYS 437
D.-H. Hou, S.S. Yang, J. Shyue, and H.L. Fraser

EFFECTS OF PROCESSING AND PROLONGED HIGH TEMPERATURE EXPOSURE ON THE MICROSTRUCTURE OF Nb-1Zr-C SHEET 443
Mehmet Uz and R.H. Titran

MICROSTRUCTURES, DEFECTS AND DEFORMATION MECHANISMS IN VANADIUM MODIFIED Nb_3Al 453
L.S. Smith, M. Aindow, and M.H. Loretto

*Invited Paper

PART VII: REFRACTORY ALLOYS: MULTIPHASE MATERIALS AND COMPOSITES

*PROPERTIES OF MICROLAMINATED INTERMETALLIC-REFRACTORY METAL COMPOSITES 461
R.G. Rowe, D.W. Skelly, M. Larsen, J. Heathcote, G. Lucas, and G.R. Odette

TENSILE AND STRESS-RUPTURE BEHAVIOR OF HAFNIUM CARBIDE DISPERSED MOLYBDENUM AND TUNGSTEN BASE ALLOY WIRES 473
H.M. Yun and R.H. Titran

MICROSTRUCTURAL EVOLUTION AND DENSIFICATION KINETICS DURING SINTERING OF OXIDE-DISPERSED TUNGSTEN ALLOYS 483
Li-Chyong Chen and Bernard P. Bewlay

*MICROSTRUCTURES AND MECHANICAL BEHAVIOR OF Nb-Ti BASE BETA + SILICIDE ALLOYS 491
P.R. Subramanian, M.G. Mendiratta, and D.M. Dimiduk

EFFECTS OF ENVIRONMENTAL EXPOSURE ON DUCTILE-PHASE TOUGHENING IN NIOBIUM SILICIDE-NIOBIUM COMPOSITES 503
Joseph D. Rigney, Preet M. Singh, and John J. Lewandowski

THE EFFECTS OF IN-SITU PROCESSING METHODS ON THE MICROSTRUCTURE AND FRACTURE TOUGHNESS OF V-V$_3$Si COMPOSITES 511
M.J. Strum, G.A. Henshall, B.P. Bewlay, J.A. Sutliff, and M.R. Jackson

PART VIII: APPLICATIONS OF REFRACTORY ALLOYS

*PROCESSING, PROPERTIES AND APPLICATIONS OF HIGH-TEMPERATURE NIOBIUM ALLOYS 519
C. Craig Wojcik

*APPLICATION OF TUNGSTEN ALLOYS IN THE LIGHTING INDUSTRY 531
L. Bartha

POTASSIUM IN GRAIN BOUNDARIES OF TUNGSTEN 537
Milan R. Vukcevich

CREEP CHARACTERISTICS OF TUNGSTEN WIRES 547
Wego Wang

SINTERING BEHAVIOR OF Ba_2CaWO_6-DOPED-TUNGSTEN 553
J.A. Rudd and B.P. Bewlay

VARIOUS PROPERTIES OF SPUTTERED Ta_xAl_{1-x} FILMS 559
V.J. Minkiewicz, J.O. Moore, G. Keller, S.J. Woodman, D. Dobbertin, R. Savoy, and J.M. Eldridge

AUTHOR INDEX 565

SUBJECT INDEX 567

*Invited Paper

Preface

This volume is the written proceedings of Symposium F on High Temperature Silicides and Refractory Alloys, which was held in conjunction with the 1993 Fall Materials Research Society Meeting in Boston, Massachusetts, November 28-December 2, 1993. This symposium was very successful with 82 oral presentations, over four days.

The first two days were devoted to recent developments in silicides and the last two days to refractory alloys. This response is a reflection of the growing interest in refractory metal based silicides, in particular, $MoSi_2$, and the continued development of commercial refractory alloys such as W, Mo, Ta, and Nb-based alloys. The symposium covered synthesis, processing, microstructures, mechanical properties, oxidation behavior, composites, multiphase materials and applications. Significant advances were evident in all these areas.

The symposium was sponsored by The Office of Naval Research, Osram-Sylvania Inc., and the General Electric Company. We are very grateful for their support. We are also pleased to acknowledge the support of the staff at MRS for their assistance in assembling both the program and the proceedings. Finally, we would like to thank the session chairs, the manuscript services, the speakers and all those who contributed to the success of this symposium.

C.L. Briant
J.J. Petrovic
B.P. Bewlay
A.K. Vasudevan
H.A. Lipsitt

January 1994

Acknowledgments

Financial support for this symposium was provided by The Office of Naval Research, Osram-Sylvania Inc., and General Electric Company. We are very grateful to them for this support for without it the symposium could not have been so successful. The papers in this proceedings were reviewed on-site following the MRS procedures. We gratefully acknowledge the contributions of the session chairs and all the other key readers of the manuscripts.

MATERIALS RESEARCH SOCIETY SYMPOSIUM PROCEEDINGS

Volume 297— Amorphous Silicon Technology—1993, E.A. Schiff, M.J. Thompson, P.G. LeComber, A. Madan, K. Tanaka, 1993, ISBN: 1-55899-193-X

Volume 298— Silicon-Based Optoelectronic Materials, R.T. Collins, M.A. Tischler, G. Abstreiter, M.L. Thewalt, 1993, ISBN: 1-55899-194-8

Volume 299— Infrared Detectors—Materials, Processing, and Devices, A. Appelbaum, L.R. Dawson, 1993, ISBN: 1-55899-195-6

Volume 300— III-V Electronic and Photonic Device Fabrication and Performance, K.S. Jones, S.J. Pearton, H. Kanber, 1993, ISBN: 1-55899-196-4

Volume 301— Rare-Earth Doped Semiconductors, G.S. Pomrenke, P.B. Klein, D.W. Langer, 1993, ISBN: 1-55899-197-2

Volume 302— Semiconductors for Room-Temperature Radiation Detector Applications, R.B. James, P. Siffert, T.E. Schlesinger, L. Franks, 1993, ISBN: 1-55899-198-0

Volume 303— Rapid Thermal and Integrated Processing II, J.C. Gelpey, J.K. Elliott, J.J. Wortman, A. Ajmera, 1993, ISBN: 1-55899-199-9

Volume 304— Polymer/Inorganic Interfaces, R.L. Opila, A.W. Czanderna, F.J. Boerio, 1993, ISBN: 1-55899-200-6

Volume 305— High-Performance Polymers and Polymer Matrix Composites, R.K. Eby, R.C. Evers, D. Wilson, M.A. Meador, 1993, ISBN: 1-55899-201-4

Volume 306— Materials Aspects of X-Ray Lithography, G.K. Celler, J.R. Maldonado, 1993, ISBN: 1-55899-202-2

Volume 307— Applications of Synchrotron Radiation Techniques to Materials Science, D.L. Perry, R. Stockbauer, N. Shinn, K. D'Amico, L. Terminello, 1993, ISBN: 1-55899-203-0

Volume 308— Thin Films—Stresses and Mechanical Properties IV, P.H. Townsend, J. Sanchez, C-Y. Li, T.P. Weihs, 1993, ISBN: 1-55899-204-9

Volume 309— Materials Reliability in Microelectronics III, K. Rodbell, B. Filter, P. Ho, H. Frost, 1993, ISBN: 1-55899-205-7

Volume 310— Ferroelectric Thin Films III, E.R. Myers, B.A. Tuttle, S.B. Desu, P.K. Larsen, 1993, ISBN: 1-55899-206-5

Volume 311— Phase Transformations in Thin Films—Thermodynamics and Kinetics, M. Atzmon, J.M.E. Harper, A.L. Greer, M.R. Libera, 1993, ISBN: 1-55899-207-3

Volume 312— Common Themes and Mechanisms of Epitaxial Growth, P. Fuoss, J. Tsao, D.W. Kisker, A. Zangwill, T.F. Kuech, 1993, ISBN: 1-55899-208-1

Volume 313— Magnetic Ultrathin Films, Multilayers and Surfaces/Magnetic Interfaces—Physics and Characterization (2 Volume Set), C. Chappert, R.F.C. Farrow, B.T. Jonker, R. Clarke, P. Grünberg, K.M. Krishnan, S. Tsunashima/ E.E. Marinero, T. Egami, C. Rau, S.A. Chambers, 1993, ISBN: 1-55899-211-1

Volume 314— Joining and Adhesion of Advanced Inorganic Materials, A.H. Carim, D.S. Schwartz, R.S. Silberglitt, R.E. Loehman, 1993, ISBN: 1-55899-212-X

Volume 315— Surface Chemical Cleaning and Passivation for Semiconductor Processing, G.S. Higashi, E.A. Irene, T. Ohmi, 1993, ISBN: 1-55899-213-8

MATERIALS RESEARCH SOCIETY SYMPOSIUM PROCEEDINGS

Volume 316— Materials Synthesis and Processing Using Ion Beams, R.J. Culbertson, K.S. Jones, O.W. Holland, K. Maex, 1994, ISBN: 1-55899-215-4

Volume 317— Mechanisms of Thin Film Evolution, S.M. Yalisove, C.V. Thompson, D.J. Eaglesham, 1994, ISBN: 1-55899-216-2

Volume 318— Interface Control of Electrical, Chemical, and Mechanical Properties, S.P. Murarka, T. Ohmi, K. Rose, T. Seidel, 1994, ISBN: 1-55899-217-0

Volume 319— Defect-Interface Interactions, E.P. Kvam, A.H. King, M.J. Mills, T.D. Sands, V. Vitek, 1994, ISBN: 1-55899-218-9

Volume 320— Silicides, Germanides, and Their Interfaces, R.W. Fathauer, L. Schowalter, S. Mantl, K.N. Tu, 1994, ISBN: 1-55899-219-7

Volume 321— Crystallization and Related Phenomena in Amorphous Materials, M. Libera, T.E. Haynes, P. Cebe, J. Dickinson, 1994, ISBN: 1-55899-220-0

Volume 322— High-Temperature Silicides and Refractory Alloys, B.P. Bewlay, J.J. Petrovic, C.L. Briant, A.K. Vasudevan, H.A. Lipsitt, 1994, ISBN: 1-55899-221-9

Volume 323— Electronic Packaging Materials Science VII, R. Pollak, P. Børgesen, H. Yamada, K.F. Jensen, 1994, ISBN: 1-55899-222-7

Volume 324— Diagnostic Techniques for Semiconductor Materials Processing, O.J. Glembocki, F.H. Pollak, S.W. Pang, G. Larrabee, G.M. Crean, 1994, ISBN: 1-55899-223-5

Volume 325— Physics and Applications of Defects in Advanced Semiconductors, M.O. Manasreh, M. Lannoo, H.J. von Bardeleben, E.L. Hu, G.S. Pomrenke, D.N. Talwar, 1994, ISBN: 1-55899-224-3

Volume 326— Growth, Processing, and Characterization of Semiconductor Heterostructures, G. Gumbs, S. Luryi, B. Weiss, G.W. Wicks, 1994, ISBN: 1-55899-225-1

Volume 327— Covalent Ceramics II: Non-Oxides, A.R. Barron, G.S. Fischman, M.A. Fury, A.F. Hepp, 1994, ISBN: 1-55899-226-X

Volume 328— Electrical, Optical, and Magnetic Properties of Organic Solid State Materials, A.F. Garito, A. K-Y. Jen, C. Y-C. Lee, L.R. Dalton, 1994, ISBN: 1-55899-227-8

Volume 329— New Materials for Advanced Solid State Lasers, B.H.T. Chai, T.Y. Fan, S.A. Payne, A. Cassanho, T.H. Allik, 1994, ISBN: 1-55899-228-6

Volume 330— Biomolecular Materials By Design, H. Bayley, D. Kaplan, M. Navia, 1994, ISBN: 1-55899-229-4

Volume 331— Biomaterials for Drug and Cell Delivery, A.G. Mikos, R. Murphy, H. Bernstein, N.A. Peppas, 1994, ISBN: 1-55899-230-8

Volume 332— Determining Nanoscale Physical Properties of Materials by Microscopy and Spectroscopy, M. Sarikaya, M. Isaacson, H.K. Wickramasighe, 1994, ISBN: 1-55899-231-6

Volume 333— Scientific Basis for Nuclear Waste Management XVII, A. Barkatt, R. Van Konynenburg, 1994, ISBN: 1-55899-232-4

Volume 334— Gas-Phase and Surface Chemistry in Electronic Materials Processing, T.J. Mountziaris, P.R. Westmoreland, F.T.J. Smith, G.R. Paz-Pujalt, 1994, ISBN: 1-55899-233-2

Volume 335— Metal-Organic Chemical Vapor Deposition of Electronic Ceramics, S.B. Desu, D.B. Beach, B.W. Wessels, S. Gokoglu, 1994, ISBN: 1-55899-234-0

Prior Materials Research Society Symposium Proceedings available by contacting Materials Research Society

PART I

Silicide Microstructures and Deformation

OVERVIEW OF HIGH TEMPERATURE STRUCTURAL SILICIDES

J.J. PETROVIC* AND A.K. VASUDEVAN**
*Materials Division, Group MTL-4, Los Alamos National Laboratory, Los Alamos, NM 87545
**Office of Naval Research, Code 4421, 800 North Quincy St., Arlington, VA 22217-5660

ABSTRACT

High temperature structural silicides represent an important new class of structural materials, with significant potential applications in the range of 1200-1600 °C under oxidizing and aggressive environments. Silicides, particularly those based on $MoSi_2$, are considered to be promising due to their combination of high melting point, elevated temperature oxidation resistance, brittle-to-ductile transition, and electrical conductivity. Possible structural uses for silicides include their application as matrices in structural silicide composites, as reinforcements for structural ceramic matrix composites, as high temperature joining materials for structural ceramic components, and as oxidation-resistant coatings for refractory metals and carbon-based materials. The historical development of structural silicides, their potential applications, and important issues related to their use are discussed.

INTRODUCTION

High temperature structural materials that can be used in oxidizing environments in the range of 1200-1600 °C constitute an enabling materials technology for a wide range of applications in the industrial, aerospace, and automotive arenas. Potential uses include industrial furnace elements and fixturing, power generation components, high temperature heat exchangers, gas burners and igniters, high temperature filters, aircraft turbine engine hot section components such as blades, vanes, combustors, nozzles, and seals, and automotive components such as turbocharger rotors, valves, glow plugs, and advanced turbine engine parts. There is increasing interest in silicide-based compounds for such applications. In this temperature range, for oxidation and strength reasons, the choice of materials is limited to the silicon-based structural ceramics such as Si_3N_4 and SiC, and to the new class of "high temperature structural silicides" [1].

While the number of known silicide compounds is large, potential silicides for elevated temperature applications are essentially those based on refractory and transition metals, such as $MoSi_2$, WSi_2, $TiSi_2$, $CrSi_2$, $CoSi_2$, Mo_5Si_3, and Ti_5Si_3. Of such materials, $MoSi_2$ is presently the most promising and the most developed, due to its combination of high melting point, superb elevated temperature oxidation resistance, brittle-to-ductile transition, and electrical conductivity [2]. Structural uses for silicides include their application as matrices in structural silicide composites, as reinforcements for structural ceramic composites, as high temperature joining materials for structural ceramics, and as oxidation-resistant coatings for refractory metals and carbon-based materials. The purpose of the present discourse is to provide an overview regarding these materials.

Mat. Res. Soc. Symp. Proc. Vol. 322. ©1994 Materials Research Society

HISTORICAL PERSPECTIVE:

A brief historical perspective on the development of structural silicides is given here. A more detailed history of the development of structural silicides, with emphasis on $MoSi_2$ materials, is given in Reference [1]. W.A. Maxwell was the first person to suggest the use of a silicide, $MoSi_2$, as a high temperature structural material. He performed interesting research on structural silicides in the early 1950's at NACA, the predecessor to NASA [3]. Unfortunately, Maxwell's thoughtful initial work was not continued due to the fact that, at that time, the high temperature structural materials community was not yet ready to deal with brittle materials. In the early 1970's, E. Fitzer in Germany began examinations of $MoSi_2$ matrix composites reinforced with additions of Al_2O_3, SiC, and Nb [4]. This work led Fitzer's colleague, J. Schlichting, to publish a detailed review article in 1978, suggesting the use of $MoSi_2$ as a matrix material for high temperature structural composites [5].

Two important structural silicide articles were published in 1985. The first was an article by Fitzer and Remmele describing work on Nb wire-$MoSi_2$ matrix composites with improved room temperature mechanical properties [6]. In the second article, Gac and Petrovic indicated the feasibility of SiC whisker-$MoSi_2$ matrix composites, showing improvements in room temperature strength and fracture toughness [7]. In 1988, Carter demonstrated SiC whisker-$MoSi_2$ matrix composites with mechanical property levels within the range of high temperature engineering applications [8]. In 1990, Umakoshi et. al. published investigations of the mechanical behavior of $MoSi_2$ single crystals, which indicated interesting elevated temperature properties [9]. As a result of the growing interest in structural silicides, the First High Temperature Structural Silicides Workshop, sponsored by the Office of Naval Research, was held in November 1991 at the National Institute of Standards and Technology in Gaithersburg, Maryland. This Workshop consisted of 32 presentations in the areas of silicide materials, processing, processing-properties, microstructures, oxidation, mechanical properties, and coatings. Reference [1] contains the proceedings from this Workshop.

SILICIDE MATRIX COMPOSITES

For silicides to be used as a basis for high temperature structural materials, both their high and low temperature mechanical properties must be improved. This requires significant improvements in high temperature strength and creep resistance, and in low temperature fracture toughness. However, it is important that composite strategies adopted do not degrade either the intermediate or the elevated temperature oxidation resistance of the composite to a significant extent.

A number of composite approaches for silicides have been employed to date [1]. Reinforcement morphologies have included continuous fibers, discontinuous particulate or whisker phases, and microlaminates. Reinforcement materials have been both oxide and non-oxide ceramics, as well as refractory metals. Fabrication techniques for composites have involved hot pressing/hot isostatic pressing, melting, plasma spraying, mechanical alloying, microlamination, in-situ syntheis, and combustion synthesis.

Composite approaches have been shown to significantly improve the mechanical properties of $MoSi_2$-based structural silicides [1,2]. For example, the use of SiC whisker

reinforcements has been demonstrated to reduce elevated temperature creep rates by three orders of magnitude over that of unreinforced $MoSi_2$. Creep rates can also be reduced by alloying with substitutional species such as WSi_2. Continuous fiber reinforcements have yielded $MoSi_2$-based composites with room temperature fracture toughness values in excess of 15 MPa $m^{1/2}$. Toughness values of 7.8 MPa $m^{1/2}$ have been obtained with discontinuous ZrO_2 particulate reinforcements.

It is useful to compare $MoSi_2$-based structural silicides to silicon-based structural ceramics (Si_3N_4, SiC), since both of these material classes are candidates for 1200-1600 °C structural applications [2]. The two central issues for the application of such materials are those of reliability and cost, and a comparison of these aspects is given in Table 1.

Table I. Comparison of $MoSi_2$-Based Structural Silicides and Silicon-Based Structural Ceramics

RELIABILITY ADVANTAGES

$MoSi_2$-Based Structural Silicides:

- O Brittle-to-ductile transition in a useful temperature range
  - o Potential higher fracture toughness at operating temperatures
- O Alloying may be extensively employed to improve mechanical properties
- O Thermodynamically stable with a wide range of ceramic reinforcements
- O Thermal expansion coefficients a closer match to metals, thus easier to join to metals

Silicon-Based Structural Ceramics:

- O No intermediate temperature oxidation "pest"
- O Somewhat more creep resistant, at least at present
- O Lower thermal expansion coefficients, thus lower thermal stresses

COST ADVANTAGES

$MoSi_2$-Based Structural Silicides:

- O Can be electro-discharge machined, thus lower cost machining
- O Can be melted, thus more versatility in processing
- O Easer to densify, no densification aids required

Silicon-Based Structural Ceramics:

- O None

Currently, there is a slight reliability advantage of the $MoSi_2$-based structural silicides over the silicon-based structural ceramics. With further development of the structural silicides (which are currently at an early stage in comparison to the more mature structural ceramics), a more dramatic reliability advantage is likely to emerge, as issues of structural silicide creep resistance, fracture toughness, and intermediate temperature oxidation behavior are addressed. However, Table 1 clearly shows that there is a distinct cost advantage of the structural silicides over the structural ceramics. Because the silicides can be electro-discharge machined, their machining costs will be significantly lower than the structural ceramics, which must be diamond machined. Furthermore, unlike the structural ceramics which thermally

decompose rather than melt, the silicides can be melted, leading to more versatility in processing since melting techniques such as plasma spraying can be employed. Finally, the silicides are easier to densify, and do not require the densification aids which must be employed for structural ceramics.

SILICIDE REINFORCEMENT OF CERAMIC MATRIX COMPOSITES

An area that is little explored at present but which is potentially of major importance is the use of silicides to improve both the reliability and cost of structural ceramics [2]. For example, above its brittle-to-ductile transition temperature, $MoSi_2$ can be employed as an oxidation-resistant, ductile phase in a ceramic matrix composite. This presents the opportunity to significantly improve the elevated temperature mechanical properties of the composite, such as strength, high temperature fracture toughness, creep, and slow crack growth resistance. Such property improvements would constitute an important reliability benefit. Additionally, at suitable volume fraction and morphology, the $MoSi_2$ phase may also improve the machinability of ceramic matrix composites by allowing for electro-discharge machining (EDM). This would constitute a major cost benefit.

There is very little published work in this area to date. The work that has been done, however, definitely indicates a substantial improvement in elevated temperature mechanical properties by incorporating a $MoSi_2$ silicide phase into SiC and Si_3N_4 structural ceramic matrices [10,11]. Although no silicide phase work on benefits to ceramic machinability has yet been published, such benefits are also anticipated in view of published results with electrically conductive carbide, nitride, and boride phases in structural ceramic matrix materials such as Si_3N_4. However, these carbide, nitride and boride additions do not possess the high temperature oxidation resistance of silicides, and this fact has limited their usefulness.

SILICIDE HIGH TEMPERATURE JOINING MATERIALS

The high temperature joining of structural ceramic components has been a longstanding difficulty. Structural ceramics such as Si_3N_4 and SiC possess thermal expansion coefficients significantly lower than most metals, leading to mismatch stress problems. In addition, conventional brazing metal alloys do not have sufficient elevated temperature oxidation resistance. Silicides may have potential uses as higher temperature brazing materials for the structural ceramics. Only one investigation has been performed to date in this area. This study demonstrated that $MoSi_2$ and $TiSi_2$ may be employed as braze joining materials for SiC [12]. Sound joints were obtained by heating in the range of 1750-1950 ^{o}C, and no reactions with SiC were observed.

SILICIDE COATINGS

Silicide based materials may have applications as advanced high temperature coatings for refractory metals. Important factors for coatings of this type include coating oxidation resistance, thermal stability and strength, high temperature chemical compatibility of the

coating with the substrate, and thermal expansion coefficient mismatch between coating and substrate. Recent work has shown that $MoSi_2$ based materials can provide an excellent high temperature coating for niobium [13]. $(Mo,W)(Si,Ge)_2$ coatings on niobium survived 200 one hour cycles at 1370 °C in air and 60 one hour cycles at 1540 °C in air, due to formation of a protective glassy film.

The use of silicides to coat carbon and carbon-carbon composite materials has not been explored to any great extent as of the present time, although the potential for such coatings may exist. One aspect here is the fact that silicides tend to react with carbon (for example, $MoSi_2$ reacts to form CMo_5Si_3, the so-called Nowotny phase), which may necessitate the use of reaction barrier layers.

SIGNIFICANT ISSUES WITH SILICIDES

There are several significant issues which must be addressed in order to promote the use of silicides in high temperature structural applications. These issues include minimizing or eliminating the intermediate temperature oxidation pest behavior, increasing low temperature fracture toughness, improving high temperature creep resistance, and obtaining basic material properties.

Many silicides exhibit intermediate temperature accelerated oxidation, or even oxidation pest behavior (catastrophic oxidation) under certain conditions. For example, in $MoSi_2$ intermediate temperature (500 °C) accelerated oxidation and pest behavior occurs due to the retention of MoO_3 as a solid oxidation product, whose volume expansion can produce microcracking. Means to minimize or eliminate this behavior include minimization of porosity and microcracking, pre-oxidation formation of a continuous SiO_2 surface layer, alloying to alter oxide characteristics and oxidation mechanisms, and the use of metal coatings.

Improving low temperature fracture toughness is a significant issue. For many applications, room temperature fracture toughness values below 10 MPa $m^{1/2}$ will be adequate, but for some high performance applications higher toughness levels will be necessary. Composite strategies developed or in development for high toughness structural ceramics should also be applicable to the silicides. Improvements in elevated temperature creep resistance may be achieved by the minimization or elimination of glassy phases which promote grain boundary sliding in preference to dislocation creep mechanisms. Dispersion strengthening through the use of nanosized reinforcement phases dispersed intragranularly in a relatively large grained material should produce a highly creep resistant microstructure.

Lastly, there are currently substantial gaps in the description and understanding of the fundamental material properties of the silicides. Areas where little basic information exists include self-diffusion coefficients and diffusion mechanisms, single crystal properties, characterizations of ductile-to-brittle transitions and the factors which influence them, oxidation mechanisms, and sintering behavior. It will be necessary to obtain this basic information in order to be able to optimize the silicide materials for engineering applications.

ACKNOWLEDGEMENTS

Research on high temperature structural silicides at the Los Alamos National Laboratory has been made possible by funding support from the U.S. Department of Energy and the Office of Naval Research.

REFERENCES

1. High Temperature Structural Silicides, edited by A.K. Vasudevan and J.J. Petrovic (Elsevier Science Publishers, Amsterdam, 1992); Mat. Sci. Eng., **A155**, 1-274 (1992).

2. J.J. Petrovic, MRS Bulletin, **XVIII**, 35 (1993).

3. W.A. Maxwell, NACA Research Memorandum RM-E52B06, (1952).

4. E. Fitzer, O. Rubisch, J. Schlichting, and I. Sewdas, Spec. Ceram., **6**, 24 (1973).

5. J. Schlichting, High Temp.-High Press., **10**, 241 (1978).

6. E. Fitzer and W. Remmele, in Proc. 5th Int. Conf. on Composite Materials, ICCM-V, edited by W.C. Harrigan, Jr., J. Strife, and A.K. Dhingra, (AIME, Warrendale, PA, 1985), pp. 515-530.

7. F.D. Gac and J.J. Petrovic, J. Am. Ceram. Soc., **68**, C200 (1985).

8. D.H. Carter, MS Thesis, Massachusetts Institute of Technology, 1988; D.H. Carter, W.S. Gibbs, and J.J. Petrovic, Proc. 3rd Int. Symp. on Ceramic Materials and Components for Engines, (American Ceramic Society, 1989), pp. 977-986.

9. Y. Umakoshi, T. Sakagami, T. Hirano, and T. Yamane, Acta Metall. Mater., **38**, 909 (1990).

10. C.B. Lim, T. Yano, and T. Iseki, J. Mat. Sci., **24**, 4144 (1989).

11. J.J. Petrovic and R.E. Honnell, J. Mat. Sci. Lett., **9**, 1083 (1990).

12. T.J. Moore, J. Am. Ceram. Soc., **68**, C151 (1985).

13. A. Mueller, G. Wang, R.A. Rapp, E.L. Courtright, and T.A. Kircher, Mat. Sci. Eng., **A155**, 199 (1992).

PLASTIC BEHAVIOR AND DEFORMATION STRUCTURE OF SILICIDE SINGLE CRYSTALS WITH TRANSITION METALS AT HIGH TEMPERATURES

Y. UMAKOSHI, T. NAKASHIMA*, T. NAKANO and E. YANAGISAWA

Department of Materials Science and Engineering, Faculty of Engineering,
Osaka University, 2-1, Yamada-oka, Suita, Osaka 565 Japan
* Sumitomo Metal Industries, Ltd., Wakayama, Japan

ABSTRACT

The mechanical and plastic behaviors of refractory silicide single crystals with $C11_b$ ($MoSi_2$), C40 ($CrSi_2$, $TaSi_2$ and $NbSi_2$), $D8_8$ (Ti_5Si_3) and C1 ($CoSi_2$ and $(Co_{0.9}Ni_{0.1})Si_2$) structures were investigated. The C40-type silicides were deformed by (0001)<11$\bar{2}$0> slip. Their yield stress decreased sharply with increasing temperature but $NbSi_2$ and $TaSi_2$ which were deformable even at low temperatures, exhibited anomalous strengthening around 1350°C. Deformation of Ti_5Si_3 whose ductile-brittle transition occurred around 1300°C was controlled by twins and the brittle fracture occurred on the basal plane. In $CoSi_2$ the {001}<100> slip was only activated at ambient temperatures but addition of Ni activated {110}<1$\bar{1}$0> slip as secondary slip system and improved the ductility. The creep behavior of $MoSi_2$ and $CrSi_2$ single crystals were also investigated and was found to be controlled by the viscous and glide motion of dislocations.

INTRODUCTION

New, extremely high-temperature tolerant materials for service at more than 1500°C are required for aircraft gas turbines and spacecraft airframes. From the viewpoint of specific gravity, elastic modulus, high-temperature strength and oxidation resistance, several transition metal silicides with high silicon content are among the potential candidates for such ultra-high temperature structural materials from a compilation of about 300 binary metallic and metal-metalloid compounds that melt above 1500°C [1]. At high temperatures the silicides exhibit excellent oxidation resistance since silicon atoms form viscous and protective SiO_2 films which can infiltrate and cover micro cracks generated during the operating process.

In general, silicides have an intricate crystal structure and can rarely be deformed. From crystal symmetry considerations, melting point and high-temperature strength, we should look for several silicides with the $C11_b$ structure based on the b.c.t. lattice, and C40 and $D8_8$ structures based on the h.c.p. lattice.

Some MSi_2-type silicides with the elements Mo, W and Re are known to crystallize into the $C11_b$ structure. Since the $C11_b$ structure is a long-period ordered structure derived by stacking up three b.c.c. lattices and then compressing them along the long period axis, their silicides possess the deformation characteristics of b.c.c. crystals. The {110}<$\bar{3}$31] and {103}<$\bar{3}$31] slips which correspond to the {110}<1$\bar{1}$1> slips in the b.c.c. lattices were observed in $MoSi_2$ at around 1000°C, and with increasing temperature <100]-and <110]-slips were activated [2, 3]. From the viewpoint of activated slip systems, polycrystalline $MoSi_2$ is expected to have ductility since the number of slip systems is enough to satisfy the von Mises criterion. However, even single crystals were brittle extremely at low temperatures and the transition from ductile to brittle behavior occurred around 900°C.

One of the approaches to improve the ductility and fracture toughness is to develop quasi-binary disilicides with two-phase microstructures composed of the $C11_b$ and C40 phases [4]. Detailed informations are needed on the mechanical properties and plastic characteristics of both C40-type and $C11_b$-type silicides to understand the plastic behavior

Mat. Res. Soc. Symp. Proc. Vol. 322. ©1994 Materials Research Society

of the component phases in quasi-binary silicide composites. However, to our knowledge only limited studies on the slip system and the temperature dependence of the critical resolved shear stress (CRSS) of $CrSi_2$ with the C40 structure have been reported using single crystals [5].

For application to high-temperature structural components, not only high temperature strength but also creep resistance which is even more important is required. The creep behavior of polycrystalline $MoSi_2$ and $MoSi_2$-based composites reinforced with SiC whiskers has been investigated [6] but studies have not been made on the creep mechanism or dislocation structure using single crystals.

In this paper, current knowledge of the slip behavior and deformation mechanism of the $C11_b$-type and C40-type disilicides including creep deformation is reviewed based on the results of our recent studies on $MoSi_2$ with the $C11_b$ structure and $CrSi_2$, $TaSi_2$ and $NbSi_2$ with the C40 structure.

$CoSi_2$ with the C1 structure exhibits excellent oxidation resistance and some ductility even at low temperature because of its f.c.c.-based structure. It is of considerable interest as one of the duplex phases to improve the fracture toughness of silicide composites, although the melting point of $CoSi_2$ is not high (T_m=1326°C). $CoSi_2$ is primarily deformed by {001}<100> slip systems and when the orientation of samples is controlled for the {001}<100>-slip, some fracture strains are obtained in single crystals even at room temperature [7]. Polycrystalline $CoSi_2$, however shows high ductile-brittle transition temperature and therefore, activation of additional slip systems is required to improve ductility. The effect of the addition of Ni to $CoSi_2$ on operative slip systems and plastic behaviors is also described.

Ti_5Si_3 with the $D8_8$ structure is also a potential candidate as a refractory material. The mechanical properties of polycrystalline Ti_5Si_3 and unidirectionally solidified eutectic α Ti-Ti_5Si_3 alloys [8], and the oxidation resistance of ternary $(Ti, X)_5Si_3$ (X=V, Nb) have been investigated but no detailed study on plastic behavior has been reported. Deformation and fracture mechanisms of Ti_5Si_3 single crystals are also presented together with the deformation structure.

EXPERIMENTAL PROCEDURE

The master ingots of binary MSi_2 (M=Mo, Cr, Ta, Nb or Co) and Ti_5Si_3, and ternary $(Co_{0.9}Ni_{0.1})Si_2$ silicides were prepared by melting high-purity raw materials in a plasma arc furnace. Single crystals of the binary and ternary silicides were grown from these ingots by the floating zone method using an NEC SC-35HD single crystal growth apparatus at growth rates of 5 and 10mm/h under a high-purity argon gas flow. Specimens for compression and creep tests (approximately 2.5×2.5mm in cross-section and 7mm long) with selected orientations were cut from the single crystals by spark machining and mechanically polished using diamond paste to observe surface slip markings. Compression tests were conducted on an Instron-type testing machine in a purified argon gas atmosphere or in a vacuum at a nominal strain rate of $1.4\times10^{-4}s^{-1}$ at temperature ranging from 20 to 1500°C. Slip patterns were then examined with an optical microscope using Nomarski interference contrast. Creep tests of $MoSi_2$ and $CrSi_2$ single crystals were conducted under compression in an argon gas atmosphere. The displacement of specimens was measured with a linear variable-differential transducer.

Thin-foil specimens for electron microscopy were cut first from deformed specimens by spark machining and finally ion-milled by Ar bombardment to perforation. The thin foils were examined in a Hitachi H-800 electron microscope operated at 200KV.

RESULTS AND DISCUSSION

($C11_b$- type silicides)

$MoSi_2$ is extremely brittle even in single crystals at low temperatures but it becomes deformable above 900°C. Activation of 1/2<$\bar{3}$31] dislocations which are thought to dissociate into three 1/6<$\bar{3}$31] superpartials bound by APBs was observed around 900°C. The slip occurred on both closely packed {110) and {103) planes at all tested temperatures between 900 and 1500°C [2, 3]. The ductility was remarkably improved and the fracture strain sharply increased accompanied by rapid decrease of the yield stress with increasing temperature above 1200°C where <100]-and <110]-type dislocations were activated as shown in Fig.1. Although the yield stress depends strongly on the strain rate, the low strain rate

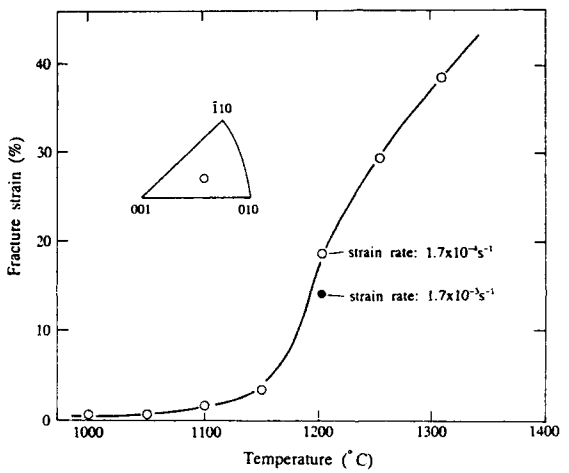


Fig.1 Temperature dependence of fracture strain for $MoSi_2$ single crystals.

sensitivity of fracture strain around 1200°C suggests that adequate fracture toughness is provided at high operating temperatures. Dislocation networks composed of <100] and <110] dislocations were observed in $MoSi_2$ deformed at 1300°C. The climb mobility of the <100] and <110] dislocations is already high and a dynamic recovery process takes place during deformation.

To improve the ductility of $MoSi_2$ at low temperature, an approach to activate 1/2<111> dislocations was done based on the phase stability of the $C11_b$ with respect to the C40 sructure. A 1/2[111] dislocation can be dissociated into two 1/4[111] partial dislocations bound by a stacking fault [3, 9]. If the stacking fault with a fault vector of 1/4[111] is introduced on a ($\bar{1}$10) plane in the $C11_b$ structure, the atomic arrangements and the stacking sequence on the ($\bar{1}$10) become equivalent to those on the (0001) plane in the C40 structure. Addition of alloying elements which destabilize the $C11_b$ structure of $MoSi_2$ with respect to the C40 structure decreases the stacking fault energy resulting in the ductility improvement. A sign of ductility improvement was noticed in the stress-strain curves for $(Mo_{0.97}Cr_{0.03})Si_2$ single crystals [3].

Figure 2 shows the early stages of the creep curves of $MoSi_2$ single crystals at the applied stresses of 15.2, 30.3, 49.6 and 100 MPa at 1400°C. The curves show a primary

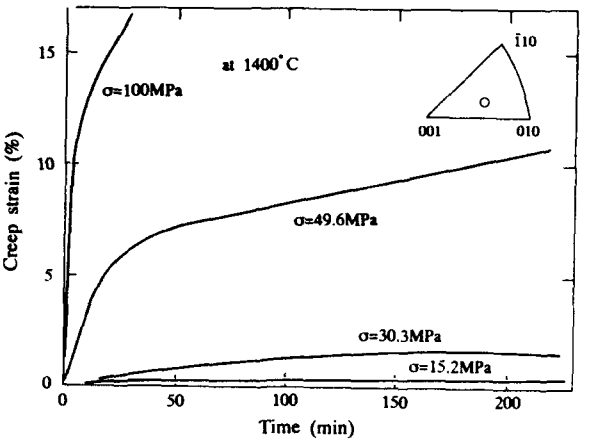


Fig.2 Creep curves of $MoSi_2$ single crystals deformed at 1400°C.

transient followed by a long period of steady-state creep with minimum creep rate by which the creep behavior can be evaluated. The empirical power law creep relation represents the strain rate at the steady-state creep as a function of the applied stress.

$$\dot{\varepsilon}=A\sigma^{n}\exp(-\Delta H/kT)$$

where $\dot{\varepsilon}$ is the steady-state creep rate, A is a constant, σ is the applied stress, ΔH is the activation energy and n is the stress exponent and depends on the rate controlling process. The stress exponent n was determined to be 3 from the slope of a straight line by plotting the logarithm of the strain rate as a function of the logarithm of the applied stress at 1200°C as shown in Fig.3. The n value of 3 suggests that the creep of $MoSi_2$ is controlled by the viscous motion of dislocations. At high temperatures the climb mobility of <100] and <110] dislocations is already high and the formation of dislocation networks proceeds as shown in Fig.4. The slower the dislocation creep, the larger the contribution of diffusion creep becomes. Evidence of the transition from the dislocation creep (n=3) to the diffusion creep (n=1) was found in $MoSi_2$ single crystals crept at 1400°C under low applied stress of 15.2 MPa . From the logarithm plots of the steady state creep rate as a

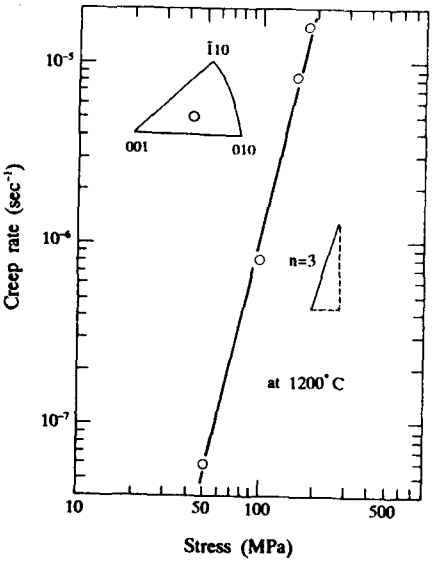


Fig.3 Variation of the creep rate of $MoSi_2$ single crystals deformed at 1200°C with the applied stress.

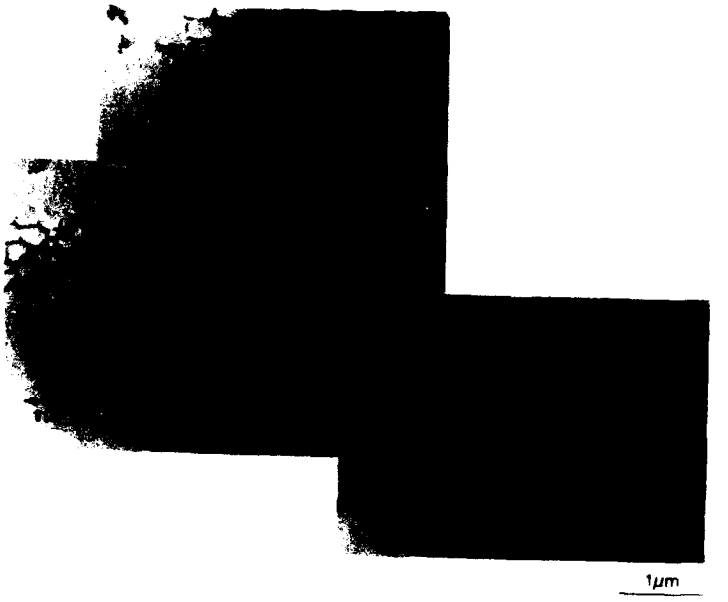


Fig.4 Dislocation structures in $MoSi_2$ single crystals deformed at 1200°C with the applied stress.

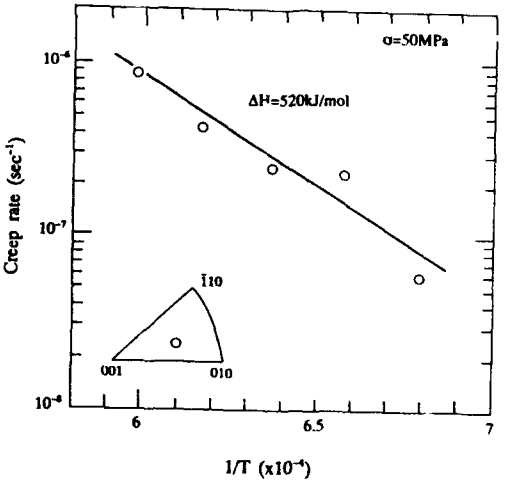


Fig.5 Creep rate of $MoSi_2$ single crystals as a function of reciprocal values of temperature under 50MPa.

function of the reciprocal temperature as shown in Fig.5, the apparent activation energy was determined to be 520KJ/mol. This value is rather higher than previous result of ΔH=433KJ/mol for polycrystalline $MoSi_2$ [10]. Orientation dependence of operative dislocations and the effect of grain boundaries might be responsible for the difference.

(C40-type silicides)

Although possible slip planes are expected to be (0001) and {11$\bar{2}$0} planes from the crystal structure of C40-type, the (0001)<11$\bar{2}$0>-slips are only operative in $CrSi_2$. The $CrSi_2$ single crystals are deformable above 700°C and the yield stress decreases monotonically with increasing temperature. The stress-strain curves exhibited considerable work hardening after yielding below 900°C, but at higher temperatures they exhibit a yield drop followed by a very gradual work hardening or sometimes work softening, and an improvement in ductility. Hexagonal networks composed of three types of 1/3<11$\bar{2}$0> dislocations are formed as shown in Fig.6. On the (0001) plane, 1/3[2$\bar{1}\bar{1}$0] dislocation was confirmed to be dissociated into two 1/6[2$\bar{1}\bar{1}$0] partial dislocations combined with a superlattice intrinsic stacking fault(SISF) as shown in Fig.7. The cross-slip or climb dissociation of some segments of the paired partials, which may provided an additional stress to the motion of the entire dislocations and exhibit the plastic anisotropy, is expected to occur during moving on the (0001). However, the CRSS for (0001)<11$\bar{2}$0> slip did not depend on crystal orientation and it decreased continuously with increasing temperature.

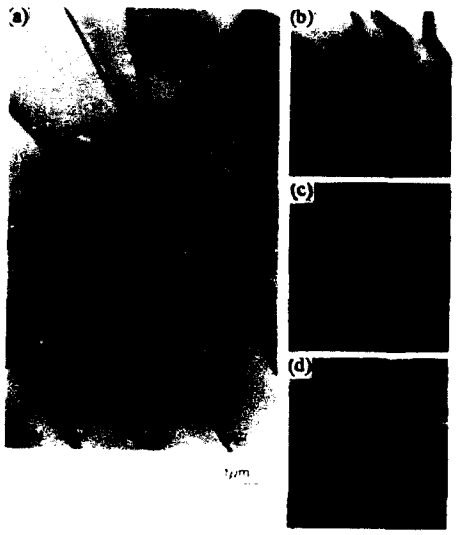


Fig.6 Dislocation networks of $CrSi_2$ single crystals deformed at 1300°C; (a)g=11$\bar{2}$0 ,(b)g=02$\bar{2}$0, (c)g=$\bar{2}$200, (d)g=20$\bar{2}$0.

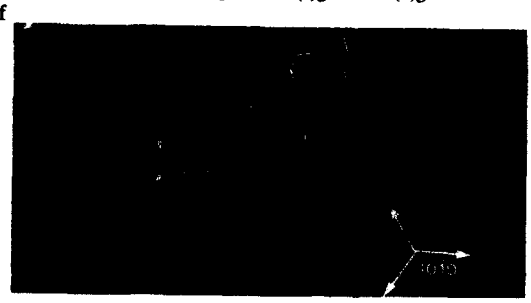


Fig.7 Weak beam image of dissociated 1/3[11$\bar{2}$0] dislocation in $CrSi_2$ deformed at 1000°C.

The creep test of $CrSi_2$ single crystals was carried out at a temperature between 900 and 1050°C under applied stress of between 2 and 40 MPa. The creep curves showed a long period of steady-state creep after primary regime in single crystals, while a primary region followed by inverse creep with no development into a

steady-state creep was observed in polycrystalline $CrSi_2$ tested above 1000°C. The stress exponent n and the apparent activation energy for creep of $CrSi_2$ single crystals were determined to be 2.9 and 360kJ/mol from measurements of the temperature and applied stress dependence of the steady-state creep rate. Numerous isolated 1/3<11$\bar{2}$0>-type dislocations were observed on the basal plane in $CrSi_2$ single crystals crept at 1000°C. These results strongly suggest that the creep of $CrSi_2$ is controlled by the viscous and glide motion of 1/3<11$\bar{2}$0>-type dislocations.

$NbSi_2$ (2200°C) and $TaSi_2$ (1930°C) have higher melting temperature than $CrSi_2$ (1550°C). The high melting temperature which is closely related to the strong bonds is thought to be disastrous for ductility of intermetallics. However, a distinct plastic flow was observed in the stress-strain curve of $NbSi_2$ single crystal even at room temperature and a sharp increase in ductility occurred with increasing temperature as shown in Fig.8. Serrations in the stress-strain curves appeared at high temperatures and became remarkable between 1200 and 140 0°C. The transition from ductile to brittle behavior of $TaSi_2$ single crystals shifted to 300°C but the stress-strain curves were similar to those of $NbSi_2$.

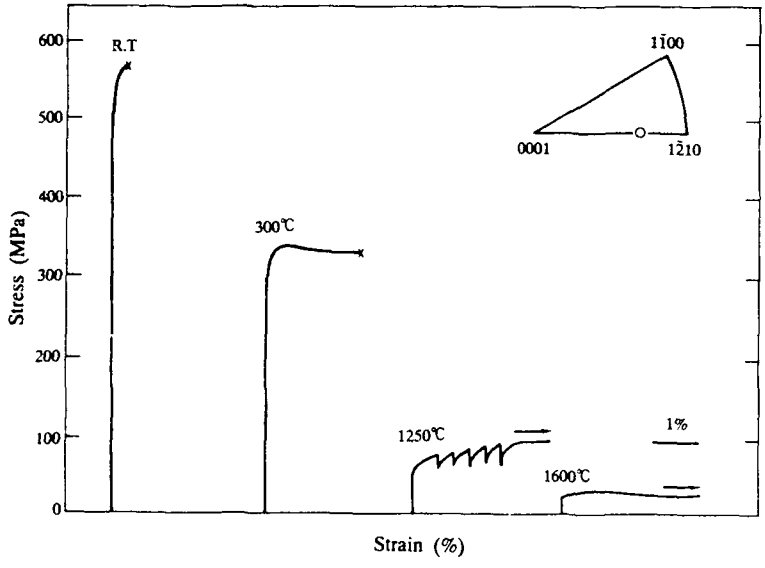


Fig.8 Stress-strain curves of $NbSi_2$ single crystals.

Temperature dependence of the yield stress of $NbSi_2$ and $TaSi_2$ single crystals, together with that of $CrSi_2$ is given in Fig.9. The yield stress of $NbSi_2$ and $TaSi_2$ decreased rapidly with increasing temperature and then increased reaching an anomalous peak around 1350°C. The yield stress of $NbSi_2$ and $TaSi_2$ at low temperature is not high enough as expected from their melting points, but the anomalous strengthening above 1000°C is attractive for high-temperature structural application. The basal slip was confirmed in the temperature range below the anomalous peak but the anomalous strengthening mechanism is not yet clear. Investigations on orientation dependence of the CRSS and the anomalous peak temperature of $NbSi_2$ and $TaSi_2$ single crystals are now in progress.

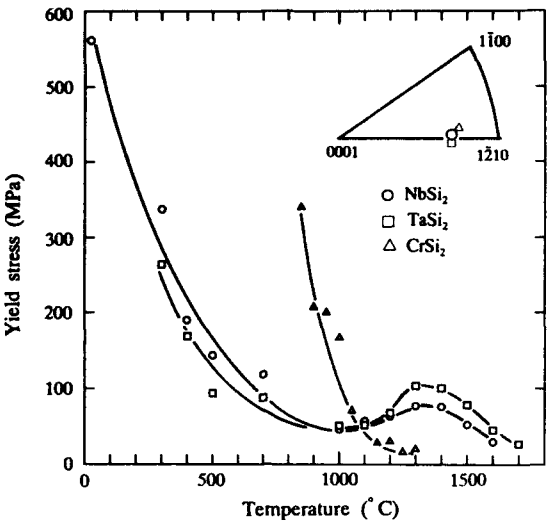


Fig.9 Temperature dependence of yield stress of $CrSi_2$, $TaSi_2$ and $NbSi_2$ single crystals.

($D8_8$-type silicide)

Ti_5Si_3 crystallizes in the hexagonal $D8_8$ structure whose stacking sequence on the basal planes is ABACA$\cdots$. The atomic arrangements of B and C layers are related by 180° rotation about the c axis relative to each other. Ti_5Si_3 single crystals are extremely brittle at low temperature but they become deformable above 1300°C. The yield stress depends strongly on the crystal orientations and decreases rapidly with increasing temperature as shown in Fig.10. The closed triangle indicates fracture stress of the tested specimen instead of yield stress since the specimens broke within a straight region of the stress-strain relationship.

Deformation twins were very often observed in deformed samples. Figure 11 shows a twin in T_5Si_3 single crystal deformed at 1500°C, whose twin plane lies almost

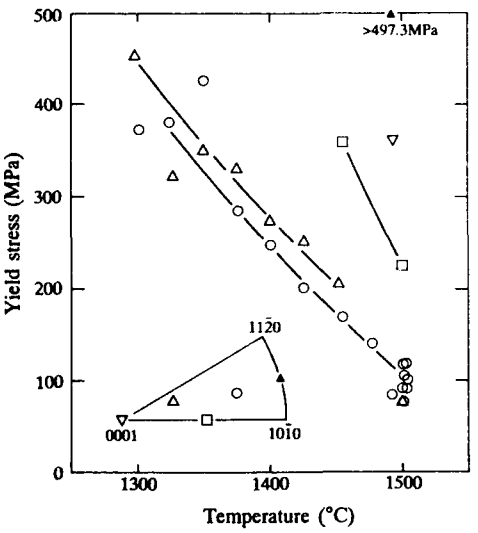


Fig.10 Temperature dependence of yield stress of Ti_5Si_3 single crystals.

parallel to an incident electron beam. From the diffraction spots which were taken from the matrix and the combined area of the matrix and the twin, the twin plane was determined to be $(10\bar{1}2)$. In consideration of an activated twinning system in a hexagonal lattice, a twinning system of $\{10\bar{1}2\}<\bar{1}011>$ may be possible in Ti_5Si_3 crystals.

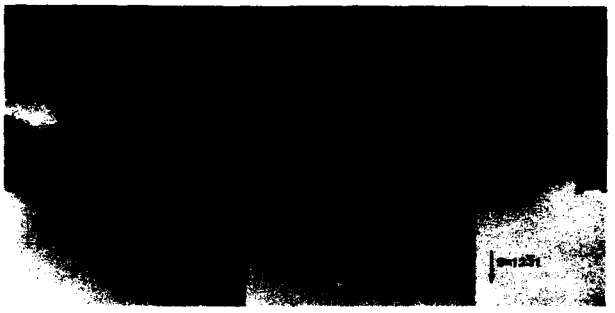


Fig.11 A twin in Ti_5Si_3 single crystal deformed at 1500°C.

Figure 12 shows the CRSS for the $\{10\bar{1}2\}<\bar{1}011>$ system calculated from the data in Fig.10. The data on samples with orientations on the $[11\bar{2}0]$-$[10\bar{1}0]$ boundary and

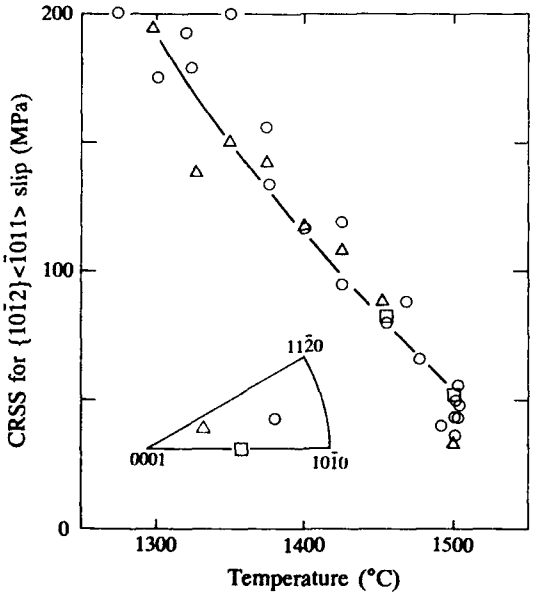


Fig.12 Temperature dependence of CRSS for $\{10\bar{1}2\}<\bar{1}011>$ of Ti_5Si_3 single crystals.

near the [0001] are excluded from the figure since these samples did not exhibit a marked plastic flow. The good agreement of the CRSS with the Schmid law suggests that the deformation of Ti_5Si_3 single crystals may be controlled by the $\{10\bar{1}2\}<10\bar{1}\bar{1}>$ twins.

From the atomic arrangements on the basal plane, a possible slip system is $(0001)<11\bar{2}0>$ but the basal slip has not been observed. The brittle fracture occurred very often on the basal plane in samples with orientations where only a small shear stress component for the $\{10\bar{1}2\}<10\bar{1}\bar{1}>$ twin deformation was provided. Our recent measurements of the thermal expansion coefficient of Ti_5Si_3 single crystals showed the thermal expansion coefficient along the [0001] direction to be about 4 times more higher than that along the $[\bar{2}110]$ direction [11]. Since the thermal expansion is due to the thermal vibration on the basis of the repulsive and attractive forces between atoms, the higher thermal expansion coefficient along the [0001] direction suggests a weak bonding force along this direction, causing the brittle fracture to occur on the (0001) plane.

(C1-type silicides)

In crystals with the cubic C1 structure various slip systems of $\{001\}<110>$, $\{110\}<1\bar{1}0>$, $\{111\}<1\bar{1}0>$ and $\{001\}<100>$ are expected to occur. The difference in operative slip systems of C1-type compounds depends on the difference in the electrostatic nature of the core structure. For example, the $\{001\}<1\bar{1}0>$-slip is primarily activated in the ionic compounds such as CaF_2, BaF_2 and SrF_2, while the metallically bonded compounds such as TiH_2 and ZrH_2 are deformed by $\{111\}<1\bar{1}0>$ slip. $CoSi_2$ which has a combined character of strong covalent and metallic bonding exhibits 2–4% fracture strains in single crystals even at room temperature. However, it cannot be deformed in polycrystalline form since only the $\{001\}<100>$ slip is activated and the von Mises criterion cannot be satisfied, while activation of $\{111\}<1\bar{1}0>$ and $\{110\}<1\bar{1}0>$ slips with increasing temperature provides a rapid increase in ductility[7]. Addition of small amount of Ni which is expected to increase the character of metallic bonding activated $\{110\}$-slip as secondary slip in the sample deformed along $[\bar{1}23]$ as shown in Fig.13 and the ductility was improved.

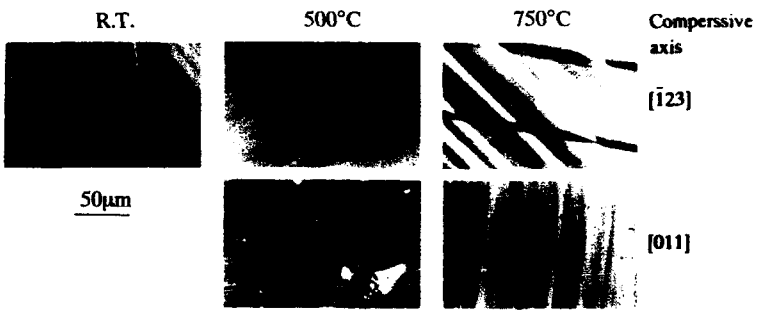


Fig.13 Slip traces of $(Co_{0.9}Ni_{0.1})Si_2$ single crystals.

$CoSi_2$ and $(Co_{0.9}Ni_{0.1})Si_2$ single crystals show similar temperature dependence of the CRSS for$\{100\}<001>$-slip as shown in Fig.14. The steep temperature dependence of the CRSS below 200°C suggests that deformation of $CoSi_2$ and $(Co_{0.9}Ni_{0.1})Si_2$ is controlled by the Peierls mechanism as predicted by Takeuchi [12], while at 500°C high activation volume of $323b^3$ was obtained for $(Co_{0.9}Ni_{0.1})Si_2$ single crystals. The lower CRSS of $(Co_{0.9}Ni_{0.1})Si_2$

in comparison with $CoSi_2$ at low temperatures suggests that addition of Ni reduces the covalent bonding force resulting in improve ductility.

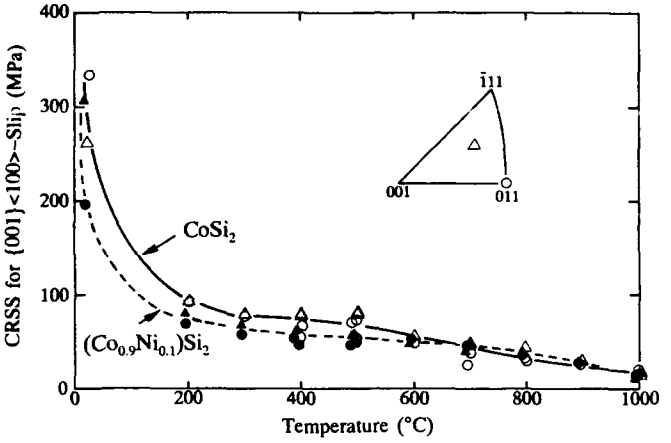


Fig.14 Temperature dependence of CRSS for {100}<100>-slip in $CoSi_2$ and $(Co_{0.9}Ni_{0.1})Si_2$ single crystals.

CONCLUDING REMARKS

$MoSi_2$ is believed to be an attractive candidate of refractory materials operating above 1500°C. Although a hopeful indication was noted in the ductility improvement for $MoSi_2$ with a small addition of Cr, it is very difficult to pursue good ductility in single phase through alloying design and thermo-mechanical processing. A target in developing of refractory silicides should be to focus on the improvement of toughness using multi-phase microstructures. The transition metal silicides described in this paper may be suitable for oxidation resistance at high temperature because of their high silicon content. For silicide composites high strength is guaranteed by $MoSi_2$-phase as a matrix, while the ductility and toughness should be improved by dispersed phases with sufficient ductility at low temperature. A good sign in low-temperature ductility of $TaSi_2$ and $NbSi_2$, together with anomalous strengthening around 1350°C is attractive for usage as a dispersed phase. $CoSi_2$ is also of interest as a dispersed phase in silicide composites since a small added amount of Ni activates {110}<$\bar{1}$10> slips in addition to {001}<100> slips and sufficient slip systems for continuous plasticity of polycrystals are provided, although the melting point limits its operating temperature below about 1300°C. Good ductility at low temperature as well as conventional alloys cannot be expected for refractory silicides, but in sharp contrast to ceramics the silicides can be deformed by the motion of dislocations and become ductile at high operating temperature. Composites composed of quasi-binary and ternary silicide phases with the $C11_b$, C40 and C1 structure may be able to improve fracture toughness at low temperature and overcome difficult barriers in the development of structural materials for use at extremely high temperature.

ACKNOWLEDGEMENTS

Y. Umakoshi would like to thank for a research grant to Fundamental Research Developing Association for Shipbuilding and Offshore. This work was partly supported by a Grant-in Aid for Scientific Research and Development from the Ministry of Education, Science and Culture of Japan.

REFERENCES

1. R. L. Fleischer, J. Metals, **37**, 16(1985).
2. Y. Umakoshi, T. Sakagami, T. Yamane and T. Hirano, Acta Metall. Mater. **38**, 909(1990).
3. Y. Umakoshi, T. Hirano, T Sakagami and T. Yamane, in High Temperature Aluminides and Intermetallics, edited by S. H. Whang, C. T. Liu, D. P. Pope and J. O. Stiegler (TMS, Warrendale, PA, 1990)p.111.
4. A. K. Vasudévan and J. J. Petrovic, Mater. Sci. Engn., **A155**, 1(1992).
5. Y. Umakoshi, T. Nakashima, T. Yamane and H. Senba, in Intermetallic Compounds -Structure and Mechanical Properties-, edited by O Izumi, (Jap. Inst. Metals, Sendai, 1991)p.639.
6. M. J. Maloney and R. J. Hecht, Mater. Sci. Engn., **A155**, 19(1992).
7. I. Ito, H. Inui, T. Hirano and M. Yamaguchi, Mater. Sci. Engn., **A152**, 153(1992).
8. G. Frommeyer, R. Rosenkraz and C. Ldecke, Z. Metallk., **81**, 307(1990).
9. S. A. Maloy, A. H. Heur, J. J. Lewandowski and T. E. Mitchell, Acta metall. mater., **40**, 3159(1992).
10. K. Sadananda, C. R. Feng, H. Jones and J. Petrovic, Mat. Sci. Engn. **A155**, 227(1992).
11. T. Nakashima and Y. Umakoshi, Phil. Mag. Lett., **66**, 317(1992).
12. S. Takeuchi, T. Hashimoto and T. Shibuya, J. Mater. Sci., **27**, 1380(1992).

THE TEMPERATURE AND STRAIN RATE DEPENDENCE OF THE FLOW STRESS IN $MoSi_2$ SINGLE CRYSTALS

S.A. Maloy*, T.E. Mitchell*, John J. Petrovic**, A.H. Heuer***, J.J. Lewandowski***,
*Center for Materials Science, MS-K765, Los Alamos National Laboratory, Los Alamos, NM 87545
**MST-4, MS-G771, Los Alamos National Laboratory, Los Alamos, NM 87545
***Department of Materials Science and Engineering, Case Western Reserve University, Cleveland, OH 44106

Abstract

The temperature dependence of the flow stress and deformation mechanisms of single crystal $MoSi_2$ have been determined for compression along three different orientations, [001], [021] and [771], at two different strain rates, $1x10^{-5}$/s and $1x10^{-4}$/s, and at temperatures between 900 and 1600°C. The flow stress along [021] is slightly higher than that along [771] while both orientations gave a much lower flow stress than that along [001]. Along [021], slip occurs on the {110}1/2<111> slip system between 1000 and 1200°C, while at 1300-1400°C, slip occurs on the {013}<100> slip system. Along [771], deformation occurs by the {011}<100> slip system while cross-slip onto {013} and {01$\bar{1}$} planes is observed at 1000-1300°C except that slip occurs on the {013}1/2<331> slip system at 1000-1100°C for faster strain rates. Along [001], slip occurs on the {013}1/2<331> system at 900-1100°C while slip is observed on the {011}1/2<111> system at 1300-1600°C. Strain rate jump tests from $1x10^{-5}$/s to $5x10^{-5}$/s at 1100°C revealed a stress exponent of 7 along [771] and 20 along [021], while a rate jump test from $1x10^{-5}$/s to $2x\ 10^{-5}$/s along [001] at 1400°C gave a stress exponent of 3.9.

Introduction

$MoSi_2$ is a candidate material for high temperature structural applications as it has excellent oxidation resistance [1], a reasonable toughness above 1000°C [2], and high creep and yield strength when reinforced with SiC [3].

$MoSi_2$ has a body centered tetragonal structure, space group I4/mmm and lattice parameters: a=0.3204 nm, c=0.7848 nm [4]. According to conventional dislocation theory, the most likely perfect dislocations have Burgers vectors with the shortest lattice translations, and glide on the densest packed planes. Thus, we expect <100> dislocations with b=0.3204 nm should be most common, followed by 1/2<111> and <110> dislocations, both with b=0.4531 nm. These latter vectors have the same length because of the hexagonal symmetry of the {110} plane. The next two possible Burgers vectors are much longer, 1/2<331> and [001], both with b=0.7848 nm (again the same length because of the hexagonal symmetry of the (110) plane). The densest packed planes, in terms of both Mo and Si atoms, are {110} and {013} [5]. Thus, elementary dislocation theory would predict the {013}<100>, {1$\bar{1}$0}<110> or {110}1/2<111>, slip systems should have the lowest Peierls stresses. The possible slip systems in $MoSi_2$ are shown in Table I and are labelled A-H in order of decreasing d/b (where d is the planar spacing and b is the Burgers vector), since the Peierls stress is predicted to decrease with increasing d/b [6].

The purpose of the present work was to study the deformation behavior of single crystal $MoSi_2$ at high temperatures. Single crystals of $MoSi_2$ oriented along [001], [021], or [771] were deformed in compression between 900 and 1600°C. For compression along [001], the Schmid factors are zero for all slip systems except for {013}1/2<331> (H) and {011}1/2<111> (I), thereby eliminating slip on the expected easy slip systems. For compression along [021], the Schmid factors are high for the expected easy slip systems {013}<100> (A), {110}1/2<111> (D) and {001}<100> (E), while along [771], the Schmid factors are high for slip on {013}<100> (A), {010}<100> (B) and {011}<100> (F) (Table 1). Along [001], [021], and [771], the strain rate sensitivity was determined by performing rate jump tests at 1400, 1100, and 1100°C, respectively. This paper will provide a summary of an in depth study on the mechanical properties of single crystal $MoSi_2$. For a more detailed description of results see Maloy (1993) [7] and Maloy et al. (1993) [8].

Mat. Res. Soc. Symp. Proc. Vol. 322. ©1994 Materials Research Society

Table I Schmid Factors and d/b Values for Possible Slip Systems when Compressed along [021], [001], and [771].

	Slip System	d (nm)	b (nm)	d/b	Schmid Factors [001]	[021]	[771]
A	{013}<100>	0.202	0.3204	0.630	0	0.38	0.42
B	{010}<100>	0.160	0.3204	0.499	0	0	0.46
C	{110}<110>	0.226	0.4531	0.499	0	0.20	0
D	{110}1/2<111>	0.226	0.4531	0.499	0	0.40	0.20
E	{001}<100>	0.131	0.3204	0.409	0	0.48	0.17
F	{011}<100>	0.0989	0.3204	0.309	0	0.17	0.5
G	{110}1/2<331>	0.226	0.7848	0.288	0	0.36	0.12
H	{013}1/2<331>	0.202	0.7848	0.257	0.39	0.46	0.45
I	{011}1/2<111>	0.0989	0.4531	0.218	0.33	0.40	0.38

Experimental Procedure

Single crystals of $MoSi_2$ were grown with orientations along [001], [021], and [771] using $MoSi_2$ seeds by the Czochralski technique at McMaster University by J. Garrett. Rectangular parallelepipeds were cut, ground to approximately 1.5x1.5x5mm^3, and polished through 1μm diamond paste. Samples were deformed at strain rates of either $1x10^{-4}$/s or $1x10^{-5}$/s at temperatures between 900 and 1600°C on Instron testing machines equipped with high temperature furnaces for testing in either vacuum or argon. SiC or single crystal YAG pads were used; BN powder on the ends of each specimen served as a high temperature lubricant. Slip traces were observed on the specimen surface after testing using an optical microscope with Nomarski contrast imaging techniques. Thin sections from each specimen were cut parallel to the slip plane after deformation. If no slip traces were observed, a foil was cut perpendicular to the compression direction. Standard procedures were used to ion mill samples to electron transparency. The foils were examined in a Philips CM30 transmission electron microscope (TEM) operating at 300 kV. Standard **g.b** and trace analyses were performed to determine the Burgers vectors of the dislocations and their slip planes.

A small amount of Mo_5Si_3 (~2 vol.%) was present in as-grown single crystals due to Si-loss during growth. The second phase content was determined by grinding a small piece of each single crystal into -300 mesh powder and quantifying using X-ray diffraction techniques. The C, N, O and H contents of each single crystal were determined by Leco* analysis with the highest impurity being C (< 91 wt. ppm) followed by O (< 39 ppm) and H (< 5 ppm).

Results

Mechanical Properties

The yield stress of single crystal $MoSi_2$ was determined by compression along [021], [771], and [001], and the results are shown in Figure 1. The yield stresses in the [001] orientation are much higher than those in the [021] and [771] orientations. For compression in the [001] orientation at 900-1100°C, the band shown in figure 1 starting at ~600 MPa and ending at ~1400 MPa represents yielding, which occurred by a series of load drops followed by elastic reloading until the test was stopped at the load limit of the testing machine. At 1200°C, the sample was loaded to the load limit of the testing machine without yielding (as noted by an arrow pointing upward). At temperatures above 1200°C the yield stress sharply decreases with decreasing strain rate and increasing temperature. For deformation along [771] and [021], the yield stress is not very sensitive to strain rate and decreases with increasing temperature. At 1000°C along [771] and [021], cracking occurred before a yield point was observed.

* Leco Corporation, 3000 Lakeview Ave., St. Joseph, MI 49085-2396

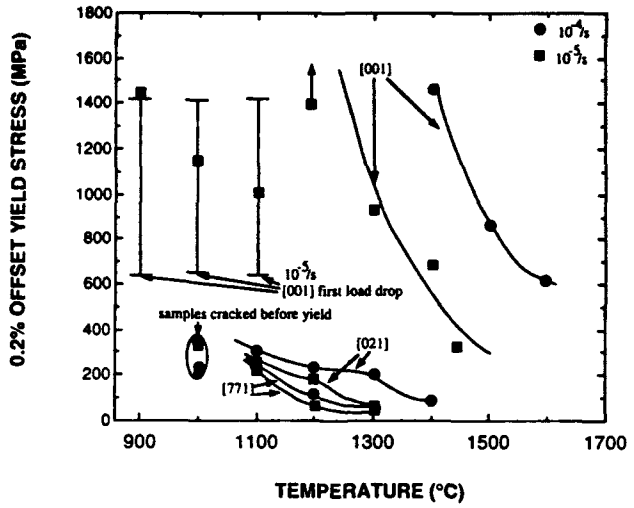


Fig. 1 Plot of 0.2% offset yield stress vs. temperature for deformation at two strain rates and along [001], [021] and [771].

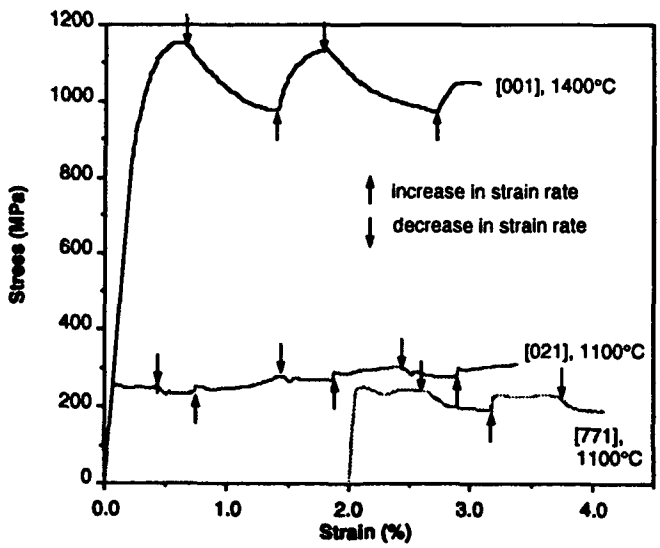


Fig. 2 Stress/strain curves for rate jump tests performed in compression along [001] at 1400°C and [771] and [021] at 1100°C. Along [001], the rate was change from $2x10^{-5}$ to $1x10^{-5}$/s while along [771] and [021] the strain rate was changed from $5x10^{-5}$/s to $1x10^{-5}$/s (arrowed).

Rate jump tests were performed at 1100°C along [021] and [771] and at 1400°C along [001] as shown in Figure 2. For the test performed along [021], a stress exponent of 20 was observed, while for the test performed along [771], a slightly larger stress exponent of 7 was observed. Finally, for the test performed along [001] a stress exponent of 3.9 was found. The stress exponents are in close agreement with those obtained from separate tests performed at strain rates of $1x10^{-5}$/s and $1/10^{-4}$/s.

Slip Trace Analysis

The slip trace analyses made after deformation along [001], [021], and [771] are summarized in Table II. The characteristics of the slip traces varied depending on the temperature and compression axis. For example, for deformation along [001] at 900°C, very fine {013} slip traces were observed while the slip traces observed at 1000 and 1100°C were also fine but inclined by ten degrees to the angle expected for {013} slip. At higher temperatures, no slip traces were observed. For deformation along [021], distinct {110} slip traces were observed after deformation at 1000-1200°C, while at higher temperatures, slightly curved {013} slip traces were observed. Finally, for deformation along [771], {013} slip traces were observed after deformation at 1000-1100°C at a strain rate of $1x10^{-4}$/s and at 1000°C at a strain rate of $1x10^{-5}$/s. For deformation along [771] at higher temperatures and both strain rates, primary slip occurred on {011} planes, while cross-slip was observed on {013}, and $\{01\bar{1}\}$ planes.

TEM Analysis

The dislocations' Burgers vectors and their glide planes determined from detailed TEM analyses are also summarized in Table II. For deformation along [001] at 900-1100°C, 1/2<331> dislocations were observed lying in the {013} plane. The 1/2<331> dislocations were often observed to be decomposed into 1/2<111> and <110> dislocations (a further explanation of the decomposition is given by Maloy et al. (1993) [9]). The extent of the decomposition reaction increases with temperature, thereby effectively immobilizing the 1/2<331> dislocation at

Table II Summary of Slip Trace and TEM Analyses

Orientation	Temperature (°C)	Strain Rate (/s)	Slip Traces	Dislocations' Burgers vector	Plane	Slip System
[001]	1400-1600	10^{-4}	none	<100>, <110> 1/2<111>	(001) {110}	I
	900-1100	10^{-5}	{013}	1/2<331>, 1/2<111>, <110>	{013}	H
	1200-1400	10^{-5}	none	<100>, <110> 1/2<111>	(001) {110}	I
[021]	1000-1200	10^{-4} and 10^{-5}	{110}	1/2<111>	{110}	D
	1300-1400	10^{-4} and 10^{-5}	{013}	<100>	(001)	A
[771]	1000-1100	10^{-4}	{013}	1/2<331>, 1/2<111>, <110>	{013}	H
	1200-1300	10^{-4}	{011} cross-slip	<100>	{011}	F
	1000	10^{-5}	{013} cross-slip	<100>	{011}	A
	1100-1300	10^{-5}	{011} cross-slip	<100>	{011}	F

temperatures above 1100°C. After deformation at higher temperatures, <100> and <110> dislocations were observed in the form of low angle grain boundaries, while in some areas, 1/2<111> dislocations were also observed, often lying on the {110} plane. The <100> and <110> dislocations result from reaction of 1/2<111> dislocations.

For deformation along [021], 1/2<111> dislocations on {110} planes were observed at 1000-1200°C while <100> dislocations lying on the (001) plane were found at 1300-1400°C. Finally, for deformation along [771], at 1000-1100°C and a strain rate of 10^{-4}/s, 1/2<331> dislocations were observed lying on the {013} plane. As observed for deformation along [001], the 1/2<331> dislocations were decomposed into 1/2<111> and <110> dislocations. For deformation at other temperatures, <100> dislocations were found on the {011} plane and the formation of low angle boundaries occurred during deformation at 1300°C.

Discussion

From the slip trace and TEM investigations, the active slip systems were determined and are listed in Table II. The slip systems are labelled as per Table I. For deformation along [001] at 1300-1600°C, <100>, <110> and 1/2<111> dislocations are observed. Since the Schmid factor is zero for deformation via the <100> and <110> dislocations and on the {110} plane, it is assumed that the <100> and <110> dislocations are formed by reaction of 1/2<111> dislocations gliding on the {011} plane (slip system I). For deformation along [021] at temperatures of 1300-1400°C, the dislocations observed lie on the (001) plane. Since the slip traces involve slip on the {013} plane, it is assumed that the dislocations climb after deformation via the {013}<100> slip system (A) to position themselves on the (001) plane. For deformation along [771] at 1000°C, <100> dislocations are observed lying on {011} planes. Since the slip traces reveal cross-slip from {013} to {011} planes, it is assumed that the majority of slip occurs on the {013} plane via slip system A.

Therefore, slip occurs on five different slip systems, depending on the orientation of the compression axis, temperature and strain rate at which the test was performed. When deforming in the hard orientation, [001], slip must occur via slip systems with long Burgers vectors and rather open slip planes (H and I). On the other hand, when deforming in the easy orientations, [021] and [771], slip may occur by means of slip systems with short Burgers vectors and dense slip planes (D, A and F). Slip only occurs on a slip system with a long Burgers vector and the second densest slip plane ({013}1/2<331>) when deforming along [771] at low temperatures and high strain rates.

The rate jump tests reveal information about dislocation motion in $MoSi_2$. The highest stress exponent (20) is obtained for deformation along [021] at 1100°C. At this temperature deformation occurs via the {110}1/2<111> slip system (D). The 1/2<111> dislocation can dissociate by glide into two 1/4<111> partials separated by a superlattice intrinsic stacking fault with an energy of approximately 255 mJ/m^2 (Evans et al. 1993 [10], Maloy 1993 [7]) on the {110} plane. This lowers the Peierls stress for glide on this slip system which eases glide on slip system D and may be the cause of the high stress exponent. The next highest stress exponent (7) was recorded for deformation along [771] at 1100°C. At this temperature and strain rate, deformation occurs by glide on the {011}<100> slip system, although cross-slip is observed on the {013} and {01$\bar{1}$} planes. Although the lowest stresses are recorded for slip on the {011}<100> system (F), the cross-slipped segments may hinder dislocation motion, yielding a lower stress exponent than was measured along [021]. The lowest stress exponent (3.9) is found for deformation along [001] at 1400°C. At this temperature, deformation occurs via glide on the {011}1/2<111> slip system (I). The yield stress is high and many low angle boundaries are observed after deformation suggesting that the Peierls stress is high and climb is occurring. This may be the reason for such a low stress exponent.

Conclusions

1) The temperature dependence of the flow stress in single crystal $MoSi_2$ has been determined at temperatures between 900 and 1600°C at strain rates of 10^{-4}/s and 10^{-5}/s. The flow stress in the

[001] orientation is an order of magnitude higher than that measured in the [771] orientation at 1300°C. The flow stress decreases sharply with increasing temperature.
2) Five different slip systems can be activated, depending on the temperature and strain rate at which the test is performed: {013}<100> (A), {110}1/2<111> (D), {011}<100> (F), {013}1/2<331> (H) and {011}1/2<111> (I). Slip systems involving the densest planes, (A, D and H), are activated at temperatures of 900-1200°C while those involving the shortest Burgers vectors are activated at 1200-1600°C (A,F, and I).
3) To investigate the strain rate sensitivity of single crystal $MoSi_2$, rate jump tests were performed at 1400°C along [001] and 1100°C along [021] and [771] giving stress exponents of 3.9, 7, and 20 respectively.

Acknowledgments
This work was supported by the U.S. Department of Energy and (in part) by the DARPA-ONR at CWRU. We are grateful to J. Garrett at McMaster University for growing the $MoSi_2$ single crystals used for this research.

References

1. E. Fitzer, Ceramic Trans., **10**, 19-49 (1989).

2. S.A. Maloy, J.J. Lewandowski, A.H. Heuer and J.J. Petrovic, J. Am. Ceram. Soc., **74** (10), 2704-2706 (1991).

3. K. Sadanada, C.R. Feng, H. Jones and J.J. Petrovic, Mat. Sci. and Engrg., **A155**, 227-239, (1992).

4. T.A.Adler and C.R. Houska, J. Am. Ceram. Soc. **61**(3), 182-183, (1978).

5. O. Unal, J.J. Petrovic, D.H. Carter, and T.E. Mitchell, J. Am. Ceram. Soc., **73**, 1752 (1990).

6. V. Vitek, in Dislocations and Properties of Real Materials, (The Institute of Metals, London, 1984), pp. 30-50.

7. S. A. Maloy, Ph. D. thesis, Case Western Reserve University, Cleveland, OH (1993).

8. S. A. Maloy, T.E. Mitchell, J.J. Lewandowski, and A.H. Heuer, to be submitted to Acta Met. & Mater (1993).

9. S.A. Maloy, T.E. Mitchell, J.J. Lewandowski, and A.H. Heuer, Phil. Mag. Letters, **67**(5), 313-321 (1993).

10. D.J. Evans, S.A. Court, P.M. Hazzledine, and H.L. Fraser, Phil. Mag. Letters, **67**(5), 331-341, (1993).

CHARACTERIZATION OF STRUCTURE AND MECHANICAL PROPERTIES OF $MoSi_2$-SiC NANOLAYER COMPOSITES

H. KUNG, T. R. JERVIS, J-P. HIRVONEN*, M. NASTASI, AND T. E. MITCHELL
Los Alamos National Laboratory, Los Alamos, NM 87545, U.S.A.
*Technical Research Centre of Finland, Espoo, Finland

ABSTRACT

A systematic study of the structure-mechanical properties relationship is reported for $MoSi_2$-SiC nanolayer composites. Alternating layers of $MoSi_2$ and SiC were synthesized by DC-magnetron and rf-diode sputtering, respectively. Cross-sectional transmission electron microscopy was used to examine three distinct reactions in the specimens when exposed to different annealing conditions: crystallization and phase transformation of $MoSi_2$, crystallization of SiC, and spheroidization of the layer structures. Nanoindentation was employed to characterize the mechanical response as a function of the structural changes. As-sputtered material exhibits amorphous structures in both types of layers and has a hardness of 11GPa and a modulus of 217GPa. Subsequent heat treatment induces crystallization of $MoSi_2$ to form the C40 structure at 500°C and SiC to form the α structure at 700°C. The crystallization process is directly responsible for the hardness and modulus increase in the multilayers. A hardness of 24GPa and a modulus of 340GPa can be achieved through crystallizing both $MoSi_2$ and SiC layers. Annealing at 900°C for 2h causes the transformation of $MoSi_2$ into the $C11_b$ structure, as well as spheroidization of the layering to form a nanocrystalline equiaxed microstructure. A slight degradation in hardness but not in modulus is observed accompanying the layer break-down.

INTRODUCTION

Enhancement of mechanical properties of nanoscale materials has been predicted and observed in a number of multilayer structures [1-2]. Specifically, metal-metal systems have shown increased yield and fracture strength [2-3]. The availability of fine scale high strength materials may extend the applications of multilayered films into high temperature environments, such as protective surface coatings for high temperature structural applications. Therefore, the transformation of phases and the stability of layering are particularly important. This study examines both issues for $MoSi_2$-SiC multilayer structures.

$MoSi_2$ is a potential matrix material for high temperature structural composites due to its high melting temperature and good oxidation resistance at elevated temperatures [4]. The two major drawbacks for structural applications are inadequate high temperature strength and poor low temperature ductility. The need for composite additions has become the focus of extensive investigations in recent years [5]. On the other hand, SiC, being elastically hard and brittle, has been used as a reinforcing second phase in various intermetallic and ceramic compound matrices. Specifically, the addition of SiC whiskers has provided significant improvement in the high temperature yield strength of $MoSi_2$ [6].

In a previous report [7], it was shown that these $MoSi_2$-SiC multilayers exhibit superior oxidation resistance and significant hardness increase through annealing at 500°C. In this study, we have systematically investigated both the evolution of phases and the stability of layers by varying the heat treating conditions. By monitoring the changes in hardness and modulus with different structural changes, a trend in the structure-mechanical properties relationship can be established in these multilayers.

Mat. Res. Soc. Symp. Proc. Vol. 322. ©1994 Materials Research Society

EXPERIMENTAL PROCEDURE

Alternating layers of $MoSi_2$ and SiC were prepared by sputter deposition at a pressure of 1.33Pa with an argon flow of 10sccm/min. Prior to deposition the chamber was evacuated down to a pressure of 10^{-4} Pa. Silicon (111) substrates were used for most of the depositions. $MoSi_2$ was sputtered from a planar magnetron target at a DC power of 100-200W. Silicon carbide was sputtered from a SiC diode target at an rf power of 130-200W. The deposition rates of $MoSi_2$ and SiC were 32 and 7nm/min, respectively, at a power of 200W. The $MoSi_2$-SiC layered composites were prepared by cyclically passing the samples beneath the two targets at such a rate and target power that the constituent SiC layers had a nominal thickness of 3nm and $MoSi_2$ layers 10nm. A total of 90 sublayers of each kind were produced for each film. The multilayers were then annealed at 500, 600, 700, 800°C for 1h and 900°C for 2h, respectively, in a vacuum of 10^{-8} torr.

Investigation of the surface hardness was performed using an indentation load-depth sensing apparatus, commercially available as a Nanoindenter™ [8,9]. This instrument directly measures the load on a triangular pyramid diamond indenter tip as a function of displacement from the surface. Hardness is determined from the load data using the relation:

$$H=L(h)/A(h),$$

where L(h) is the measured load, and A(h) is the projected area of the indent as a function of the plastic depth h. The area function is determined by an iterative process involving indents into materials of known isotropic properties [9]. Measurements were made under a constant load rate of 20mN-sec^{-1} to a nominal depth of 70nm. Typically nine indents were made on each sample and the data averaged. The depth of the indents was chosen to be less than 10% of the total thickness of the nanolayered composites [10]. As discussed by Doerner and Nix [11], the actual depth of the indent includes the plastic depth as well as the elastic recovery of the material as the indenter is removed. Following their analysis, we used the unloading portion of the curve to estimate the elastic contribution to the total displacement. This analysis assumes a homogeneous material, rather than a layered surface structure, but the limitation on the depth of the indentation should validate this assumption.

As-deposited and annealed multilayers were made into cross-sectional transmission electron microscopy (XTEM) specimens and were examined using conventional and high resolution transmission electron microscopy (HRTEM) on a Phillips CM30ST microscope operating at 300kV. Optical diffractograms were taken from the lattice images; the patterns were then analyzed to identify the phase and orientation of each pattern.

RESULTS

Microstructural Characterization

Fig. 1(a) shows the XTEM image of the as-deposited multilayers. The average layer thickness was estimated to be 15nm and 2.7nm for $MoSi_2$ and SiC layers respectively. Selected area diffraction (SAD) patterns taken from the multilayered region revealed the amorphous structure as is represented by the diffuse rings in Fig. 1(b). Annealing the multilayers at 500°C for 1h induces crystallization of the amorphous $MoSi_2$ to form the hexagonal C40 structure which is a metastable structure of $MoSi_2$ [12]. SiC, on the other hand, remains amorphous.

Fig. 2(a), taken after annealing at 700°C, shows that the layer structure is preserved. Careful examination of the SAD pattern (Fig. 2(b)) indicates the presence of a few extra spots (indicated by circles) superimposed on the continuous ring patterns of the polycrystalline C40 structure. Analysis of the extra spots discloses that these extra reflections can be matched to the 6H structure and possibly other polytypes of α-SiC. XTEM image of an 800°C 1h-annealed multilayers is shown in Fig. 3(a). The two major differences between the 700° and 800°C annealed specimens are that the $MoSi_2$ layer dimension changes and the SiC layer morphology changes.

The average grain size within the $MoSi_2$ layers has increased by ~20% from 15nm to 18nm. The SiC layers have broken down to form discontinuous segments. Fig 3(b) shows a HRTEM image of the layer structure. It can be seen that some parts of the SiC layers (originally ~2.7nm thick) have spheroidized to form equiaxed shaped grains (grain size ~18nm) and extended into the original $MoSi_2$ layers. As a result, the grains in the $MoSi_2$ layers has grown outward towards the adjacent $MoSi_2$ layers to take up the space originally occupied by the layered SiC. In addition to the change in layer morphology, evidence from the SAD pattern suggests the onset of the phase transformation of $MoSi_2$ to the stable tetragonal $C11_b$ structure.

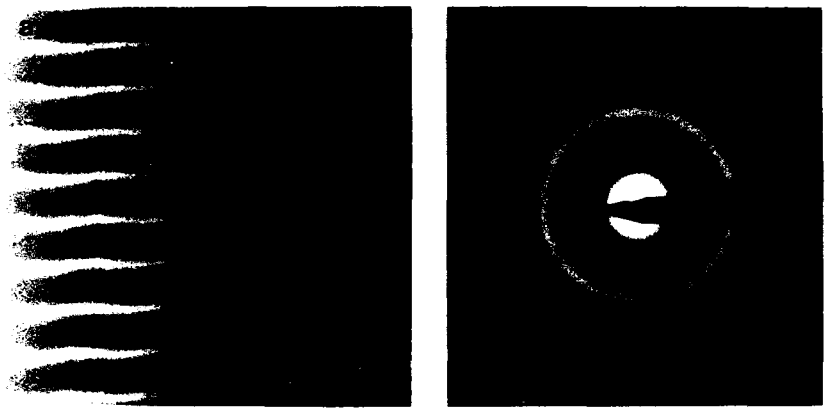


Fig. 1(a) XTEM micrograph showing the as-sputtered $MoSi_2$-SiC multilayers. Darker layers are $MoSi_2$, and the lighter layers are SiC. Fig. 1(b) Corresponding SAD pattern showing the amorphous structure in both layers.

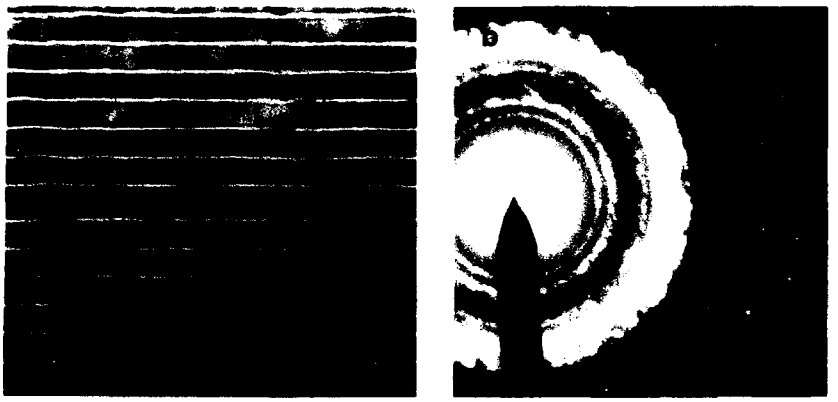


Fig. 2(a) Layered structure of $MoSi_2$-SiC multilayers annealed at 700°C for 1h. (b) SAD pattern showing extra spots corresponds to 6H structure and possibly other polytypes of α-SiC (indicated by circles) superimposed on polycrystalline rings of C40-$MoSi_2$.

900°C annealing for 2h has caused the break-down of the layered structure to form an equiaxed nanocrystalline composite. Fig. 4(a) shows a dark field image of the composite. The average grain size is in the range of 30nm, while there are a few larger grains (indicated by arrows) having diameters between 200 and 400nm. Some of the very large grains were identified to be 6H-SiC. The SAD pattern indicates that all of the C40 phase $MoSi_2$ has transformed at this temperature to form the stable $C11_b$ structure. Fig. 4(b) shows a lattice image of an interface between a $MoSi_2$ grain (d_{002}= 3.92Å) and a 6H-SiC grain ($d_{10\bar{1}4}$=2.17Å). The interface is free of any glassy phase.

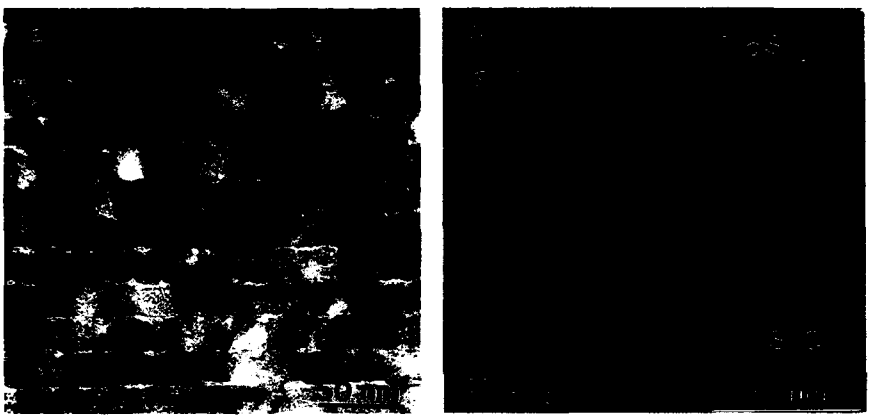


Fig. 3 (a) XTEM micrograph of an 800°C 1h-annealed multilayers. (b) HRTEM image showing evolution of layered structure: spheroidization and growth of SiC into the original $MoSi_2$ layer.

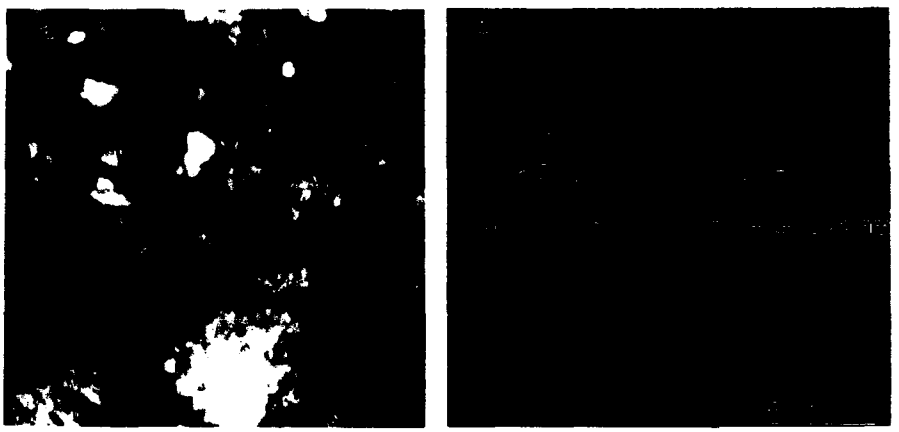


Fig. 4(a) Dark field image of a 900°C 2h-annealed composites showing equiaxed microstructure. The average grain size is ~30nm with a few large grains (as indicated by arrows) in the 300nm range. (b) HRTEM lattice image of an interface between two neighboring grains of $C11_b$-$MoSi_2$ (d_{002}= 3.92Å) and 6H-SiC ($d_{10\bar{1}4}$=2.17Å).

Nanoindentation Measurements

The hardnesses and moduli of the multilayered composites determined by nanoindentation are listed in Table I. All indents have a penetration depth less than 10% of the total thickness to avoid any influence from substrate effects. The scatter of the data is in average less than 4% of the value averaged from the nine measurements. The measured hardness and modulus of the as-sputtered multilayer are 11GPa and 217GPa, respectively. A 500°C-1h anneal has increased the hardness by almost 80% (20GPa) and the modulus by 30% (290GPa). This effect is mainly due to the crystallization of the $MoSi_2$ layers. Another significant change in hardness and modulus occurred after a 700°C annealing for 1h. An increase in hardness to 24GPa and in modulus to 326GPa corresponds well with the evidence of the SiC layer being crystallized at temperature at or above 700°C in the multilayers.

Not much change in either hardness or modulus was detected by increasing the annealing temperature to 800°C even though the layering started to show signs of breaking down. After the layers spheroidized at 900°C, a slight decrease in hardness was observed from 23.8 to 21.6GPa, perhaps due to grain size effect, while the modulus remained at ~340GPa.

Table I Hardness and Modulus of $MoSi_2$-SiC Multilayered Films

Condition	Layer Structure	Phase: $MoSi_2$ / SiC	Hardness (GPa)	Modulus (GPa)
As-Sputtered	Layered	Both Amorphous	11.5	217
500°C-1h	Layered	C40 / Amorphous	20.8	290
700°C-1h	Layered	C40 / α	24.0	326
800°C-1h	Partially Layered	C40+$C11_b$/α	23.8	344
900°C-2h	Equiaxed	$C11_b$/α	21.6	338

DISCUSSION

The phase transformation behavior of $MoSi_2$ layers within the multilayers agrees well with that of single phase $MoSi_2$ films [13,14]. It has been shown that, at ~500°C, the C40 structure crystallizes from the amorphous structure, while at temperatures above 800°C it starts to transform to the $C11_b$ structure. This agreement suggests that the presence of SiC layers pose no influence on the crystallization process of $MoSi_2$ within the temperature range studied.

The clue to the onset of layer spheroidization was obtained by examining the 800°C 1h-annealed multilayers. The significant growth and coarsening of SiC into $MoSi_2$ layers, as compared to the relatively mild grain growth in $MoSi_2$ layers, suggests that the coarsening process may be favorable both thermodynamically and kinetically. One obvious driving force is the reduction in interfacial area/energy through spheroidization. It has also been shown that the carbon self diffusion rate through grain boundaries in SiC is several orders of magnitude larger than either carbon or silicon lattice diffusion [15]. On the other hand, the diffusion of Mo and Si in $MoSi_2$ is very slow below ~1200°C [16]. No quantitative comparison can be made of the self diffusion coefficients of Mo, Si and C due to the scarcity of comparable diffusion data. It can only be speculated that the abundance in interface area may provide favorable diffusion paths for C (and possibly also Si) to complete the growth process.

It has been demonstrated in this study that the mechanical properties are directly related to the crystallization process in multilayered films. Significant improvement in both hardness and modulus can be achieved through crystallization of both $MoSi_2$ and SiC layers while still maintaining the layering structure. A maximum hardness value of 24GPa was obtained, which is higher than either single crystal $MoSi_2$, 10GPa (nanoindentation) [17], or reaction sintered $MoSi_2$-

30v/oSiC, 14.2GPa (microindentation) [18]. One possible explanation for the high hardness value is the nanocrystalline structure of these films.

The preservation of the nanocrystalline structure (grain size ~30nm) after 900°C annealing may be attributed to two factors. One is the slow diffusion process in $MoSi_2$ at this temperature. Secondly, the presence of homogeneously distributed SiC among the matrix may be imposing constraints on the $MoSi_2$ grain boundaries to prevent severe grain growth. The maintenance of high hardness even after layer break-down shows the potential of the multilayers to be used for high temperature coating applications. Future experiments have been planned to investigate the effect of prolonged high temperature exposure on the mechanical properties.

CONCLUSIONS

Amorphous structures are present in the as-sputtered multilayers. Crystallization of $MoSi_2$ and SiC layers significantly increases the hardness and modulus. A maximum hardness of 24GPa and a modulus of 326GPa are obtained through annealing at 700°C for 1h where layered $MoSi_2$ (C40) and SiC (α plus other polytypes) remain stable. The onset of layer spheroidization starts when annealing at ~800°C. Increasing the temperature to 900°C for 2h causes the complete layer break-down to form a nanocrystalline equiaxed microstructure and the transformation of $MoSi_2$ to the C11b structure. A slight decrease in hardness is observed accompanying this structural change.

ACKNOWLEDGMENTS

HK would like to acknowledge the DOE Distinguished Postdoctoral Research Program for sponsoring her fellowship at Los Alamos National Laboratory. This research is also supported in part by a DOE program in Basic Energy Sciences/Advanced Energy Project.

REFERENCES

1. J.S. Koehler, Phys. Rev. **B2**, 547 (1970).
2. S.L. Lehoczky, J. Appl. Phys. **49**, 5479 (1978).
3. S.L. Lehoczky, Phys. Rev. Lett. **41**, 1814 (1978).
4. S.M. Tuominen, J. Less-Common Met. **81**, 249 (1981).
5. R.M. Aikin, Jr., Ceram. Eng. Sci. Proc. **12**, 1643 (1991).
6. J.J. Petrovic, R.E. Honnell, Ceram. Eng. Sci. Proc. **11**, 734 (1990).
7. J-P. Hirvonen, R. Lappalainen, H. Kattelus, J. Lidonen, I. Suni, H. Kung, T.R. Jervis and M. Nastasi in Nanophase and Nanocomposite materials, edited by J.C. Parker and G.J. Thomas (Mater. Res. Soc. Proc. **286** Pittsburgh, PA, 1992) pp. 373-378.
8. W.C. Oliver, R. Hutchings, and J.B. Pethica, ASTM Spec. Tech. Pub. 889, 90 (1986).
9. W.C. Oliver and G.M. Pharr, J. Mater. Res. 7, 1564 (1992).
10. B.D. Fabes, W.C. Oliver, R.A. McKee and F.J. Walker, J. Mater. Res. 7, 3056 (1992).
11. M.F. Doerner and W.D. Nix, J. Mater. Res. 1, 601 (1986).
12. W.J. Boettinger, J.H. Perepezko and P.S. Frankwicz, Mat. Sci. Eng A155, 33 (1992).
13. T.C. Chou and T.G. Nieh, Thin Solid Films 214, 48 (1992).
14. H. Kung, T.R. Jervis, J-P. Hirvonen, M. Nastasi and T.E. Mitchell (to be published).
15. J.D. Hong, M.H.Hon and R.F. Davis, Mater. Sci. Monogr. **6**, 409 (1980).
16. E. Fitzer, Berg-Hüttenmänn, Monatsh, Leobun **97**, 81 (1952).
17. C.M. Czarnik, T.R. Jervis, M. Nastasi and R. Gibala, this symposium.
18. C.H. Henager, J.L. Brinhall, and J.P. Hirth, Scripta metall.mater. **26**, 585 (1992).

SYNTHESIS AND PROPERTIES OF *IN-SITU* $MoSi_2$/SiC COMPOSITES

S. JAYASHANKAR, S.E. RIDDLE, AND M. J. KAUFMAN
Department of Materials Science and Engineering, University of Florida,
Gainesville, FL 32611

ABSTRACT

Compositionally-tailored, silica-free, $MoSi_2$/SiC composites with SiC content ranging from 0 to 40 percent were synthesized through a novel processing scheme involving mechanical alloying and *in-situ* reactions for the formation of the reinforcement. Room temperature indentation fracture toughness and hardness measurements were obtained from these silica-free composites and were compared with values obtained from silica-containing, conventionally-processed $MoSi_2$/SiC composites.

INTRODUCTION

Conventional powder processing techniques for the fabrication of $MoSi_2$ result in the incorporation of silica (originally present as a surface layer on the powders) into the consolidated samples. The presence of silica is believed to be detrimental, since the particles may serve as crack nucleation sites at lower temperatures, while enhancing grain boundary sliding at temperatures above the softening point of silica. Additionally, the overall matrix stoichiometry is altered. Considerable efforts have therefore been made to eliminate or control the silica content through the addition of deoxidants such as carbon [1-4] and erbium [5], through clean processing [6,7], and through surface etching of the powders prior to consolidation [1].

In order to achieve the dual objective of silica elimination and control of the stoichiometry, a novel process combining mechanical alloying with the carbothermal reduction of silica has been used to synthesize $MoSi_2$/SiC composites [2,4]. While mechanical alloying would result in a microstructurally uniform and compositionally homogeneous alloy of the desired stoichiometry, the carbothermal reduction would reduce the silica to SiC. Furthermore, $MoSi_2$/SiC composites with varying amounts of SiC could be produced by suitable control of the starting compositions of the powders derived from the mechanical alloying process.

EXPERIMENTAL

Processing

The study focused on the processing and property evaluation of silica-free $MoSi_2$/SiC composites with reinforcement contents of 20 and 40 volume percent (v/o) produced through mechanical alloying and in-situ displacement reactions. For this purpose, elemental powders of molybdenum (3-7 μm, Johnson Matthey), silicon (98% pure, -325 mesh, Cerac), and carbon (99.5 % pure, -300 mesh, Johnson Matthey) were subjected to mechanical attrition for a period of at least 24 hours. The choice of powder compositions was based on the 1600°C isotherm of the Mo-Si-C system as proposed by several workers [8,9] (see Fig. 1). Nominal compositions were chosen in the $MoSi_2$ + SiC + CMo_5Si_3 (Nowotny phase) three phase field, close to the

Mat. Res. Soc. Symp. Proc. Vol. 322. ©1994 Materials Research Society

$MoSi_2$-SiC tie line so that the volume fraction of undesirable phases would be kept to a minimum; these corresponded to 20 and 40 v/o SiC (hereafter designated as MA20 and MA40). Details concerning the processing rationale and the microstructural evolution during mechanical alloying and hot consolidation can be found elsewhere [4, 10].

To achieve the optimum microstructure in the MA materials, the consolidation process is carried out in two stages. The MA powder is loaded in dies and a very low pressure (less than 10 MPa) is applied on the cold compact, so that the sample has sufficient open porosity for the entrapped gases to escape during the degassing and silica reduction reactions. The sample is ramped up to 1500°C and held at that temperature for at least 30 minutes to deoxidize the matrix. Subsequently, it is heated to 1650°C under an argon environment (7 psi) and densified for an hour under a uniaxial pressure of 35-40 MPa. The pressure on the compact is subsequently released and the sample cooled to room temperature at 10°C/min.

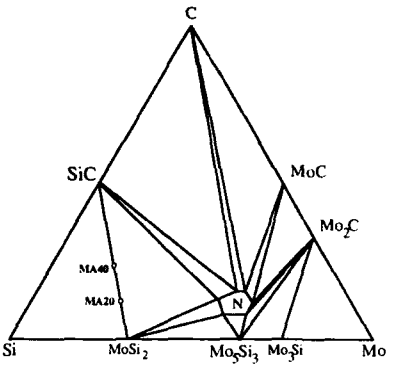
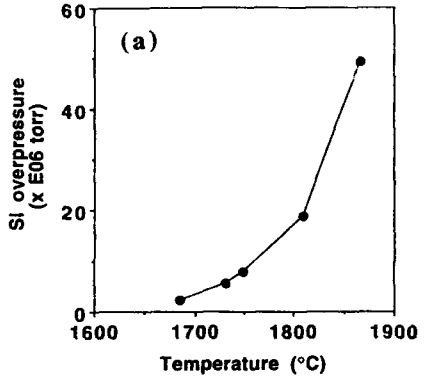


Fig.1 Schematic of the ternary Mo-Si-C isotherm at 1600°C as proposed by Nowotny et al. [9].

It should be noted that processing variables such as the temperature and the partial pressures need to be carefully controlled while processing $MoSi_2$ and $MoSi_2$/SiC composites. As Fig. 2a clearly indicates, the equilibrium dissociation pressure of Si over $MoSi_2$ increases rapidly above 1650°C [11,12]. Thus, conditions typically present during vacuum hot pressing, such as high temperatures and low vacuum levels would



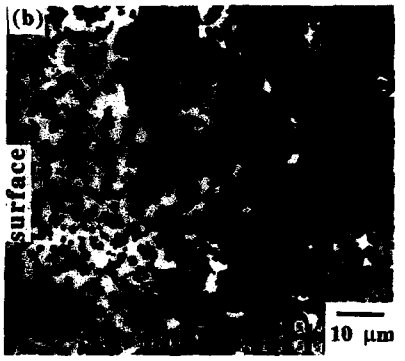


Fig. 2.(a) Equilibrium dissociation pressures of Si over $MoSi_2$, as adapted from [12].
(b) BEI of the surface of a MA40 sample hot pressed at 1700°C, showing silicon depletion. Light phase is the Nowotny phase, grey phase is $MoSi_2$ and dark phase is SiC.

result in the progressive volatilization of elemental silicon from the silicide and result in substantial weight losses. Such a volatilization reaction would be exemplified by the loss of elemental silicon from the surface of the sample, and the resultant formation of a Mo-rich phase

such as Mo_5Si_3 or the Nowotny phase. Fig. 2b is a backscattered electron image of the surface of the MA40 material that had undergone silicon volatilization after being hot pressed under a vacuum of less than 10^{-3} torr at 1700°C for 1 h. Similar effects have been reported during the processing of monolithic $MoSi_2$ [13].

For purposes of comparison, composites with 20 and 40 v/o SiC reinforcement were fabricated using the conventional approach of dry blending $MoSi_2$ (99.9% pure, -325 mesh, Johnson Matthey) and SiC powders (< 1 μm average diameter, 99.9% pure, Cerac) in the appropriate proportions followed by hot consolidation (hereafter designated as C20 and C40). Monolithic $MoSi_2$ was also processed from commercial $MoSi_2$ powder (99.9% pure, -325 mesh, Johnson Matthey). In order to facilitate the meaningful comparison of properties between the conventionally processed and compositionally tailored in-situ composites produced by mechanical alloying, the size distribution of the SiC powders was chosen such that they matched the reinforcement sizes in the *in-situ* processed material. Hot pressing of the conventionally processed composites was performed in graphite dies under a vacuum of 10^{-3} torr or better, with a pressure of 35 MPa at 1600°C for a hold time of 1 h. Subsequently, samples were cooled at the rate of 10°C/min to room temperature.

Specimens for microstructural characterization and Vickers indentation measurements were electro discharge machined, ground to remove the recast layer, and polished to a 1 μm diamond finish. Microstructural analysis of the consolidated samples was performed on a JEOL 6400 SEM equipped with a Tracor Northern EDS unit with light element detection capabilities, while phase analysis of the consolidated mechanically alloyed samples was conducted by XRD using Ni-filtered Cu K_α radiation on a Philips APD 3720 diffractometer with digital data acquisition. Since $MoSi_2$ responds well to polarized light, grain size measurements in the composites and the monolithic material were performed using cross-polarized light microscopy. Bulk density and open porosity measurements were also made on all the hot pressed samples using the Archimedes method with deionized water as the liquid medium.

Hardness and Fracture Toughness

Vickers microhardness indentations, each at least 3 mm apart (to minimize interactions between neighboring cracks) were made on the surfaces of the samples polished to 1 μm diamond finish. The indentation loads spanned a range from 49 N to 245 N for a contact time of 15 s, with a minimum of 4 indentations per indent load per sample. The minimum indentation loads were selected so as to achieve a minimum value of 2 for the ratio of the half penny crack radius (c) and half the diagonal of the Vickers impression, a requirement recommended in conventional practice for toughness measurements by indentation. In the case of the monolithic $MoSi_2$ (examined as a control sample), extensive microcracking around the indenter prevented the formation of well defined cracks for loads up to 196 N, in part due to the large grain size. The lengths of the indent diagonals (2a) and the radial cracks (2c) were measured and the hardness (H) and fracture toughness (K_c) were calculated using the following equations [14]:

$$H = P/\alpha a^2 \quad (1)$$

and

$$K_c = \delta (E/H)^{1/2} (P/c)^{3/2} \quad (2)$$

where P is the peak indentation load, $\alpha = 2$ for a Vickers indenter, δ is a material independent constant ($\delta = 0.016$) and E is the Young's modulus of the material. The Young's moduli of the

composites were calculated using literature values for $MoSi_2$ [15] and SiC [16] and assuming the rule of mixtures behavior (Voight bound).

RESULTS AND DISCUSSION

Bulk density measurements of the various composites prepared during this study show that near full densities (99% or greater) were achieved for the in-situ composites and the conventionally processed (CP) composites for compositions up to 40 v/o SiC. It should be noted that the estimation of the theoretical density of the in-situ composites was made after determining the actual volume fraction of SiC in the composite through standard point count techniques. The results of near-complete densification for the in-situ composites are significant from the standpoint of processing, since it involved the deoxidization of SiO_2 and the effective removal of the product gases CO and CO_2 in order to avoid gas porosity in the samples.

Microstructures

Fig. 3a shows a backscattered electron image of the hot pressed specimen MA20. The microstructure consists of a uniform distribution of 1-2 μm sized low Z particles dispersed in an intermediate-Z matrix. XRD and EDS analysis together indicated that the low Z phase is SiC, while the intermediate Z phase is $MoSi_2$. In addition, minor amounts (< 1v/o) of the high Z Nowotny phase were observed. Furthermore, the relative volume fractions of these phases were found to agree very well with the location of the nominal powder compositions in the 1600°C Mo-Si-C isotherm of Nowotny. The grain size of the $MoSi_2$ was relatively uniform and between 6-8 μm. Polarized light microscopy indicated that the SiC particles were located primarily at the $MoSi_2$ grain boundaries. Occasionally, large SiC grains were also observed. Previous TEM analysis of similarly processed material [4] revealed that the grain boundaries were free of the siliceous intergranular phase.

The microstructure of the hot-pressed MA40 alloy (Fig. 3b) shows a dispersion of SiC in the $MoSi_2$ matrix. However, the SiC size is considerably larger and the distribution considerably more inhomogeneous than the MA20 material, possibly due to the diffusion-controlled coarsening of SiC brought about by the smaller interparticle spacing associated with high volume fraction of SiC. Indeed, the presence of necks between adjacent SiC particles as in Fig 3b is indicative of coarsening by coalescence. This coarsening leads to a wider size distribution and a higher mean particle size, and results in a wide variation in the $MoSi_2$ grain size distribution due to varying Zener drag on the grain boundaries. The $MoSi_2$ grain size varies between 2 and 7 μm, with the mean grain size close to 5 μm The SiC is irregularly shaped, with a size range from 1 -10 μm.

The microstructures of the conventionally-processed (CP) composites C20 and C40 are shown in Figs. 4a and 4b and are typified by an inhomogeneous distribution of the SiC particles. These microstructures are characterized by particle-free islands of $MoSi_2$ surrounded by a network of irregularly shaped SiC particles. It should be recognized that in this case, the inhomogeneous distribution is due to the relative starting powder sizes of the $MoSi_2$ and SiC. The size of the SiC is much greater than the initial starting size of less than 1 μm, indicative of its coarsening during consolidation. Both of these microstructures are exemplified by a wide distribution of matrix and reinforcement grain sizes. The C20 composite has a $MoSi_2$ grain size range ranging from 2 - 10 μm, with a mean of 7 μm, while for the C40 composite, these values

range from 2 - 8 μm, with a mean of around 5 μm. These relatively wide distributions in the matrix and reinforcement grain sizes are significant since they may enhance the magnitude of the thermal mismatch stresses between the two phases.

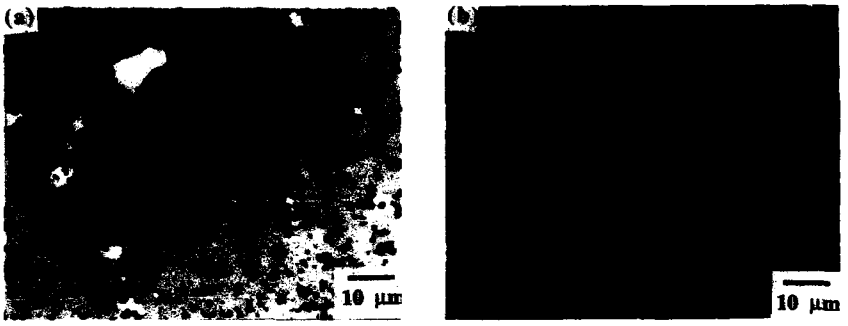


Fig. 3 BEI of (a) MA20 and (b) MA40. Phase designations are the same as that of Fig. 2b.

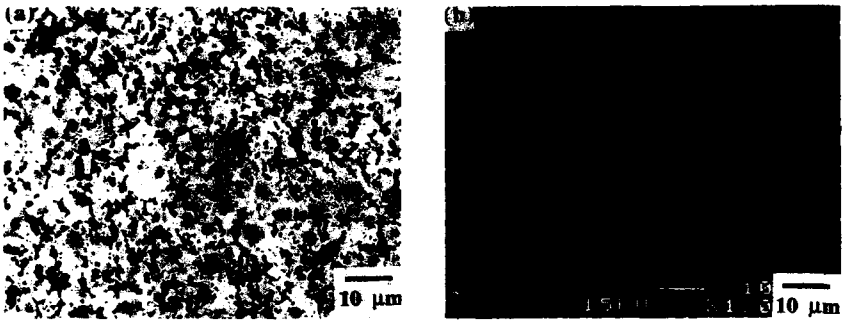


Fig. 4 Secondary Electron Image of (a) C20 and (b) C40.

Properties

Fig. 5 shows the variation of the Vickers Hardness as a function of reinforcement content of the composites. For the purpose of comparison, the hardness of the composites as predicted by a simple rule of mixtures is also plotted. It should be noted that while the hardness values of single phase $MoSi_2$ (~20 μm grain size) studied in this investigation is 8.56± 0.5 GPa, a slightly higher value was used in the rule of mixtures calculation in order to account for the smaller grain size of the matrix in the composites (~10 μm or less). Indeed, previous studies [13] on monolithic $MoSi_2$ have shown the hardness to be structure sensitive, with slight increases with decreasing grain size. The hardness value of SiC used in the rule of mixtures estimation was 25 GPa [17].

The results show that the room temperature hardnesses of the $MoSi_2$/SiC composites increase with increasing SiC content. For all reinforcement contents, the hardnesses of the in-situ composites were slightly higher than the CP composites, with the difference increasing with increasing reinforcement content. Microstructural comparison between the CP and in-situ processed composites at 40 v/o SiC loading show no marked differences in the matrix or

reinforcement grain sizes or in their spatial distribution to account for the observed differences. However, it may be of significance that the content of the intergranular silica phase in these composites are substantially different, with the MA material containing little or no silica. Specifically, the presence of the viscous glass phase at elevated temperatures might play a significant role in the relaxation of the thermal contraction stresses generated during cooldown by the CTE mismatch between the reinforcement and matrix phases.

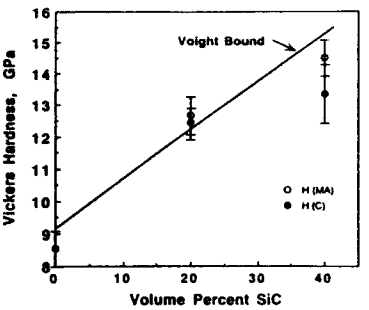


Fig. 5 Vickers Hardness of CP and MA composites as a function of SiC content.

Figs. 6a and 6b shows the variation of the fracture toughness with SiC content for the in-situ processed and CP composites respectively for various indentation loads, with each data point representing the average of at least 4 indentations. It is seen that the fracture toughness of the in-situ composites monotonically increases through 40 v/o of reinforcement, while the toughnesses of the CP composites seems to saturate at around 20 v/o and remains constant thereafter. This trend in the toughness variations with increasing reinforcement content for the conventionally processed material is consistent with earlier data [18]. Furthermore, the peak toughness values obtained in the composites processed using the CP as well as the MA approaches are almost identical at around 4.5 MPa. $m^{1/2}$. This is possibly the limit of toughening for SiC particulate reinforced $MoSi_2$.

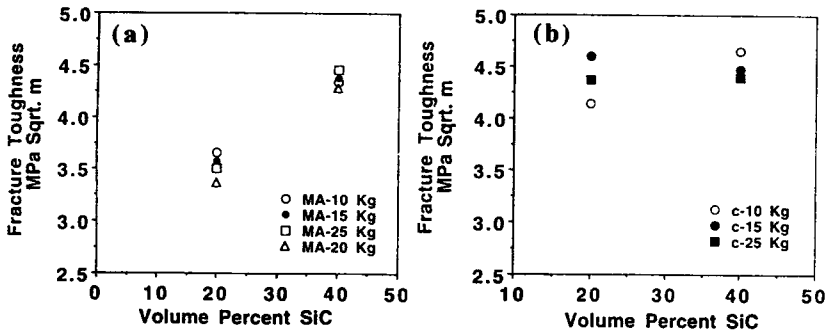


Fig. 6 Indentation fracture toughnesses of (a) MA and (b) CP $MoSi_2$/SiC composites as a function of SiC content.

The data in Figs. 6a and 6b also indicates that the toughnesses are constant and do not show any variations with the crack length, at least for the range of indentation loads used in this investigation. The only possible exception to this trend is the indentation response of the C20 material, which seemingly shows a marginal increase in K_c with indentation load.

Microstructural observations of the crack path seem to support the trends in the toughness values. Examination of the crack path of the MA20 material under polarized light as well as in

the SEM (Fig. 7a) revealed that the crack propagation was relatively straight, with a substantial portion of the crack length being transgranular and through the silicide matrix. A limited amount of crack deflection was also evident. For the most part, the cracks appeared to propagate through the matrix, and in some instances, the crack cut through the SiC particles. The absence of any interfacial debonding along the $MoSi_2$/SiC interface suggests that the strength of this interface is high and hence, does not contribute to toughening.

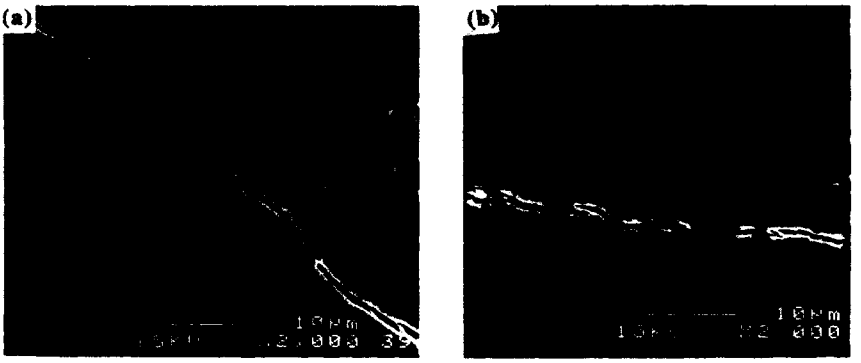


Fig. 7 Crack path arising from a Vickers indentation in (a) MA20 and (b) C40 composite.

Investigation of the crack path in the microstructures of the C20, C40 and MA40 materials showed that all three materials displayed similar crack-microstructure interactions. Considering the C40 material as a representative example (Fig. 7b), a small amount of crack deflection due to the SiC particles is observed. Evidence of some crack branching is seen, although it does not appear to be extensive. A larger portion of the crack segments were observed to run along the $MoSi_2$/SiC interface as well as through the SiC particles, when compared to the MA20 material. Presumably, these differences could have contributed to the increased toughness in the case of the C20, C40 and MA20 materials. Alternatively, it is also conceivable that the large differences in the CTEs between the $MoSi_2$ and SiC at the processing temperatures ($\Delta\alpha$ = ~4 x 10^{-6} at 1000°C) could lead to thermally-induced microcracking, thereby contributing to increased toughnesses, with the magnitude of the thermal mismatch stresses being higher for a wide grain size distribution, such as the C40 and MA40 materials than for a uniform, fine grained microstructure such as the MA20. The propagation of the cracks through the SiC particles rather than being deflected around them is also not surprising since the lower CTE of the SiC particles compared to the matrix would cause radial compressive stresses within the SiC particles and tensile hoop stresses around the SiC particle in the $MoSi_2$ matrix thereby causing the crack to be attracted towards the particles [19].

The results of the room temperature indentation fracture toughness measurements thus seem to indicate that the intergranular glass phase does not influence the toughness as much as the uniformity of the microstructure. However, it should be noted that K_c determinations based on direct crack length measurements are rather inaccurate and have a high degree of error. Additional testing using at least one other large crack technique will be necessary to verify the trends in toughnesses.

SUMMARY AND CONCLUSIONS

$MoSi_2$/SiC composites containing up to 40 v/o SiC have been fabricated using a novel processing technique involving mechanical alloying, carbothermal reduction of silica and in-situ displacement reactions. These composites are essentially free of grain boundary silica that is otherwise present in powder processed $MoSi_2$ matrix composites which have not been deoxidized. Homogeneous distributions of the reinforcing phase are observed for SiC contents up to 20 v/o, while higher loadings lead to inhomogeneities brought about by the diffusion-controlled coarsening of the SiC due to reduced interparticle distances. Preliminary property evaluations using indentation measurements indicate that the peak room temperature fracture toughnesses for the silica-free $MoSi_2$/SiC composites are similar to those of the CP composites indicating that microstructural uniformity, rather than the presence or absence of silica, controls the toughnesses in these composites.

ACKNOWLEDGMENTS

This work was supported through a Grant (No. MDA972-88-J-1006) from the Advanced Research Projects Agency. We would like to acknowledge valuable discussions with Prof. J.J. Mecholsky, A. Costa e Silva, Z. Chen and L. Hehn.

REFERENCES

1. W.A. Maxwell, NACA RM E52B06, 1952.
2. S. Jayashankar and M. J. Kaufman, Scripta Metallurgica et Materialia, **26**, 1245 (1992).
3. S.A. Maloy, A.H. Heuer, J.J. Lewandowski and J.J. Petrovic, J. Am. Ceram. Soc. **74** 2704 (1991).
4. S. Jayashankar and M. J. Kaufman, Journal of Materials Research, **8**, 1428 (1993).
5. D.P. Mason and D.C. Van Aken, Mat. Res. Soc. Symp.Proc. **273**, 289 (1992).
6. D.A. Hardwick, P.L. Martin and R. J. Moores, Scripta Metall. **27**, 391 (1992).
7. R. B. Schwarz, S.R. Srinivasan, J. J. Petrovic and C. J. Maggiore, Mater. Sci. Eng. **A155**, 75 (1992).
8. A. Costa e Silva and M. J. Kaufman, to appear in Met. Trans. **25A** (1994).
9. H. Nowotny, E. Parthe, R. Kieffer and F. Benesovsky, Monatsh. Chemie **85**, 255 (1954).
10. S. E. Riddle, S. Jayashankar and M.J. Kaufman, Mat. Res. Soc. Symp. Proc. (this proceedings).
11. T. G. Chart, Metal Science **8**, 344 (1974).
12. A.W. Searcy and A. G. Tharp, J. Phys. Chem. **64**, 1539 (1960).
13. R. K. Wade and J. J. Petrovic, J. Am. Ceram. Soc. **75**, 3160 (1992).
14. G.R. Anstis, P. Chantikul, B.R. Lawn and D. B. Marshall, J. Am. Ceram. Soc. **64**, 533 (1981).
15. M. Nakamura, S. Matsumoto, and T. Hirano, J. Mat. Sci **25**, 3309 (1990).
16. "Engineering Property Data on Selected Ceramics, Vol. 2, Carbides" , Metals and Ceramics Information Center Report No. MCIC-HB-07 vol II, Batelle Columbus Laboratories, Columbus, Ohio, (1979).
17. Y. Ohya, M.J. Hoffman, and G. Petzow, J. Am. Ceram. Soc. **75** , 2479 (1992).
18. A. K. Bhattacharya and J.J. Petrovic, J. Am. Ceram. Soc. **74**, 2700 (1991).
19. R. Rice, Ceram. Eng. Sci. Proc. **8**, 605 (1987).

THE EFFECT OF DEFORMATION AND REINFORCEMENT PARTICLES ON THE GRAIN GROWTH BEHAVIOR OF $MoSi_2$

AJOY BASU AND AMIT GHOSH
Department of Materials Science & Engineering, University of Michigan, Ann Arbor, MI.

ABSTRACT

The grain growth behavior of polycrystalline $MoSi_2$ and composites containing SiC particulates has been studied in the temperature range of 1200-1800°C during static annealing as well as under concurrent deformation conditions. Monolithic $MoSi_2$, with ~ 26 μm grain size appears to be extremely resistant to grain growth up to 1500°C. However, the grain growth rate above this temperature is quite rapid. When particulate reinforcements are used to reduce the grain size of $MoSi_2$ to 4.4 μm, a stable microstructure is maintained up to 1500°C. Accelerated grain growth kinetics are observed at 1800°C under conditions of large plastic strain. This enhanced grain boundary mobility is associated with particle sweeping and particle agglomeration effects. At lower temperatures, where dislocation creep is the more dominant deformation mechanism these effects are absent. In the presence of a Si concentration gradient extremely high growth rates of columnar $MoSi_2$ grains have been observed during reaction synthesis of $MoSi_2$.

INTRODUCTION

Developmental efforts on $MoSi_2$ and its composites are underway to meet the challenges of high temperature applications in future turbine engines [1-2]. Microstructural stability of reinforced $MoSi_2$ is a subject of interest from the standpoint of processing and fabrication of these materials, as well as during service at high temperature. Processing often requires large scale plastic flow as in forging and extrusion, involving changes in grain size, texture and morphology[3]. At this time, adequate information is not available regarding the magnitudes of such changes and their relationship to the changes occurring during static annealing. Among various processes of synthesis of brittle intermetallics, reaction synthesis from elemental constituents has also been used[4]. Such processes may offer the opportunity to produce textured materials with columnar grain morphology. The objective of the present study has been to examine the microstructural changes during several processing conditions, including hot pressing, forging, static annealing and reaction synthesis.

EXPERIMENTAL WORK

Monolithic $MoSi_2$ was prepared from $MoSi_2$ powder (-325 mesh) procured from Cerac Inc. SiC particulates used in preparing composites were obtained from H.C. Stark. A slurry milling technique was used to mix the matrix powder with SiCp to develop a intimate mixture of fine scale constituents. The powder mixtures were hot pressed in a graphite die at 1700°C for 2 hours under 28 MPa pressure. Figure 1 shows the optical microstructure of the consolidated materials. The monolithic material consists of roughly equiaxed grains, with an average intercept of 26 μm. This material also contains small spherical SiO_2 particles located primarily at the $MoSi_2$ grain boundaries and a small amount of residual porosity. The addition of SiC particles as a fine dispersion acts to pin the $MoSi_2$ grain boundaries in the composite and produce a stable matrix grain size of 4.6 μm.

Mat. Res. Soc. Symp. Proc. Vol. 322. ©1994 Materials Research Society



Fig. 1. Micrographs of (a) Monolithic $MoSi_2$ and (b) $MoSi_2$/20% SiCp under cross polarized light in hot pressed condition. The pressing direction is horizontal.

Grain Growth Studies

Static and dynamic grain growth experiments were performed at 1500 and 1800°C on samples cut from the consolidated billets. Static annealing at 1500°C was done in air for 72 and 168 hours using a Kanthal resistance furnace manufactured by CM Furnaces. The 1800°C tests were conducted for 8 and 24 hours under an argon environment using a Centorr furnace. Static annealing of the composite at 1800°C could not be accomplished due to reaction between the matrix and the reinforcement phase which produced extensive void formation. Grain growth under concurrent deformation conditions were studied successfully however, since large cavities were absent in these. Dynamic grain growth was studied from rectangular samples, 3 x 3 x 6 mm^3 in dimension, deformed at a strain rate of ~ 5 x 10^{-4} s^{-1} between SiC platens to strain levels of ~ 0.69 and ~ 2 at the same temperatures. The microstructures of the tested samples were compared to the initial microstructures.

Reaction Synthesis

Grain growth during reaction synthesis of $MoSi_2$ from its elemental constituents was studied during columnar growth of $MoSi_2$ in a Mo-Si diffusion couple. This was performed by subjecting a layer of Si sandwiched between Mo sheets, 1.6 mm in thickness, under a pressure of ~ 55 MPa for ~ 6 hours, at 1300 and 1500°C (~ 100°C below and above the melting point of Si respectively). This provided a measure of grain growth under a Si concentration gradient.

Texture Development

Texture development during compressive deformation of the composite at 1800°C was examined by comparing the {101} and the {002} pole figures of a forged sample to that of the hot pressed material. The pole figures were obtained from the plane perpendicular to the pressing axis using a Schulz goniometer attached to a Rigaku x-ray generator. An attempt to determine the growth orientation of the columnar $MoSi_2$ grains during reaction synthesis was made by using an electron back scattering technique. Here the polished cross sectional surface of the sample is inclined at 70.4 degrees to the incident electron beam in a SEM, and the image of the reflecting Kikuchi pattern is captured by a camera focused on a phosphor screen. However, only an estimate of the growth direction can be made since the plane perpendicular to the growth direction was not studied due to a shortage of test materials.

RESULTS AND DISCUSSION

The results of static grain growth in these materials at 1500 and 1800°C is summarized by the microstructures shown in Fig. 2. At 1500°C there is little change in the grain size (d) of $MoSi_2$, (Figs. 2a, d = 25.8 μm) or its composite, (Figs. 2b, d = 4.6 μm) even after annealing for 168 hours indicating that grain boundary migration is sluggish at this temperature (0.77 Tm). However, when the temperature is increased to 1800°C (0.9 Tm) there is significant grain growth due to rapid diffusion. Figure 2c shows large equiaxed grains of $MoSi_2$, 52.9 μm diameter, after annealing at 1800°C for 24 hours. Figures 3 and 4 show the results of dynamic grain growth in monolithic $MoSi_2$ and the composite respectively. Deformation of $MoSi_2$ to large strains (ε = 2) at 1500°C (Fig. 3a) is accompanied by grain refinement (d = 9.4 μm) indicating that deformation at this temperature is dominated by dislocation processes. Additionally, grain boundary microcracking is also visible as this high strain level. Deformation at 1800°C produced a microstructure consisting of large equiaxed grains (Figs. 3b, d = 41.2 μm) which indicate that diffusional processes have a more significant contribution to the deformation mechanism at this temperature. Consequently microcracking is also eliminated The deformation of the composite material also shows similar results (Fig. 4). At 1500°C, where dislocation creep is prevalent, as shown in Ref. 5, the deformed microstructure consists of slightly refined $MoSi_2$ grains (Figs. 4a, d = 4.2 μm) which are flattened perpendicular to the compression axis (aspect ratio = 2.0). However, at 1800°C, a bimodal grain structure develops, which consists of large equiaxed $MoSi_2$ grains free from SiCp (d = 54.3 μm) and particle agglomerated regions with small, flattened grains (d = 6.5 μm) bounded by SiC particulates (Figs. 4b & 4c). The growth of the $MoSi_2$ grains is accompanied by the sweeping of the SiC particles by the migrating grain boundaries which results in the agglomeration of particles at the boundaries.

Data from the microstructural examinations is summarized in Figs. 5 and 6. Figure 5 compares the rates of static grain growth to that of dynamic grain growth in the monolithic and the composite materials at 1500 an 1800°C. The results show that while there is little grain growth at 1500°C during static annealing, large plastic deformation under conditions of dislocation creep results in substantial grain refinement (Fig. 5a). The extent of refinement is less in the composite material where the initial microstructure is much finer. However, under conditions of diffusional creep there is significant grain growth in both materials sincethe rate of dynamic grain growth is faster than that of static grain growth (Fig. 5b). This type of behavior has been observed in other materials[6-8].



Fig. 2. Optical micrographs showing grain growth after static annealing: (a) monolithic $MoSi_2$ at 1500°C for 168 h, (b) $MoSi_2$/20% SiCp at 1500°C for 168 h and (c) $MoSi_2$ at 1800°C for 24 h. It is worth noting that the extent of dynamic grain growth in the composite is greater than that in the unreinforced material despite the presence of boundary pinning particles in the former.

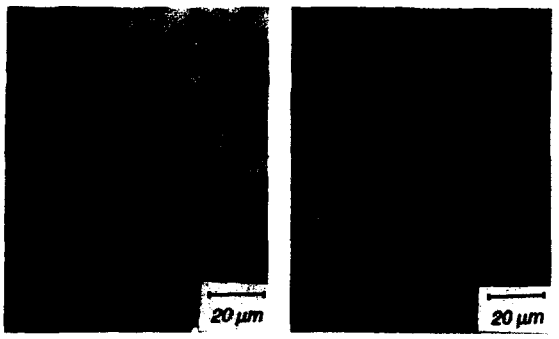


Fig. 3. The effect of compressive strain on the microstrucutre of $MoSi_2$: (a) Deformed at 1500°C ($\varepsilon = 2.0$) and (b) Deformed at 1800°C ($\varepsilon = 1.7$). Compression axis is vertical.

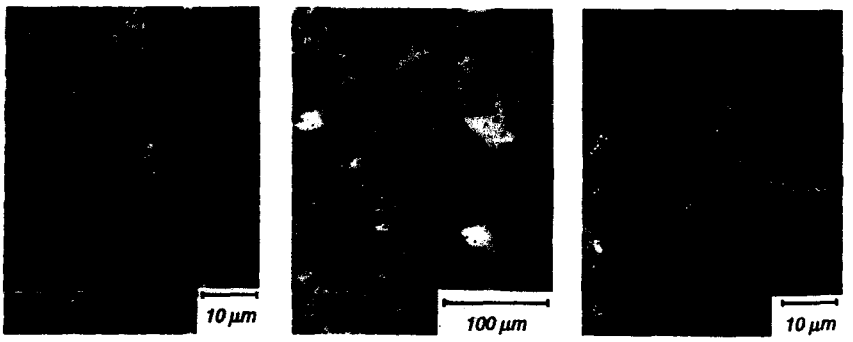


Fig. 4. The effect of compressive strain on the microstructure of $MoSi_2$/20% SiCp composite: (a) Deformed at 1500°C ($\varepsilon = 2.0$), (b) Deformed at 1800°C ($\varepsilon = 2.0$) and (c) Detailed structure of region A. Compression axis is vertical.

The temperature dependence of microstructural changes occurring during dynamic grain growth in the composite is shown in Fig. 6. Up to 1500°C, there is a slight refinement in the matrix grain size but deformation results in an increase in the grain aspect ratio from ~ 1.1 to ~ 2.0. But with an increase in temperature to 1800°C the enhanced diffusional activity leads to significant grain growth accompanied by particle sweeping and agglomeration, as discussed in Ref. 9-11. The large $MoSi_2$ matrix grains in the particle free region are equiaxed with an aspect ratio significantly lower than that within the agglomerated region.

The accelerated rate of dynamic grain growth in the particulate reinforced material can be explained on the basis of a simple model as shown in Fig. 7. Normal grain growth occurs by the migration of the boundaries of smaller grains towards their centers of curvature. The presence of particles on boundaries can lead to local stress concentration under applied load and enhanced slip. The resulting perturbation of the grain boundary region around the particles aids in enhanced diffusional flow of atoms tunneling into the larger grains due to curvature induced pressure in the smaller grains behind the particles. The addition of these atoms behind the particles causes the particles to be swept along with the migrating grain boundary. Thus at extremely high temperature under conditions of rapid diffusional processes, the presence of particles can result in accelerated diffusional kinetics and particle sweeping.

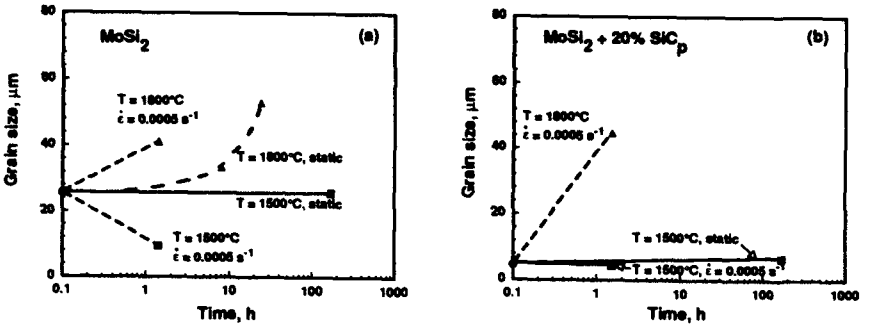


Fig. 5. Comparison between static and dynamic grain growth in (a) Monolithic $MoSi_2$ and (b) $MoSi_2$/20% SiCp composite.

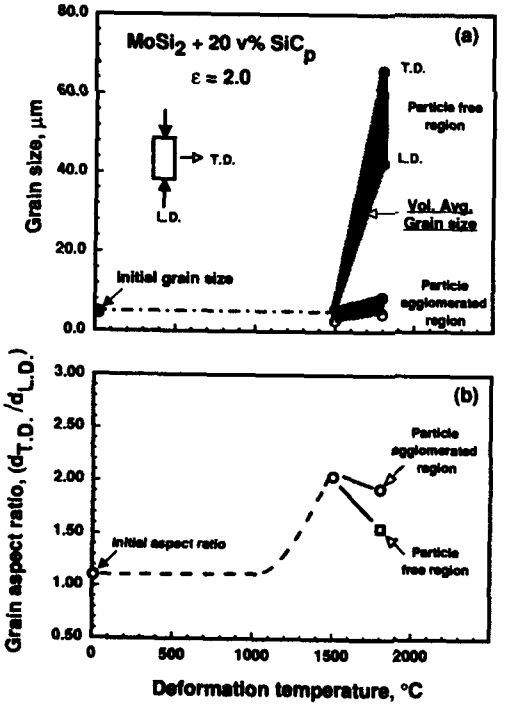


Fig. 6 Grain size and aspect ratio of the matrix grains after deformation of $MoSi_2$/20% SiCp composite at 1500 and 1800°C. Deformation at the higher temperature is associated with particle sweeping and particle agglomeration effects which result in a bi-modal microstructure.

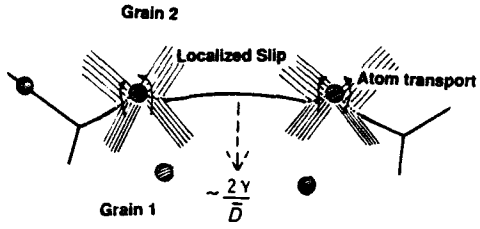


Fig. 7. Schematic of a model for accelerated grain growth and particle sweeping kinetics observed in particulate reinforced composites during deformation at elevated temperatures, involving diffusion.

The deformation of the composite at 1800°C also results in the development of texture within the material. Figure 8 compares the {101} pole figure of the deformed sample to that of the hot pressed material. It is seen that as a result of deformation there is a 60 degree redistribution of the {101} planes away from the center. Similar comparison of the {002} poles showed an intensification of the poles at the center after forging. It is believed that this {002} fiber texture formation is probably due to {001}<110> slip in $MoSi_2$[12].

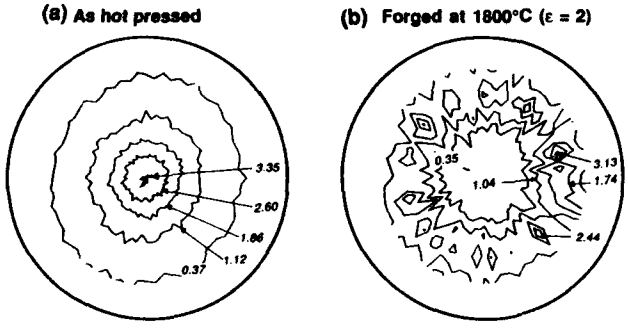


Fig. 8. {101} pole figures from a plane normal to the pressing direction of $MoSi_2$/20% SiCp: (a) as hot pressed and (b) as forged at 1800°C ($\varepsilon = 2.0$). Forging redistributes {101} poles away from the compression axis and promotes {002} fiber texture.

Fig. 9 shows $MoSi_2$ formed by direct reaction between Mo and Si. The reaction rate at 1300°C is much slower than the rate at 1500°C (Fig. 9). This is consistent with the observation that the melting point of Si is 1410°C and that the reaction at 1500°C is occurring between Mo and molten Si as compared a solid state reaction between the phases at 1300°C. The reaction layer consists of long columnar grains of $MoSi_2$ with smaller equiaxed grains at their tip, and a very small region of Mo_5Si_3 between Mo metal and $MoSi_2$. Fig. 10 shows the grain size of $MoSi_2$ at the different reaction temperatures as a function of reaction time. The grains formed at 1500°C are much longer than those formed at 1300°C. However, the difference between the width of the grains formed at the two temperatures is much less than the difference in the length of the grains. The reaction is thought to occur by the dissolution of Mo into Si and the subsequent precipitation of $MoSi_2$ at the Mo_5Si_3/Si interface. The first formed $MoSi_2$ grains are

thus spherical in shape. Subsequent formation of $MoSi_2$ is controlled by the rate at which Si diffuses along the $MoSi_2$ boundaries and reaches the $Mo_5Si_3/MoSi_2$ interface. This results in the growth of $MoSi_2$ as long columnar grains. An initial analysis of Kikuchi patterns of these grains suggest <001> as a probable growth direction, thereby indicating the possibility of producing strongly textured $MoSi_2$ by this method.

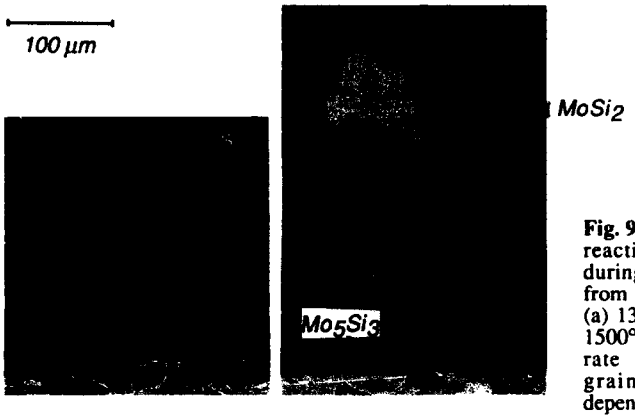


Fig. 9. Micrographs showing reaction products formed during synthesis of $MoSi_2$ from elemental constituents: (a) 1300°C for 5.5 h and (b) 1500°C for 6 h. The growth rate of columnar $MoSi_2$ grains is temperature dependent.

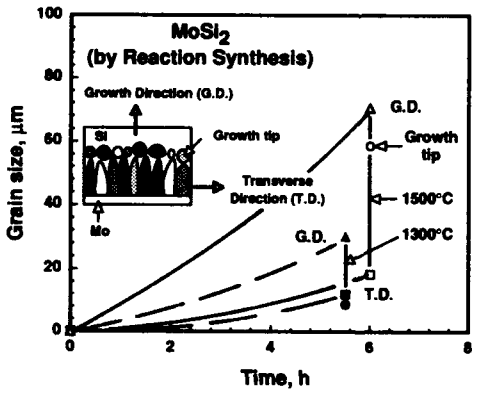


Fig. 10. Grain growth kinetics of $MoSi_2$ during reaction synthesis along the $MoSi_2$ growth direction and transverse to this direction at 1300 and 1500°C.

CONCLUSIONS

(1) $MoSi_2$ and $MoSi_2$/20% SiCp composite do not undergo static grain growth at 1500°C. Due to dislocation creep at this temperature, there is significant grain refinement in monolithic $MoSi_2$ after severe compressive deformation ($\varepsilon = 2.0$). Grain boundary microcracking is also observed in $MoSi_2$ but not in the composite due to its finer size.

(2) At 1800°C, $MoSi_2$ undergoes significant grain growth during static annealing. Under dynamic conditions both the materials undergo accelerated grain growth kinetics. The extent of growth in the composite material is greater than that in $MoSi_2$, and is accompanied by particle sweeping and agglomeration effects. These effects result in the formation of a bimodal microstructure. A model is proposed to explain the particle sweeping and accelerated grain growth behavior.

(3) Reaction synthesis of $MoSi_2$ from its elemental constituents results in the growth of columnar $MoSi_2$ grains at 1500°C and 1300°C. The rate of grain growth under a Si concentration gradient is considerably faster than that involving static of dynamic grain growth in $MoSi_2$ or its composite.

(4) Large amount of forging deformation of $MoSi_2$/SiCp composite generated {002} fiber texture, possibly resulting from {001}<110> slip.

REFERENCES

1. A.K. Vasudevan and J.J. Petrovic, Mat. Sci. and Eng., **A155** 1 (1992).
2. F.D. Gac and J.J. Petrovic, J. Am. Ceram. Soc., **68** c 200 (1985).
3. Deformation, Processing and Structure, Ed. G. Krauss, Published by ASM.
4. Combustion and Plasma Synthesis of High-Temperature Materials, Eds. Z.A. Munir and J.B. Holt, VCH Publishers Inc. NY (1990).
5. A.K. Ghosh and A.K. Basu, Critical Issues in the Development of High-Temperature Structural Materials, Eds. Stoloff, Duquette and Giamei, TMS book (1993).
6. M.A. Clark and T.H. Alden, Acta Metall., **21** 1195 (1973)
7. P. Cotterill and P.R. Mould, Recrystallization and Grain Growth in Metals, John Wiley & Sons NY (1976)
8. M.W. Mahoney and A.K. Ghosh, Met. Trans. A, **18A**, 653 (1987)
9. Migration of Macroscopic Inclusions in Solids, Ya. E. Geguzin and M.A. Krivoglaz, Consultants Bureau NY (1973)
10. Li Changmo and M. Hillert, Acta Metall., **30**, 1133 (1983)
11. R.W. Balluffi and J.W. Cahn, Acta Metall., **29**, 493 (1981)
12. H. Kung, Research performed at the University of Michigan, 1991 and reported in Ref. 5.

ACKNOWLEDGEMENTS

The authors acknowledge the financial support of this work by the U.S. Air Force through URI Grant No. DoD-G-AFOSR-90-0141 (Dr. A.H. Rosenstein, Grant Monitor).

$C11_b$-C40 TRANSFORMATION-INDUCED 1/4<111> FAULTS IN $MoSi_2$

B.K. KAD, K.S. VECCHIO, *B.P. BEWLAY and R.J. ASARO
Department of Applied Mechanics & Engineering Sciences,
University of California-San Diego, LaJolla, CA 92093-0411.
*GE Corporate Research & Development, Schenectady, NY 12301.

ABSTRACT

Previous experimental evidence for the transformation of $MoSi_2$ from the high temperature C40 structure to the low temperature $C11_b$ structure has been re-examined such that the fault character and the existence of the C40 structure is now questioned. New observations of faults in single crystals prepared over a range of growth rates from 1cm/hr to 30cm/hr are presented. Transformation-induced stacking faults, which were previously described as 1/4<111> lying on {110), have been re-identified as 1/6[001] condensation faults on (001). These faults were probably produced by silicon loss during crystal growth. The contribution that these faults may make to macroscopic strain under the action of diffusion-assisted mechanisms at elevated temperatures is discussed.

INTRODUCTION

$MoSi_2$ is presently under consideration as a high temperature structural material because it offers an attractive combination of excellent oxidation resistance, high melting point (2020°C), and reasonable specific strength at high temperatures [1, 2]. However, $MoSi_2$ has a brittle to ductile transition temperature (BDTT) at ~1000°C, with only limited plasticity above the BDTT. Three aspects of the high temperature ductile behavior have been examined in single crystals: 1) the plastic behavior is extremely strain rate sensitive [3], suggesting the possibility of time dependent phenomena, 2) there is significant evidence of climb dominated segments lying in non-slip planes, and 3) transformations may play a role in enhancing plasticity [4]. The first two phenomena relate to enhanced diffusion-based mechanisms; the strain rate sensitivity has been observed experimentally [3]. The last phenomenon relates to the polymorphic transformation from the low temperature $C11_b$ to the high temperature C40 structure [4, 5].

The current evaluation of the binary Mo-Si phase diagram [6] shows two allotropes of the line compound $MoSi_2$. The first is the hexagonal C40, which is stable between the melting temperature (2020°C) and ~1900°C. The second is the tetragonal $C11_b$, which is stable from ~1900°C to room temperature. Tetragonal $C11_b$-$MoSi_2$ can be generated by ABAB stacking on {110) planes, both layers being chemically equivalent. Hexagonal C40-$MoSi_2$ has ABCABC stacking on {0001) planes, where each of the A, B, C layers are chemically equivalent to those in $C11_b$-$MoSi_2$. Considering $C11_b$ as the reference structure, the $C11_b$ structure can be transformed to the C40 structure by 1/4<111> partial displacement on {110) planes.

Previous evidence for the $C11_b$-> C40 shear transformation was presented by Umakoshi et al [4] for a $MoSi_2$ single crystal compressed in an orientation close to [210]. They suggested that high temperature ductility can be derived as a result of the transformation from the $C11_b$ to the C40 structure since this activates 1/4<111> partial dislocations and creates pure stacking

Mat. Res. Soc. Symp. Proc. Vol. 322. ©1994 Materials Research Society

faults in $MoSi_2$. Additionally, it was suggested that alloying elements that destabilize the $C11_b$ with respect to the C40 structure by the activation of stacking faults may also enhance ductility [5].

The evidence for the $C11_b$->C40 transformation has been questioned recently because in equilibrium phase diagram studies of high purity $MoSi_2$, the C40 phase was not detected [7]. Metastable C40-$MoSi_2$ can also be generated by undercooling the melt below the metastable melting point of the C40 phase, and the occurrence of the liquid->C40->$C11_b$ transformation can be accounted for by metastable transformations in impure $MoSi_2$, such as carbon stabilized C40-$MoSi_2$. However, even under these circumstances, the possible transformation in the opposite direction of high purity $MoSi_2$ from the $C11_b$ to C40 structure is unlikely.

Numerous faults were observed previously on {110) planes in rapidly solidified metastable $MoSi_2$ [8], but these faults were not 1/4<111> type. The dislocation dissociations in single crystal $MoSi_2$, as reported by Umakoshi et al [4, 5], are significantly large. However, Evans et al [9] reported only small dissociations (~65Å) of the 1/2<111> dislocation on {110) in polycrystalline $MoSi_2$ deformed under similar conditions. Thus in polycrystalline $MoSi_2$, the partials are tightly bound and do not follow the scheme of large scale 1/4<111> partials sweeping on 1/2{110) planes, as proposed by Umakoshi et al [4].

In order to examine the inconsistencies in the nature of the faults, the $C11_b$->C40 transformation and the microstructures in the reported data, the previous data was re-examined. Table I shows previously obtained experimental contrast [4] for a typical fault (R_F) and the partial (b_p) together with the $\mathbf{g}.\mathbf{R}_F$, $\mathbf{g}.\mathbf{b}_p$ tabulations for the diffracting vectors used in the analysis. The image recorded with g=1$\bar{1}$0 offers the clearest invisibility for the bounding partial as well as the stacking fault. Thus, the choice of stacking fault partial is either 1/4[111] or 1/4[11$\bar{1}$]. However, in each case the dislocation partial visibility and the fault contrast is not matched consistently for the remaining diffracting conditions, as shown in Table I. For the case of the bounding partial, at least three images should reveal no fault contrast (i.e., $\mathbf{g}.\mathbf{R}_F$= 0, integer), whereas only one invisibility was presented [4]. Table I also shows the computed contrast for $\mathbf{b}_p$=1/n[001] (n=1/2, 1/6), and in these cases the experimental contrast can be matched correctly with the computed contrast assuming the $\mathbf{g}.\mathbf{b}_p$=0 criteria. Additionally, it was proposed that the faults lie on {110) planes. However, it appears that for g=002, the projection width of the fault is reduced to a line indicating that perhaps the fault lies in the (001) plane or one close to it; for the fault to lie in {110) the g=002 has to be parallel to the fault. In the present paper, faults in as-solidified single crystals will be described in detail together with mechanisms for their formation.

Table I: Fault Analysis of experimental data extracted from Umakoshi et al [4]. The six diffracting conditions are listed as presented in the published literature along with the 'computed' and 'experimental' fault contrast. The experimental data has an excellent match with a fault vector of 1/2[001] or 1/6[001], and not 1/4<111>, as suggested previously.

					experimental	
$\mathbf{g}.\mathbf{R}_F$	1/4[111]	1/4[11$\bar{1}$]	1/2[001]	1/6[001]	Fault	Partial
($\bar{1}$03)	1/2	1	V	V	V	V
(1$\bar{1}$0)	0	0	I	I	I	I
($\bar{2}$11)	0	-1/2	V	V	V	V
(0$\bar{1}$3)	1/2	-1	V	V	V	V
(002)	1/2	-1/2	V	V	?	V
($\bar{2}$1$\bar{3}$)	0	-1/2	V	V	V	V

EXPERIMENTAL

$MoSi_2$ was prepared by induction melting high purity elemental molybdenum and silicon in a segmented water-cooled copper crucible under an atmosphere of high purity argon prior to crystal growth. Single crystals of $MoSi_2$ were grown using the Czochralski method from the same crucible [10], at growth velocities of 30cm/hr and 12cm/hr, and also by the optical imaging float zone technique using a growth rate of 1cm/hr, as described by Kimura et al [11]. TEM disks were sliced and slurry drilled from the single crystals. Thin foils were prepared by ion milling,and examined in a Phillips CM-30 transmission electron microscope operating at 100-300kV.

RESULTS

In crystals grown at the lowest velocity of 1 cm/hr, a low density of <100] dislocations was observed in the as-grown crystals, as shown in Fig. 1. The dislocation in Fig 1(a) exhibited a $\mathbf{g.b}=0$ type of contrast for $\mathbf{g}=103$, as shown in Fig. 1(b), and $\mathbf{g}=\bar{2}00$, as shown in Fig. 1(f), yielding a fault vector = 010. Trace analysis indicated that the dislocation segments had line directions close to [100] and [110] such that the edge and the mixed segments of the dislocation were confined to the (001) plane. The stacking fault imaged, Fig. 1(a) and Fig. 1(b), exhibited a $\mathbf{g}.\mathbf{R}_F=0$, integer type contrast for $\mathbf{g}=\bar{1}10$, Fig. 1(c), $\mathbf{g}=110$, Fig. 1(d), $\mathbf{g}=0\bar{2}0$, Fig. 1(e), and $\mathbf{g}=\bar{2}00$, Fig. 1(f), yielding a $\mathbf{R}_F=1/x[001]$, where x=1/6 or 1/2. Further details about the fault plane and the leading partial are given in Fig. 2 for a similar fault.

Both the stacking fault and the bounding partial were visible for $\mathbf{g}=0\bar{1}3$, Fig. 2(a), and $\mathbf{g}=\bar{1}0\bar{3}$, Fig. 2(b). The stacking fault exhibited a $\mathbf{g}.\mathbf{R}_f=0$ or integer type of contrast for $\mathbf{g}=1\bar{1}0$, Fig. 2(c), $\mathbf{g}=110$, Fig. 2(d), $\mathbf{g}=0\bar{2}0$, Fig. 2(e), and $\mathbf{g}=\bar{2}00$ Fig. 2(f), thus indicating an $\mathbf{R}_f=1/n[001]$. The partial exhibited a $\mathbf{g}.\mathbf{b}=0$ and $\mathbf{g}.\mathbf{b}\times\mathbf{u}\neq 0$ type of contrast for $\mathbf{g}=1\bar{1}0$, Fig. 2(c), $\mathbf{g}=110$, Fig. 2(d), $\mathbf{g}=0\bar{2}0$, Fig. 2(e), and $\mathbf{g}=\bar{2}00$ Fig. 2(f). Trace analysis indicated that the fault was spread out on the (001) plane with the line directions ($\mathbf{u}_i$) of the curved partial as A=100 and B=010. Thus, both A and B exhibited a $\mathbf{g}.\mathbf{b}\times\mathbf{u}=0$ type of contrast for $\mathbf{g}=\bar{2}00$, Fig. 2(f), and $\mathbf{g}=0\bar{2}0$, Fig. 2(e), respectively. Conventional dark field imaging and $\pm$ g contrast reversal indicated the contrast was of the intrinsic type. In crystals grown at 30cm/hr no [001] faults were identified. In some areas Mo_5Si_3 rod precipitates were observed aligned along <110] in crystals grown of the range of growth rates.

DISCUSSION

The experimental observations of [001] faults in the present study are essentially similar to those presented by Umakoshi et al.[4] in deformed single crystals. However, in the present study the faults were observed in the as-solidified crystals, whereas Umakoshi et al.[4] only reported them in deformed crystals. It is also surprising that the [001] faults were generated previously during compression of single crystals in the [210] orientation, because there is no net normal stress or shear stress on the (001) plane. It is more likely that the faults, which have been previously attributed to deformation [4], were in fact present in the as-solidified crystals, as was observed in the present study.

There are two possible mechanisms for the formation of the [001] faults. First, they could be produced by condensation of vacancies, and second, they could be created by removal of

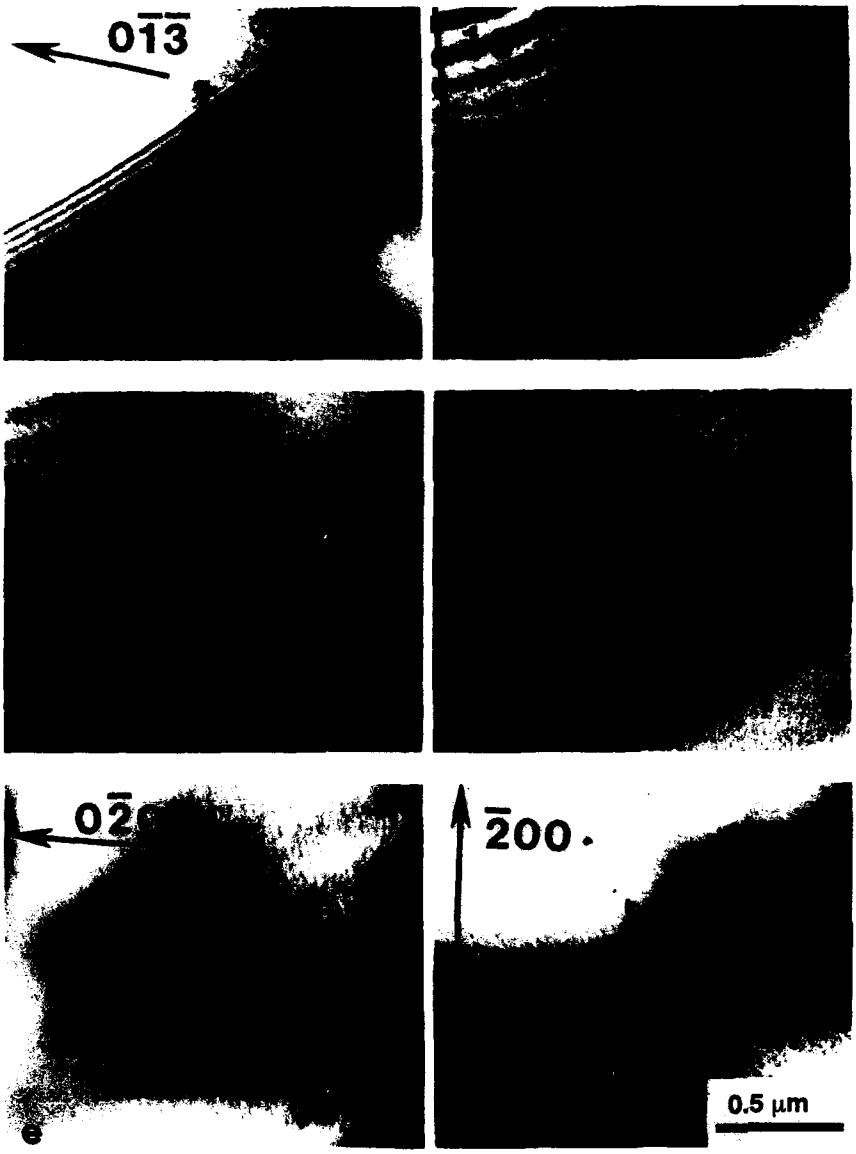


Figure 1. TEM micrographs of <100] dislocations observed in single crystal $MoSi_2$ grown at ≈1cm/hr. a) $\mathbf{g} = 0\bar{1}\bar{3}$, $\mathbf{B} \approx [\bar{3}31]$, b) $\mathbf{g} = 103$, $\mathbf{B} \approx [\bar{3}31]$, c) $\mathbf{g} = \bar{1}10$, $\mathbf{B} \approx [\bar{1}\bar{1}1]$, d) $\mathbf{g} = 110$, $\mathbf{B} \approx [001]$, e) $\mathbf{g} = 0\bar{2}0$, $\mathbf{B} \approx [001]$, g) $\mathbf{g} = \bar{2}00$, $\mathbf{B} \approx [001]$. The dislocation appears to interact with the stacking fault and is spread out on the (001) plane of the fault.

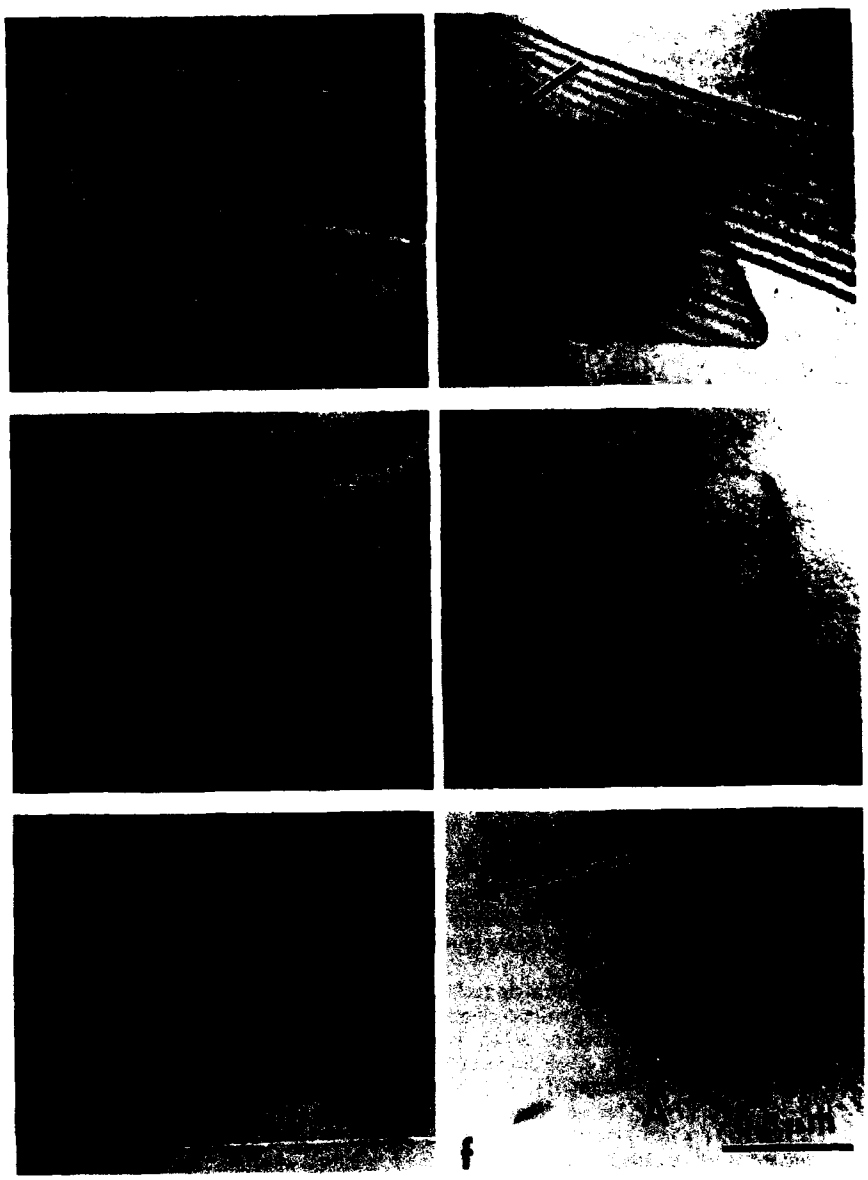


Figure 2. TEM micrographs of 1/6[001] (001)condensation faults. a) $\mathbf{g} = 0\bar{1}3$, $\mathbf{B} \approx [\bar{3}31]$, b) $\mathbf{g} = 10\bar{3}$, $\mathbf{B} \approx [\bar{3}31]$, c) $\mathbf{g} = 1\bar{1}0$, $\mathbf{B} \approx [001]$, d) $\mathbf{g} = 110$, $\mathbf{B} \approx [001]$, e) $\mathbf{g} = 0\bar{2}0$, $\mathbf{B} \approx [001]$, f) $\mathbf{g} = \bar{2}00$, $\mathbf{B} \approx [001]$. Dislocation segments A and B have line directions [100] and [010], respectively

silicon from the $MoSi_2$ unit cell. The first mechanism is unlikely because no such condensation faults were observed in rapidly quenched specimens studied previously [8], or in crystals grown at faster growth rates. The second mechanism is more likely, since the observation of such faults can be related to high temperature exposure of the crystal during growth and/or mechanical testing, where the problem of silicon volatilization is well recognised [12]. For stacking in the [001] direction of the $C11_b$, the unit cell is made up of seven different layers, 3-Mo layers and 4-Si layers, as shown in Fig. 3.

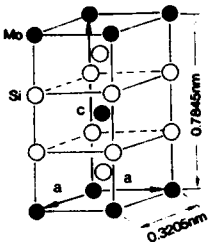


Figure 3. The unit cell of $C11_b$ $MoSi_2$.

The unit cell consists of sheets of Mo and Si atoms on the (001) planes with 1/6[001] + 1/2<110], i.e. 1/6<331], displacements between them. The chemistry can be altered by eliminating either the Mo sheets or Si sheets of atoms, for example, single or double layers of silicon atoms may be removed to create 1/6[001] and 1/3[001] faults respectively. Similarly, a 1/2[001] fault can be generated by removal of Si and Mo atoms in the ratio of 2:1; thus there is no deviation from stoichiometry associated with this fault. With regard to the data obtained in the present study, a 1/3[001] fault is excluded because of the strong fault contrast observed for $\mathbf{g}=0\bar{1}3$, as shown in Fig. 2(a), and $\mathbf{g}=\bar{1}03$, as shown in Fig. 2(b), and so a 1/6[001] vector is most likely.

At growth rates of more than 12cm/hr no faults were observed, whereas [001] condensation faults were observed at slower growth rates. This indicates that the mechanism of fault formation is indeed related to the exposure to high temperature for extended periods of time during crystal growth at slow rates. In this regard the suggestion that fault formation is associated with silicon loss appears plausible. The degree of silicon volatilization depends on the temperature of the melt, overall time of melting, ambient pressure, growth rate and temperature gradient, as discussed by Lograsso [12]. The contribution of the vacancy condensation mechanism to fault formation is therefore less likely because it would be expected to be more dominant at the higher growth velocities.

At elevated temperatures, pre-existing faults in single crystals may grow upon testing in the creep regime based on diffusion assisted climb arguments and generate condensation loops of the form observed by Umakoshi et al.[4]. Indeed, [001] faults could expand on the (001) plane and produce strain [13]. Such climb would be activated by a component of stress acting normal to the plane of the fault (001). This could lead to an increase in the size of faults when testing in the [001] orientation. The likelihood of this is increased because the <100] dislocations, are not activated at this orientation. However, climb assisted expansion of the [001] loops can only produce a small amount of strain in the ε_{zz} direction. Further to the issue of high temperature plasticity, these faults are also significant barriers to dislocations with burgers vectors not contained in the (001) plane, because the periodicity of the lattice will

introduce some APB components. An example of such a barrier is derived from the spreading of the <100] dislocations on to the [001] plane of the fault, as shown in Fig. 1.

SUMMARY

Faults that were observed in $MoSi_2$ single crystals were identified as simple 1/6[001] condensation faults. These faults were observed in single crystals that were grown at 1cm/hr, but not in crystals grown at 12cm/hr or faster. These 1/6[001] faults are consistent with the removal of complete Si layers from the $C11_b$ $MoSi_2$ structure. It is proposed that these faults result from loss of silicon at high temperatures during crystal growth. At faster growth rates, where the residence time at high temperatures is shorter, the faults are essentially absent. These faults can act as general barriers to the motion of more mobile dislocation segments and therefore reduce plasticity, although at elevated temperatures they may produce some strain by climb assisted mechanisms.

ACKNOWLEDGMENTS

The authors are grateful to Dr. T. Hirano, Dr. C.T. Liu and Claudette McKamey for providing the single crystal grown at 1cm/hr. This research was performed under AFOSR contract #91-0427 with Program Managers Dr. A.H. Rosenstein and Dr. C.H. Ward.

REFERENCES

1. J.J. Petrovic, MRS Bulletin **13**(6), 35-40 (1993).
2. P.J. Meschter and D.S. Schwartz, JOM **41** (11), 52-55 (1989).
3. R. Gibala, A.K. Gosh, D.C. Van Aken, D.J. Srolovitz, A. Basu, D.P. Mason and W. Wang, Mat. Sci. and Eng. **A155**, 147-152 (1992).
4. Y. Umakoshi, T. Sakagami, T. Yamane and T. Hirano, Phil. Mag. Lett. **59**, 159-164 (1989).
5. Y. Umakoshi, T. Sakagami, T. Hirano and T.Yamane, Acta. Met. **38**, 909-915 (1990).
6. T. B. Massalski (ed.), 1990, Binary Alloy Phase Diagrams, American Society for Metals, Metals Park, OH.
7. W.J. Boettinger, J.H. Perepezko and P.S. Frankwicz, Mat. Sci. and Eng. **A155**, 33-44 (1992).
8. B.K. Kad, K.S. Vecchio and R.J. Asaro, MRS Symp. Proc. **288**, 1123-1128 (1993).
9. D.J. Evans, S.A. Court, P.M. Hazzledine and H.L. Fraser, Phil. Mag. Lett. **67**, 331-341 (1993).
10. O. Thomas, J.P. Senateur and R. Madar, Solid State Com. **55** (7), 629-633 (1985).
11. K. K. nura, M. Nakmura and T. Hirano, Mat. Sci and Eng. **25**, 2487 (1990).
12. T. A. Lograsso, Mat. Sci and Eng. **A155**, 115-119 (1992).
13. G.W. Groves and A. Kelly, Phil. Mag. **19**, 977 (1969).

PART II

Silicide Synthesis and Processing

IN-SITU PROCESSING OF $MoSi_2$-BASE COMPOSITES

N. Patibandla, W.B. Hillig, M.R. Ramakrishnan, D.E. Alman* and N.S. Stoloff

Center for Composite Materials and Structures, and Department of Materials Engineering

Rensselaer Polytechnic Institute

Troy, NY 12180

ABSTRACT

Three different methods of preparing $MoSi_2$ and composites reinforced with ceramic fibers by reactive in-situ processing are described. Reactive powder sintering (co-synthesis) of elemental powders, chemical vapor infiltration/deposition and reactive vapor infiltration are examined. Monolithic $MoSi_2$, SiC particle-reinforced $MoSi_2$ or fibrous $MoSi_2$ composites reinforced with Nicalon fiber were prepared. The advantages and disadvantages of these processes relative to more traditional processing techniques such as HIPing of prealloyed powders, mechanical alloying and a reported in-situ displacement reactions are discussed.

1. INTRODUCTION

Molybdenum disilicide, referred to as an intermetallic or a ceramic, has a high melting point (2030°C), low density (6.24 g/cm^3) and excellent high temperature oxidation resistance. However, it has a low fracture toughness at room temperature [1,2] *(brittle as a ceramic)* and poor high temperature strength [3,4] *(softens like a metal)*. Improvements in both these characteristics have been observed when $MoSi_2$ is reinforced with SiC particles or SiC whiskers [3-8]. It is now clear that further improvements in toughness and strength can be obtained by using continuous fiber reinforcements [9]. Therefore, processing of continuous fiber $MoSi_2$ matrix composites is the subject matter of this paper.

We have primarily explored three processing techniques namely: *Reactive Powder sintering (RPS)* (also referred as Reactive co-synthesis), *Chemical Vapor Infiltration (CVI)* and a new technique called *Reactive Vapor Infiltration (RVI)*. Each route offers the potential of near net shape processing, allows placement of short or continuous fibers reinforcements and results in its own characteristic microstructure.

Reactive powder sintering: RPS is a relatively straightforward process in which elemental powders are intimately mixed in stoichiometric proportions and then heated to desired temperatures. The reaction typically is sufficiently exothermic to become self-sustaining.

Chemical Vapor Infiltration: CVI is a relatively lower temperature processing technique primarily used in processing of fiber reinforced ceramic matrix composites. Over the last decade or so variants of CVI, such as thermal gradient CVI, forced flow CVI and pulsed CVI, have been experimented with and are presently used in processing of SiC matrix composites. In the present work, isothermal CVI is considered as a potential processing route.

Reactive vapor Infiltration: RVI is also a variant of CVI. We have developed this technique to overcome the limitations of CVI. Briefly, the process involves the conversion of a shaped porous preform made from the parent metal powder(s) and reinforcing fibers interspersed in the desired orientation(s).

* Present address: US Bureau of Mines, Albany Reserach Center, Albany, OR 97321

Mat. Res. Soc. Symp. Proc. Vol. 322. ©1994 Materials Research Society

2. REACTIVE POWDER SINTERING (REACTIVE CO-SYNTHESIS)

A powder processing-type technique such as RPS is relatively straight forward, inexpensive and a variety shapes can be produced to near net sizes. To synthesize SiC(p)/$MoSi_2$ composites *in situ*, stoichiometric proportions of Mo and Si, and Si and C powders were filled into separate glass jars and mixed using a turbula type mixer for one hour. These powder mixtures were then blended to a composition of $MoSi_2$/10v% SiC and mixed as above. The powder mixture was then placed inside a niobium foil lined polyurethane mold bag and CIPed at 200 MPa. The green compacts were placed in alumina sintering boats and loaded into a sintering furnace which was then evacuated to a pressure of 10^{-9} MPa (10^{-5} torr). The compacts were heated to 300° C at a rate of 15° C/min, held for one hour, heated to 1550° C again at a rate of 15° C/min, held for 15 minutes and then furnace cooled.

The sintered samples retained their general shape but were not completely dense. They could be easily powdered with a mortar and pestle. A powder diffraction pattern taken from a co-synthesized sample is shown in Fig. 1. The pattern clearly shows the reaction products to be $MoSi_2$ and SiC *only*. Note the absence (at XRD detection limits) of molybdenum carbides (Mo_2C or Mo_5Si_3C), and lower molybdenum silicides (Mo_5Si_3 or Mo_3Si) which are also thermodynamically possible. Some of the co-synthesized samples were HIPed at 1350° C and 172 MPa for one hour in a niobium foil lined titanium HIP can. A typical microstructure of the consolidated sample is shown in Fig. 2. Note the presence of large SiC particles within the $MoSi_2$ matrix. More detailed descriptions of the sample preparation and results are published elsewhere [10,11].

We have demonstrated RPS to be a viable route for *in situ* processing of SiC particulate-reinforced $MoSi_2$ composites. We are currently employing the technique to fabricate composite samples with aligned fibers. In view of the thermal expansion mismatch-induced matrix cracking reported for SiC fiber (Ta-coated/uncoated Textron SCS-6 or sigma) reinforced $MoSi_2$ [12], we are experimenting with Al_2O_3 fibers. We are using a hand lay-up technique for interspersing the fibers between the layers of premixed elemental powders. The compact is then cold isostatically pressed (CIPed) into the desired shape and processed further. The composite matrix is expected to be purer than commercial prealloyed $MoSi_2$ which is generally found to have significant levels of second phase particles [13-15]. RPS also is expected to be superior to both mechanical alloying [16], which employs a milling step and is therefore, unsuitable for processing of fiber reinforced composites and a solid state displacement reaction technique [14] in which the volume fraction of SiC reinforcement is dictated by a chemical reaction between Mo_2C and Si.

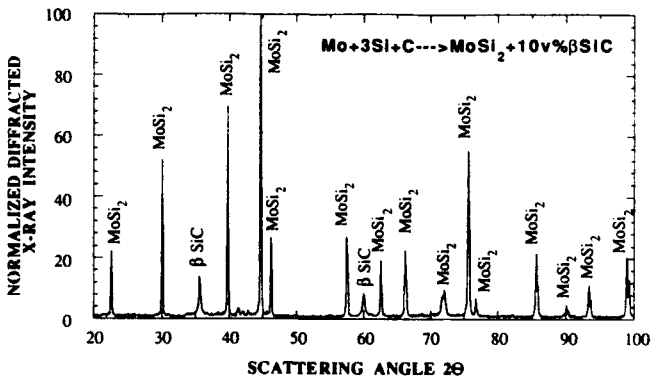


Fig. 1. A representative XRD pattern for reactively co-synthesized $MoSi_2$/SiC.



Fig. 2. A microstructure (polarized light) of HIPed reactive co-synthesized $MoSi_2$/10v% SiC showing large SiC particles in $MoSi_2$ matrix.

3. CHEMICAL VAPOR INFILTRATION/DEPOSITION

Chemical Vapor Infiltration (CVI) offers a route for producing near net shape structural components. In this method the matrix phase is deposited inside a 2- or 3-dimensional fiber preform, hence the name *infiltration*. Prior to CVI, it is almost always necessary to establish the deposition conditions on flat samples, meaning conditions for CVD. Most CVD processes are controlled by either kinetics or thermodynamics or both. Irrespective of the kinetic factors, thermodynamic feasibility of a particular chemical reaction responsible for the deposition needs to be established first. In CVD of $MoSi_2$, three different precursors, listed below, have been used by earlier researchers [17-19]:

Mixture of molybdenum hexa-fluoride (MoF_6) and silane (SiH_4) [17]

Mixture of molybdenum penta-chloride ($MoCl_5$) and silane (SiH_4) [18]

Mixture of molybdenum penta-chloride ($MoCl_5$) and silicon tetra-chloride ($SiCl_4$) [19].

Hydrogen is generally added to the above precursor systems to facilitate reduction of the halide precursors. The conditions of deposition in all three cases were established empirically. In the present investigation, CVD of $MoSi_2$ from the above precursor systems is analyzed from a thermodynamic view point and deposition conditions for obtaining exclusive $MoSi_2$ deposits are established. Such an analysis is critical, when $MoSi_2$ is intended for use as a high temperature structural material, because excess silicon limits the service temperatures to its melting point, 1414°C and excess Mo adversely affects the oxidation behavior of $MoSi_2$.

A detailed descriptions of the thermodynamic analysis and calculation methods are published elsewhere [20,21]. To illustrate typical results from these analyses, a plot of thermodynamic yield of the condensed phases vs. the ratio of $SiCl_4/MoCl_5$ in the inlet gas for the $MoCl_5$-$SiCl_4$-H_2 precursor is shown in Fig. 3. These calculations were conducted at a temperature of 1000°C and a reactor pressure of 133 Pa for SiCl4/MoCl5 ratios less than 10 and $H/Cl \geq 1.0$. The following conclusions can be drawn from this analysis:

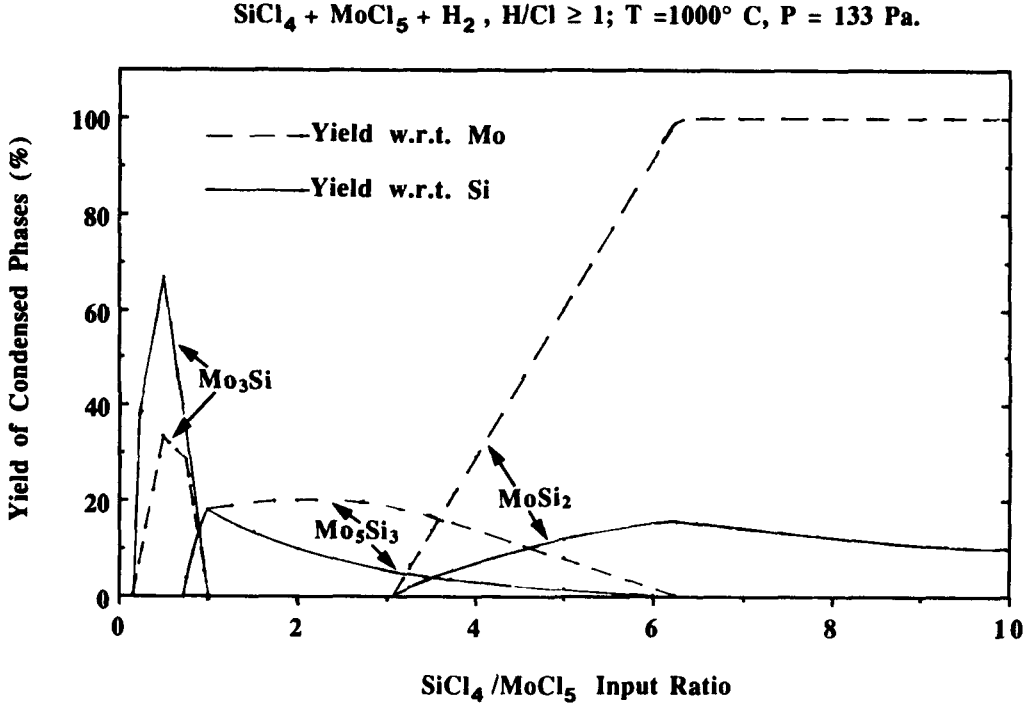


Fig. 3 Thermodynamic yield of condensed phases as a function of $SiCl_4/MoCl_5$ ratio of $SiCl_4$-$MoCl_5$-H_2 precursor with H/Cl ratios of ≥ 1.0 at 1000°C and 133 Pa.

At high $SiCl_4/MoCl_5$ ratios (6.3 and above) the only condensed phase is $MoSi_2$, meaning the activity of silicon at these ratios is less than one and therefore is not codeposited as is the case for the other two systems examined.

The lower silicide phases, Mo_5Si_3 and Mo_3Si, are codeposited at $SiCl_4/MoCl_5$ ratios below 6.3.

The yield of $MoSi_2$ with respect to Si is relatively low with a maximum of about 16% at the $SiCl_4/MoCl_5$ ratio of 6.3, indicating an inefficient utilization of $SiCl_4$.

Based on similar analyses, the following conclusions may be drawn for the other two systems:

Deposition of exclusive $MoSi_2$ is possible in the MoF_6-SiH_4 system when the SiH_4/MoF_6 ratio in the precursor is 3.5. Otherwise, one of the lower molybdenum silicides (Mo_5Si_3 and Mo_3Si) or elemental molybdenum or elemental silicon is codeposited.

Deposites exclusively of $MoSi_2$ can be obtained in the $MoCl_5$-SiH_4 system with $SiH_4/MoCl_5$ ratios between 2.4 and 3.5.

Therefore, based on thermodynamics alone, the $SiCl_4$-$MoCl_5$-H_2 system appears to be the most suitable for deposition of exclusive $MoSi_2$ deposits.

In our experiments to deposit $MoSi_2$ from $MoCl_5$-$SiCl_4$-H_2, we observed deposition rates of the order of 0.10 to 0.15 μm/min at temperatures between 1000° and 1200°C and a pressure of 2.0 torr. Use of higher temperatures led to the formation of powdery deposits indicating gas phase nucleation. Also, the handling of hygroscopic $MoCl_5$ was tedious and hazardous. The deposits were mixtures of silicon and molybdenum but not stiochiometric $MoSi_2$. The relative amounts of Si and Mo varied depending on the flow rates of precursors but never $MoSi_2$. Based on these observations CVI was considered to be non-feasible and non-economical in processing of structural components of $MoSi_2$.

4. REACTIVE VAPOR INFILTRATION (RVI) TECHNIQUE

To overcome the limitations of the CVI/CVD processing of $MoSi_2$ structural components, we have conceived and developed a new technique that retains certain features of CVD. We term our new process Reactive Vapor Infiltration (RVI). In this process a loosely compacted porous preform containing molybdenum powder is exposed to a gaseous silicon precursor at temperatures slightly below the melting point of silicon. In the present work, silicon vapor was supplied through a gas phase decomposition of silicon tetrachloride ($SiCl_4$) in presence of hydrogen (H_2).

To establish the feasibility of this technique, first we prepared monolithic $MoSi_2$ samples as follows: commercial grade molybdenum powder was pressed into pellets at room temperature to a pressure of 152 MPa (22 ksi). The molybdenum pellets were of size 38 mm in length, 6.4 mm in width, and 1.2 to 1.5 mm in thickness. After measuring initial weight and thickness of these pellets, porosity of the Mo-compacts was estimated to be about 44%. The Mo pellets were suspended into the hot zone of a graphite furnace at a temperature between 1100° and 1400°C and a pressure of 1.3 Pa using a silicon vapor precursor of 325 cm^3/min. H_2 and 25 cm^3/min. $SiCl_4$. The siliciding experiments were run for the desired number of hours (2 to 72 hrs). Further details on the RVI experimental procedure are available from our earlier publications [22,23].

4.1 RVI - KINETICS AND MICROSTRUCTURE

The silicide layer growth kinetics were measured at temperatures between 1100° and 1400°C and a pressure of 270 Pa (2 torr). The kinetics were followed by monitoring the thickness of the silicide layers measured on cross-sections of partially silicided molybdenum samples using an optical microscope with a micrometer attachment. A plot showing the thickness of the silicide layer grown on molybdenum samples as a function of siliciding time are shown Fig. 4. The data plotted in this figure indicate parabolic kinetics. The rate constants measured from this data are compared with the data of Gage and Bartlett [24] and the data of Cox and Brown [25] (see Fig. 5). Our data conform to

$$K\ (cm^2/s) = 1.3 \exp\left(\frac{-216\pm5\ kJ/mol}{RT}\right) \quad (1)$$

with an activation energy similar to the one reported by the other two investigators who grew the silicide layers using a pack-cementation approach. The absolute values of our data are consistent with those of Gage and Bartlett [24], who used thickness derived kinetics, and are higher by a factor of three than the data reported by Cox and Brown [25] who used weight gain measurements to obtain their rate constants.

Using a simple reaction-diffusion analysis, Orszagh and Vander Poorten [26] related the diffusivity (D) of the element responsible for the growth of the silicide layer to the measured parabolic rate constant (K). This relation can be modified to read as

$$D = \frac{K\,\Omega}{\Delta C} \quad (2)$$

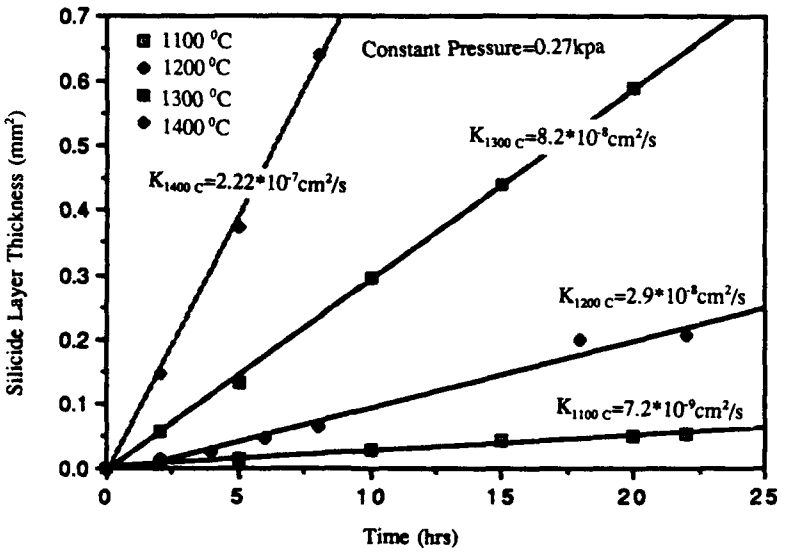


Fig. 4. Silicide layer thickness vs. time showing the parabolic nature of the RVI [illegible]s.

where, Ω is the molar concentration of the diffusing species in the silicide (0.082 moles/cm^3 for Si in $MoSi_2$) and ΔC is its concentration gradient (mole/cm^3) across the growing silicide layer. The best estimate of ΔC may be the nonstoichiometry of the silicide layer. Based on earlier work edited by Pascal [27], the Si-nonstoichiometry in $MoSi_2$ may be considered to be about 0.2% which is equivalent to 1.6×10^{-4} moles/cm^3. Substituting these numbers into the above equation, the diffusion coefficient of Si in $MoSi_2$ is estimated to be

$$D_{Si} = 6.7X10^2 \exp\left(\frac{-216\pm5 \text{ kJ/mol}}{RT}\right) \quad (3)$$

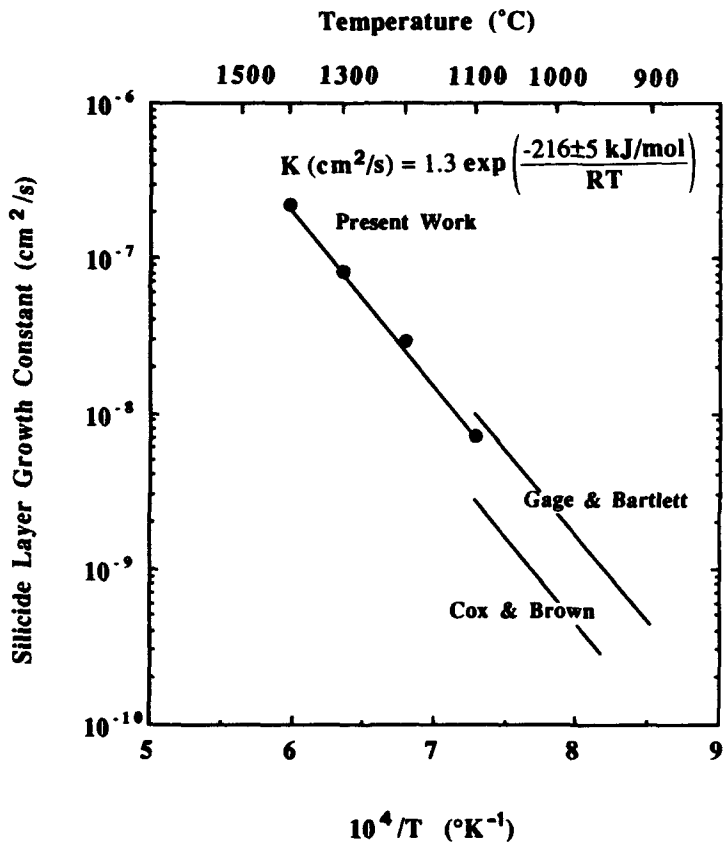


Fig. 5. Silicide layer growth constant as a function of temperature. Also shown are the data of Gage and Bartlett [24] and Cox and Brown [25].

The microstructure of the silicide layers is shown in a fracture cross-section, see Fig. 6. Note the coherency of the interfaces between the unsilicided molybdenum and the silicide layers and the absence of major structural defects such as voids. The microstructual examinations conducted on polished cross-sections of partially silicided samples indicated the presence of a Mo_5Si_3 interface layer between the external $MoSi_2$ layer and the unsilicided core. The microstructural evaluation in the RVI process has been reported in detail [22,23]. Compositional analysis conducted on the samples using x-ray photo-electron spectroscopy indicated that the oxygen contamination in the RVI processed samples is 0.3 at% or less.

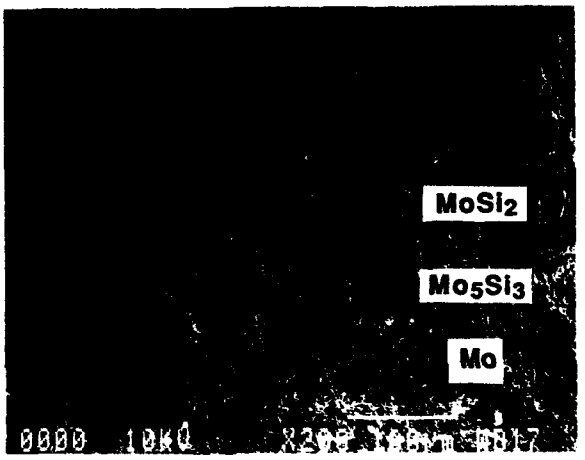


Fig. 6. Fractoragraph of a partially silicided RVI sample (1200°C, 0.27 kPa).

4.2. RVI - COMPOSITE PROCESSING

The short fiber reinforced composite samples were fabricated by completely siliciding mixtures of molybdenum powder and 5 to 10 v% chopped (desized) Nicalon SiC fibers of approximately 0.5 mm length. The continuous fiber composites were made by interspersing (via hand lay-up) the fibers and the preform powder. In both cases the compacts were formed into pellets of 38 mm in length, 6.4 mm in width, and 1 to 2 mm in thickness by pressing at a pressure of 152 MPa (22 ksi) and room temperature. Once fabricated these preforms were exposed to silicon vapor to convert Mo containing powder-phase to $MoSi_2$ in a manner similar to the one described in Sec. 2.1. The initial weight and dimensions of these pellets were measured and the porosity of the compacts was estimated to be between 43 and 45%.

A fracture section of a composite sample silicided at 1200°C is shown in Fig. 7. The Nicalon fibers show a rough surface morphology indicating that some chemical reaction occurred during RVI processing. It is noteworthy that the fibers seem to bond weakly to the $MoSi_2$ matrix as evidenced by the fiber-sections sticking out normal to the fracture surface (photographic plane) and the in-plane grooves left behind by fibers that have fallen off.



Fig.7. Fracture section of a RVI processed composite sample showing chopped Nicalon-SiC fiber (10v%) in $MoSi_2$ matrix.

We are encouraged that there appears to be weak bonding between Nicalon-SiC fibers and the $MoSi_2$ matrix. Such a weak fiber/matrix interface is expected to improve the toughness of the composite. However, the density of the composite at this stage of our work is about 92%, i.e. the density of RVI processed monolithic $MoSi_2$. Therefore, we are considering HIPing as a final densification step. To improve upon the accommodation of the volumetric expansion, we are experimenting with powders of different particle sizes and with powders containing different Mo-Si phases.

In addition, we are presently synthesizing continuous fiber reinforced composite samples. In view of the thermal expansion mismatch, alluded to in earlier sections, between the SiC fibers and $MoSi_2$ matrix, we are presently experimenting with Al_2O_3 fibers.

5. SUMMARY

The $MoSi_2$ matrix composites have potential for extended use at high temperatures, possibly up to 1600°C in such applications as heat engines. Conventional processing techniques such as hot-pressing require high temperatures of the order of 1600°C to achieve full density is not possible at temperatures below 1700°C. These high temperature processing routes restrict the usable reinforcements to those that are thermally and chemically stable at those processing temperatures.

Currently, our efforts include processing of $MoSi_2$ matrix composites using both reactive co-synthesis and reactive vapor infiltration routes. Both these routes use relatively lower temperatures, yield a purer matrix phase, allow the placement of fiber reinforcements in required orientation and quantity, and also fabrication to a near net shape and size. This approach will also provide a better sense of microstructure and properties of a single class of composites prepared by two different techniques.

ACKNOWLEDGMENT

The authors acknowledgde the financial suppot from Advanced Research Projects Agency (ARPA) and New York State Energy Research and Development Authority (NYSERDA) under the contract numbers N00014-92-J-1779 and 1544-EEED-POP-91 respectively.

REFERENCES

1. D. H. Carter and G. H. Hurley, J. Am. Ceram. Soc., **74**, C70 (1987)

2. D. H. Carter, J. J. Petrovic, R. E. Honnel and W. S. Gibbs, Ceram. Eng. Sci. Proc., **10**, 1121 (1989)

3. F. D. Gac and J. J. Petrovic, J. Am. Ceram. Soc., **68**, C200 (1985)

4. W. S. Gibbs, J. J. Petrovic and R. E. Honnel, Ceram. Eng. Sci. Proc., **8**, 645 (1987)

5. D. H. Carter, W. S. Gibbs and J. J. Petrovic in Proc. Third Int. Symp. Ceramic Materials and Components for Engines (Am. Ceram. Soc., Westerville, OH,1989) p. 977.

6. C. B. Lim, T. Yano and T. Iseki, J. Mater. Sci., **24**, 4144 (1989)

7. K. Sadananda, H. Jones, J. Feng, J. J. Petrovic and A. K. Vasudevan, Ceram. Eng. Sci. Proc., **12**, 1671 (1991)

8. R. M. Aiken, Jr., Ceram. Eng. Sci. Proc., **10**, 1643 (1991)

9. D. E. Alman and N. S. Stoloff in Intermetallic Matrix Composites II, Edited by D. B. Mirade, D. L. Auton and J. A. Graves, (MRS Symp. Proc., **273**, Pittsburgh, PA, 1992) p. 247.

10. D. E. Alman and N. S. Stoloff, Scripta Metall., **28**, 1525 (1993)

11. D. E. Alman, Ph.D Thesis, Rensselaer Polytechnic Institute, (1993)

12. M. J. Maloney and R. J. Hecht, Mat. Sci. and Eng., A155, 19 (1992)

13. S. Jayashankar and M. J. Kaufman, Scripta Metall., **26**, 1245 (1992)

14. C. H. Henager, Jr., J. L. Brimhall and J. P. Hirth, Scripta Metall., **26**, 585 (1992)

15. J. D. Cotton, Y. S. Kim and M. J. Kaufman, Mat. Sci. and Eng., **A144**, 287 (1991)

16. S. Jayashankar and M. J. Kaufman, J. Mater. Res., **8**, 1428 (1993)

17. G. A. West and K.W. Beeson in Proc. 10th Int. Conf. on CVD, Edited by G. W. Cullen, (The Electrochem. Soc., Pennington, NJ, 1987), p. 720

18. S. Inoue, N Toyokura, T. Nakamura, M. Maeda and M. Takagi, J. Electrochem. Soc., **130**, 1603 (1983).

19. D. E. R. Kehr in Proc. 6th Int. Conf. on CVD, Edited by L.F. Donaghey and P. Rai-Choudhury, (The Electrochem. Soc, Pennigton, NJ, 1977), p. 511.

20. N. Patibandla and W. B. Hillig, to appear in J. Mater. Synthesis and Processing

21. K. L. Luthra and H.S. Spacil, J. Electrochem. Soc., **129**, 649 (1982)

22. N. Patibandla and W. B. Hillig, J. Am. Ceram. Soc., **76**, 1630 (1993).

23. N. Patibandla, W. B. Hillig and M. R. Ramakrishnan in Proc. of the Ceramic Matrix Composites Symp. of the 95th Annual Meeting, (Am. Ceram. Soc., Westerville, OH). (in press)

24. P. R. Gage and R. W. Bartlett, Trans. Met. Soc. AIME **233**, 832 (1965).

25. A. R. Cox and R. Brown, J. Less-Common Metals, **6**, 51 (1964).

26. J. Orszagh and H. Vander Porten, Rev. int. Htes Temp. et Refract. **11**, 109 (1974).

27. P. Pascal, editor, *Nouveau Traite de Chimie Minerale*, Masson et Cie, Paris (1963).

VACUUM PLASMA SPRAY FORMING OF HIGH TEMPERATURE SILICIDES

S.Sampath and H.Herman
Thermal Spray Laboratory
Department of Materials Science and Engineering
State University of New York
Stony Brook, NY 11794-2275

ABSTRACT

Molybdenum disilicide and its composites have been fabricated by a number of researchers in recent years through vacuum plasma spray (VPS) forming. VPS is capable of producing dense, fine grained deposits of these high temperature intermetallics and is a promising technique for near-net-shape manufacturing. Reviewed here is VPS forming of high temperature silicide intermetallics, principally $MoSi_2$ and its composites. A discussion will be given of the processing-structure-properties relationship of the spray formed silicide.

INTRODUCTION

In recent years, intermetallics and intermetallic matrix composites have been the subject of considerable research interest for potential high strength, high temperature structural applications. The refractory metal disilicides, in particular, $MoSi_2$, are leading contenders in the search for high performance refractory materials for heat engine and related aerospace requirements [1]. $MoSi_2$ has a high melting point (2030°C), with an essentially temperature independent yield stress of 300 MPa. $MoSi_2$ has excellent oxidation resistance, having traditionally been employed as a heating element material in air furnaces for high temperatures up to 1800°C. The compound is near brittle at room temperature, with a DBTT at approximately 925°C, above which the material is strong and ductile, but beyond 1250°C a range of softness sets in, leading to creep rupture deficiencies [2]. Compositing strategies such as SiC, TiC, etc., have been proposed to enhance creep resistance at high temperatures [2-5]. Ductile phase toughening using Nb wires has also been considered as a mechanism of room temperature toughening [6].

Rapid solidification of intermetallic compounds has attracted attention in recent years, due to the potential for producing chemically homogeneous, fine-grained microstructures [7]. However, the necessity for ultra-high cooling rates imposes restrictions on specimen size: generally, rapidly solidified material is produced in the form of ribbon, flake or powder[8]. Plasma spray processing, a well established technique for producing protective coatings, offers an alternate method of consolidation of these materials into potentially useful forms, while retaining the benefits of rapid solidification rate (RSR) processing. Compared to other RSR approaches, plasma spraying offers the advantages of large throughputs (kg/hr), high density, and the ability to deposit objects of near-net bulk forms.

The benefits of rapid solidification through plasma spraying of Ni-based superalloys have been explored in the past as an alternate manufacturing methodology. For instance, researchers at General Electric have examined a number of vacuum plasma spray (VPS; also referred as "low pressure plasma spray - LPPS") formed Ni-based alloy shapes and have obtained improved yield and tensile strengths as compared to other processing techniques [9-11]. Their results indicate that the rapid solidification of the molten droplets occurs during deposition in a low pressure environment, the deposits achieving nearly theoretical density. In another example, Chang et al compared the mechanical properties of melt-spun, hot-isostatic pressed, and plasma sprayed Ni_3Al-B alloys and found that plasma sprayed specimens had the highest yield and tensile strengths [12]. As noted by Taub et al a key advantage of plasma processing is the capacity to produce rapidly solidified free-standing near-net forms, thus obviating the need for post-spray thermo-mechanical processing [13].

Mat. Res. Soc. Symp. Proc. Vol. 322. ©1994 Materials Research Society

Plasma spray processing of composites represents a synthesis of rapid solidification and composite materials technology. It is a near-net-shape composite manufacturing process, in which co-deposition combines melting, blending and consolidation into a single step, readily allowing the formation of continuous, discontinuous, or laminated composite structures. Tiwari et al used dual-feed co-deposition to produce TiB_2-reinforced Ni_3Al composites, the free-standing structures displaying mechanical properties which were superior to those obtained using other processing techniques [14]. This was attributed to enhanced particle-matrix bonding obtained by the VPS process.

THE PROCESS

Plasma spraying , is a technique of "thermal spraying", in which feedstock powder, wire or rod is melted in a hot flame, propelled to an appropriately prepared substrate, where solidification occurs, forming a thick film deposit, or, as discussed here, a thick section which can be removed from the substrate. D.C. and R.F. thermal, near-ambient pressure plasmas are extensively used in the materials processing industries for extractive metallurgy, melting, deposition, and evaporation. The traditional D.C. arc plasma gun, which was developed as a heat source over three decades ago, has been extensively used to spray deposit protective coatings. The D.C. plasma is formed typically between a tungsten cathode and a water-cooled copper anode by the ionization of gases such as Ar or N_2 with additions of secondary gases such as He or H_2. It is into this exiting, high temperature, plasma flame that powdered feedstock material (10 - 90 μm in diameter) is introduced by a carrier gas. The particles melt in transit without vaporizing excessively, are accelerated, and impinge onto the substrate where they flatten and solidify at cooling rates similar to those achieved in rapid solidification processes. The deposit is formed by successive impingement of these molten droplets.

Due to the high temperature of the plasma core (~10-15,000K), virtually any refractory material can be melted and deposited, the only criteria being that the material not decompose. Thus, the process allows the processing of metals, alloys, and, in particular, intermetallics and ceramics. The evolution of controlled atmosphere plasma spraying, such as inert shrouded spraying and vacuum plasma spraying (actually, VPS operates at pressures in the range of 50 mbar) has considerably expanded the capabilities of the process to produce dense, oxide-free deposits. Vacuum D.C. plasma spray typically achieves high particle velocities (200 - 500 m/s), with attendant high impact velocities, yielding deposits of near theoretical density [15].

Although conventional air plasma spraying (plasma spraying in ambient environment or APS) leads to rapid solidification [16], the deposits contain defects such as porosity, non-continuous interlamellar bonds, oxide inclusions, etc., as well as process-related residual stresses. VPS can circumvent these microstructural deficiencies and yield highly dense deposits, which are relatively stress-free. In VPS, although the solidification is rapid, the deposit undergoes in-process annealing due to the almost continuous exposure of the deposit to the end of the high temperature (> 800°C) flame. In fact, this self-annealing can be beneficial, since it provides stress-relief, recrystallization, and results in enhanced interparticle bonding [15, 17]. The reduction in residual stresses permits build-up of very thick deposits, and, thus, VPS can be viewed as an effective means for consolidation of powders and composites for the production of free-standing forms for high performance applications [18].

VPS FORMED $MoSi_2$ INTERMETALLICS

One of the earliest reported uses of vacuum plasma spraying of $MoSi_2$ was in the production of protective coatings. Henne and Weber studied VPS deposited $MoSi_2$ coatings on Mo substrates to form an adherent oxidation-resistant coating [19-20]. Due to large differences in thermal expansion coefficients between Mo and $MoSi_2$, the coatings experienced transverse cracks. Although this difference in thermal expansion is of some concern for coatings production, when treated properly thermal expansion mismatch allows the facile separation of thick intermetallic deposits from the substrate to produce free-standing forms [21-22].



Fig.1: Scanning electron micrograph of VPS $MoSi_2$ cross-section.



Fig.2: Scanning electron micrograph of hot-pressed $MoSi_2$.

Microstructures and Phase Formation

In Fig.1 is shown typical cross-sectional microstructure view of the VPS-formed $MoSi_2$ deposit, produced using $MoSi_2$ powder feedstock of particle size 5 to 45 μm. The deposit, which appear to approximate a wrought metallurgical microstructure, typically display greater than 98% theoretical density in the as-sprayed condition; Table I [21]. The microstructure shows fine pores and the grain structure is not revealed under these imaging conditions. For comparison, the microstructures of hot-pressed $MoSi_2$, produced from a similar powder, is shown in Fig.2. The hot pressed specimen of similar density displays a coarser grain structure and larger pores. Figure 3 shows a transmission electron micrograph of VPS-formed $MoSi_2$, revealing a bimodal distribution of grains. The grain size is in the range of 0.1- 0.6 μm. This type of submicron, equiaxed microstructure is commonly observed in VPS deposits and has been attributed to recrystallization occurring during the spray process; i.e., "self-annealing" [15]. Castro et al have reported similar grain size distributions in VPS-formed $MoSi_2$ [23].

Table I: Density and Phase Characteristics of VPS formed $MoSi_2$ [21].

Condition	Deposit Density g/cc	Oxygen Content (%)	Phases
Powder	-	0.24	t-$MoSi_2$, Mo_5Si_3(trace)
$MoSi_2$ - Hot Pressed	6.22	0.29	t-$MoSi_2$, Mo_5Si_3*
As-VPS-sprayed	6.17	0.30	h-$MoSi_2$, t-$MoSi_2$, Mo_5Si_3*
Annealed 1100°C / 2h	6.15	0.45	t-$MoSi_2$, h-$MoSi_2$* , Mo_5Si_3*
Annealed 1100°C / 24h	6.02	0.28	t-$MoSi_2$, h-$MoSi_2$* , Mo_5Si_3*

t-$MoSi_2$ (tetragonal), h-$MoSi_2$ (hexagonal), * - Present as Minor Phases

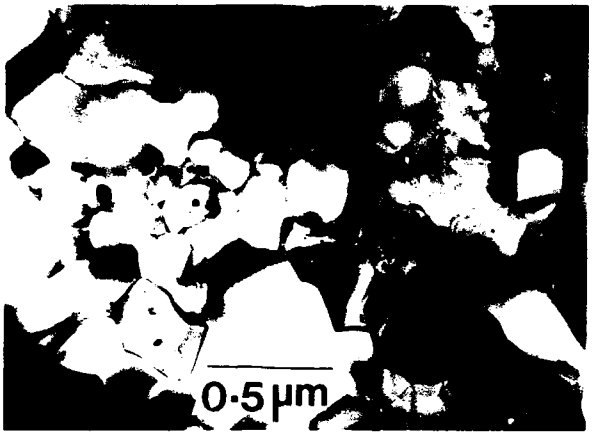


Fig.3: Transmission electron micrograph of a vacuum plasma spray formed $MoSi_2$ revealing a fine grained microstructure

The X-ray diffraction pattern of the as-received powder reveals an essentially equilibrium tetragonal single-phase structure (t -$MoSi_2$). However, a metastable hexagonal $MoSi_2$ allotrope (h-$MoSi_2$) has been observed in the as-sprayed condition: Table I [21]. Annealing of the as-sprayed specimen at 1100°C leads to an irreversible transformation of h-$MoSi_2$ -> t-$MoSi_2$. Tiwari et al have shown that h-$MoSi_2$ is a major phase in the as-sprayed deposit [21]. Upon annealing, there is a considerable decrease in h-$MoSi_2$ peak intensity accompanied by an increase in the t-$MoSi_2$ peak intensity, suggesting that the h-$MoSi_2$ phase is metastable at room temperature. In a recent work, Ohmori and Fukuoka have also shown the substantial presence of the hexagonal $MoSi_2$ phase in the VPS deposit [24]. They observed the hexagonal to tetragonal transformation upon heating to about 950°C. Mitchell et al observed twins in the VPS $MoSi_2$ attributed to the hexagonal-tetragonal transformation at high temperatures [25]. In another study, Shaw et al have examined the microstructural evolution of $MoSi_2$, plasma sprayed in an atmospheric pressure inert gas chamber and found considerable Si volatilization, resulting in the formation of several Mo-rich silicide phases with significant compositional variations [26]. Annealing at 1500°C resulted in the formation of the Mo_3Si phase.

The above results are not surprising since plasma spraying commonly yields RSR-induced metastable phases [16]. On examination of the phase diagram [27] it is seen that h-$MoSi_2$ is a high temperature allotrope (1900 -2030°C) and this phase is retained at room temperature during plasma spraying. It is clear that inert gas chamber spraying alone is not sufficient to overcome the Si volatilization and that a low-pressure, oxygen-free environment is required to retain the appropriate chemistry and homogeneity such that the single phase tetragonal $MoSi_2$ can be obtained through subsequent annealing.

Composite Microstructures

A variety of composite reinforcements have been added to $MoSi_2$ through VPS. Using premixed powders, Tiwari et al produced TiB_2- and SiC-reinforced $MoSi_2$-matrix composites [22]. The TiB_2 reinforcements in the $MoSi_2$ matrix had a splat-like morphology resulting from concurrent melting of both the components in the plasma flame; Fig.4. However, this was not the case for SiC-reinforced $MoSi_2$, because SiC sublimates at 3000°C instead of melting.

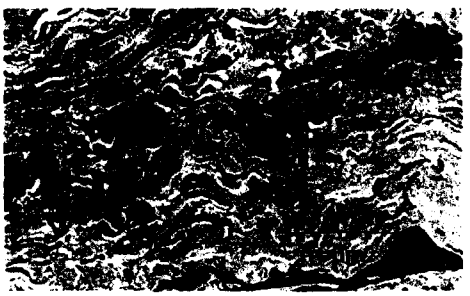


Fig.4: Backscattered electron micrograph of VPS formed $MoSi_2$-TiB_2 composite [21].



Fig.5: Scanning electron micrograph of VPS formed $MoSi_2$-SiC composite [22].

Thus, unlike TiB_2 , the SiC distributed as particulates, retain their pre-sprayed morphology; Fig.5. No apparent interfacial reaction was observed between the matrix and reinforcements. This is attributed to the high rate deposition process, which prevents particle-matrix interfacial reactions.

In order to enhance fracture toughness at temperatures below 1000°C, the ductile-brittle transition temperature, a ductile phase can be incorporated into the intermetallic matrix. Such is the case for Ta-reinforced $MoSi_2$, which was VPS-processed by Castro et al [28], who obtained microstructures similar to the plate-like morphology observed for the TiB_2 reinforcement [21]. Alman et al produced $MoSi_2$ - Al_2O_3 laminates by alternate deposition of the two powders [29]. These deposits, which were of relatively low overall density (82-96%), were produc·' in an inert gas filled chambe, at ambient pressure. However, post-spray annealing was sufficient to fully densify the laminates.

Currently exploratory research is underway at Stony Brook involving VPS forming of pre-alloyed / pre-composited $MoSi_2$ + 20 vol% SiC and $MoSi_2$-WSi_2+ 20 vol% SiC powders, which were produced by Osram Sylvania Inc. (Towanda, PA) using solid state sintering methods. The microstructures and mechanical properties of these deposits are being investigated. It is the contention of the authors that the use of pre-composited powders would enable substantially enhanced reinforcement loading during VPS forming.

Mechanical Properties

Both room temperature and high temperature mechanical properties of VPS- formed $MoSi_2$ and composites have been reported. In Table II are summarized room temperature mechanical properties [22]. The high Vickers microhardness (1200 VHN) of unreinforced as-sprayed $MoSi_2$ has been attributed to the fine grain size of the spray-formed product [22]. Further, the indentation fracture toughness and the flexural strength of the as-sprayed $MoSi_2$ are substantially greater than that for hot-pressed material. Annealing leads to a lower hardness, in conjunction with increases in indentation fracture toughness and flexural strength. It is important to note that annealing at 1100°C did not lead to significant grain growth or changes in microstructure. These greatly improved properties of VPS $MoSi_2$ are attributed to the fine-grained microstructure.

Table II: Room temperature mechanical properties silicide composites [22].

Material Condition	Hardness VHN	Bend Strength MPa	Fracture Toughness MPa $m^{1/2}$
$MoSi_2$ as-sprayed	1201	280	4.7
$MoSi_2$ annealed 1100/2 hrs	1203	310	4.8
$MoSi_2$ annealed 1100/24 hrs	1093	364	5.9
$MoSi_2$ + 4 vol% SiC as-sprayed	1228	300	5.4
$MoSi_2$+4 vol% SiC annealed 1100/24h	1160	410	7.9
$MoSi_2$ + 20 vol% TiB_2 as-sprayed	1057	380	6.1
$MoSi_2$ hot-pressed	950	185	2.9

The addition of composite reinforcements, for example, in the form of TiB_2 and SiC, leads to considerable increases in flexural strength and fracture toughness over their monolithic counterparts. Although a relatively small (4 volume %) incorporation of SiC leads to only a nominal increase in strength, a large increase in fracture toughness is observed [22]. Where-as strength increases may be attributed to enhanced particle-matrix bonds, leading to improved load transfer, the large increase in fracture toughness can likely be attributed to enhanced crack deflection and branching processes [1]. The rationale for the strong particle-matrix bond in the VPS-processed composites is that the temperature of processing is at least 800°C, thereby promoting good wetting of the reinforcement by the matrix. However, the short time of processing eliminates the occurrence of any large scale interfacial reactions, which may have a detrimental influence on the overall strength of the VPS deposit. Similar strengthening effects were observed in a related study of VPS-formed Ni_3Al-matrix TiB_2 composite [14].

Alman and co-workers, plasma spraying $MoSi_2$ in an inert gas chamber at ambient pressure, observed that microhardness increased with plasma current [29]. Since it is known that increased power leads to increased gas and, thus, greater particle velocity, it must be concluded that the higher hardness is the result of an overall greater deposit density. Upon subsequent annealing of the deposit, a decrease in hardness was observed [26]. Further, as seen in Table II, a decrease in hardness is observed with subsequent annealing of the VPS deposits, which, as demonstrated by Tiwari et al, is associated with grain growth [22]. This is further evidence that in-process spray parameters, which determine power and flame (and, thus, substrate) temperature, are crucially important for optimizing the process relative to deposit properties.

The studies of Castro et al and Jeng et al have shown increased hardness and indentation fracture toughness of VPS-formed $MoSi_2$ and Ta-reinforced $MoSi_2$ [28,30], which is in agreement with the results of Tiwari et al [22], where the indentation fracture toughness of VPS-formed $MoSi_2$ is found to be greater than hot-pressed $MoSi_2$ (4.7 versus 2.9 MPa $m^{1/2}$), both materials being of similar as-processed density. Castro et al also reported anistropy in fracture toughness between the spray direction and the direction parallel to the deposit surface, which is, of course, associated with the lamellar nature of the deposit [28]. It is the opinion of the authors that this anistropy, although common for most thermal spray deposits, can be diminished in VPS by promoting self-annealing during spraying. It is for this reason that no substantial anistropy in indentation fracture toughness was observed in the work of the authors and co-workers [22]. This was further confirmed by Jeng et al who showed only a small difference in indentation fracture toughness between the spray direction and the direction parallel to the deposit in VPS-formed SiC-reinforced $MoSi_2$ [30].

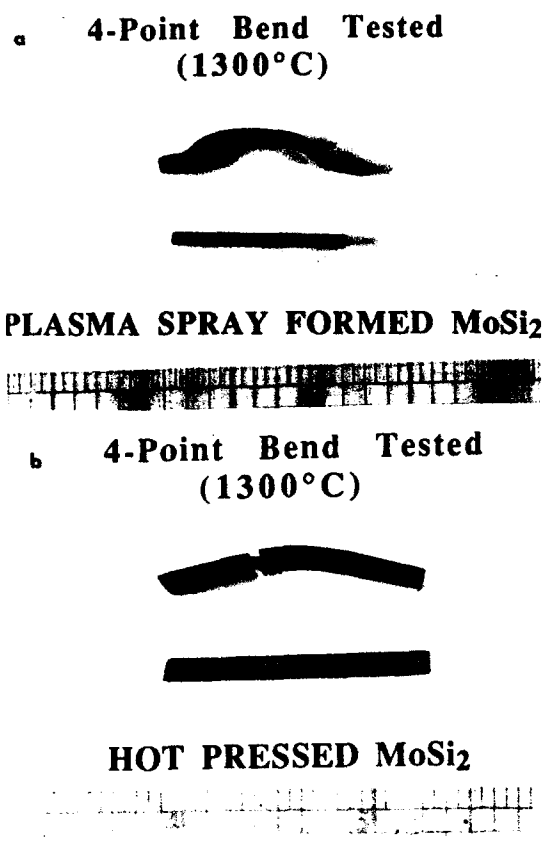


Fig.6: $MoSi_2$ test coupons before and after four-point bend testing at 1300°C. (a) VPS (b) Hot-pressed.

Elevated temperature (1300°C) four-point bend tests on VPS-formed and hot-pressed $MoSi_2$ are shown in Fig.6 [22]. Clearly, the VPS-formed specimen shows a high degree of ductility. In fact, these values may be underestimated due to limitations of the experimental conditions. The mechanism of such a high degree of plasticity may be related to a creep-like or superplastic behavior. The role of microstructure needs to be identified. This result, in conjunction with the increased room temperature toughness of the VPS $MoSi_2$ in comparison with hot pressed $MoSi_2$, suggests interesting ideas for future research.

Jeng et al have reported on creep behavior of VPS SiC/$MoSi_2$ composites at 1350°C and compared it to the creep behavior of powder metallurgy based $MoSi_2$ and SiC/$MoSi_2$ [31]. Their results show that creep resistance of the VPS composite was lower than that of the powder metallurgy counterparts. This was attributed to grain boundary sliding and amorphous SiO_2 at grain boundaries. However, no significant grain size relationship was identified which could be a potentially important factor in these materials.

Oxidation Studies

Isothermal and cyclic oxidation studies were conducted on VPS formed unreinforced and composite $MoSi_2$; Table III [22]. Unreinforced $MoSi_2$ showed no measurable mass gain after cyclic oxidation testing for 168 h. It was noted that the specimen size was small and hence the oxidation, if any, would not have been detectable at shorter testing periods. However, other researchers have reported significant mass gains during cyclic oxidation of hot isostatically pressed $MoSi_2$ at 500°C [32].

Table III: Isothermal Oxidation of VPS formed $MoSi_2$ and its Composites [22].

Material	Specific Weight Gain (mgs/sq.cm.)	
	24 hrs	96 hrs
$MoSi_2$	0	0.716
$MoSi_2$ + SiC	0	0.852
$MoSi_2$ + TiB_2	22.52	35.37

During isothermal oxidation at 1000°C, both $MoSi_2$ and SiC-$MoSi_2$ showed no mass gain after 24 h and minimal oxidation after 96 h. The mass gain for SiC-$MoSi_2$ was greater than that for unreinforced MoSi2. However, the TiB_2 reinforced $MoSi_2$ showed significant degradation under isothermal oxidation conditions. Following the isothermal oxidation tests the specimen showed the presence of a yellowish-colored oxide scale, related to the presence of TiO_2. Similar oxidation results were reported by Cook et al for oxidation behavior of $MoSi_2$, SiC-$MoSi_2$ and TiB_2-$MoSi_2$ materials processed by the XD™ process [33].

Recently, Beatrice and Worrell have conducted 1500°C and 1600°C oxidation studies on the VPS $MoSi_2$ specimens produced at SUNY-Stony Brook [34]. Preliminary results indicate comparable oxidation behavior with hot-pressed $MoSi_2$. Further analysis is underway to obtain a more definitive mechanism of the high temperature oxidation behavior of the VPS-processed $MoSi_2$.

Aqueous Corrosion

Halada et al have examined the aqueous corrosion behavior of VPS and hot-pressed $MoSi_2$ in a 4M HCl solution [35]. The electrochemical polarization curves indicated that both samples displayed a significantly higher passive current density as well as much higher breakdown potential as compared to Mo. Further examination of the surfaces using variable angle x-ray photo-electron spectroscopy revealed a dense film of $Mo_{0.05}SiO_2$. The data revealed a large passive film formed on both VPS and hot-pressed $MoSi_2$, with the passive film slightly thicker (42Å vs 34Å) for the hot-pressed specimen. These results indicate excellent aqueous corrosion resistance of $MoSi_2$.

SUMMARY AND CONCLUSIONS

The investigations described in this review demonstrate the capabilities of vacuum plasma spray to process near-net, free-standing structures of refractory silicide intermetallics. The process enables the fabrication of dense, monolithic and composite structures. The high temperature plasma flame offers an ideal route for one-step processing of these refractory intermetallics and their composites. The unique attributes of plasma spraying in its inherent versatility offers the potential for processing continuous, discontinuous and laminated composites. The properties of the VPS formed silicides and silicide composites are promising, although substantial improvements in room temperature fracture toughness is still wanting. Further work is required to address the critical aspects of process-structure-property relationships, especially as it relates to the deposit formation, rapid solidification and metastable microstructures during VPS processing. The oxidation and aqueous corrosion behavior of the VPS formed silicides are excellent, which suggests possible applications as coatings against environmental degradation.

REFERENCES

1. A.K.Vasudevan and J.J.Petrovic, Mat.Sci. & Eng., **A155**, 1 (1992).
2. P.J.Meschter and D.S.Schwartz, J. Metals, **11**, 52 (1989).
3. W.S.Gibbs, J.J.Petrovic and R.E.Honnell, Ceram. Eng.Sci. Proc., **8(7-8)**. 645 (1987).
4. F.D.Gac and J.J.Petrovic, J.Am.Ceram.Soc., **68(8)**, C-200 (1985).
5. J.M.Yang, W.Kai and S.M.Jeng, Scripta Met. **23**, 1953 (1989).
6. E.Fitzer and W.Remmele, Proc. 5th Int. Conf. on Comp. Matls. edited by W.C.Harrigan Jr., J.Strife and A.K.Dhingra (The Metallurgical Society, PA, 1985), pp.515-530.
7. C.C.Koch, Int. Materials Reviews, **33(4)**, 201 (1988).
8. D.Apelian in Plasma Processing and Synthesis of Materials, edited by J.Szekely and D.Apelian (Mater.Res.Soc.Proc. **30**, Pittsburgh, PA 1984) pp. 91-100.
9. M.R.Jackson, J.R.Rairden, J.S.Smith and R.W.Smith, J.Metals, Nov. (1981) 23.

10. A.M.Johnson, J.S.Kelm, R.W.Smashey, D.V.Rigney and T.G.Wakeman, Rapid Solidification Processing - Priniciples and Technologies III, Edited by R.Mehrabian (Conference Proceedings, Gaithersburg, MD 1982) pp. 650-661.
11. A.M.Ritter and M.R.Jackson, Rapid Solidification Processing - Priniciples and Technologies-III, Edited by R.Mehrabian (Conference Proceedings, Gaithersburg, MD 1982) pp. 270-275.
12. K.M.Chang, A.I.Taub and S.C.Huang, High Temperature Ordered Intermetallics, edited by C.C.Koch,C.T.Liu and N.S.Stoloff (Mat.Res.Soc.Proc.**39**,Pittsburgh,PA 1985)pp.335-342.
13. A.I.Taub, M.R.Jackson, S.C.Huang and E.L.Hall in Rapidly Solidified Alloys and their Mechanical and Magnetic Properties edited by B.C.Giessen, D.Polk and A.I.Taub (Mat.Res.Soc.Proc. **58**, Pittsburgh, PA, 1986) pp.389-394.
14. R.Tiwari, H.Herman, S.Sampath and B.Gudmundsson, Mat.Sci. and Eng. **A144**, 127 (1991).
15. S.Sampath and H.Herman, Thermal Spray Technology - New Ideas and Processes, edited by D.L.Houck (Proceedings of National Thermal Spray Conference,Cincinnati, OH 1988) pp1-8.
16. S.Safai and H.Herman, Thin Solid Films **45**, 295 (1977).
17. K.Murakami, T.Okamoto, Y.Miyamoto and S.Nakazono, Mat.Sci. and Eng., **A117**, 207 (1989).
18. S.Sampath and H.Herman, J. Metals, **25(7)**, 42 (1993).
19. R.Henne and W.Weber, High Temperatures - High Pressures **14**, 237 (1982).
20. R.Henne and W.Weber, High Temperatures - High Pressures **18**, 232 (1986).
21. R.Tiwari, H.Herman and S.Sampath, High Temperature Ordered Intermetallics, edited by (Mat.Res.Soc.Proc. **213**, Pittsburgh, PA, 1991) pp.807-813.
22. R.Tiwari, H.Herman and S.Sampath, Mat.Sci. and Eng. **A155**, 95 (1992).
23. R.G.Castro, R.W.Smith, A.D.Rollet and P.W.Stanek, Mat.Sci, & Eng., **A155**, 101 (1992).
24. A. Ohmori and M.Fukuoka in Thermal Spray Coatings: Research, Design and Applications, edited by C.C.Berndt and T.F.Bernecki (Proceedings of National Thermal Spray Conference, Anaheim, CA, 1993) pp.433-437.
25. T.E.Mitchell, R.G.Castro, J.J.Petrovic, S.A.Maloy, O.Unal and M.M.Chadwick, Mat.Sci. & Eng. A155, 241 (1992).
26. K.G.Shaw, J.A.Trogolo and T.Moses in Powder Production and Spray Forming, edited by J.M.Capus and R.M.German, (Advances in Powder Metallurgy & Particulate Materials, Vol.1, APMI, Princeton, NJ 1992) pp. 363-375.
27. A.B.Gokhale and G.J.Abbaschian in Binary Alloy Phase Diagrams, edited by T.B.Massalski (ASM International, Materials Park, OH 1986).
28. R.G.Castro, R.W.Smith, A.D.Rollet and P.W.Stanek, Scripta Met. **26**, 207 (1992).
29. D.E.Alman, K.G.Shaw, N.S.Stoloff and K.Rajan, Mat.Sci.&Eng. **A155**, 85 (1992).
30. Y.L.Jeng, E.J.Lavernia, J.Wolfenstine, D.E.Bailey and A.Sickinger, Scripta Met. **28**, 453 (1993).
31. Y.L.Jeng, E.J.Lavernia, J.Wolfenstine, D.E.Bailey and A.Sickinger, Scripta Met. **29**, 107 (1993).
32. P.J.Meschter, Met.Trans. A, **23A**, 1763 (1992).
33. J.Cook, R.Mahapatra, E.W.Lee, A.Khan and J.Waldman, Ceram.Eng.Sci.Proc., **12(9-10)** 1656 (1991).
34. P.Beatrice and W.Worrell, (private communication).
35. G.P.Halada, C.R.Clayton, H.Herman, S.Sampath and R.Tiwari, to be published in Proceeding of the Electrochemical Society Meeting, Honolulu, 1993.

Fabrication and Testing of Plasma-Spray Formed $MoSi_2$ and $MoSi_2$ Composite Tubes

R.G. Castro*, J.R. Hellmann**, A.E. Segall** and D.L. Shelleman**
*Los Alamos National Laboratory, Materials Division, Los Alamos, NM 87545
**Pennsylvania State University, Center for Advanced Materials, University Park, PA 16802

ABSTRACT

Plasma-spray forming has been used to fabricate thick-wall tubes of $MoSi_2$ and $MoSi_2$ containing concentric layers of Al_2O_3. This process is being investigated as a potential fabrication method for producing tubular components of $MoSi_2$ and $MoSi_2$ composites for use in high temperature fuel-burner applications. Results will be reported on the spray forming method used to produce tubes of various sizes. The room temperature strength of pure $MoSi_2$ tubes in the as-deposited condition, and after heat-treating at 1500 °C for 2 hours in vacuum, will also be reported. The strength of plasma sprayed $MoSi_2$ tubes were measured via diametral compression of O-ring and C-ring sections in air at room temperature. Qualification of the strength distribution was based on Weibull statistical theory.

INTRODUCTION

Various processing methods are currently under investigation for producing and synthesis $MoSi_2$ and $MoSi_2$ composites [1]. In many cases, conventional powder consolidation approaches are being utilized to produce dense shapes of $MoSi_2$ and $MoSi_2$ composites for testing and evaluation at high and low temperatures. Very little attention is currently focused on extending these processing/manufacturing techniques beyond small scale laboratory operations to the actual fabrication of prototype/near-net shape components. In order to show viability of $MoSi_2$ for industrial applications, prototype components will need to be fabricated for on-site industrial testing.

Plasma-spraying of $MoSi_2$ has been shown to be a viable processing method for producing high density deposits of $MoSi_2$ with the processing flexibility to manufacture discontinuous [2,3,4], continuous [5], and in situ [6,7] reinforced composites of $MoSi_2$. This processing technology offers a number of important advantages such as combined melting, solidification and consolidation all in one processing step, fine-grained microstructures, chemical homogeneity and the capability for near-net shape manufacturing.

In this study, thick-walled tubes of $MoSi_2$ and $MoSi_2$ containing concentric layers of Al_2O_3 were fabricated using the plasma-spray forming process. Various tube sizes, and tubes with composite microstructures intentionally graded through the tube wall, were produced to demonstrate the flexibility of this process. Discussions will focus on the fabrication results and the strengths of $MoSi_2$ tubes in the as-sprayed condition and after elevated temperature exposure at 1500°C for 2 hours in vacuum.

EXPERIMENTAL PROCEDURE

Plasma-spray forming

Plasma-spray forming of the $MoSi_2$ and $MoSi_2/Al_2O_3$ tubes were done using the low pressure plasma spray chamber at Los Alamos National Laboratory. This chamber is equipped with an SG-100 Plasmadyne torch and duel powder feeding capabilities for spraying alternate

Mat. Res. Soc. Symp. Proc. Vol. 322. ©1994 Materials Research Society

layers of $MoSi_2$ and Al_2O_3. The $MoSi_2$ powder used in this investigation was purchased from CERAC Inc. The powder had a purity of 99.5% with an average particle size of 65 μm. X-ray diffraction analysis confirmed the presence of tetragonal $MoSi_2$ with a trace of Mo_5Si_3. The oxygen content of the powder was approximately 1600 ppm. METCO-105 Al_2O_3 powder, with a particle size range of 5 to 20μm, was used to produce the reinforcing Al_2O_3 layers. Parameters used to produce the spray formed $MoSi_2$ and $MoSi_2/Al_2O_3$ tubes are given in Table I.

TABLE I. Parameters used for plasma-spray forming $MoSi_2$ and $MoSi_2/Al_2O_3$ tubes

Parameters	Values
Amps (A)	600
Volts (V)	36
Plasma Gas (slm)	25-Ar
Auxiliary Gas (slm)	25-He
Powder Gas (slm)	10-Ar
Feed rate (g/min)	7.6
Spray distance (cm)	15.24
Chamber pressure (torr)	450
Anode/Cathode	145/129
Rotation (rpm)	500
Substrate translation (ipm)	39

The starting powders were deposited on graphite rods which were used as sacrifical mandrels. Graphite rod sizes ranging from 6.35mm to 22.2mm were used to produce $MoSi_2$ and $MoSi_2/Al_2O_3$ tubes, with tube wall thicknesses ranging from 2.00mm to 7.00mm. Following spray forming, the graphite rods were drilled out and the remaining graphite was removed by oxidation in an air furnace at 800°C.

Room temperature testing of $MoSi_2$ tubes

The room temperature tube strength of plasma-sprayed $MoSi_2$ was determined by testing "O"-ring and "C"-ring samples sectioned from spray formed tubes of approximately 15.24cm in length with an inside diameter of 6.35mm and a outside diameter of 9.00mm. Machining procedures to produce the O-ring and C-ring samples for room temperature strength testing are given in reference [8]. The samples were tested under two different conditions, (1) the as-sprayed condition and (2) after vacuum heat-treating at 1500°C for 2 hrs. Specimens were loaded in diametral compression in order to sample the flaw populations contribution to failure at the inner and outer tube surfaces. Strength testing was performed at room temperature in air on an Instron testing machine equipped with an 890N (200lb) compression load cell. Prior to loading, a small piece of Al_2O_3 felt (1.6mm thick) was placed between the re-crystallized alumina loading rams and the specimens. The alumina felt was used to redistribute the load under the loading rams. A small preload 1.78N (0.4lb) was used to hold the specimens in place prior to loading to failure. All specimens were loaded at a strain rate of 3.13×10^{-4}/sec. Based on the peak load at fracture, and the specimen dimensions, the maximum stress at fracture was calculated and used to perform Weibull statistical analysis of the strength distributions. Optical and scanning electron microscopy was used to evaluate the microstructures of the as-sprayed and annealed O-ring and C-ring samples, and their fracture surfaces after testing. Density measurements were conducted using water immersion.

RESULTS AND DISCUSSION

$MoSi_2$ and $MoSi_2/Al_2O_3$ tubes

Examples of tubes fabricated by the plasma-spray forming process are given in Figure 1. The various lengths and wall thicknesses of the tubes in this figure demonstrates the flexibility of plasma-spray forming for producing tubular products. Cross-sections of each tube, which were imaged by scanning electron microscopy (SEM), are given in Figure 2. The $MoSi_2/Al_2O_3$ composites are comprised of concentric ring microstructures (Figures 2 (b) and (c)) which were produced by alternating between $MoSi_2$ and Al_2O_3 powder feeders during the spray-forming process. Figure 2 (b) shows a uniform spacing of $MoSi_2$ and Al_2O_3 layers through the wall thickness of the tube. The variation in the Al_2O_3 and $MoSi_2$ layer thicknesses in Figure 2 (c) was intentionally done to grade the tube cross-section from thicker $MoSi_2$ layers in the center regions of the tube to thinner $MoSi_2$ layers on the outer regions of the tube, with the outer tube surface eventually coated with a thick layer of Al_2O_3 (not shown on this tube). Fabrication of tubes with this type of graded/layered microstructure is under investigation for potential applications which require O_2 gas injection on the inside diameter of the tube and liquid metal compatibility on the outside diameter of the tube. During tube fabrication, cracking was observed along the length of the spray-formed tube. The crack/microstructure interactions and crack propagation that occurred along the $MoSi_2$ layer is shown in Figure 3 (a). Cracks were observed to have propagated through the outside three layers of the tube but did not extend through the thickness of the tube. The outside features of the tube showed an "onion skin" effect where the outside three layers separated from the tube, Figure 3 (b). The electron backscattered image in Figure 3 (b) shows cracks terminating and separating along the $MoSi_2$ layer. Crack propagation along the $MoSi_2$ layer (as opposed to the interface or Al_2O_3 layer) may result from the lower fracture toughness of the $MoSi_2$ layer (3.0 MPa $m^{1/2}$) when compared to Al_2O_3 (5.0 MPa $m^{1/2}$). Cracks were not observed in the $MoSi_2/Al_2O_3$ tubes which were fabricated with uniform $MoSi_2$ and Al_2O_3 layer thicknesses, Figure 2 (b).

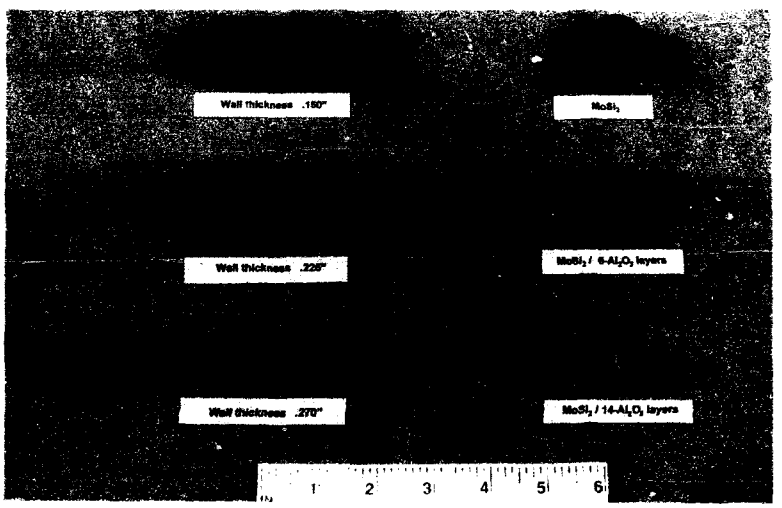


Figure 1. Photograph of plasma-spray formed tubes of $MoSi_2$ and $MoSi_2$ containing alternating layers of Al_2O_3.

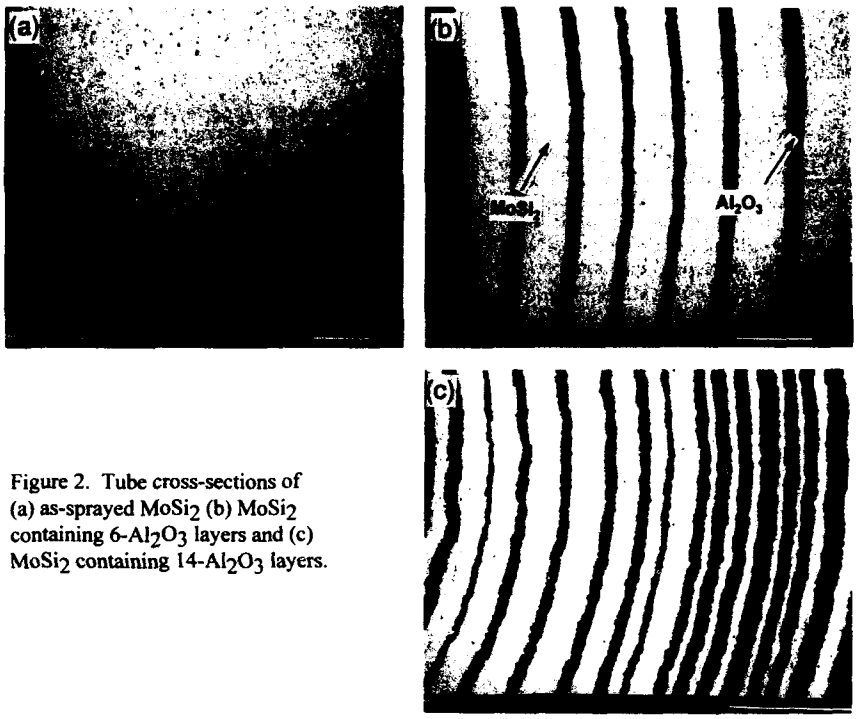


Figure 2. Tube cross-sections of (a) as-sprayed $MoSi_2$ (b) $MoSi_2$ containing 6-Al_2O_3 layers and (c) $MoSi_2$ containing 14-Al_2O_3 layers.

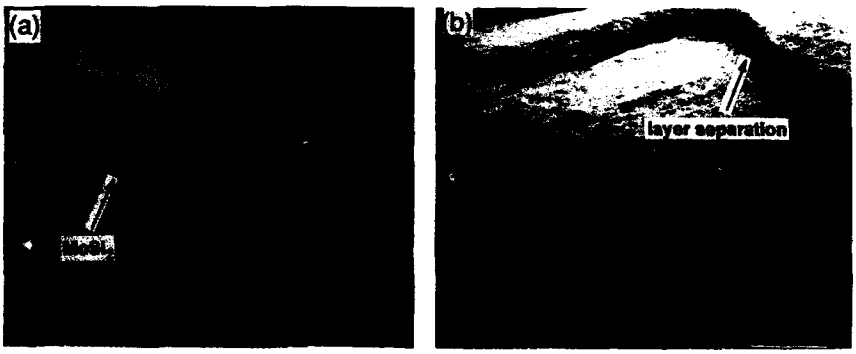


Figure 3. Crack/microstructure interactions in $MoSi_2/Al_2O_3$ tubes. (a) crack propagation along $MoSi_2$ layer (b) layer separation on outside surface of the tube.

"O"-ring and "C"-ring test results

Table II. summarizes the specimen geometry, Weibull characteristic strength (strength at 63% failure probability; σ_o) and modulus (m) for the as-sprayed and heat-treated $MoSi_2$ tubes. The heat-treated samples exhibited significantly higher characteristic strength in both the C-ring and O-ring samples then did the as-sprayed material. The increased strength can be attributed to the increase in relative density from 91% to 95% after heat-treating. Fractography revealed that in all instances failure initiated from residual porosity which intersected the sample surfaces. Interestingly, although the C-ring and O-ring strengths are essentially equivalent in the as-sprayed condition, the C-ring strength is significantly larger then the O-ring strength after heat-treatment. This suggests that the flaw population on the inner and outer tube walls are modified by heat-treatment, and is the topic of studies currently under way.

Table II. Specimen geometry, Weibull characteristic strengths and modulus for as-sprayed and heat-treated $MoSi_2$.

MATERIAL	SPECIMEN GEOMETRY	# OF SPECIMENS	WEIBULL MODULUS LR[b]	WEIBULL MODULUS ML[c]	CHARACTERISTIC[a] STRENGTH (MPa*m) LR[b]	CHARACTERISTIC[a] STRENGTH (MPa*m) ML[c]
AS-SPRAYED	C-RINGS	10	$12.6^{18.9}_{8.4}$	$13.0^{17.6}_{7.2}$	$141.1^{147.4}_{135.1}$	$141.0^{148.4}_{134.2}$
	O-RINGS	10	$14.0^{21.6}_{9.3}$	$13.6^{18.4}_{7.5}$	$136.5^{141.9}_{131.3}$	$136.6^{143.4}_{130.3}$
H.T.1500°C 2HR.	C-RINGS	10	$8.2^{12.3}_{5.5}$	$10.9^{14.8}_{6.0}$	$306.2^{327.3}_{286.5}$	$303.1^{322.2}_{285.7}$
	O-RINGS	10	$8.3^{12.5}_{5.5}$	$8.0^{10.8}_{4.4}$	$225.8^{241.2}_{211.4}$	$226.0^{245.6}_{208.5}$

a- Strength at a 63% failure probability.
b- Linear Regression Analysis [9]
c- Maximum Likelihood Analysis [10]

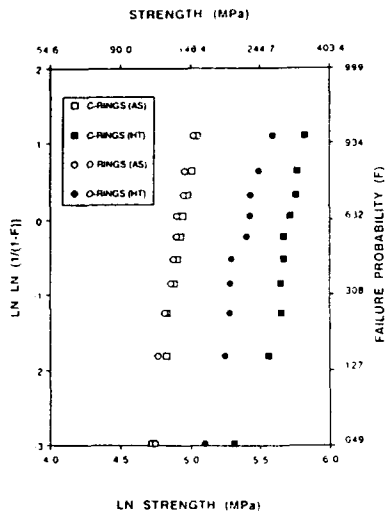


Figure 4. Room temperature Weibull strength distributions for both as-sprayed (AS) and heat-treated (HT) $MoSi_2$ C-ring and O-ring specimens.

A graphical representation of the experimentally obtained strength distributions for both the as-sprayed (AS) and heat-treated (HT) material is given in Figure 4. All strength distributions tend to be well behaved (no outliers were identified) which suggests that single flaw populations are present.

SUMMARY

Plasma-spray forming was used to fabricate tubular $MoSi_2$ and $MoSi_2/Al_2O_3$ layered composites of various wall thicknesses and lengths. The feasibility of initially grading the Al_2O_3 layer thickness and spacing through the tube wall was demonstrated. However cracking was observed in the outer $MoSi_2$ layers.

The strengths of plasma-spray formed $MoSi_2$ tubes were measured via diametral compression of C-ring and O-ring sections in both the as-sprayed and after heat-treatment at 1500 ^{0}C for 2 hrs in vacuum. Weibull analysis of the strength distributions revealed that heat treatment provided a significant strength enhancement (40-54% in characteristic strength) but at the expense of a broadened strength distribution (i.e., lower Weibull moduli for heat-treated specimens). The strength enhancement was attributed to the increased densification of the tubes from 91% to 95%. Fractographic analysis revealed that all failures intitated at the surfaces and were associated with residual porosity.

REFERENCES

1. Proceedings of the First High Temperature Structural Silicides Workshop, Gaithersburg, ML. Ed., A.K. Vasudevan and J.J. Petrovic, Elsevier Science Publishers, Amsterdam, November (1991).
2. R. Tiwari, S. Sampath and H. Herman, Mat. Res. Soc. Symp. Proc., 213 (1991) 807.
3. R.G. Castro, R.W. Smith, A.D. Rollett and P.W. Stanek, Mat. Sci. Eng., A155 (1992)95.
4. Y.L. Jeng, J. Wolfenstine and E.J. Lavernia, Scripta Metall. et Mater., 28(4) (1993) 453.
5. D.E. Alman, K.G. Shaw, N.S. Stoloff and K. Rajan, Mat. Sci and Eng., A155 (1992) 85.
6. R.G. Castro, H. Kung and P.W. Stanek, *"Reactive Plasma Spraying of $MoSi_2$ Using a Ar/10% CH_4 Powder Carrier Gas"* accepted for publication in Mater. Sci. Eng. A.(Oct 1993).
7. Z.Z. Mutasim and R.W. Smith, Proc. 4th National Thermal Spray Conf., edited by T.F. Bewecki, (ASM International, Pittsburgh, 1991) 273.
8. O.M. Jadaan, D.L. Shelleman, J.C. Conway, Jr., J.J. Mecholsky, Jr., and R.E. Tressler, J. of Testing and Evaluation, JTEVA, 19(3) (1991) 181.
9. R.B. Abernethy, J.E. Breneman, C.H. Medlin and G.L. Reinman, "Weibull Analysis Handbook," Final Report, AFWAL-TR-83-2079, 1983.
10. C.A. Johnson, and W.T. Tucker, "Advanced Statistical Concepts of Facture in Brittle Materials," Ceramic Technology for Advanced Heat Engines Project, Phase II Final Report, Draft Copy (1992).

THE APPLICATION OF REACTIVE HOT COMPACTION AND IN-SITU COATING TECHNIQUES TO INTERMETALLIC MATRIX COMPOSITES

H. Doty, M. Somerday, and R. Abbaschian, University of Florida, Dept. of Materials Science and Engineering, Gainesville, Florida

ABSTRACT

An overview of the application of the reactive hot compaction (RHC) process to fabricate various intermetallics such as silicides and aluminides is presented. Specific examples with the in-situ formation of diffusion barrier coatings on refractory metal reinforcements during RHC are also given. The processing involves blending the elemental powders with pre-treated refractory metal filaments and reactively synthesizing the mixture at elevated temperatures. During this process, the treated surfaces of the filaments react with one of the components (e.g. Al for aluminides or Si for silicides) to form in-situ a protective surface coating. The important influence of the RHC reaction sequence and rate on the consolidation of the composite are discussed. Finally, the fracture toughness of the composites are related to the various toughening mechanisms, with special emphasis on the role of the interfacial layer.

INTRODUCTION

Many intermetallics possess combinations of properties, such as high melting temperature, low density and good corrosion resistance, which designers desire for the next generation of high-temperature structural materials. These materials are needed to replace current nickel- and cobalt-based superalloys in applications which require operating temperatures near and above the melting temperatures of these alloys. However, attractive properties of intermetallics are accompanied by low temperature damage tolerance, low high temperature strength and excessive creep. A large effort is underway to understand the basic mechanisms responsible for the behavior of these materials, particularly in light of the sporadic reports of ductility[1,2], superplasticity[3] and anomalous plasticity[4] in certain intermetallics. The anticipated outcome comprises a combination of alloying, processing and thermomechanical treatments to control the mechanical behavior of certain intermetallic alloy systems[2].

Among intermetallics, the silicides, especially $MoSi_2$, possess many of the properties sought in future high temperature materials. $MoSi_2$ has a melting temperature of 2030°C and a density of 6.31 g/cm^3 and has excellent high temperature oxidation resistance due to the formation of a surface coating of SiO_2 upon reaction with oxygen in the atmosphere. Monolithic $MoSi_2$ is not acceptable as a structural material for engine applications because of its room-temperature brittleness and decreased high-temperature strength. As such, it becomes necessary to toughen the material below its DBTT (at $\approx$1000°C), while also improving its high

Mat. Res. Soc. Symp. Proc. Vol. 322. ©1994 Materials Research Society

temperature strength. Alloying and addition of thermomechanically compatible reinforcements to the matrix are two possible means to achieve this goal.

One method of alloying involves solution strengthening of $MoSi_2$ with WSi_2. WSi_2 has the same crystal structure and lattice parameters as $MoSi_2$, and the two silicides form solid-solution alloys. In a study by Petrovic and Honnell of $MoSi_2$/SiC composites[5], materials made with a matrix of 50 mol% $MoSi_2$-50 mol% WSi_2 alloys showed an improvement in high temperature yield strength over monolithic $MoSi_2$ matrix composites. Schwarz et al.[6] also observed improved mechanical properties in $MoSi_2$-WSi_2 alloys. In this work, elemental Mo, W, and Si powders were mechanically alloyed in the proper proportions to form in situ solid solutions. These displayed a high temperature yield strength of approximately 175 MPa at 1200°C, seven times higher than that of monolithic $MoSi_2$.

Alternatively, other researchers are developing compositing schemes to compensate for the brittle nature of silicides via different combinations of energy dissipating mechanisms which become activated during fracture. Intermetallic matrix composites (IMCs) are commonly divided into two broad categories based on the nature of the reinforcement; (a) ductile reinforced IMCs or (b) brittle reinforced IMCs. In each group, there are different processing methods of fabrication for both natural and artificial composites. In general, natural composites are systems which form the matrix and reinforcement during processing from precursor materials, such as directional eutectic solidification, as such the composite components are thermodynamically compatible. Artificial composites, on the other hand, require separate preparation of the reinforcement and the matrix followed by their combination and are generally not thermodynamically stable, especially at elevated temperatures[7]. This commonly necessitates the application of diffusion barriers at the interface to minimize chemical interactions.

The mechanism or mechanisms which dominate during fracture in a given composite system depends on the geometry, rate and magnitude of loading, the elastic properties of the matrix and reinforcement and the nature of bonding and roughness of the interface. Nevertheless, the dominant energy dissipation mechanism during fracture is usually quite different in IMCs with ductile reinforcements as compared to brittle reinforcements, although there is a large area of overlap in their behavior. In addition, the dominant mechanism can change locally as a crack propagates through the microstructure[8]. Figure 1 schematically shows the operation of crack bridging, crack front debonding, wake debonding and fiber pullout. For a more complete description, the reader is referred to descriptions of fiber pullout[9,10], crack bridging[9,10,11,12,13], residual stress[14], crack blunting[8,12], interfacial debonding[8,10,11], multiple matrix cracking[8] and microcracking[8], given in the literature.

FABRICATION TECHNIQUES

The high melting temperatures of intermetallics and the associated increased chemical reactivities limit the availability of suitable container materials for the processing of intermetallic composites from the molten state. In addition, the high processing temperatures cause extensive reaction between the matrix and the reinforcement. Nevertheless, some investigators have achieved success in producing IMCs via melt infiltration processes[15], electromagnetic levitation[16] and directional solidification of eutectic alloys[7,18,19,20,21].

The most general success in producing intermetallic matrix composites has come in the powder processing area. Initially these materials were produced via sintering of pre-alloyed powders formed by a gas-atomizing technique or by crushing and ball milling arc-method ingots.

More recently, due to the lack of availability of pre-alloyed powders and various processing advantages, other powder processes such as self-propagating high-temperature synthesis and reactive hot compaction have been developed to produce a wide array of IMs and IMCs[7,22,23].

Self-propagating high-temperature synthesis (SHS) is the term used to describe a process in which reactants, usually elemental constituents, when ignited, spontaneously transform to products due to the exothermic heat of formation. Both reactants and products are condensed phases. Several other terms are also applied to this process, such as gasless combustion synthesis, self-propagation combustion and self-sustaining synthesis. SHS has received considerable attention as an alternative to conventional powder metallurgy (PM) and ceramic processing due to several advantages. These potential advantages include lower energy consumption resulting from less heat input and shorter processing times, lower capital investment resulting from process simplicity, and higher product purity due to less reaction with the processing environment. The steps involved in an SHS process, schematically shown in Figure 2, are elemental powder preparation, cold compaction, and ignition/combustion. At this point, the formation of the product composition is complete although there are generally unacceptably high levels of porosity.

The study of utilizing exothermic solid-solid reactions for the production of refractory compounds such as oxides nitrides and borides has been reported by former Soviet researchers for over two decades[24]. Others have reported the successful fabrication of intermetallics such as $MoSi_2$[25,26] other silicides such as Mo_5Si_3, Ti_5Si_3 and $ZrSi$[27,28] and various aluminides, notably $NbAl_3$[7,29], $NiAl$[22,30,31,32], Ni_3Al[31,33] and $TiAl$[34].

The SHS reaction is characterized by the relationships between the melting and boiling temperatures of the reactants and the adiabatic temperature of the reaction[35]. The adiabatic temperature is the peak temperature to which the products are raised under adiabatic conditions due to the heat evolved by the exothermic reaction. This heat drives the propagation of the combustion wave by heating the adjacent reactants. Merzhanov[35] devised a classification system to describe SHS reaction mechanism by the state of the reactants (solid, liquid or gas) at the reaction adiabatic temperature. Of the six combinations possible (the product is assumed to be solid), when the adiabatic temperature lies between the melting point of the reactants, the molten reactant spreads at a high rate throughout the compact, resulting in the highest velocity of combustion. This is also known as liquid phase sintering (LPS). Complete solid state combustion occurs when the adiabatic temperature is less than both reactant melting temperatures, resulting in the lowest combustion velocities.

SHS composites are formed by either mechanically adding the reinforcement to the reactant mixture or when the product consists of two or more materials formed from the reactants. Both of these are the basis of specific processes which have been developed to produce certain IMCs which are described in detail below.

In pure SHS, the reaction rate and the state of the product are determined by the thermodynamics and kinetics of the combustion reaction. In many cases, this occurs in an explosive manner leading to a product which, although it is of the desired composition, the physical form has been degraded by excessive heating, or it contains large amounts of porosity and must be further processed to generate the desired densification and physical form.

Reactive Hot Compaction

Reactive hot compaction (RHC) is the name given to a group of processes developed

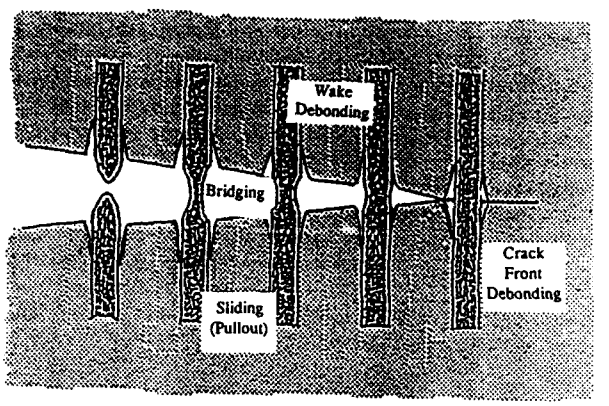


Figure 1. Schematic of fiber reinforced composite toughening mechanisms.

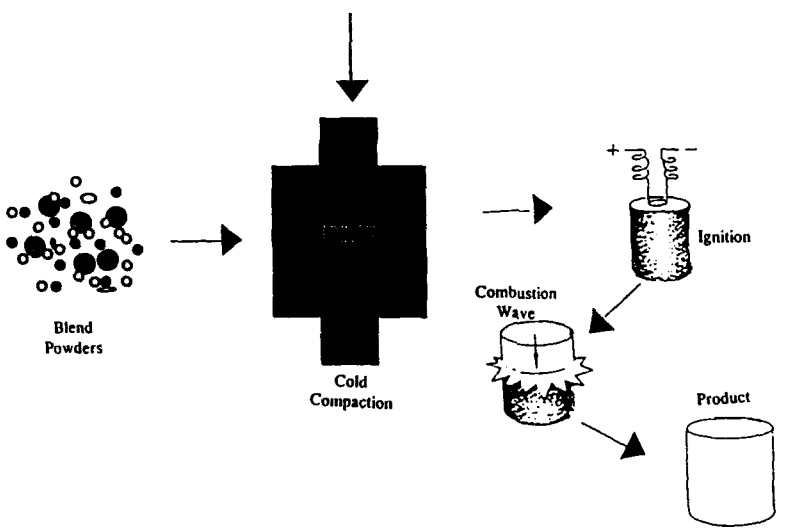


Figure 2. Typical steps in self-propagating high temperature synthesis.
(adopted from [24])

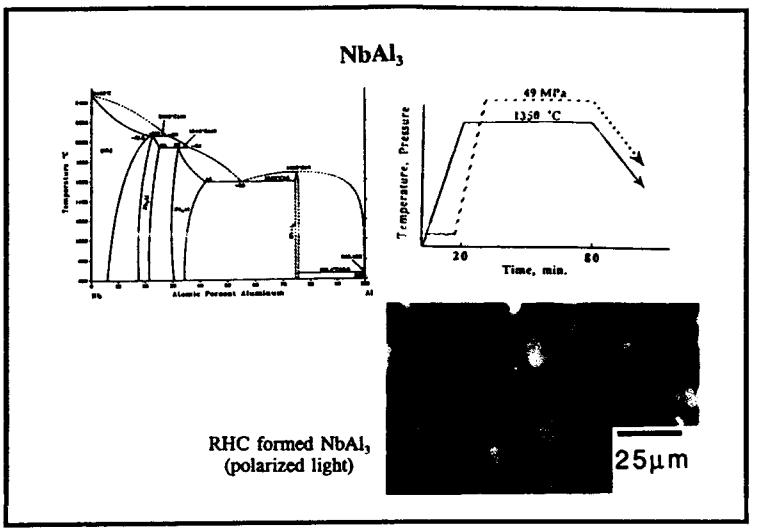
from SHS which make use of external variables to control the reaction so that a more useful product is formed. RHC is a volumetric combustion process as the reactants are heated uniformly within a die to the reaction temperature. Thus, the reaction initiates at many sites throughout the mixture of reactants. The application of pressure is utilized to aid densification and the addition of pre-reacted reactant or an inert material, such as Al_2O_3 particles has been shown to slow the reaction by absorbing some of the heat of formation of the product[32,36].

Figure 3 shows a general description of the RHC process as applied to NiAl and $NbAl_3$. The important variables used to control the reaction rate and consolidation are: the shape and size distribution of the reactants, the shape and size distribution of the inert particles (if any), green density of the compact, heating rate, maximum temperature, the timing and magnitude of the externally applied load and the atmosphere. As a subgroup of SHS, RHC shares many features in common; the reactants are blended and usually cold compacted prior to initiating the reaction. The degree of cold compaction determined as a percentage of theoretical density can have a great impact on the reaction rate and sequence. Deevi[25] has reported that for Mo + 2Si powders, increasing the green density of the cold compact from 51% to 59% of theoretical resulted in the possibility of forming $MoSi_2$ directly without any of the intermediate Mo_5Si_3 phase. It appears that increasing the density improves the interfacial contact between the reactant particles, providing more sites for the initiation of the reaction, decreasing the distances required for mass transport, thus decreasing compositional fluctuation in the product. On the other hand, higher interparticle contact also increases the effective heat transfer of the powder mass, leading to faster conduction of the heat of formation from the interface. This can lead to loss of the self-propagating characteristic in some RHC systems[7].

The effect of particle size on the structure of the product during RHC can be quite dramatic. In producing $NbAl_3$, Lu[37] found that by increasing the Nb particle size distribution from $< 10\mu m$ to 10-30μm, the as reacted microstructure contained a second phase of Nb_2Al with a central Nb core, whereas the smaller Nb particles produced only the 2 phase $NbAl_3$-Nb_2Al mixture. Subsequent annealing eliminated the Nb cores via a diffusion controlled process and increased the volume fraction of Nb_2Al.

Figure 4 shows the effect of heating rate on the temperatures and peak heights on DTA scans during RHC of $NbAl_3$[37]. Increasing the heating rate is seen to initially shift the initiation of the formation reaction to higher temperatures, then it drops back somewhat. This is probably the result of two competing processes, at very low heating rates, intermediate products have time to form via diffusion controlled solid-solid reactions, as the heating rate is raised, the initiation is shifted to higher temperatures due to the inertia of the system but coincidentally there is less time for intermediate product formation and thus reducing that barrier to the main reaction initiation. At some heating rate, here between 20°C/min. and 30°C/min., the intermediate reaction product becomes negligible eliminating this barrier to the reaction initiation. Also, increasing the heating rate increases the peak temperature. Consequently, the synthesis reaction is accelerated by higher diffusivity and shorter diffusion distances[38,39]

Philpot, et al.[40] studied the effect of heating rate on the combustion synthesis of nickel aluminides. They found two exotherms at very low heating rates, whose temperatures increased with heating rates; at higher rates (>2°C/min.) only one exotherm occurred. In both cases, the first (or only) peak occurred below the melting point of Al, indicating a solid-solid reaction. In all cases where two peaks were observed, the highest temperature of the first peak was always below the initiation temperature of the second peak. They concluded that when the heat generated by the first reaction is sufficiently high, it initiates the second (liquid phase) reaction



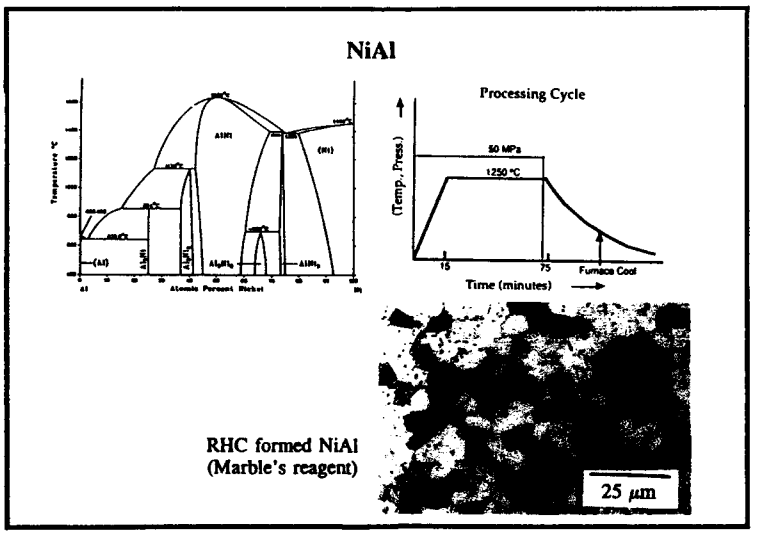


Figure 3. Typical Reactive Hot Compaction hot press schedules. A. Transient Liquid Phase. B. All solid state reactions.

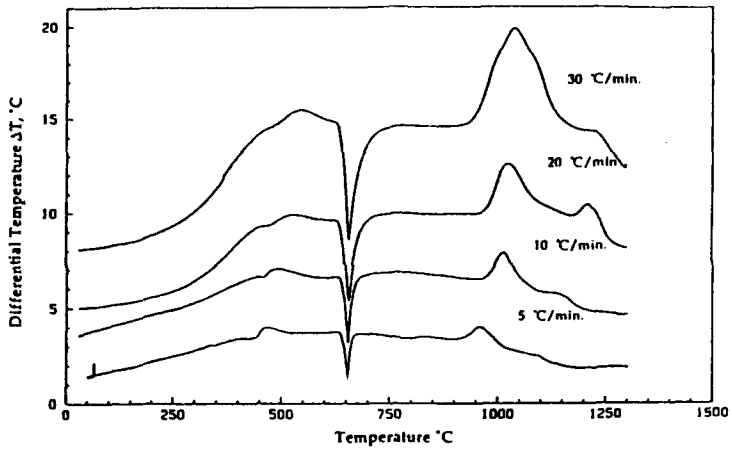
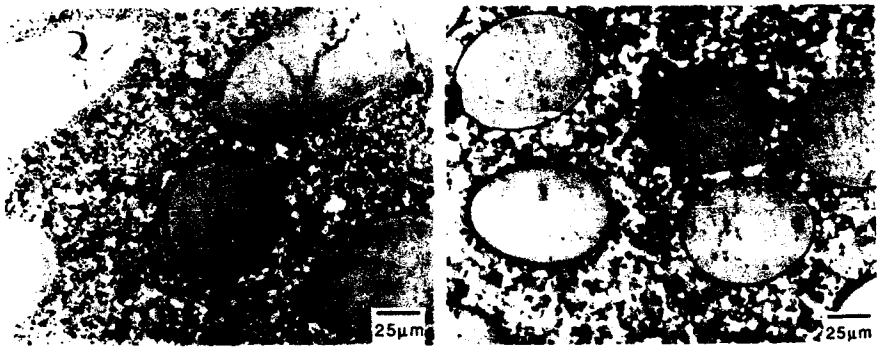


Figure 4. DTA profile of Nb and Al powder samples ($NbAl_3$ composition) performed at four heating rates indicated[37].



(a) (b)

Figure 5. Micrographs showing the effectiveness of the in-situ formed Al_2O_3 diffusion barrier in as-hot pressed $Nb/NbAl_3$ composites. (a) uncoated (b) in-situ alumina coated.

and thus changes the system from two peaks to one, which incorporates both reactions.

The effects of externally applied pressure is related to the green density effect mentioned above. In addition, the timing of the pressure application relative to the reaction sequence plays an important role in the densification of the product. It seems that the application of the pressure during the transient reactions is the most appropriate, as earlier pressurization might lead to premature or incomplete reactions, whereas pressurization after the reactions would only be hot deformation of a porous mass, requiring further solid-state diffusion to achieve full density.

Transient liquid phase sintering, or liquid phase sintering (LPS) is a variation of RHC in which one of the reactants melts, or the system goes through a low temperature eutectic at temperature below the ignition temperature during heat up[42]. This molten constituent easily flows throughout the compact by capillary forces and fills in many of the inter-particle voids aiding in densification and increasing the reaction rate. Anton[42] also reports the elimination of severe fiber damage normally associated with the consolidation of brittle fiber reinforced IMCs when LPS techniques are employed. In the process, external pressure was applied to the system at the melting temperature of Al in FP Alumina/$TaAl_3$, prior to the initiation of the intermetallic-forming reaction, followed by a further homogenizing anneal at 1200°C, presumably still under pressure. This reportedly resulted in a fully dense microstructure. Lu[7] on the other hand, waited until after the reaction was complete to apply external pressure to RHC Nb/$NbAl_3$ composites and reported less then 2% porosity in the microstructure. In DRC[32] the pressure is applied at room temperature prior to heating. This eliminates Al melting since the increased contact causes the NiAl-formation reaction to initiate at 600°C, and results in a fully dense microstructure after holding at 800°C for 30 minutes. In this reaction sequence, the microstructure is not homogeneous but contains a mixture of Ni_3Al and off stoichiometry NiAl. This is homogenized by a 30 minute anneal at 1200°C.

Solid-Solid Reactions

Solid-solid reactions occur when the adiabatic temperature is below the melting temperatures of the constituents. Thus, the reaction initiates and propagates throughout the compact without the formation of a separate liquid phase, although the intense localized heating caused by highly exothermic intermetallic reactions can give rise to local fusion zone which is quickly cooled by conduction. The presence of local fusion zones is the probable mechanism allowing 100% densification in very short processing times in the Dynamic Reactive Compaction process briefly described by Doty, et al.[32] This system normally forms by LPS as the Al melts below the reaction temperature, but the application of pressure is shown to initiate the reaction prior to Al melting.

In-situ synthesis of $MoSi_2$-SiC composites via solid state displacement reactions[30] and co-synthesis[31] have been recently reported. The former makes use of the reaction Mo_2C + Si -> $MoSi_2$ + SiC, while the latter utilizes the elemental powders to produce the same phases.

Mechanical alloying is a variation of the solid-solid reactive processing of intermetallics. In this process elemental powders are mixed at very high energy levels in a ball mixer. The impact and grinding of the balls on the powder provides the energy to initiate the reaction sporadically during the process and to reduce the particle size of the product. Bieler, et al.[43] reported mechanically alloying Ni and Al powder in liquid Nitrogen to eliminate the heat of reaction (cryomilling) and reported the formation of NiAl-AlN nanocomposites via reaction

and thus changes the system from two peaks to one, which incorporates both reactions.

The effects of externally applied pressure is related to the green density effect mentioned above. In addition, the timing of the pressure application relative to the reaction sequence plays an important role in the densification of the product. It seems that the application of the pressure during the transient reactions is the most appropriate, as earlier pressurization might lead to premature or incomplete reactions, whereas pressurization after the reactions would only be hot deformation of a porous mass, requiring further solid-state diffusion to achieve full density.

Transient liquid phase sintering, or liquid phase sintering (LPS) is a variation of RHC in which one of the reactants melts, or the system goes through a low temperature eutectic at temperature below the ignition temperature during heat up[42]. This molten constituent easily flows throughout the compact by capillary forces and fills in many of the inter-particle voids aiding in densification and increasing the reaction rate. Anton[42] also reports the elimination of severe fiber damage normally associated with the consolidation of brittle fiber reinforced IMCs when LPS techniques are employed. In the process, external pressure was applied to the system at the melting temperature of Al in FP Alumina/$TaAl_3$, prior to the initiation of the intermetallic-forming reaction, followed by a further homogenizing anneal at 1200°C, presumably still under pressure. This reportedly resulted in a fully dense microstructure. Lu[7] on the other hand, waited until after the reaction was complete to apply external pressure to RHC Nb/$NbAl_3$ composites and reported less then 2% porosity in the microstructure. In DRC[32] the pressure is applied at room temperature prior to heating. This eliminates Al melting since the increased contact causes the NiAl-formation reaction to initiate at 600°C, and results in a fully dense microstructure after holding at 800°C for 30 minutes. In this reaction sequence, the microstructure is not homogeneous but contains a mixture of Ni_3Al and off stoichiometry NiAl. This is homogenized by a 30 minute anneal at 1200°C.

Solid-Solid Reactions

Solid-solid reactions occur when the adiabatic temperature is below the melting temperatures of the constituents. Thus, the reaction initiates and propagates throughout the compact without the formation of a separate liquid phase, although the intense localized heating caused by highly exothermic intermetallic reactions can give rise to local fusion zone which is quickly cooled by conduction. The presence of local fusion zones is the probable mechanism allowing 100% densification in very short processing times in the Dynamic Reactive Compaction process briefly described by Doty, et al.[32] This system normally forms by LPS as the Al melts below the reaction temperature, but the application of pressure is shown to initiate the reaction prior to Al melting.

In-situ synthesis of $MoSi_2$-SiC composites via solid state displacement reactions[30] and co-synthesis[31] have been recently reported. The former makes use of the reaction Mo_2C + Si -> $MoSi_2$ + SiC, while the latter utilizes the elemental powders to produce the same phases.

Mechanical alloying is a variation of the solid-solid reactive processing of intermetallics. In this process elemental powders are mixed at very high energy levels in a ball mixer. The impact and grinding of the balls on the powder provides the energy to initiate the reaction sporadically during the process and to reduce the particle size of the product. Bieler, et al.[43] reported mechanically alloying Ni and Al powder in liquid Nitrogen to eliminate the heat of reaction (cryomilling) and reported the formation of NiAl-AlN nanocomposites via reaction

synthesis.

Jayashankar and Kaufman[44] also mechanically alloyed $MoSi_2$ with C to reduce the silica at grain boundaries. Weight losses during processing were reported (4% at 1550°C and below, 8% at 1700°C), although to a much lesser extent than that observed previously[45]. This study[44] suggested that above 1700°C, the weight loss is caused by the volatization of silicon from the matrix. Therefore, control of temperature and vacuum conditions could be utilized to prevent weight loss.

Costa é Silva and Kaufman[46] have also used mechanical alloying and in situ deoxidation of $MoSi_2$ to reduce the silica phase. In this study, varying amounts of aluminum were alloyed with $MoSi_2$ powders then hot pressed. Aluminum additions, up to 4.1 wt%, resulted in formation of α-Al_2O_3 out of all oxide inclusions. Increased wt% of aluminum resulted in formation of a $Mo(SiAl)_2$ phase. The volume of alumina formed was approximately 60% of that of the initial silica. These alloyed composites showed a slight increase in indentation fracture toughness (4.3 $MPa\sqrt{m}$ for the alloy as compared to 3.6 for the monolithic matrix). Srinivasan and Schwarz[47] also report fabrication of ultrafine structures in $MoSi_2$ based alloys via mechanical alloying. The structures were fully dense, but still lacked room temperature ductility.

DEVELOPMENT OF COMPOSITES VIA RHC PROCESSES

Each alloy/reinforcement system presents a unique set of thermodynamic and kinetic factors. For successful intermetallic matrix composites to be fabricated via RHC, the process must be optimized based upon the specifics of the application. These parameters not only control the reaction sequence and rate but also the density and the microstructure of the resulting IMC. Since many of the IMC systems under development are artificial composites, and thus a state of non-equilibrium likely exists between matrix and reinforcement. It is therefore necessary to control the interaction between the reinforcement and the matrix via application of a diffusion barrier coating at the interface. The interfacial coating must perform at least 3 functions. First, it must prevent the chemical interaction between the matrix and the reinforcement throughout the temperature range of exposure, both during manufacture and in service. The coating must also provide the proper degree of bonding required by the composite to aid strengthening and/or toughening since the interface has been shown to control fracture mechanisms[9,11,12]. Finally, the coating must also withstand and transfer the stresses induced by differential expansion rates of the matrix and reinforcement due to thermal cycling and mechanical loading.

An example of such an interface coating during RHC was reported for ductile filament reinforced NiAl[32] and $NbAl_3$[7]. In both of these cases, the ductile reinforcement (Nb) was preoxidized to form a surface layer of Nb_2O_5. Subsequent elevated temperature processing converted the Nb_2O_5 to Al_2O_3 prior to any discernable matrix/reinforcement interaction. Although the results were similar, the processing routes, necessitated by the individual systems were different. For $NbAl_3$, heating caused the melting of Al which spreads throughout the remaining Nb powder, providing ample opportunity for both transient liquid phase sintering to aid densification and direct contact between liquid Al and the oxidized Nb surfaces. This allowed a uniform Al_2O_3 interface to develop, followed by diffusion controlled completion of the conversion from Nb_2O_5 to Al_2O_3. In NiAl on the other hand, the synthesis reaction initiates prior to the melting of aluminum and proceeds by generating intense localized heat which may cause a very small local molten zone briefly as the reaction progresses before the heat is

conducted away. It seems that the wide solubility range of NiAl allows easy transfer of Al atoms to the Nb reinforcement to reduce the Nb_2O_5 to Al_2O_3 which is aided by the intense local heating.

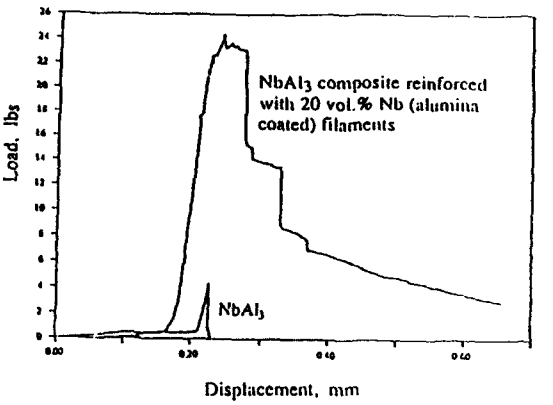
Figure 5 shows the results of high temperature annealing of RHC-produced $NbAl_3$ both with and without the in-situ diffusion barrier coating[37]. Excessive interaction is seen between the matrix and reinforcement in the absence of the diffusion barrier whereas with the coating, the integrity of the interface is maintained for 100 hrs. at 1200°C. Figure 6 gives the results of Four Point Bend Testing of chevron-notched bars of RHC $Nb/NbAl_3$ composites with and without the interfacial coating compared to monolithic $NbAl_3$. For the coated specimen, the load rises sharply, then oscillates over a relatively stable load, indicating matrix fracture. Then the load decreases in a stepwise manner indicating fiber pull-out and failure of multiple fibers in succession. The uncoated fibers, however, are characterized by a strongly bonded interface and the fibers failed in a ductile mode, due to multiple matrix cracking of the brittle ($\approx 2MPa\sqrt{m}$) $NbAl_3$ matrix, allowing the formation of a discrete "gage length" to allow ductile failure. Although the toughnesses were similar in the as-processed condition, the inherently unstable nature of the uncoated interface, as shown in Figure 5, will degrade the properties over time as the reinforcement is consumed by the reaction products.

In a study by Costa e Silva and Kaufman[41], diffusion barriers for Nb filaments in a $MoSi_2$ matrix were formed following the procedure described by Doty and Abbaschian[32]. After an oxide coating was formed on the surface of the filaments, these filaments were hot pressed with a $MoSi_2$/10.4 wt% Al mixture, forming an in situ alumina coating on the filaments. In addition, the aluminum also acted as a deoxidant in the $MoSi_2$ matrix. The analysis of these samples[41] revealed that the matrix/reinforcement interaction was substantially reduced by the coating.

MECHANICAL PROPERTIES

Monolithic silicides have been toughened by adding reinforcements to the matrix before processing. For example, SiC is frequently composited with $MoSi_2$ due to its thermodynamic stability with the matrix, in addition to its high melting point, excellent oxidation resistance, and high modulus. Several studies[48,49,50,51] have reported improvements in the fracture toughness of a $MoSi_2$/SiC composite over the base $MoSi_2$ matrix. Figure 8 shows the effect of a small addition of carbon (2 wt. %) on the fracture toughness of $MoSi_2$ as a function of temperature, compared to monolithic $MoSi_2$[46]. It was noted that the whiskers were strongly bonded to the matrix; therefore, fiber pullout was not the significant contribution to the observed increased toughness. Suggested explanations for the toughness increases[49,50] are crack deflection due to the residual stresses caused by the difference between the CTE's of $MoSi_2$ and SiC. Bhattacharya and Petrovic[49] concluded that the fracture toughness of a $MoSi_2$/SiC composite is dependent on the amount of SiC added. They found that toughness was optimized at a 20 vol% content of SiC particles. At this level, indentation fracture toughness was increased from 2.85 $MPa\sqrt{m}$ in the monolithic $MoSi_2$ to approximately 4 in the composites. Figure 9 shows the effect of increasing volume fraction SiC and TiB_2 on the yield stress as a function of temperature[52].

The addition of brittle reinforcements and mechanical alloying to silicide matrices has also been shown to reduce creep[53,54,55,56]. Two studies[53,54] have used mechanical alloying and SiC additions to improve the creep resistance. Since WSi_2 has a higher melting point and elastic



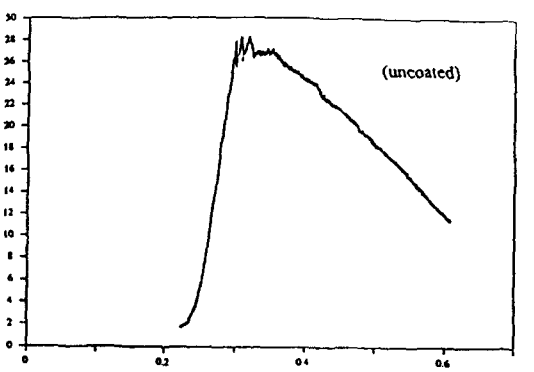
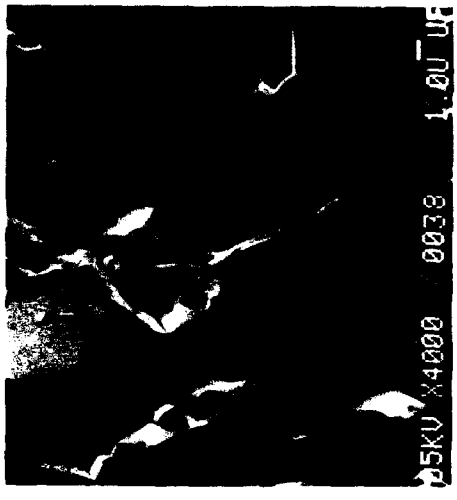


Figure 6. Typical vs. Elongation curves showing mechanical response of strongly bonded (uncoated) and weakly bonded (coated) interfaces[37].



(a)



(b)

Figure 7. SEM micrographs of fracture surfaces (a) unalloyed $MoSi_2$ and (b) $MoSi_2$ with aluminum addition[41]. The particles in (a) are SiO_2 and the particles in (b) are Al_2O_3.

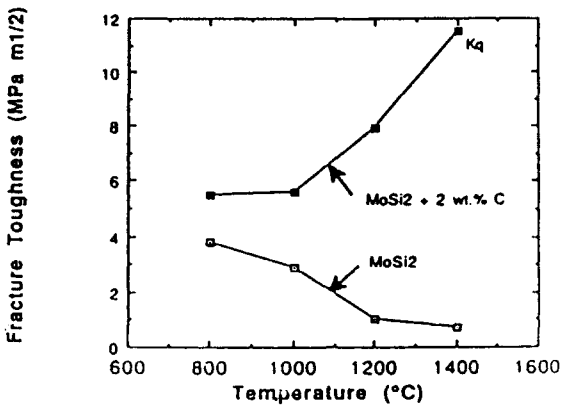


Figure 8. Fracture toughness vs. temperature of $MoSi_2$ and $MoSi_2$ with 2 wt% C[50].

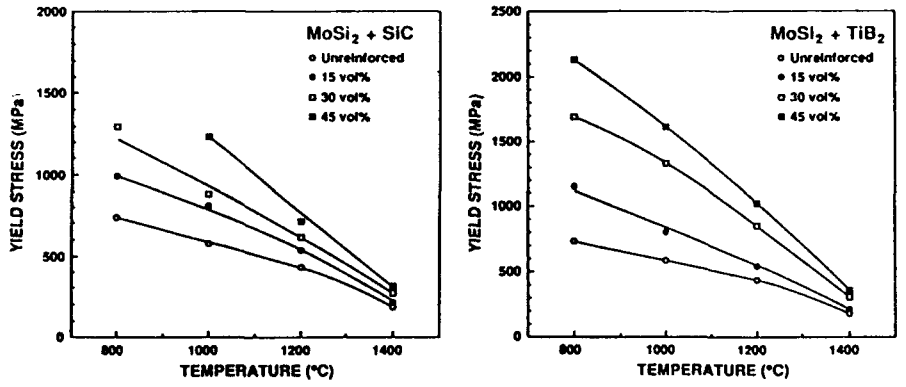


Figure 9. Compressive yield stress vs. temperature for $MoSi_2$ composites formed in situ with varying vol% of (a) SiC and (b) TiB_2[52].

modulus than $MoSi_2$, it is expected that alloying with $MoSi_2$ would decrease creep rates. This was demonstrated[54,55], although Sadananda et al.[54] found it to be more pronounced at temperatures below 1300°C. It was also shown that additions of SiC whiskers were successful in decreasing creep rates by impeding the motion of dislocations and grain boundaries, thus decreasing the deformation process in the matrix.

In recent studies[57,58,59], zirconia particles have been added to a $MoSi_2$ matrix in order to improve the room temperature fracture toughness. Metastable zirconia particles transform to a more stable crystallographic form by means of a martensitic transformation, either when cooled or when stressed in the vicinity of an advancing crack tip. The volume change associated with this transformation causes increased dislocation density and matrix microcracking, leading to increased fracture toughness in these composites. The degree of toughening is dependent upon volume fraction of zirconia, transformation zone and particle size, and alloying additions to the zirconia[57].

Petrovic et al.[57,59] used partially stabilized (with Y_2O_3) and unstabilized ZrO_2 to reinforce a $MoSi_2$ matrix. The best improvement in room temperature fracture toughness was seen in the unstabilized ZrO_2, with an improvement from 2.6 MPa$\sqrt{m}$ for pure $MoSi_2$ to 7.8 for the ZrO_2 toughened matrix[59]. They also noted the necessity of a homogeneous distribution of particles in the matrix, something which had been achieved in other composites through in situ processes[7,32]. Another study[58] showed a slight increase in material properties of $ZrO_2/MoSi_2$ composites over base $MoSi_2$ and cited grain bridging and crack branching as two likely contributions to the increased toughness.

The toughness of silicides has shown substantial improvement with the addition of ductile reinforcements in many systems including $MoSi_2$/Nb[52,60,61], Nb_5Si_3/Nb, and Cr_3Si/Cr[62]. The increased toughness is attributed to crack bridging and energy dissipated in plastic deformation of the ductile ligaments. However, the ductile reinforcements often used in silicide composites, refractory metals, possess poor oxidation resistance, a problem compounded at elevated temperatures. Therefore, the recognition of suitable coatings for these refractory metals reinforcements is necessary to reduce interphase diffusion in service.

Coatings can also promote fiber debonding from the matrix, reducing matrix constraint on the fiber, thus allowing the fiber to plastically deform as expected. If the reinforcement is not coated, the reaction with the matrix will be strong and hence the bond there will also be strong. Oxides of zirconium[52,61,63], and aluminum[8,52,60,61,63,64] have all been shown to be successful in reducing the reaction between $MoSi_2$ and Nb. A more dense oxide coating provided better diffusion protection[52,65] something achieved when a physical vapor deposited (PVD) coating was used instead of a sol-gel coating[64]. These studies[65] noted that the coatings were not effective if cracked, something which could occur if the coatings were too thick[64,65] or damaged during processing. Xiao and Abbaschian[8,52,64] have done extensive research using Al_2O_3 and ZrO_2 coatings on Nb laminates in a $MoSi_2$ matrix, investigating the resulting effects on interfacial fracture toughness and consequently composite mechanical behavior. Both oxides are stable in these composites. Moreover, Al_2O_3, Nb, and $MoSi_2$, have coefficients of thermal expansion (CTE) which correlate well, which should help prevent residual stresses during processing. ZrO_2 has a slightly higher CTE.

In their study[8,52,63], 20 vol% Nb/$MoSi_2$ composites were made in three states: uncoated Nb, Nb coated with Al_2O_3, and Nb coated with ZrO_2. In the uncoated-Nb composite, the Nb and $MoSi_2$ reacted extensively to form a significant multiphase region. In the coated-Nb samples, the width of the interaction region was reduced significantly. Also, the number and

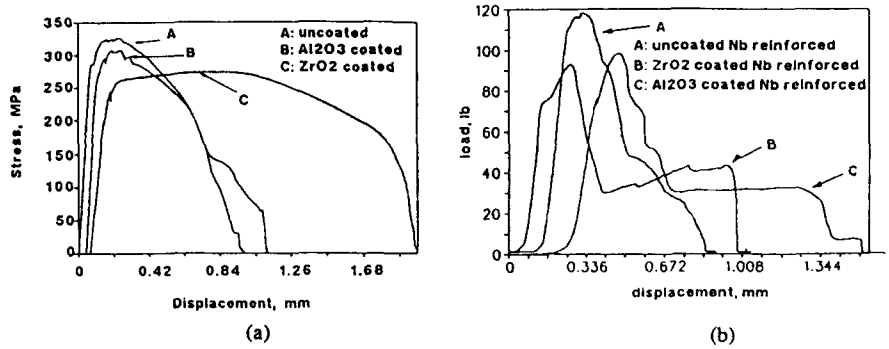


Figure 10. Results of mechanical testing performed on $MoSi_2$-20 vol% laminate Nb composites showing the effects of coating the Nb laminates[52]. (a) is stress-displacement curves from pre-cracked tensile specimens and (b) is load-displacement curves from bend specimens.

type of interphases produced were changed. The composition of the interphases indicated that the coatings effectively suppressed diffusion of molybdenum and niobium across the coatings, and, in the case of the Al_2O_3 coating, silicon as well.

As the reactions at the interface change, so does the fracture energy at the interface. This in turn will determine how much debonding occurs at the interface. Low fracture energy leads to increased debonding and therefore less reinforcement constraint. The less the reinforcement is constrained, the more it is allowed to plastically deform and continue to bridge the crack[52]. In another study by Xiao and Abbaschian[8], the oxide coating was found to reduce the fracture energy at the interface. The ZrO_2-coated Nb composite showed the least fracture energy, the uncoated the greatest, thus demonstrating the inverse relation of decohesion length to interface fracture energy.

The results of tensile testing demonstrate the relationship between the coating, debond length, and composite mechanical properties[8,52]. The uncoated foil composite systems demonstrated the highest peak load, followed by the Al_2O_3-coated, then the ZrO_2-coated foils. However, the ZrO_2-coated Nb shows the highest work of rupture, measured as the area under the load-displacement curve. These results demonstrate that as the decohesion length decreases, so does the work of rupture, but the peak load increases. Four-point bend tests were conducted on the same composites to determine fracture toughness. It was found that the coated systems show an increase in the load carried in the latter part of the curve. At this stage, the ductile reinforcement is participating heavily in the fracture process, due to interface debonding to relieve foil constraint in the matrix. As a result, the area under the load-displacement curve is much greater in the coated-Nb composites.

The amount of the constraint can be seen through examination of the characteristics of the fracture surfaces of the ruptured Nb foils[52] in the $MoSi_2$ matrix. The Al_2O_3-coated Nb showed ductile rupture while the ZrO_2-coated and uncoated Nb showed mixed mode fracture (dimple rupture and cleavage). These results seem to contradict the above logic concerning debond length and expected reinforcement ductility. One possible explanation for these results is embrittlement of the Nb foils[52] by oxygen present in the ZrO_2 coating.

The curves from the tensile and bend tests demonstrate trends in peak stress and total energy to fracture for uncoated and coated laminate composites. They seem to indicate that whether or not strong bonding is desired depends upon the criterion used for toughness[8,52]. Thus, if peak load is the criterion, strong interfaces are preferable, but if work of fracture is used, a weak interface is desirable.

SUMMARY

The fabrication difficulties associated with high temperature structural materials have been reduced significantly in the case of many intermetallics and intermetallic matrix composite by utilizing reactive processing techniques. Extremes of temperature and pressure are no longer required to fabricate IMCs and thus their deleterious effects have been greatly diminished. A variety of techniques has been developed to exploit the wide range of reaction dynamics accompanying each specific system, and to impose control over the reaction sequence or the reaction rate to facilitate the formation of a specific reaction product or to enhance densification.

Various in-situ processes have been developed to form IMCs via reactive processing. Interfacial coatings and reinforcements have been formed during processing by manipulation of the reactants and/or the reaction sequence itself.

Finally, the effect of increased control over the processing parameters has had a beneficial impact on both the integrity of the composite and the mechanical properties. The processing variables can be used to develop interfaces with desired chemical and mechanical properties.

ACKNOWLEDGEMENT

The authors gratefully acknowledge the support of the Advanced Research Project Agency (ARPA) and the Air Force Office of Scientific Research - University Research Initiative (AFOSR-URI).

REFERENCES

1. K.H. Hahn and K. Vedula, Scripta Met. **23**, 7-12 (1989).
2. J.E. Hack, J.M. Brzeski and R. Darolia, Scripta Met. **27**, 1259-1263 (1992).
3. D.F. Larhman, R.D. Field and R. Darolia, (Mat. Res. Soc. Symp. Proc. **213**, Boston, MA, 1991) pp. 603-607.
4. S.M. Barinov and V.I. Kotenev, Izvestiya Akademii Nauk SSSR. Metally. **1**, 94-97 (1986).
5. J.J. Petrovic and R.E. Honnell: Ceram. Eng. Sci. Proc., **11**, 734-744 (1990).
6. R.B. Schwarz, S.R. Srinivasan, J.J. Petrovic, and C.J. Maggiore, Mat. Sci. Eng. **A155**, 75-83 (1992).
7. L. Lu, Y.S. Kim, A.B. Gokhale and R. Abbaschian, Mat. Res. Soc. Proc. **194**, 79-87 (1990).
8. L. Xiao and R. Abbaschian, to be published in Met. Trans.
9. A.G. Evans, M.Y. He and J.W. Hutchison, J. Am. Ceram. Soc. **72** (12), 2300-2303 (1989).
10. A.G. Evans, J. Am. Ceram. Soc. **73** (2), 187-206 (1990).

11. P.A. Mataga, Acta. Metall. **37** (12), 3349-3359 (1989).
12. L. Xiao and R. Abbaschian, Met. Trans. A. **24A**, 403-415 (1993).
13. A.G. Evans and D.B. Marshall, Acta Metall. **37** (10), 2567-2583 (1989).
14. L.S. Sigl, PA. Mataga, B.J. Dalgleish, R.M. McMeeking and A.G. Evans, Acta. Metall. **36** (4), 945-953 (1988).
15. S. Nourbakhsh, H. Margolin and F.L. Liang, in Solidification of Metal Matrix Composites, edited by P. Rohatgi (TMS, 1990), pp. 103-114.
16. A.B. Gokhale, L. Lu and R. Abbaschian, in Solidification of Metal Matrix Composites, edited by P. Rohatgi (TMS, 1990), pp. 115-131.
17. J.J. Valencia, C. McCullough, J. Rosler, C.G. Levi and R. Mehrabian, in Solidification of Metal Matrix Composites, edited by P. Rohatgi (TMS, 1990), pp. 133-150.
18. D.R. Johnson, S.M. Joslin, B.F. Oliver, R.D. Noebe and J.D. Wittenberger, (Mat. Res. Soc. Symp. **273**, San Francisco, CA, 1992) pp. 87-92.
19. F.E. Heredia and J.J. Valencia, (Mat. Res. Soc. Symp. Proc. **273**, San Francisco, CA, 1992) pp. 197-204.
20. A. Misra, R.D. Noebe and R. Gibala, ibid., **273**, 205-210 (1992).
21. B.P. Bewlay, K-M. Chang, J.A. Sutliff and M.R. Jackson, ibid., **273**, 417-423 (1992).
22. K.S. Kumar, S.K. Mannan and R.K. Viswanadham, Acta Metall. Mater. **40** (6), 1201-1222 (1992).
23. B. Huang, J. Vallone, C.F. Klein and M.J. Luton, (Mat. Res. Soc. Symp. Proc. **273**, San FRancisco, CA, 1992) pp. 171-176.
24. W.L. Frankhouser, K.W. Brendley, M.C. Kieszek and S.T. Sullivan, Gasless Combustion Synthesis of Refractory Compounds. (Noyes Publications, Park Ridge, NJ, 1985), p. 10.
25. S.C. Deevi, Mat. Sci. Eng. **A149**, 241-251 (1992).
26. S.B. Bhaduri, Scripta. Met. **27**, 1277-1281 (1992).
27. T.S. Azatyan, V.M. Maltsev, A.G. Merzhanov and V.A. Seznev, Comb. Expl. Shock Waves. **15**, 35 (1979).
28. A.R. Sarkisyan, S.K. Dolukhanyan and I.P. Borvinskya, Comb. Expl. Shock Waves. **15**, 95 (1979).
29. K. Barmak, K.R. Coffey, D.A. Rudman and S. Foner, J. Appl. Phys. **67** (12), 7313-7322 (1990).
30. C.H. Henager, Jr., J.L. Brimhall, J.S. Vetrano and J.P. Hirth, (Mat.Res.Soc.Symp.Proc. **273**, San Francisco, CA, 1992)pp. 281-287.
31. D.E. Alman and N.S. Stoloff, Scripta Metall. Mater., **28**(12), 1525-1530 (1993).
32. H. Doty and R. Abbaschian, (ICCM-9 Conf. Proc. **1**, Madrid, Spain, 1993) pp.
33. R.M. German and A. Bose, Mat. Sci. Eng. **A107**, 107-116, (1989).
34. J.H. Moll, C.F. Yolton and B.J. McTiernan, Int. J.P. Met. **26** (2), 149-155 (1990).
35. J. Subrahmanyam and M. Vijayakumar, J. Mater. Sci. **27**, ?? (1992).
36. D.E. Alman and N.S. Stoloff, Int. J.P. Met. **27** (1), 29-41 (1991).
37. L. Lu, Master's Thesis, University of Florida, 1991.
38. A. Bose, B. Moore, R.M. German and N.S. Stoloff, J. of Metals. **9**, 14-17 (1988).
39. H.E. Kissinger, Analytical Chemistry. **29**, 169-177 (1957).
40. K.A. Philpot, Z.A. Munir and J.B. Holt, J. Mat. Sci. **22**, 159-169 (1987).
41. A. Costa e Silva and M.J. Kaufman, to be published in Proceedings and Fabrication of Advanced Materials for High Temperature Applications III, V.A. Ravi and T.S. Srivatsan eds.
42. D.L. Anton (Mat. Res. Soc. Symp. Proc. **120**, San Francisco, CA, 1988) pp. 57-64.
43. T.R. Bieler, R.D. Noebe, J.D. Whittenberger and J.J. Luton, (Mat. Res. Soc. Symp. Proc. **273**, SAn Francisco, CA, 1992) pp.165-170.
44. S. Jayashankar and M.J. Kaufman, J. Mater. Res. **8**, 1428-1441 (1993).
45. Stuart A. Maloy, John J. Lewandowski, and Arthur H. Heuer, Mat. Sci. Eng. **A155**, 159-163 (1992).
46. A. Costa e Silva and M.J. Kaufman, Scripta Met. **29**, 1141-1145 (1993).
47. S.R. Srinivasan and R.B. Schwarz, (Met. Pow. Ind. Fed. Conf. Proc. 7, San Francisco, CA, 1992)pp. 345-358.
48. J.M. Yang, S.M. Jeng, (Mat. Res. Soc. Symp. Proc. **194**, San Francisco, CA, 1990)pp. 139-146.
49. Arun K. Bhattacharya and John J. Petrovic, J. Am. Ceram. Soc. **74**, 2700-2703 (1991).
50. Frank D. Gac and John J. Petrovic, J. Am. Cer. Soc. **68**, C-200-C-201 (1985).
51. W.S. Gibbs, J.J. Petrovic, and R.E. Honnell, Ceram. Eng. Sci. Proc. **8**, 645-648 (1987).
52. L. Xiao and R. Abbaschian, Mat. Sci. Eng. **A155**, 135-145 (1992).
53. M. Suzuki, S.R. Nutt, and R.M. Aiken, Jr., Mat. Sci. Eng. **A162**, 73-82 (1993).

54. K. Sadananda, C.R. Feng, H. Jones, and J.J. Petrovic, Mat. Sci. Eng. **A155**, 227-239 (1992).
55. S. Bose, Mat. Sci. Eng. **A155**, 217-225 (1992).
56. S.M. Widerhorn, R.J. Gettings, D.E. Roberts, C. Ostertag, and J.J. Petrovic, Mat. Sci. Eng. **A155**, 209-215 (1992).
57. J.J. Petrovic, A.K. Bhattacharya, R.E. Honnell, T.E. Mitchell, R.K. Wade, and K.J. McClellan, Mat. Sci. Eng. **A155**, 259-266 (1992).
58. Arun K. Bhattacharya and John J. Petrovic, J. Am. Cer. Soc. **75**, 23-27 (1992).
59. J.J. Petrovic, R.E. Honnell, T.E. Mitchell, R.K. Wade, and K.J. McClellan, Ceram. Eng. Sci. Proc. **12**, 1633-1642 (1991).
60. L. Shaw and R. Abbaschian, submitted to Acta metall. mater.
61. L. Xiao, Y.S. Kim, R. Abbaschian, and R.J. Hecht, Mat. Sci. Eng. **A144**, 277-285 (1991).
62. Jan Kajuch, Joseph D. Rigney, and John J. Lewandowski, Mat. Sci. Eng. **A155**, 59-65 (1992).
63. L. Xiao and R. Abbaschian, Met. Trans. **23A**, 1-10 (1992).
64. L. Xiao and R. Abbaschian, unpublished work.
65. Michael J. Maloney and Ralph J. Hecht, Mat. Sci. Eng. **A155**, 19-31 (1992).

SINTERING OF $MoSi_2$

J.J. PETROVIC AND J.S. IDASETIMA
Materials Division, Group MTL-4, Los Alamos National Laboratory, Los Alamos, NM 87545

ABSTRACT

Despite the fundamental nature of sintering and its importance as a low cost fabrication process, little information exists on the sintering behavior of the structural silicide $MoSi_2$. The sintering of commercial $MoSi_2$ powders in the range of 1-10 μm was investigated as a function of sintering temperature, sintering time, and sintering atmosphere. Initial densities for uniaxially cold pressed powders were in the range of 47-56% theoretical. A maximum sintered density of 90% of theoretical was achieved for 1 μm $MoSi_2$ powders after sintering for 100 hours at 1600 °C in an argon atmosphere. Larger 10 μm $MoSi_2$ powders achieved lower sintered densities under these conditions. Avenues to optimize the sintering behavior of $MoSi_2$ are suggested.

INTRODUCTION

The borderline ceramic-intermetallic compound $MoSi_2$ is considered to be a promising high temperature structural material due to its combination of high melting point, superb elevated temperature oxidation resistance, brittle-to-ductile transition, and electrical conductivity [1]. Because of their high melting points, most ceramic materials are fabricated into consolidated shapes by the pressing and sintering of powders, and there has been a tremendous amount of research performed on the sintering of ceramics. Sintering is an attractive processing route because it is a simple, inexpensive processing approach of importance to commercial applications. However, somewhat surprisingly, there has been very little work performed on the sintering of $MoSi_2$ and $MoSi_2$ composites. Previous work on the sintering of $MoSi_2$ has been performed by Fitzer et.al. [2,3]. The purpose of the present investigation was to provide information on the sintering of $MoSi_2$ powders as a function of powder size, temperature, time, and sintering atmosphere.

EXPERIMENTAL

The commercial $MoSi_2$ powders employed for this study were H.C. Starck Grade A and Grade C. The Grade A material has an average particle size of approximately 10 μm, while the Grade C material has an average particle size of approximately 1 μm. The Grade A material is reported to contain 0.5 wt.% oxygen, while the Grade C contains 2.0 wt.% oxygen. These powders were uniaxially cold pressed into green bodies of dimensions 12.7 mm diameter by approximately 6.35 mm thickness at a pressure of 138 MPa. No binders were used in the green pressing. The Grade A material exhibited an average green density of

Mat. Res. Soc. Symp. Proc. Vol. 322. ©1994 Materials Research Society

56% of theoretical, while the Grade C material showed an average green density of 47% of theoretical.

A high temperature dilatometer was employed to measure the change in length of the green bodies during continuous heating to a temperature of 1550 °C. The heating rate in these dilatometer runs was approximately 3 °C/minute. Dilatometer runs were performed in atmospheres of argon, argon-6 % hydrogen, and 10^{-3} torr vacuum. Isothermal sintering runs were performed for one hour holds at temperatures of 1300, 1400, 1500, and 1600 °C, and for times of 1 hour, 10 hours, and 100 hours at 1600 °C. Heating rates for these isothermal runs were approximately 15 °C/minute. All isothermal sintering runs were performed in an argon atmosphere.

Sintered densities were measured both geometrically on the sintered specimens, and by the liquid immersion technique for porous materials described by Pennings and Grellner [4]. A water medium was employed for the immersion density measurements. Optical and SEM microscopy was employed to characterize sintered microstructures, and to detect any phases formed as a result of the sintering process.

RESULTS AND DISCUSSION

Dilatometer Results

The results of dilatometer sintering runs on the $MoSi_2$ powders are shown in Figure 1.

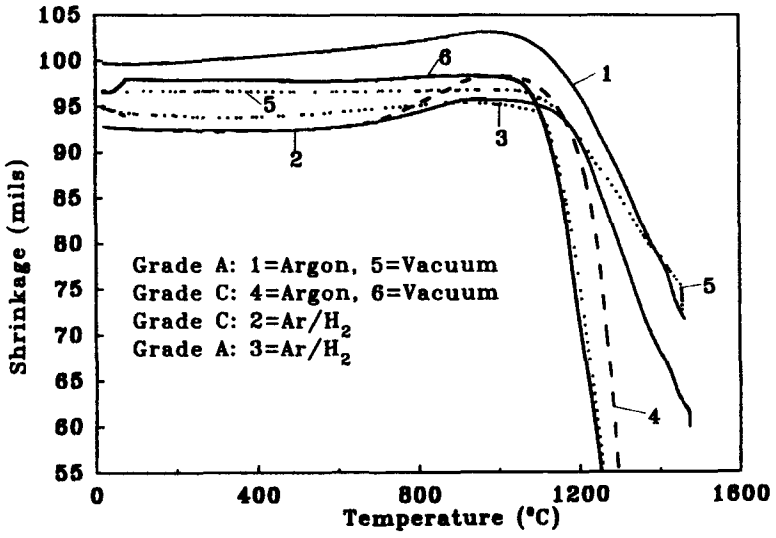


Figure 1. Dilatometer Results for Starck Grade A and Grade C $MoSi_2$ Powders

These dilatometer results clearly show that the onset of $MoSi_2$ sintering occurs at a temperature of 1100 °C. Sintering atmosphere has little effect on this initial sintering temperature. The slight increase in length observed in some of the sintering runs at approximately 1000 °C is not understood at the present time. The Grade C material exhibits a higher sintering rate than the Grade A material, due to its finer particle size. The presence of hydrogen in the sintering atmosphere appears to accelerate the rate of sintering somewhat. Faster sintering in hydrogen-containing atmospheres has also been observed previously for $MoSi_2$ [2]. A vacuum atmosphere accelerates sintering slightly for both the Grade A and Grade C materials. Fitzer et.al. [2] have reported that weight losses occur during the vacuum sintering of $MoSi_2$.

Isothermal Sintering

Isothermal sintering results are shown in Figures 2 and 3. In Figures 2 and 3, both the measured geometric % theoretical density and the measured immersion % theoretical density are plotted. Immersion densities tended to be higher than geometric densities. Generally, density increases with increasing sintering temperature, as expected. The extent of densification is significantly greater for the Grade C material as compared to the Grade A material, despite the fact that the Grade C material had the lower initial green density. For a one hour hold at 1600 °C, the maximum density attained by the Grade C material was 85% density, while the maximum density for the Grade A material was only 65% density. As shown in Figure 3, sintering time had only a secondary effect on the extent of sintering at 1600 °C. Most of the densification took place within a ten hour sintering time.

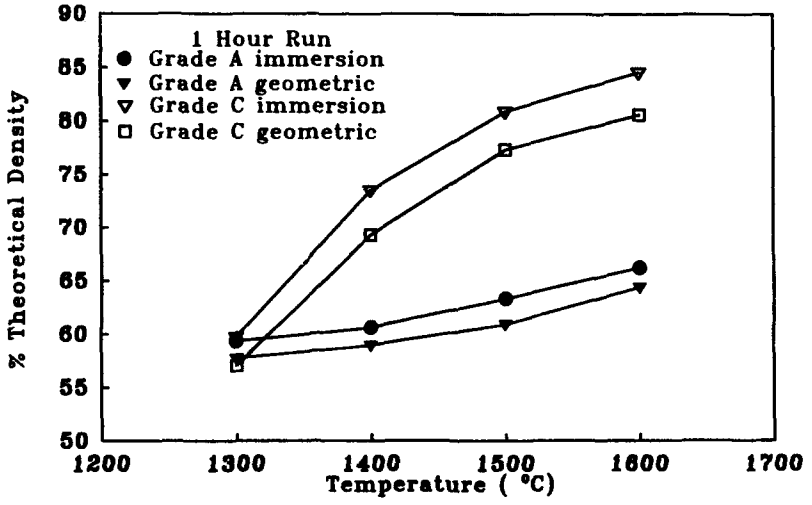


Figure 2. $MoSi_2$ Sintered Density versus Temperature

A maximum density of 90% theoretical was attained for the Grade C material after a 100 hour hold at 1600 °C. The reason for the lower immersion density value of the Grade A material at a 100 hour sintering time is not known at present.

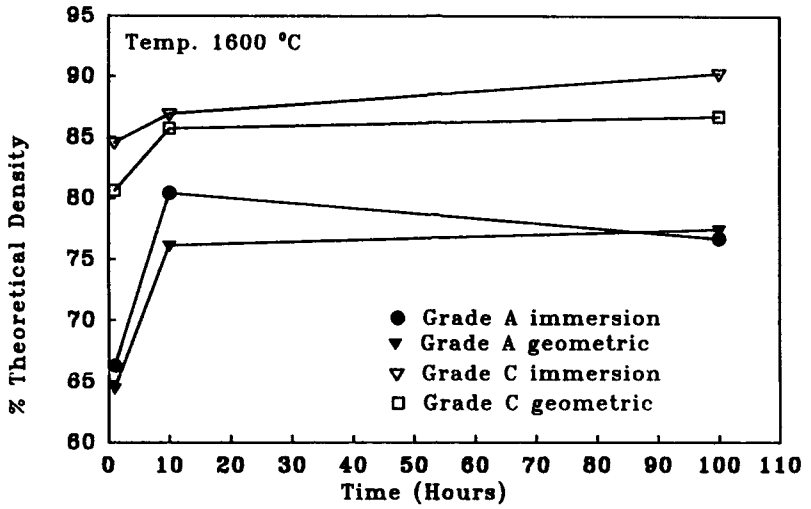


Figure 3. $MoSi_2$ Sintered Density versus Time

Sintered microstructures exhibited classical sintering features. Extensive neck formation was observed in Grade A and Grade C materials sintered for 1 hour at 1300 °C, while interconnected porosity was observed for 1 hour sintering at 1600 °C. An isolated porosity microstructure was seen in the Grade C material sintered for 100 hours at 1600 °C. Although not detected by x-ray diffraction, SEM analysis showed the presence of the Mo_5Si_3 phase in the Grade C material sintered for 100 hours at 1600 °C in argon. The formation of this phase was also noted by Fitzer et.al. [2] after sintering for 3 hours at 1700 °C in a hydrogen atmosphere. The Mo_5Si_3 phase likely results due to Si loss occurring during the sintering process.

Sintering Theory

The current state of sintering theory has been nicely summarized recently by Hansen et.al. [5]. These authors also present a combined-stage sintering model which can describe all the three stages of the sintering process. Stage 1 sintering involves the initial formation of necks between sintering particles. Stage 2 sintering is associated with extensive neck formation and the development of an interconnected network of porosity. In Stage 3 sintering, pores have become isolated from each other. In Hansen et.al., the cell sintering

geometry proposed by DeHoff [6] is employed to describe the various stages of sintering in a continuous fashion. This is coupled to a fundamental sintering model of a grain boundary intersecting a pore, which is considered to apply to all stages of sintering. The Hansen model results in the following expression for the change in length of a body during sintering [5]:

$$d \ln L/dt = (\gamma\Omega/kT)(\delta D_b \Gamma_b/G^4 + D_v \Gamma_v/G^3) \quad (1)$$

In this expression, L is the sintering specimen instantaneous length, γ is the surface energy, Ω is the atomic volume, k is Boltzmann's constant, T is absolute temperature, δ is the grain boundary diffusion width, D_b is the grain boundary diffusion coefficient, D_v is the volume difffusion coefficient, and G is the particle or grain diameter.

In Equation (1), the terms Γ_b and Γ_v are a function of scaling factors which represent specific features of the microstructure that influence the kinetics of sintering. These terms contain information that describes the driving force of the microstructure for sintering (curvature), efficiency for diffusional transport (mean diffusion distance and area available for diffusion), and the rate at which mass transport is converted to shrinkage (base to centroid distance and grain boundary area). Hansen et.al. [5] have provided estimates of these terms as a function of density during sintering.

The present sintering results for $MoSi_2$ have shown that sintering is more rapid for finer initial powder particles than for coarser particles. This is consistent with the predictions of Equation 1. At present, very little information is available concerning diffusion coefficients in $MoSi_2$. From oxidation experiments, the activation energy for Si diffusion in $MoSi_2$ is reported to be 250 kJ/mole [7,8]. From creep experiments, Sadananda et.al. [9] have indicated that the activation energy for Mo diffusion in $MoSi_2$ is in the range of 350-540 kJ/mole, and more likely closer to 350 kJ/mole. These very limited diffusion data might suggest that Mo is the slower diffusing species in $MoSi_2$, and would then control the sintering behavior of $MoSi_2$. However, at the present time this is a very tentative conclusion at best. In many ceramic materials, grain boundary diffusion often tends to dominate over volume diffusion during the sintering of ceramic powders. Currently, no grain boundary diffusion data exist for $MoSi_2$.

ASSESSMENT OF $MoSi_2$ SINTERING

The sintering of $MoSi_2$ powders begins at a temperature of 1100 ^oC. The extent of sintering increases with decreasing powder size, and shows some sensitivity to the sintering environment. Hydrogen-containing environments may promote the sintering process. A sintering temperature of at least 1600 ^oC is required to sinter 1 μm powders to density levels in the range of 85-90% theoretical density in times less than 100 hours. Larger size $MoSi_2$ powders exhibit lower levels of densification under these conditions. Silicon loss during sintering can result in the formation of an Mo_5Si_3 second phase in the sintered microstructure.

Key aspects to increasing the sintered density of $MoSi_2$ powders involve green density, sintering temperature, and sintering atmosphere. It is generally observed for ceramic

powders that, under fixed sintering conditions, the final sintered density is roughly proportional to the initial green density. Thus, increasing the green density to as high an initial level as possible is clearly desirable. This can often be achieved by increasing pressing pressures (as with cold isostatic pressing), and by employing bimodal or multimodal particle size distributions. Generally, increasing the sintering temperature promotes the level of densification much more than increasing the sintering time. Larger particle size $MoSi_2$ powders will require sintering temperatures in excess of 1600 °C, probably in the range of 1700-1800 °C. Silicon loss at these higher temperatures may lead to significant levels of in-situ Mo_5Si_3 phase in the sintered microstructures, but this may actually be desirable if the second phase formation leads to mechanical property improvements. Finally, hydrogen-containing sintering atmospheres appear to promote the sintering of $MoSi_2$, possibly by reducing silica layers present on $MoSi_2$ powders.

ACKNOWLEDGEMENTS

The authors acknowledge the Office of Naval Research for sponsorship of this research, and useful discussions with Dr. A.K. Vasudevan at ONR. One of the authors (JSI) would like to express appreciation to the Historically Black Colleges and Universities (HBCU) Program for support while at the Los Alamos National Laboratory.

REFERENCES

1. J.J. Petrovic, MRS Bulletin, **XVIII**, 35 (1993).
2. E. Fitzer, K. Reinmuth, and H. Schnabel, Arch. Eisenhuettenwas., **40**, 895 (1969).
3. E. Fitzer, Arch. Eisenhuettenwas., **44**, 703 (1973).
4. E.C.M. Pennings and W. Grellner, J. Am. Ceram. Soc., **72**, 1268 (1989).
5. J.D. Hansen, R.P. Rusin, M-H. Teng, and D.L. Johnson, J. Am. Ceram. Soc., **75**, 1129 (1992).
6. R.T. DeHoff, in Sintering and Heterogeneous Catalysis, edited by G.C. Kuczynski, A.E. Miller, and G.A. Sargent (Plenum Press, New York, 1984), pp. 23-34.
7. R.W. Bartlett, P.R. Gage, and P.A. Larssen, Trans. AIME, **230**, 1528 (1964).
8. P. Kofstad, in High-Temperature Oxidation of Metals (John Wiley & Sons, New York, 1966), p. 300.
9. K. Sadananda, C.R. Feng, H. Jones, and J. Petrovic, Mat. Sci. Eng., **A155**, 227 (1992).

COMBUSTION SYNTHESIS OF $MoSi_2$ AND $MoSi_2$-COMPOSITES.

K. MONROE, S. GOVINDARAJAN, J.J. MOORE, B. MISHRA, D.L. OLSON, and J. DISAM*. Dept. of Metallurgical and Materials Eng., Colorado School of Mines, Golden, CO 80401. *Schott Glaswerke, Mainz, Germany.

ABSTRACT

$MoSi_2$ and $MoSi_2$-composites are potential candidate materials for both high-temperature coatings and structural components. The application of combustion synthesis and hot pressing in the production of dense $MoSi_2$ and $MoSi_2$- composites, i.e., $MoSi_2$-SiC, $MoSi_2$-Mo, is currently being studied. Selection of compositions was based on oxidation resistance, thermal expansion, thermodynamic stability, and compatibility. Functionally-graded materials (FGM's) of these composite material systems are also currently being studied.

INTRODUCTION

In recent years, intermetallics have been studied because of their potential use for high temperature structural applications. Molybdenum disilicide and it's composites have been shown to be excellent candidate materials due to their high-temperature oxidation resistance[1,2] . The primary factors that have contributed to the choice of $MoSi_2$ as a matrix material for high temperature structural composites or coatings are: (1) a high melting point of around 2300K; (2) low density (6.24g/cc) when compared with nickel-based superalloys; (3) superior oxidation resistance; (4) high temperature strength; and (5) high thermal and electrical conductivity.

However, $MoSi_2$ is very brittle and exhibits low toughness at room temperature, has poor strength and creep resistance, and can also exhibit "pesting" between 673K and 873K[3]. During the last two decades, there has been a strong research effort directed towards the development of $MoSi_2$-based composites [1,2,4]. Amongst these composites, $MoSi_2$-SiC appears to offer the best combination of oxidation resistance and mechanical properties. Self-propagating high temperature (combustion) synthesis (SHS) has been used in some cases to produce these composites[5-7]. It is well established[6,7] that an exothermic reaction system becomes self propagating when $(\Delta H^\circ_{f,\,298} / C^\circ_{P,298}) > 2000$, where $\Delta H^\circ_{f,\,298}$, $C^\circ_{P,298}$ are the heat of formation (reaction) and heat capacity, respectively, of the products, e.g. $MoSi_2$.

Based on these considerations, a program for assessing different processing routes and the effects of different processing parameters on the production of $MoSi_2$, $MoSi_2$-SiC composites and functionally-graded composite materials was initiated. In order to achieve a dense product, hot pressing has been used in conjunction with simultaneous combustion synthesis. The preliminary results are discussed below.

EXPERIMENTAL PROCEDURE

Molybdenum (<10μm), silicon (<7μm) and carbon (<20μm) powders were compacted under loads varying from 454kg to 3178kg in a 13mm (diam.) die to provide a range in green density from 53% to 63%. In the case of the functionally-graded material (FGM) samples, individual

Mat. Res. Soc. Symp. Proc. Vol. 322. ©1994 Materials Research Society

layers of varying stoichiometry to provide varying ratios of $MoSi_2$:SiC were mixed and manually stacked, one above the other, prior to compaction. Three different processing routes were followed. SHS was carried out in the propagating mode in an argon-filled chamber (Figure 1) and the green pellet ignited by a tungsten coil. The ignition (T_{ig}) and combustion (T_c) temperatures were determined by a thermocouple (W-26wt%Re/W-5wt%Re) inserted in the sample as well as an infrared pyrometer. Simultaneous combustion synthesis, in which the whole pellet is heated to T_{ig} and ignites simultaneously, was also ignited using a second reaction chamber (Figure 2). A combination of simultaneous combustion synthesis and hot pressing was also carried out in a third reaction system (Figure 3). On detection of the reaction exotherm, the sample was hot pressed under an applied pressure of up to 4680psi (32.3MPa). The samples were characterized using optical and scanning electron microscopy, X-ray diffraction (XRD), and density measurements were made using immersion in water and steam techniques.

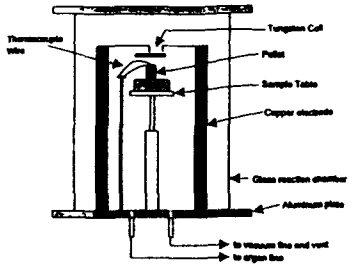


Figure 1. Schematic representation of the self-propagating combustion synthesis chamber.

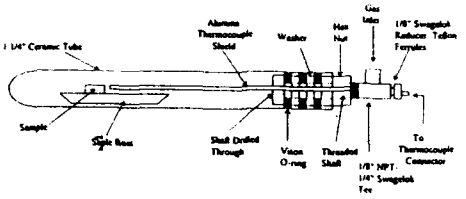


Figure 2. Schematic representation of the simultaneous combustion synthesis chamber.

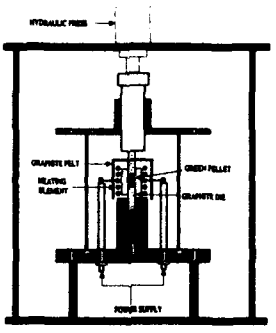


Figure 3. Schematic representation of the simultaneous combustion and hot pressing chamber.

RESULTS AND DISCUSSION

SHS of $MoSi_2$ using the propagating mode

SHS experiments conducted in the propagating mode using Mo and Si stoichiometric ratios corresponding to $MoSi_2$ with green densities from 53% to 63% resulted in a decrease in the combustion temperature with increasing green density. This decrease was ascribed to the increased heat losses resulting from higher thermal conductivities of samples with increasing green density. The reacted samples consistently exhibited around 60% pores irrespective of green density and is largely due to the molar volume change accompanying the reaction (around -40% for $MoSi_2$[8]). Therefore, hot pressing was needed to achieve higher densities. X-ray diffraction analysis on the reacted samples indicated complete reaction to $MoSi_2$, with no traces of Mo_3Si or Mo_5Si_3. Scanning electron microscopy (SEM) of the reacted samples indicated a distinct variation in morphology between the top (closest to the tungsten heating coil) and bottom (where the reaction terminated) of the sample. Significant melting and a high level of porosity was observed at the top of the sample - a direct effect of the heating coil. These preliminary results confirmed the possibility of producing $MoSi_2$ by the propagating mode of SHS and the necessity of resorting to hot pressing to achieve dense products.

SHS of Functionally-Graded Materials (FGM's) of $MoSi_2$ + X SiC by the propagating mode

A FGM of $MoSi_2$ (CTE = $9.7 \times 10^{-6} K^{-1}$ at 1873K)+ X SiC (CTE = $6.2 \times 10^{-6} K^{-1}$ at 1873K) with a gradually varying CTE profile was designed. A six-layer FGM was designed with X varying as follows: 0, 0.25, 0.5, 1.0, 1.5 and 2.0. The samples were heated from the $MoSi_2$ - rich sides and were found to react about 33% through the sample, with the reaction quenching out at higher levels of SiC, i.e. X>0.5. An interesting observation was the fact that the sample height (and, consequently, the heating rate) strongly affected the extent of the reaction. XRD analysis of the partially reacted samples showed $MoSi_2$, SiC, and small amounts of unreacted Mo, Si and C to be present. SEM photomicrographs of the partially reacted samples revealed melting had occurred at the top of the sample (i.e. $MoSi_2$ rich layer, close to the tungsten ignition coil) while unreacted graphite graphite flakes were present in the region where the reaction had quenched out. The size of the $MoSi_2$ grains was approximately 1-3μm.

FGM samples composed of 3 layers (X = 0, 0.25, and 0.5) reacted fully in the propagating mode, and XRD analysis again confirmed $MoSi_2$, and SiC to be present with small amounts of Si and C. The unreacted Si and C is possibly due to the large graphite particle size and the fact that individual particles of Si and C may not be in intimate contact at these low stoichiometries. This can be overcome by using finer particle sizes (e.g. carbon black). As with $MoSi_2$, the samples exhibited a distinct variation in morphology of products between the top and bottom. Based on the above results, it was concluded that to minimize porosity and enhance the conditions required for the reaction to go to completion, the best processing route would be to use simultaneous combustion (SC) and hot pressing (HP).

Synthesis of Individual Layers of $MoSi_2$ + X SiC by Simultaneous Combustion (SC) and Hot Pressing(HP) Procedures

Four reactions were studied for use in the synthesis of $MoSi_2$ + X SiC, as follows:

$$Mo + 2\,Si + X\,SiC \rightarrow MoSi_2 + X\,SiC \quad (1)$$

$$Mo + (2+X)\,Si + X\,C \rightarrow MoSi_2 + X\,SiC \quad (2)$$

$$1/2\,Mo_2C + 5/2\,Si + X/2\,SiC \rightarrow MoSi_2 + (1+X)/2\,SiC \quad (3)$$

$$1/2\,Mo_2C + (4+X)/2\,Si + (X-1)/2\,C \rightarrow MoSi_2 + X/2\,SiC \quad (4)$$

The most exothermic reactions are (2) and (4), with both reactions fully reacting in the simultaneous combustion and hot pressing modes when X was less than 1. The samples were hot pressed just after observing the exotherm on the thermocouple. A pressure of 33MPa was applied at this point and reapplied once a minute for 5 minutes, then held for 5 minutes, at 1873K. All reactions were conducted in an argon atmosphere. Reactions (1) and (3) were incompletely reacted, with $MoSi_2$, SiC, and varying amounts of Si and C observed in the X-ray diffraction data. Reactions (1) and (3) used SiC as a diluent, and because these reactions are not highly exothermic, they are unable to fully react under these conditions. Examination of the photomicrographs (Figure 4 (a,b)) and XRD analysis of the products from reaction (2) show both the center (a) and surface (b) to be fully reacted for values of $X \leq 0.5$. The average density was determined to be 89% of the theoretical density, but it is evident from the photomicrographs that the surface is very porous while the center is extremely dense. Further research will be carried out on reactions (2) and (4), with varying amounts of SiC used to build the FGM layers.

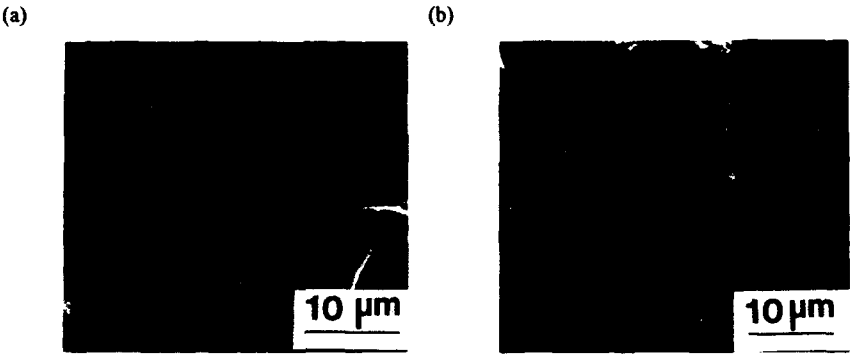


Figure 4. Center (a) and surface (b) regions of the reaction [$Mo+2.5Si+0.5C \rightarrow MoSi_2+0.5SiC$] synthesized by simultaneous combustion and hot pressing in argon.

Synthesis of $MoSi_2$ + X SiC by Simultaneous Combustion and Hot Pressing in Vacuum

The reaction [$1/2\,Mo_2C + 3\,Si + 1/2\,C \rightarrow MoSi_2 + SiC$] was reacted and hot pressed in a vacuum atmosphere. Preliminary results appear to be very promising, in that the samples which were reacted under vacuum have a much more uniform structure throughout the sample than

those reacted in argon. This is most likely due to the lack of gas being trapped in the sample. The microstructure of the center (a) and surface (b) of a sample which was pressed under atmospheric loading (no applied force) are shown in Figures 5 (a) and (b) respectively. Very uniform porosity and microstructures were observed in both regions of the sample. Future work will be conducted using hot pressing at much higher loads.

(a) (b)

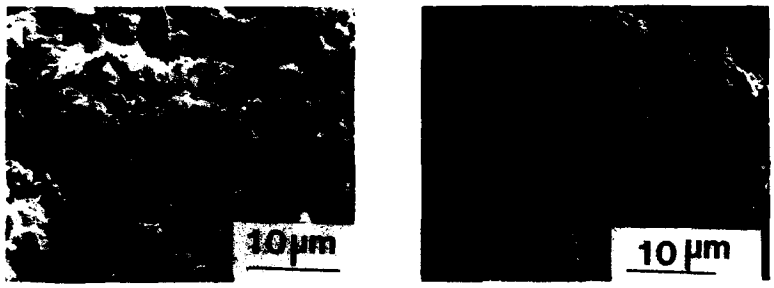


Figure 5. The center (a) and surface (b) of the reaction [1/2Mo_2C+3Si+1/2C → $MoSi_2$ +SiC] synthesized by simultaneous combustion in a vacuum atmosphere without hot pressing.

Discussion

The enthalpy-temperature diagrams for the synthesis of $MoSi_2$ + X SiC are shown in Figure 6. The SiC additives (X SiC) to the SHS reactants act as "diluents" and reduce the adiabatic temperatures. The resulting microstructure of the product phases has been shown to be controlled by T_c, in that lowering T_c will refine the particle size of the phases and, therefore, affects the mechanical properties[9]. Examination of the enthalpy-temperature data and the criteria for a reaction to be self-sustaining suggest that the formation of $MoSi_2$ by SHS is possible, as shown experimentally. However, addition of X SiC reduces the exothermicity of the reaction and at a certain level, the reaction will quench out. In the case of FGM's, the presence of 100% $MoSi_2$ layers in the top of the samples provides sufficient heat to allow the reaction to propagate past the layers where the reaction should have theoretically been quenched out. Consequently, the use of SHS experiments on individual layers of the FGM, to predict the extent to which the reaction will propagate, may not be a suitable indicator.

CONCLUSIONS

(1) Pure $MoSi_2$ has been synthesized by reacting stoichiometric proportions of Mo and Si, using the SHS technique. The product porosity was ~ 60%, irrespective of the initial green density.
(2) Functionally-graded materials $MoSi_2$ + X SiC were produced using the propagating mode of SHS. The reaction quenched out at higher concentrations of SiC, i.e. when X>0.5. Below X=0.5, the product was $MoSi_2$, SiC, and small amounts of unreacted Si and C.

(3) Individual layers of $MoSi_2$ + X SiC were produced by the simultaneous combustion and hot pressing modes. The most exothermic reactions appear to be the following:

$$Mo + (2+X)\ Si + X\ C \rightarrow MoSi_2 + X\ SiC$$

$$1/2\ Mo_2C + (4+X)/2\ Si + (X-1)/2\ C \rightarrow MoSi_2 + X/2\ SiC$$

Photomicrographs of the reacted samples showed uneven porosity throughout the sample. Product phases were $MoSi_2$ and SiC as found by X-ray diffraction.

(4) $1/2\ Mo_2C + 3\ Si + 1/2\ C \rightarrow MoSi_2 +$ SiC reacted by simultaneous combustion in a vacuum atmosphere had more uniform porosity than samples reacted in argon. This process may provide dense, uniform hot pressed microstructures and further research will be done in this area.

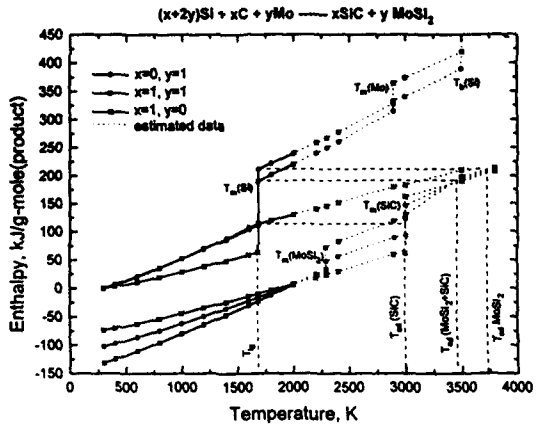


Figure 6. Enthalpy-Temperature diagram for the X SiC + Y $MoSi_2$ system.

REFERENCES

1. A.K. Vasudivan and J.J. Petrovic, *Materials Science and Engineering*, A155, 1992, p.1.
2. J. Schlichting, *High Temperatures-High Pressures*, 10, 1978, p.241.
3. E. Fitzer, *Warmfeste und Korrosionbestandige Sinterwerkstoffe*, 2, Plansee Seminar, 19-23 June 1955, Rutte/Tirol, F. Benesovsky ed., Springer, Vienna, 1956, p.56.
4. D.H. Carter, J.J. Petrovic, R.E. Honnell and W.S. Gibbs, *Ceram. Eng. Sci. Proc.*, 10, 1989, p.1121-29.
5. V.N. Bloshenko, V.V.Bokii and I.P. Borovinskaya, *Combus. Explos. Shock Waves*, 21, 1985, p.202.
6. S. Zhang and Z.A. Munir, *J. Mater. Sci.*, 26, 1991, p.3685-88.
7. N.P. Novikov, I.P. Borovinskaya and A.G. Merzhanov, *Combustion Processes in Chemical Technology and Metallurgy*, A.G. Merzhanov, editor, Chernogolovka, USSR, 1975, p.174.
8. S. Jandhyala, *J. Amer Ceram. Soc.*, 75 (12), 1992, p.1.
9. H.J. Feng, J.J. Moore and D.G. Wirth, "Combustion Synthesis of Dense Ceramic-Metal Composites" in Proceedings of the Symposium on Ceramic Matrix Composites, 1993, Annual American Ceramic Society Conference, Cincinatti, April 1993, to be published by American Ceramic Society.

COMBUSTION SYNTHESIS OF MOLYBDENUM DISILICIDE AND ITS COMPOSITES

SEETHARAMA C. DEEVI
Research and Development Center, Philip Morris, USA, Richmond, VA 23234-2269.

ABSTRACT

A combustion wave originating from an exothermic reaction between Mo and Si propagates through the reactants converting Mo-2Si mixture to $MoSi_2$. X-ray analysis of the product confirmed that the product is single phase $MoSi_2$ with no second phase or reactants when combustion synthesis experiments were carried out in argon. The oxygen content of the product was 0.22 wt.%. When the mixture was reacted under pressure in a hot press, the product obtained was also $MoSi_2$, and a theoretical density up to 92% could be achieved. Heating of a mixture of Mo and Si with C leads to the formation of $MoSi_2$ with a dispersed SiC phase.

INTRODUCTION

Among the silicides of transition metals, molybdenum disilicide ($MoSi_2$) is an attractive candidate for high temperature structural applications, due to its high melting point of 2020 °C, stable electrical resistance over long periods of time, self-healing ability due to the formation of a highly protective and continuous amorphous silica layer, and excellent oxidation and thermal shock resistance [1]. Several methods have been reported for the synthesis of $MoSi_2$. Brewer et al [2] synthesized high-melting silicides of Mo by mixing and heating 100 to 400 mesh powders of Mo and Si to the desired temperature in an Ar atmosphere using an induction furnace at temperatures of 1657 °C to 2157 °C with times ranging from 3 to 68 min. Cherniack and Elliot [2] reported that the densities of $MoSi_2$ increased up to 1650 to 1700 °C, and at a temperature of 1750 °C and 150 min, $MoSi_2$ decomposed in the interior and formed Mo_5Si_3. The use of $MoSi_2$ as a structural material was thought to be limited to 1700 °C owing to the internal formation and agglomeration of Mo_5Si_3, while Mo_5Si_3 was also believed to be responsible for the difficulty in fabricating sound $MoSi_2$ bodies by sintering at the temperatures necessary for densification. $MoSi_2$ is also produced using a thermite mix consisting of 41.75% MoO_3, 10.8% Al, 38.6% of ferrosilicon, 6.6% of limestone, and flourspar [3]. The literature indicates several other methods for the production of $MoSi_2$: ranging from reduction of MoO_3 with SiC and carbon, siliciding of molybdenum powder, powder pressing and sintering, arc - melting, and hot pressing [4].

In contrast to the techniques discussed above, combustion synthesis or self - propagating high temperature synthesis (SHS) based on heterogeneous combustion between molybdenum and silicon has been shown to be effective in preparing a single phase tetragonal $MoSi_2$ with high purity [5-10]. Sarkisyan et al [6] were the first to report combustion velocities and behavior of mixtures of Mo-Si with different amounts of Si in argon using metal powders of size < 50μm, and Si of size < 30 μm. At low compact diameters (< 20 mm), the product was multiphase consisting of $MoSi_2$ and Mo_5Si_3 along with Mo and Si. Deevi [7,8] and Zhang and Munir [9] further investigated the synthesis aspects of $MoSi_2$ based on Mo+2Si mixtures.

In this paper, features of combustion synthesis of $MoSi_2$ and application of combustion synthesis to the densification of $MoSi_2$ and its composites will be presented.

Mat. Res. Soc. Symp. Proc. Vol. 322. ©1994 Materials Research Society

EXPERIMENTAL METHODOLOGY

Molybdenum (Mo) and silicon (Si) powders used in the present work were as received powders from Alfa Products with Mo size of <63 μm, and Si size of ≤ 47 μm, whose average particle sizes correspond to 13.3 μm, and 12.6 μm respectively. Cylindrical compacts of Mo-2Si mixture of approximately 30 mm in length were obtained by applying pressure uniaxially on both sides of the powder. Combustion synthesis experiments were carried out in a stainless steel chamber with two 12.5 cm quartz windows. Experiments were carried out either in a stagnant vacuum of 5 to 10 microns or stagnant argon pressure of 1.2 Kg/cm^2 [7]. Ignition was achieved by supplying current to a tungsten ignition coil for a few seconds. Temperature measurements were carried out using tungsten - 5% rhenium vs tungsten - 26% rhenium thermocouples.

Hot pressing of Mo-2Si mixture, and a mixture of 49.81% of Mo, 43.84% Si, and 6.25% C (all by weight) was carried out by pressing at different temperatures in the range 1100 to 1600 ^oC in argon with a pressure of 100 - 300 Kg/cm^2 for 30 min.

COMBUSTION SYNTHESIS OF $MoSi_2$

Combustion synthesis is based on the ability of the reactants, Mo and Si, to react exothermically once ignited, converting the reactants to products as a combustion wave progresses through the reactants. This is illustrated in Fig. 1 with a set of photographs taken during the combustion wave propagation in Mo-2Si mixture. Formation of $MoSi_2$ is accompanied by a heat release of 31.0 k. cal/Mo atom, and this corresponds to an adiabatic temperature of 1627 ^oC [7]. The observed temperature agrees with the calculated temperature, and is higher than the melting temperature of Si, but lower than the melting temperatures of Mo and $MoSi_2$.

Combustion wave velocities of Mo-2Si mixture obtained in vacuum and argon [Fig. 2] show an increase with increase in green density due to an effective increase of thermal conductivity, and reduction of porosity [7]. The combustion wave propagated at a lower velocity in vacuum than in argon. The maximum combustion temperature noted in vacuum was 1423 ^oC as opposed to 1613 ^oC in argon, and the temperature remained at its maximum temperature for seven seconds in vacuum. In vacuum, conduction is mainly by particle-particle contact and therefore, the sample remained at its maximum temperature for seven seconds due to the continuation of the exothermic diffusional reaction between Mo and Si powders. In contrast to the behavior observed in vacuum, the temperature profile obtained in argon at 1.2 atm. indicated that the product remained at its maximum combustion temperature for less than a second.

A product of the linear combustion velocities (cm/min) of compacts of uniform cross-sectional area (cm^2), and densities of the compacts (g/cm^3) provides the volumetric mass conversion rates of Mo+2Si into $MoSi_2$. The mass conversion rates shown in Fig. 3 indicate that they are dependent upon (a) density of the compact, (b) the atmosphere, and (c) the diameter of the compact. The mass conversion rates vary from 25 g/min to 130 g/min, and it is interesting to note that when a compact of Mo+2Si is ignited, $MoSi_2$ can be synthesized at a rate of 130 g/min. X - ray diffraction analysis of combustion synthesized powders obtained after grinding of the compacts showed that the conversion to $MoSi_2$ was complete in argon (Fig. 4), while about 91% of the reactants were converted to $MoSi_2$ in vacuum. This illustrates not only the simplicity of the technique but also reflects its viability as a manufacturing process. Combustion synthesized product was analyzed for impurities and oxygen content, and the oxygen content of combustion synthesized $MoSi_2$ was 0.22 wt.%, which is lower than the weighted average oxygen contents of the reactants [7]. This is also lower or comparable to the oxygen contents reported by several investigators [1,4]

The heating rates calculated in combustion synthesis (based on the time-temperature profiles) indicate that a heating rate of ~48,000 ^oC/min was obtained in argon. The combustion



Fig. 1. Photographs of Passage of Combustion Front in Mo-2Si Mixture in Argon.

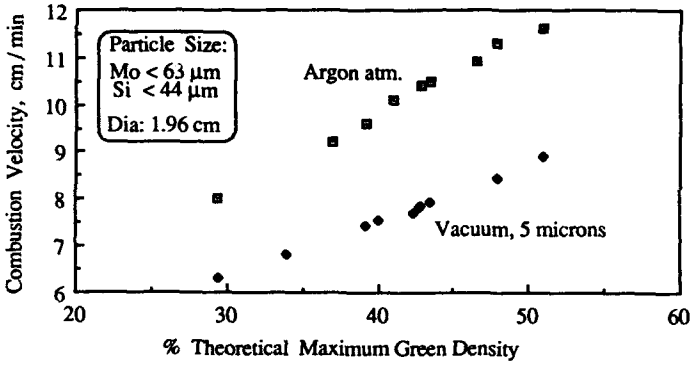


Fig. 2. Variation of Combustion Velocities on the % Theoretical Maximum Green Density (%TMD) of Compacts

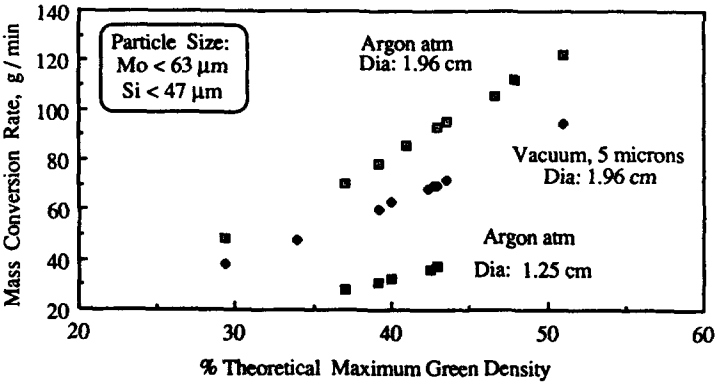


Fig. 3. Dependence of Mass Conversion Rate on % Theoretical Maximum Green Density (%TMD) of Compacts.

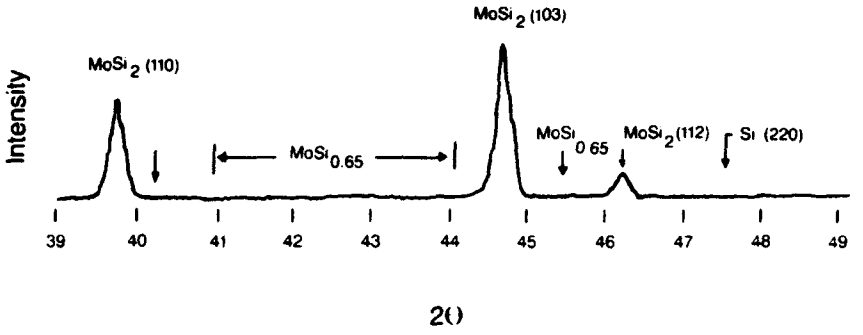


Fig. 4. X-ray Diffractogram of a Combustion Synthesized MoSi2 indicative of a single phase, MoSi2, with no unreacted elements.

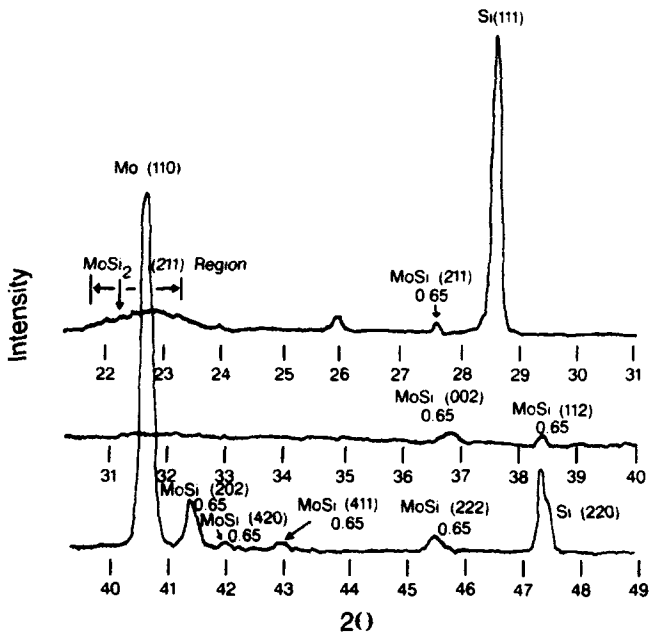


Fig. 5. X- ray diffractogram of a Compact of Mo-2Si of 51% theoretical density heated in Argon to 1260 °C at 5 °C/min. Note the peaks corresponding to $MoSi_{0.65}$ (which are referred to as Mo_5Si_3).

temperature of the reaction is sufficiently higher than the melting point of the diffusing species, i.e. Si, and therefore liquid Si diffuses into Mo giving rise to $MoSi_2$ phase. In most conventional processes, reactants are heated at a much lower heating rate, which will favor solid-solid diffusional reactions prior to the melting point of Si [7,8].

An understanding of diffusional and interfacial reactions was attempted by heating various combinations of particle sizes of Mo-2Si in the temperature range 300 to 1900 K using a high temperature differential thermal analyzer (DTA). A detailed account of the results is presented elsewhere [8]. In summary, DTA experiments showed two exotherms at low heating rates in the range 5 to 100 °C/min, and a single exotherm above 100 °C/min. The first exotherm, occurring prior to the melting of Si, was identified by X-ray analysis as due to the formation of Mo_5Si_3 (Fig.5). The second exotherm represents the formation of $MoSi_2$ and the exothermicity of the second exotherm increased with increase of heating rate. The exothermicity of the first reaction and the amount of Mo_5Si_3 formed decreased with increase of heating rate and above 150 °C/min only a single exotherm was observed, with the formation of single phase $MoSi_2$. X-ray examination of the products obtained at different heating rates confirmed that at heating rates above 150 °C/min, the probability of formation of Mo_5Si_3 is negligible since diffusional time for solid-solid diffusional reactions is very limited [8].

The $MoSi_2$ synthesized by combustion synthesis is porous with a porosity in the range of 30 to 50%, and the compact can easily be crushed to obtain powder. If densification is achieved by the application of pressure, combustion synthesis becomes an attractive technique to obtain dense materials. Densification was carried out by hot pressing mixtures of Mo + 2Si in the temperature range 1100 to 1600 °C. A single phase $MoSi_2$ was observed in all cases when the hot press temperature was above 1350 °C. At the melting point of Si, i.e at 1410 °C, application of pressure in the range 100 Kg/cm^2 did not cause any significant densification(Fig. 6a). At 1450 °C, the sample densified to about 85% of theoretical density, while a maximum density of 92% was achieved at a temperature of 1550 °C with a pressure of 250 Kg/cm^2 (Fig. 6b). Hot pressing of a mixture of Mo,Si, and C to obtain $MoSi_2$-SiC also resulted in densification with densities approaching 95% (Fig. 6c and 6d). A detailed account of the microstructural observations, X- ray phases, and densification curves will be presented at a later stage. Composites of $MoSi_2$-Al_2O_3 were also prepared by heating a mixture of MoO_3, Si and Al similar to a thermite mixture, and the reaction originated with the melting of Al. Thermal analysis revealed several different reactions, and the reaction was found to be extremely rapid with larger sample sizes of 500 mg and at heating rates above 50 °C/min.

CONCLUSIONS

Single phase $MoSi_2$ can be synthesized from elemental powders of Mo and Si using SHS technique. Mass conversion rates showed that SHS is a viable technique for rapid production of $MoSi_2$ from the elements. The combustion velocities, and hence the conversion rates were lower in vacuum as compared to argon atmosphere. The low combustion temperature in vacuum accounts for the lower conversion efficiency of Mo and Si powders to $MoSi_2$.

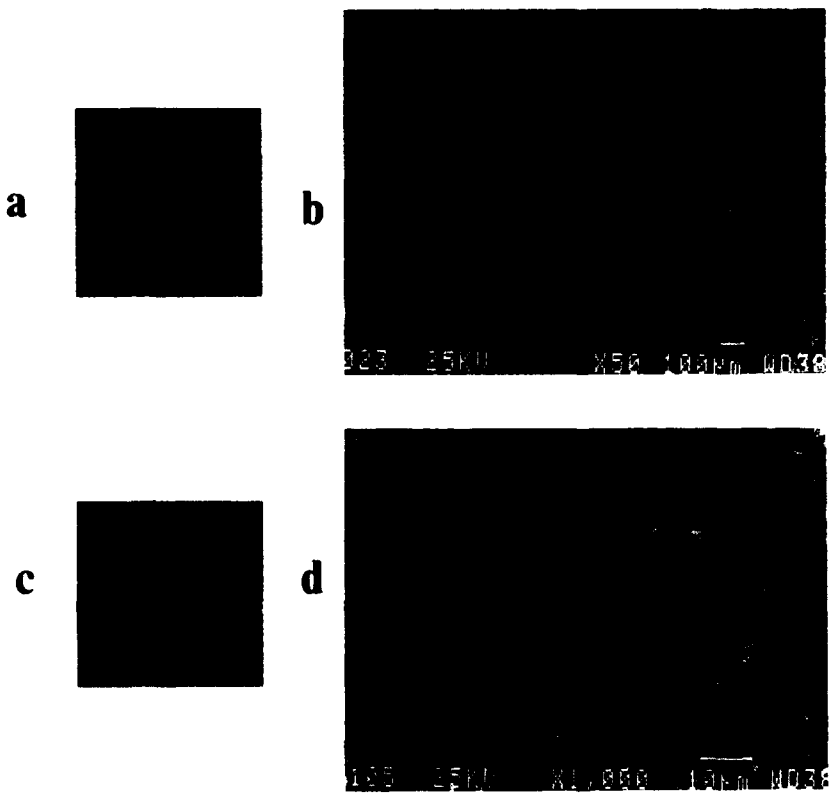


Fig. 6. Micrographs of Hot Pressed Mo+2Si Mixtures, and a Mixture of Mo, Si, and C to give rise to $MoSi_2$-SiC. (a) Mo+2Si, hot pressed at 1410 °C for 30 min (b) Mo+2Si, hot pressed at 1450 °C for 30 min, (c) Mo, Si, and C, hot pressed at 1550 °C for 30 min, and (d) Mo, Si, and C, hot pressed at 1500 °C for 30 min.

REFERENCES

1. See articles in A.K. Vasudevan, and J.J. Petrovic, High Temperature Structural Silicides, Proc. of First High - Temperature Structural Silicides Workshop. (Elsevier Science Publishers, B.V. Amsterdam, 1992).
2. L. Brewer, A.W. Searcy, D.H. Templeton, and C.H. Dauben, J. Am. Ceram. Soc., 33(10), 291 (1950); G.B. Cherniack and A. G. Elliot, ibid., 47(3), 136 (1964).
3. D.H. Killeffer, and A. Linz, Molybdenum Compounds: Their Chemistry and Technology., (Interscience Publishers, New York, 1952), p.11.
4. J. Schlichting, High Temperatures-High Pressures, 10(3), 241 (1978).
5. A. R. Sarkisyan, S.K. Dolukhanyan, I.P. Borovinskaya, and A.G. Merzhanov, Fizika Goreniya i Vzryva, 14(3), 49, (1977).
6. L. M. Sheppard, Adv. Mat. Processes, 2, 25, (1986).
7. S. C. Deevi, J. Mat. Science., 26 , 3343, (1991).
8. S.C. Deevi, Mat. Sci. Engg., A149, 241 (1992).
9. S. Zhang and Z.A. Munir, J. Mat. Sci., 26, 3685, (1991).
10. J.J. Moore, to be published in Processing and Fabrication of Advanced Ceramic Materials, edited by V.A. Ravi, T.S. Srivatasan, and J.J Moore, (TMS, Warrandale, PA, 1994).

SYNTHESIS AND CHARACTERIZATION OF METAL SILICIDE/SILICON CARBIDE COMPOSITES BY LOW TEMPERATURE SOLID-STATE REACTIONS.

D. ZENG†, M. J. HAMPDEN-SMITH† AND L.-M. WANG††
†Department of Chemistry and Center for Micro-Engineered Ceramics, ††Department of Earth and Planetary Science, University of New Mexico, Albuquerque, NM 87131.

ABSTRACT

Co-reduction of mixtures of $MoCl_3(THF)_3$ and $SiCl_4$ in THF using $Li/C_{10}H_8$ or both $Li/C_{10}H_8$ and $LiBEt_3H$ resulted in formation and separation of black powders which upon thermal annealing at temperatures ranging from 750°C to 1100°C produced crystalline molybdenum silicide and silicon carbide composite. Co-reduction of mixtures of WCl_4 and $GeBr_4$ with $LiBEt_3H$ in THF formed W_2C and elemental Ge which upon thermal treatment at 750°C for 4 hours generated a small amount of crystalline W_5Ge_3.

INTRODUCTION

Solid-state displacement reactions between Mo_2C and Si forms molybdenum silicide and silicon carbide composite on heating for 1350°C for 2 hours followed by 1700°C for 1 hour.[1] We have recently demonstrated that nanometer-sized metal carbides, M_2C (M = Cr, Mo and W)[2-5] react with micrometer-sized silicon powder to form the corresponding metal silicide and silicon carbide composites under milder reaction conditions (1000°C/4 hours),[6] probably as a result of high surface energy of the M_2C particles. In this work we report the co-reduction of mixture of $MoCl_3(THF)_3$ and $SiCl_4$, WCl_4 and $GeBr_4$.

EXPERIMENTAL PROCEDURES

(i).Co-reduction of a mixture of $MoCl_3(THF)_3$ and $SiCl_4$ in THF by $Li/C_{10}H_8$

Lithium metal (1.15 gram, 164.3 mmole) and $C_{10}H_8$ (20.95 gram, 163.7 mmole) were mixed in 300 mL of THF and stirred for 12 hours to form a dark-green solution. This solution was then transferred to a 100 mL red-brown THF suspension of $MoCl_3(THF)_3$ (5.00 gram, 12.0 mmole) and $SiCl_4$ (4.07 gram, 23.9 mmole) while stirring. The dark-green color of $Li/C_{10}H_8$ disappeared rapidly during the initial addition of $Li/C_{10}H_8$/THF. The reaction mixture become darker as addition of $Li/C_{10}H_8$/THF progressed, and an exothermic reaction was observed. The mixture was stirred at room temperature for 48 hours to form a homogenous black suspension. This suspension was centrifuged at 2000 rpm for 45 minutes to precipitate a black solid. The black solid was washed with THF and dried under vacuum to give 1.69 gram of black powder. Black powder contains high percentage of carbon, 37.56%. Heating this powder to 1100°C under vacuum formed molybdenum silicide and silicon carbide.

(ii).Co-reduction of a mixture of $MoCl_3(THF)_3$ and $SiCl_4$ in THF by both $Li/C_{10}H_8$ and $LiBEt_3H$

Lithium metal (0.79 gram, 112.86 mmole) and $C_{10}H_8$ (14.23 gram, 111.17 mmole) were mixed in 100 mL of THF and allowed to stir for 12 hours to form dark-green

Mat. Res. Soc. Symp. Proc. Vol. 322. ©1994 Materials Research Society

solution. This solution was then transferred to a 70 mL red-brown THF suspension of $MoCl_3(THF)_3$ (6.00 gram, 14.35 mmole) and $SiCl_4$ (5.34 gram, 31.41 mmole) while stirring. The dark-green color disappeared rapidly during the initial addition of $Li/C_{10}H_8$/THF. A black suspension was formed at the end of addition of $Li/C_{10}H_8$/THF. After further stirring for 30 minutes, 1.0M THF solution of $LiBEt_3H$ (80 mL, 80 mmole) was added and stirred for another 5 hours at room temperature to form a homogenous black suspension. The suspension was centrifuged at 2000 rpm for 45 minutes to precipitate black solid. The black solid was separated and was washed with THF and then was dried under vacuum to give 0.82 gram black powder. The powder was heated to 1050°C under vacuum to form molybdenum silicide and silicon carbide.

(iii).Co-reduction of a mixture of WCl_4 and $GeBr_4$ in THF by $LiBEt_3H$.

WCl_4 (2.00 gram, 6.13 mmole) and $GeBr_4$ (4.82 gram, 12.26 mmole) was mixed in 150 mL THF. Into this mixture, 1.0M $LiBEt_3H$ (75.0 mL in THF, 75.0 mmole) was transferred at room temperature while stirring. Gas evolution and a color change from black to dark brown and finally back to black was observed. The reaction mixture was stirred at room temperature overnight, resulting in a formation of black suspension. Centrifuging for 10 minutes precipitated the black solid, which after washing with THF and drying under vacuum, yielded 2.05 gram black powder composed of W_2C and elemental Ge, a yield of 100 % based on the formation of mixture of W_2C and Ge.

RESULTS AND DISCUSSION

The reduction of a mixture of $MoCl_3(THF)_3$ and two molar equivalents of $SiCl_4$ by $Li/C_{10}H_8$ in THF resulted in formation of a homogeneous black suspension, from which a black powder was separated by centrifuging. Elemental analysis of the black powder showed a high carbon and hydrogen content that appears to be associated with the electron carrier (naphthalene). Both scanning electron microscopy (SEM) and transmission electron microscopy (TEM) showed no discrete particles within the resolution limit of the

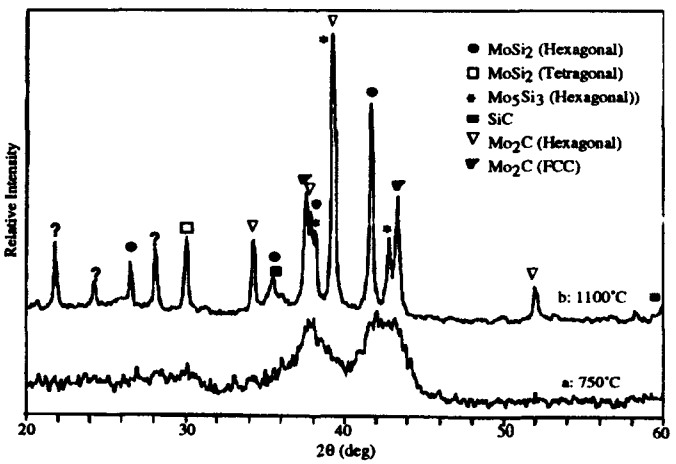


Figure 1. XRD patterns of the 750°C (a) and 1100°C (b) annealed sample.

instrument. The electron diffraction and X-ray powder diffraction data showed that the black powder is amorphous material resulting in no diffraction but only one broad peak at $2\theta \sim 20^{\circ}$. After the sample was heated to 500°C for 4 hours, SEM revealed the presence of large dense particles. X-ray powder diffraction of the 500°C annealed sample did not show sufficient peak sharpening for phase identification. The sample was heated to 750°C for 4 hours and the resulting X-ray diffraction pattern is shown in Figure 1a. The diffraction maximum centered at d = 2.4 Å was assigned to FCC Mo_2C, and the peak at d = 2.1 Å to 2.2 Å was assigned to the mixture of $MoSi_2$ and Mo_5Si_3. This assignment was confirmed by the X-ray powder diffraction pattern taken for the sample after heating to 1100°C for 4 hours as shown in Figure 1b. The diffraction peaks at 1.54 Å and 2.51 Å were assigned to SiC which may result from reaction between Mo_2C and elemental silicon powder at 750°C or higher. The formation of molybdenum silicide and silicon carbide is consistent with the formation of amorphous molybdenum carbide and elemental silicon powders during the co-reduction step. We have studied the reduction of $MoCl_3(THF)_3$ in THF by using $Li/C_{10}H_8$ as reducing agent separately and observed the formation of amorphous Mo_2C which upon heating crystallized to form FCC Mo_2C.[4] Further heating resulted in phase transition from FCC to hexagonal phase of Mo_2C. We are currently unable to assign those peaks labeled by "?".

The reduction of mixture of $MoCl_3(THF)_3$ and two equivalents of $SiCl_4$ in THF with 7 molar equivalents of $Li/C_{10}H_8$ followed by 4 molar equivalents of $LiBEt_3H$ also resulted in formation of a homogeneous black solution from which a black powder was isolated by centrifuging. The grain size of the black powder is about 2 - 4 μm as shown by both SEM and TEM. Energy dispersive spectroscopy from both SEM and TEM showed the presence of Mo and Si only, no chlorine was detected within the detection limit of the instrument. High magnification TEM further revealed that the grains are composed of ~ 1 nm sized particles. Electron diffraction and X-ray powder diffraction showed that the

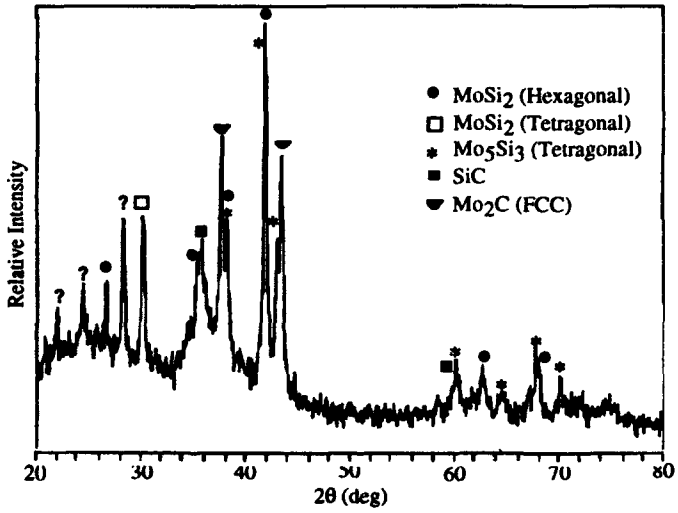


Figure 2. XRD pattern of 1050°C annealed sample

material is amorphous. To assist the phase identification of the material, the sample was annealed at 900°C and 1050°C, and X-ray powder diffraction of 1050°C annealed sample showed the presence of $MoSi_2$ and Mo_5Si_3 phases as shown in Figure 2. The diffraction peaks at 2.51 Å and 1.54 Å were assigned to SiC formed by solid-state displacement reaction between Mo_2C and elemental silicon powder. The peaks labeled by "?" are consistent with those as shown in Figure 1, and again we are unable to assign these peaks.

In order to investigate the co-reduction using $LiBEt_3H$ as reducing agent, and at the same time avoiding the possible formation of SiH_4 as a dangerous by-product, a mixture of WCl_4 and two equivalents of $GeBr_4$ were chosen as the starting materials. This mixture, suspended in THF, was reduced with 12 molar equivalents of $LiBEt_3H$. Again, a homogeneous black solution was formed from which black powder was isolated in high yield, Variable temperature X-ray powder diffraction of this black powder showed only the presence of W_2C and elemental Ge at 390°C (Figure 3a). When the sample was treated

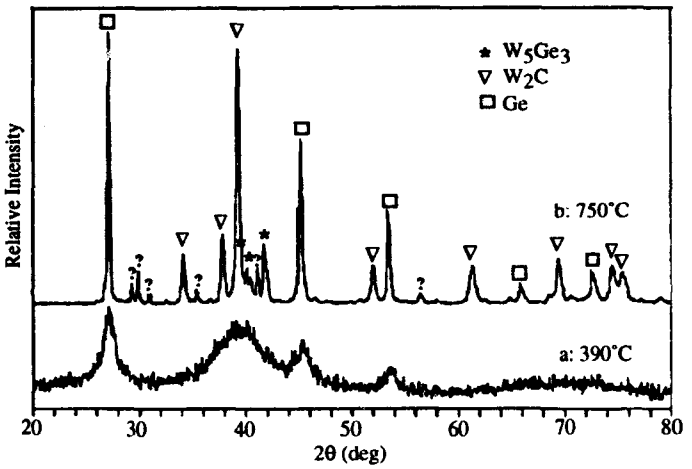


Figure 3. XRD pattern of 390°C and 750°C annealed sample.

at 750°C for 4 hours, X-ray powder diffraction (Figure 3b) showed presence of a small amount of W_5Ge_3 formed through a solid state displacement reaction between W_2C and elemental germanium. There are a few small peaks labeled by "?" are not indexed as a result of inability to assign them.

CONCLUSIONS

In summary, co-reduction by using $Li/C_{10}H_8$ alone or both $Li/C_{10}H_8$ and $LiBEt_3H$ as reducing agents in THF solution resulted in formation of black suspension from which black powder can be separated. The black powders are believed to be a mixture of amorphous Mo_2C and elemental silicon powder. Upon thermal treatment, $MoSi_2$, Mo_5Si_3 and SiC were formed via solid-state reactions between Mo_2C and silicon powder. Co-reduction of mixture of WCl_4 and $GeBr_4$ with $LiBEt_3H$ in THF solution at room temperature forms W_2C and elemental Ge which upon thermal treatment resulted in formation of tungsten germanide.

ACKNOWLEDGEMENTS

We thank the Office of Naval Research, Chemistry and Department of Materials Research for funding this research (ONR N00014-91-J-1258) and the National Science Foundation Chemical Instrumentation Program for the purchase of a low-field NMR spectrometer. We also thank the Department of Earth and Planetary Sciences at the University of New Mexico for maintenance of X-ray powder diffractometer and transmission electron microscope. The author also thank Ms. X. Qiu for assistance in obtaining the TEM data.

REFERENCES

1. C.H. Henager, and J.L. Brimhall, Scripta Metallugica 26, 585 (1992).
2. D. Zeng, and M.J. Hampden-Smith, Chem. Mater. 4, 968 (1992).
3. D. Zeng, and M.J. Hampden-Smith, Chem. Mater. 5, 681 (1993).
4. D. Zeng, M.J. Hampden-Smith, and L.-M. Wang, presented at the Fall Materials Research Society Meeting, Boston, 1993.
5. D. Zeng, M.J. Hampden-Smith, and A. Datye, in Chemical Processes in Inorganic Materials: Metal and Semiconducter Clusters and Colloids, edited by J.S. Bradley, P.D. Persans, G. Schmid and R.R. Chianelli (Mat. Res. Soc. Symp. Proc., Pittsburgh, 1992) v. 272, p. 103.
6. D. Zeng, M.J. Hampden-Smith, and L. Wang, J. Mat. Chem. 3, 321 (1993).

SYNTHESIS OF HIGH-TEMPERATURE SILICIDES VIA RAPID SOLID-STATE METATHESIS

Richard M. Jacubinas and Richard B. Kaner
Department of Chemistry and Biochemistry and the Solid State Science Center, University of California, Los Angeles, Los Angeles, CA 90024-1569

ABSTRACT

$MoSi_2$ has a very favorable combination of materials properties, including a high melting point (2020°C), high strength at elevated temperatures, and resistance to high temperature oxidation and corrosion. These properties make it a good candidate for a high-temperature structural material; however, it has very poor ductility. A great deal of research has focused on improving the ductility of this alloy through various preparative routes. We have synthesized $MoSi_2$, as well as WSi_2, $TaSi_2$, and $NbSi_2$, using rapid solid-state metathesis reactions between a high oxidation state metal halide and an alkaline earth silicide. These reactions take advantage of the large exothermic heat of formation of the alkaline earth halide and can reach temperatures as high as the melting point of the product silicides. In addition, this approach yields crystalline products in seconds. The synthetic technique will be discussed along with characterization results.

INTRODUCTION

Interest in producing $MoSi_2$ and other silicides stems from their potential use as high-temperature structural materials. The desirable properties of such a compound are present in $MoSi_2$[1], specifically, moderate density (6.24 g/cm^3), high melting point (2020°C), and resistance to high temperature oxidation. Significant drawbacks to the successful implementation of $MoSi_2$ as a structural material are its low temperature ductility and lack of high temperature strength. Research is currently being pursued to improve these properties, including the addition of a ductile phase, such as Nb, and alloying with, for example, WSi_2[1]. Unfortunately, Nb has a deleterious effect on the high temperature oxidation resistance[2].

Conventional methods for producing $MoSi_2$ involve heating elemental powders together for several hours[3]. Other methods of bulk synthesis reported include self-propagating high temperature synthesis (SHS)[4], mechanical alloying[5,6], and solid-state displacement[7]. While all of these techniques produce the desired products, they are hampered by the amount of time and energy they require to complete the reactions.

Rapid solid-state metathesis reactions (SSM) are a relatively new method used to produce crystalline products in seconds[8,9]. The general synthetic technique involves combining a high oxidation state metal halide with an alkali or alkaline earth species which then react in seconds to form product. In the synthesis of $MoSi_2$, for example, $MoCl_5$ is reacted with Mg_2Si. The formation of the by-product salt ($MgCl_2$) drives this process and results in very exothermic reactions. In this work, rapid SSM reactions are used to synthesize intermetallic alloys.

EXPERIMENTAL

The metal halides, $MoCl_5$ (Aesar, 99.6%), WCl_6 (Aesar), $NbCl_5$ (Aldrich, 99.9+%), and $TaCl_5$ (Aldrich, 99.9%), were all purified by vapor phase transport prior to use. Mg_2Si (Aldrich, 99+%) was used as received.

All reactions were performed in a He-filled drybox. The reactants were ground together with a mortar and pestle and then placed in a stainless steel reaction vessel, similar to those

Mat. Res. Soc. Symp. Proc. Vol. 322. ©1994 Materials Research Society

used for calorimetry. The reactions were initiated with a resistively heated nichrome wire. The resulting highly exothermic reaction was complete in seconds. The products were washed with methanol to remove salt and any unreacted precursors. In addition, aqua regia was used to remove any byproduct molybdenum.

Powder X-ray diffraction was performed on a locally automated Crystal Logic diffractometer with graphite monochromated Cu Kα radiation in 0.1° 2θ increments with 2 second count times, except for $MoSi_2$ in which 0.05° 2θ increments with 3 second count times was used. Scanning electron microscopy (SEM) and energy dispersive X-ray analysis (EDAX) were performed on a Cambridge Stereoscope 250 SEM equipped with a Tracor Northern EDAX TN2000 spectrometer. The samples were mounted on graphite discs with colloidal graphite paste (Ted Pella Inc.).

RESULTS AND DISCUSSION

The reactions were all balanced to produce a stoichiometric amount of salt:

$$8\ MCl_5 + 10\ Mg_2Si \longrightarrow 20\ MgCl_2 + M_8Si_{10}\ (M = Mo, Nb, Ta) \qquad (1)$$

$$2\ WCl_6 + 3\ Mg_2Si \longrightarrow 6\ MgCl_2 + W_2Si_3 \qquad (2)$$

The reaction products were identified through X-ray diffraction (Figure 1) and compared to standard patterns[10]. The X-ray results suggest that equations (1) and (2) are more accurately written as:

$$8\ MCl_5 + 10\ Mg_2Si \longrightarrow 20\ MgCl_2 + 5\ MSi_2 + 3\ M\ (M = Mo, Nb, Ta) \qquad (3)$$

$$4\ WCl_6 + 6\ Mg_2Si \longrightarrow 12\ MgCl_2 + 3\ WSi_2 + W \qquad (4)$$

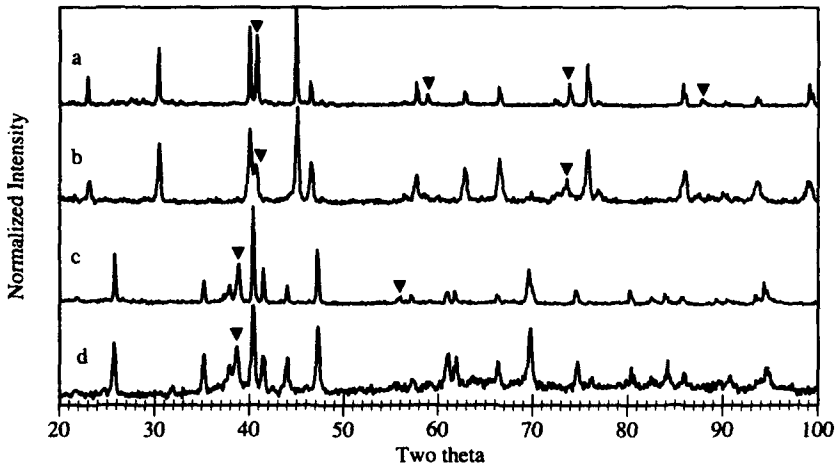


Figure 1. X-ray diffraction patterns of: (a) $MoSi_2$ products, (b) WSi_2 products, (c) $NbSi_2$ products, and (d) $TaSi_2$ products. ▼ denotes Mo, W, Nb, or Ta. The unlabeled peaks are assigned to the MSi_2 phase.

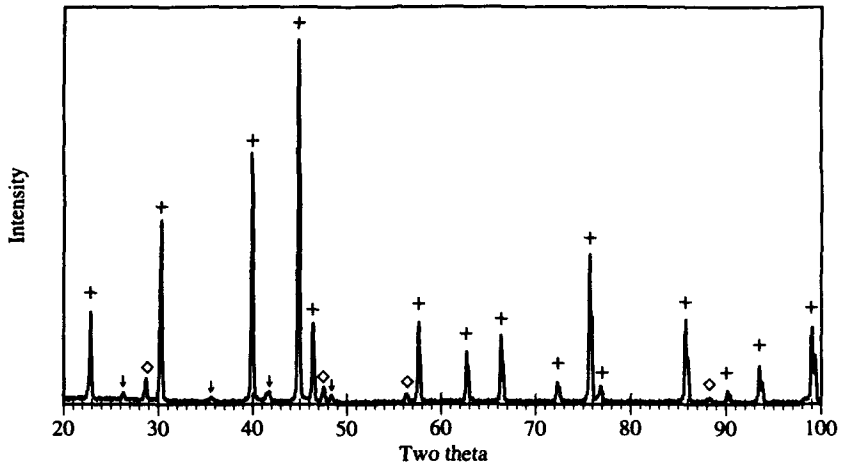


Figure 2: X-ray difffraction pattern of the $MoSi_2$ reaction product washed in aqua regia. + denotes α-$MoSi_2$, ↓ denotes β-$MoSi_2$, and ◇ denotes Si.

When the byproduct molybdenum was washed away using aqua regia, the two phases of $MoSi_2$, α and β, are readily apparent (Figure 2). The presence of small amounts of elemental Si is taken to indicate incomplete reaction of the Mg_2Si with the metal halide.

On the basis of the Mo-Si phase diagram[11], the thermodynamic phases predicted to be present at room temperature are Mo_5Si_3 and α-$MoSi_2$. However, in the SSM synthesis, no evidence was found in the X-ray diffraction pattern for Mo_5Si_3. According to equation (1), the Mo:Si starting ratio is 4:5, which places it in a region between these two phases. It is likely that $MoSi_2$ is the first phase to nucleate and is quenched to room temperature before further reaction can occur. This result exemplifies the non-equilibrium nature of these reactions.

When an adiabatic situation is assumed in which the entire enthalpy of reaction is used to heat only the products and not the surroundings, an adiabatic temperature (T_{ad}) can be calculated[4]. The T_{ad}'s for these reactions are calculated using temperature dependent heat capacities and heats of transformation of the products, as well as the overall heat of reaction[12] (see Table I). The boiling point of $MgCl_2$ is 1710K while $MoSi_2$ melts at 2293K. In all cases, the reactions theoretically reach **at least** the boiling point of $MgCl_2$. This may explain the rapid nature of these reactions since solid-state diffusion increases at higher temperatures and can be even more rapid if a molten flux is present.

In SHS reactions, T_{ad} has been used as an indicator of self-propagating behavior; when T_{ad} is greater than approximately 1800K, a self-propagating reaction is expected.[4] In contrast, all the reactions performed in this work are self-propagating, even though two cases fail to meet this condition. This is further evidence for enhanced solid-state diffusion which would lead to a lower threshold for self-propagating behavior. In addition, attempts to synthesize $MoSi_2$ using a combination of the elements and the same reaction conditions were unsuccessful.

Preliminary SEM analysis of the $MoSi_2$ product after washing in aqua regia indicates a range of particle sizes from approximately 0.5 μm to 10 μm. In addition, X-ray line broadening shows that the product is at least as crystalline as typical standards. Semi-quantitative EDAX analysis verifies a slight silicon enrichment as indicated by the X-ray

Table I
Calculated T_{ad}

Silicide produced	T_{ad} (K)
$MoSi_2$	2293
WSi_2	2373
$NbSi_2$	1710
$TaSi_2$	1710

diffraction pattern.

One of the ways in which the properties of $MoSi_2$ can be improved is through alloying with other silicides. The preparation of a mixed metal halide precursor is straightforward[13]. The two halides, after being individually purified via vapor phase transport, are melted together and then shaken vigorously after removal from the oven, causing rapid cooling. The material is inspected visually for homogeneity and then used in the SSM reactions. Initial results indicate that when a 1:1 $MoCl_5$•WCl_6 precursor is used, a single phase silicide is obtained. In contrast, when a 1:1 $MoCl_5$•$NbCl_5$ precursor is used, several silicide phases are present. This can be understood by realizing that $MoSi_2$ and WSi_2 have the same $C11_b$ crystal structure, while $NbSi_2$ has a C40 crystal structure. Thus, while the $(Mo,W)Si_2$ product is likely a substitutional solid solution, the niobium and molybdenum products are likely an intimate mixture of different phases. Further work is in progress to clarify these results.

CONCLUSIONS

SSM reactions provide a quick method for the preparation of transition metal silicides. The formation of a molten flux likely enhances solid-state diffusion, resulting in rapid formation of single phase, highly crystalline disilicides. Preliminary results indicate that solid-solution formation using SSM reactions is possible and further work will elucidate the parameters necessary for successful synthesis of the desired products.

ACKNOWLEDGEMENTS

The authors wish to thank E.G. Gillan, Dr. J.B. Wiley, and Dr. R.E. Treece for helpful discussions. Funding was provided by the National Science Foundation and a David and Lucile Packard Foundation Fellowship in Science and Engineering.

REFERENCES

1 A.K. Vasudévan and J.J. Petrovic, Mater. Sci. Eng. **A155** (1-2), 1 (1992).
2 P.J. Meschter, Scrip. Metall. **25**, 521 (1991).
3 S. Zhang and Z.A. Munir, J. Mater. Sci. **26** (13), 3685 (1991).
4 Z.A. Munir, Amer. Ceram. Soc. Bull. **67** (2), 342 (1988).
5 G. Le Caer, E. Bauer-Grosse, A. Pianelli, E. Bouzy, P. Matteazzi, J. Mater. Sci. **25**, 4726 (1990).
6 R.B. Schwarz, S.R. Srinivasan, J.J. Petrovic, C.J. Maggiore, Mater. Sci. Eng. **A155** (1-2), 75 (1992).
7 C.H. Henager and J.L. Brimhall, Scrip. Metall. **26**, 585 (1992).
8 J.B. Wiley and R.B. Kaner, Science **255**, 1093 (1992).

9 R.E. Treece, E.G. Gillan, R.M. Jacubinas, J.B. Wiley, and R.B. Kaner in *Better Ceramics Through Chemistry V*, edited by M.J. Hampden-Smith, W.G. Klemperer, and C.J. Brinkman (Mat. Res. Soc. Symp. Proc. **271**, Pittsburgh, PA, 1992) pp. 169-174.
10 JCPDS, Powder Diffraction File, Inorganic Phases, edited by W.C. McClune (JCPDS International Centre for Diffraction Data, Pennsylvania, 1988).
11 *Binary Alloy Phase Diagrams*, 2nd ed., edited by T.B. Massalski (ASM International, Ohio, 1990), p. 2666.
12 O. Kubaschewski and C.B. Alcock, *Metallurgical Thermochemistry*, 5th ed. (Pergamon Press Inc., New York, 1979), p. 268.
13 P.R. Bonneau and R.B. Kaner, Inorg. Chem., in press.

SYNTHESIS AND PROPERTIES OF $MoSi_2$/SiC PROCESSED BY LOW PRESSURE PLASMA CO-INJECTION AND DEPOSITION

D.E. Lawrynowicz, J. Wolfenstine, S. Nutt*, and E.J. Lavernia
Materials Science and Engineering
Department of Mechanical and Aerospace Engineering
University of California, Irvine, CA 92717-3975
*Division of Engineering, Brown University, Providence, RI 02912

D.E. Bailey and A. Sickinger
Electro-Plasma, Inc., Irvine, CA 92714

ABSTRACT

Low-pressure plasma deposition (LPPD) and co-injection has been used to fabricate a $MoSi_2$ composite reinforced with 15 μm SiC particles. The microstructure and creep behavior of the LPPD processed composite are reported and discussed. Scanning electron microscopy (SEM) and transmission electron microscopy (TEM) showed the structure of the composite to be lamellar and energy dispersive X-ray analysis (EDAX) identified the phases present in the material as: $MoSi_2$, Mo_5Si_3, SiO_2, and SiC. Density characterization revealed a porosity of less than 1.0 vol. %, indicating a nearly fully dense material. A high concentration of SiO_2 (~8.0 vol. %) present in the $MoSi_2$/SiC composite may be attributed to possible contamination of the starting powders before or during LPPD. Sublimation of SiC during co-injection led to a low volume fraction (< 2.0 vol. %) of reinforcement in the composite. The creep rate of the LPPD $MoSi_2$/SiC was higher relative to that of $MoSi_2$/SiC composites fabricated by powder metallurgy (PM) techniques. On the basis of the results of this study it has become evident that alternative processing methods such as LPPD *in-situ* processing may be better suited for the fabrication of elevated volume fraction $MoSi_2$/SiC composites.

Mat. Res. Soc. Symp. Proc. Vol. 322. ©1994 Materials Research Society

INTRODUCTION

In recent years, many intermetallic compounds such as aluminides and silicides have been extensively evaluated for high temperature structural applications [1,2]. Considerable attention has been directed towards refractory metal silicides as a result of their favorable elevated temperature characteristics. In particular, molybdenum disilicide ($MoSi_2$) has become a leading candidate matrix material for elevated temperature composites [2]. Its unique combination of physical attributes, which include: moderate density of 6.31 g/cm^3, high melting point of ~2030 °C, excellent oxidation resistance and high modulus at elevated temperatures [3-5], make it an integral part of continuing research for viable high temperature structural materials. The addition of second phases such as SiC improves the elevated temperature creep resistance and fracture toughness of the notoriously brittle monolithic $MoSi_2$ [5-9]. Currently, most of the SiC-reinforced $MoSi_2$ composites have been fabricated using conventional powder metallurgy (PM) techniques or solid-state reactions [7,9,10]. Inspection of the available scientific literature reveals a limited exploration of other alternative innovative synthesis techniques such as plasma spraying of $MoSi_2$/SiC composites [11]. This processing method is reported to provide further improvements in the mechanical properties through microstructural refinement as well as the prospect of near-net shape manufacturing [12].

It is suggested that the best overall mechanical properties (i.e., creep resistance, fracture toughness, etc.) of $MoSi_2$/SiC are realized when ~30 vol. % SiC is incorporated in the matrix [13]. Currently, plasma spray processing of $MoSi_2$/SiC has only been able to achieve up to ~ 10 vol. % SiC in the $MoSi_2$ matrix [4,13,14]. In view of these findings, the present study was undertaken with the objective of fabricating a high SiC content (~ 25 vol. %) reinforced $MoSi_2$ composite using low-pressure plasma deposition (LPPD). Accordingly, the microstructure and creep behavior of the plasma sprayed composite are discussed.

EXPERIMENTAL PROCEDURES

Processing

The experimental procedure used in the present investigation is described as follows. The $MoSi_2$ powders were obtained from CERAC (Milwaukee, WI) and ranged in size from 10-44 μm. The SiC powder had an average size of 15 μm and was obtained from Exolon-ESK (Tonawanda, NY). The $MoSi_2$ and SiC powders were combined in a 50-50 vol. % ratio in a blender and mixed until a uniform distribution was achieved. The LPPD processing experiments were conducted at Electro-Plasma Inc. (Irvine, CA) using an EPI-LPPS ™ system capable of spraying a wide variety of materials under high deposition rates with a number of different operating configurations. The present experiment utilized the co-injection capabilities of the plasma system. Two separate hoppers were used to feed two separate injection ports. One hopper contained the 50 vol. % $MoSi_2$-50 vol. % SiC mixture and the other hopper contained 100% SiC. The SiC injection port was positioned as far down into the plasma stream as physically possible in order to minimize the temperature the SiC would encounter in an effort to avoid sublimation of the SiC. The target substrate was a 150 mm x 150 mm x 5 mm molybdenum plate controlled by a two axis target manipulator. The choice of substrate material was based on minimizing thermal expansion differences between the substrate and the deposited material [12]. A summary of the primary processing parameters is shown in Table I. The resultant LPPD $MoSi_2$/SiC material exhibited a discoidal geometry of approximately 6 mm in thickness. The deposited composite was then removed from the substrate, sectioned and prepared for microstructural and mechanical characterization studies following established procedures.

Table I LPPD Processing Parameters

Plasma Unit	EPI-LPPS System
Plasma Gun	EPI-03CP
Voltage (Volts)	66
Current (Amps)	1400
Arc Gas Flow Rate - Ar (SLPM)	104
Second Gas - H_2 (SLPM)	15
Powder Gas Flow Rate $MoSi_2$+SiC - Ar (SLPM)	6
Powder Gas Flow Rate SiC - Ar (SLPM)	5
Powder Feed Rate SiC (g/min)	50
Powder Feed Rate $MoSi_2$+SiC (g/min)	50
Spray Distance (mm)	30.5
Spray Time (min)	45
Atmosphere (Pa)	$3x10^4$

Characterization

Scanning (SEM) and transmission electron microscope (TEM) analysis of the microstructural features was conducted on polished, unetched $MoSi_2$/SiC samples. The composition of the LPPD processed composite was analyzed using X-ray diffraction measurements. The density of the $MoSi_2$/SiC composite material was determined on as spray-deposited samples utilizing Archimede's principle. Porosity quantification was determined using image analysis of polished sections. These measurements were conducted in accordance with ASTM standards. The creep specimens evaluated in this investigation were rectangular parallelepipeds with a height to width ratio of approximately 2:1, with typical dimensions of 3.0 mm x 3.0 mm x 6.0 mm. The specimens were loaded perpendicular to the plasma spray direction and were deformed to a total true strain of approximately 0.15. After deformation, the samples were cooled rapidly under load to preserve any structures developed during creep.

RESULTS AND DISCUSSION

Image analysis characterization conducted on several representative random areas revealed a total porosity of less than 1.0 vol. %, indicating a nearly fully dense material. The density of the $MoSi_2$/SiC composite was measured to be 6.03 g/cm^3. From previous studies [4,13], the theoretical density of a 20 vol. % SiC reinforced $MoSi_2$ composite should be ~5.70 g/cm^3 (under the assumption that only $MoSi_2$ (6.31 g/cm^3) and SiC (3.21 g/cm^3) are present in the material). This result suggests that the composite material fabricated in this study contains less than 20 vol. % SiC. The discrepancy may be accounted for by the possible sublimation of SiC at elevated temperatures (>3500 °C) similar to those present in a plasma arc (4000-10^4 °C) [8]. In addition, SiC particles are readily dragged by the plasma stream as a result of their low density (3.21 g/cm^3). These two factors lead to significant loss of SiC during plasma spraying, and as a consequence, can account for the observed density difference. The loss of SiC may be minimized by utilizing an external injection nozzle that would deliver the SiC powder at the surface of the substrate as opposed to inside the plasma gun. Also, *in-situ* plasma spray fabrication of $MoSi_2$/SiC composites promises the capability of forming higher volume fraction SiC-reinforced $MoSi_2$ composites. These two approaches will be the focus of future experiments which will assess the viability of these alternative processing methods.

SEM Analysis

SEM images of transverse sections (perpendicular to the spray direction) of the spray formed composite revealed a wavy microstructure consisting of alternating layers of three different phases (see Figure 1) which were subsequently quantified by energy dispersive X-ray (EDAX) analysis. The higher magnification SEM micrograph of Figure 2 reveals consistent results.

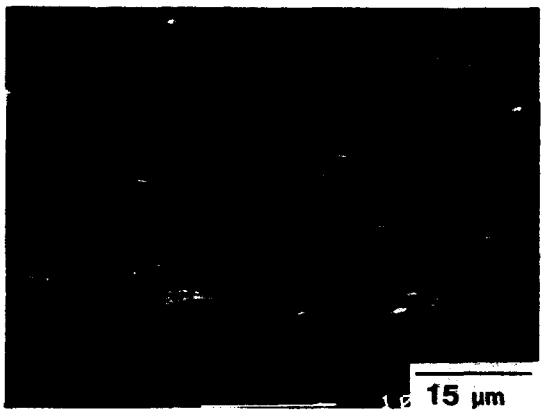


Figure 1 Transverse section of sprayed composite

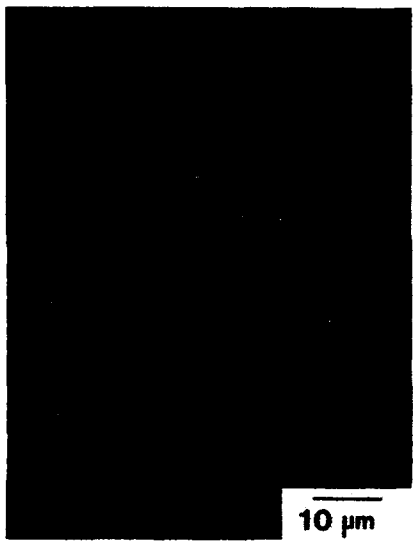


Figure 2 Magnified transverse section identifying phases: arrow # 1):SiO_2, #2): $MoSi_2$, #3): Mo_5Si_3

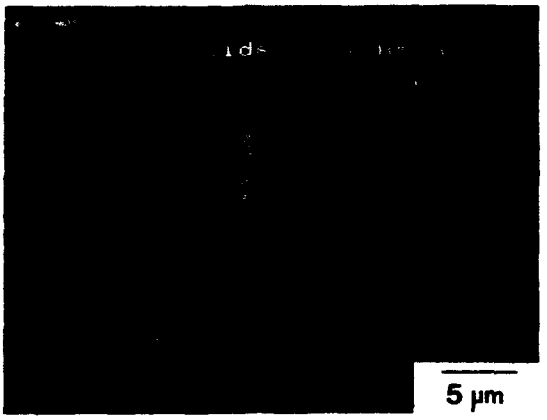


Figure 3 Magnified area of Figure 2 showing SiC (arrow # 1) SiO_2 (arrow # 2)

The wavy microstructure with limited porosity (< 1.0 vol. %) suggests that the $MoSi_2$/SiC droplets arrived at the deposition surface in a fully liquid condition, eventually spreading in the transverse direction. This process caused elongated flattened grains to be present in the microstructure. This result is consistent with the findings of Castro et al. who reported similar observations [16-17]. The dark phase identified by arrow 1 in Figure 2 was quantified by EDAX to be SiO_2, and comprised on average ~ 8.0 vol. % of the microstructure. The light gray phase denoted by arrow 2 in Figure 2 is comprised of 43.5 at. % Si and 56.5 at. % Mo which most likely corresponds to Mo_5Si_3. The dark gray phase numbered 3 in Figure 2 contains 66.2 at. % Si and 33.8 at. % Mo consistent with the $MoSi_2$ phase. The grain size of the composite varied with different phases. The $MoSi_2$ phase had a grain size which ranged from 2-10 µm while the Mo_5Si_3 phase had a 1-7 µm grain size range. A high magnification of a selected area of the micrograph of Figure 2 shows one of the few visible SiC particles (see Figure 3). Arrow 1 in Figure 3 points to a SiC particle and arrow 2 in Figure 3 identifies the associated SiO_2 phase found attached to SiC in nearly all of the randomly selected SiC particles found in the prepared samples. These results suggest that an oxidation reaction may have occurred at the location of SiC and the SiO_2 formed adjacent to those areas.

TEM Analysis

TEM observations revealed long stringers of layered phases present in the microstructure. This result were consistent with the previous microscopy analysis. Selected area diffraction (SAD) patterns of the various phases of the microstructure confirmed the presence of $MoSi_2$ and Mo_5Si_3. Figure 4 shows the lamellar structure, consistent with the SEM results, made up of alternating layers of $MoSi_2$ and Mo_5Si_3. In addition, a substantial concentration of the SiO_2 phase was also present. Figure 5 shows a glassy SiO_2 layer (arrow 1) present at a prior droplet boundary of $MoSi_2$. Similar SiO_2 features were observed in other samples and similar findings in plasma sprayed $MoSi_2$ have been reported by Maloy et al. [18-20]. The average particle size of the SiO_2

phase varied from 0.25-5 μm. SiC particles were observed less frequently. Figure 6 shows a typical SiC inclusion found in the microstucture. Very few of these particles were identified in the samples which were examined. In addition, the TEM revealed regions of dual-phase finely mixed $MoSi_2$ and Mo_5Si_3 (see Figure 7). This dual-phase mixture was present at various locations in the



Figure 4 Lamellar structure, arrow # 1: $MoSi_2$,arrow # 2: Mo_5Si_3



Figure 5 Glassy phase SiO_2 (arrow # 1) surrounded by Mo_5Si_3 (arrow # 2) and $MoSi_2$ (arrow # 3)



Figure 6 SiC inclusion (arrow #1)



Figure 7 Dual-phase region made up of both $MoSi_2$ and Mo_5Si_3 (arrow #1)

microstructure. The size of the dual-phase varied from thin bands (<0.1 μm) to larger areas up to several μm thick and 10 μm long. X-ray diffraction of the bulk material reconfirmed the presence of Mo_5Si_3, $MoSi_2$, SiO_2 and trace amounts (< 2.0 vol. %) of SiC.

Creep

The creep data for the as-sprayed and heat treated $MoSi_2$/SiC composite is shown in Figure 8 on a plot of logarithm steady-state creep rate vs. logarithm applied stress. Also shown on the Figure 8 is data for a PM $MoSi_2$/SiC [21]. The slope of the curves is equal to the stress exponent, n. From Figure 8 several important points are noted. First, the creep rate of the plasma sprayed $MoSi_2$/SiC material is faster than that for the PM composite over the entire stress range investigated. Second, different stress exponents are exhibited by the plasma sprayed (n~2.3) and the PM (n~3.3) materials. Third, as the annealing time increases the creep rate for the plasma sprayed material decreases.

Microstructural examination of the deformed specimens revealed very little change in grain morphology and size, as a result of deformation. In addition, there was only a slight increase in dislocation density due to deformation.

The stress exponent of about 2, combined with the microstructural observations that the grains remained equiaxed with almost no increase in dislocation density due to deformation, suggests that the creep behavior of the fine grained plasma prayed material is controlled by a grain boundary sliding mechanism. In contrast, it has been postulated that the creep behavior of the PM $MoSi_2$/SiC is controlled by a dislocation mechanism [21]. For the case of a grain boundary sliding mechanism it is observed that the creep rate is a function of the grain size [4,22]. In general, as the grain size increases the creep rate decreases. The results shown in Figure 8 are in agreement with this suggestion.

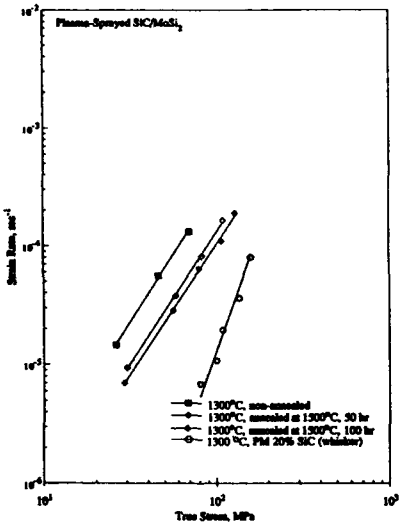


Figure 8 Creep curves comparing results of present study

The possible reasons why the creep rate for the plasma sprayed SiC reinforced $MoSi_2$ is higher than that for the PM SiC reinforced $MoSi_2$ are as follows: 1) lower volume fraction of SiC reinforcement (2 versus 20 vol. %), 2) lower aspect ratio (particulate versus whisker), 3) smaller grain size (5 versus 10 μm) and 4) the presence of an amorphous boundary phase at prior droplet boundaries in the plasma sprayed material. However, the presence of silica grain boundary phases has also been noted in some PM monolithic and reinforced $MoSi_2$ [13,14]. Further work is currently underway to identify the most important reason for the difference, and to increase the creep resistance of the plasma sprayed SiC reinforced $MoSi_2$.

CONCLUSIONS

The $MoSi_2$/SiC composite material formed by plasma spray, co-injection and deposition elucidated several aspects of the processing method and its effect on the material properties. First, sublimation of SiC during co-injection leads to a low volume fraction of reinforcement in the composite. Second, the high concentration of SiO_2 present in the microstructure can be attributed to possible contamination of the starting powders before or during LPPD and volatilization of SiC. The microstructure of the $MoSi_2$/SiC composite formed by LPPD was >99 % dense and contained the following phases:

SiC	~	2.0 %
SiO_2	~	8.0 %
Mo_5Si_3	~	20.0 %
$MoSi_2$	~	70.0 %

The creep rate of the LPPD $MoSi_2$/SiC is higher relative to PM $MoSi_2$/SiC composites. The creep rate of the LPPD $MoSi_2$/SiC decreased with an increase in grain size. It is proposed the creep behavior of LPPD $MoSi_2$/SiC is controled by a grain boundary sliding mechanism. As a result of this investigation, it was determined that LPPD and co-injection of $MoSi_2$/SiC is not an effective processing alternative for this composite. Future work will investigate LPPD *in-situ* reaction of SiC in $MoSi_2$ as yet another processing option for this composite system.

ACKNOWLEDGMENTS

The authors would like to acknowledge an Air Force Office of Scientific Research Augmentation Award for Science and Engineering Research Training (AASERT no. 442530-22537) and Electro-Plasma Inc. (Irvine, CA) for financial support and encouragement. Support from the office of Naval Research for SRN is also acknowledged. The authors would also like to acknowledge financial support from the National Science Foundation under grant no. DMR-9122365 for the acquisition of the X-ray diffraction facility. The authors would like to thank Dr. Bill Long from Exolon-ESK (Tonawanda, NY) for providing the SiC powders. In addition, the authors would like to acknowledge the excellent microanalysis and materials characterization performed by Janusz K. Terlecki at PhotoMetrics, Inc. (Huntington Beach, CA).

REFERENCES

1. X. Liang, H.K. Kim, J.C. Earthman, and E.J. Lavernia, Mater. Sci. Eng. **A153**, 646-653, (1992).

2. C.T. Sims, N.S. Stoloff, and W.C. Hagel, eds., Superalloys II (John Wiley & Sons, New York, 1987), pp. 519-549.

3. J. Schlichting, High Temperatures-High Pressures, **10**, 241 (1978).

4. Y.L. Jeng, J. Wolfenstine, E.J. Lavernia, D.E. Bailey, and A. Sickinger, Scripta Metall. **28**, 453 (1993).

5. Y.L. Jeng, E.J. Lavernia, J. Wolfenstine, D.E. Bailey, and A. Sickinger, Scripta Metall. **29**, 107 (1993).

6. F.D. Gac and J.J. Petrovic, J. Am. Ceram. Soc. **68**, C-200 (1985).

7. D.H. Carter and G.F. Hurley, J. Am. Ceram. Soc. **70**, C-79 (1987).

8. W.S. Gibbs, J.J. Petrovic, and R.E. Honnell, Ceram. Eng. Sci. Proc. **8**, 645 (1987).

9. D.H. Carter, J.J. Petrovic, R.E. Honnell, and W.S. Gibbs, Ceram Eng. Sci. Proc. **10**, 1121 (1989).

10. A.K. Bhattacharya and J.J. Petrovic, J. Am. Ceram. Soc. **74**, 2700 (1991).

11. M.L. Thorpe, "Thermal Spray," Adv. Mater. Proc. **5**, 50-62, (1993).

12. J. Karthikeyan, R. Ratnaraj, A.J. Hill, Y.C. Fayman and C.C. Berndt, in Thermal Plasma Coating: Properties, Processes and Applications, edited by T.F. Bernecki (ASM International, Materials Park,Ohio.1992) .

13. A.K. Vasudevan and J.J. Petrovic, Mater. Sci. Eng. A155, 1-17, (1992).

14. Y.L. Jeng and E.J. Lavernia, submitted for publication in Mater. Sci. Eng., Oct. 1993.

15. R.G. Castro, R.W. Smith, A.D. Rollett, and P.W. Stanek, Scripta Metall. **26**, 207 (1992).

16. R.G. Castro, R.W. Smith, A.D. Rollett, and P.W. Stanek, Mater. Sci. Eng. **A155**, 101 (1992).

17. R.G. Castro, H. Kung, and P.W. Stanek, accepted for publication in Mater. Sci. Eng., Oct. 1993.

18. S.A. Maloy, A.H. Heuer, J.J. Lewandowski, and J.J. Petrovic, J. Am. Ceram. Soc. **74**, 2704-2706 (1991).

19. S.A. Maloy, J.J. Lewandowski, A.H. Heuer, and J.J. Petrovic, Mater. Sci. Eng. **A155**, 159 (1992).

20. N.S. Jacobson, K.N. Lee, S.A. Maloy, and A.H. Heuer, J. Am. Ceram. Soc. **76** (8), 2005-2009 (1993).

21. K. Sadananda and C.R. Feng, Mater. Sci. Eng. **A170**, 199 (1993).

22. M. Suzuki, S.R. Nutt, and R.M. Aikin, Jr., Mater. Sci. Eng. **A162**, 73 (1993).

THERMO-CHEMICAL SYNTHESIS OF NANOSTRUCTURED CHROMIUM SILICIDE / SILICON CARBIDE AND MOLYBDENUM SILICIDE / SILICON CARBIDE COMPOSITE POWDERS

Ping Luo*, Peter R. Strutt and Kenneth E. Gonsalves**
* Connecticut Advanced Technology Center for Precision Manufacturing and Department of Metallurgy, University of Connecticut, Storrs, CT 06269
**Institute of Materials Science, Polymer Program, University of Connecticut, CT 06269

ABSTRACT

Intermetallic silicides and silicon carbide composites are potential useful materials in high temperature applications requiring superior strength combined with enhanced fracture toughness. This paper presents results obtained on these materials in nanostructured form, since structural reduction to this scale offers a way for achieving unique properties.

Chromium silicide / silicon carbide and molybdenum silicide / silicon carbide composite powders were readily synthesized by thermal conversion from spray dried precomposites at 1250°C. Basically, the process involves spray drying the aqueous chemical solution to a precomposite, followed by thermal conversion in a tube furnace reactor. The phases present in the composites are hexagonal $Cr_{5-X}Si_{3-X}C_{X+Y}$ ($Cr_5Si_3C_X$) / cubic β-SiC and tetragonal $MoSi_2$, hexagonal $Mo_5Si_3C_X$/ cubic β-SiC. The volume fraction of these phases can be controlled through the solution preparation of the precursors. Characterization of composite powders include x-ray diffraction spectrometry (XRD), scanning electron microscopy (SEM) and transmission electron microscopy (TEM). Particle size distribution of the synthesized chromium silicide and silicon carbide composite was conducted by a computerized image analyzer and the statistical result was obtained.

INTRODUCTION

Advanced material systems for service at high temperatures up to temperature 1600°C must combine strength, creep strength, fracture toughness and high thermal conductivity. The latter is now of considerable importance in applications where rapid heat dissipation is necessary. Although carbon / carbon and ceramic / ceramic composites are now being developed for high temperature applications, these materials have inherent limitations [1]. Uncoated carbon /carbon composites for example, have poor oxidation resistance and ceramic / ceramic composites are brittle over the operative temperature range. Consequently, intermetallic-matrix composites are of considerable potential importance because they can have good fracture toughness at high temperatures. Studies of potential intermetallic phases and reinforcing phases (with requisite strength and elastic modulus) indicate the intermetallic silicides and silicon carbide to be a good candidates for composites.

Composites having ultrafine microstructures is a concept that can provide the means for achieving isotropic properties and optimized fracture toughness. Additionally, there is the important concept of super strength, when a high volume fraction (>50%) of submicron particles are embedded into a ductile matrix. This unusually high strength depends solely on the inverse particle diameter and particle-matrix interfacial properties. It is temperature independent and is maintained even at the matrix melting temperature. The preceding aspects illustrate some of the

Mat. Res. Soc. Symp. Proc. Vol. 322. ©1994 Materials Research Society

benefits to be gained by synthesizing large amounts of composites possessing nanostructures such as chromium silicide and molybdenum silicide /silicon carbide. Although the thermodynamic compatibility of such systems has been calculated, the processing capability needs to be developed for producing the structures on a sufficiently nanoscale. Recent works [1,2,3] have shown, for instance, that molybdenum silicide powders containing silicon carbide can be produced by rapid solidification or conventional hot pressing techniques. With these techniques, however, the dispersoids are too coarse for achieving the desirable properties. This structural scale limitation may be overcome by developing appropriate chemical precursors and processing routes to produce silicide matrix nanoparticles, dispersion strengthened by silicon carbide nanoparticles. Based on newly developed synthesis technologies at the University of Connecticut [4,5,6], a solution chemical synthesis route is selected for synthesizing a chromium silicide / molybdenum silicide and silicon carbide nanocomposite. The approach involves (i) the spray drying of water soluble inorganic compounds to form an intermediate precursor, and (ii) thermal chemical conversion of the intermediate precursor to form the final product material at an elevated temperature in a dynamic gas environment.

EXPERIMENTAL

Chromium chloride ($CrCl_3$) or molybdenum chloride ($MoCl_5$), sodium methylsiliconate ($CH_3Si(ONa)_3$) with 30wt% water and dextrose (D-Glucose $C_6H_{12}O_6$) were dissolved in distilled water to produce an aqueous solution. Spray drying of the precursor was performed in a spray dryer. The solution was pumped from a feed tank into the spray nozzle. Atomization was achieved using compressed air. The resulting powder was cyclone separated from the flowing gas stream. The intermediate precursor powders were placed in an alumina crucible in a tube furnace. The system was cyclically evacuated to 10^{-3} torr and flushed with argon gas several times, and then back filled with argon gas to near ambient pressure. During this process operation, the system was maintained under an argon flow rate of 70 cc/min.

CHARACTERIZATION

X-ray Analysis

X-ray diffraction analysis provides detailed information of the crystalline structural characteristics (crystalline phase formations). Fig.1 shows the x-ray spectra for the synthesis of chromium silicide and silicon carbide composites at the 1250°C. Samples were prepared from different solution precursors where the concentration ratios of chromium chloride ($CrCl_3$), sodium methylsiliconate ($CH_3Si(ONa)_3$) and D-Glucose ($C_6H_{12}O_6$) were 1:3:1, 1:2:1, and 1:4:2.

The analysis revealed the chromium silicide phase has a hexagonal structure and the modification is $Cr_{5-X}Si_{3-Y}C_{X+Y}(Cr_5Si_3C_X)$; silicon carbide has a cubic structure and the modification is $\beta-SiC$. *Silicon dioxide cristolbalite SiO_2 presented as crystalline phases in the composite* for the samples prepared from the solution precursors where the molar ratios 1:3:1 and 1:2:1 but not 1:4:2. By increasing the processing temperature up to temperature 1300°C, SiO_2 cristolbalite phase disappearing for the sample 1:2:1. (Fig.2). It suggests that the silicon dioxide phase as impurity of the final composite can be controlled by optimizing the Cr, Si, and C ratios of the precursors and the processing temperatures.

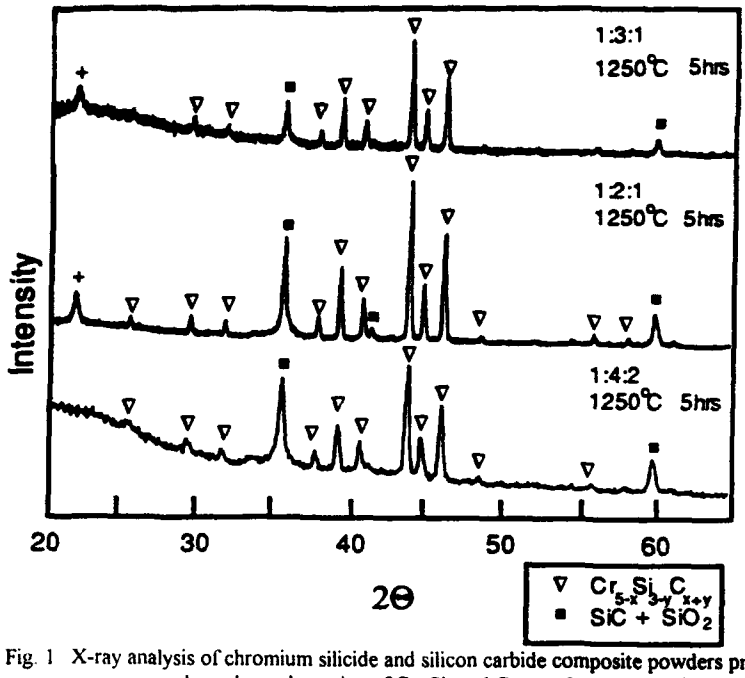


Fig. 1 X-ray analysis of chromium silicide and silicon carbide composite powders produced from precursors where the molar ratios of Cr, Si, and C are 1:3:1, 1:2:1 and 1:4:2 at 1250°C for 5 hours.

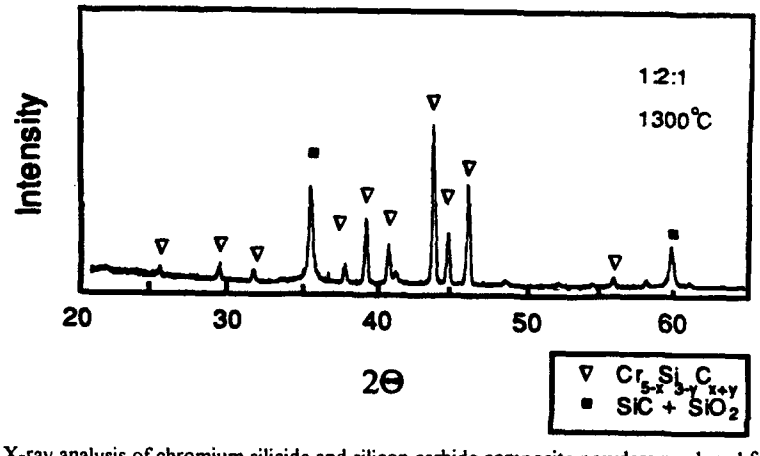


Fig. 2 X-ray analysis of chromium silicide and silicon carbide composite powders produced from the precursor with Cr, Si, and C molar ratio in 1:2:1 at 1300°C for 3.5 hours.

Molybdenum silicide and silicon carbide composite was prepared from a precursor made of molybdenum chloride ($MoCl_5$) and sodium methylsiliconate ($CH_3Si(ONa)_3$) and D-Glucose ($C_6H_{12}O_6$), where the molar ratio of Mo, Si and C was 1:4:2. The process was followed by a thermal chemical treatment at 1300°C for 5 hours. The synthesized final composite was revealed by the x-ray analysis and the analytical result is shown in Fig.3. The contained phases of the synthesized composite were identified as tetragonal $MoSi_2$, hexagonal $Mo_5Si_3C_x$, and cubic β-SiC. It was found that different phase modifications of molybdenum silicides and chromium silicides were produced in the synthesized composite even though they were produced from the solution precursors with the same molar ratios. This result might due to the differences between $CrCl_3$ and $MoCl_5$. that the ionic status of chromium is in the 3^+ and of molybdenum is in 5^+. A slight difference in the reaction paths involved may affect on the silicide formation.

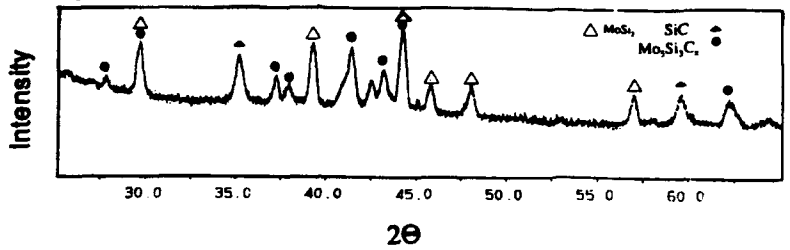


Fig. 3 X-ray analysis of molybdenum silicide and silicon carbide composite powders produced at 1250°C for 5 hours.

Electron Microscopy Examinations

Morphological examinations of the synthesized powders were performed using SEM and TEM. Fig.4 is a SEM micrograph of the powders, which shows transparent and hollow structures under the electron beam. These particles were observed and examined using the TEM. Studies revealed these powders are nanostructured agglomerates, each agglomerate is in the nanometer size, and these agglomerates are platelets with the hexagonal or cubic shapes (Fig.5).



Fig. 4 Scanning electron microscopy (SEM) examination shows the morphology of the synthesized chromium silicide and silicon carbide composite powder.

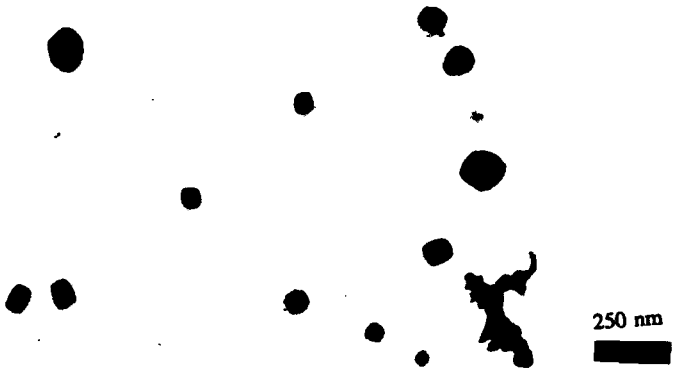


Fig. 5 Transmission electron microscopy (TEM) examination shows the shapes of the particulates of the synthesized chromium silicide and silicon carbide composite powder.

Particle size distribution

Image analysis was applied to investigate the particle size distribution. A SEM picture of the agglomerated composite powder was taken and imported into a image analyzer. The diameters of these particles were measured on the screen and statistically calculated. Fig.6 shows the size distribution of the agglomerated particles which were produced at 1250°C for 5 hours. The agglomerated particles have the average (mean) size of 1.12 μm. The maximum size is 3.72 μm and the minimum size is 0.0438 μm. 90% of the measured particles are in the size range below to 2 μm. It is difficult to measure the minimum particle size because very tiny particles which are below 0.1 m are not able to be counted from the SEM picture. In order to analyze the particulate of the agglomeration, sample powders were analyzed using the high resolution TEM. Fig. 7 shows the size distribution of the particulate. The average (mean) value of the size is 50.47 nm, the maximum value is 92 nm. The minimum value is 13.6 nm. The particulate size distribution is in the type of the Gauss-distribution.

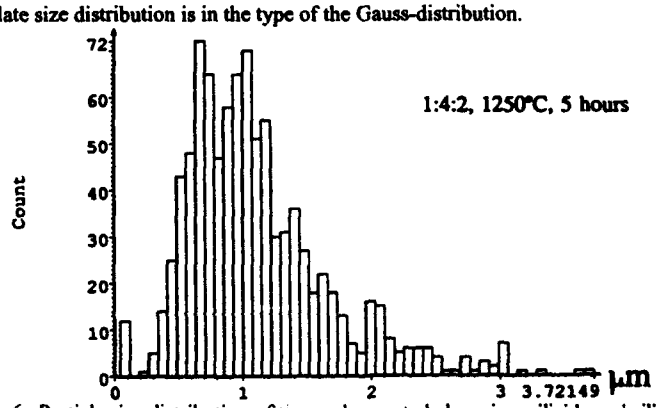


Fig. 6 Particle size distribution of the agglomerated chromium silicide and silicon carbide composite powders.

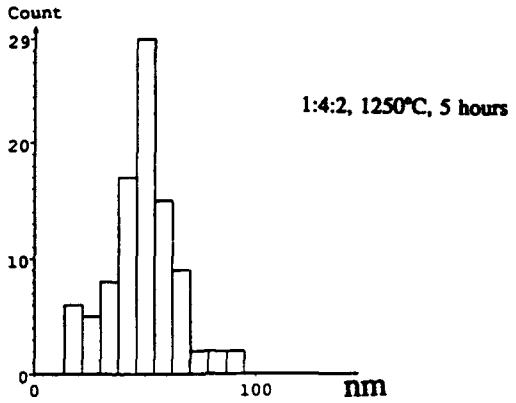


Fig. 7 Particle size distribution of the particulates of chromium silicide and silicon carbide composite powders

CONCLUSION

A process for the synthesis of nanostructured chromium silicide/ molybdenum silicide and silicon carbide composites has been developed. This paper mainly emphasizes the merit of a materials synthesis technique that involves the thermo-chemical materials processing concepts. Silicon carbides in both intermetallic composites show the cubic structure and β- SiC modification. Intermetallic silicides are in the hexagonal and tetragonal structures and the modifications were identified as $Cr_{5-X}Si_{3-Y}C_{X+Y}(Cr_5Si_3C_X)$, $Mo_5Si_3C_X$ and $MoSi_2$. The agglomerated powders are in the spherical shape and have a mean value around 1 μm diameter. The particulates are in the cubic and hexagonal shapes and have a mean value around 50 nm length. Knowledge obtained in this study can be easily extended to the synthesis of other nanostructured intermetallic silicides and silicon carbide systems.

REFERENCES

1. P.J. Meschter and D.S. Schwartz, J. Metals, 52 (1989)

2. W.S. Gibbs, J.J. Petrovic, and R.E. Honnell, Ceram. Eng. Sci. Proc., **8**, 645 (1987)

3. A.K. Vasudevan and J.J. Petrovic, Mat. Sci. and Eng., A, **155**, 1 (1992)

4. P. Luo, P.R. Strutt, and T.D. Xiao, Mat. Sci. and Eng., B, **17**, 126 (1993)

5. K.E. Gonsalves, P.R. Strutt, T.D. Xiao, and P.G. Klemens, J. of Mater. Sci. **27**, 3231 (1992)

6. T.D. Xiao, K.E. Gonsalves, P.R. Strutt, and P.G. Klemens, J. of Mater. Sci. **28**, 1334 (1993)

PART III

Silicide Mechanical Behavior and Problems

A REVIEW OF CREEP OF SILICIDES AND COMPOSITES

K. SADANANDA AND C.R. FENG
Materials Science and Technology Division, Naval Research Laboratory, Washington D.C. 20375

ABSTRACT

A review of creep behavior of molybdenum disilicides and their composites is presented. Creep rates of these silicides are compared with those of other high temperature materials such as superalloys, ceramic-ceramic composites, intermetallics including aluminides (nickel and titanium), berylides (vanadium and niobium), and refractory metals(molybdenum and tungsten). Creep rates of silicides are shown to be very sensitive to grain size even in the power-law creep regime with grain size exponent of the order of five and above. In addition, the results show that with increase in volume fraction of reinforcements there is a decrease in creep rates for volume percentages less than 25%. To achieve significant improvement in creep strength volume percentages of reinforcements greater than 25% are required. This weakening effect at low volume percentages is related to accompanying decrease in grain size with the addition of reinforcements. Addition of carbon to $MoSi_2$ eliminated the silica present at grain boundaries and converted it to SiC. The SiC thus formed, inhibited grain growth during hot pressing. Thus although addition of carbon enhanced creep resistance, its effect is masked by the accompanying decrease in grain size. Thus, grain size plays a dominant role in the creep of molydisilicide composites. It is shown that among all the materials molybdenum disilicides possess very high creep resistance comparable to ceramic-ceramic composites.

INTRODUCTION

Creep and oxidation resistance is a limiting factor for many high temperature applications. For temperatures below 1000°C , nickel base superalloys are being used extensively as structural materials in propulsion systems. The strength of these alloys is primarily due to the presence of a high volume fraction of an intermetallic Ni_3Al as coherent precipitates in a fcc matrix. Above 900°C the precipitates go into solution, and the strength drops precipitously. Distribution of dispersoids by mechanical alloying could retain some amount of strengthening, but since the volume fraction and the size of these dispersoids are small, the improvement in creep strength is only marginal.

For temperature greater than 1000°C , the competing materials are, refractory alloys, intermetallics and ceramics. There are two disadvantages with refractory alloys, particularly bcc metals. First, they are extremely susesptable to oxidation, and second, because of their open crystal structure, their creep resistance is lower than that expected based on their melting point. Coming to the structural ceramics, most of them are

Mat. Res. Soc. Symp. Proc. Vol. 322. ©1994 Materials Research Society

brittle even in the range of 1000-1400°C. The only alternate is intermetallics. Among the intermetallics, aluminides and silicides are the two most important class of materials that have high potential for application at high temperatures, because of their high resistance to oxidation due to the formation protective layers of aluminia or silica. Some aluminides and berylides have an additional advantage due to their high specific strength. In recent years, $MoSi_2$- based systems have been explored as alternatives to ceramics, because of their metallic nature, oxidation resistance, and significant ductility at temperatures above 1000°C . Attempts are being made to optimize the strength of these silicides by alloying and by using particulate and/or whisker reinforcements. Molybdenum disilicide is currently being used as a heating element for high temperature furnaces. In this report, we review extensive creep studies conducted at the Naval Research Laboratory on a variety of $MoSi_2$- based systems[1-8] and compare the creep data with those published in the literature on similar systems [9-16].

CREEP OF MOLYBDENUM DISILICIDE BASED SYSTEMS

Creep behavior of $MoSi_2$ has been studied by several investigators, and Table I provides the data in terms of materials, processing conditions and the microstructural details of the systems studied. The specific size, aspect ratio and distribution of the SiC particulates and whiskers in the $MoSi_2$ matrix that we have tested have been studied in detail and discussed elsewhere[7]. These materials were obtained from Los Alamos Laboratory. Most of the materials listed in Table I were obtained through powder processing route by hot pressing or hot isostatic pressing for densification. Initial and final grain sizes, processing conditions, and final distribution of particulates are different for each material as shown in Table I. Because of these differences in processing and final microstructure care should be exercised in comparing the results of one material with the other. Both our effort and the effort by Weiderhorn et al.[9,16] involved testing of the same materials from Los Alamos and, therefore, the results can be compared on a one-to-one to basis. We present below review of our results in terms of the effect of microstructural and metallurgical variables on the creep behavior. Later we compare our results with those of Weiderhorn et al. as well as the with the results of other workers listed in Table I.

Effect of Grain Size

Fig. 1 shows the effect of grain size on the creep rates in monolithic $MoSi_2$ at 1200°C[8]. The following points may be noted from the figure: (a) with increase in grain size from 14 to 25 μm, creep rates decreased by more than two orders of magnitude, (b) the decrease is more pronounced at low stresses, (c) although the decrease is monotonic with increase in grain size, the decrement is not a smooth function of the grain size, and (d) over the range of applied stresses, the stress-strain exponent varies from n=2 to n=5 for small grain sizes, and from n=4 to n=9 for large grain sizes. Normally the grain size effect is observed in metallic or ceramic systems in the Newtonian viscous regime with stress exponent n=1 but not in the power-law regime [18]. In the power-law regime, the grain size dependence is not normally

TABLE I: Materials, Microstructural Parameters and Processing Conditions

Material	Processing	Proc. T. °C	Grain Size µm	Ref.
$MoSi_2$	Hot pressing	-	-	Maxwell
$MoSi_2$	HIPing	1800	20	Suzuki et al
$MoSi_2$	Hot pressing	1600-1650	-	Bose
$MoSi_2$	HIPing	1650-1700	30	Bose
$MoSi_2$	HIPing	1700	30	Ghosh et al
$MoSi_2$	Hot pressing	1820	18	Sadananda et al
$MoSi_2$, single crystal <210>		-	-	Bose
$(Mo,W)Si_2$	Hot pressing	1600-1650	-	Bose
$(Mo,W)Si_2$	Hot pressing	1650	13	Sadananda et al
$MoSi_2$+20v%SiC_w	Hot pressing	1600-1650	-	Bose
$MoSi_2$+18v%SiC_w	HIPing	1650-1700	10	Bose
$MoSi_2$+20v%SiC_w	HIPing	1700	7	Ghosh et al
$MoSi_2$+20v%SiC_w	Hot pressing	1815	18	Sadananda et al
$(Mo,W)Si_2$+20v%SiC_w	Hot pressing	1900	19	Sadananda et al
$(Mo,W)Si_2$+20v%SiC_w *	Hot pressing	1900	20	Wiederhorn et al
$MoSi_2$+20v%SiC_p	HIPing	1350	-	Deve et al
$MoSi_2$+20v%SiC_p/Mo	HIPing	1350	-	Deve et al
$MoSi_2$+20v%SiC_p	HIPing	1700	3	Ghosh et al
XD $MoSi_2$+30v%SiC_p	HIPing	1600	10	Suzuki et al
$MoSi_2$+20v%$Er_2Mo_3Si_{4p}$	-	-	-	Patrick et al
$MoSi_2$+20v%CaO_p	-	-	29	Patrick et al
$MoSi_2$-45v%Mo_5Si_3	Hot pressing	-	7, 15	Mosan et al
$MoSi_2$-45v%Mo_5Si_3,DS	Direct. solid.	-	7	Mosan et al
$MoSi_2$+5v%SiC_p	Hot pressing	1850	10	Sadananda et al
$MoSi_2$+10v%SiC_p	Hot pressing	1850	8	Sadananda et al
$MoSi_2$+20v%SiC_p	Hot pressing	1850	6.5	Sadananda et al
$MoSi_2$+30v%SiC_p	Hot pressing	1850	5.5	Sadananda et al
$MoSi_2$+40v%SiC_p	Hot pressing	1850	5	Sadananda et al
$MoSi_2$+5v%SiC_p	Hot pressing	1850	-	Wiederhorn et al
$MoSi_2$+10v%SiC_p	Hot pressing	1850	-	Wiederhorn et al
$MoSi_2$+20v%SiC_p	Hot pressing	1850	-	Wiederhorn et al
$MoSi_2$+30v%SiC_p	Hot pressing	1850	-	Wiederhorn et al
$MoSi_2$+40v%SiC_p	Hot pressing	1850	-	Wiederhorn et al
$MoSi_2$+9v%SiC	Plasma spray	-	-	Jeng et al
$(Mo,W)Si_2$+20v%SiC_p	HIPing	1600-1650	-	Bose
$(Mo,W)Si_2$+20v%SiC_p+10Nb p	HIPing	1600-1650	-	Bose
$MoSi_2$+1wt%C	Hot pressing	1800, 1600	15, 5	Sadananda et al
$MoSi_2$+2wt%C	Hot pressing	1800	7	Sadananda et al
$MoSi_2$+4wt%C	Hot pressing	1800	6	Sadananda et al

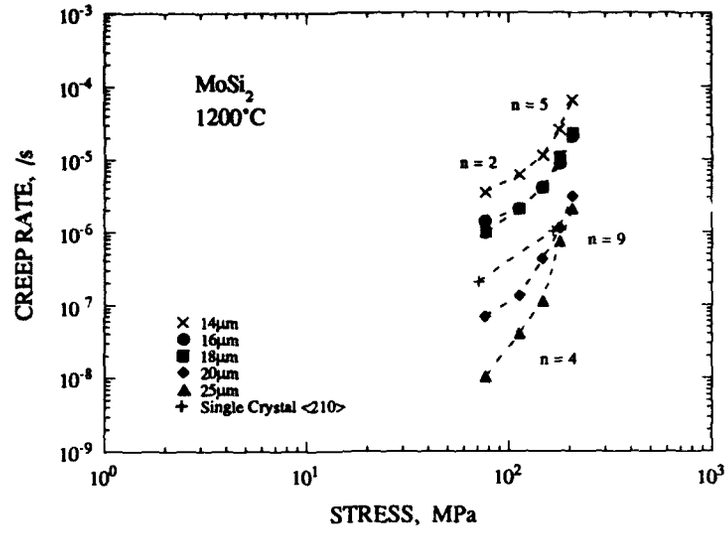


Fig. 1. Effect of grain size on the creep of $MoSi_2$

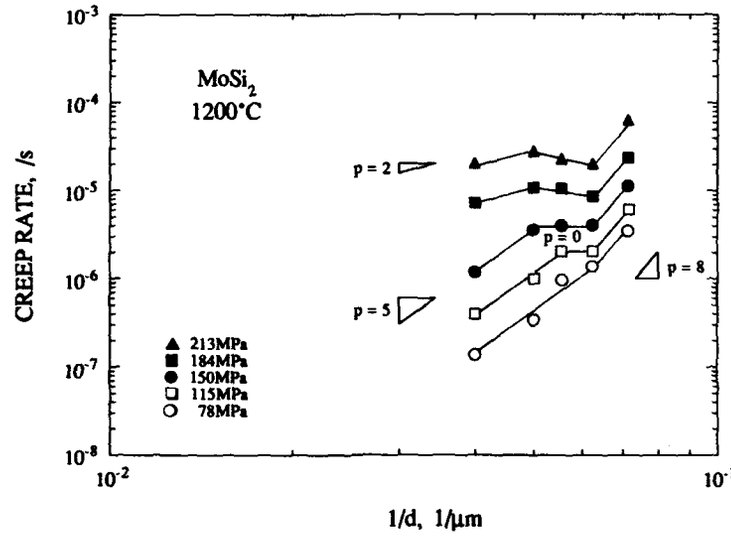


Fig. 2. Grain size exponents in the power-law creep regime for $MoSi_2$

observed since the controlling mechanism consists of the dislocation glide and climb. The dislocation free path in the power-law creep regime is smaller than the grain size, and therefore the grain boundaries are not expected to play a dominant role in the dislocation climb. To analyze the grain size effect further, we have plotted log of creep rate as a function of log of 1/d, where d is the grain size. Fig. 2 shows that the grain-size exponent varies from 5 to 8 in the low stress regime. With increase in stress the data appears to indicate the there is an intermediate grain size regime where the effect disappears. Normally, the grain size exponent is 2 for Nabarro- Herring creep involving bulk diffusion of vacancies, and it is 3 for Cobel creep involving grain boundary diffusion. High grain boundary exponents of the order of 5 and above have been rarely observed. Thus there are two puzzling factors in relation to grain size effect: (a) that the grain size effect is significant in the power-law creep regime and that (2) the grain size exponent is greater than three; it is of the order of 5 and above for the most of the creep range. We note that the grain size effect was also observed in other intermetallic systems and this aspect was discussed earlier[8].

Effect of Alloying

In order to improve the creep resistance of $MoSi_2$ system, two alloying additions were considered. From the phase diagram, $MoSi_2$ is essentially a line compound and does not tolerate solubility of molybdenum or silicon. Any excess silicon added during processing gets oxidized as amorphous silica and forms a glassy phase at the grain boundaries. This glassy phase causes free grain boundary sliding accentuating creep deformation. To eliminate the silica, carbon is added during processing which converts silica to SiC. SiC forms particulates and reinforces the matrix $MoSi_2$ and hence should improve its creep resistance. The other alloying effect that was considered was the addition of WSi_2, which, because of its identical crystal structure, forms an extended solid solution with $MoSi_2$. We will consider the effects of both carbon and WSi_2 on the creep behavior of $MoSi_2$.

Figure 3 shows the effect of creep rates with carbon addition. All the specimens were hot pressed at the same temperature. It appears from the curves that carbon has very little effect since the creep rates are essentially the same as the base material with carbon varying from zero to 4%. However the analysis indicates that there is a small decrease in grain size with increase in carbon content. Microstructural examination shows that this decrease in grain size is related to the formation of particulates of SiC which inhibit the grain growth during hot pressing. Fig. 4 shows the TEM micrographs of (a) monolithic material with grain boundary silica (b) reduction of silica by carbon to from SiC, and (c) SiC particulates in a reinforced material. In (b), in addition to SiC, precipitates of CMo_5Si_3 were also noted at the grain boundaries. This precipitate could only have formed by an additional reaction of C with $MoSi_2$. C can remove Si from $MoSi_2$ to form additional SiC thus reducing molybdenum disilicide to a lower silicide. It is important therefore to add just enough C to reduce all the silica but not the molydisilicide. In order to consider the effect of the addition of carbon on creep without the masking effect of the grain size, we have compared the materials that processed at different hot pressed temperatures that resulted in very nearly the same grain size (within the errors measurement). Real effect of carbon addition(at constant grain size) is shown in Fig. 5. In comparison to Fig. 3, the effect

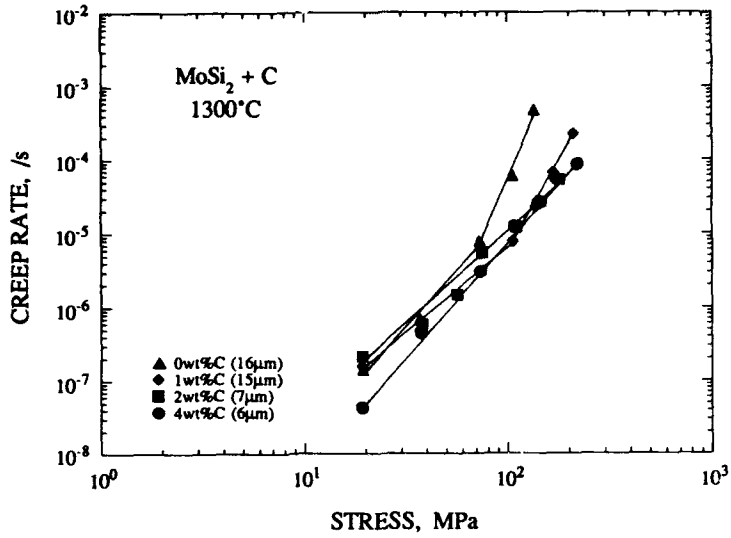


Fig. 3. Effect of carbon addition on creep of $MoSi_2$

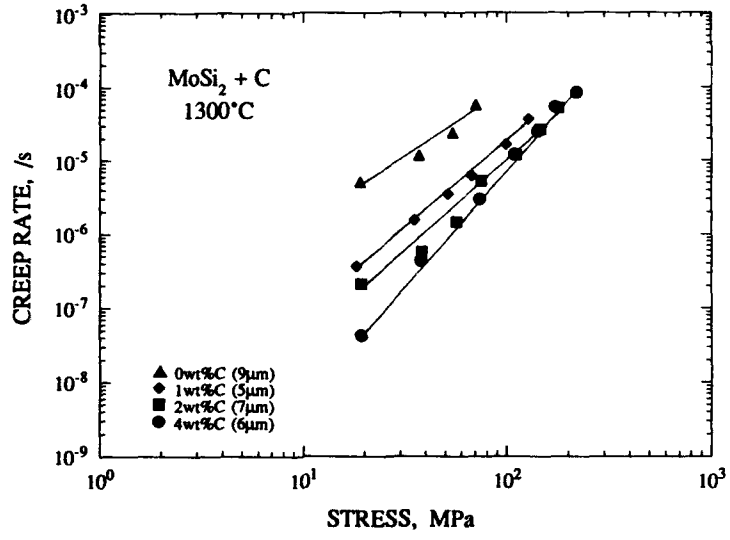


Fig. 5. Effect of carbon on creep of $MoSi_2$ at constant grain size.

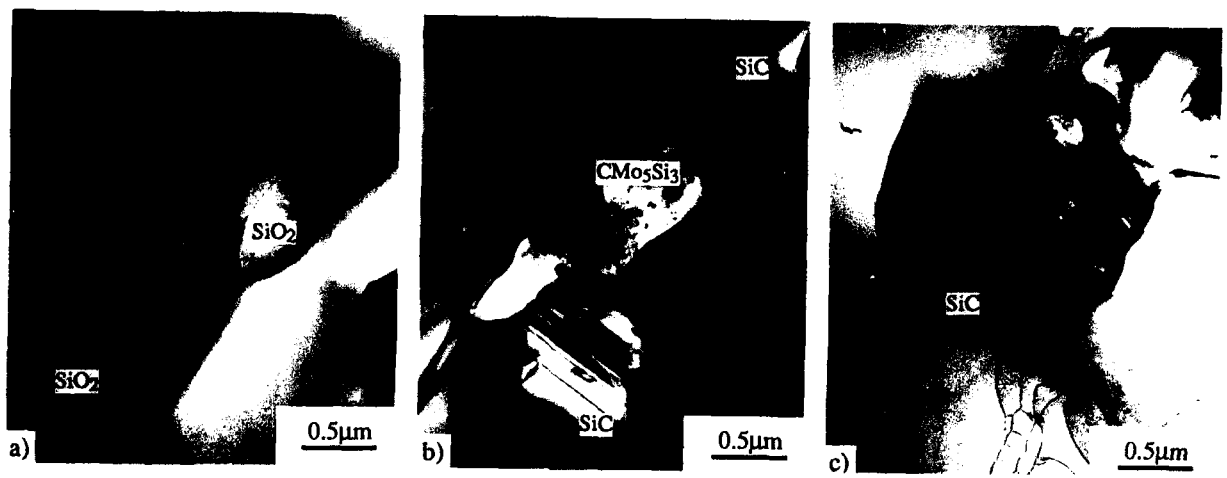


Fig. 4 TEM micrographs (a) $MoSi_2$ with silica present (b) Addition of carbon to convert silica to SiC and (c) SiC particulate reinforced $MoSi_2$ composite

of carbon addition is clearly evident. Addition of C enhances creep resistance first by eliminating the undesirable silica and second by replacing it by the desirable SiC which contributes to composite strengthening. The effect of reinforcement per se on the creep rates is discussed in the next section.

Fig. 6 shows the effect of alloying with WSi_2 which has higher melting temperature. The crystal structures of both silicides are the same with the lattice parameters along a=b axis and c axis differing less than 0.3% (For $MoSi_2$, a=b =3.202 and c = 7.851 Å, while for WSi_2 they respectively are 3.211 and 7.868 Å, a lattice mismatch of less than 3%). Thus Mo and W are clearly interchangeable and they form extended solid solutions. Creep behavior of both monolithic systems and their composites have been investigated extensively[2-8] and the results are shown in Fig. 6. Creep rates in the alloy are lower than that in $MoSi_2$, the enhancement due to alloying may be more if one considers the added effect due to grain size since the grain size is lower in the alloy than in $MoSi_2$. The effect of alloying however disappears with increasing temperature to 1400°C . The alloying effect is also obvious in the composite with 20% SiC whiskers. The alloy composite is significantly stronger than the $MoSi_2$ composite. Note the change in the slopes (stress exponents) between the monolithic and the composites and is due to the presence of reinforcements rather than alloying. Similarly it was shown earlier that the activation energy for creep also increased by alloying and since the melting point of WSi_2 is higher than that of $MoSi_2$.

Effect of SiC Reinforcements

Fig. 6 shows the effect of 20%SiC whisker reinforcement on creep rates in both $MoSi_2$ and in the alloy $(Mo,W)Si_2$. The reinforcement enhances the creep rates and also increases slightly the creep exponent. To clearly evaluate the effect of reinforcement on the creep behavior, several volume fractions of SiC particulates were considered and the results are shown in Fig. 7. In this figure, we have also compared the data obtained using tensile tests by Weiderhorn et al [17] on a similar material. Following conclusions can be reached from the results: (a) with the increase in volume fraction of reinforcements the creep rates increase and reach a maximum and then decrease for volume fraction greater than 20%, (b) notable increase in creep resistance observed only when volume fractions are greater than 30%. (c) the creep rates under compression and tension are essentially the same except for the 40% volume fraction, (c) for 40% volume fraction, the creep rates in tension are much lower than those under compression, and (d) since the data in tension is based on only one specimen it is not clear at this stage whether the observed difference at 40% vol. fraction is a true material behavior. That the results under tension and compression do not differ significantly can also be seen in Fig. 8 where identical whisker reinforced materials were compared [2,7,9].

Just as with carbon addition, where the effect of carbon is masked by the superimposed effect of grain size, the true effect of particulate volume fraction is masked by the effect of the associated reduction of grain size. As shown earlier and as evident from the Table I that the with increase in volume fraction of particulates the grain size decreases until the it plateaus at high volume factions greater than 30%.

The reinforcement strengthening effect SiC formed by the addition of carbon can now become clear when creep rates with carbon addition are compared with those with

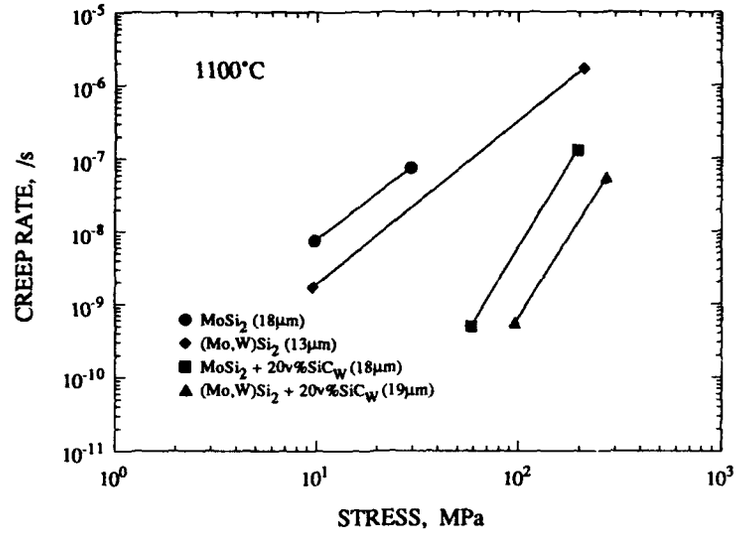


Fig. 6. Effect of alloying with WSi_2 on creep of monolithic and composite $MoSi_2$

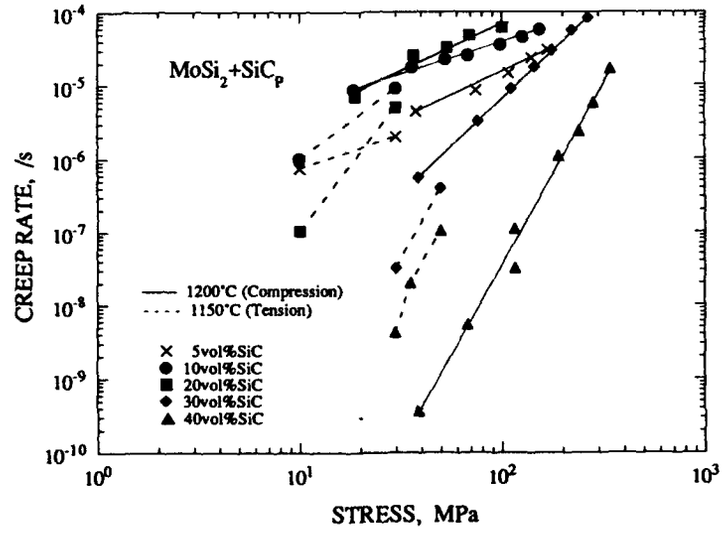


Fig. 7 Effect of volume fraction of SiC particulates on creep of $MoSi_2$

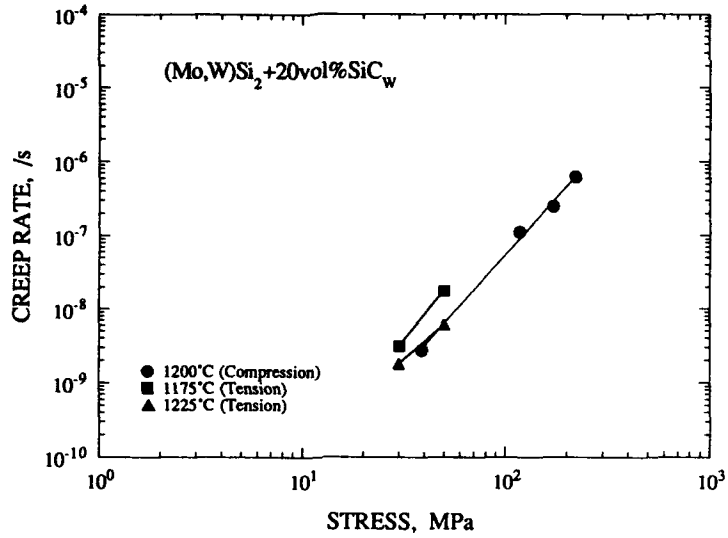


Fig. 8 Tension versus compression creep for whisker reinforced composite

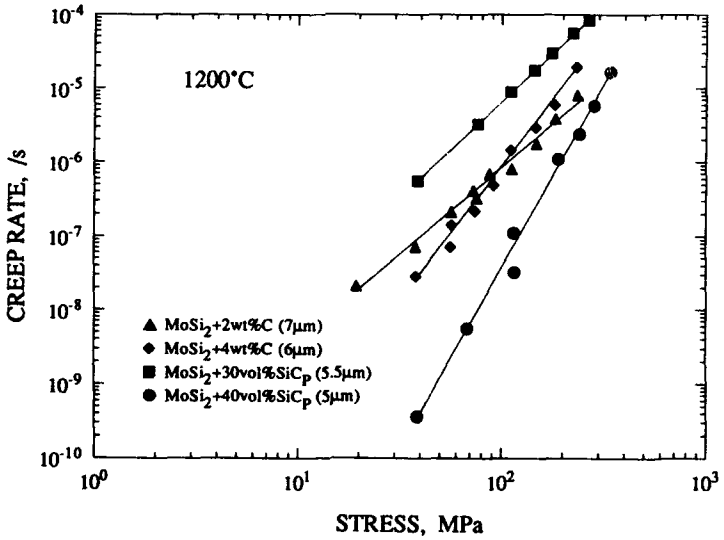


Fig. 9 Creep of $MoSi_2$ with carbon addition in relation to creep of SiC particulate reinforced $MoSi_2$

the addition of SiC particle reinforcement. Fig. 9 shows that the data for 2 and 4% carbon addition falls in between the data for 30 and 40% SiC particulate reinforced material(grain sizes are nearly the same). The results imply that there is nearly 35% volume fraction of SiC formed with the addition of carbon. It is possible that some of the SiC resulted through the reduction of $MoSi_2$ to Mo_5Si_3.

Fig. 10 show summary of all the data on particulate reinforced $MoSi_2$- based composites. Since grain size is one of the important parameters that influences the creep behavior, we have specified the reported grain sizes for each system. Table II provides the complete list of the materials, test temperatures, reported stress exponents and activation energies for all the $MoSi_2$ based systems. Recognizing that the grain size exponent is of the order of 5, and above particularly at low stresses (Fig. 2), care should be exercised in ranking materials. For example, the 20% vol. frac. of CaO appears to be better than 20% vol. frac. of SiC, but the grain size of the CaO reinforced material is at least 4 times larger than that in the SiC reinforced material [11]. Therefore reduction in creep rates in CaO materials could be partly due to increase in grain size. Most striking result in all is that creep rates in the Los Alamos materials with $MoSi_2$ with 40% vol. frac. with grain size of 5 μm, in XD material with 30% vol. frac. with grain size of 10 μm [15] and in directionally solidified eutectic material[16] with 45% MoSi2 with grain size of 7 μm all nearly equal. On equivalent grain size basis, the Los Alamos material may fare better. The fact remains, however, that significant improvement in creep rates of $MoSi_2$ can be achieved through particulate reinforcements.

Comparison of Creep of $MoSi_2$ with Creep of Other Materials

As discussed in the introduction, for high temperature applications, $MoSi_2$ has to compete with the currently available ceramic-ceramic systems. Fig. 11 compares the creep rates of $MoSi_2$ with 20% SiC whisker reinforced materials with that of Si_3N_4 reinforced with 30% SiC whiskers.[19] Creep rates are comparable with ceramic-ceramic composite although the volume fraction of the reinforcement is 10% lower. The other advantages such as high ductility and ease of machinability would outweigh the performance of the $MoSi_2$ system

Finally, Fig. 12 shows the comparison of creep of $MoSi_2$- based composites with the other potential candidate materials for high temperature applications. Clearly $MoSi_2$ - based composites have a superior performance than currently used superalloys [20], all high temperature aluminides [7,8,21], berylides [22,23], refractory metals [24,25] that have been tested so far. The creep rates are comparable with the ceramic-ceramic system. Thus the current research efforts have established that MoSi2-based system is not just for academic interest but has a high potential for application in the temperatures greater than 1000°C. It is now only a question of optimizing the microstructure for additional improvement in properties, and for enhancing the ambient temperature toughness.

SUMMARY AND CONCLUSIONS

Creep behavior of $MoSi_2$ based systems has been reviewed. The effect of grain

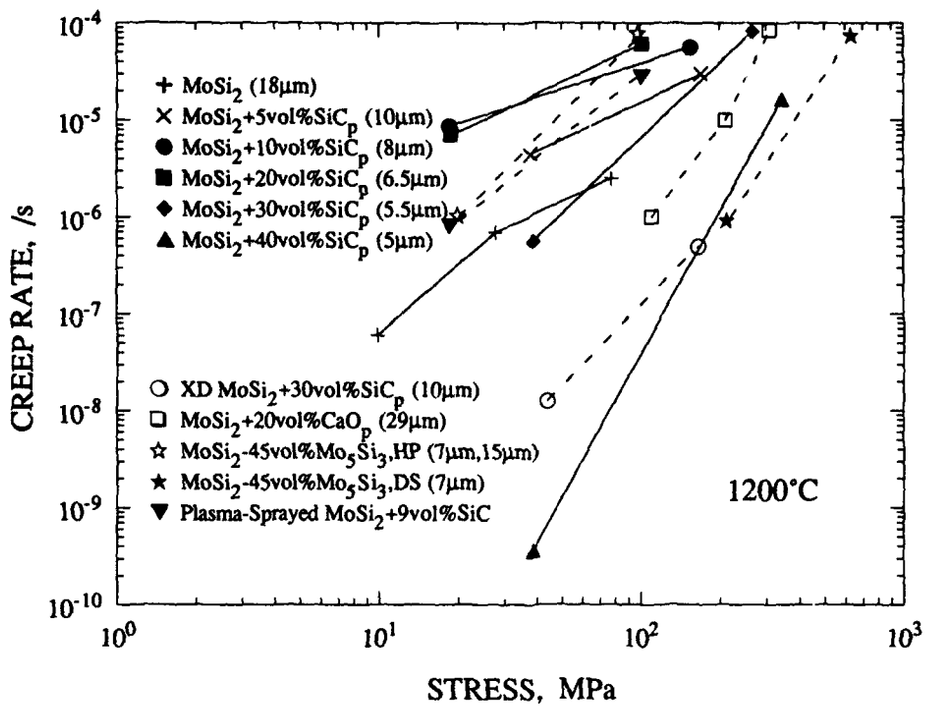


Fig. 10. Comparison of all creep data on particulate reinforced $MoSi_2$ composites

TABLE II : Creep Data for $MoSi_2$

Material	Temp., °C	Stress, MPa	n	Act. Eng., kJ/mol	Ref.
$MoSi_2$	1093-1371	8-70	1.3	-	Maxwell
$MoSi_2$	1200	42-130	3.5	-	Suzuki et al
$MoSi_2$, HP	1200	35-70	2.8	-	Bose
$MoSi_2$, HIP	1200	35-70	2.8	-	Bose
$MoSi_2$	1100-1400	10-80	1.7, 4.4	372	Ghosh et al
$MoSi_2$	1100-1300	10-80	2	433	Sadananda et al
$MoSi_2$, single crystal <210>	1200	70-170	2	-	Bose
$MoSi_2$*	1200	10-50	2.7	-	Ghosh et al
$(Mo,W)Si_2$	1200	35-70	1.6	-	Bose
$(Mo,W)Si_2$	1100-1400	2-200	2.4, 3.6	536	Sadananda et al
$MoSi_2$+20v%SiC_w	1200	35-70	3.1	-	Bose
$MoSi_2$+18v%SiC_w	1200	35-100	3.1	-	Bose
$MoSi_2$+20v%SiC_w	1200	100-250	3.1	-	Ghosh et al
$MoSi_2$+20v%SiC_w	1100-1450	20-200	3.3, 5.2	596	Sadananda et al
$(Mo,W)Si_2$+20v%SiC_w	1100-1400	8-250	2, 4	-	Sadananda et al
$(Mo,W)Si_2$+20v%SiC_w *	1175	30-50	3.2	557	Wiederhorn et al
$(Mo,W)Si_2$+20v%SiC_w*	1225	30-50	2.3	557	Wiederhorn et al
$MoSi_2$+20v%SiC_p	1100	40-90	5	-	Deve et al
$MoSi_2$+20v%SiC_p/Mo	1100	70-150	3	-	Deve et al
$MoSi_2$+20v%SiC_p	1200	8-100	3.1	-	Ghosh et al
XD $MoSi_2$+30v%SiC_p	1050-1300	[illegible]	3.5	430	Suzuki et al
$MoSi_2$+20v%$Er_2Mo_3Si_{4p}$	1200-1300	[illegible]	3.5	-	Patrick et al
$MoSi_2$+20v%CaO_p	1200	[illegible]	3.5	-	Patrick et al
$MoSi_2$-45v%Mo_5Si_3,HP	1200-1300	10-[illegible]	2.5, 3.5	-	Mosan et al
$MoSi_2$-45v%Mo_5Si_3,DS	1100-1300	150-1000	4.5	300	Mosan et al
$MoSi_2$+5v%SiC_p	1100-1200	20-180	1	460	Sadananda et al
$MoSi_2$+10v%SiC_p	1100-1200	20-250	1	460	Sadananda et al
$MoSi_2$+20v%SiC_p	900-1200	15-450	1, 4	460	Sadananda et al
$MoSi_2$+30v%SiC_p	1100-1200	35-300	3, 5.7	460	Sadananda et al
$MoSi_2$+40v%SiC_p	1000-1200	40-400	5	460	Sadananda et al
$MoSi_2$+5v%SiC_p*	1050-1150	10-30	1	815	Wiederhorn et al
$MoSi_2$+10v%SiC_p*	1050-1150	10-30	3	575	Wiederhorn et al
$MoSi_2$+20v%SiC_p*	1050-1150	10-30	5	894	Wiederhorn et al
$MoSi_2$+30v%SiC_p*	1150-1250	30-50	5	684	Wiederhorn et al
$MoSi_2$+40v%SiC_p*	1100-1200	30-50	5, 10	628	Wiederhorn et al
$MoSi_2$+9v%SiC	1100-1500	10-100	1.5, 2.5	190, 300	Jeng et al
$(Mo, W)Si_2$+20v%SiC_p	1200	50-100	2.5	-	Bose
$(Mo,W)Si_2$+20v%SiC_p+10Nb	1200	65-120	3.5	-	Bose
$MoSi_2$+1wt%C	1200-1400	20-250	2, 5	460	Sadananda et al
$MoSi_2$+2wt%C	1000-1400	20-300	3	460	Sadananda et al
$MoSi_2$+4wt%C	1200-1400	20-250	3	460	Sadananda et al

* Tensile Creep Test

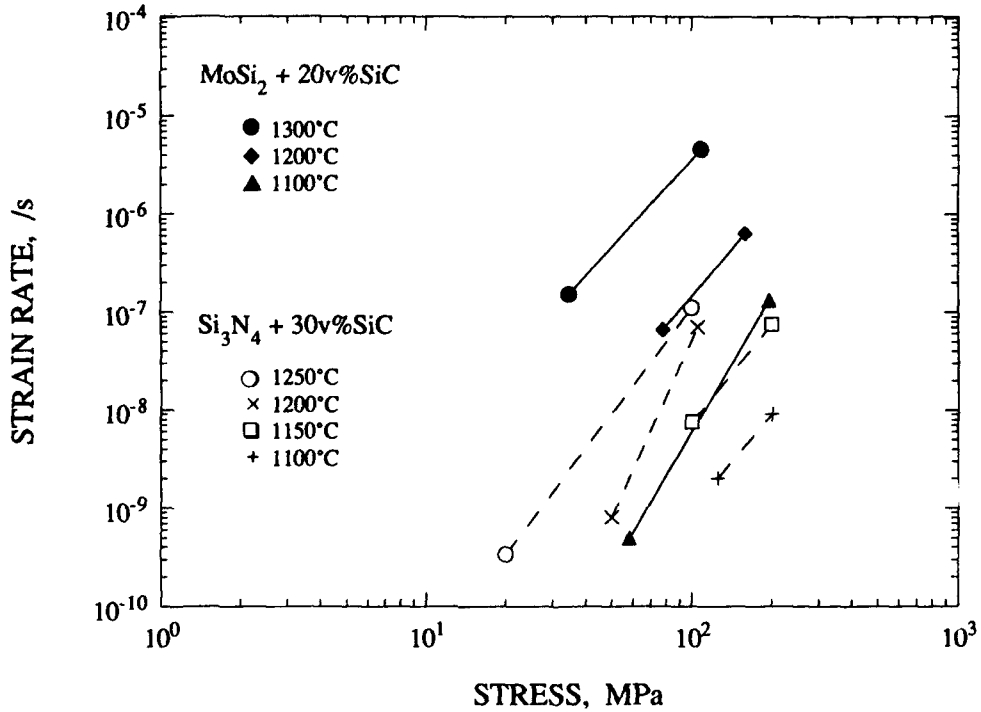


Fig. 11. Comparison of creep of $MoSi_2$ composites with creep of ceramic-ceramic composites

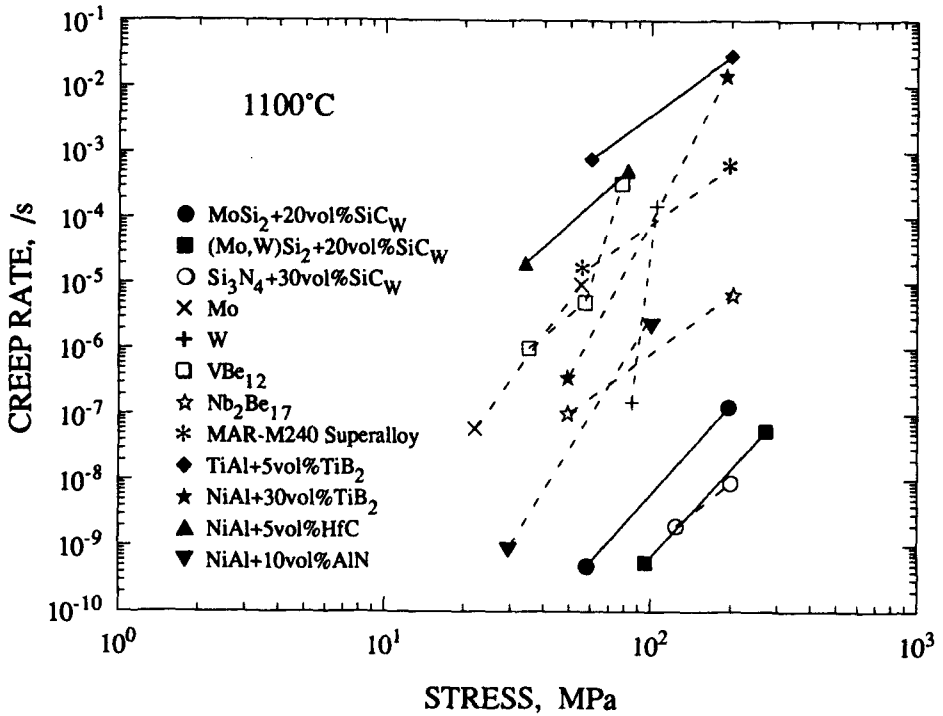


Fig. 12. Comparison of creep of $MoSi_2$ - based systems with that of other high temperature materials

size, effect of alloy additions, effect of reinforcements, combined effect of alloying and reinforcement have been studied as a function of stress and temperature. It shown that effect of grain size and reinforcement are significant. While the addition of reinforcement enhances creep resistance of the composite, the accompanying reduction in grain size reduces creep resistance, and a balance of the two determines the resulting creep behavior. It was emphasized that care should be exercised in comparing the results of different materials that were processed differently.

Creep rates of $MoSi_2$ material is compared with the those of other candidate materials for high temperature application and it is shown that they are far superior than superalloys, advanced aluminides, berylides, refractory metals etc. and their creep rates are comparable to ceramic-ceramic composites. The conclusion is that $MoSi_2$ has a high potential for application at temperatures greater than 1000 C. Future efforts should address the optimization of the microstructure for additional improvement in creep resistance and for the improvement in low temperature fracture toughness.

REFERENCES

1. K. Sadananda, H. Jones, J. Feng, J. J. Petrovic, and A.K. Vasudevan, Ceram. Eng. Sci. Eng. Proc., **12**, 1671-1678 (1991).

2. K. Sadananda, C.R.Feng, H. Jones, and J.J. Petrovic, Mater. Sci. Eng., **A155**, 227-239. (1992)

3. K. Sadananda and C.R. Feng., in Proc. Processing, Fabrications, and Manufacturing of Composite Materials, edited by T.S. Srivatsan and E.J. Lavernia, (American Society of Mechanical Engineers, New York) MID, **35**, 23-245 (1992).

4. K. Sadananda and C.R. Feng., in Advanced Composites '93, edited by T.Chandra, T.S. Dingra, (TMS Publication, Warrendale, PA), 603-610 (1993).

5. K. Sadananda and C.R. Feng., Processing and Fabrication of Advanced Materials for High temperature Applications - II, edited by V.A. Ravi and T.S. Srivatsan,(TMS publication, Warrendale PA) , 331 (1993)

6. K. Sadananda and C.R. Feng, in "Aspects of High Temperature Deformation and Fracture in Crystalline Materials, edited by Hosoi et al. (Japan Institute of Metals, Tokyo) 391 (1993).

7. K. Sadananda and C.R. Feng, Mater. Sci. Engrg., **A170**, (1993) 199-214.

8. K. Sadananda and C.R. Feng, J. J. Petrovic., in Int. Symp. on Structural Intermetallics, Seven Springs Symp. In Press (1993).

9. S.M. Weiderhorn, R.J. Gettings, D.E. Roberts, C. Ostertag and J.J. Petrovic, Mat. Sci. Engrg., **A155**, 217-226 (1992).

10. S. Bose, Mat. Sci. Engrg., **A155**, 217-226 (1992).

11. A. K. Ghosh, and A. Basu, in Critical Issues in the Development of High Temperature Structural Materials, edited by N. S. Stoloff et al. (TMS Publication, Warrendale) (1993)

12. W.A. Maxwell, Some Stress-Rupture and Creep Properties of Molybdenum Disilicide in the Range of 1600-2000ºF, NACA RME52D09, (1952).

13. H.E. Deve, C.H. Weber, N. Maloney, Mat. Sci. Engrg., **A153**, 668 (1992)

14. Y. Umakoshi, Bull. Jpn. Inst. Metals. **30**, 72 (1991).

15. M. Suzuki and S.R. Nutt and R. M. Aiken, Jr., Mater. Sci. Engrg., **A162**, 73 (1993).

16. D.P. Mason and D.C. Van Aken, in High Temperature Ordered Intermetallics, edited by I, Baker, R. Doralia, J. D. Whittenberger and M.H. Yoo, (Mater. Res. Soc. Proc. **286**, Pittsburgh, 1992) 1129-1134; D. K. Patrick D.C. Van Aken, ibid., pp 1135-1141;

17 J. D. French and S. M. Weiderhorn, Presented at the 1993 MRS Fall meeting, Boston, MA 1993

18 M. F. Ashby and L. M. Brown, "Perspectives in Creep Fracture", Pergmon Press, Oxford, 1983).

19 B.J. Hokey, S.M. Weiderhorn, W. Liu, J.G. Baldoni and S.T. Buljan, J. Mater. Sci. **26**, 1991, 3931

20. M.J. Donachie (ed) "Superalloys - Source Book", American Society of Metals, Metals Park, OH, 1984.

21.T.R. Bieler, J.D. Whittenberger and M.J. Luton, in High Temperature Ordered Intermetallics, edited by I, Baker, R. Doralia, J. D. Whittenberger and M.H. Yoo, (Mater. Res. Soc. Proc. **286**, Pittsburgh, 1992) pp 1149-1154; C.R. Feng and K. Sadananda, ibid., pp. 1155-1160.

22. T.G. Nieh, J. Wadsworth, F.C. Grensing, J.M. Yang, J. Mater. Sci. **27** (1992) pp 2660-2664.

23. T.G. Nieh, J. Wadsworth, T.C. chou, D. Owen and A.H. Chokshi, J. Mater. Res. **8**, 757-763 (1993).

24 L.V. Pavlinov and V. N. Bikov, Fiz. Met. i Metalloved, **18**, 459, (1964)

25. S.L. Robinson, O.D. Sherby, Acta Met. **17**, 109 (1969).

PLASTICITY ENHANCEMENT PROCESSES IN $MoSi_2$-BASE MATERIALS

R. GIBALA, H. CHANG AND C.M. CZARNIK
Department Of Materials Science And Engineering,
The University Of Michigan, Ann Arbor, MI 48109-2136

ABSTRACT

Low temperature plasticity enhancement processes observed in body-centered cubic metals and B2 ordered alloys can be observed in $MoSi_2$ in appropriate stress-temperature-strain rate regimes. We illustrate effects of surface films (ZrO_2) and dispersoids (TiC) in enhancing plasticity of $MoSi_2$ in the ductile-to-brittle transition range of temperatures, 900-1400°C. We also show, through experiments involving high temperature (1300°C) prestrain, that effective operation of dislocation generation processes can extend the low temperature range to which $MoSi_2$ can be plastically deformed. These results illustrate that approaches to enhance toughness of $MoSi_2$ need not be limited to ductile phases characterized by weak interfaces.

INTRODUCTION

Ordered intermetallic compounds such as $MoSi_2$ possess many desirable engineering properties, e.g. high stiffness, high thermal conductivity, low density, excellent environmental resistance, and potentially high strength at elevated temperatures. However, a major difficulty in the application of $MoSi_2$ as a structural material has been a lack of adequate ductility and fracture toughness at relatively low temperatures. "Low" temperatures for $MoSi_2$ are as high as 900°C-1400°C. At the lower end of this temperature range, $MoSi_2$ exhibits very limited plasticity, even in compression of high purity single crystals [1-4]. Only toward the higher of these temperatures, with the onset of dislocation climb and diffusional creep processes (5-7), does $MoSi_2$ exhibit significant plasticity in compression, bending and tension in both single crystals and polycrystalline materials [1-8]. Within this temperature range, $MoSi_2$ undergoes a brittle-to-ductile fracture transition that appears to be dislocation-mobility or dislocation-density limited.

Many approaches have been taken to reduce the brittle-to-ductile transition temperature (BDTT) of $MoSi_2$ or to enhance the capability for plastic flow and obtain increased toughness at relatively low temperatures. Approaches include but are not limited to solid solution alloying, second-phase microstructural control, ductile phase toughening, and thermomechanical manipulation of grain size and texture (9). In this paper, we examine three specific methods of plasticity enhancement that have proven effective previously in body-centered cubic refractory metals such as Nb, Ta, Mo and W, and B2 ordered intermetallic alloys such as NiAl and FeAl: high temperature prestrain, surface film coatings and second phase particles [10,11]. Such results have demonstrated that the ductility of bcc metals and B2 ordered alloys can be greatly enhanced by these methods because dislocation-mobility or dislocation-density limitations can be overcome. The dislocation-mobility limitation follows, for example, from the large difference in intrinsic mobility between edge and screw dislocations in the bcc structure and in B2 ordered alloys which deform by the motion of <111> dislocations [12]. The dislocation-density limitation arises from a lack of sufficient numbers of surface or internal dislocation sources [10,13]. For $MoSi_2$, insufficient knowledge exists concerning the relative mobilities of edge and screw dislocations, and information on the different dislocation types <100>, <110>, 1/2 <111> and 1/2 <331>, their glide planes, and the operative slip systems as a function of temperature, strain rate and crystallographic orientation is only recently being developed [4,14,15]. Inspite of this new information, it is clear that there is minimal dislocation plasticity below ~900°C at normal strain rates [14], except perhaps under hardness indentations [16].

Mat. Res. Soc. Symp. Proc. Vol. 322. ©1994 Materials Research Society

Because $MoSi_2$ exhibits qualitatively similar dependences of the yield strength on temperature, strain rate and crystallographic orientation as bcc metals and B2 ordered alloys, it is important to examine $MoSi_2$ for possible plasticity enhancement by processes that are operative in these materials. The purpose of this paper is to determine the extent to which the plastic deformation of $MoSi_2$ at and below the BDTT is bcc/B2-like in its sensitivity to high temperature prestrain, surface films and second phases.

EXPERIMENTAL

Most of the experimental procedures have been described in detail in other papers or theses given as references to this paper. Only those procedures that pertain to the particular results described or discussed in this paper are given here.

Materials

All experiments on monolithic polycrystalline $MoSi_2$ were done on powder processed materials. Most experiments were performed on -325 mesh $MoSi_2$ powder obtained from Cerac, Incorporated. Some work was done on high purity, oxide-free powders prepared by mechanical alloying by Dr. R. Schwarz of Los Alamos National Laboratory [17]. Most monolithic materials were tested in the hot-pressed condition. Hot pressing was done uniaxially in grafoil-lined graphite dies in argon at temperatures in the range 1600-1700°C for 1/2 to 2 hours at pressures of 25-30 MPa. Some materials were additionally HIPed at 1800°C for 1.5 hours at 200 MPa. The approximately equiaxed grain size was typically about 30 μm, and the materials were about 95-98% of theoretical density. No preferential texture was noted. Surface film coating experiments utilized PVD electron beam deposition of ZrO_2 films approximately 100 nm thick at 50°C.

Some experiments were performed on single crystals of $MoSi_2$ prepared by the Czochralski method by J.D. Garrett of McMaster University [16]. The growth rate of these crystals was approximately 180 mm/h, and crystal pulling was done in a high purity, Ti-gettered atmosphere.

$MoSi_2$-TiC particulate composites were prepared by powder processing in attempts to disclose second-phase-induced plasticity enhancement. TiC powders of 2.5-4 μm size with the stoichiometry $TiC_{0.95}$ were dry blended in a ball mill for 20 h with the commercial $MoSi_2$ powders described above in proportions to produce $MoSi_2$-10, 15 and 20 vol.% TiC composites. These materials were given identical hot pressing/HIPing treatments given to the monolithic $MoSi_2$ materials with which they were to be compared. The composites were usually 92-98% dense. The grain size of the $MoSi_2$ matrix was approximately 15-25 μm in these materials. The TiC particles were well distributed throughout the composite volume, but because of agglomeration varied in size from 5 μm to 45 μm, with a mean size of 10 μm. Because of the large sensitivity of yield strength and creep resistance on grain size, only monolithic $MoSi_2$ and $MoSi_2$-TiC composites with nearly the same grain size (30 μm and 25 μm, respectively) are compared.

Mechanical Testing

Most mechanical testing of $MoSi_2$ and $MoSi_2$-TiC composites was done in compression at a constant extension rate corresponding to an initial strain rate of 10^{-4} s^{-1} on specimens that were 6 mm x 3 mm x 3 mm in dimensions. Tests were done on an Instron Model 4507 machine in argon at temperatures in the range of 750-1300°C. Yttria was used as a platen lubricant to minimize friction.

To examine surface film effects in ZrO_2-coated $MoSi_2$, we used microhardness indentation techniques. Diamond Vickers indentations at loads of 0.5 to 1 kgf were made at temperatures of 25-1300°C with a Nikon QM hot hardness tester, with an average of at least five measurements made at each temperature. The $MoSi_2$ specimens were typically coated over one half of the indentation surface so that hardness measurements of uncoated and coated materials could be made on the same specimen at the same time.

Microstructural Characterization

All materials were examined by visible-light optical, scanning electron, and transmission electron microscopies. Optical and SEM methods were employed to determine grain size, grain shape, second phase structure and distribution, and deformation and fracture path morphologies on fracture surfaces and side surfaces. Conventional TEM on a JEOL 2000FX microscope was used to determine deformation behavior between phases in the two-phase microstructures and to analyze the dislocation substructures in each phase.

RESULTS AND DISCUSSION

This section of the paper discusses experimental results which disclose effects of high temperature prestrain, surface films and particulate additions on the plasticity of $MoSi_2$. In each case, we make reference to previous results obtained in our laboratories and elsewhere for bcc metals and B2 ordered alloys for comparison with $MoSi_2$. The intent is to demonstrate that dislocations "injected" into $MoSi_2$ by high temperature prestrain or generated into the matrix from strong, adherent interfaces associated with surface films or second phases afford plasticity that would not ordinarily occur in the unprestrained, uncoated or unalloyed matrix.

Prestrain Effects

The effects of prestrain-enhanced changes in plasticity of bcc metals and B2 ordered alloys are well established. For example, Sethi and Gibala [13] have shown that the flow stress at 77 K of high purity Nb and Ta single crystals can be reduced by prestrain at higher athermal temperatures such as 295 K and 400 K, respectively, because of the sensitivity of the flow stress to the mobile dislocation density. Similarly, many investigators have demonstrated that yield points observed in impure bcc metals, low dislocation-density semiconductors and other dislocation-deprived materials can be eliminated by prestrain [18]. Hack and co-workers [19] have shown enhancement of the fracture toughness of NiAl by prestrain in single crystals with apparently well-pinned initial dislocation densities. These results plus recent experiments by Maloy [4] showing modestly enhanced plasticity of [001] oriented single crystals of $MoSi_2$ from surface abrasion led us to examine prestrain as a means of plasticity enhancement in $MoSi_2$.

The hot pressed polycrystalline material examined in these experiments had a 30 μm grain size and approximately 5% SiO_2 particles dispersed throughout the matrix at grain boundaries and within grain interiors. Stress-strain curves in compression for this material over the temperature range 800°C-1300°C are shown in Fig. 1. At 1100°C-1300°C, the material exhibits appreciable dislocation plasticity in compression, albeit with increasing amounts of concurrent microcrack damage with decreasing temperature. At 1300°C, there is virtually no microcrack damage after 1% plastic strain. We have used this as the high temperature prestrain in experiments described below on $MoSi_2$ deformed at lower temperatures. As the test temperature is lowered below 1000°C, the unprestrained material exhibits a well-rounded yield point such as shown at 900°C in Fig. 1. At lower temperatures such as 850°C, there is limited plasticity and obvious macrocracking in compression. At 800°C and below, there is no observable plastic deformation before brittle fracture occurs.

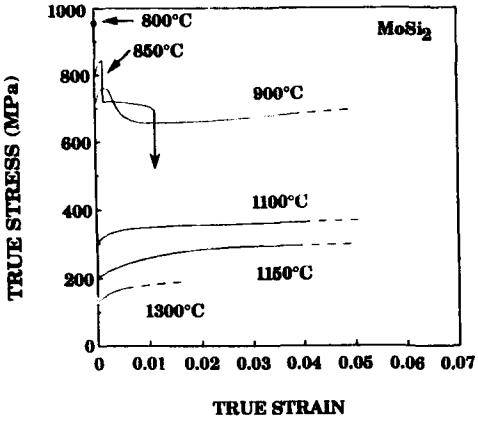


Figure 1. True stress-true strain curves in compression for hot-pressed polycrystalline $MoSi_2$ at 800°C-1300°C.

Two major effects of prestrain at 1300°C on the mechanical behavior at lower temperatures are noted, as illustrated in Fig. 2. (a) The yield point observed in unprestrained materials deformed at temperatures such as 900°C is eliminated by the prestrain (Fig. 2(a)). (b) The limited plasticity exhibited by materials deformed at temperatures below 900°C is greatly enhanced by the high temperature prestrain (Fig. 2(b)). Note in Fig. 2(a) that the unprestrained and prestrained materials deform at about the same flow stress, typical of dislocation-pinned or dislocation-density limited materials. TEM observations of both materials deformed to 1% plastic strain disclose high dislocation densities, up to 10^{14} m/m^3, demonstrating the major role of dislocation plasticity in the deformation. The most prominent slip systems in these materials were <100> {011} and <100> {013} [20]. Fig. 2(b) shows that at temperatures such as 800°C, at which the unprestrained material exhibits no plasticity, there is significant plasticity afforded by prestrain at 1300°C. Note there is even modest plasticity of nearly 2% at 750°C, although it is accompanied by macrocracking.

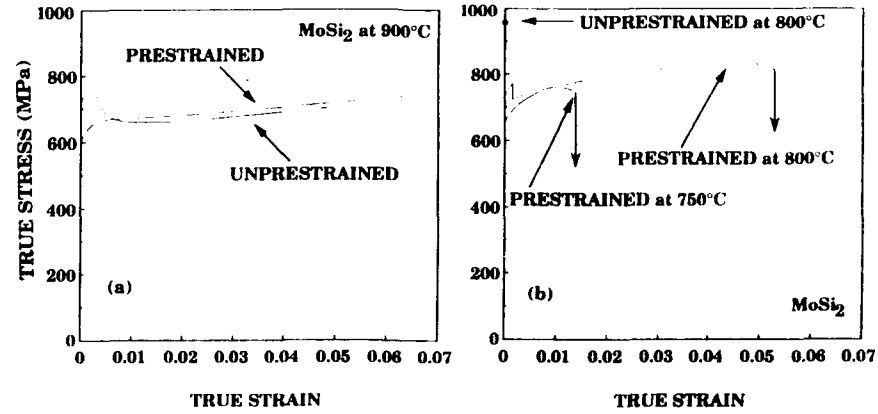


Figure 2. True stress-true strain curves in compression of polycrystalline $MoSi_2$ (a) at 900°C, showing elimination of the yield point by prestrain at 1300°C, and (b) at 750°C and 800°C, showing enhanced plastic flow by prestrain at 1300°C.

These results represent the first report of plastic flow of $MoSi_2$ at temperatures as low as 750°C. Although the results are encouraging, the importance of observing concurrent micro- and macrocracking must be emphasized. The damage resilience of the polycrystalline $MoSi_2$ is associated with the ability of the polycrystalline grain structure to stop crack propagation during deformation, as metallographic observations as a function of plastic strain at these low temperatures attest [20]. In general, finer grained $MoSi_2$ and $MoSi_2$-based composites are stronger and more crack resistant at these temperatures but weaker at elevated temperatures than their larger-grained counterparts [21]. Single crystals, without obvious crack-blunting microstructures, exhibit negligible plasticity below 900°C-1000°C [1-4] and only small plasticity compared to that obtained in polycrystalline materials at higher temperatures. Figure 3 compares the plasticity of an [001] single crystal deformed at 1250°C to the much larger plasticity of the polycrystalline material described in Figure 1 at 1200°C and 900°C. Future research on single crystalline $MoSi_2$ should investigate prestraining of the type done here and the incorporation of crack-arresting second-phase microstructures as a means of enhancing plasticity.

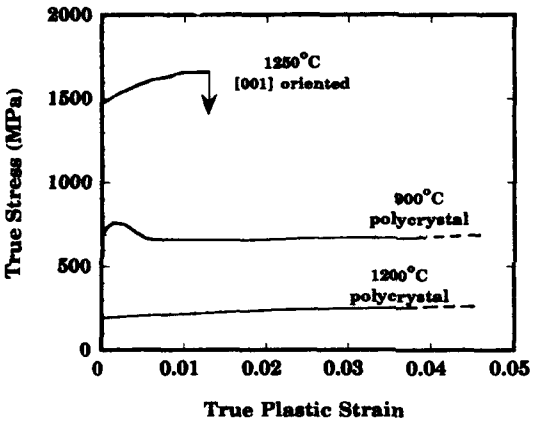


Figure 3. Plasticity in compression of an [001] oriented single crystal of $MoSi_2$ at 1250°C compared to that of polycrystalline $MoSi_2$ at similar and lower temperatures.

Surface Film Effects

A large number of investigations have demonstrated that surface films on bcc metals [10, 13] and B2 ordered alloys [10,11,22,23], in single crystal or polycrystalline form, can enhance the plasticity of the substrate material. The usual manifestation of such surface film softening is reduced yield and flow stresses and increased strains to failure in tension, compression and cyclic deformation. These effects occur at relatively low homologous temperatures, e.g. $T \leq 0.2T_m$, where T_m is the absolute melting temperature. Such temperatures are near or below the BDTT, but at temperatures high enough that intrinsic dislocation mobility is significant. Although the temperature range of 900°C -1400°C represents higher homologous temperatures for $MoSi_2$, the previously discussed prestrain experiments suggest use of these temperatures for investigation of film effects in terms of the requisite roles of dislocation mobility and dislocation generation processes.

Surface film softening was investigated in various polycrystalline $MoSi_2$ materials and in [001] single crystals coated with 100 nm thick PVD-deposited ZrO_2. ZrO_2 was chosen as a surface film because it forms adherently on $MoSi_2$ when deposited by low-temperature PVD methods. Adherence is important in order to develop the necessary elastic and plastic constraint for dislocation generation at the film-substrate interface. In addition, research by Petrovic and co-workers [24] has demonstrated that $MoSi_2$ composites containing ZrO_2 particles exhibit toughening that is not observed in ZrO_2-free materials. The results on two different

polycrystalline materials, a hot-pressed material of commercial powder from Cerac, Incorporated and a hot-pressed high purity material prepared by mechanical alloying [17], are given in this paper. Results on single crystals are given elsewhere [25].

Our initial experiments to investigate possible surface film softening of $MoSi_2$ by ZrO_2 films have employed hardness indentation testing at temperatures from 25-1300°C, as described earlier in this paper. Hardness testing offers the advantage of utilizing deformation under a large, essentially hydrostatic compressive stress state at large effective stresses and strain rates. Hence dislocation glide plasticity is the operative deformation mechanism under these conditions throughout this temperature range of hardness measurements [26]. Such conditions are optimum for observation of film softening, because of its occurrence in bcc metals and B2 ordered alloys at relatively low homologous temperatures where the temperature dependence of the flow stress is very large and where only dislocation glide mechanisms are operative. In $MoSi_2$, the temperature dependence of the flow stress in compression is very large over the temperature range 900-1400°C, but the dominant dislocation mechanism changes from glide, to glide/climb, to climb, to diffusional creep with increasing temperature in this temperature range for simple slow strain rate monotonic testing [5]. Consequently, hardness testing offers a mechanistic simplicity that other testing does not. Results of compression testing of film-coated $MoSi_2$ are reported elsewhere [25].

The results of experiments on commercial hot-pressed $MoSi_2$ and mechanical alloyed hot-pressed $MoSi_2$ are given in Fig. 4. Both uncoated materials exhibit a large decrease in hardness as a function of temperature. The lower purity commercial $MoSi_2$ is harder at all temperatures than the higher purity mechanical alloyed material, as expected. Both coated materials exhibit a large decrease in hardness relative to that of the respective uncoated materials. The amount of film-induced softening is larger for the higher purity material, again as expected [10]. It should be emphasized that the ZrO_2 films are approximately 0.1 μm in thickness compared to hardness indentation depths of about 10 ± 5 μm. Hence the hardness test is sampling almost entirely the plastic zone of the substrate and not film properties. Experiments on single crystals, including use of nanoindentation techniques, elucidate more clearly the role of the film in the hardness behavior in these film-coated materials [25,27].

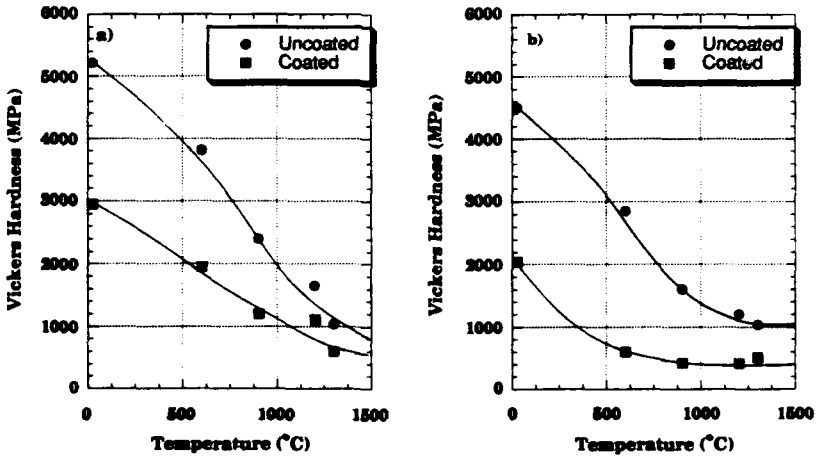


Figure 4. Temperature dependence of the Vickers hardness of uncoated and ZrO_2-coated polycrystalline $MoSi_2$. (a) Commercially pure hot-pressed $MoSi_2$. (b) Mechanical alloyed $MoSi_2$.

Effects of Second-Phase Interfaces

Internal interfaces associated with second-phase precipitates or dispersoids in $MoSi_2$ should be capable of acting as effective dislocation sources in the same manner as for bcc metals and B2 ordered alloys [10,11]. We have been successful in observing enhanced dislocation generation due to the incorporation of TiC particles in $MoSi_2$ [28]. TiC is extremely hard at room temperature, but deforms appreciably with increasing temperature above 600-800°C. At temperatures above 900°C as a particulate addition to $MoSi_2$, it undergoes substantial deformation prior to the $MoSi_2$ matrix and can therefore lead to enhanced dislocation generation into the $MoSi_2$. Figure 5 gives an example of the deformation undergone by TiC particles during deformation of $MoSi_2$-10 vol.% TiC composites deformed 0.5% at 1150°C. The diffraction conditions are ones which also show enhanced multiplication of dislocations into the $MoSi_2$ matrix effected by deformation incompatibility at the particle-matrix interface. Most of the dislocations are of the <100> type, mainly on {011} and {013} planes.

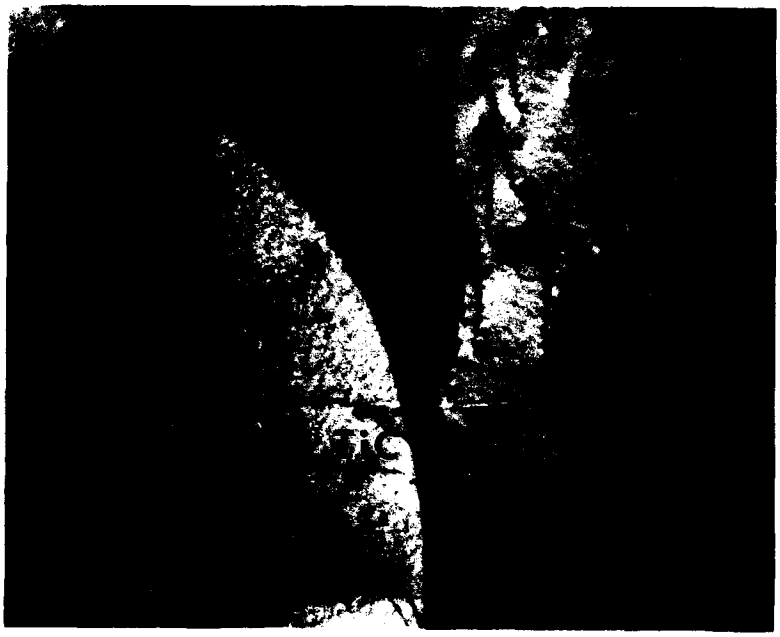


Figure 5. TEM micrograph of dislocation substructures in a TiC particle and the adjacent $MoSi_2$ matrix in a $MoSi_2$-10 vol.% TiC composite deformed 0.5% at 1150°C. **B** = [110], **g** = 002.

Some representative mechanical behavior data for hot pressed and HIPed $MoSi_2$ and a $MoSi_2$-10% TiC composite are given in Fig. 6(a). Both materials are approximately 98% of theoretical density and have nearly the same grain size (28 μm and 25 μm, respectively). The composite has a larger strength and exhibits a comparable plasticity in compression to that of the monolithic $MoSi_2$ at 1150°C. The composite reaches a steady-state of zero work hardening at much smaller strains than monolithic $MoSi_2$, as expected from more efficient dislocation pumping from interface sources. There is also extensive low-angle boundary formation by dislocation recovery processes in the vicinity of the TiC particles at small strains that is not

observed in monolithic $MoSi_2$ [28]. This observation is associated with the more effective dislocation generation processes in the $MoSi_2$-TiC composites. Such processes should allow plastic deformation of the composite to low temperatures as observed for the prestrained monolithic material, but we have not yet investigated this. In Figure 6(b), we illustrate significant plasticity of a composite at 900°C inspite of appreciable particle strengthening by TiC. Future work will be directed toward improving plasticity in the composites at these low temperatures.

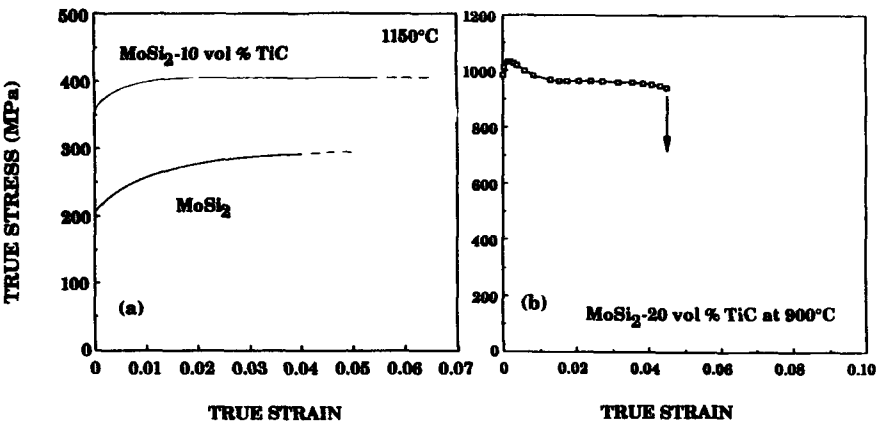


Figure 6. Mechanical behavior of $MoSi_2$ and $MoSi_2$-TiC particulate composites. (a) Comparison of stress-strain curves at 1150°C. (b) Deformation of a composite at 900°C.

SUMMARY

We have successfully demonstrated enhanced plasticity and dislocation activity in $MoSi_2$ by high temperature prestrain, surface films, and internal interfaces associated with second-phase particulates. These results offer evidence that enhanced plasticity of $MoSi_2$ can be realized from manipulation of dislocation density and dislocation source density by microstructural methods. The plasticity enhancement by high temperature prestrain occurs from dislocation injection into the dislocation-density limited material and activation of dislocation sources not available in the unprestrained material. The observed enhancements of plasticity by surface films and second phases occur because of the conditions of constrained deformation at the film-substrate and particle-matrix interfaces which are effective in introducing glissile dislocations into the otherwise brittle substrate/matrix material. These observations offer hope that optimized microstructural control of $MoSi_2$ will lead to enhanced toughness in future engineering applications. However, such approaches must take into account the microcrack damage accumulation processes which occur concurrently during plastic deformation.

ACKNOWLEDGMENTS

Various parts of this research have been individually supported by the National Science Foundation, Grant No. DMR 9102414, Dr. Bruce A. MacDonald, Program Director, and by the Air Force Office of Scientific Research, Grant No. DoD-G-AFOSR-90-0141 and DoD-G-F49620-93-1-0289, Dr. Alan H. Rosenstein, Director. We also acknowledge the Department of Energy for fellowship support that enabled two of us (R.G., C.M.C.) to do portions of the research on surface film softening of $MoSi_2$ in the Center for Materials Science at Los Alamos National Laboratory.

REFERENCES

1. Y. Umakoshi, T. Sakagami, T. Hirano and T. Yamane, Acta Metall. Mater. 38, 909 (1990).
2. Y. Umakoshi, T. Hirano, T. Sakagami and T. Yamane, High Temperature Aluminides and Intermetallics, S.H. Whang et al., TMS, Warrendale, PA, p. 111, 1990.
3. K. Kimura, M. Nakamura and T. Hirano J. Mater. Sci. 25, 2487 (1990).
4. S.A. Maloy, Ph.D. Thesis, Case Western Reserve University, Cleveland, Ohio, 1993.
5. R. Gibala, A.K. Ghosh, D.C. Van Aken, D.J. Srolovitz, A. Basu, H. Chang, D.P. Mason and W. Yang, Mater. Sci. Eng. A155, 147 (1992).
6. K. Sadananda, C.R. Feng, H. Jones and J.J. Petrovic, Mater. Sci. Eng. A155, 227 (1992)
7. K. Sadananda and C.R. Feng, High Temperature Silicides and Refractory Alloys, B.P. Bewlay et al., eds., MRS Symposium Series 322 (1994).
8. R.M. Aikin, Jr., Scripta Metall. Mater. 26, 1025 (1992).
9. A.K. Vasudevan and J.J. Petrovic, Mater. Sci. Eng. A155, 1 (1992).
10. R.D. Noebe and R. Gibala, Structure and Deformation of Boundaries, K. Subramanian and M.A. Imam, eds., The Metallurgical Society, AIME, Warrendale, PA, p. 89, 1986.
11. R.D. Noebe, A. Misra and R. Gibala, ISIJ International 31, 1172 (1991).
12. M. Yamaguchi, Mechanical Properties of BCC Metals, M. Meshi, ed., TMS-AIME, Warrendale, PA, p. 31, 1982.
13. V.K. Sethi and R. Gibala, Phil. Mag. 37, 419 (1978).
14. S.A. Maloy, A.H. Heuer, J.J. Lewandowski and T.E. Mitchell, Acta Metall. Mater. 40, 3159 (1992).
15. T.E. Mitchell, High Temperature Silicides and Refractory Alloys, B.P. Bewlay et al., eds., MRS Symposium Series 322 (1994).
16. P.H. Boldt, J.D. Embury, and G.C. Weatherly, Mater. Sci. Eng. A155, 251 (1992).
17. R.B. Schwarz, S.R. Srinivasan, J.J. Petrovic and C.J. Maggiore, Mater. Sci. Eng. A155, 75 (1992).
18. W.G. Johnston, J. Appl. Phys. 33, 2716 (1962).
19. J.E. Hack, J.M. Brzeski and R. Darolia, Scripta Metall. Mater. 27, 1259 (1992).
20. H. Chang and R. Gibala, High Temperature Silicides and Refractory Alloys, B.P. Bewlay et al., eds., MRS Symposium Series 322 (1994).
21. A.K. Ghosh and A. Basu, High Temperature Silicides and Refractory Alloys, B.P. Bewlay et al., eds., MRS Symposium Series 322 (1994).
22. R.D. Noebe and R. Gibala, Scripta Metall. 20, 1635 (1986).
23. K.J. Bowman, S.E. Hartfield-Wünsch and R. Gibala, Scripta Metall. Mater. 26, 1529 (1992).
24. J.J. Petrovic, A.K. Bhattacharya, R.E. Honnell, T.E. Mitchell, R.K. Wade, and K.J. McClellan, Mater. Sci. Eng. 155A, 259 (1992).
25. C.M. Czarnik, R. Gibala, M. Nastasi and J.D. Garrett, High Temperature Silicides and Refractory Alloys, B.P. Bewlay et al., eds., MRS Symposium Series 322 (1994).
26. W.B. Li, J.L. Henshall, R.M. Hooper and K.E. Easterling, Acta Metall. Mater. 39, 3099 (1991).
27. C.M. Czarnik, M.S. Thesis, University of Michigan, Ann Arbor, MI, 1993.
28. H. Chang, H. Kung and R. Gibala, Intermetallic Matrix Composites II, D.B. Miracle et al., eds., MRS Symposium Series 273, 253 (1992).

FILM SOFTENING EFFECTS OF ZrO_2 ON $MoSi_2$

C. M. CZARNIK, R. GIBALA, M. NASTASI* AND J. D. GARRETT**
The University of Michigan, Department of Materials Science and Engineering, Ann Arbor, MI 48109-2136
*Materials Science Technology Div., Los Alamos National Laboratory, Los Alamos, NM 87545
**Institute for Materials Research, McMaster University, Hamilton ONT, Canada, L8S 4M1

ABSTRACT

We have investigated the effect of thin films of ZrO_2 on the mechanical behavior of [001] single-crystalline $MoSi_2$. Previous work in our laboratories has shown there to be a 20-40% reduction in hardness in coated samples relative to the corresponding uncoated samples. We now compare fracture around the indentations as a function of thickness. Thicker ZrO_2 coatings reduce radial crack length around the indentation through the intrinsic compressive stress at the film/substrate interface. In addition, ZrO_2-coated materials tested in compression at 1250°C exhibit approximately twice the plastic strain of uncoated materials, indicating that reduction in hardness is associated with enhanced plasticity from dislocation activity associated with the film/substrate interface.

INTRODUCTION

$MoSi_2$ exhibits properties of low density, excellent oxidation resistance, high stiffness, high thermal conductivity, and potential high strength at elevated temperatures. However, limited ductility at intermediate temperatures (<1300°C) and poor strength at elevated temperatures (>1300°C) have been major drawbacks. There have been attempts to enhance the plasticity of this material in the brittle-to-ductile transition temperature region (900-1300°C) [1]. Some of these methods include solid solution alloying, grain size manipulation, and second-phase toughening. However, none of these methods has been singularly successful in solving all of the problems associated with a brittle material such as $MoSi_2$.

The aim of this research involves the use of deposited surface films in an attempt to improve the deformation characteristics of $MoSi_2$. Previous work has demonstrated a film softening effect in many bcc metals and B2 ordered alloys at relatively low homologous temperatures ($T < 0.2T_m$) [2]. The application of surface oxide films has substantialiy increased the ductility of these bcc and B2 materials. $MoSi_2$ is similar to these materials in a few important respects: it has a bcc-like unit cell, it is a dislocation glide-limited material, and there is a marked temperature dependence of the yield strength. There is also a yield stress dependence on crystal orientation in compression tests. All these dependencies suggest that film softening might occur in the $MoSi_2$ system. ZrO_2 was chosen as a possible film after discussions with Petrovic et al. regarding use of ZrO_2 particles as a potential toughening addition to hot-pressed $MoSi_2$ material. Their investigations have shown that there is no significant chemical reaction between ZrO_2 and the $MoSi_2$ matrix [3]. The thermal expansion coefficient for ZrO_2 is close to that of $MoSi_2$, thus reducing possible thermal stresses. Our previous research on hardness testing of ZrO_2 coated $MoSi_2$ has shown a 20-40% decrease in hardness relative to the uncoated material [4]. In this paper, we examine the effect of film thickness on the film-induced reduction in hardness and examine the effect of these films on the yield stress in compression.

EXPERIMENTAL

The single crystalline $MoSi_2$ was grown from high purity Si (Johnson Matthey) and Mo (GTE Products) arc melted in a high purity Ar atmosphere to form a single button. The Czochralski technique of crystal growing was employed to pull single crystals from these buttons at a rate of 240 mm/hour. Crystals were pulled in a high purity argon atmosphere further purified

Mat. Res. Soc. Symp. Proc. Vol. 322. ©1994 Materials Research Society

by passing the gas through a Ti getter. All single crystals were grown from an [001] seed crystal in an attempt to align the crystals in the "hard" orientation for $MoSi_2$ [5]. Sample preparation for the compression tests involved coring 3 mm diameter x 6 mm length samples from the single crystals. A Laue back reflection method was used to orient the crystal to within 3° of the [001] axis prior to final shaping of the specimens. An AEGIE Electro-Discharge Machining (EDM) unit was used to section single crystals through a combination of wire cutting and coring. Subsequent Laue measurements confirmed that the crystals were oriented to within 2° of the [001] direction.

All coatings were deposited by electron beam evaporation under high vacuum conditions. Partial pressures of O_2 and H_2O in the deposition chamber just prior to deposition were less than $1x10^{-6}$ Torr. The deposition rate for all coatings was 1 nm/second. Surface films of SiO_2 and ZrO_2 were deposited from their respective commercial crystalline sources using a single electron beam gun. Carbon samples were coated to analyze composition of the deposited film by Rutherford Backscattering Spectroscopy (RBS). Also, films were deposited onto Al_2O_3 substrates for thickness measurement. A Dektak profilometer was employed to calibrate the deposited thickness of films to an accuracy of $\pm$ 4 nm and to measure final deposited thicknesses. All films were of stoichiometric composition within 5%.

We used a motor driven rotating shaft to coat the cylindrical compression samples inside the deposition chamber. Five or six compression samples were attached end-to-end to the rotating rod by an epoxy. The rod rotated at a speed of 2 revolutions/second to ensure a uniform coating over the whole sample. Total deposition times were on the order of 2 minutes. We attached a carbon sample to the end of the compression samples for RBS analysis.

An Instron machine was utilized for all compression testing. All testing was performed in a high purity Ar atmosphere at 1250°C at a nominal strain rate of 10^{-4} s^{-1}. Testing continued until major cracking occurred in the sample, or the sample catastrophically failed. In one case the test was prematurely halted because the extension limits of the apparatus were reached. Dense SiC platens were employed to compress the single crystalline $MoSi_2$ and the platens showed little or no sign of indentation after tests. BN was used to coat the SiC platens prior to compression testing.

Samples for hardness measurements were prepared by coating half of the surface with 120 nm ZrO_2. This allowed testing of uncoated and coated areas on the same sample at the same time. It also kept constant the orientation between crystallographic directions and indenter edges. Indentations were then made at loads 0.5-1 kgf for 5 seconds. We used a diamond Vickers indenter for all hardness tests.

Intrinsic stress in the deposited film was measured by an Ionic wafer deflection gauge. The system was originally designed to measure intrinsic stress in thin films deposited on Si wafers. It was modified to allow measurements on smaller Si beams. Three measurements were made on each coated sample, and three such samples were tested with adequate results, i.e. the deflection was in the measurable range of the machine after coating. The stress measurement system employed a fiber optic bundle that shined light on the Si surface. From detection of varying amounts of light reflected from the sample, a distance between light head and sample could be determined to high accuracy. From this distance and the radius of the contact points for the beam we can determine a change in radius of curvature for the film-substrate composite due to intrinsic stresses.

RESULTS AND DISCUSSION

Compression Tests

Compression tests were performed on single crystal samples at 1250°C. Results for the 120 nm ZrO_2 coated compression samples are shown in Fig. 1. Coated samples exhibit approximately twice the plastic deformation of uncoated samples, i.e. 2.7 - (>) 3.0% strain in ZrO_2 coated materials compared to 1 - 1.3% in uncoated materials. The uncoated samples failed catastrophically during testing, with only bits of powder left after compression tests. On the other hand, the coated samples deformed plastically, with one sample exhibiting a large degree of shear.

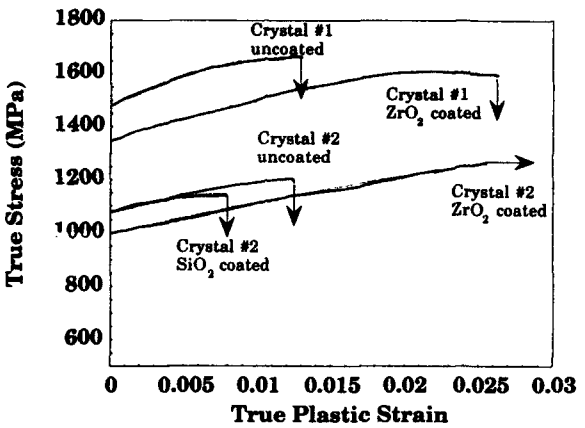


Fig. 1 True stress as a function of true plastic strain for uncoated, ZrO_2 coated and SiO_2 coated [001] oriented single crystalline $MoSi_2$.

Samples were prepared from two different single crystals grown at different times. Each of the two uncoated single crystals exhibited a different yield strength as well as a different total plastic strain. This could be due to different amounts of Mo_5Si_3 in the each crystal. However, in each case the coated materials exhibited greater plastic strains.

Fig. 1 also shows the effect of an SiO_2 coating on single crystal compression. Additional SiO_2 coating over that associated with the formation of the thin natural oxide did not lead to an increase in plasticity. In fact, there is a slight decrease in the plasticity of the SiO_2 coated sample in Fig. 1. There was no significant effect of the coating on the yield stress of the material as there was for ZrO_2 coated material. The SiO_2 coated sample failed by the formation of vertical cracks, such that there were only long splinters of SiO_2 coated single crystal $MoSi_2$ after test completion. However, the ZrO_2 sample is still intact after undergoing twice the plastic strain of the uncoated sample.

Intrinsic and Extrinsic Stresses

The Ionic stress analyzer measures the change in deflection of a wafer between the uncoated and coated situations. Using this information, we calculate a value of intrinsic stress in our film. Using values for ZrO_2 on Si, we find that the stress in our as-deposited films is approximately 70 MPa (tensile in the film, compressive in the substrate). Comparing this value to values obtained by other investigators, we find that Scheuerman measured the stress in other electron-beam deposited ZrO_2 films to be 25 MPa [6]. These measurements were on different substrates than $MoSi_2$. Hoffman has pointed out that the intrinsic stress of a deposited film does not seem to change much with varying substrates [7].

The intrinsic stress involves only stresses due to deposition; considerations such as thermal expansion differences are extrinsic stresses. In many cases, the value of extrinsic stress can greatly exceed the value of intrinsic stress. The coefficients of thermal expansion (CTE) of

$MoSi_2$ and ZrO_2 are very similar over the range of temperatures up to 1250°C. From the CTE difference at 1200°C, we find that the strain due to thermal expansion mismatch is less than 0.25% at these relatively high temperatures. However, our ZrO_2 film is not completely dense, so the exact CTE difference is unknown. Because the ZrO_2 film shows no sign of spalling at 1200°C, it is likely that the extrinsic stresses are not excessively large.

From the calculations described above, we know that the intrinsic stress of the $ZrO_2/MoSi_2$ composite system is of the order of 70 MPa. This additional compressive stress at the surface would tend to prevent the nucleation and propagation of surface cracks in the matrix. In addition, this compressive stress, for deformation in compression, would allow dislocation generation at stress concentrators at the interface. Thus, the film in this case can serve two important functions. The relatively large intrinsic stress prevents cracks from nucleating at surface sites and also increases the plastic deformation in the bulk. This combination of effects manifests itself during compression testing as significantly enhanced plasticity.

Failure of Compression Samples

The manner of failure in the uncoated compression samples suggests that the propagation of especially large numbers of cracks throughout the sample was responsible for its failure. These were most likely cracks that nucleated at the surface and propagated inward during loading. The ZrO_2 coating had a significant effect on this crack propagation, both in delaying crack nucleation at the surface thus also delaying catastrophic failure.

We see a much different behavior for the SiO_2 coated compression samples. The total strain of these samples is approximately the same as the uncoated samples, but the samples failed by the formation of a few vertical cracks rather than the multiple crack propagation as in the uncoated material. The film constrained the material enough to prevent large-scale multiple crack nucleation. However, it did not have the same effect as the ZrO_2 coating. SiO_2, the natural oxide layer on $MoSi_2$, evidently cannot rigidly constrain the substrate sufficiently during deformation in such a manner as to generate additional dislocations in compression, at least not when it is artifically thickened by PVD methods used in this investigation.

Hardness Tests

Our previous work has shown a 20-40% reduction in hardness for single crystal and polycrystalline $MoSi_2$ with 120 nm ZrO_2 coatings [4]. We also see this reduction in hardness for ZrO_2 films of varying thickness (see Fig. 2). There is a large drop in hardness for 120 nm films, but additional coating thicknesses do not give additionally reduced hardness.

When we examine the indentations, we find that the variation in film thickness has a large effect on the indentation-induced cracking behavior. Fracture toughness of a brittle material is often approximated by measuring the lengths of radial cracks extending from an indentation. The indentations of uncoated and coated materials are shown in Fig. 3. Indentation into uncoated $MoSi_2$ causes long radial cracks extending from the edges of the indentation as shown in (a). These radial lengths are on the order of 30 μm. Similarly, the 120 nm film has long radial cracks extending from the corners that are about 30 μm in length. Films of 240 nm thickness markedly reduce the amount of radial cracking associated with the indentation to about 15μm. The thickest films (480 nm) effectively eliminate all radial cracking.

It is likely that the intrinsic stress in the deposited film is responsible for this abrupt change in radial cracking behavior. The film induces a compressive stress in the substrate, which should make crack nucleation in the substrate more difficult. At larger film thicknesses, this stress is apparently sufficient to prevent any radial cracks from extending in the substrate. There is a change from radial crack formation to lateral crack formation along the interface between ZrO_2 and the substrate. Hence, we see delamination of the film around the corners of the microindentation. The interface in this case serves as a relatively weak path for crack propagation.

Despite film delamination at regions corresponding to the edges of the indenter, the film remains adherent to the substrate underneath the indenter, as seen in Fig. 3. This adherent

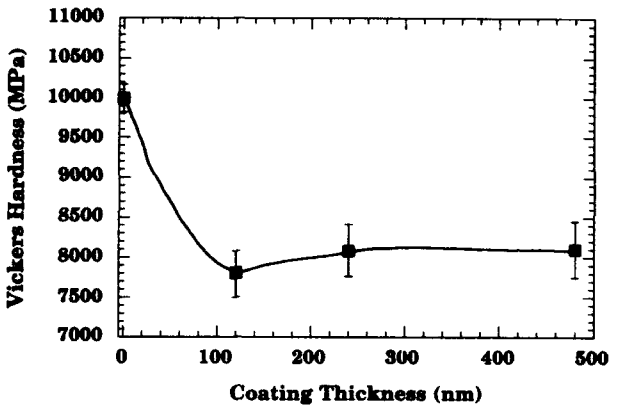


Figure 2. Vickers hardness of [001] $MoSi_2$ samples as a function of ZrO_2 film thickness on $MoSi_2$.

area suggests that the film deforms with the substrate with increasing loads. In addition, it suggests that the film remains adherent to the substrate during the entire loading cycle. If lateral fracture of the film were to occur during the loading cycle, we would expect to see indentations where the film has cracked or spalled from the area under the indenter. However, this is not the case for any of the films in this investigation. It is more likely that this lateral fracture occurs during the unloading cycle of the hardness test. A model for indentation testing proposed by Chiang et al. predicts very large residual stresses underneath an indenter during the unloading cycle [8]. It is therefore likely that the lateral fracture seen in the thicker coatings occurs during the unloading portion of hardness testing.

SUMMARY

When the hardness data is obtained in conjunction with the compression testing data, it is apparent that there is enhanced plasticity by dislocation motion occurring in ZrO_2 film-coated $MoSi_2$. From previous studies in other less brittle materials, we know that interfaces such as surface films and second phases can be dislocation sources under applied stress. A similar mechanism probably operates in this system, except that the brittle cracking behavior of material must also be taken into account. It is likely that the film prevents nucleation and/or propagation of cracks at the surface, in addition to providing nucleation sites for additional dislocations. This would explain the increased plasticity in ZrO_2 coated materials over uncoated ones. The constraint of the adherent surface film could effectively be pumping dislocations into the substrate at the film/substrate interface, thereby reducing crack nucleation, crack propagation or both.

ACKNOWLEDGMENTS

The portions of this research carried out at the University of Michigan were supported by the National Science Foundation, Grant No. DMR 9102414. C.M. Czarnik also acknowledges Department of Energy fellowship support which enabled him to do major portions of this research in the Center for Materials Science at Los Alamos National Laboratory. J.D. Garrett also acknowledges the support of the Ontario Council for Materials Research.

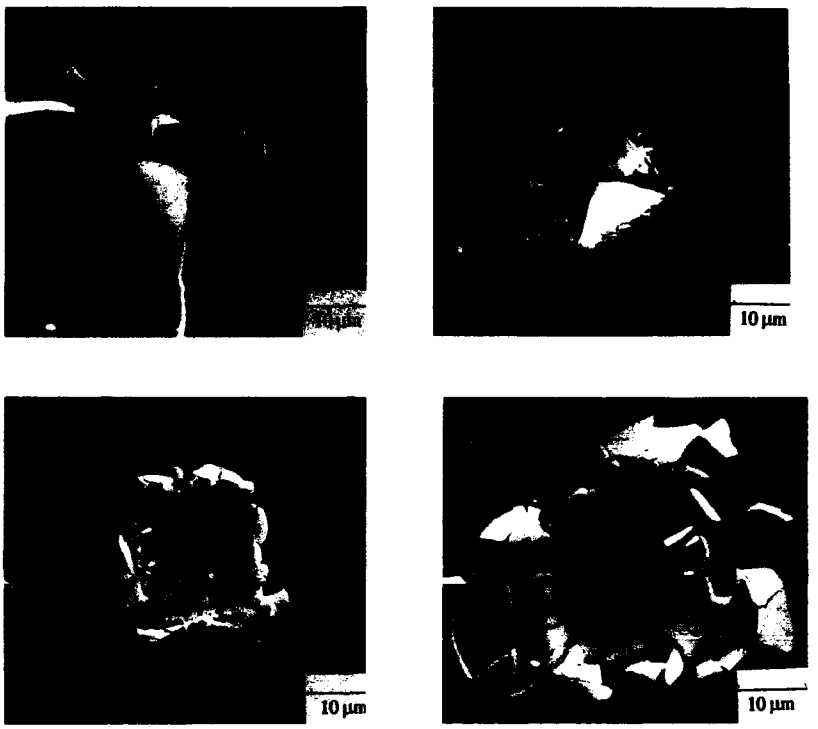


Figure 3. a) Indentation of an uncoated specimen. Radial crack length is about 30 μm. b) Indentation through a 120 nm ZrO_2 coating. The radial crack length is also about 30 μm, and there are small amounts of lateral fracture surrounding the indentation. c) Indentation through 240 nm ZrO_2 coating. Radial crack length is reduced to 15 μm, but the lateral cracking is more prevalent than for the 120 nm coatings. d) Indentation through 480 nm ZrO_2 coating. Radial cracking has been eliminated, but the lateral cracking around the indentation is substantial.

REFERENCES

1. A.K. Vasudevan and J.J. Petrovic, Mater. Sci. Eng. A155, 1 (1992).
2. R.D. Noebe and R. Gibala, Structure and Deformation of Boundaries, K. Subramanian and M.S. Iman, eds., TMS-AIME, Warrendale, PA, p. 89, 1986.
3. J.J. Petrovic, A.K. Bhattacharya, R.E. Honnell, T.E. Mitchell, R.K. Wade and K.J. McClellan, Mater. Sci. Eng. A155, 259 (1992).
4. C.M. Czarnik, R. Gibala, M.A. Nastasi, R.B. Schwarz, S.R. Srinivasan and J.J. Petrovic, Mat. Res. Soc., 288 (1993).
5. Y. Umakoshi, T. Hirano, T. Sakagami and T. Yamane, Scripta Metall. 23, 87 (1989).
6. R. Scheuerman, Stresses in Dielectric Films, Thin Film Dielectrics, F. Vratny ed., 561 (1969).
7. R. W. Hoffman, Physics of Thin Films, Vol. 3. Academic Press, New York, (1966).
8. S.S. Chiang, D.B. Marshall and A.G. Evans, J. Appl. Phys. 53, 298 (1982).

STRENGTH AND TOUGHNESS OF SILICIDE MATRIX MATERIALS CONSOLIDATED BY HOT ISOSTATIC PRESSING

R. SURYANARAYANAN, S. M. L. SASTRY AND K. L. JERINA
Materials Science & Engineering Program, Department of Mechanical Engineering
Washington University, St. Louis MO 63130

Abstract

Substantial improvements have been reported in high temperature strength and creep resistance, and room temperature fracture toughness of molybdenum disilicide ($MoSi_2$) reinforced with ductile or brittle reinforcements. The influence of Hot Isostatic Pressing (HIP) process parameters on the mechanical properties of $MoSi_2$ based alloys was studied. Monolithic $MoSi_2$ powder and $MoSi_2$ powder blended with either niobium powder or silicon carbide whisker reinforcements were consolidated by HIP at 1200 – 1400°C, 207 MPa, and 1 - 4 hrs. The HIP'ed compacts were characterized for compression strength and creep resistance at 1100-1300°C. Fracture toughness was measured on single edge notched rectangular specimens at room temperature. Mechanical properties were correlated with post-HIP microstructural features.

INTRODUCTION

The intermetallic compound, molybdenum disilicide ($MoSi_2$) has been considered as a potential material for advanced high temperature structural applications [1]. This has been primarily due to its high melting temperature, good oxidation resistance, compatibility with reinforcement materials, and attractive mechanical properties with a potential for improvement by reinforcements or alloying additions. The present study utilizes silicon carbide (SiC) as a brittle whisker reinforcement and niobium (Nb) as a ductile particulate reinforcement.

Hot Isostatic Pressing (HIP) has been one of the common powder consolidation methods for these materials. Alman et al [2] have reported that for P/M processed $MoSi_2$ and its composites, HIP was necessary to achieve complete densification, even for samples processed initially by hot pressing. The objectives of the present investigation were (i) to determine optimum HIP process parameters in order to minimize porosity and matrix-reinforcement interactions, reduce deleterious secondary phases, and refine grain structure, and (ii) to characterize mechanical properties of consolidated samples as a function of HIP process parameters. Details of optimization of HIP consolidation are described elsewhere [3]. We report here the elevated temperature strength, creep resistance and room temperature fracture toughness of the consolidated alloys.

EXPERIMENTAL METHODS

Hot Isostatic Pressing

The $MoSi_2$ powder (45μm, 99.5 % purity) and the Nb powder (Coarse : 75-180μm, 99.8 % purity; Fine : 45μm, 99.5 % purity) were procured from Cerac, Inc., Milwaukee, WI. The SiC whiskers (15.5μm × 1.6μm) were procured from ART, Inc., Buffalo, NY. In the case of composites, the matrix and reinforcement particles (20 vol. %) were mechanically blended for more than 12 hours. The powder was poured into cylindrical Nb cans sealed on one end by tungsten inert gas (TIG) welding, degassed for several hours at 250°C, and sealed on the other end by electron beam welding. The cans were then HIP'ed in an argon atmosphere at 207 MPa (30 ksi) pressure, at three different temperatures ($1200°C, 1300°C, 1400°C$) and two time intervals (52 min and 4 hrs) for each type of material under study. Density measurements were performed on samples by the Archimedes principle method.

Mat. Res. Soc. Symp. Proc. Vol. 322. ©1994 Materials Research Society

Mechanical Properties

Compression Strength

Compacts of $MoSi_2$, $MoSi_2$ - Nb, and $MoSi_2$ - SiC produced for the consolidation experiments [3] were machined into rectangular pieces by electro discharge machining. Specimens tested were the highest density samples of $MoSi_2$, $MoSi_2$ - Nb, and $MoSi_2$ - SiC. Specimens were approximately 10mm × 6mm × 3mm in size. Specimens were soaked at the test temperatures of 1100 and 1300°C before loading. Compression tests were performed on a MTS closed loop servohydraulic test machine at an initial strain rate of 5×10^{-4} sec^{-1}.

Creep

Specimens were tested under constant load compression, in the temperature range of 1100°C to 1300°C, using SiC platens and push rods. The displacement of the lower cross head of the MTS testing machine was recorded as a function of time. The incremental load method was used once steady state creep was attained at a particular load.

Fracture Toughness

A single edge notch was introduced in the middle of each specimen using a 0.3mm diamond cutting wheel. The rectangular specimens were approximately 25mm × 6mm × 3mm and the initial crack lengths produced by the diamond wheel were approximately 2.5 mm. Specimens were loaded monotonically to failure under three point bending. Fracture toughness measurements of fatigue pre-cracked and non-precracked specimens of $MoSi_2$ based materials indicated no significant differences [4]. Furthermore, it has been suggested by Fleck and Smith [5], and Barnby et al [6], who worked on sintered steel as model material, that fatigue pre-cracking is an unnecessary precursor to fracture toughness testing in some material systems. It is likely, therefore, that the notch root radius is not a sensitive parameter in these brittle materials. No fatigue precracking was, therefore, done for any of the specimens tested. Fracture surface morphologies of the most dense and the least dense samples in each type of material were studied in a HITACHI S4500 Scanning Electron Microscope. Fracture mode was identified in each case.

RESULTS AND DISCUSSION

Compression Strength

The compressive yield strengths of the highest density samples of $MoSi_2$, $MoSi_2$ - Nb, and $MoSi_2$ - SiC, along with results of earlier studies, are shown in Table I. Compression strength data for the monolithic case shows that attractive strength is retained at least until 1300°C. Measured strength at 1100°C is much higher than data reported in the literature for similar temperatures. This may be due to lower levels of the silica rich grain boundary phase in the present case than in earlier studies where consolidation was carried out at much higher temperatures. Optimal processing, therefore, may be a means of reducing the undesirable silica phase in the matrix.

In the case of the Nb reinforced composite, strengths at 1100°C and 1300°C are comparable to values reported in previous studies at similar temperatures. Samples showed buckling at the later stages of compression at both test temperatures.

Table I: Effect of temperature on the compression strength (in MPa) of $MoSi_2$ based materials

Monolithic $MoSi_2$

T (°C)	$\dot{\epsilon}$	1050	1100	1150	1200	1250	1300	1350	1400
Ref.[7]	5×10^{-4}	594		493		305		222	
Ref.[8]	7×10^{-5}				325				194
Present work	5×10^{-4}		826.7				394.4		

$MoSi_2$ - Nb

T (°C)	1050	1100	1150	1250	1300	1350
Ref.[7]	513		392	286		156
Present work		450.2			265.5	

$MoSi_2$ - SiC

T (°C)	1100	1200	1300	1400
Ref.[9], flexure		236		39
Ref.[10], flexure		394		73
Present work	295.8		171	

The strengths are lower in $MoSi_2$ - SiC specimens compared to the other two cases. Compression strengths of the present work are only comparable with the 4-point flexural strengths of Refs. [9] and [10]. The lower strengths at these temperatures may be attributed to a larger amount of the grain boundary Si-rich phase that may be viscous at these temperatures. As suggested by Maloy et al [11] a small addition of carbon to $MoSi_2$ can reduce this problem since carbon acts as a deoxidant thereby removing the silica grain boundary phase. Samples were crumbled after $\sim$ 2.5% deformation, indicating the absence of appreciable plastic deformation in this case. Optical micrographs of the SiC reinforced material showed an agglomeration of the SiC whiskers, possibly due to electrostatic attractions [3]. This agglomeration of the SiC whiskers causes regions of the composite to be highly brittle compared to the matrix. This could be a major reason for the low strengths in this material. A better distribution of the whiskers in the matrix may lead to a significantly higher strength value than measured in the present study.

Creep Resistance

Figure 1 shows the steady state creep rate as a function of applied stress for the three materials at different temperatures. The slopes of the regression fit lines (corresponding to the power law creep (PLC) exponents) are noted in the figure. The stress exponents are comparable to results of earlier studies on $MoSi_2$ and $MoSi_2$ - SiC [1,2]. The creep rates of $MoSi_2$ - Nb are higher at both temperatures compared to the monolithic case. The creep rates of $MoSi_2$ - SiC is slightly lower than the monolithic material. This small difference in creep rates is contrary to the significantly lower creep rates obtained for $MoSi_2$ - SiC in earlier studies [12,13]. One possible explanation for this discrepancy is the low density of the $MoSi_2$ - SiC specimen, approximately 96 %, compared to the nearly theoretical dense specimens used by earlier workers. Also, the much smaller grain sizes in the SiC reinforced case may enhance the kinetics of Mo diffusion in $MoSi_2$, the rate controlling step in the kinetics of creep of $MoSi_2$ [13], which may lead to higher creep rates. The average creep exponents for $MoSi_2$, $MoSi_2$ - Nb, and $MoSi_2$ - SiC in the 1200° - 1300°C temperature range are 2.2, 2.55, and 2.41, respectively. The exponent for the Nb reinforced material varies from 2.06 at 1300°C to 4.02 at 1100°C. A plot of creep rate versus reciprocal temperature gave

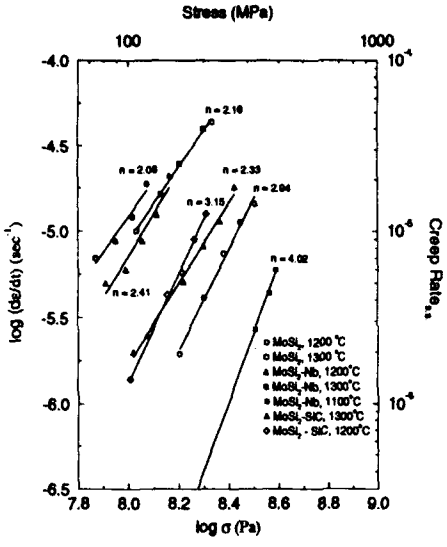


Figure 1: Steady state creep rate as a function of applied stress for $MoSi_2$, $MoSi_2$ - Nb, and $MoSi_2$ - SiC.

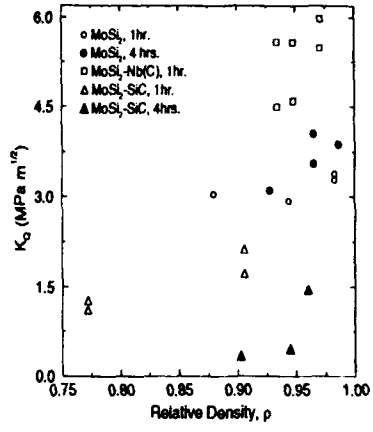


Figure 2: Toughness as a function of relative density for monolithic $MoSi_2$, $MoSi_2$ - Nb, and $MoSi_2$ - SiC

the activation energy of 160 kJ/mol for the $MoSi_2$ - Nb materi

Fracture Toughness

Monolithic $MoSi_2$:

Figure 2 shows the results of fracture toughness vs. relative density for monolithic $MoSi_2$ and $MoSi_2$ composites. For relative density less than 0.95, K_Q values are relatively constant at $\sim$ 3 MPa $\sqrt{m}$ and increases to $\sim$ 3.3 MPa $\sqrt{m}$ and $\sim$ 4.0 MPa $\sqrt{m}$ for powders consolidated for 1 hr. and 4 hrs., respectively. The toughness value increase above 95% density corresponds to the consolidation stage where pores become isolated and spherical in shape. This increase in toughness is not surprising because at lower levels of density pores are interconnected and cracks have existing channels to propagate through, leading to earlier failure. Fracture surface studies [3] show that, for the sample consolidated at 1400°C, fine grained regions fracture by an intergranular mode and coarse grained regions show cleavage fracture.

$MoSi_2$ - 20 vol.% Nb:

Ductile reinforcements have been used effectively to increase fracture toughness properties of brittle matrices [7]. However, the resulting composites are unstable at elevated temperatures because, for example, niobium reacts with $MoSi_2$ forming brittle intermetallics at the interface. The formation of these compounds degrades the toughening effect. Some investigators have studied the effectiveness of inert diffusion barrier coatings like Al_2O_3, ZrO_2 [14], and Y_2O_3 [15] to counter this problem. As an alternative to the coating approach, the

methodology of the present investigation was to reduce the HIP temperature to a minimum without compromising on the level of density, thereby, minimizing the reaction products at the interface.

Toughness variation as a function of relative density for the matrix reinforced with coarse Nb powder is shown in Figure 2. $MoSi_2$ reinforced with 20 vol. % coarse Nb particles showed the maximum resistance to crack propagation among all the materials in this study. At low densities (93-95%) K_Q remained close to 5 MPa $\sqrt{m}$ and increased to $\sim$ 5.7 MPa $\sqrt{m}$ at higher densities. This is approximately a 35-40% increase in K_Q compared to the unreinforced matrix.

Fracture surface analysis of the Nb particle region [3] shows that it undergoes brittle cleavage fracture which means that crack blunting and crack bridging mechanisms are unlikely in this material. The matrix may be constraining the deformation of the Nb particles near the crack tip, causing a state of plane strain, leading to brittle failure. The $MoSi_2$-Nb reaction zone may cause the initial crack length in the Nb particle to be high enough, resulting again in a plane strain state. It leads to the conclusion that optimal HIP processing alone will not be sufficient for the requisite toughness improvement of this composite. In addition to optimal HIP, the $MoSi_2$ /Nb interface needs to be engineered to enhance its effectiveness in toughening, for example, by coatings.

$MoSi_2$ - 20 vol.% SiC:

Figure 2 shows the toughness increase in $MoSi_2$ - SiC with increasing relative density. The resistance to crack propagation in this case is considerably less than for monolithic and Nb reinforced $MoSi_2$. Carter and Hurley [16] reported a 54% increase in fracture toughness in this material compared with the unreinforced matrix. The fracture toughness values in the present study are considerably lower than in earlier studies. The primary reason for this difference is that the samples in the present study have been consolidated to much lower levels of density (96 %) than those in previous studies where samples were consolidated to near theoretical densities.

Micrographs of the $MoSi_2$ - SiC composite show clumping of SiC whiskers that are either rod shaped or stacked equiaxed SiC grains [3]. This agglomeration produces highly brittle regions (in comparison to the matrix), which may be another reason for the low fracture resistance of the SiC reinforced materials in this study. The general behavior of K_Q versus relative density in this case is similar to the other two cases investigated. The sudden increase in toughness values after reaching density values greater than 90% is similar to the conclusions of Fleck and Smith [5].

CONCLUSIONS

1. Yield strengths of monolithic $MoSi_2$ were found to be greater than that for $MoSi_2$ - Nb, which were in turn greater than those for $MoSi_2$ - SiC, at test temperatures of 1100 and 1300°C. The low strength of the SiC reinforced material is probably due to the higher level of porosity in the material. The larger level of grain boundary silica phase in this composite, which may be viscous at high temperatures, is probably another reason for the low strength measured for this material.

2. At a particular applied stress, the creep rates are higher in $MoSi_2$ - Nb than in monolithic $MoSi_2$, and $MoSi_2$ - SiC. The PLC exponents for monolithic $MoSi_2$ and $MoSi_2$ - SiC are comparable to the values obtained in other studies. The PLC exponent for $MoSi_2$ - Nb is 2.2, with a PLC activation energy of 160 kJ/mol.

3. Room temperature fracture is predominantly cleavage for $MoSi_2$ and $MoSi_2$ - Nb samples with densities close to theoretical values. Toughness values are almost constant until a relative density of $\sim$ 95% is achieved. This level of density corresponds closely to the range where there is a change in the nature of porosity from being interconnected (cusp shape) to being isolated (spherical shape). However, in all three cases, as relative density changes from $\sim$ 95% to 100%, there is a disproportionate increase in toughness values.

4. $MoSi_2$ - Nb was found to have the maximum resistance to crack propagation, followed by $MoSi_2$ and $MoSi_2$ - SiC, in that order. The uncharacteristically low fracture toughness of $MoSi_2$ - SiC is probably due to the relatively low density level (primarily interconnected porosity) in this case compared to the other two and/or because of the agglomeration of the SiC whiskers.

ACKNOWLEDGEMENTS

This research was conducted under AFOSR contract # F49620-90-C-0030.

REFERENCES

1. A. K. Vasudevan and J. J. Petrovic, Mater. Sci. Engg. A, **155**, 1-17 (1992).
2. D. E. Alman, K. G. Shaw, N. S. Stollof, and K. Rajan, Mater. Sci. Engg. A, **155**, 85-93 (1992).
3. R. Suryanarayanan, S. M. L. Sastry, and K. L. Jerina, presented at the 122nd TMS Annual Meeting & Exhibition, Denver, CO, February, 1993 (unpublished).
4. D. S. Schwartz, Technical Report MDC 92-Q0409, McDonnell Douglas Aerospace, St. Louis MO 63166, 1992.
5. N. A. Fleck and R. A. Smith, Powder Metall., **3**, 121-125 (1981).
6. J. T. Barnby, D. C. Ghosh, and K. Dinsdak, Powder Metall., **16**, 55 (1973).
7. W. O. Soboyejo, K. T. Venkateswara Rao, S. M. L. Sastry, and R. O. Ritchie, Metall. Trans. A, **24**, 585-600 (1993).
8. R. M. Aikin Jr., Scripta Metall. Mater., **26**, 1025-30 (1992).
9. W. S. Gibbs, J. J. Petrovic, and R. E. Honell, Ceram. Eng. Sci. Proc., **8**, 645-48 (1987).
10. J. J. Petrovic and R. E. Honell, Ceram. Eng. Sci. Proc., **11** (7-8), 734-44 (1990).
11. S. Maloy, A. H. Heuer, J. J. Lewandowski, and J. J. Petrovic, J. Amer. Ceram. Soc., **74**, 2704 (1991).
12. H. E. Deve, C. H. Weber, and M. Maloney, Mater. Sci. Eng. A, **155**, 668-75 (1992).
13. K. Sadananda, C. R. Feng, H. Jones, and J. J. Petrovic, Mater. Sci. Eng. A, **155**, 227-39 (1992).
14. L. Xiao and R. Abbaschian, Mater. Sci. Eng. A, **155**, 135-45 (1992).
15. T. C. Lu, A. G. Evans, R. J. Hecht, and R. Mehrabian, Acta Metall. Mater., **39** (8), 1853-62 (1991).
16. D. H. Carter and G. F. Hurley, J. Amer. Ceram. Soc., **70** (4), C79-C81 (1987).

CREEP BEHAVIOR OF $MoSi_2$-SiC COMPOSITES

DARRYL P. BUTT,* STUART A. MALOY, H. KUNG, DAVID A. KORZEKWA, and JOHN J. PETROVIC
Materials Division, P.O. Box 1663, M.S. G755, Los Alamos National Laboratory, Los Alamos, New Mexico 87545

ABSTRACT

Using a cylindrical indenter, the indentation creep behavior of hot pressed and HIPed $MoSi_2$-SiC composites containing 0-40% SiC by volume, was characterized at 1000-1200°C, 258-362 MPa. The addition of SiC affects the creep behavior of $MoSi_2$ in a complex manner by pinning grain boundaries during pressing, thus leading to smaller $MoSi_2$ grains; by obstructing or altering both dislocation motion and grain boundary sliding; and by increasing the overall yield stress of the material. Comparisons are made between indentation and compressive creep studies. It is shown that under certain conditions, compressive creep and indentation creep measurements yield comparable results after correcting for effective stresses and strain rates beneath the indenter.

INTRODUCTION

Molybdenum disilicide ($MoSi_2$) is a candidate high temperature structural material due, in particular, to its excellent high temperature oxidation resistance, good high temperature strength, high melting point, and high thermal conductivity.[1] However, because of its open crystal structure, one of the major limitations in the use of $MoSi_2$ at elevated temperatures is its poor creep resistance. The purpose of this work was to improve the creep resistance of $MoSi_2$ by reinforcing it with a relatively rigid particulate: silicon carbide (SiC).

The creep behavior of the $MoSi_2$-SiC composites was characterized using an indentation creep method. Various investigators have used indentation or impression creep techniques to characterize the creep behavior of materials.[2-5] A flat, cylindrical indenter, as used in these studies, appears to be the best geometry for indentation creep measurements because the stress and material hardness do not decrease with time, as is the case with other indenters such as Knoop and Vickers. Since the stress and material hardness remain constant during the indentation creep test, steady state creep can be observed. The general equation governing indentation creep for a cylindrical indenter is as follows:

$$\dot{\varepsilon}_{ss}^{i} = \frac{v}{2a} A(G.S.)^{-m} \left(\frac{\sigma_{app}}{B}\right)^{n} \exp\left(\frac{-Q}{RT}\right) \quad (1)$$

Contrast equation (1) with the equation for compressive creep:

$$\dot{\varepsilon}_{ss}^{c} = A(G.S.)^{-m} (\sigma_{app})^{n} \exp\left(\frac{-Q}{RT}\right) \quad (2)$$

In equations (1) and (2), $\dot{\varepsilon}_{ss}$ is the steady state creep rate where the subscripts *i* and *c* denote indentation and compressive creep rates, respectively; G.S. is the grain size; m is the grain size exponent; σ_{app} is the applied stress (or the stress on the indenter or punch); n is the stress exponent; Q is the activation energy; and RT has its usual meaning. The equations differ in that equation (1) contains two additional terms: v/2a and B, where v is the velocity of the punch, 2a is the punch diameter, and B is a stress correction factor. The term v/2a, derived by Yu and Li through finite element analysis,[2] converts the punch velocity to an approximate, effective material

* Author to whom correspondence should be addressed.

Mat. Res. Soc. Symp. Proc. Vol. 322. ©1994 Materials Research Society

strain rate. The term B has apparently not previously been evaluated in detail for the axisymmetric case. For plane strain conditions, B has been shown to be equal to $1+\pi/2$ for specimens with dimensions effectively infinitely large compared to the indenter diameter.[6] Through finite element modeling of the axisymmetric case, we derived values for B ranging from 2.74 to 2.77 depending on the assumed strain rate sensitivity.[7] Thus, B appears to have a relatively minor strain rate sensitivity. In the studies described below, we assumed B equaled 2.75. Note that the results of our finite element analyses are preliminary.

In order to make a direct comparison between the indentation and compressive creep techniques, as others have proposed is viable,[4] specimens produced in our laboratory were sent to the Naval Research Laboratory (NRL) in Washington, D.C. for compressive creep tests. In this way direct comparisons could be made between the two techniques using identical materials. The results of NRL tests have been reported in detail elsewhere.[8]

EXPERIMENTAL

Specimens of $MoSi_2$-SiC containing 0, 5, 10, 20, 30, and 40 volume percent SiC were produced by hot pressing and hot isostatically pressing (HIPing). The starting materials were H. C. Stark 3 μm $MoSi_2$ and 0.5 μm SiC powders. The powders were combined and vibratory milled for 1 hour using tungsten carbide grinding media. The blends were then hot pressed into 2.5 cm diameter x 6 mm thick disks at 1850°C, 20 MPa yielding compacts with ≈95% theoretical density. Specimens were cut in half and with half being sent to NRL for compressive creep testing. Specimens of each composition were then additionally HIPed at 1800°C, 206 MPa yielding compacts with ≈97% theoretical density. Approximately 1 cm x 6 mm x 5 mm specimens were cut from the compacts for indentation creep tests.

In all cases, specimens were tested using a 1 mm diameter by 1.2 cm long Cercom polycrystalline alumina EBON-A indenter. This material was found to have excellent mechanical properties for this application and did not react measurably with the test materials. Three other materials† were evaluated for use as indenters but did not perform satisfactorily due to poor creep or fracture resistance. Specimens were heated to 1000°C, 1100°C, or 1200°C at approximately 50°C/min, the system was equilibrated for 2 hours or longer at which point a static load was applied providing a stress on the indenter of 258, 310, or 363 MPa. The indentation creep direction was parallel to the hot pressing direction. The duration of experiments ranged from a few hours to approximately 1 week depending on the material and test conditions. Displacements (punch velocities) were measured using an LVDT and data were converted to effective strains or strain rates using equation (1).

Selected specimens were cut in half, parallel to the indentation direction and were polished back to near the center of the z-axis of the indenter. One TEM specimen (20% SiC, 1200°C, 310 MPa) was similarly prepared. Although not covered in detail in this paper, microstructures of the as received and post-mortem specimens were characterized using TEM, SEM, and optical microscopy.[7]

RESULTS AND DISCUSSION

Figure 1 shows a comparison of the steady state indentation creep behavior of the HIPed and hot pressed $MoSi_2$-SiC composites tested at 1200°C. The stress on the indenter was 310 MPa, which is estimated to provide an estimated effective stress, σ_{eff}, on the sample of 113 MPa (i.e., $\sigma_{app}/2.75$). As is apparent from figure 1, the HIPed and hot pressed materials behaved similarly except in the case of the pure material, where the HIPed material had somewhat superior creep resistance. As will become clearer in the discussion to follow, the HIPed $MoSi_2$ exhibited a

† Cercom Hot Pressed SiC, Cercom PAD SiC_w reinforced Al_2O_3, and Sapphikon Sapphire Rod.

slower creep rate because the grains were somewhat larger than obtained during hot pressing (see figure 2).

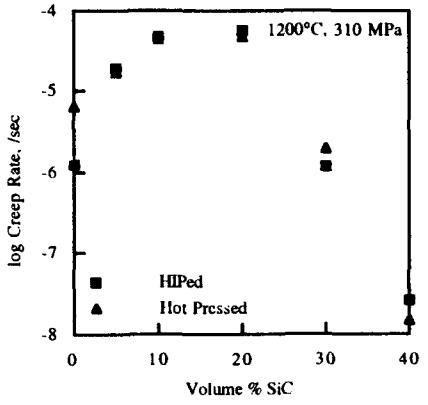


Figure 1. Effect of SiC additions on the creep of $MoSi_2$-SiC composites at 1200°C, 310 MPa on the indenter.

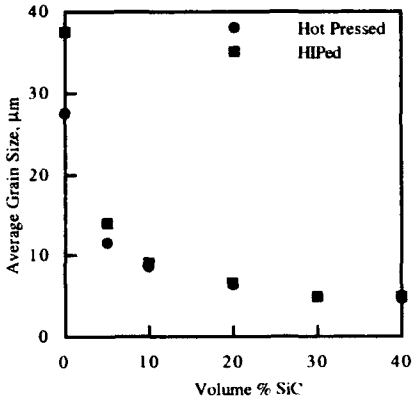


Figure 2. Effect of SiC additions on the average grain size of $MoSi_2$.



Figure 3. Optical micrograph of polished cross-section through indentation zone of pure $MoSi_2$ tested at 1200°C, 310 MPa on the indenter.



Figure 4. Optical micrograph showing intergranular cavitation in the deviatoric stress zone shown in figure 3.

The complex relationship between creep rate and SiC content, shown in figure 1, is associated with a number of factors. The creep rate increases significantly between 0 and 20% SiC, appearing to go through a maximum near 15% SiC, due to the corresponding decrease in the $MoSi_2$ grain size (see figure 2). As equation (1) indicates, the strain rate decreases with increasing grain size, providing the grain size exponent, m, is greater than zero. Sadananda *et al.*[8] observed grain size exponents for pure $MoSi_2$ in compression that varied between approximately 5 and 17 depending on the materials and test conditions. In order to have a non-zero value for m, a boundary mechanism must be operable.[9] Figures 3 and 4 show polished regions from a cross-section taken through the indentation zone of the pure $MoSi_2$. As can be seen in figure 3, there is a relatively dense hydrostatic zone below the indentation. There is a deviatoric stress region surrounding the hydrostatic zone where a significant amount of cavitation is apparent. As shown in figure 4, the cavitation occurs primarily along grain boundaries. Thus, the effects of microstructure and grain size suggest that creep in the pure material is rate limited or

partially rate limited by unaccommodated (or partially accommodated) grain boundary sliding. Unaccommodated grain boundary sliding was also observed in specimens containing 5, 10, and 20% SiC, however, the degree of cavitation decreased significantly with increasing SiC content. At 30 and 40% SiC, little cavitation could be seen optically or by SEM. This would be expected since small grains are more able to accommodate grain sliding than are large grains.

In addition to the obvious effect that SiC has on the $MoSi_2$-SiC grain size, SiC may affect the creep behavior in at least three other ways: by pinning grains thus inhibiting grain boundary sliding, by increasing the overall yield stress of the composite, and by chemically reducing and subsequently removing amorphous silica from the material thereby removing the "lubricant" that provides easy grain boundary sliding and cavity formation. Due to the limited amount of data available, it is not possible to statistically sort out the importance of each of these mechanisms in inhibiting creep. However, TEM investigations provided substantial evidence that the latter mechanism is quite important. As shown in figure 5, the pure $MoSi_2$ contained a significant percentage of amorphous phase both in the form of inclusions and along grain boundaries. Only a few isolated pockets of SiO_2 and no apparent grain boundary phase was observed via TEM investigations of materials containing SiC.[7] Similar observations have been made by others.[10-11] Based on thermodynamic analyses and Knudsen cell mass spectrometry, Jacobson *et al.*[11] proposed that SiC reduces SiO_2 in the $MoSi_2$ compact according to the reaction:

$$SiC + 2SiO_2 \rightarrow 3SiO(g) + CO(g) \qquad (3)$$

Thus, SiC reduces SiO_2 to gaseous species that apparently can escape readily during processing. The kinetics of this process are not currently understood.

As exemplified in figure 6, TEM studies of a $MoSi_2$-20% SiC indentation creep specimen tested at 1200°C, 310 MPa on the indenter, revealed that, in addition to grain boundary sliding, there was significant plastic deformation of the $MoSi_2$ crystals. Most of the deformation resulted from the formation of [100] dislocations, but a variety of other deformation processes were observed including the formation of stacking faults. Based on the data collected to date it appears that the indentation creep of pure $MoSi_2$ is dominated by unaccommodated grain boundary sliding, while at high concentrations of SiC creep may be dominated by plastic deformation or grain boundary sliding accommodated by plastic deformation. Further details of the micromechanisms of creep will be reported later in a more comprehensive paper.[7]



Figure 5. TEM micrograph showing significant amorphous silica (arrows) in pure $MoSi_2$.



Figure 6. TEM micrograph showing a region in the deviatoric stress zone of a hot pressed $MoSi_2$-20% SiC composite showing highly deformed crystals.

As noted above, a secondary objective of this research was to assess whether direct correlations could be made between indentation and compressive creep tests. Figures 7 and 8 show comparisons of the steady state creep rates for the two test configurations at 1200°C and 1100°C, respectively. As described above, the comparisons were made by assuming the effective stress on the indentation sample equaled σ_{app}/B. The compressive creep data were taken from figures provided by Sadananda *et al.*[8] As the figures below show, agreement between the two tests was relatively good, particularly at 1200°C. However, in order to make legitimate comparisons between the two test techniques, the stress and grain size exponents and activation energies for creep should be similar, that is, the mechanisms of creep must be the same. Figures 9 and 10 compare the stress exponents and activation energies, respectively, for indentation and compres-

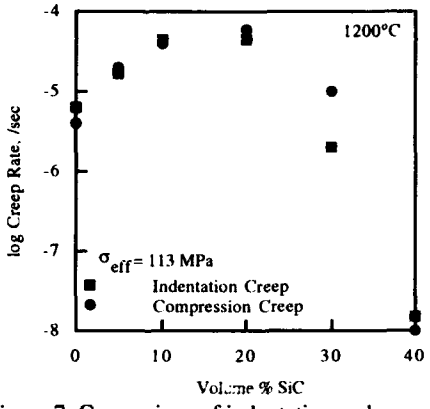


Figure 7. Comparison of indentation and compressive creep behavior of hot pressed $MoSi_2$-SiC composites at 1200°C. The stress or effective stress was 113 MPa.

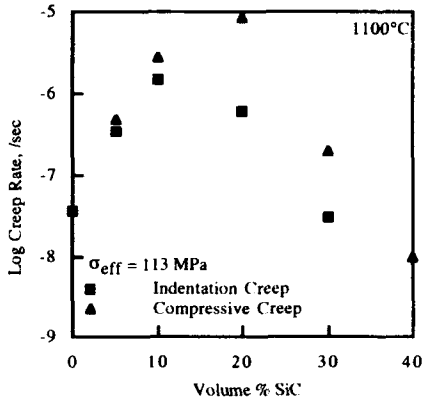


Figure 8. Comparison of indentation and compressive creep behavior of hot pressed $MoSi_2$-SiC composites at 1100°C. The stress or effective stress was 113 MPa.

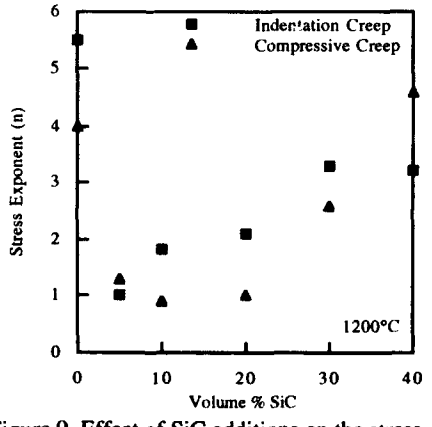


Figure 9. Effect of SiC additions on the stress exponent for creep, comparing indentation to compressive creep at 1200°C.

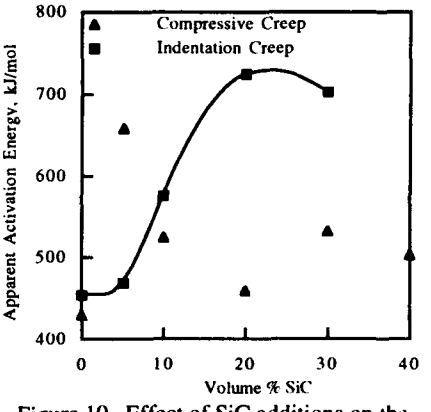


Figure 10. Effect of SiC additions on the activation energy for creep, comparing indentation to compressive creep at 1000 to 1200°C, at a stress or effective stress of 113 MPa.

sive creep. (Values of grain size exponents for indentation creep have not yet been measured.) Figure 9 shows that the stress exponents for indentation and compressive creep follow very similar trends. However, figure 10 shows there are significant differences in the activation energies for indentation and compressive creep suggesting different mechanisms. Therefore, the agreement between the creep rates shown in figures 7 and 8 may be purely fortuitous. Thus, investigators should be cautious in making any comparisons between the two test methods.

CONCLUDING REMARKS

Studies of the indentation creep behavior of $MoSi_2$-SiC composites demonstrated that SiC has a complex effect on creep by reducing the $MoSi_2$ grain size, removing amorphous SiO_2, inhibiting grain boundary sliding, and increasing the overall yield stress of the material. The creep of pure $MoSi_2$ appears to be dominated by unaccommodated grain boundary sliding, while creep of materials with higher concentrations of SiC appears to be dominated by grain boundary sliding accommodated or partially accommodated by plastic deformation, or possibly by pure plastic deformation. Comparisons made between indentation and compressive creep yielded a rather contradictory result: creep rates and stress exponents were in reasonable agreement, while activation energies for creep were quite different.

ACKNOWLEDGMENTS

This work was supported by the U.S. Department of Energy, Advanced Industrial Concepts Program.

REFERENCES

1. A. K. Vasudevan and J. J. Petrovic, *Mat. Sci. and Engr.*, **A155**, 1-17 (1992).

2. E. C. Yu and J. C. M. Li, *Phil. Mag.*, **36** [4] 811-825 (1977); *J. Mater. Sci.*, **12**, 2214-2222 (1977).

3. S. N. G. Chu and J. C. M. Li, *J. Mater. Sci.*, **12**, 2200-2208 (1977); *Mat. Sci. and Engr.*, **39**, 1-10 (1979).

4. B. Roebuck and E. A. Almond, *J. Mater. Sci. Lett.*, **1**, 519-521 (1982).

5. W. B. Li and R. Warren, *Acta Metall. Mater.*, **41** [10] 3065-3069 (1993).

6. W. A. Backofen, Deformation Processing, Addison-Wesley Publishing Co., Reading, Ma, pp. 135, 1972.

7. D. P. Butt, S. A. Maloy, H. Kung, D. A. Korzekwa, and J. J. Petrovic, to be submitted to *J. Am. Ceram. Soc.*

8. K. Sadananda, C. R. Feng, H. N. Jones, and J. J. Petrovic, *Mat. Sci. and Engr.*, **A155**, 227-239 (1992); in Structural Intermetallics, Proceedings of the First International Symposium on Structural Intermetallics, R. Dardia *et al.* (Eds.), TMS, Pittsburgh, PA, 809-818, 1993.

9. T. G. Langdon, in Deformation of Ceramic Materials, pp 101-126, R. C. Bradt and R. E. Tressler (Eds.), Plenum Press, New York, NY (1975).

10. J. D. Cotton, Y. S. Kim, and M. J. Kaufman, *Mater. Sci. and Engr.*, **A144**, 287-291 (1991).

11. Y. S. Kim, M. R. Johnson, R. Abbaschian, and M. J. Kaufman, in High-Temperature Ordered Intermetallic Alloys IV, Mat. Res. Soc. Symp. Proc., Vol. 213, 839-845 (1991).

12. N. S. Jacobson, K. N. Lee, S. A. Maloy, and A. H. Heuer, *J. Am. Ceram. Soc.*, **76** [8] 2005-2009 (1993).

CREEP RUPTURE OF $MoSi_2/SiC_p$ COMPOSITES

JONATHAN D. FRENCH*, SHELDON M. WIEDERHORN* AND JOHN J. PETROVIC**
*National Institute of Standards and Technology, Gaithersburg, MD 20899
**Los Alamos National Laboratory, Los Alamos, NM 97545

ABSTRACT

We studied the creep rupture of a series of $MoSi_2$ materials reinforced with SiC particles. Particulate contents were in the range of 0 to 40 volume percent. Temperature and stress ranges were 1050°C to 1200°C and 10 MPa to 50 MPa, which gave failures ranging from 1 hour to 1500 hours. The creep curves show an extensive tertiary regime, accounting for 25-95% of the total lifetime. Tertiary creep increases with increasing stress and temperature. Cavitation occurs throughout the creep life, and tertiary creep is associated with the linkage of cavities into large cracks. The creep life improves with increasing SiC particle content, with a concurrent loss of creep ductility. Significant improvement occurs only when the particle content is greater than 30 volume percent. Our studies suggest that the creep and creep rupture behavior of $MoSi_2$ can be further improved by increasing the content of SiC particles.

INTRODUCTION

Intermetallic silicides, such as $MoSi_2$, have recently become the subject of numerous research efforts as high temperature structural materials [1]. Current superalloys are limited to temperatures below ~1100°C [2], and the high melting point and excellent oxidation resistance of $MoSi_2$ make it an attractive candidate for high temperature structural applications [3]. However, poor high-temperature creep strength, and low fracture toughness below ~1000°C are impediments to the use of $MoSi_2$ as a structural material. Improvements in these properties have been achieved through the use of SiC particle and whisker reinforcements, and alloy additions, such as WSi_2 [4-6].

The majority of creep data on these materials was collected in compression [6-7]; such data do not provide enough information for design of high temperature structures. First, compression tests provide no details regarding the failure behavior, and second, many ceramics creep faster in tension than compression [8-10]. Therefore, the objectives of this work are to characterize the creep rupture behavior of $MoSi_2$ reinforced with silicon carbide particles (SiC_p) and to compare these materials to other high temperature engineering materials.

EXPERIMENTAL DETAILS

Mechanically mixed powders of $MoSi_2$ and SiC, 0 - 40 vol% SiC, were hot-pressed at 1850°C for 1/2 hour at 30 MPa in a grafoil-lined 1-1/4 inch ID graphite die, with BN powder as the release agent. Hot-pressing was followed by containerless hot-isostatic pressing at 1800°C for 1/2 hour at 207 MPa. All billets were produced at Los Alamos National Laboratory. Dog-bone specimens, 30 mm long with a 2 mm thickness, were machined from the billets. The gauge length was approximately 10 mm long, and 2 mm by 2 mm square cross-section. Due to the limited material available, only 6 - 8 specimens could be made of each composition.

Mat. Res. Soc. Symp. Proc. Vol. 322. ©1994 Materials Research Society

Tensile loads were applied to the specimen through pressure in an air cylinder attached to SiC pull-rods [11]. Load was transferred to the specimen by 2.4 mm diameter Si_3N_4 pins. The gauge length was measured by laser extensometry, which measured the separation of two SiC flags attached to the specimen. The system is able to measure the flag separation with a precision of ±1 μm [11]. The temperature and stress ranges tested, 1050°C to 1200°C and 10 MPa to 50 MPa, gave failures between 1 hour and 1500 hours.

RESULTS AND DISCUSSION

As with metals, these materials exhibit primary and extensive tertiary creep during the rupture tests. The contribution from each regime is stress and temperature dependent. Typical creep curves for these composites are plotted in Figure 1, for the 40 vol% SiC_p composition. The effect of stress and temperature on the shape of the creep curves is clearly shown. The contribution of tertiary creep and primary creep to the total creep strain show opposite trends. Larger tertiary creep regimes are seen with an increase in stress or temperature. Conversely, the primary stage is larger at lower stress and temperature. Tertiary creep accounts for 25-95% to the total creep strain for all runs. In all cases, very little secondary creep occurred, i.e., the time of constant (minimum) creep rate is small compared to the total creep life. Hence a constant

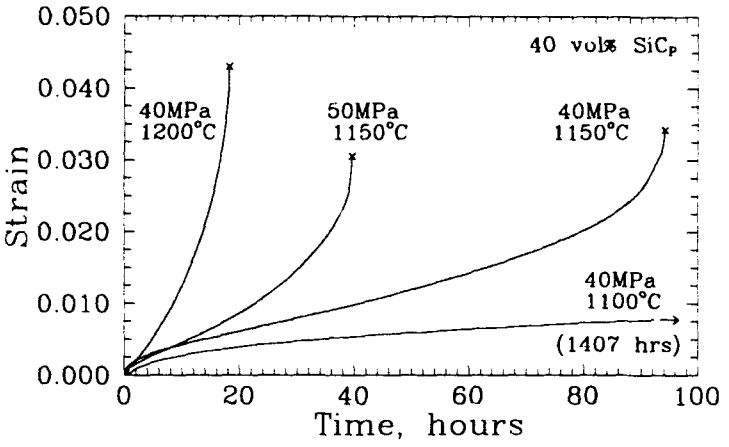


Figure 1. Typical creep curves for the $MoSi_2/SiC_p$ composites, 40 vol% SiC_p is shown.

deformation structure, or balance between strain-hardening and recovery processes that characterize steady state creep, does not occur during creep of these materials.

The addition of SiC_p reinforcement improves the creep rupture life of $MoSi_2$ (Figure 2), especially for the 30 and 40 vol% SiC_p compositions. The increase in creep life with increasing SiC_p content is concurrent with a loss of creep ductility. Specifically, typical strains-to-failure for the 5 vol% SiC_p composition are about 10-15%, compared with the 3-4% strains-to-failure for the 40 vol% SiC_p material. Cavitation, at interfaces between $MoSi_2$ and SiC particles, occurs throughout the creep life. The onset of tertiary creep coincides with the linkage of

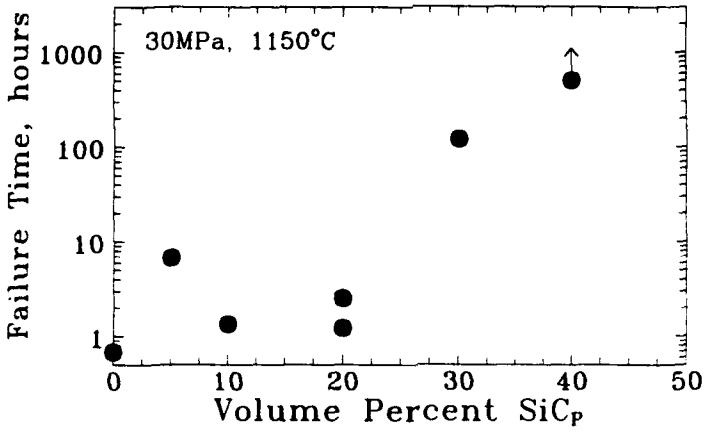


Figure 2. The effect of SiC_p content on the rupture time of $MoSi_2$, 30 MPa, 1150°C.

cavities into cracks and the subsequent growth of these cracks as shown in Figure 3 for the 40 vol% SiC_p composition.

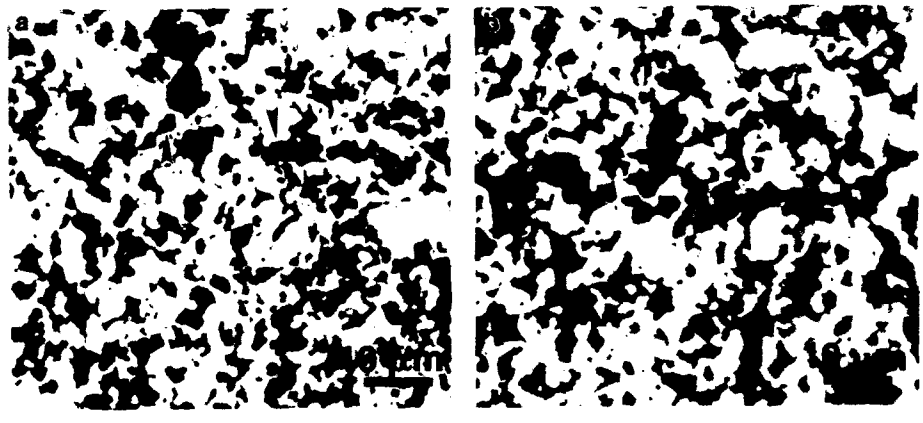


Figure 3. Optical micrographs of crept specimens (40 vol% SiC_p), (a) primary creep regime (arrows indicate cavities), and (b) failed specimen. The tensile stress axis is in the vertical direction.

By determining the temperature and stress dependence of the failure time, a failure map can be generated to compare the behavior of these materials (Figure 4). Significant improvement in the creep rupture life of $MoSi_2$ is achieved when the reinforcement content is greater than 30 vol%. We believe this improvement in behavior is due to the formation of a

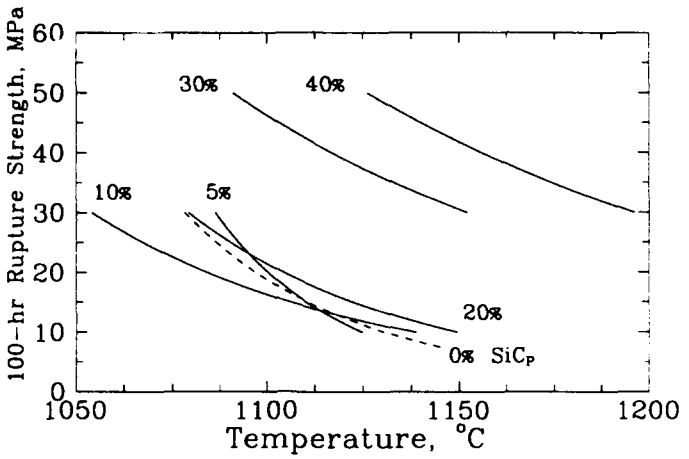


Figure 4. Failure map for the $MoSi_2/SiC_p$ composites. Solid lines are calculated from the experimental data (long-time and short-time tests), dashed line is an estimate from short-time data.

rigid skeleton by the SiC particles. For SiC concentrations of 20% and lower the skeleton does not form and the deformation of the matrix dominates the behavior. The failure map also allows us to compare these materials to other high temperature engineering materials. Figure 5 compares the rupture strength of the $MoSi_2/SiC_p$ composites, a nickel-based superalloy (MAR-M246) [12] and two commercial grades of silicon nitride [13,14]. NT154 represents a state-of-

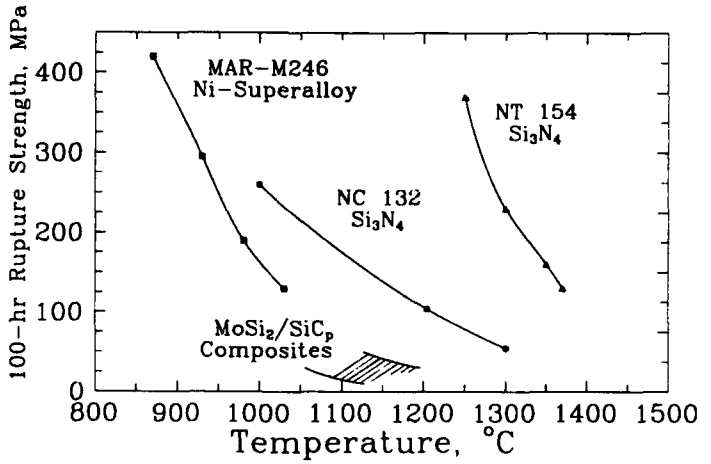


Figure 5. Comparison between the $MoSi_2/SiC_p$ composites and other engineering materials.

the-art creep-resistant silicon nitride (4 wt% yttria sintering additive, crystallized second phase) made by Norton-TRW[1]. NC132 is also a commercial hot-pressed silicon nitride made by Norton Co., representing the state-of-the-art 10 years ago (magnesia sintering aid, glassy second phase). Significant improvement of the creep and creep rupture properties of silicon nitride have been made through the enormous research efforts over the last decade. Clearly the $MoSi_2/SiC_p$ composites need dramatic improvement in creep strength to compete with these other engineering materials for high-temperature applications. The low creep strength of the $MoSi_2$ materials is likely due to the presence of silica in pockets at the grain boundaries, resulting from oxygen in the starting powder.

The trend in Figure 4 suggests that the addition of even larger particulate contents to $MoSi_2$, 60 to 80 volume percent, is likely to give dramatic improvements in the creep strength of this material. We base this conclusion on observations made on siliconized silicon carbide [8]. The addition of silicon carbide to silicon in fractions that range from 60 to 90 volume percent produces ceramics that are functional at temperatures up to 1300°C. We feel that an increase in particle content from 40 vol% to 60 to 80 volume percent will produce a comparable change in creep performance. In addition, the matrix could be modified, through various alloy additions. For instance, WSi_2 improves the high-temperature strength and creep resistance of $MoSi_2$ [6]. The use of carbon as a dopant to react with the oxygen on the surface of $MoSi_2$ powders to eliminate the internal silica has also been shown to improve the properties of $MoSi_2$ [15]. These matrix modifications, in addition to a very high SiC particulate fractions, are likely to produce a material better suited for high temperature structural applications.

SUMMARY

1. $MoSi_2/SiC_p$ composites exhibit creep curves similar to metals, with extensive tertiary creep regimes. Cavitation plays an important role in the creep rupture behavior.
2. Significant improvement in the creep rupture life of $MoSi_2$ is observed when the SiC_p reinforcement content is equal to or greater than 30 vol%, where the reinforcement forms a rigid skeleton.
3. Despite the SiC reinforcement these materials have low creep strength, likely due to silica in pockets at the grain boundaries, resulting from SiO_2 on the surface of the starting powder.
4. Dramatic improvement of $MoSi_2$ composites is required for these materials to be competitive with other engineering materials (e.g. superalloys and Si_3N_4) for high-temperature structural applications. This research indicates this improvement could be accomplished with higher loadings of SiC particles.

REFERENCES

1. High Temperature Structural Silicides, A. Vasudevan and J. Petrovic editors (Elsevier Science Publishers, Amsterdam, 1992).
2. C. Sims and W. Hagel, The Superalloys (J. Wiley and Sons, Inc, New York, 1972).
3. J. Cook, R. Mahapatra, E. Lee, A. Khan and J. Waldman, Ceram. Eng. Sci. Proc., 12[9-10] 1656 (1991).

[1]Use of commercial designations does not imply endorsement by the National Institute of Standards and Technology.

4. D. Carter and G. Hurley, J. Am. Ceram. Soc., **70** (4), C79 (1987).
5. J. Petrovic and R. Honnel, Ceram. Eng. Sci. Proc., **11** (9-10), 734 (1990).
6. K. Sadananda, C. Feng, H. Jones and J. Petrovic, Mater. Sci. Eng., **A155**, 227 (1992).
7. K. Sadananda, C. Feng, H. Jones and J. Petrovic, Int. Symp. Str. Intermetall., in press (1993).
8. S. M. Wiederhorn, D. E. Roberts, T-J Chuang and L. Chuck, J. Am. Ceram. Soc. **71** (7), 602 (1988).
9. S. M. Wiederhorn, R. J. Gettings, D. E. Roberts, C. Ostertag and J. Petrovic, Mater Sci. Eng., **A155**, 209 (1992).
10. W. E. Luecke and S. M. Wiederhorn in Silicon Nitride 93, edited by M. J. Hoffman, P. F. Becher and G. Petzow (Trans Tech Publications Ltd, Switzerland, 1994), p. 587
11. D. F. Carroll, S. M. Wiederhorn and D. E. Roberts, J. Am. Ceram. Soc. **72** (9), 1610 (1989).
12. R. Hertzberg, Deformation and Fracture of Engineering Materials, 1st Edition (John Wiley and Sons, New York, 1976).
13. R. Govila, J. Am. Ceram. Soc., **65** (1), 15 (1982).
14. S. M. Wiederhorn, B. J. Hockey, D. C. Cranmer and R. Yeckley, J. Mater. Sci. **28**, 445 (1993).
15. S. Maloy, A. H. Heuer, J. Lewandowski and J. Petrovic, J. Am. Ceram. Soc., **74** (10), 2704 (1991).

MICROCRACKING, STRAIN RATE AND LARGE STRAIN DEFORMATION EFFECTS IN MOLYBDENUM DISILICIDE

D. A. HARDWICK AND P. L. MARTIN
Rockwell International Science Center, 1049 Camino Dos Rios, Thousand Oaks, CA 91360

ABSTRACT

High purity molybdenum disilicide was deformed in compression to strains ranging from 5 to >50%. The deformation was accomplished at temperatures in the range 1200°-1400°C and at strain rates from 10^{-3} to 10^{-5} sec^{-1}. The strength of this high purity material was found to be at least twice that of $MoSi_2$ produced by the hot pressing of commercial powder. Microstructural examination revealed that subgrain formation resulted from modest strains (≈10%) while dynamic recrystallization was observed following large strains. Transmission microscopy revealed a significant change in the dislocation substructure after straining as the temperature was increased from 1300°C to 1400°C.

INTRODUCTION

Molybdenum disilicide ($MoSi_2$) is an intermetallic compound that combines a high melting point (2293K) with excellent resistance to high temperature oxidation [1, 2]. These attributes make it a candidate structural material for use at temperatures in the 1200°-1600°C range. At ambient and moderate temperatures $MoSi_2$ is brittle, but once the ductile-to-brittle transition temperature (DBTT) is exceeded, it rapidly loses strength. The actual value of the DBTT has been a subject of some debate [3-6]. However, the oxygen content of $MoSi_2$ is often not reported but it could have a determining influence on the DBTT. The oxygen will be present as SiO_2 located at grain boundaries, triple points and within the grains [7, 8]. The behavior of the silica may dominate the material response at high temperatures, analogous to the dominant effect of sintering aids on the creep behavior in some ceramics [9]. While the presence of silica may lower the DBTT [4], this effect must be achieved at the expense of material strength. The present investigation was undertaken to provide additional information on the intrinsic deformation behavior of polycrystalline $MoSi_2$ through deformation of high purity material with a low oxygen content.

EXPERIMENTAL PROCEDURE

The $MoSi_2$ was produced by reaction synthesis during HIP processing. High purity powders of molybdenum (600 wppm oxygen) and silicon (20 wppm oxygen) in the correct weight ratio to ensure stoichiometric $MoSi_2$ were ball milled in vacuum to ensure an intimate mixture of the powders. The powder mixture was cold isostatically pressed at 200 MPa for 30 minutes, lathe turned to size and placed within cylindrical Ta HIP cans that were evacuated at 350°C prior to sealing. All of the powder handling and machining steps were done in a low oxygen, inert gas environment to limit oxygen exposure and reduce SiO_2 contamination. HIP'ing was carried out at 200 MPa and a maximum furnace temperature of 1400°C. More complete details of the processing have been published elsewhere [10]. Right circular cylinders

Mat. Res. Soc. Symp. Proc. Vol. 322. ©1994 Materials Research Society

for compression testing were electro-discharge-machined from the HIP compacts; an average cylinder was 9.5mm in diameter by 10mm long. The ends of the cylinders were polished flat and perpendicular to the cylinder axis. Compression testing was performed over a range of strain rates from $1x10^{-3}$ to $1x10^{-5}$ sec^{-1}. All testing was conducted in a vacuum of $5x10^{-3}$ Pa or better and at temperatures in the range 1200° to 1400°C. The majority of the tests were terminated at strains of 5-6% but some were allowed to proceed to higher strains, up to ≈50% at 1300°C at 10^{-4} and 10^{-5} sec^{-1}. The compression platens were silicon nitride and the specimens were lubricated with boron nitride to reduce frictional effects. After testing, the cylinders were sectioned vertically and the microstructures examined optically and in the SEM. Specimens for TEM examination were prepared by ion milling and examined at 300keV in a Philips CM30.

RESULTS AND DISCUSSION

The reaction synthesized $MoSi_2$ after HIP processing contained <1000wppm oxygen, as determined by standard vacuum fusion techniques, and was fully dense. Figure 1 shows that the microstructure of $MoSi_2$ prior to compression testing had an average grain size of 40μm. The remnant silica particles were randomly distributed. A small volume fraction of Mo_5Si_3 was present at $MoSi_2$ grain boundaries and triple points.

The 0.2% offset yield stress as a function of temperature and strain rate is plotted in Figure 2. Lines are drawn through the data at the lower strain rates to facilitate data interpretation. Also plotted in Figure 2 is data from Petrovic et al. [11] on the strength of hot pressed commercial $MoSi_2$ powder tested in bending at a constant cross-head rate of 0.05mm/min, i.e. a strain rate of $1.2x10^{-5}$ sec^{-1}. The oxygen content of this material was not reported but if we assume that it is fully dense, then the strength decriment must be attributable to a high silica content. Viscous flow of the silica would promote grain boundary sliding as a deformation mechanism and lead to lower strengths. Our data is comparable with that obtained by Aikin on testing fully dense $MoSi_2$ containing 610 wppm oxygen [3, 12].

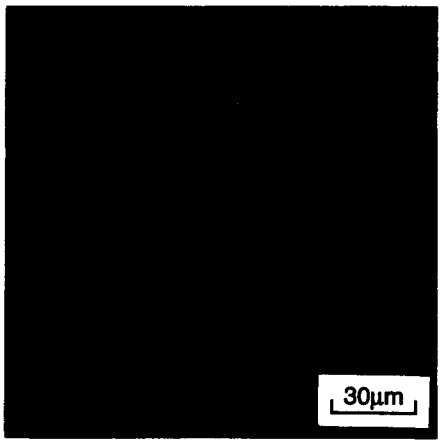


Figure 1: Microstructure of $MoSi_2$ produced by reaction HIP processing from elemental powders. Oxygen-590wppm.

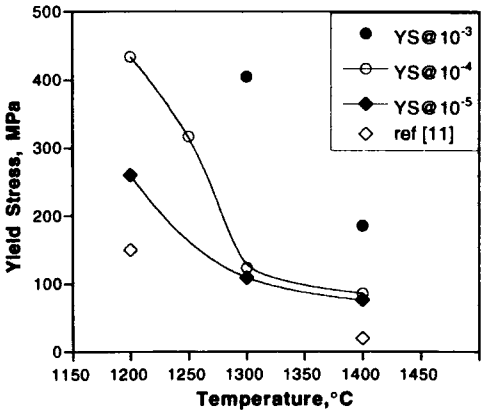


Figure 2: Compressive stress at 0.2% strain as a function of temperature and strain rate.

Metallographic examination of low strain samples, i.e. samples deformed to plastic strains ≤15%, with polarized light revealed that the grain boundaries, which were quite straight prior to deformation as shown in Figure 1, had developed a wavy character. The degree of waviness was greatest in samples that had received the highest amount of strain. Figure 3(a) shows a sample compressed 8.7% at 1250°C while the sample in Figure 3(b) was strained 15.2% at 1300°C; both were strained at a rate of 10^{-4} sec^{-1}. Both samples exhibit the wavy grain boundary effect but it is most prominent in the more highly strained sample.

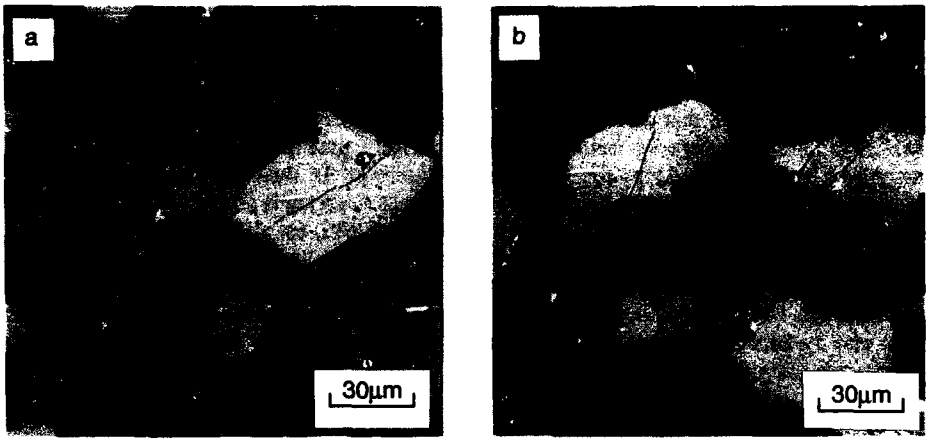


Figure 3: Microstructure in polarized light of specimens deformed (a) 8.7% at 1250°C and (b) 15.2% at 1300°C. Both specimens were compressed at an initial rate of 10^{-4} sec^{-1}.

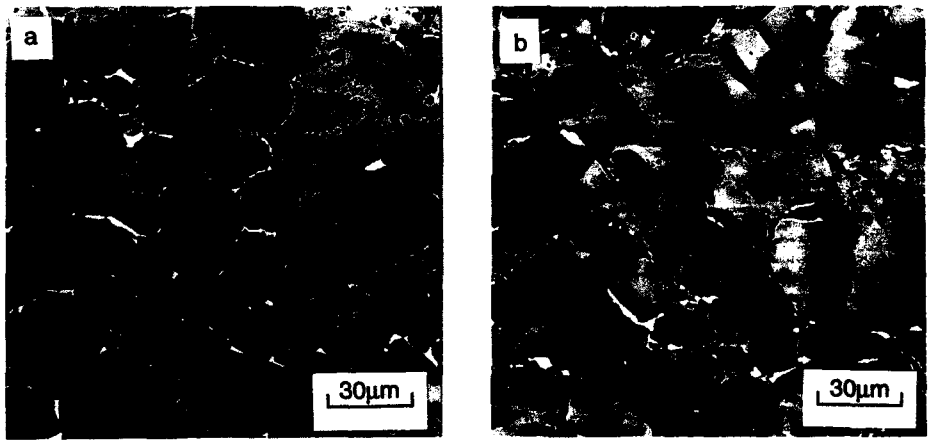


Figure 4: Microstructure revealed by backscatter SEM contrast of the samples shown in Figure 3

Examination of these same samples using backscatter contrast in the SEM reveals further differences. Backscatter imaging delineates the minor orientation differences that arise from subgrains. This contrast is well developed in the more highly strained sample of Figure 3(b) but almost absent in Figure 3(a). Examination at higher magnification showed that the waviness of the grain boundaries is associated with individual subgrains within the grains. Regardless of strain rate, deformation at 1400°C resulted in grain growth. Temperature alone was not sufficient to cause grain growth at 1400°C; a sample held at this temperature for 1 hour (a typical time to completion for a straining experiment) did not exhibit grain growth.

Figures 3 and 4 reveal another feature of these deformed samples: microcracking. None of the samples exhibited cracking on the external surfaces; this held true even for the specimens strained plastically to ≈50%. However, metallographic examination of samples sectioned longitudinally revealed that all of the samples contained internal cracks. At low strains, the interiors of the specimens contained transgranular cracks; typically, these cracks traversed just one or two grains before stopping, as shown in Figure 3. In their barreled regions, these specimens also contained intergranular cracks. Such microcracking is probably the direct result of the large variation in the critical resolved shear stress (CRSS) for glide of variously oriented $MoSi_2$ grains [13]; some orientations will be more amenable to slip than others leading to stress concentrations at grain boundaries with certain orientations. Intergranular separation could also arise from this phenomenon as adjacent grains may be unable to deform cooperatively. This effect may be exacerbated by the tensile stresses that will develop in the barreled regions of compression samples.

The microcracking was not reflected in the recorded stress-strain curves; these exhibited the usual non-linearity associated with normal plasticity and work hardening. The majority of previous investigators have not reported microcracking. In impure, high silica material, microcracking may not occur as the stress could be dissipated through viscous sliding of the grain boundary silica film before the critical stress to nucleate transgranular cracks could be achieved. The only other reported incidence of stable, transgranular microcracks was in the work of Maloy et al. [14] where transgranular micro-cracking and a non-linear load vs. displacement trace was obtained in C-containing material tested in notched bending at 1400°C.

The deformation of $MoSi_2$ to very large strains was also investigated. To avoid grain growth, samples were strained at 1300°C at strain rates of 10^{-4} and 10^{-5} sec^{-1}. The microstructure of the sample strained 48.5% at 10^{-5} sec^{-1} was quite similar to that shown in Figures 3(b) and 4(b). There was only minor distortion of the grain shape in response to the imposed strain and very limited evidence of recrystallization. On the other hand, the microstructure after 57.3% strain at 10^{-4} sec^{-1} consisted of pancake shaped grains plus significant regions of recrystallized grains. This is shown in the polarized light micrograph in Figure 5(a). The backscatter constrast micrograph in Figure 5(b) reveals the extent of subgrain formation within the deformed grains. Through dynamic recrystallization, the initially coarse microstructure has been refined significantly and it would be very interesting to know the strength of fine grained, high purity $MoSi_2$. However, the high level of strain imparted to these samples resulted in significant barreling and intergranular separation throughout much of the volume of the compression sample. The micrographs of Figure 5 were taken in the central region of the sample where grain boundary separation was minimal. The absence of significant grain refinement at the same temperature, 1300°C, but the lower strain rate of 10^{-5} sec^{-1} indicates that there is a delicate balance between the processes of grain refinement and grain coarsening at this temperature. Straining at higher temperatures would have to be done at strain

rates higher than 10^{-4} sec^{-1} to achieve similar grain refinement and grain boundary separation may remain a problem. At higher temperatures, thermally-activated modes of dislocation motion such as climb that would limit stress concentrations (and therefore microcracking), will also hinder grain refinement. To achieve grain refinement, the straining must be done in a strain rate regime where such mechanisms are inoperative.

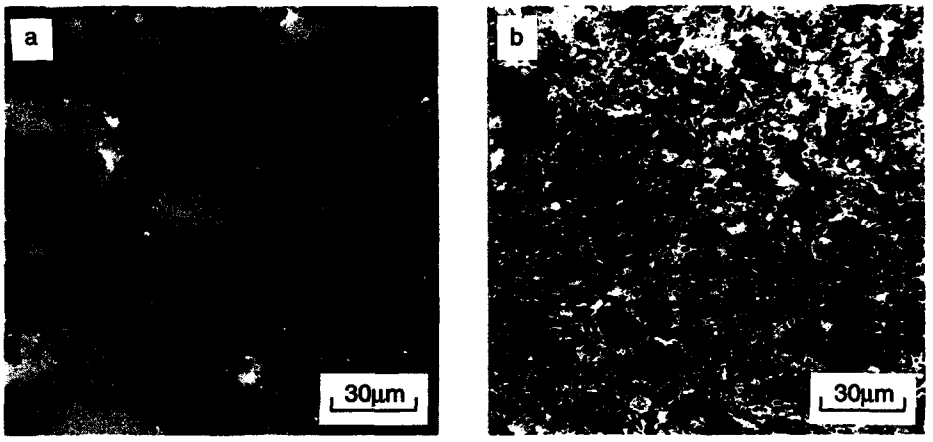


Figure 5: Microstructure of $MoSi_2$ strained to 57.3% as revealed by (a) polarized light and (b) backscatter contrast in the SEM.

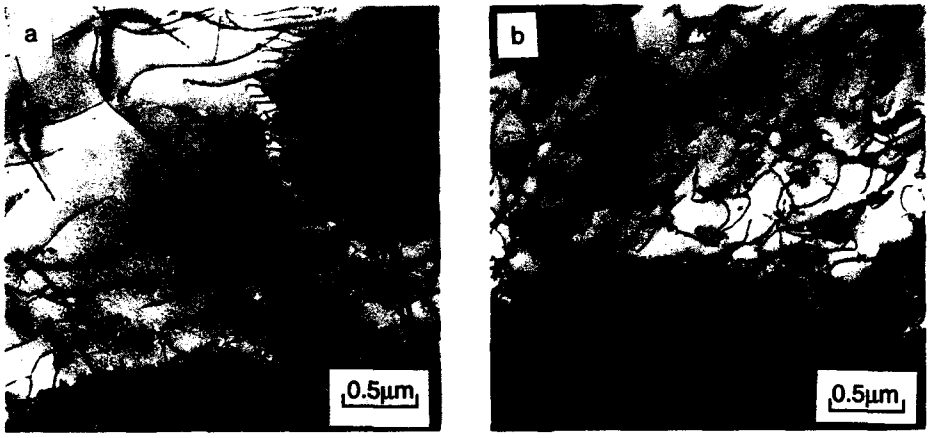


Figure 6: Dislocation substructure developed after straining at (a)1300°C and (b) 1400°C.

TEM examination revealed that straining at 1300°C and 1400°C gave rise to very different dislocation substructures; this is illustrated in Figure 6. At 1300°C, the dislocation segments are quite straight and tend to form arrays and low angle boundaries within the microstructure. At

1400°C the dislocations are quite wavy and many loops are observed. These may be indicative of thermally activated mechanisms such as dislocation climb. Work is continuing to gain a more quantitative understanding of the differences between these two dislocation substructures. However, we can conclude that there is a significant change in deformation character between 1300°C and 1400°C. This may offer definitive evidence for the intrinsic DBTT of $MoSi_2$ falling between 1300°C and 1400°C.

SUMMARY

The strength of high purity $MoSi_2$ was found to be at least twice that of hot pressed $MoSi_2$ prepared from commercial powder. After undergoing plastic strains ≤15%, subgrains developed within the original grain structure. Grain growth occurred under the combined influence of stress and temperature at the highest temperature studied, 1400°C. At higher strain levels, ≈50%, the competitive processes of dynamic recrystallization and thermally activated deformation led to grain size refinement at 1300°C after straining at 10^{-4} sec^{-1} but not at 10^{-5} sec^{-1}. The change in dislocation substructure that occurs between 1300°C and 1400°C provides corroborating evidence for the intrinsic DBTT of $MoSi_2$ occurring in this temperature range.

ACKNOWLEDGEMENTS

Supported by the U.S. Air Force Office of Scientific Research, Contract F49620-91-C-0027.

REFERENCES

1. P. J. Meschter and D. S. Schwartz, JOM, **4** (11), 52 (1989).
2. P. J. Meschter, Met. Trans A., **23A**, 1763 (1992).
3. R. M. Aikin, Jr, Scripta Metall. Mater. **26**, 1025 (1992).
4. S. R. Srinivasen, R. B. Schwartz and J. D. Embury, Mat. Res. Soc. Proc. **288**, (1993) pp 1099-1104.
5. J. Schlichting, High Temperatures-High Pressures, **10** (3), 241 (1978).
6. S. N. Patankar and J. J. Lewandowski, Mat. Res. Soc. Proc. **288**, (1993) pp 829-834.
7. J. D. Cotton, Y. S. Kim and M. J. Kaufmann, Mater. Sci. Eng., **A144**, 287 (1991).
8. S. Maloy, A. H. Heuer, J. J. Lewandowski and J. J. Petrovic, J. Am. Ceram. Soc., **74** (10), 2704 (1991).
9. D. W. Richerson, Amer. Ceram. Soc. Bull., **52** (7), 560 (1973).
10. D.A. Hardwick, P.L. Martin and R.J. Moores, Scripta Metall. Mater., **27**, 391 (1992).
11. D. H. Carter, J. J. Petrovic, R. E. Honnell and W. S. Gibbs, Ceram. Eng. Sci. Proc., **10**, 1121 (1989).
12. D. A. Hardwick, P. L. Martin, S, N, Patankar and J. J. Lewandowski, in Proc.International Symposium on Structural Intermetallics, (1993) pp 665-674.
13. T. Hirano, N. Nakamura, K. Kimura and Y. Umakoshi, Ceram. Eng. Sci. Proc. **12** (9-10) 1619 (1991).
14. S. Maloy, J. J. Lewandowski and A. H. Heuer, Mater. Sci. Eng., **A155**, 159 (1992).

THE EFFECT OF GRAIN SIZE AND SiC PARTICULATES ON THE STRENGTH AND DUCTILITY OF $MoSi_2$

AMIT K. GHOSH AND AJOY BASU
Department of Materials Science & Engineering, University of Michigan, Ann Arbor, MI 48109-2136

ABSTRACT

Monolithic $MoSi_2$ and $MoSi_2$ reinforced with SiC particulate reinforcements have been produced with widely varying grain sizes. Monotonic compression behavior of these materials has been examined in the temperature range of room temperature to 1200°C. Based on these results, the ductile-to-brittle transition temperature at low deformation rate of $MoSi_2$ and its composite appears to be near 900°C and may decrease slightly with decreasing grain size. Tension and compression creep behavior of these materials were also studied between 1100 and 1400°C. Creep strength of the matrix decreases with decreasing grain size even in the nominally dislocation climb-glide regime. While 20 vol% SiC particulates provide a reasonable amount of creep strengthening of the fine grain $MoSi_2$ matrix, strengthening due to coarser grain size can be significantly higher in these materials. These results parallel those on other intermetallics.

INTRODUCTION

$MoSi_2$ intermetallics, in monolithic form and reinforced with SiC particulates and whiskers, have potential application in future gas turbine engines. Aikin and others have suggested that grain boundary SiO_2 (if present as a viscous layer) can lower mechanical strength in these materials [1-2], although SiO_2 is primarily observed as spherical particles and not as grain boundary films in $MoSi_2$. Attempts are being made to produce clean alloys by addition of SiO_2 removers (e.g., C, Er, CaO, etc.) [3-6] and to improve the mechanical properties of $MoSi_2$ by synthesizing composites with hard ceramic phases as well as ductile metallic phases [6-8]. SiC reinforcement has shown excellent bonding characteristics with $MoSi_2$ [5], and it also rids the SiO_2 inclusions from $MoSi_2$ grain boundaries via chemical reaction. Furthermore, the addition of SiC whiskers have shown the possibility of creep strengthening of $MoSi_2$ [9-10] while SiC particulates have shown grain refinement and apparent weakening [11]. It was also shown recently [11] that grain boundary microcracking damage can occur during creep which produces a dependence on the imposed stress state - tensile vs. compressive. The objective of this paper is to examine the effects of grain size and damage in $MoSi_2$ and its composite containing SiC particulate reinforcements and combine results from prior work to show their effects on strength, toughness, and creep behavior.

EXPERIMENTAL WORK

Material Synthesis

$MoSi_2$ powder (-325 mesh) was used for consolidating monolithic $MoSi_2$. Particulate reinforced composites were prepared by mixing $MoSi_2$ powder with 20 vol% powder of SiC. The SiC_p powder was from H.C. Stark Co. of Germany, with an average particle size of 0.7 μm, while the $MoSi_2$ powder was from Cerac, Inc., Milwaukee, WI with an average particle size of 5 μm. For the composite, a slurry milling approach was used to develop a homogeneous mixture of fine scale constituents. The powder mixtures were hot pressed in a

Mat. Res. Soc. Symp. Proc. Vol. 322. ©1994 Materials Research Society

graphite die at 1700°C for 2 hours under 28 MPa pressure. Hot pressed billets were cut and a portion HIPed at 1700°C for 90 min under 200 MPa pressure.

Characterization of Microstructure

The optical micrographs of $MoSi_2$ and its composite are shown in Fig. 1. The average grain size of monolithic $MoSi_2$ was 30 μm while that of SiC_p reinforced material was 3 μm. The monolithic material showed small spherical SiO_2 particles on the grain boundaries and a small amount of porosity; the total volume of both was approximately 5%. Previous work with high resolution TEM showed that the interface between SiC and $MoSi_2$ is free from contaminants but does not appear to have an orientation relationship [5]. The reinforcement agglomerates were always located on grain boundaries, and the void density was approximately 6%.

Compression and Tension Tests

Rectangular samples, 3 mm x 3 mm x 6 mm, were cut from the billets and compression tests were conducted in the temperature range of room temperature to 1200°C by pressing the samples between rigid SiC platens in an argon environment. The tests were conducted on an Instron machine fitted with a Centorr furnace. The first set of tests were conducted at a constant $\dot{\epsilon}$ of $10^{-5}s^{-1}$ between room temperature and 1200°C. For tests within the range of 1100-1400°C, step strain rate tests were carried out by first straining the sample at a strain rate of $10^{-4}s^{-1}$ to a steady level of stress, followed by decremental step strain rate tests. Steady stress values were achieved at each strain rate level which were subsequently used to plot log $\dot{\epsilon}$ vs. log σ plots. Constant stress creep tests were also performed by maintaining increasing load with continued creep strain under the assumption of constant specimen volume. Crosshead displacement corrected for machine compliance was used to determine sample strain. Normal creep curves with primary, secondary and tertiary regions were observed. Minimum creep rates determined from these curves were plotted as a function of stress.

From the cylindrical billets, slices were cut perpendicular to their axes and reduced gauge section for tensile specimens with large grip tabs was machined by EDM. The specimen cross-section was 3 mm x 3 mm and the gauge length was 6 mm. A special SiC grip was fabricated to pull the tabs from beneath them (i.e., edge loading not face loading). Constant stress creep tests were conducted in a manner described previously for the compression tests. Typically several load levels were explored from each specimen. The onset of tertiary creep (or fracture) was found to occur at much smaller strain levels and more abruptly than in compression.

EXPERIMENTAL RESULTS AND DISCUSSION

Compression Test Results

Stress-strain curves for monolithic $MoSi_2$ and $MoSi_2$/20%SiC composite are shown in Fig. 2. At a strain rate of $10^{-5}s^{-1}$, neither material showed plastic behavior at room temperature, although the composite has a significantly higher fracture strength. With increasing test temperature (800°C and above) yielding is clearly found to occur. Yielding in the matrix is followed by strain softening indicative of concurrent microstructural damage. However, in monolithic $MoSi_2$, strain hardening is seen at compressive strain greater than 0.02, possibly indicating that dislocation storage processes are beginning to occur. Yield strength of the composite between 25°C and 1000°C is much greater than that of monolithic $MoSi_2$, due to a combination of grain boundary strengthening and load sharing by elastic SiC reinforcements.

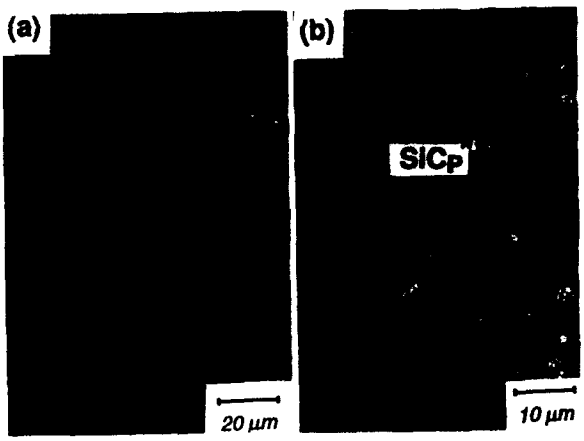


Fig. 1. Microstructures of hot-pressed $MoSi_2$ and $MoSi_2$/ 20%SiC composite. Hot pressing direction is vertical

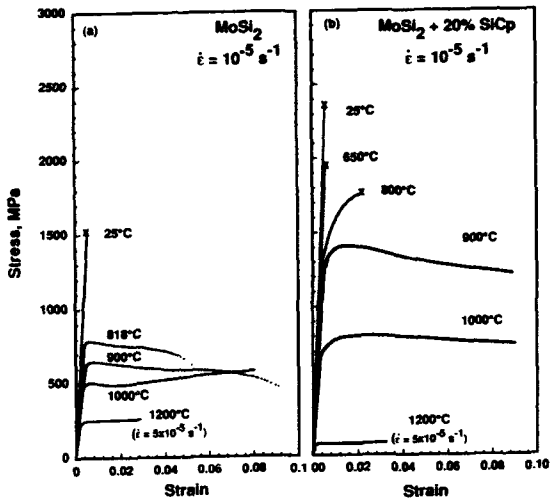


Fig. 2. Stress-strain curves in compression for monolithic $MoSi_2$ and $MoSi_2$/20% SiC composite at various temperatures. x indicates sample fracture. Data without x indicate samples exhibiting greater than 10% strain before fracture.



Fig. 3. TEM dark field micrograph of $MoSi_2$ deformed at 900°C in compression which shows 1/2<331> Burgers vector (Photo Courtesy of H. Kung.)

Strain hardening following yielding is also much greater for the composite, indicating possibly a strong interface between SiC and $MoSi_2$, and constrained deformation of the $MoSi_2$ matrix [12]. The suggestion of crystallographic slip processes as above is consistent with the observation of dislocations in $MoSi_2$ deformed at 900°C (see Fig. 3), which has also been reported by other investigators [5,11,13].

Figures 4a and 4b show yield strength and fracture energy as a function of test temperature for the two materials. The strain-to-fracture is not shown in all plots in Fig. 2 but the area under these curves to fracture has been computed as a function of temperature and plotted in Fig. 4b as fracture energy. It is clear that the addition of SiC_p significantly enhances the strength and fracture energy of $MoSi_2$. The yield strength of the composite begins to fall off more rapidly above 800°C, eventually exhibiting a weaker behavior than the matrix. Figure 5a shows microstructural damage in monolithic $MoSi_2$ during compression, compared to the lack of visible damage in the fine grain composite (Fig. 5b). At 1000°C and a strain rate of $10^{-5}s^{-1}$ intergranular cracks occur in $MoSi_2$, however, at higher strain rates and lower temperatures, transgranular cracks have also been observed. The microcracking process leads to a decrease in the apparent elastic modulus (Fig. 5c), determined from partial unload-reload tests.

Creep Test Results

Figure 6 shows strain rate vs. stress data for $MoSi_2$ at 1200°C from creep, and step-strain rate tests in compression, as well as from tension creep tests. An average curve drawn through the scatter in this data shows a stress exponent (n) for creep of about 4.3 at high stresses and 3.0 at the low stresses, which is indicative of dislocation creep [14-15]. The tension data shows a 40-50% weakening relative to compression. It also shows an n of 2.7 (at low stresses), this lower value being a possible result of concurrent grain boundary microcracking aided by diffusion (Fig. 7). Figure 8 shows step-strain rate test data for 1300°C, 1300°C, and 1400°C as compared with the compression curve for 1200°C from Fig. 6. This family of curves clearly illustrates a decreasing n with increasing temperature, indicating an increasing contribution of diffusional creep at the higher temperature. Transmission Electron Microscopy of dislocation structure of specimens deformed at 1300°C indicated the formation of dislocation cells and subgrains [11] as further evidence for the glide-climb process. The dislocations which were identified are of the following types: {010}<100>, {011}<100>, {013}<100>, {001}<110> and {101}1/2<111>. All high temperature data from Fig. 8 were plotted in the form of Zener-Hollomon parameter ($Z = \dot{\varepsilon} \exp(Q/RT)$) [11], exhibiting an activation energy for creep in the range of 310 to 372 kJ/mol. The combination of mechanical data and grain boundary cracking results strongly suggest that dislocation climb-glide creep in this material is accompanied by grain boundary sliding, and at low stresses and above 1300°C sliding is accommodated by diffusional processes.[11]

The effect of reinforcements on composite strength is shown in Fig. 9, along with data on SiC_w composite from Refs. 9 and 11. A significant weakening relative to $MoSi_2$ (solid line) was observed for the 20% SiC_p reinforced composite (g.s. 3μm). $MoSi_2$/20%SiC_w from Ref.11 (g.s. 7μm) showed a somewhat lesser weakening effect. The data of Sadananda et al. [9] for SiC_w reinforced $MoSi_2$ (g.s.18μm) showed strengthening over monolithic $MoSi_2$. The values of n for the composites were not significantly different from that of the matrix and were in the range of 3 to 3.4. The apparently unusual creep weakening of the composite is due to a finer matrix grain size, and not from included SiO_2 or damage, nor is it unique to $MoSi_2$ [11]. The effect of matrix grain size on dislocation climb-glide creep is shown in Fig. 10 with other data taken from the literature [16-18]. A number of intermetallic alloy systems are represented at a homologous temperature of about 0.6, within the climb-controlled creep ($3.4 \leq n \leq 5.7$) regime. A grain size dependence is visible for each intermetallic alloy. Using a simple relationship $\sigma = Bd^p$, where σ is stress for a fixed creep strain rate $\dot{\varepsilon}$, d = grain size, and B = a temperature dependent constant, the grain size exponent, p, is found to be within the range 0.43-0.76. It should be noted that similar grain size dependence at 0.5 Tm was found by

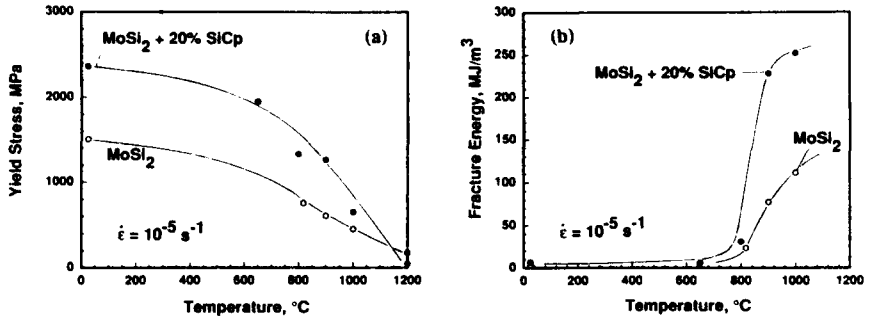


Fig. 4. Yield stress and fracture energy in slow compression test as a function of test temperature

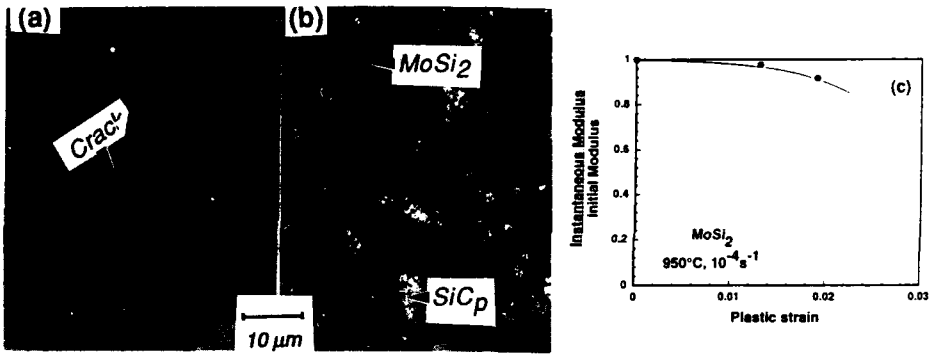


Fig. 5. (a) Intergranular cracking in $MoSi_2$ after compression at $\varepsilon = 10^{-5}s^{-1}$ (T = 1000°C), (b) no cracking in $MoSi_2$/SiC under similar conditions, (c) Loss of elastic modulus with strain

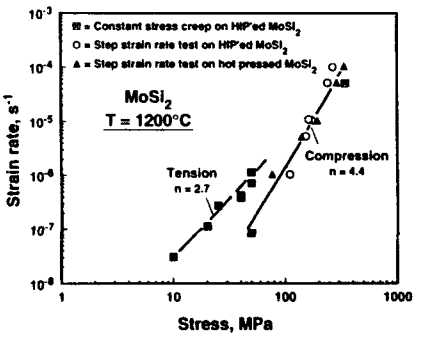


Fig. 6. Step strain rate and creep test results for $MoSi_2$ under compression and tension loading at 1200°C.

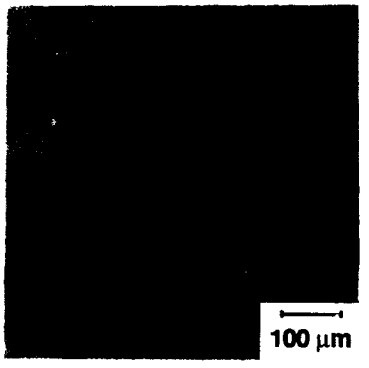


Fig. 7. Intergranular cracking during tensile creep of $MoSi_2$ at 1200°C, load axis vertical

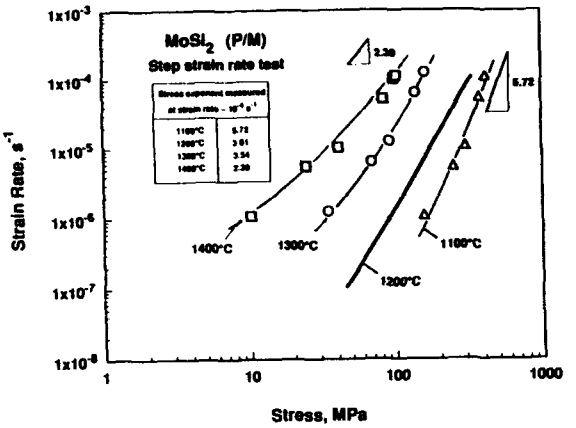


Fig. 8. Step strain rate test data in compression for $MoSi_2$ at several temperatures, compared with the curve for compression from Fig.6. Stress exponents (n) at $10^{-4}s^{-1}$ are: 5.7 (1100°C), 3.8 (1200°C), 3.5 (1300°C) and 2.4 (1400°C).

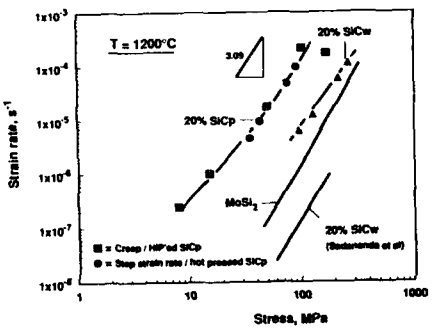


Fig. 9. Compression creep data for $MoSi_2$ composites (data points) from Refs. 9 and 11 and monolithic $MoSi_2$ from Fig. 6

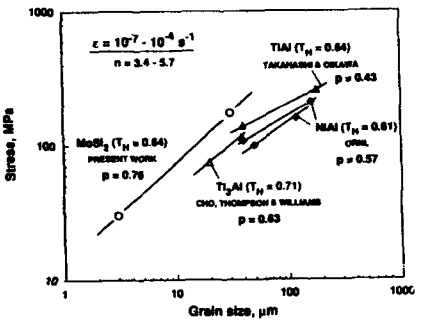


Fig. 10. Creep strength at constant strain rate as a function of grain size for a variety of intermetallic alloys from Refs. 16-18 are compared with $MoSi_2$ data (1200°C) (T_H = homologous temperature)

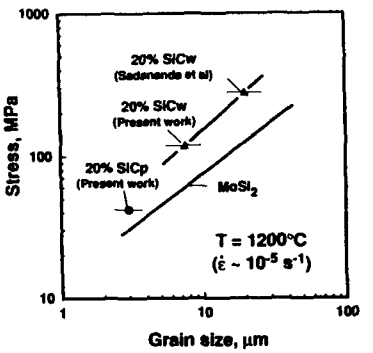


Fig. 11. Stress vs. grain size for monolithic $MoSi_2$ from Fig. 9, compared with data for various composites from Fig. 8 for the same strain rate.

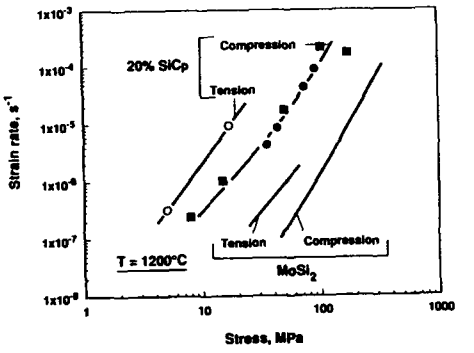


Fig. 12. Strain rate vs. stress data for $MoSi_2$ and $MoSi_2$/20%SiC_p under compression

Barrett, Lytton and Sherby [19] for copper for grain sizes below 100 μm,the magnitude of this effect becoming negligible for grain sizes larger than 100 μm.

With grain size dependence of the matrix behavior in mind, the creep strength for $MoSi_2$ and its composites at $\dot{\varepsilon} = 10^{-5}s^{-1}$ is plotted in Fig. 11 as a function of grain size. All composites are found to be stronger relative to their own matrices, (i.e., for the same grain size). SiC_w reinforcements appear to provide greater strengthening relative to the matrix than SiC_p due to higher aspect ratio. A simple model was developed [11] to explain the grain size dependence of dislocation creep in which grain boundary sliding is accommodated by localized deformation in the grain corner regions. Creep rate based on this model can be expressed in a simple form as:

$$\dot{\varepsilon} = \left(A + A_1 / d^3\right)\sigma^n \qquad (1)$$

where A and A_1 are constants, and d is the grain size. This creep equation combines a strongly grain size dependent part with a grain size independent part in an overall dislocation creep framework. The level of strengthening predicted by this model is in agreement with observations.

Damage also plays an important role in composite strength. Microcracking during creep can decrease the strength level if no superimposed pressure exists on the grain boundaries. In tensile tests, there is a net tensile stress component normal to the grain boundaries aiding in the boundary opening up during grain stretching and boundary sliding. The strain increment from this provides enhanced creep rate in tension for both the matrix and the composite (Fig. 12). This strength differential effect is perhaps slightly greater for the fine grain composite.

CONCLUSIONS

(1) Yielding of $MoSi_2$ is observed under slow strain rate compression at or above 800°C. Addition of SiC_P to $MoSi_2$ leads to grain refinement and significant strengthenening, the magnitude of which decreases with increasing temperature, eventually vanishing around 1100°C. It also produces increased strain hardening rate and considerable toughening under slow strain rate compressive deformation.

(2) Between 1100 and 1400°C, $MoSi_2$ deforms primarily by dislocation climb-controlled creep, with concurrent grain boundary sliding. Creep stress exponents vary between 4 and 2. Sliding is accommodated by dislocation creep at 1100 and 1200°C, and diffusional creep at higher temperatures.

(3) A grain size dependence of creep strength is observed for grain sizes 30 μm and less with an exponent of 0.76 for grain size. Creep strength increases with increasing grain size, eventually saturating around 100 μm size, a behavior common with other intermetallics and some metals.

(4) Addition of SiC_p and SiC_w reinforcements to $MoSi_2$ matrix produce creep strengthening relative to the matrix present within the composites. However, relative to coarse grain matrix, weakening often occurs because reinforcement addition can cause significant grain refinement.

(5) Creep strengths of $MoSi_2$ and its composites are lower in tension than in compression because grain boundaries are prevented from separating readily during compression testing. Composites with a greater flaw density within reinforcement regions are more sensitive to this strength differential effect.

ACKNOWLEDGEMENTS

The authors acknowledge the financial support of this work through the U.S. Air Force URI Grant No. DOD-G-AFOSR-90-0141 (Dr. A.H. Rosenstein, Grant Monitor).

REFERENCES

1. R.M. Aikin, Scripta Metall., **26**, 1025 (1992).
2. J.J. Petrovic (private communication).
3. S. Maloy, J.J. Lewandowski, A.H. Heuer, and J.J. Petrovic, J. Mater. Sci. and Eng., **A155**, 159 (1992).
4. D.P. Mason and D.C. VanAken,(Mat. Res. Soc. Symp. Proc., **273**, 1992) p. 289.
5. A.K. Ghosh, A. Basu and H. Kung,(Mat. Res. Soc. Symp. Proc., **273**, 1992) p. 259.
6. A. Basu and A.K. Ghosh in Advanced Metal Matrix Composites for Elevated Temperatures, (ASM International Symp. Proc., Metals Park, OH, 1991) p. 41.
7. M.J. Maloney, DARPA Contract Report, No. N00014-87-C0862, High Temperature Materials Workshop, Wright Patterson AFB, February, 1991.
8. L. Xiao and R. Abbaschian in Advanced Metal Matrix Composites for Elevated Temperatures, (ASM
9. K. Sadananda, C.R. Feng, H. Jones, and J.J. Petrovic, J. Mater. Sci. and Eng., **A155**, 227 (1992).
10. S.M. Wiederhorn, R.J. Gettings, D.E. Roberts, C. Osterag, and J.J. Petrovic, Mater. Sci. and Eng., **A155** (1992).
11. A.K. Ghosh and A. Basu, "Microstructural Effects on Creep Strengthening of $MoSi_2$ Matrix Composites," in Critical Issues in the Development of High Temperature Structural Materials edited by N.S. Stoloff, D.J. Duquette, and A.F. Giamei (TMS, 1993).
12. M.F. Ashby, Chapter 3 in Strengthening Methods in Crystals, Edited by A. Kelly and R.B. Nickolson, (Halsted Press Division, John Wiley & Sons, New York, 1971), p.137
13. Y. Umakoshi, J. Sennami and T. Yamane, (Proc. Fall Meeting of Jap. Inst. Metals, 1990) p. 279.
14. J. Weertman, J. Applied Phys., **28**, 362 (1957).
15. J. Weertman and J.R. Weertman, Physical Metallurgy, edited by R.W. Cahn (North Holland, Amsterdam, 1965) p. 736.
16. Oak Ridge National Lab Report, ORNL-DWG 85-16426, 1985.
17. T. Takahashi and H. Oikawa, (Mat. Res. Soc. Symp. Proc., **213**, 1991) p. 721.
18. W. Cho, A.W. Thompson, and J.C. Williams, Met. Trans. A, **21A**, 641 (1990).
19. C.R. Barrett, J.L. Lytton, and O.D. Sherby, Trans. of AIME, **239**, 170 (1967).

PLASTICITY OF $MoSi_2$ BELOW 900°C

H. CHANG AND R. GIBALA
Department of Materials Science and Engineering
University of Michigan, Ann Arbor, MI 48109

ABSTRACT

The mechanical behavior of polycrystalline $MoSi_2$ tested in compression at temperatures from 750°C to 950°C has been investigated. This material can be deformed to several percent strain without fracture at temperatures as low as 900°C. This same material prestrained at 1300°C and subsequently tested at lower temperatures can be deformed to substantial strain at 800°C, and even exhibits modest plasticity at 750°C. Both prestrained and unprestrained materials exhibit microcracking combined with dislocation substructures containing high densities of dislocations. Unprestrained $MoSi_2$ exhibits a yield point in this temperature range which does not exist when it is prestrained. The stress-strain curves of the prestrained material in this temperature range are similar qualitatively to those of the unprestrained material at 1100°C and above. These observations suggest that at these temperatures $MoSi_2$ is a dislocation density limited material which can deform by dislocation plasticity processes if a sufficient dislocation density is available.

INTRODUCTION

Polycrystalline $MoSi_2$ has been observed in previous investigations to deform in compression to substantial strains at temperatures above approximately 1100°C to 1400°C [1-4]. Examinations of the dislocation substructures after these tests reveal high densities of dislocations consistent with deformation by dislocation plasticity processes. As the temperature decreases, however, $MoSi_2$ exhibits decreasing plasticity before brittle fracture occurs. Kim et al. have reported plasticity at 1070°C and above but no plasticity at 860°C for polycrystalline $MoSi_2$ in compression, while Aikin has reported failure after one to two percent strain at 800°C [3,4].

The prevalence of cracking exhibited by $MoSi_2$ at these lower temperatures raises the question of whether or not dislocation processes can occur at all in this temperature range. This current work investigates the plasticity of $MoSi_2$ in this temperature range to determine if it can be enhanced by introducing dislocations through prestrain at elevated temperatures.

EXPERIMENTAL PROCEDURE

The monolithic $MoSi_2$ used was hot pressed and subsequently HIPed from a commercially available powder, a nominally 5 to 6 micron powder from CERAC, Inc. Hot pressing was performed in argon at 1700°C for one hour at 29.4 MPa. HIPing was done at 1800°C for 1.5 hours at 200 MPa. The density of the material after HIPing is approximately 98%, with an average grain size of approximately

Mat. Res. Soc. Symp. Proc. Vol. 322. ©1994 Materials Research Society

30 μm. The microstructure of this material has been described previously [1].

All mechanical testing was performed in compression at a constant crosshead speed corresponding to an initial strain rate of 10^{-4} s^{-1}. The unprestrained $MoSi_2$ was tested between 800°C and 950°C. Prestrain was performed at 1300°C, usually to approximately 1% true strain. These specimens were cooled to room temperature and subsequently tested between 750°C and 950°C. Testing was performed on 6 mm x 3 mm x 3 mm specimens in an argon atmosphere furnace in an Instron Model 4507 testing machine.

Conventional transmission electron microscopy (TEM) was performed using a JEOL 2000FX microscope operating at 200 kV. Foils were mechanically thinned by hand grinding, dimpling and ion milling.

RESULTS AND DISCUSSION

Figure 1 shows the stress-strain behavior of $MoSi_2$ at temperatures from 1150°C to 1300°C. The material exhibits deformation to substantial strain with no indications of imminent fracture at the strains at which the tests were stopped. The 1300°C test represents the prestrain conditions used in this investigation. The TEM micrograph is representative of the dislocation substructure generated in the material during the prestrain, in which the primary Burgers vector observed is of <100> type.

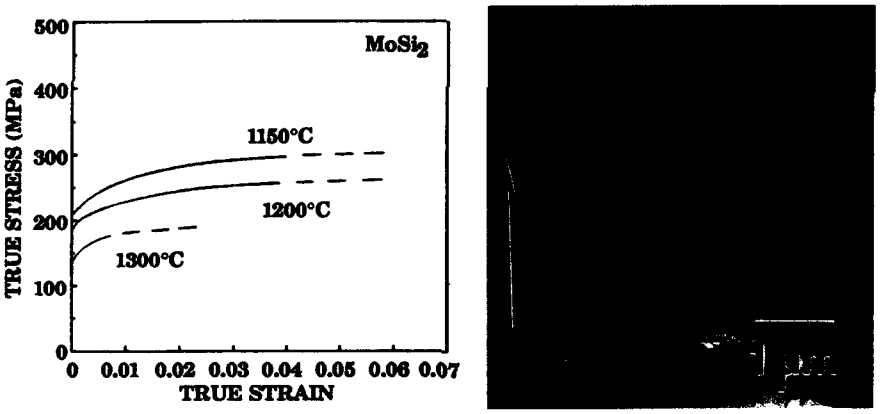


Figure 1. Stress-strain curves of unprestrained $MoSi_2$ at 1150°C, 1200°C and 1300°C in (a), with the substructure of the 1300°C test shown in (b). $\mathbf{B} = [3\bar{3}1]$ $\mathbf{g} = 110$.

Figure 2 shows the stress-strain behavior of $MoSi_2$ in both unprestrained and prestrained condition at 900°C and 950°C. In the unprestrained $MoSi_2$, the stress increases to a maximum after yielding, but then the material exhibits a gradual yield drop over the first half percent of plastic strain. The stress decreases to a minimum and increases slightly with continuing deformation. For the tests shown in Figure 2, there was no indication of imminent fracture at the strains at which the tests were stopped. The curves in Figure 2 demonstrate that

polycrystalline $MoSi_2$ can be deformed in compression to at least several percent strain at temperatures as low as 900°C.

One of the effects of prestrain at 1300°C is the elimination of the stress drop present in the unprestrained material. This prestrained material instead yields and strain hardens at about the same strain rate as unprestrained $MoSi_2$ deformed at 1150°C and 1200°C, where dislocation generation occurs readily. Moreover, as Figure 2 shows, the stress level of plastic flow after prestrain is close to that of the unprestrained material after the stress drop. Thus it appears that providing the material with an initial dislocation density through high temperature prestrain eliminates the stress drop and the material flows by dislocation motion at the stress level which the unprestrained material flows at after the stress drop. This behavior also suggests that the stress drop is a classical yield point phenomenon due to an insufficient dislocation density at these temperatures in the initial stage of plastic deformation, and that the stress drop arises from a rapid increase in dislocation density when the applied stress is sufficiently large enough to generate dislocations.

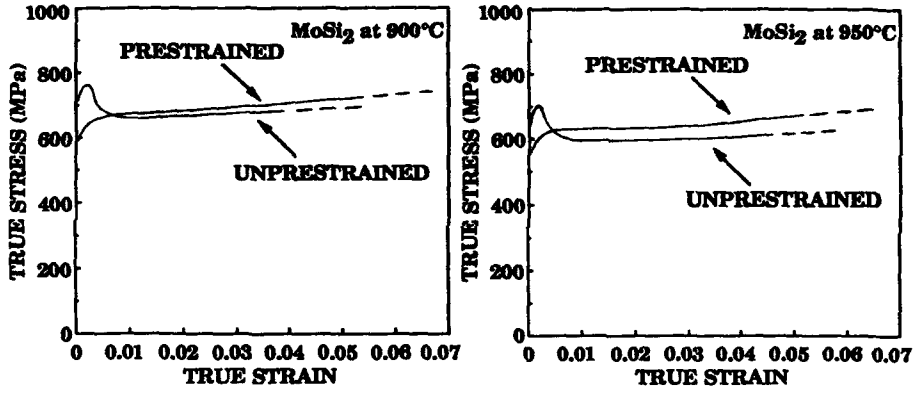


Figure 2. Stress-strain curves of $MoSi_2$ at (a) 900°C and at (b) 950°C.

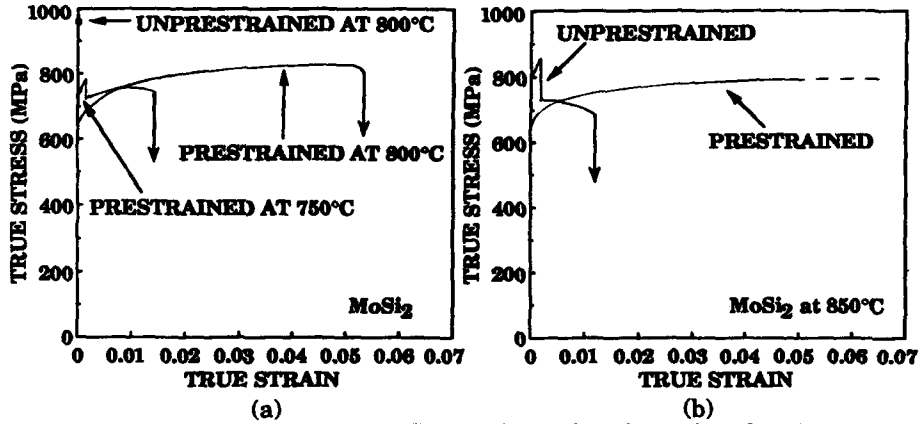


Figure 3. Stress-strain curves of $MoSi_2$ at (a) 750°C and 800°C and at (b) 850°C.

Figure 3 shows the deformation behavior from 750°C to 850°C. The unprestrained material exhibits fracture with no plasticity at 750°C and 800°C. Some plasticity occurs at 850°C, but the propagation of large axial cracks within the specimen soon after yield, as evidenced by the instantaneous stress drop, resulted in fracture after small additional strain. In contrast, the prestrained material exhibits substantial deformation at both 800°C and 850°C, and some deformation is even present at 750°C. Thus, the use of high temperature prestrain has enhanced the plasticity of $MoSi_2$ by attaining plastic deformation to lower temperatures than that possible without prestrain.

Figure 4 shows the appearance of a specimen of prestrained $MoSi_2$ after testing at 800°C to 5% strain. Large cracks of length visible to the unaided eye exist in this and many of the specimens tested at these lower temperatures. These 1 mm to 4 mm long cracks exist at both small and large strains, depending apparently upon whether or not conditions favorable for coalescence of microcracks occurred in a given specimen. In Figure 4, a large crack has grown to near imminent fracture.



Figure 4. Specimen of $MoSi_2$ after testing at 1300°C to 1% strain and at 800°C to 5% strain. The compression direction is horizontal in this figure.



Figure 5. Microcracking in unprestrained $MoSi_2$ tested at 900°C to 1% strain. The compression direction is horizontal in this figure. Both transgranular and intergranular microcracks are present.

Microcracking is observed in all the tests presented in this investigation. Figure 5 shows the microcracking present in unprestrained $MoSi_2$ tested at 900°C to approximately 1% strain. This cross section is approximately 0.5 mm into the interior of the specimen. Both transgranular and intergranular microcracks are observed. These cracks represent damage in the material which with continued deformation would be expected to increase until coalescence resulting in fracture occurs. The prestrained material also exhibits large numbers of microcracks, and the amount does not to a first approximation appear different from that in the unprestrained material. The presence of microcracking has also been investigated as a function of strain in the unprestrained material deformed at 900°C. Microcracking is observed even after only 0.3% strain, corresponding to the beginning of the yield drop just after the maximum stress obtained. Thus microcracking appears to originate at very low plastic strains.

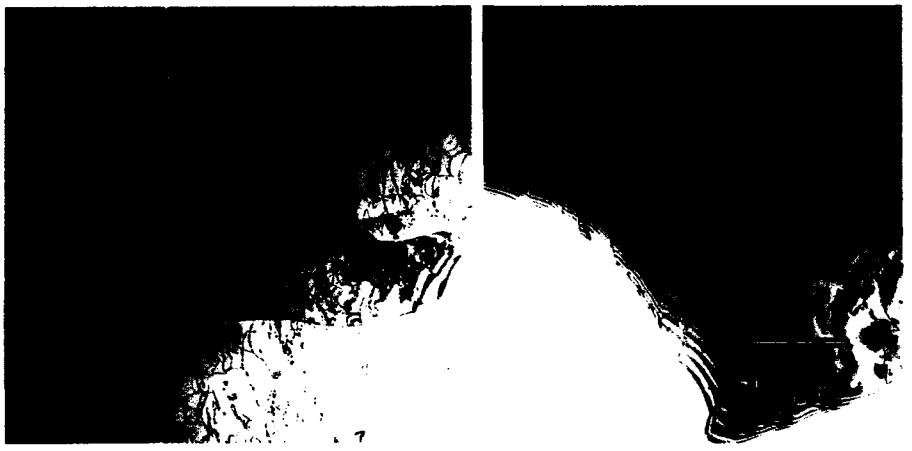


Figure 6. Dislocation substructure within one grain of unprestrained $MoSi_2$ tested at 900°C to 1% strain. $\mathbf{B} = [110]$ $\mathbf{g} \approx \bar{1}10$.

Figure 6 shows the dislocation substructure observed by TEM within one grain of unprestrained material tested at 900°C to 1% strain, which is the strain at the minimum stress after the yield drop. Figure 7 gives similar data for prestrained material tested at 800°C to 5% strain. The micrographs reveal extremely high dislocation densities in both materials. Dislocation tangles, as well as, upon examination at higher magnification, evidence of loop and debris formation are both prevalent in the substructures, consistent with the occurrence of significant amounts of dislocation interactions during plastic flow. These dense dislocation substructures reveal the dominance of dislocation processes in the plasticity of several percent strain obtained in these tests. Microcracking is present from the onset of plastic deformation, but the dislocations evidently occur concurrently and contribute substantially to the plastic strain.

Burgers vector analysis conducted on the dislocations represented in Figures 6 and 7 reveal Burgers vectors mostly of <100> type. At higher temperatures, such as shown in Figure 1 for 1300°C, the most often observed Burgers vector is also <100>. Thus, the prevalent Burgers vector in the deformation does not appear to change between higher and lower temperatures.

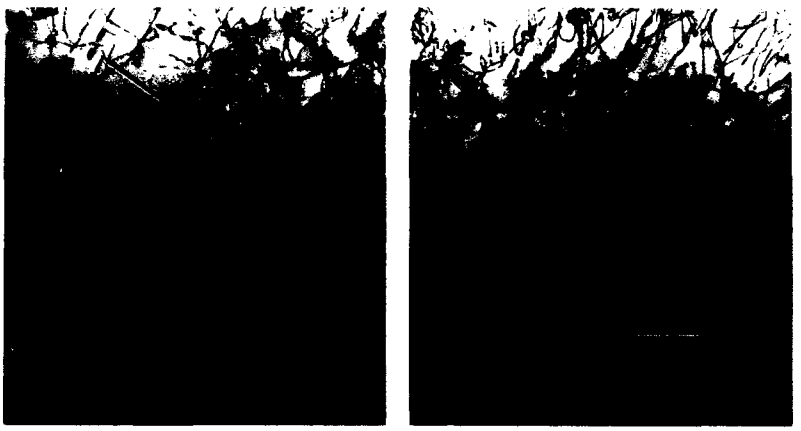


Figure 7. Dislocation substructure within one grain of $MoSi_2$ prestrained at 1300°C to 1% strain and then tested at 800°C to 5% strain. $\mathbf{B} = [331]$ $\mathbf{g} = \bar{1}10$.

SUMMARY

Polycrystalline $MoSi_2$ was tested in compression between 750°C and 950°C both with and without prestrain at 1300°C. Prestraining the material allows significant deformation to occur at temperatures lower than what can be attained in unprestrained material. Both microcracking and high densities of dislocations exist in the materials after testing. Unprestrained $MoSi_2$ exhibits a yield point in this temperature range which disappears when it is prestrained. These results suggest that $MoSi_2$ is a dislocation density limited material in the temperature range of 950°C and below which, however, exhibits increased plasticity when dislocations are introduced by high temperature prestrain.

ACKNOWLEDGEMENT

This research is funded by the Air Force Office of Scientific Research under the University Research Initiative Program, Dr. Alan H. Rosenstein, Program Director, Grant Nos. DOD-G-AFOSR-90-0141 and DOD-G-F49620-93-0289.

REFERENCES

1. H. Chang, H. Kung and R. Gibala in Intermetallic Matrix Composites II, edited by D. B. Miracle, D. L. Anton and J. A. Graves (Mater. Res. Soc. Proc. 273, Pittsburgh, PA, 1992) pp. 253-258.
2. D. J. Evans, S.A. Court, P. M. Hazzledine and H. L. Fraser, Phil. Mag. Lett., 67 (5), 331 (1993).
3. Y. S. Kim, M. R. Johnson, R. Abbaschian and M. J. Kaufman in High Temperature Ordered Intermetallic Alloys IV, edited by L. Johnson, J. Stiegler and D. Pope (Mater. Res. Soc. Proc. 213, Pittsburgh, PA, 1991) pp. 839-845.
4. R. M. Aikin, Jr., Scripta Metall. et Mater., 26 (7), 1025 (1992).

BRITTLE COMPOSITES MODELING: Comparisons with $MoSi_2/ZrO_2$

S. P. Chen, R. LeSar and A. D. Rollett
Los Alamos National Laboratory, Los Alamos, NM 87545, USA

ABSTRACT

We have calculated the mechanical properties of brittle composites with spring-network (SN) model. The composites that we studied involve the transformation toughening effects and the accompanying micro-cracking. Our simulation results are consistent with experiments of $MoSi_2$ toughened with ZrO_2. By monitoring the stress changes due to the transformation and micro-cracking we are able to separate, for the first time, the contributions from these two competing effects. We also found that the fracture toughness of the composite increases as the modulus, interfacial cohesion of particle increases.

INTRODUCTION

Potential high temperature structural materials such as intermetallics and ceramics suffer room temperature brittleness and have low fracture toughness [1, 2]. This low temperature brittleness prevents the wide-spread use of these materials. One way to improve the materials fracture toughness is to make use of composite toughening, notably by transformation toughening, crack deflection and whisker toughening. The calculation of the fracture toughness of composites has been a very difficult task [3].

We used a "spring-network model" (SN) model [4, 5] to include the effects of microstructure, second-phase particle toughening and micro-cracking phenomena. We treat the system as a two-dimensional triangular lattice of nodes, each of which is connected to its six nearest neighbors by elastic springs. The microstructure is generated with a Potts model. Transformation of a second-phase particle is modeled by irreversibly increasing the equilibrium spring length when the mean stress on the second-phase particle exceeds a prescribed critical stress, σ_c. Cracking of a bond is modeled by irreversibly cutting the bond when the corresponding breaking length is reached. We assigned a 1% increase in the length of the springs (e^T=0.01) connected to second phase particles upon transformation to mimic the $MoSi_2/ZrO_2$ composite. The breaking length for the bulk bonds is 1.005 and for the grain boundaries and second phase particles are 1.003. We note that this choice of breaking strains ensures that there should be a mixture of trans- and intergranular fracture in polycrystals [6]. Finally, we choose a mean stress criterion for transformations with critical stresses σ_{cj} of 0.0005, 0.0010, and 0.0015 and other values (for j equal to 1, 2 and 3, respectively) to test the effect of σ_c on the enhancement of the fracture toughness. Also the second phase particles are randomly distributed in the matrix with a particle size of 1 node (labeled

Mat. Res. Soc. Symp. Proc. Vol. 322. ©1994 Materials Research Society

as Sj in the figures, where j representing composites with a transformation stress of σ_{cj}) or cluster of 7 nodes (labeled as Lj in the figures) to study the microstructural effects on the fracture toughness.

RESULTS AND COMPARISONS WITH EXPERIMENTS AND THEORIES

In this section, we describe our method of calculating fracture toughness and present results on the increase of fracture toughness, ΔK_{1C}, as a function of the dilatational strain, e^T, volume fraction of particles, f, and the critical transformation stress, σ_C. We then compared these results with available experimental measurements in $MoSi_2/ZrO_2$ (ZTM) [7], Al_2O_3/ZrO_2 (ZTA) [8] and the continuum theory [1, 8, 9].

The local stress, σ_L, for composites with second phase particles is linearly related to the local stress intensity, K_L. The reduction of the stress (or ΔK) over the block of nodes can be monitored as a function of the number of particles transformed as the strain (or stress) is applied. The increase of the fracture toughness is described by

$$\Delta K_{1C} = K_\infty - K_L = \alpha(\sigma_\infty - \sigma_L) = \alpha(-\Delta\sigma_{xx}) \qquad (1),$$

where α is a constant that depends on the simulation cell. The α is never calculated because only ratios with pure matrix are needed. It has been shown by continuum fracture mechanics [1, 8, 9] that the increase of the fracture toughness, ΔK, due to the transformation is represented by

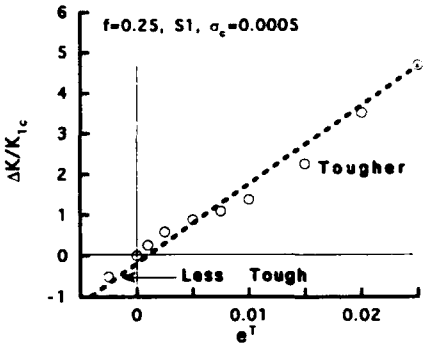
$$\Delta K = \alpha_1 \, E e^T f (\sigma_C)^{-1} / (1-\nu) \qquad (2),$$

where α_1 is a constant, E is the modulus, ν is the Poisson's ratio.

First, we held all parameters the same except the value of e^T to study the dependence of ΔK_{1C} on e^T. We found that for $e^T > 0$ the composite is tougher than the single phase material so it is good for transformation strain to be large and positive if massive micro-cracking (shattering of the sample) can be avoided [10]. On the other hand, if e^T is negative the composite is less tough than the matrix material because the transformed particles increase the tensile stress on the crack [10]. As shown in Fig. 1, ΔK is linear in e^T. Unfortunately, there has been no independent experimental studies on the linear dependence of e^T. Therefore, direct comparisons with experiments are not possible at this moment. This linear dependence is consistent with the continuum results (eq. 2).

Second, we assume all the parameters the same except f and calculated the ΔK as a function of the volume fraction of particles. The volume fraction dependence of ΔK has been shown previously by Chen et al [4, 5]. It was found that the increase in

Fig. 1: (a) The ΔK is plotted as a function of dilatational transformation strain, e^T.



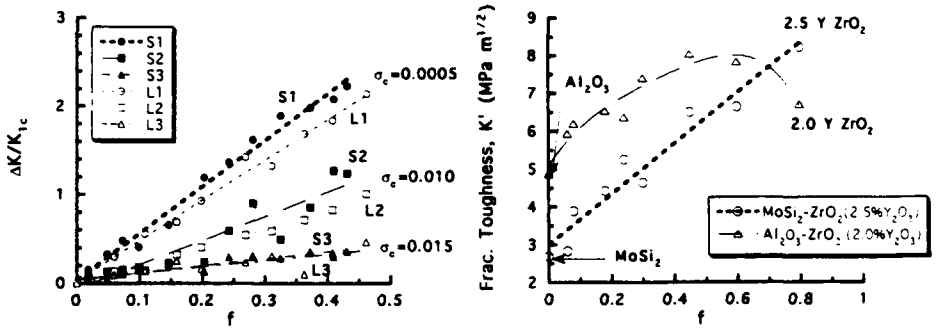


Fig. 2: The ΔK is plotted as a function of f for (a) small (Si's) and large particles (Li's) with several σ_C's. (b) The experimental ΔK is plotted as a function of f for $MoSi_2/ZrO_2$ (ZTM) and Al_2O_3/ZrO_2 (ZTA).

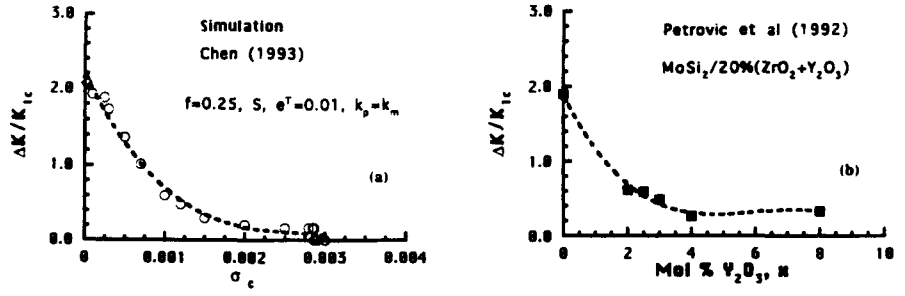


Fig. 3: (a) The ΔK is plotted as a function of the critical transformation stress, σ_C. (b) The experimental ΔK of the ZTM is plotted as a function of x (Mole percentage of Y_2O_3 stabilizer in ZrO_2 particles). These two curves of simulation and ZTM (both fitted to a 3rd order polynomial) are strikingly similar.

the fracture toughness associated with the transformation toughening is linear in f, for small and large particles (Fig. 2a). We noted that the increases of the composite toughness with large particles or the particles which clusters are smaller than the composites with small particles (assuming the same σ_c). The measurement of ΔK indicates a linear dependence of f of ZrO_2 in ZTM [7] shown in Fig. 2b is a direct confirmation of the simulation results. This calculated linear dependence is also consistent with the theory of continuum mechanics as represented by eq. (2).

The third way in changing the composite fracture toughness is to modify the critical transformation stress of the particles, σ_c. The change in σ_c can be achieved by the addition of stabilizers like in transforming ZrO_2 particles. The alloying of Y_2O_3 in ZrO_2 increases the critical transformation stress [1, 2]. We found the simulation results (Fig. 3a) are in good agreement with experiments of the $MoSi_2/ZrO_2(+ Y_2O_3)$ composites (Fig. 3b)[7]. A direct comparison with continuum theory (eq. 2) reveals some new features. We found that for different stress levels the ΔK versus σ_c curve can be broken into two regions:

(a) for large σ_c (> 0.0003), $\Delta K = \beta_1 \sigma_c^{-1.3}$,

(b) for small σ_c (< 0.0003), $\Delta K = \beta_2 \sigma_c^{-0.05} \simeq \beta_2$ (3)

where β_1 and β_2 are constants. For high σ_c, the simulation results indicate a less toughening than the results predicted by eq. (2). This indicates that the continuum theory is overestimating the transformation toughening effect by treating every transformation event as an independent event.

BEYOND EXISTING EXPERIMENTS & THEORIES

In Fig. 4a, we show that for $k_p=k_i=k_m=1.0$, the contribution to the fracture toughness from the transformation (open circle), the micro-crack (open triangle) and the total fracture toughness (solid circle) as a function of f. The contributions due to the transformations and micro-cracking are linear in f. For the micro-cracking part, we found that the contribution from the micro-cracking is 100% of the fracture toughness at f=0.0 (pure matrix material) and decreases as f increases. For the composites with the largest f (0.45) studied, the micro-cracking has a negative contribution to the fracture toughness due to the extensive cracking. We further study the effect of the modulus of the transforming particles on the fracture toughness. The modulus of the particle, E_p, is proportional to the particle's force constant, k_p. Therefore, the ratio of the moduli equals the ratio of corresponding force constants, e.g., $E_p/E_m = k_p/k_m$. As shown in Fig. 4b, the K' dependence on k_p is almost linear except for the composite with the largest k_p where the increase in K' starts to saturate. The composite with k_p larger than the matrix has a K' larger than the one with a smaller k_p. This connection of K' with k_p is easy to see by noting that the particle with larger modulus

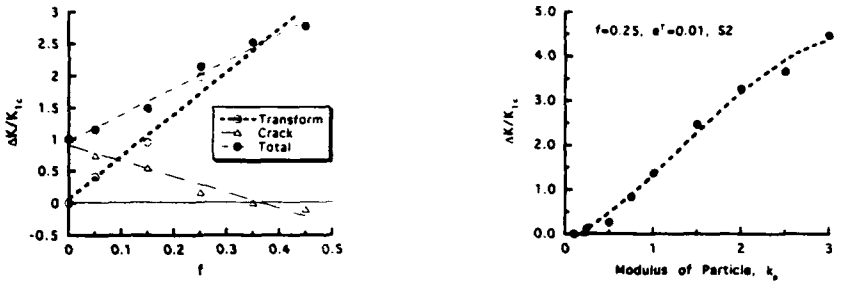


Fig. 4: (a) The fracture toughness, K' (transformation, crack, and total) is plotted as a function of f. (b) The total fracture toughness K' is plotted as a function of particle force constant, k_p ($=E_p/E_m$).

will shrink less after the relaxation. Therefore, the transformed particle puts more compressive stress on the matrix and creates a larger stress reduction or cracks shielding. Assuming the rule of mixture applies to the modulus, we can rewrite eq. (2) and eq. (3) to include explicitly the contribution from the modulus change and collective effects:

$$\Delta K = \alpha\ Em\ [(1-f) + fE_p/E_m]\ e^T f(\sigma_c)^{-1.3}\ /(1-\nu) \qquad (4).$$

This formula can be used as a predictive tool to select future tougheners.

In this part, we investigate the influence of the particle-matrix interfacial cohesion by varying the breaking distance of the nodes, r^b_{pm}, on the fracture toughness of the composites with second-phase particles. The results indicate that the stronger the interfacial cohesion, r_{pm}, is the larger the increase of the fracture toughness, ΔK_{1c}, will be (Fig. 5).

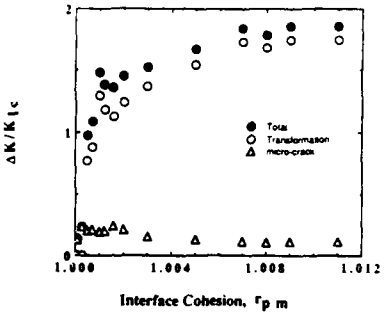


Fig. 5 : (a) The ΔK is plotted as a function of the particle-matrix interfacial cohesion, r_{pm}. The contributions due to the transformation are much larger than the contributions derived from micro-cracking.

The results indicate that the transformation toughening is the dominant cause of the increase in ΔK_{1c}, while the micro-cracking

only provides less than 10% of the toughening when r_{pm} is relatively large. For weak interfaces, none of the particles were transformed because high stresses can not be transferred from the matrix to the particles with cracking of the interfacial bonds. Therefore, only micro-crackings near the particles are providing the toughening at the level of 0.1 to 0.2 of the original value of K_{1c}. The composite with a smaller r_{pm} has a larger ΔK due to micro-cracking but the total K' is much smaller than the one with large r_{pm}.

It has been shown [4, 5] that with the same critical stress the composite with smaller particles with linear particle to grain size ratio of $R_{p/g}$=0.17 is tougher than the composites with large particles with $R_{p/g}$=0.46 (Fig. 2a). This result does not take into account of a possible change in the critical transformation stress as a function of the particle size that may existed in the real systems [11, 12]. Therefore, this result indicates clustering of particles (large particles) is detrimental to the fracture resistance of composites.

CONCLUSIONS

The simulation results on composite fracture toughness presented above using Spring-Network model are in good agreement with the available experiments and continuum theory. Using particles with characteristics like large dilatational transformation strain, large volume fraction, small transformation stress, large particle modulus, strong particle-matrix cohesion, and uniform distributions of transformable particles are beneficial in making tougher composites.

Acknowledgment: We would like to thank J. Petrovic, and R. Castro for helpful discussions. This work is supported by U. S. Department of Energy, Office of Industrial Technologies.

References:

1. A. G. Evans, J. Am. Ceram. Soc., 73, 187 (1990).
2. D. J. Green, R. H. J. Hannink, and M. V. Swain, "Transformation Toughening of Ceramics", CRC Press, Boca Raton, Florida (1989).
3. M. F. Ashby, Acta Metall. et Mat., 41, 1313 (1993).
4. S. P. Chen, J. Mat. Res. (submitted).
5. S. P. Chen, R. Lesar and A. D. Rollett, Scr. Met. et Mat., 28, 1393 (1993).
6. R. K. Wade and J. J. Petrovic, J. Am. Ceram. Soc., 75, 1682 (1992).
7. Petrovic et al, Mat. Sci. Eng. A155, 259 (1992).
8. F. F. Lange, J. Mat. Sci., 17, 225 (1982).
9. A. Evans and R. Cannon, Acta Metall., 34, 761 (1986).
10. W. M. Kriven, J. Amer. Ceram. Soc., 71, 1021 (1988).
11. A. G. Evans et al, Acta Metall., 29, 447 (1981).
12. A. G. Evans and A. H. Heuer, J. Am. Ceram. Soc., 63, 241 (1980).

DESIGN AND SYNTHESIZE OF NEW TERNARY ZIRCONIUM SILICIDE INTERMETALLIC COMPOUNDS WITH THE 16H CRYSTAL STRUCTURE

YUKINORI IKARASHI* AND KOZO ISHIZAKI**
*Tsuruoka Kogyo Koto Senmon Gakko (Tsuruoka Nat. Coll. of Tech.)
104 Sawada Ino-oka Tsuruoka, Yamagata 997, Japan
**Nagaoka Gijyutsu-Kagaku Daigaku (Nagaoka Univ. of Tech.)
Nagaoka, Niigata 940-21, Japan

ABSTRACT

The zirconium silicide intermetallic compounds with the 16H crystal structure are good materials for high temperature structural applications, because of their high melting point and low density. Their shortcoming is low ductility. To increase ductility, the coordination numbers are increased to increase isotropy of bondings, and to have more metallic nature of bonds.

Combination of elements, silicon, zirconium and other atoms for ternary silicides are selected by theoretical consideration of the coordination numbers. As the coordination numbers increase, the atomic bonds increase metallic properties, and their ductility increases. Higher coordination numbers are obtained by substituting yttrium atoms onto zirconium 6g point set sites.

INTRODUCTION

The working temperatures of heat resistant materials, for example superalloys in gas turbines, are in the range from 700 to 1000 ℃. Materials for high temperature structural applications, which may withstand working temperatures as high as 1500 ℃, are required in various fields such as aerospace and heat engines. These materials must have high melting points, high strength, high fracture toughness, high creep resistance and low densities. Several intermetallic compounds are excellent materials for high temperature structural applications in the future.

Fleischer plotted melting point against the density of intermetallic compounds for various crystal structures [1]. Celis et al. pointed out that the 16H* crystal structure silicides have high melting points and low densities compared with other crystal structures [2]. The binary zirconium silicide with the 16H crystal structure Si_3Zr_5 has high melting point and low density, indicating that Si_3Zr_5 is a good candidate for high temperature structural applications for the next generation heat engines [2-4]. The high melting point implies also that the covalent nature of bonding in 16H crystal structure silicides is high. Therefore ductility of the 16H crystal structure silicides is likely to be low.

To improve properties of intermetallic compounds, addition of elements and composites are considered. In this work, new ternary intermetallic compounds are designed by substituting of a part of atoms without crystal structure change. Celis et al. described that it is possible to substitute a layer of zirconium atoms with titanium in Si_3Zr_5 without crystal structure changes [4,5]. Using these results, a method to design new ternary zirconium silicide is described.

To increase ductility, coordination numbers are increased to enhance isotropical nature of bondings, and to have more metallic nature of bonds. In this work, design and synthesis of new ternary zirconium silicide intermetallic compound by substituting a part of zirconium atoms with other elements to increase the metallic nature of bondings in the 16H Si_3Zr_5 structure are discussed.

---

* Structure nomenclature according to ASTM.

Mat. Res. Soc. Symp. Proc. Vol. 322. ©1994 Materials Research Society

DESIGN OF $Si_3Y_3Zr_2$

Figure 1 shows the Bravais lattice of the $(M_5Si_3)16H$ type crystal structure, where M means a metallic element. Silicon and M atoms at 6g point set are located on basal planes B and C, and M atoms at 4d point set are on basal plane A. Lattice parameters determine the nearest neighbor atomic distances. Lattice parameter **a** controls the Si(6g)–M(6g) bonding distance in basal planes B and C, for example between Si(0.00, 0.61, 0.25) and M(0.25, 0.00, 0.25). Lattice parameter **c** fixes the M(4d)–M(4d) bonding length, for example M(0.33, 0.67, 0.00)–M(0.33, 0.67, 0.50), i.e., between two basal planes A.

Using the lattice parameters **a** and **c**, the atomic positions of all atoms, and the atomic diameter of each element, the relative interatomic distance (R_d) is calculated as follows [5]:

$$R_d = (d_c - d_i) / d_i \qquad (1)$$

where, d_c is the calculated value of the interatomic distance from crystal structure and d_i is the ideal interatomic distance calculated from atomic diameters. A negative value of R_d indicates a shorter distance than the ideal one, a positive value indicates a larger distance than the ideal one, and the zero implies the ideal distance. The relative interatomic distance is used to estimate the coordination number [6].

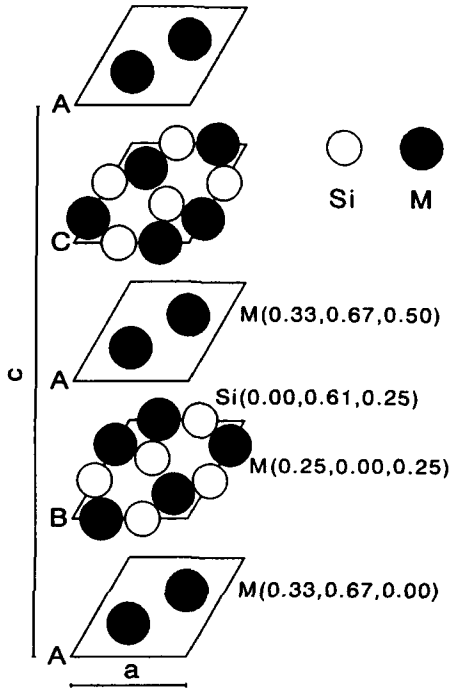


Figure 1 Schematic representation of the Si_3M_5 binary intermetallic compounds with the 16H crystal structure [2,5].

To design a new ternary zirconium silicide intermetallic compound with the 16H crystal structure, the relative interatomic distances are calculated for known binary silicide intermetallic compounds with the 16H crystal structure. In this work, the coordination numbers of a specific reference atom were defined as the number of atoms with a relative interatomic distance smaller than 0.03 (R_d <0.03) of the largest value of coordinated ones in Si_3Zr_5.

Table I shows the atomic diameter of each constituent element for binary silicide intermetallic compounds for the 16H crystal structure [7] and lattice parameters of the compounds [8] for calculation of relative interatomic distance. The silicon atomic diameter of 0.263 nm was used [7]. The coordination numbers (number of atoms with R_d less than 0.03) of binary silicides with the 16H crystal structure are shown in Table II. There is no difference of coordination numbers in these binary silicide intermetallic compounds, except Si_3Y_5. Coordination numbers of Si_3Y_5 are higher than other binary silicide intermetallic compounds, because the difference of the atomic diameter between silicon and metallic atom is the largest in this compound. This implies that the metallic nature of bonds in Si_3Y_5 is higher for the Y(6g) atoms than for other binary silicide intermetallic compounds with the 16H crystal structure. Indicating that by substituting the zirconium atoms in 6g point set of Si_3Zr_5 with yttrium atoms, the space in basal planes B and C for the atoms in 4d point set will expand and higher coordination numbers are expected.

For the calculation of the lattice parameter, the atoms are considered as quasi-rigid spheres. However, the 16H type crystal structure is complex and some of bonding distances are shorter than the ideal distance. Therefore, it is difficult to calculate the exact lattice parameters of the 16H crystal structure.

The relative interatomic distance of known binary silicide intermetallic compounds are plotted against atomic diameter in Figure 2, the 16H crystal structure assuming that the R_d value of Si(6g)-M(6g) is Si(0.00, 0.61, 0.25)-M(0.25, 0.00, 0.25) and M(4d)-M(4d) is M(0.33, 0.67, 0.00)-M(0.33, 0.67, 0.50) and bondings in $Si_3Y_3Zr_2$ are of average value. Using these values, the lattice parameters of $Si_3Y_3Zr_2$ are calculated, as **a**=0.836 nm and **c**=0.560 nm. From these lattice parameters, the coordination numbers of $Si_3Y_3Zr_2$ are calculated as shown in Table Ⅲ. Coordination numbers of $Si_3Y_3Zr_2$ are higher than Si_3Y_5. This implies that the metallic nature of bonds are probably higher than Si_3Y_5 and other binary silicide intermetallic compounds with the 16H crystal structure.

Table Ⅰ Atomic diameter of M, d, and lattice parameters **a** and **c** for binary silicide intermetallic compounds with the 16H crystal structure (M_5Si_3).

Compound		Si_3Zr_5	Si_3W_5	Si_3Ta_5	Si_3Ti_5	Si_3Y_5
d/nm		0.319	0.268	0.291	0.293	0.359
Lattice Parameter	a/nm	0.789	0.719	0.747	0.745	0.840
	c/nm	0.556	0.458	0.523	0.512	0.630

M : metal in M_5Si_3 structure

Table Ⅱ Calculated number of the nearest atoms in binary silicide intermetallic compounds with the 16H crystal structure (M_5Si_3). There is no contact between M(4d)-M(6g) and M(6g)-M(6g) bonds, except in Si_3Y_5.

Compound		Si_3Zr_5	Si_3W_5	Si_3Ta_5	Si_3Ti_5	Si_3Y_5
Si(6g)	Total	9	9	9	9	7
	M(4d)	4	4	4	4	4
	M(6g)	5	5	5	5	3
M(4d)	Total	8	8	8	8	14
	Si(6g)	6	6	6	6	6
	M(4d)	2	2	2	2	2
	M(6g)					6
M(6g)	Total	5	5	5	5	9
	Si(6g)	5	5	5	5	3
	M(4d)					4
	M(6g)					2

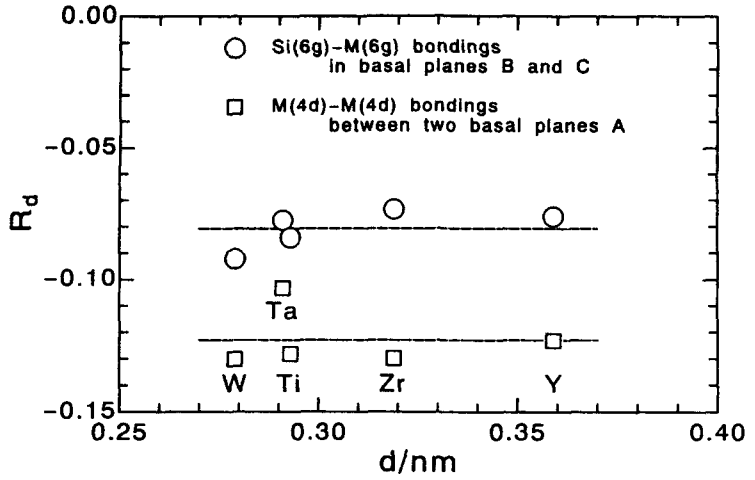


Figure 2 The relative interatomic distances (R_d) of the nearest Si(6g)–M(6g) on basal planes B and C, and M(4d)–M(4d) on two adjacent basal planes A for binary silicide intermetallic compounds with the 16H crystal structure. Dashed lines indicate average of R_d.

Table Ⅲ Calculated coordination numbers in the new ternary zirconium silicide intermetallic compounds with the 16H crystal structure $Si_3Y_3Zr_2$. The theoretical values indicate the designed $Si_3Y_3Zr_2$, and the experimental ones indicate the synthesized $Si_3Y_3Zr_2$, which is discussed later. Coordination numbers are higher than the binary silicide intermetallic compounds.

Compound		Theoretical	Experimental
Si(6g)	Total	9	7
	Zr(4d)	4	4
	Y(6g)	5	3
Zr(4d)	Total	14	14
	Si(6g)	6	6
	Zr(4d)	2	2
	Y(6g)	6	6
Y(6g)	Total	15	13
	Si(6g)	5	3
	Zr(4d)	4	4
	Y(6g)	6	6

EXPERIMENTAL PROCEDURE

Synthesis and densification of $Si_3Y_3Zr_2$

A mixture of 37.5 at.% silicon (99.5 % purity, -350 mesh), 37.5 at.% yttrium (99.9 % purity, -20 mesh) and 25.0 at.% zirconium (98.0 % purity, -350 mesh) was prepared in an alumina mortar with ethanol. After drying in vacuum, samples of the mixed powder were Cold Isostatically Pressed (CIP'ed). A reaction to form a silicide intermetallic compound was triggered by an electric arc in an argon atmosphere chamber. Samples were crushed in an alumina mortar until the powder passed through a 45 μm mesh screen.

The powder of $Si_3Y_3Zr_2$ was densified in a Spark Plasma Sintering (SPS) System (Sumitomo Coal Mining Co., Ltd.) for 5 min at 1400 ℃ under 50 MPa. The size of bulk sample is 20 mm diameter and 5 mm thickness.

Measurements of properties

Powders and bulk samples were analyzed qualitatively by X-ray diffraction in a Rigaku diffractometer of Cu-Kα_1 radiation monochromated by a graphite single crystal, operated at 40 kV and 30 mA. The patterns were obtained from 2θ=20 ° to 2θ=80 ° in steps of 0.01 ° with 0.5 ° min^{-1}. The powder was mixed with a silicon standard in order to obtain accurate lattice parameters.

After polishing bulk samples, densities were measured by the Archimedean method in toluene. Vicker's hardness was measured under a 9.8 N load.

RESULTS

Lattice parameters of experimental $Si_3Y_3Zr_2$, **a**=0.823 nm and **c**=0.608 nm, were calculated from XRD peaks (120) and (123). Using these parameters, interatomic distances were calculated to obtain the coordination numbers as shown in Table Ⅲ.

The density of $Si_3Y_3Zr_2$ is calculated from the experimentally obtained lattice parameters to be 4970 kg m^{-3}. The densified bulk sample had a density of 5060 kg m^{-3}.

Vicker's hardness of $Si_3Y_3Zr_2$ is 8.6±0.3 GPa at room temperature.

DISCUSSION

Tow Si(6g)-Y(6g) bonding distances were 7 % larger than theoretical $Si_3Y_3Zr_2$, therefore coordination numbers are lower than expected, as shown in Table Ⅲ. However, the coordination numbers of experimental $Si_3Y_3Zr_2$ are higher than any other binary silicide intermetallic compounds with the 16H crystal structure. For example, the number of Y(6g)-Y(6g) bonds increase to six of this compound compared with two of Si_3Y_5 which has the highest coordination numbers in the binary 16H system. This high coordination numbers indicate that $Si_3Y_3Zr_2$ has more metallic bonds than Si_3M_5.

The density of bulk sample is 2 % larger than the theoretical value, likely due to impurities. The density of $Si_3Y_3Zr_2$ is, however, lower than Si_3Zr_5 of 6000 kg m^{-3}, and makes it attractive for high temperature and low density structural applications.

Vicker's hardness of $Si_3Y_3Zr_2$ is 28 % lower than Si_3Zr_5 of 11.9±1.1 GPa at room temperature [3]. Lower value of hardness indicate that the strong covalent bondings are replaced by bondings with metallic nature, or the sample was not fully densified.

The melting point of $Si_3Y_3Zr_2$ was not measured. Si_3Zr_5 has a high melting point (2230 ℃) [3]. Nature of strong covalent bondings in Si_3Zr_5 are replaced by more metallic nature of bonding in $Si_3Y_3Zr_2$, and the silicon interatomic distance is 8 % larger than in Si_3Zr_5, with a value of 0.354 nm. However, melting points depends upon strength of bondings. Higher coordination numbers of $Si_3Y_3Zr_2$ indicating that total strength of bondings is higher than other intermetallic compounds. Therefore, the melting point of $Si_3Y_3Zr_2$ may

be similar to Si_3Zr_5 due to higher coordination number.

From these results, $Si_3Y_3Zr_2$ have higher ductility and lower density than Si_3Zr_5 are excellent candidates for high temperature structural applications.

CONCLUSIONS

(1) New ternary zirconium silicide intermetallic compound $Si_3Y_3Zr_2$ is designed and synthesized by substituting a layer of zirconium atoms with a layer of yttrium atoms to increase the metallic nature of bondings to obtain reasonable ductility of Si_3Zr_5 with the 16H crystal structure.
(2) Density of this compound is lower than Si_3Zr_5, making it an excellent candidate material for high temperature structural applications.
(3) The melting point of $Si_3Y_3Zr_2$ may be similar to Si_3Zr_5 due to higher coordination number.

ACKNOWLEDGEMENT

This work was supported by Grant-in-Aid for Scientific Research on Priority Areas (04239214) and Grant-in-Aid for Encouragement of Young Scientists (04855127) from the Ministry of Education, Science and Culture (MONBUSHO), Japan. The opportunity of sintering experiments of $Si_3Y_3Zr_2$ by the Spark Plasma Sintering System was kindly provided by Sumitomo Coal Mining Co., Ltd.

REFERENCES

1. R. L. Fleischer, J. Mater. Sci., **22**, 2281 (1987).
2. P. B. Celis and K. Ishizaki, J. Mater. Sci., **26**, 3497 (1991).
3. P. B. Celis, K. Ishizaki, E. Kagawa and J. Ishikawa, in Pressure Effects on Materials Processing and Design, edited by K. Ishizaki, E. Hodge, and M. Concannon (Mater. Res. Soc. Symp. Proc., **251**, Pittsburgh, PA, 1992) pp. 9-14.
4. P.B.Celis and K.Ishizaki, Bull. Iron and Steel Inst. Jpn. (Tetsu to Hagane), **78**, 26 (1992).
5. P. B. Celis, E. Kagawa and K. Ishizaki, J. Mater. Res., **6**, 2077 (1991).
6. J. Steinmetz, G. Venturini, B. Roques, N. Engel, B. Chabot and E. Parthe, Acta Cryst., **B38**, 2103-2108 (1982).
7. L. Pauling: J. American Chem. Soc., **69**, 542 (1947).
8. P. Villars and L. D. Calvert, in Pearson's Handbook of Crystallographic Data for Intermetallics (ASM, Metals Park, OH, vol.2, 1985) p.3190, p.3194, and pp.3198-3200.

PART IV

Silicide Oxidation and Properties

HIGH TEMPERATURE OXIDATION BEHAVIOR OF STRUCTURAL SILICIDES

C. E. Ramberg, P. Beatrice, K. Kurokawa, and W. L. Worrell
Department of Materials Science and Engineering, University of Pennsylvania, Philadelphia, PA 19104

ABSTRACT

The factors which control the formation of a protective silica (SiO_2) layer on structural silicides at high temperature are summarized. The thermodynamic and kinetic conditions under which both silica and a metal oxide can form are also described. Molybdenum disilicide ($MoSi_2$) forms highly protective silica scales and has the best oxidation resistance at high temperatures. Although the preparation method has little influence, the heating rate and the structure of the silica layer have significant effects on the oxidation behavior of $MoSi_2$.

INTRODUCTION

One of the inherent problems in designing structural materials for high-temperature use is their reaction with an oxidizing environment. As a result, much work has focused on developing materials with both structural integrity and oxidation resistance. This paper summarizes the conditions under which binary silicides form protective silica layers when exposed to high oxygen pressures (≈1 bar). The melting points of the structural silicides which are being considered for high temperature applications are shown in Fig. 1. Because silicon is the element providing oxidation resistance, we emphasize the most silicon-rich of the possible binary silicides, having the usual stoichiometry: $MeSi_2$. Figure 1 also shows the temperatures of the $MeSi_2$-Si eutectic, along with the lowest temperature metal-rich eutectic. The silicides of niobium, tantalum, molybdenum, and tungsten have the highest melting points and have received the most attention for high temperature applications.

The standard free energies of formation (ΔG^o_f) of oxides are useful to compare their chemical stability with that of silica. As shown in Fig. 2, the oxides of molybdenum and tungsten are much less stable than SiO_2 and are easily reduced by silicon. The oxides of tantalum and niobium are also less stable than SiO_2, but not by as large a margin as those of tungsten and molybdenum. The oxides of titanium and zirconium are more stable than SiO_2, and these metals will reduce SiO_2. In the competition for oxygen which occurs at the silicide/silica interface, the disilicides of molybdenum, niobium, tantalum and tungsten could be expected to form only a silica scale, whereas the titanium and zirconium disilicides would also form titanium or zirconium oxides and have poor oxidation resistance. However, several studies have suggested that the oxidation of $TiSi_2$ is parabolic,[1,2] implying that the oxide scale is protective. The oxide scale has a silica layer near the silicide/scale interface and islands of TiO_2 at the scale/gas interface. Titanium, which is soluble in SiO_2 up to ~10mole%,[3,4] apparently diffuses to the outer scale/gas interface, forming islands of TiO_2 and leaving a protective silica-titania glass on the inside. Zirconium disilicide may also form a mixed oxide with protective properties, but a pure silica layer has the best high-temperature oxidation resistance.

Mat. Res. Soc. Symp. Proc. Vol. 322. ©1994 Materials Research Society

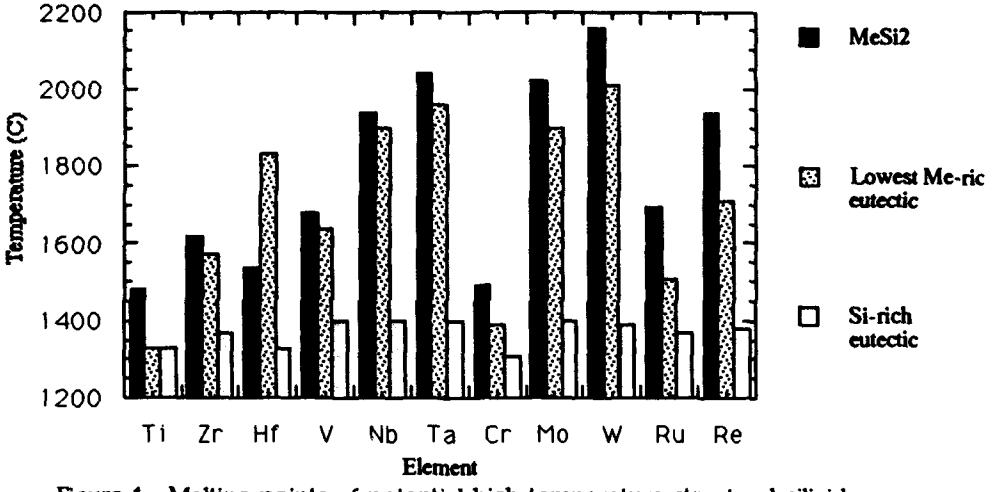


Figure 1. Melting points of potential high temperature structural silicides, with melting points of silicon-rich and metal-rich eutectics [5].

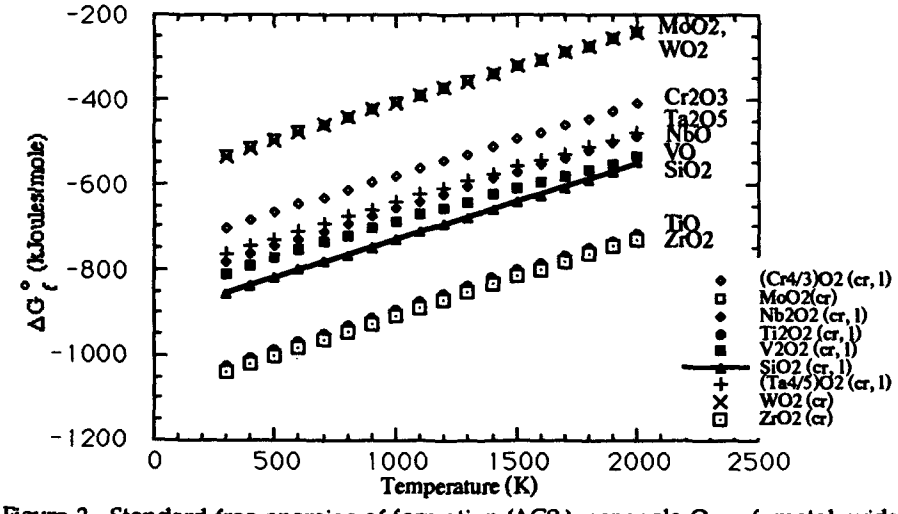


Figure 2. Standard free energies of formation (ΔG^{o}_{f}), per mole O_2, of metal oxides, based on data from JANAF tables[6].

PARABOLIC OXIDATION OF SILICIDES

The best kinetic barrier to the oxidation of silicides is a protective scale that inhibits the diffusion of oxygen or metal to or from the scale/silicide interface. Pure silica (SiO_2) is one of the most impermeable oxides at high temperatures; and disilicides that form silica scales exhibit the best oxidation resistance at high temperatures. For example, Fig. 3 shows the parabolic rate constants for the oxidation of several materials that form protective silica and alumina (Al_2O_3) scales. The low activation energy for the diffusion of oxygen in SiO_2 results in a more protective oxide scale at temperatures above ~1080°C.

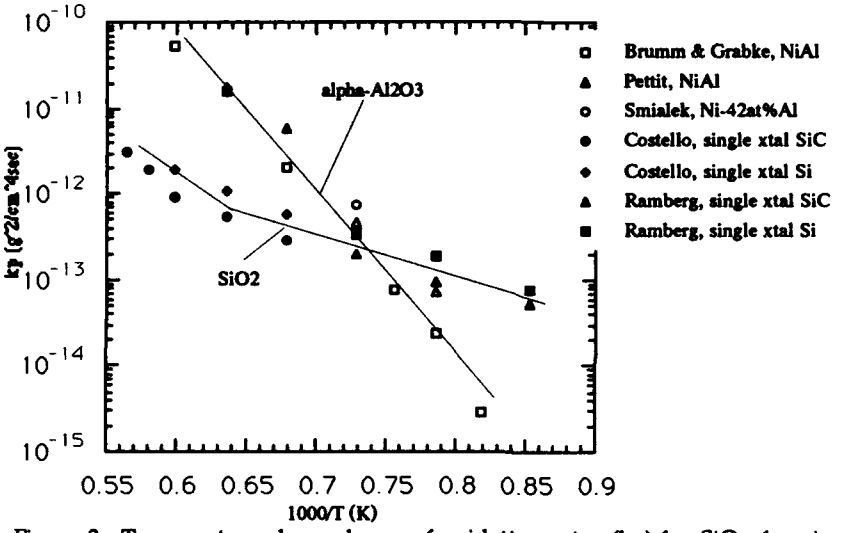


Figure 3. Temperature dependence of oxidation rates (kp) for SiO_2 forming and Al_2O_3 forming materials. Brumm and Grabke[7], 0.13 bar O_2; Pettit[8], air; Smialek[9], 0.1bar O_2; Costello and Tressler[10], 1bar O_2; Ramberg[11], 1 bar O_2.

The growth rate of a protective oxide scale has been modeled by several authors[12,13]. At high temperatures, the time dependence of the oxide thickness is described by the parabolic rate law:

$$x^2 = k_p t \qquad (1)$$

The parabolic-rate constant (k_p), has the units of either thickness^2/time or (weight/area)^2/time. These are directly related by the density of SiO_2:

$$k_{p(\text{weight/area})^2/\text{time})} = k_{p(\text{thickness}^2/\text{time})} * (2.2 g/cm^3)^2 \qquad (2)$$

The initial silica scale formed on silicides is usually amorphous, however above ~1300°C, the amorphous silica can transform to α-cristobalite. The oxygen diffusivity will change as the structure of the silica changes, and the parabolic-rate constant changes with time.

There are often conditions under which a metal oxide forms in addition to silica, and the rate constants are not due only to the growth rate of a pure silica scale. For example, formation of a gaseous metal oxide, along with the formation of silica, would result in a lower apparent rate constant, and depending upon the molecular weight of the metal in the silicide, could result in a net weight loss. Two other important assumptions are usually invo ved in the determination of parabolic rate constants. In thickness measurements, it is assumed that the scale thickness is uniform. For weight change measurements, it is assumed that the surface area of the sample is equal to the geometrically measured area. The latter assumption often leads to erroneous k_p values when the samples are cracked or have open porosity.

During the initial stages of silicide oxidation, both metal oxide and silica may form simultaneously. The diffusivity at this point is not that for SiO_2, but that for a mixed MeO_x-SiO_2 layer. For example, $TaSi_2$ or $NbSi_2$ form mixed oxides of both silica and Ta_2O_5 or Nb_2O_5 upon oxidation[14,15]. Although the niobium and tantalum silicides could eventually be protected by a thick mixed-oxide layer, spallation problems due to growth stresses become critical as scale thickness increases, and the oxide scales on $TaSi_2$ and $NbSi_2$ crack extensively[14,15].

However, $MoSi_2$ and WSi_2 form dense, protective layers of relatively pure SiO_2 when oxidized at high temperatures[16,17,18,19,20,21]. Although the molybdenum and tungsten silicides also initially form mixed oxides, the critical difference is the volatilization of the molybdenum or tungsten oxides as oxidation proceeds. Figure 4 shows the vapor pressures for some of the refractory-metal oxides. The vapor pressures of the molybdenum and tungsten oxides are orders of magnitude higher than those of niobium and tantalum. As the molybdenum or tungsten oxide formed with silica on $MoSi_2$ or WSi_2 volatilizes, the silica layer becomes more "silica rich" and oxygen transport to the silicide/scale interface decreases. This reduction in oxygen transport and the associated reduction of the oxygen activity (concentration) at the silicide/scale interface continues as the metal oxide volatilization continues. Eventually the oxygen activity at the silicide/scale interface decreases to a value where the base metal oxide is unstable, after which the molybdenum or tungsten silicide is protected by a relatively pure SiO_2 layer. Several authors have analyzed silica scales formed on $MoSi_2$ and found no molybdenum within the detection limits[16,18]. Our studies using energy dispersive spectroscopy have also failed to detect molybdenum in the silica layer. At high temperatures (> 1200 °C) volatilization is rapid, and the silica layer appears to purify within the first hour of oxidation. At lower temperatures, the weight gain is due to the formation of both the metal oxide and silica. Near the temperature where the metal oxide begins to volatilize, either a weight gain or loss could be observed. At high temperatures, where only silica is formed, the sample should gain weight slowly. This temperature-dependent behavior has been observed for powder $MoSi_2$ samples[20]. For dense samples of $MoSi_2$ having much lower specific surface area, this behavior is difficult to observe and depends on the resolution of the measuring device.

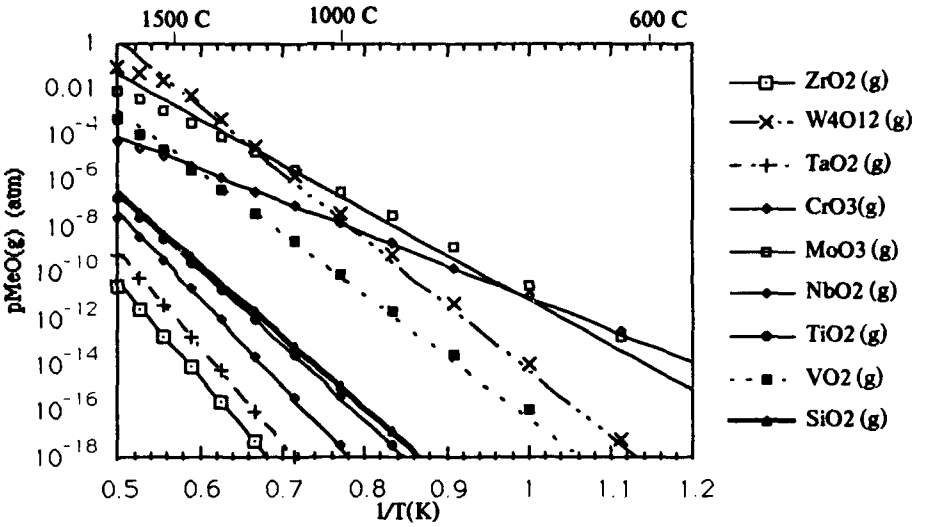


Figure 4. Equilibrium vapor pressures of some refractory-metal oxides at pO_2 = 1 atm, activity of the most stable solid oxide = 1.

When no metal oxide is formed and silicon is selectively oxidized, the silicide changes stoichiometry. Although initially high, the oxygen activity (expressed as p_{O2}) at the silica/silicide interface eventually reaches the equilibrium oxygen activity (pressure) given by:

$$p_{O_2}^{-1} = e^{\left\{\frac{-\Delta G^\circ_f}{RT}\right\}} a_{\underline{Si}} \qquad (3)$$

where ΔG°_f is the standard free energy change of the reaction:

$$\underline{Si}_{(s)} + O_{2(g)} = SiO_{2(s)} \qquad (4)$$

and $\underline{Si}$ represents silicon in the silicide. Values for ΔG°_f are given in Fig. 2. Equation (3) assumes a pure SiO_2 layer. At constant temperature, $a_{\underline{Si}}$ is not fixed in a single-phase silicide. However, if two phases in the metal-silicon binary system are present and in equilibrium (e.g., $MeSi_2$-Si or Me_5Si_3-$MeSi_2$), the activities of both the metal and silicon can be calculated from reactions such as the following:

$$zMeSi_2 = Me_zSi + (2z\text{-}1)\underline{Si} \qquad (5)$$

As the oxidation of silicon in the silicide to form SiO_2 proceeds, $a_{\underline{Si}}$ decreases (and

$a_{\underline{Me}}$ increases) in the silicide, and eventually either the lower Me_zSi silicide will form (reaction 5) or an oxide of the metal will form by the following reaction:

$$y\underline{Me} + SiO_2 = Me_yO_2 + \underline{Si} \tag{6}$$

We can estimate whether reaction (5) or (6) occurs first. For example, if the metal oxide forms instead of the Me_zSi, the ΔG^o_{rxn} for equation (6) can be used to calculate the equilibrium $a_{\underline{Si}} / a_{\underline{Me}}$ ratio established by the metal oxide and SiO_2:

$$a_{\underline{Si}} \Big/ a_{\underline{Me}}^{y} = e^{\left\{\frac{-\Delta G^o_{rxn}}{RT}\right\}} \tag{7}$$

However, when the Me_zSi forms, the ΔG^o_{rxn} for reaction (5) can be used to calculate the activity of silicon established by the two silicides:

$$a_{\underline{Si}}^{(2z-1)} = e^{\left\{\frac{-\Delta G^o_{rxn}}{RT}\right\}} \tag{8}$$

This silicon activity can be compared with the maximum silicon activity at which metal oxide would form according to Eq. (6). One first calculates the metal activity ($a_{\underline{Me}}$) at equilibrium with $MeSi_2$ and Me_zSi by rewriting Eq. (5) with the appropriate stoichiometric coefficients. This $a_{\underline{Me}}$ is then inserted into Eq. (7) to determine the maximum silicon activity ($a_{\underline{Si}}$) at which Me_yO_2 would form. If the maximum $a_{\underline{Si}}$ calculated from Eq. (7) is larger than that from Eq. (8), the metal oxide will form before another silicide. The log of the ratio $[(a_{Si})_{oxide\text{-}eq.} / (a_{Si})_{silicide\text{-}eq.}]$ is positive when the oxide first forms and negative when another silicide first forms. The temperature variation of this ratio, shown in Figure (5), indicates that all the silicides should form another silicide before the metal oxidizes. Although the thermodynamic data for the oxide free energies are well established[6], values of ΔG^o_f for the silicides are not available, and the enthalpies of formation (ΔH^o_f) at 298K[22] are used to calculate the lines shown in Fig. (5). Although the entropy of formation (ΔS^o_f) for the silicides is usually small, even a small ΔS^o_f may result in a significant $T\Delta S^o_f$ term at high temperatures. Furthermore, the activities are calculated from an $\exp(\Delta G^o_f)$ term, and small errors in ΔG^o_f can lead to large differences (orders of magnitude) in the calculated activities. Given these uncertainties and the relatively small values for $(a_{Si})_{oxide\text{-}eq.} / (a_{Si})_{silicide\text{-}eq.}$, we cannot confidently conclude that the niobium and tantalum disilicides will preferentially form another silicide. However, Fig. (5) indicates that the tungsten and molybdenum disilicides should form another silicide when oxidized at high temperatures.

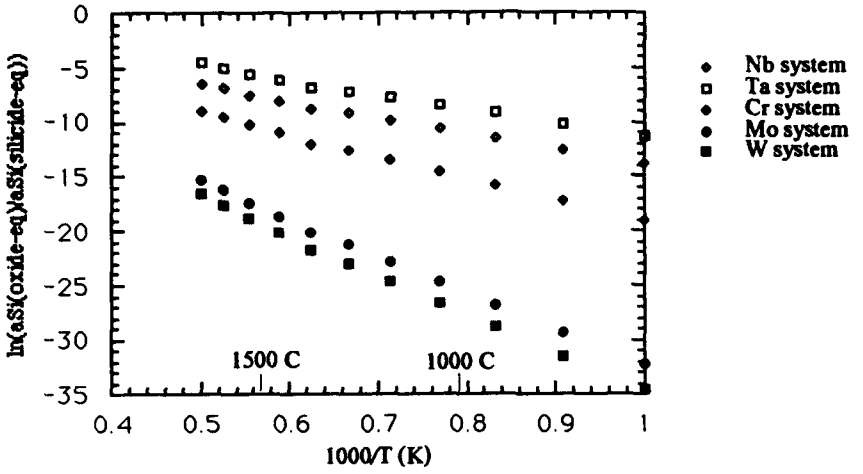


Figure 5. Temperature variation of $(a_{Si})_{oxide-eq.}/(a_{Si})_{silicide-eq.}$ Calculated using available oxide data[6] and silicide data[22]

OXIDATION OF $MoSi_2$

To complement the studies cited previously for the oxidation of $MoSi_2$[16-21], we have investigated the effects of the preparation method and heating rate on the oxidation behavior of $MoSi_2$. Hot pressed, arc melted and vacuum plasma sprayed $MoSi_2$ samples have been oxidized in 1 atm. of flowing oxygen at 1500 and 1600°C. The densities of the pure hot-pressed and vacuum plasma-sprayed samples were 95-97% and 98% of the theoretical value, respectively. However, the arc-melted specimens exhibited a high degree of cracking. The surfaces of all specimens were finished with #600 emery paper and cleaned in an ultrasonic acetone bath prior to oxidation. The specimens were placed in an alumina crucible which was suspended within an Al_2O_3 tube in a $MoSi_2$ furnace using a thin sapphire rod and a platinum wire. Direct contact between the specimens and the alumina crucible was avoided by placing some large pieces of crystalline silica between them.

A Cahn-1000 thermogravimetric balance was used to continuously measure their weight changes. Isothermal and slow-heating (SH) procedures were used to evaluate the effect of heating rate. In the isothermal procedure, the furnace was first heated to temperature, and the specimen was then suspended from the balance where it reached 1500°C within a few minutes. In the SH procedure, the suspended specimen was inserted into the furnace at room temperature and then heated at a rate of 10°C/min; in this procedure the specimen reached 1500°C after about 2.5 hours. The oxidized specimens were characterized using X-ray diffraction (XRD), scanning electron microscopy (SEM), and energy dispersive X-ray analysis (EDX).

Plots of (weight gain/area)^2 versus oxidation time (the slope of this line is k_p) for isothermal experiments at 1500°C and 1600°C are shown in Figs. 6 and 7. While the pure hot pressed $MoSi_2$ and arc-melted $MoSi_2$ samples have a constant k_p, the

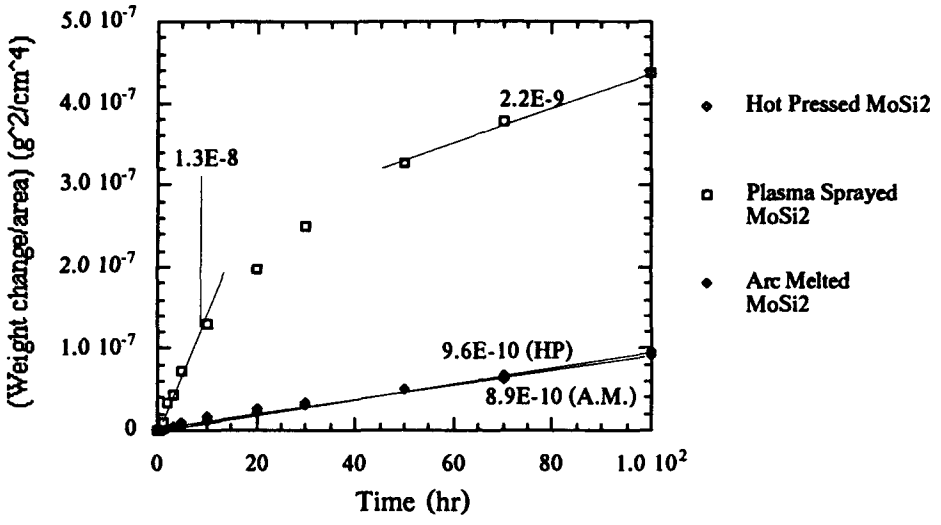


Figure 6. Isothermal oxidation at 1500 °C of $MoSi_2$ prepared by different techniques.

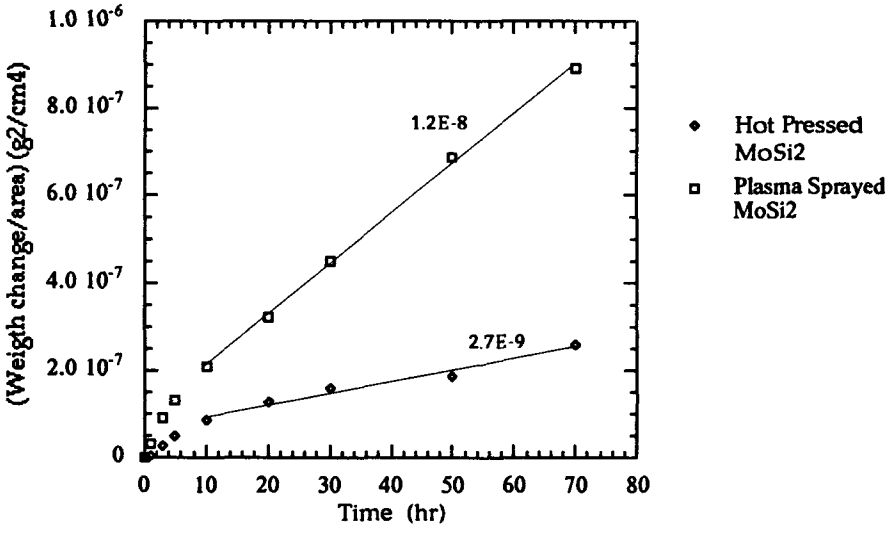


Figure 7. Isothermal oxidation at 1600 °C of $MoSi_2$ prepared by different techniques.

plasma sprayed $MoSi_2$ in Fig. 6 exhibit a changing k_p in the first 10 to 40 hours. After 100 hours of oxidation, the XRD analysis shows that the oxide layer is cristobalite, the stable crystalline phase of silica at temperatures above 1430°C. The initial short-time parabolic rate constants at 1500°C are in good agreement with those for amorphous SiO_2[10] formed on SiC, while the long time k_p is more representative of diffusion through cristobalite[23]. We are currently investigating the factors which determine the structure of the silica scale formed on $MoSi_2$ and $MoSi_2$ composites.

As shown in Table I, isothermally-oxidized $MoSi_2$ has excellent oxidation resistance at 1500 and 1600°C. Furthermore the oxidation kinetics of the arc-melted, cracked specimens are almost identical to those of the denser specimens. Thus, it appears that for isothermal, rapid-heating oxidation experiments at high temperatures, the effects of cracking are not significant.

Table I. Parabolic Rate Constants (g^2/cm^4-hr) For $MoSi_2$ Materials

Materials	1500 Slow Heat	1500 Isothermal	1600 Isothermal
Hot Pressed $MoSi_2$	7.3E-9	9.6E-10	2.7E-9
Arc Melted $MoSi_2$	1.9E-8	8.9E-10	
Plasma Sprayed $MoSi_2$		long time: 2.2E-9 short time: 1.3E-8	1.2E-8

Figure 8 shows the results of the slow heating experiments. Prior to the extended isothermal oxidation at 1500°C, the samples were slowly heated (10°C/min.) through the temperature range over which solid MoO_2 should form. The effects of this treatment were most significant for the arc-melted sample, which was highly cracked.

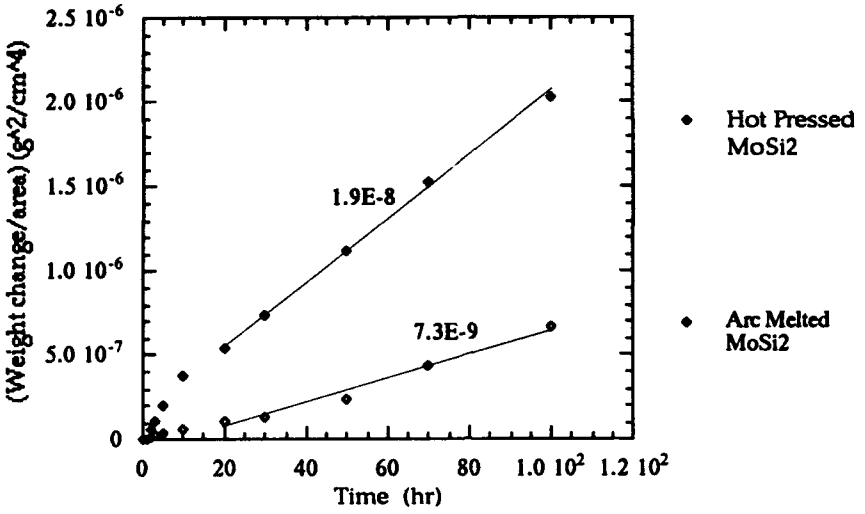


Figure 8. Oxidation at 1500°C of $MoSi_2$ prepared by different techniques. Samples were slowly heated (10°C per min.) for the first 2.5 hours.

SUMMARY AND CONCLUSIONS

The high-temperature oxidation behavior of structural silicides depends on several thermodynamic and kinetic factors. Because a pure silica layer is the preferred oxidation barrier, the silicides that form pure SiO_2 scales at high temperatures have superior oxidation resistance. Thermodynamic calculations indicate that $MoSi_2$ and WSi_2 should form another silicide and not metal oxide as the silicon activity in the disilicide decreases during extended oxidation. The volatility of the molybdenum and tungsten oxides at high temperatures can result in the "purification" of an oxide-silica duplex scale formed during exposure at lower temperatures. Molybdenum disilicide forms highly protective silica scales and has the best oxidation resistance at high temperatures. Although the preparation method has little influence, the heating rate and the structure of the silica scale have significant effects on the high-temperature oxidation behavior of $MoSi_2$.

ACKNOWLEDGMENTS

We thank Dr. John Petrovic and Dr. Sanjay Sampath for the disilicide samples and Dr. Peter Meschter for supplying some pertinent references. The financial support of the Office of Naval Research is gratefully acknowledged.

REFERENCES

[1]F.N. Schwettmann, R.A. Graff, and M. Kolodney, J. Electrochem. Soc. **118** (12), 1973-1977 (1971).

[2]A. Abba, A. Galerie, and M. Caillet, Oxid. Met. **17** (1), 43-54 (1982).

[3]P.C. Schultz and H. T. Smyth, in Amorphous Materials, edited by R. W. Douglas and B. Ellis, (John Wiley and Sons, London, 1972) p. 453-461.

[4]D. L. Evans, J. Am. Ceram. Soc. **53** [7] 418-419 (1970).

[5]Binary Alloy Phase Diagrams , Second Edition, edited by T. B. Massalski (ASM International, Materials Park, OH, 1990)

[6]J. Phys. Chem. Ref Data, Vol. 14, Suppl. 1, 1985 (JANAF Thermochemical Tables), Third Edition, edited by M. W. Chase et. al. (American Chemical Society/American Institute of Physics, 1985).

[7]M.W. Brumm and H.J. Grabke, Corr. Sci. **33** (11), 1677-1690 (1992).

[8]F.S. Pettit, Trans. AIME **239** 1296-1305 (1967).

[9]J. L. Smialek, Met. Trans. **9A** 309-320 (1978).

[10]J. A. Costello and R. E. Tressler, J. Am. Ceram. Soc. **69** (9) 674-681 (1986).

[11]C. E. Ramberg, M. S. Thesis, The Pennsylvania State University, 1992.

[12]C. Wagner, Atom Movements, p. 153-173, American Society for Metals, Cleveland OH (1951).

[13]B. E. Deal and A. S. Grove, J. App. Phys., **36** [12] 3770-3778 (1965).

[14]P. Lublin and L Sama, Am. Ceram. Soc. Bull. **46** (11), 1083-1090 (1967).

[15]H.W. Lavendel and A.G. Elliot, Trans. AIME **239** 143-148 (1967).

[16]J. Berkowitz-Mattuck and R.R. Dils, J. Electrochem. Soc. **112** (6), 583-589 (1965).

[17]E. Fitzer, Ceramic Transactions Volume 10, Corrosion and Corrosive Degradation of Advanced Ceramics, edited by R. E. Tressler and M. McNallan, The American Ceramic Society, Inc. 19-41 (1990).

[18]T. Mochizuki and M. Kashiwagi, J. Electrochem. Soc. **127** (5), 1128-1135 (1980).

[19]Y.A. Chang, J. Mat. Sci. **4** 641-643 (1969).

[20]C.D. Wirkus and D.R. Wilder, J. Am. Ceram. Soc. **49** (4), 173-177 (1966).

[21]R.W. Bartlett, J.W. McCamont, and P.R. Gage, J. Am. Ceram. Soc. **48** (11), 551-558 (1965).

[22]A.W. Searcy and L.N. Finnie, J. Am. Ceram. Soc. **45** (6), 268-273 (1962).

[23]T. Narushima, T. Goto, and T. Hirai, J. Am. Ceram. Soc. **72** (8) 1386-1390 (1989).

CYCLIC OXIDATION RESISTANCE OF $MoSi_2$/20v% Nb COMPOSITES

D.E. Alman* and N.S. Stoloff
Materials Engineering Department, Rensselaer Polytechnic Institute, Troy, New York 12180
* Present Address: U.S. Buerau of Mines, Albany Research Center, Albany, Oregon 97321

ABSTRACT

The effect of Nb morphology on the 1200°C cyclic oxidation resistance of $MoSi_2$/20v%Nb composites was investigated. Niobium was incorporated into $MoSi_2$ as particles, random short fibers and continuous aligned fibers. After oxidation, it was found all that the composites had lost weight and essentially disintegrated. This was due to spalling of both the Nb_2O_5 scale and the $MoSi_2$ matrix. The spalling of the matrix was a result of cracks originating from the oxidized Nb and propagating through the $MoSi_2$ matrix. These cracks arose from two sources: (1) the volume expansion associated with the transformation of Nb to Nb_2O_5 and (2) the difference in thermal expansion between Nb_2O_5 and $MoSi_2$. Composites with smaller diameter Nb reinforcements did not disintegrate as rapidly as composites with larger sized Nb reinforcements. This was attributed to the effect of reinforcement size on CTE mismatch cracking.

INTRODUCTION

The toughness of a variety of brittle intermetallic and ceramic matrices has been improved through the addition of ductile phases [1-7]. A few of these composites appear to be ideally suited for applications as structural materials at elevated temperatures in aggressive environments, as the ductile phase provides for toughness and the matrix provides for oxidation resistance. However, many of the ductile phases added have been refractory metals, which do not possess chemical stability in oxygen at elevated temperatures. Therefore, it is imperative to determine the effect of the addition of a ductile refractory phase on the oxidation resistance of the matrix.

Little has been reported on the oxidation resistance of ductile phase toughened composites, except by Meschter [8], who studied the 500C and 1200°C cyclic oxidation resistance of a $MoSi_2$/20v% Nb particulate composite. At 500°C, specimens exhibited weight loss on the first and each subsequent cycle, with virtually all the oxidized Nb particles spalling from the surface. X-ray diffraction revealed that MoO_3 and Nb_2O_5 were the oxide products. At 1200°C, the specimen gained weight during the first cycle; however, the sample lost weight on all subsequent cycles. Spalling of the oxidized Nb particles was not as extensive at 1200°C as at 500°C. The oxide products formed at 1200°C were Nb_2O_5 and SiO_2 on the surface of the specimen and a network of MoO_3 crystals which was deposited on the cooler walls of the tube of the oxidation furnace down stream from the specimen. The formation of MoO_3 was attributed to spalling along the $Nb_2O_5/MoSi_2$ interface, exposing fresh $MoSi_2$ which allowed for extensive vaporization of MoO_3. Fitzer and Remmele[4] examined the stabiliy of a $Mo(Si,Ge)_2$/40v% Nb aligned fibrous composite in an oxidizing environment at elevated temperatures. No mass change versus time results were reported, only changes the surface appearence were reported. They noted that during static exposure at 1200°C the Nb fibers "grew" from the surface of the specimen. This was a consequence of the difference in density of Nb and Nb_2O_5. They also reported that during thermal cycling at 1100°C the specimens were destroyed due to excessive cracking. Meschter [8], did not report this occurrence in his study; however, he did not indicate that he examined his specimens for cracking.

Recent research indicates that the toughness of $MoSi_2$ and other intermetallic matrices reinforced with Nb or other ductile phases is greatly affected by the morphology of the ductile reinforcement (i.e. size, shape and orientation) [9-14]. Thus, it is important also to determine the effect of the morphology of a ductile phase on the oxidation resistance of the matrix. This paper describes the effect of the Nb morphology (i.e particles versus random short fibers versus continuously aligned fibers) on the cyclic oxidation resistance of $MoSi_2$/20v% Nb composites.

Mat. Res. Soc. Symp. Proc. Vol. 322. ©1994 Materials Research Society

EXPERIMENTAL PROCEDURE

$MoSi_2$ composites reinforced with 20v% Nb composites were produced for this study by hot isostatic pressing mixtures of powders and fibers (vacuum encapsulated in Ti cans) at 1350°C and 172 MPa for 3 hours. The Nb was incorporated into the $MoSi_2$ as angular particles roughly 100μm in size, 800μm diameter random short fibers, 800μm diameter continuously aligned fibers, and 400μm diameter continuously aligned fibers. Complete details on the fabrication of these composites can be found elsewhere [14]. It should be mentioned that a reaction zone (primarily Nb_5Si_3 and approximately 10 μm thick) formed between the Nb and $MoSi_2$ during processing (a complete microstructural analysis can be found in references 12 and 14).

Oxidations specimens were prepared by electro-discharge machining (EDM) cylinders (6.35 mm in diameter) from the HIPed ingots. The EDM cylinders were containerless HIPed at 1350°C, and 172 MPa for 3 hours. Oxidation specimens were sectioned from the cylinders with a diamond blade to produce specimens that were nearly right circular cylinders, varying in height from approximately 6 to 9 mm. The surface of the specimens were mechanically polished through 0.3 μm Al_2O_3 paste. Prior to oxidation the dimensions and weight of each individual specimen were measured and recorded, and the specimens were ultrasonically cleaned in an acetone-alcohol mixture.

Cyclic oxidation studies were performed at 1200°C in dry laboratory air flowing though a Lindberg 1500 tube furnace at a rate of 40 cm^3/min. Each cycle consisted of placing the specimen into the furnace preheated to 1200°C and after the appropriate time interval removing the specimen from the furnace. After the specimen had cooled to room temperature (roughly 30 minutes), its weight was measured and recorded. The specimen was then placed back into the heated furnace (at 1200°C) for the next cycle. The results were plotted as specific mass (the change in the specimen's weight based on the original weight normalized for the surface area) versus oxidation time.

The duration of each of the first five cycles was 1 hour. The sixth cycle was 5 hours long and the seventh, eight and ninth cycles were 10 hours each. Any subsequent cycle was 24 hours in duration. The results dictated that only the particulate composite needed to be tested past eight cycles (30 hours exposure). After each cycle, the surface of each specimen was examined under a stereomicroscope. After testing was completed the specimens were examined by X-ray diffraction and optical and electron microscopy. To determine changes that may have resulted from exposure to oxygen after a certain time period, a few tests were repeated. However, after a pre-determined number of cycles the testing was discontinued (i.e., after the first or fifth cycle) and the specimens were sectioned for metallographic examination.

RESULTS

The oxidation results are shown in Fig. 1; specific mass change is plotted versus exposure time. All of the fibrous composites had initially gained weight on the first cycle, followed by weight loss on all subsequent cycles. The particulate composite showed the best results, as significant weight loss did not occur until the sixteenth cycle, or 208 hours of exposure (see insert in Fig. 1).

The attack of oxygen appeared to be localized at the Nb, with the Nb turning yellowish-white in color. The $MoSi_2$ matrix turned grayish in color, with a smooth clear layer appearing to have formed on the surface. X-ray diffraction detected Nb_2O_5 and $MoSi_2$ on the oxidized specimen. Presumably, amorphous SiO_2 formed on the surface of the specimens and was not detected by X-rays. Also, a network of white fibrous-like material formed down stream on cooler portions of the furnace wall; these were presumed to be MoO_3 crystals.

After 1 cycle (1 hour of exposure) the fibers appeared to have "grown" from the surface of the specimens (Fig. 2). The oxide morphology of the Nb_2O_5 scale was porous and cracks were detected in both the oxide scale and the adjacent matrix (Fig. 3). Spalled material contained only Nb_2O_5. After as few as 5 cycles, cracks were visible on the surface of the specimens and the oxide spall contained portions of fractured $MoSi_2$.

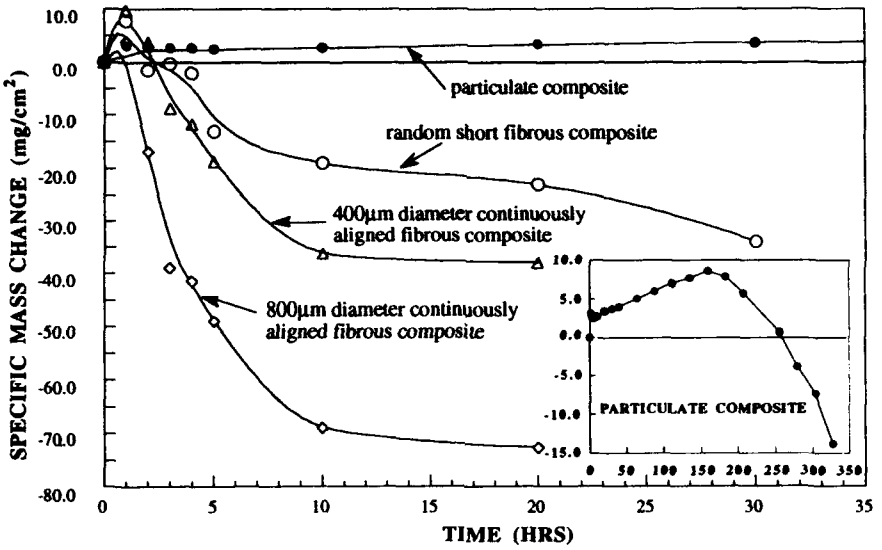


Figure 1. The cyclic oxidation behavior of $MoSi_2$/20v% Nb composites.

It should be mentioned that some of the initial weight loss displayed by the aligned fibrous composites was attributed to any fibers which transversed the entire surface oxidizing and immediately spalling from the surface. No fibers were situated entirely on the surface of the composite with the random short fibers. No fibers immediately spalled from the random short fibrous composite, thereby accounting for the slightly lower weight loss displayed by this composite. The random short fibrous composite could be considered as $MoSi_2$ containing very large Nb particles.

As with the fibrous composites, the attack of the particulate composite appeared to be localized at the Nb particles, with the particles growing from the $MoSi_2$ matrix. Significant amounts of $MoSi_2$ were not detected in the spalled material until the sixteenth cycle. However, cracks were detected originating from the particles propagating through the matrix after seven cycles (Fig.4).

DISCUSSION

Spalling of the Nb_2O_5 scale accounted for only a portion of the weight loss displayed by the composites. Some of the weight loss was attributed to the fracturing of the matrix $MoSi_2$. This was a consequence of the Nb_2O_5 scale possessing a molar volume five times greater than the molar volume of Nb (58.8 $cm^3 \cdot mol^{-1}$ for Nb_2O_5 as opposed to 10.9 $cm^3 \cdot mol^{-1}$ for Nb [15]). Thus, as the Nb inclusion oxidized to form Nb_2O_5, the physical dimensions of the inclusion increased. The $MoSi_2$ matrix accommodated for the increase in dimensions of the oxidized Nb by cracking. As the Nb_2O_5 scale "grew" from the surface the surrounding $MoSi_2$ must "move" with the scale, owing to the chemical bond between the fiber and the matrix. However, the $MoSi_2$ matrix surrounding the underlying unoxidized portion of the Nb fiber does not want to displace with the Nb_2O_5 scale. This results in a tensile stress in the matrix which was relieved by the normal (or z) type cracking (Fig. 3). If the $MoSi_2$ was not chemically bonded to Nb through the reaction zone (i.e. a weak interface exists) then this type of cracking might be avoided. Similarly any increase in diameter would be accommodated by the matrix through radial (or r)

type cracking (Fig. 2). For composites consisting of discontinuous reinforcement (particles or random short fibers), the matrix cracking also promoted further degradation as underlying Nb particles were exposed to oxygen (Fig. 4).

It is interesting to note that all types of matrix cracks (radial or r, normal or z, and debonding or θ) were observed propagating from the oxidized Nb through the matrix (Figs. 2-4). If the matrix cracking only were a result of the volume expansion associated with the formation of Nb_2O_5, then the θ or debonding cracks would not be expected, as it is unlikely that the volume expansion would cause separation along the reinforcement-matrix interface. These debonding cracks may arise from thermal expansion mismatch during cooling [16]. The stress that developed in the matrix due to the thermal expansion mismatch differences (σ_T) can be estimated by:

$$\sigma_T = E\Delta\alpha\Delta T \qquad (1)$$

where E is the modulus of $MoSi_2$, $\Delta\alpha$ is the difference between the thermal expansion coefficients and ΔT is the change in temperature (approximately 1200°C). The coefficients of thermal expansion for $MoSi_2$, Nb, and Nb_2O_5 have been reported as 8.1, 7.9 and 5.3×10^{-6}/°C, respectively [16-18]. The tensile stress developed in the $MoSi_2$ matrix arising from the CTE mismatch upon cooling from 1200°C between $MoSi_2$ and Nb was calculated as 80 MPa, and between $MoSi_2$ and Nb_2O_5 as 1150 MPa. Clearly the stress that develops in the matrix due to the CTE mismatch between the Nb_2O_5 and the $MoSi_2$ during cooling is sufficient to induce matrix cracking. Thus, the cracking of the matrix is exacerbated by the thermal expansion difference between the Nb_2O_5 scale and the $MoSi_2$ matrix.

Compared in Fig. 5 the results for this study's particulate and random short fibrous composites with the results obtained by Meschter [8]. Also shown in Fig. 5 are the results for the random short fibrous composite of the present study in which the initial cycles were 20 hours long (as were the duration of Meschter's cycles). Note that the composites with the larger sized Nb reinforcement tended "disintegrate" after one cycle, regardless of the duration of each cycle. However, the composite with the smaller sized reinforcement (the present study's particulate composite) did not begin to "disintegrate" after one cycle. This apparent size effect can be explained by the effect of reinforcement morphology on matrix cracks due to CTE mismatch. Lu et al. [16], have described a non-dimensional quantity (R) which relates the thermal expansion mismatch stress ($E\varepsilon^T = E\Delta\alpha\Delta T$) to the fracture toughness of the matrix (K_m=3 MPa$\sqrt{m}$ for $MoSi_2$) and the size of the reinforcement phase (r), by:

$$R = r\left(\frac{E\varepsilon^T}{K_m}\right)^2 \qquad (2)$$

This equation has been applied for reinforcement phase in the form of particles and fibers. For a fiber, r becomes the fiber radius, and for a particle r is equal to the particle radius. When R has a value equal to or less than unity than matrix cracking will not occur. Based on this equation, the size of the Nb_2O_5 scale must be 13.6μm (in diameter) or smaller to ensure that no matrix cracking will occur. The diameter of the forming Nb_2O_5 oxide scale on the fiber will, of course, be the diameter of the fiber; however, the size of the scale forming on a particle will approach the diameter of the particle when the particle is consumed. Consumption of Nb occurs readily at 1200°C; thus, the size of the Nb_2O_5 scale can be assumed to be equivalent to the initial diameter of the Nb. Since the radii of the Nb particles and fibers were larger than 13.6μm, matrix cracking arising from the CTE mismatch between $MoSi_2$ and Nb_2O_5 readily occurred. Lu et al [16] suggest that all forms of matrix cracking will occur profusely when R is greater than 10. The R values for the present study's fibrous composites and Meschter's particulate composite were greater than 10 (R=58, 29 and 13 to 32 for the 800, 400μm diameter fibrous composites and R=13 to 32 for Meschter's composite respectively); while the R value for the present study's

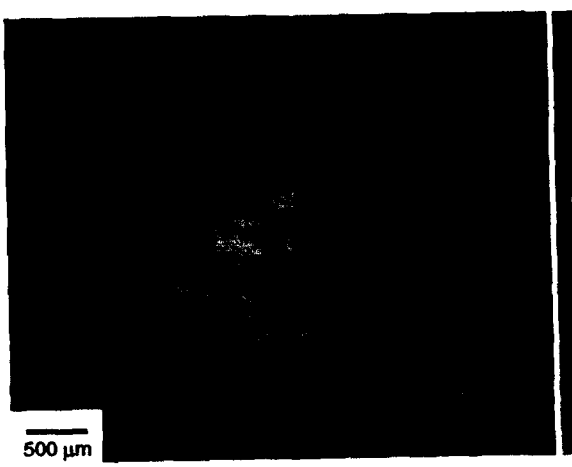


Figure 2. Oxidized Nb fibers growing from the matrix after 1 cycle (1 hour). Note the radial crack (arrow)

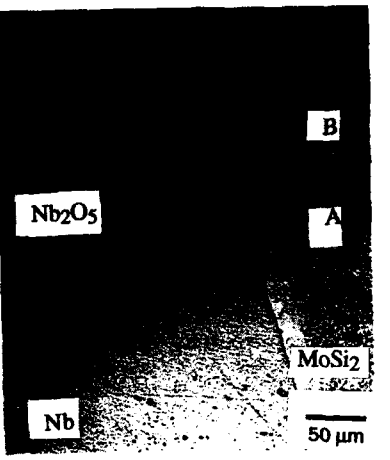


Figure 3. Cross section of oxidized specimen (800µm aligned fibers) after 1 cycle. Note the normal crack in the matrix (A), and the separation of the oxidized portion of the fiber from the matrix (B).

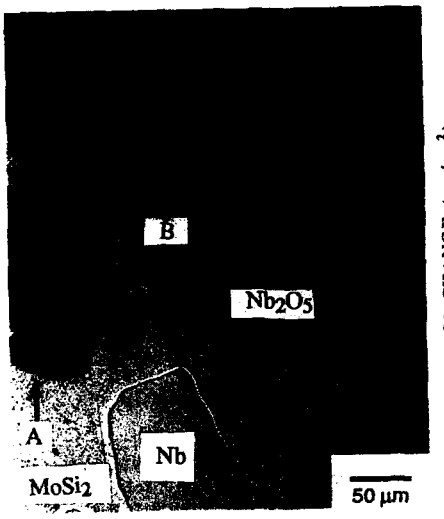


Figure 4. Cross section of the particulate composite after 7 cycles (20 hours). Note large oxidized particles separated from the matrix (A), while smaller particles did not (B).

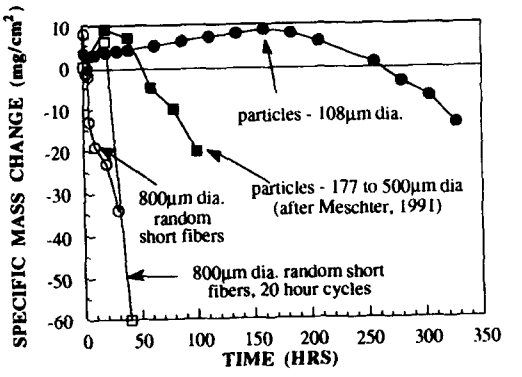


Figure 5. The effect of discontinuous reinforcement size on the cyclic oxidation behavior of $MoSi_2$/20v% Nb.

particulate composite was 8. It is interesting to note from Fig. 5 that no separation occurred between the smaller oxidized Nb particles and the $MoSi_2$ matrix. This is consistent with the argument regarding size effects on thermal expansion cracks, and would indicate that debonding between the $MoSi_2$ and the Nb_2O_5 is a result of the thermal expansion mismatch. Thus, it would appear the mismatch between the thermal expansion coefficients of $MoSi_2$ and Nb_2O_5 exacerbates the disintegration of $MoSi_2$/Nb composites during thermal cycling in an oxidizing environment, and can explain the apparent effect of size on the Nb (hence Nb_2O_5) on the cyclic oxidation behavior of these composites.

CONCLUSIONS

$MoSi_2$/20v% Nb composites disintegrated upon cyclic exposure to oxygen at 1200°C. This disintegration was attributed to the spalling of the Nb_2O_5 scale and fracturing of the $MoSi_2$ matrix. The fracturing of the matrix in the vicinity of the Nb_2O_5 was attributed to the volume expansion associated with the oxidation of Nb to form Nb_2O_5. The matrix accommodated the volume expansion by cracking, resulting in the disintegration of the composite. The matrix cracking occurred regardless of the Nb morphology (i.e particles, random short fibers, continuous aligned fibers, large diameter and small diameter fibers) incorporated into the $MoSi_2$ matrix. However, composites with smaller sized Nb inclusions tended to resist degradation (Fig. 5). The size effect was attributted to the CTE mismatch between $MoSi_2$ and the Nb_2O_5 scale, as smaller reinforcements have been found to suppress matrix cracking due to the CTE mismatch [16]. For any practical purposes, the Nb must be coated with a diffusion barrier prior to incorporation into an $MoSi_2$ matrix. Almost always, these coatings are brittle ceramics, such as Al_2O_3. During service the $MoSi_2$ matrix and Al_2O_3 coating may crack, resulting in the rapid oxidation of the Nb inclusion and degradation of the composite during thermal cycling. The results of this paper suggest that by judicious selection of the size of the Nb, a composite can be designed to possess some resistance to degradation due to oxidation.

ACKNOWLEDGEMENT

This research was supported by DARPA/ONR under Contract number N00014-86-K-0770.

REFERENCES

1. P. Hing and G.W. Groves, J. Mater. Sci., 1972, **7**, 427 (1972).
2. J.L. Chermant and F. Osterstock, J. Mater. Sci., **11**, 1939 (1976).
3. J.J. Brennen, in *Special Ceramics 6* , edited by P. Popper (The British Ceramic Reserach Association, Stoke-on-Trent, 1975), pp. 123-134.
4. E. Fitzer and W. Remmele, in *Proc. 5th Intl. Conf. on Composite Materials, ICCM-V*, edited by W.C. Harrigan, Jr., J. Strife and A.K. Dhingra (TMS, Warrendale, PA , 1985) pp. 515-530.
5. H.E. Deve and M.J. Maloney, Acta Metall., **39**, 2275 (1991).
6. H.E. Deve, A.G. Evans, G.R. Odette, R. Mehrabian, M.K. Emilliani, and R.J. Hecht, Acta Metall., **38**, 1491 (1990).
7. H.E. Deve, C.H. Weber and M. Maloney, Mater. Sci and Engr., **A153**, 668 (1992).
8. P.J. Meschter, Scripta Metall., **25**, 521 (1991).
9. K.T. Venkateswara Rao, W.O. Soboyejo and R.O. Ritchie, Metall. Trans., **23A**, 2249 (1992).
10. L. Xiao and R. Abbaschian, Metall. Trans., **24A**, 403 (1993).
11. V.C. Nardone and J. R. Strife, Metall. Trans., **22A**, 183 (1991).
12. D.E. Alman and N.S. Stoloff, in *Proc. Symposium on Fatigue and Fracture of Intermetallic Alloys* (TMS, Warrendale, PA), to be published.
13. D.E. Alman and N.S. Stoloff, in Intermetallic Matrix Composites II, edited by D.B. Miracle, D.L. Anton and J.A. Graves (MRS, **273**, Pittsburgh, Pa, 1992), pp-247-252.
14. D.E. Alman, K.G. Shaw, N.S. Stoloff and K. Rajan, Mater. Sci. and Engr., **A155**, 85 (1992).
15. O. Kubaschewski and B.E. Hopkins, J. Less-Common Metals, **2**, 172 (1960).
16. T.C. Lu, J. Yang, A.G. Evans, R. Hecht, and R. Mehrabian, Acta Metall., **39**, 1883 (1991).
17. W.R. Manning, O. Hunter, Jr., F.W. Calderwood and D.W. Stacy, J. Am. Ceram. Soc., **55**, 323 (1972).
18. M.J. Maloney, DARPA/ONR program review, Pratt and Whitney Aircraft, W. Palm Beach, Fl. Feb 27, 1990.

Thermal Fatigue of $MoSi_2$ and a $MoSi_2$-10 vol% TiC Composite

M. T. KUSH, J. W. HOLMES* and R. GIBALA
The University of Michigan, Department of Materials Science and Engineering, Ann Arbor, MI 48109-2136 and *The University of Michigan, Department of Mechanical Engineering and Applied Mechanics, Ann Arbor, MI 48109-2125

ABSTRACT

Induction heating of disk shaped specimens was used to study thermal fatigue behavior of hot pressed $MoSi_2$, hot pressed and hot isostatically pressed (HIPed) $MoSi_2$, and a $MoSi_2$-10 vol% TiC particulate composite. Specimens were subjected to 5 s, 30 s, and 300 s heating and cooling cycles between temperature limits of 700°C and 1200°C. Specimens of both the hot pressed and the hot pressed and HIPed polycrystalline $MoSi_2$ material failed by transgranular cracking on the initial temperature ramp of the 5 s and 30 s cycles. Only when the severity of the thermal cycle was reduced (300 s heating/300 s cooling) was thermal fatigue cracking avoided in the HIPed $MoSi_2$. In sharp contrast, the $MoSi_2$-10% TiC composite remained uncracked when subjected to the severe 30 s heating/30 s cooling cycle. The fatigue results are discussed with reference to the initial microstructure of the specimens and the stress-strain history of the specimens which was obtained by a thermoelastic finite element analysis.

INTRODUCTION

$MoSi_2$, which has a high melting point (2030°C) and good oxidation resistance, has been used for many years as filament elements in high-temperature furnaces. These same properties make $MoSi_2$ an attractive material for future use in high temperature structural applications in the aerospace industry. It has a low density, 6.24 g/cm^3 compared to conventional nickel based alloys, approximately 8 g/cm^3[1]. The oxidation resistance of $MoSi_2$ is attributed to the formation of a protective SiO_2 scale [2].

Although thermal fatigue resistance and cyclic oxidation behavior are primary concerns for many high temperature applications, there is very little data available for these properties. Giler[3] reported that $MoSi_2$ furnace elements could be cycled without damage from room temperature to 1650°C for 20,000 cycles. However, no information was given regarding specific temperature ramp rates of the cycles of these experiments. Giler does state however, that upon reducing the diameter of the $MoSi_2$ heating elements from 6-18 mm to 3-6 mm, and insulating the elements, heat-up times of $MoSi_2$ element furnaces could be cut from several hours to as little as 5 minutes, and cool-down times reduced from 24 hours to 15 minutes without failure. Essentially, in reducing the diameter of the elements and insulating them, extreme thermal gradients could be avoided during their use in a furnace, thus improving thermal fatigue life.

The goal of the present paper was to develop more detailed data concerning the thermal fatigue resistance of $MoSi_2$ and a $MoSi_2$-10 vol% TiC composite. This research is needed to determine initial base-line data on the thermal fatigue life of $MoSi_2$ for potential applications such as gas turbine airfoils and advanced space vehicles, where thermal gradients will invariably be seen by this material.

EXPERIMENTAL PROCEDURE AND RESULTS

Materials

Polycrystalline $MoSi_2$ billets were prepared by powder processing. The billets were fabricated from -325 mesh powder obtained from Cerac, Incorporated, Milwaukee, WI. Hot

Mat. Res. Soc. Symp. Proc. Vol. 322. ©1994 Materials Research Society

pressing was performed uniaxially in grafoil-lined graphite dies in an argon atmosphere at 1700°C. The hot pressing was conducted for 1 hr at a pressure of 30 MPa. Several of the billets were additionally HIPed at 1700°C for 1 hr at a pressure of 200 MPa. The grain size and density of each of the billets are given in Table I. Microstructure analysis showed equiaxed grains and no evidence of texture.

For comparison with the $MoSi_2$, a $MoSi_2$-TiC composite was chosen. This composite was selected because of the relatively small coefficient of thermal expansion mismatch between the $MoSi_2$ matrix (8.6×10^{-6} at 1000°C) and the TiC particles (7.7×10^{-6} at 1000°C) [5], as well as the ability of TiC to deform plastically above it's DBTT of 600-800°C[6]. The $MoSi_2$-TiC particulate composites were prepared by powder processing techniques. TiC powders were obtained from Johnson Matthey Electronics, Ward Hill, MA. TiC powders of 2.5 - 4 μm size, which were close to stoichiometric ($TiC_{0.95}$), were dry blended in a ball mill for 24 hr with the $MoSi_2$ powder described above in proportions that provided a $MoSi_2$-10 vol% TiC composite.

Table I. Grain Size and Density of Each Sample Type.

Type	Condition	Grain Size μm	Density
$MoSi_2$	Hot Pressed	30	95 %
$MoSi_2$	Hot Pressed / HIPed	5	97 %
$MoSi_2$+10vol% TiC	Hot Pressed / HIPed	5	97 %

Test Specimens

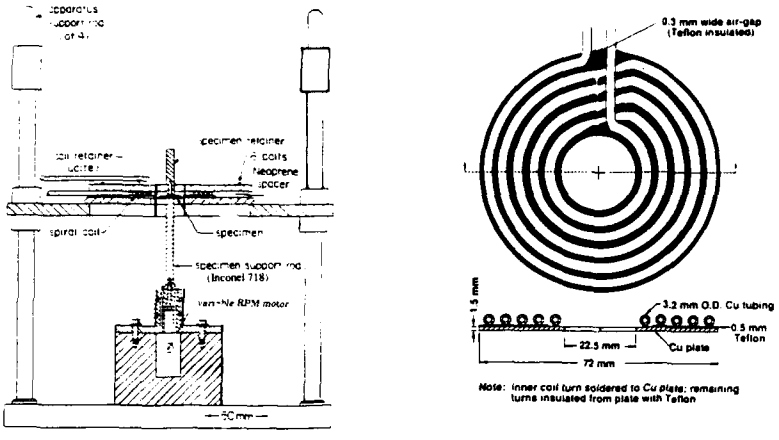
Each billet was centerless ground to 17.1 mm diameter, and disks of constant thickness of 1.8 mm were cut off of the billet by a diamond saw. Samples were mechanically polished to a 0.5 μm finish. A 1.85 mm diameter center hole was cut by a EDM (Electro Discharge Machining) technique.

Test Apparatus

Thermal fatigue was obtained by inductively heating 17.1 mm diameter disk-shaped specimens around their peripheries using a Lepel[1] 2.5 kw (450 kHz) induction generator coupled to a plate concentrator coil (see Figure 1). This technique relies upon the skin effect obtained with high frequency induction heating of metals, at 450 kHz the skin depth[2] obtained in $MoSi_2$ is approximately 0.5 mm. Under rapid heating, the shallow heating depth generates a radial temperature gradient from the specimen periphery to the cooler core. The concentrator coil was constructed with five turns of 3.2 mm diameter copper tubing. The base plate has a thickness of 1.5 mm and a 0.3 mm-wide radial air gap, which was insulated with teflon to prevent arcing. A microprocessor-based temperature controller was used to give automatic control of the induction generator power.

[1] Lepel Corporation Model T-2.5-1-KC1-B3W-T, supplied with a Research Incorporated Set-Point Programmer Model 73211.

[2] The skin depth (the depth at which the strength of the magnetic field falls to 0.3679 of its surface value) is given by $\delta = \frac{1}{2\pi}\sqrt{\frac{\rho}{\mu f}}$, where r = resistivity (abohm-cm), m = relative permeability (=1 for nonmagnetic materials), and f = frequency (Hz)[7].



1a 1b

Figure 1 Apparatus used for thermal fatigue testing of disk-shaped $MoSi_2$ specimens. (a) Schematic of test apparatus for studying thermal fatigue in air. (b) Schematic of concentrator coil.

Test specimens were positioned in the coil by placing it on a machined Inconel 718 support rod. By use of a motor, the support rod was rotated at 100 rpm during the experiments; this rotation minimizes any temperature differences around the specimen circumference caused by variations in the magnetic field intensity within the coil. This rate of spinning was also small enough to neglect effect of centrifugal stresses in the test specimens. A Mikron M78 infrared pyrometer was used to monitor the temperature of the test specimen. Pyrometer measurements agreed to within 1% of the temperature indicated by melting point standards applied to the specimen surface.

Temperature History

Test samples were subjected to two different temperature histories (see Figs. 2a and b). Figure 2a shows a 30 s heating cycle from 750°C to 1200°C, with a 30 s hold at 1200°C. followed by a convection cool for 30 s to 750°C, and a 30 s hold at 750°C. Figure 2b shows a 300 s heating from 800°C to 1200°C, with a 30 s hold at 1200°C, followed by a 300 s controlled cool to 800°C, and a 30 s hold at 800°C.

Finite-Element Modeling (FEM)

The elastic stress-strain history of the test specimens was determined using the finite element program ABAQUS[8]. For simplicity, the monolithic material was chosen to be modeled at this stage of the research. A 45° octant of the disk specimen was chosen for future modeling of the stress-strain history of composite material. The 136 element mesh used was made up of 8-node, bi-quadratic, plane-stress elements, each with nine integration points. Displacements in radial directions were constrained and shear stresses were set to zero to maintain symmetry.

Finite-Element Results

The circumferential periphery stress and strain histories for the temperature histories shown in Figs. 2a and b are given in Figs. 3a and b. The stress-strain hysteresis, which is far more pronounced in Fig. 3a, is caused by the transient thermal strains in the core relative to the periphery and not by material hysteresis. These strains differ in magnitude as a function of radius because of the nonuniform temperature and the change in elastic modulus with temperature.

THERMAL CYCLING RESULTS

All materials subjected to heating from 750°C to 1200°C in 5 s, followed by a free cool to 750°C, failed by transgranular cracking on the first heating cycle. From visual observations, the specimens failed when the temperature of the periphery had reached 800-1000°C. Periphery stress and strain were not modeled for such one cycle tests due to lack of accurate temperature history data.

Specimens of the hot-pressed $MoSi_2$ and hot-pressed and HIPed $MoSi_2$ that were subjected to heating from 750°C to 1200°C in 30 s, followed by a free cool to 750°C, also failed by transgranular cracking on the first heating cycle. Again, each specimen failed when the temperature of the periphery had reached 800-1000°C, which occurs during the first 8 to 20 s of heating. The circumferential stress along the periphery at this temperature was between 150 to 300 MPa (compressive); the corresponding stress along the inner radius was 200 to 300 MPa (tensile). In contrast to the $MoSi_2$ specimens, the $MoSi_2$-TiC composite remained uncracked even after 500 cycles.

All materials subjected to the 300 s heating and cooling cycles remained uncracked for the 500 cycle fatigue test. The stress-strain history of the periphery for this cycle is given in Fig. 3b. The peak stress along the inner radius of the specimen, from the FEM model, was 191 MPa (tension), and peak thermoelastic strain at the inner radius was 0.05%.

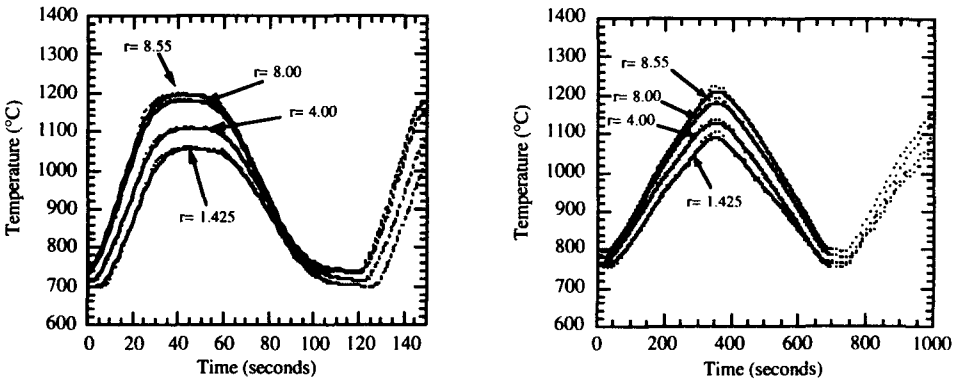


Figure 2. Temperature history of specimens used in thermal fatigue study. (a) 30s heating and 30 s cooling with 30 s hold at 1200°C. (b) 300 s heating and 300 s cooling with 30 s hold at 1200°C (all units in mm).

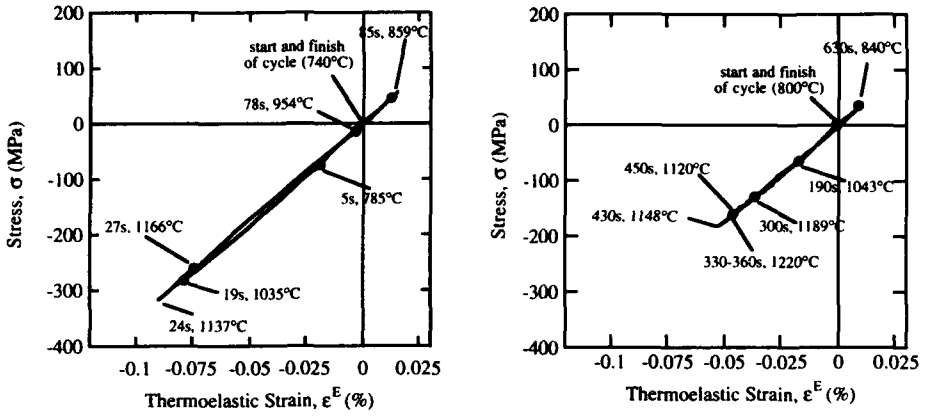


Figure 3. Circumferential stress-strain history along the periphery of disk shaped $MoSi_2$ thermal fatigue specimens. (a) 30 s heating and 30 s cooling with 30 s hold at 1200°C and (b) 300 s heating and 300 s cooling with 30 s hold at 1200°C.

When analyzing theses fatigue life data, it is important to examine related mechanical testing data. For example, Aikin reported, for a low purity $MoSi_2$ alloy, a yield stress in compression at 1000°C of 560 MPa[9]. For the same temperature, four-point bend test fracture strengths were reported to be 100 MPa. There has been no tensile strength data reported to date. Given that $MoSi_2$ is a crack sensitive material, tensile strengths would be expected to fall in this approximate stress range. During our thermal fatigue testing, the tensile stresses developed along the inner radius of the disk specimens are between 200 MPa and 300 MPa during initial heating to 800 to 1000°C for the 30 s cycle. This high tensile stress is sufficient to cause fracture along the inner radius, although fracture origins have not yet been determined. For the 5 s heating cycle, the thermal gradients are much larger, which makes the disks more sensitive to fracture. The stresses that develop along the inner radius during the 300 s cycle are near the tensile fracture strength, but apparently are not sufficient to cause fracture of the specimens.

The most significant finding of the current study is that the $MoSi_2$-TiC composite that was subjected to the 30 s heating and cooling cycle remained uncracked after the 500 cycle fatigue test. The TiC additions have obviously improved the thermal fatigue life of this material. We are currently focusing our attention on this material in an effort to identify the mechanism responsible for the enhanced thermal fatigue resistance. These results, along with more detailed studies of thermal fatigue mechanisms in $MoSi_2$ will be reported in future papers.

SUMMARY

Induction heating of disk-shaped specimens and finite element analysis of the thermal cycling data were used to study the thermal fatigue behavior of MoSi2 and a MoSi2-TiC composite, at various heating and cooling rates between 700°C and 1200°C. Monolithic MoSi2

failed upon initial heating in the first cycle except at the lowest heating rates employed. The MoSi2-TiC exhibited greatly improved thermal fatigue resistance at the much higher heating and cooling rate where a 30 s heating and cooling cycle was employed.

ACKNOWLEDGMENTS

The authors would like to acknowledge the support of this work provided by the AFOSR-URI Program, Grant No. F49620-93-0289.

REFERENCES

1. C.T.Sims and W.C.Hagel, The Superalloys, J. Wiley and Sons, Inc., 66 (1972).
2. J.B. Berkowtiz-Mattuck, and R.R.Dils, J. Electrochem. Soc., **112** [6] 583 (1965).
3. R.R. Giler, Metals Engineering Quarterly, **11,** 48 (1973).
4. J.W. Holmes, F.A. McClintock, K.S. O'Hara, and M.E. Connors, Low Cycle Fatigue,ASTM STP 942, H.D. Solomon et al., eds., ASTM, Philadelphia, PA, 672 (1987).
5. Y.S. Touloukian, R.K. Kirby, R.E. Taylor, and T.Y.R. Lee, Thermophysical Properties of Matter, IFI/Plenum, New York, NY, **13** (1973).
6. D. Miracle and H. Lipsitt, J. Am Ceram. Soc. **66**, 592 (1983).
7. P.G.Simpson, Induction Heating: Coil and System Design, McGraw-Hill Book Company, Inc., New York, 5 (1960).
8. ABAQUS Users Manual, Hibbitt, Karlsson, and Sorensen, Inc., Providence, R.I., (1982).
9. R.M. Aikin, Jr., Scripta Metall. Mater. **26**, 1025 (1992).

SURFACE OXIDATION MECHANISMS OF MOLYBDENUM DISILICIDE IN HIGH-TEMPERATURE COMBUSTION ENVIRONMENTS

WEN-YI LIN AND ROBERT F. SPEYER
School of Materials Science and Engineering, Georgia Institute of Technology, Atlanta, Georgia 30332

ABSTRACT

The stability of $MoSi_2$ was studied at 1600°C in combustion products with an incoming gas to air ratio of 1:6.7 and compared to results in a 1:10 environment. Oxidation was investigated using periodic weight measurements and characterization using XRD, SEM, and EDS. Passive oxidation was observed; $MoSi_2$ was oxidized by H_2O and CO_2 to form Mo_5Si_3 and SiO_2. The amorphous silica product formed a surface layer and reduced the oxidation rate as it coarsened. $MoO_{3(g)}$ did not form which was in agreement with the thermodynamic (SOLGASMIX-PV) prediction that it would only form in the presence of molecular oxygen. A good agreement was observed between the measured and calculated weight gains based on the surface layer thickness.

INTRODUCTION

Molybdenum disilicide is a valuable material for a variety of high-temperature applications, given its high melting point and excellent oxidation resistance[1]. Numerous studies on the oxidation of $MoSi_2$ in O_2, air, or oxygen-inert gas atmospheres have been reported[2]-[7]. However, combustion products ($CO_{2(g)}$ and $H_2O_{(g)}$) corrosion of $MoSi_2$ has not as yet been thoroughly evaluated. Combustion environments are commonly encountered in a wide variety of industrial applications, such as glass melting and metal heat treating.

$MoSi_2$ has demonstrated distinctly different oxidation behavior depending on oxygen partial pressure and temperature. At high temperature and oxygen partial pressure, e.g. 1420°C and $>10^4$ Pa, it has been reported to oxidize to form volatile molybdenum trioxide and amorphous silica[4]. Continued exposure leads to the formation of a silica surface layer through which molecular oxygen must diffuse. As the protective coating coarsens, the oxygen concentration gradient is reduced and thus oxidation is retarded. This is referred to as a passive oxidation behavior.

Below 600°C (at 10^5 Pa of dry oxygen), the sublimation of solid MoO_3 is limited, which in turn inhibits the formation of a continuous glassy surface layer of SiO_2[5]. The formation of $MoO_{3(s)}$ in microcracks has been argued to extend them, ultimately turning the material to powder[6]. This has been referred to as $MoSi_2$ pest. At low oxygen partial pressure (< 266 Pa), molybdenum disilicide oxidizes to form SiO gas, instead of SiO_2 glass[7], wherein no protection against further oxidation is provided by the oxidation product (SiO gas). This process is referred to as active oxidation. Silicon monoxide gas has also been shown to form a significant partial pressure above 1700°C and at an oxygen partial pressure of 1330 Pa, resulting in ruptured surface layers[7].

In our previous work[8], the stability of $MoSi_2$ exposed to combustion products at a natural gas to air ratio of 1:10 ("stoichiometric") at 1370° and 1600°C was investigated. The current work focuses on a combustion environment with an excess of natural gas ("rich") in order to understand the effects of a less oxidizing atmosphere on surface layer formation.

Mat. Res. Soc. Symp. Proc. Vol. 322. ©1994 Materials Research Society

EXPERIMENTAL PROCEDURE

SOLGASMIX-PV[9], used in an earlier study[8], was utilized to simulate the phase equilibria between combustion products and materials as a function of natural gas to air ratio at 1600°C. In addition to the original JANAF database[10], some thermodynamic data were obtained from F*A*C*T (Facility for the Analysis of Chemical Thermodynamics)[11]. Excessive natural gas and air relative to the solid phases were used as input for the simulation to best emulate the reactions amongst a flowing gas and a test coupon. The input data for the starting composition of natural gas is listed elsewhere[8].

Test specimens were cut from a $MoSi_2$ rod (Kanthal Super 33) and then polished with 600-grit SiC abrasive paper and subsequently with 1 μm diamond paste. The specimens were cleaned in ultrasonic deionized water baths and dried before testing. Two flow meters were utilized to control the flow rates of air and natural gas so that the ratio of 1:6.7 was maintained. A burner was used to generate combustion products which propagated through a mullite tube chamber. The central portion of the mullite tube was maintained at 1600°C in a controlled fashion (Innovative Thermal Systems) using a $MoSi_2$ resistance heating element furnace. A mass spectrometer (Ametek Dycor Quadropole Gas Analyzer) with a fused silica capillary was used to analyze the chamber atmosphere. A platinum-10% rhodium wire was used to suspend a reticulated alumina basket where the sample was set during the test.

Independent specimens for each exposure time were used to minimize the effects of spalling of SiO_2 layers with repeated thermal cycles with the same specimen. After exposure, each specimen was weighed using a digital balance (Mettler AE-240) with a resolution of 0.01 mg. The exposed surface areas were determined by dimensional measurements of rectangular specimen wafers using a calipers with a measurement precision of 0.01 mm.

The crystalline phases of the sample surfaces before and after exposure were investigated using an X-ray diffractometer (XRD, Philips PW1800) with a time constant of 1 second and a step size of 0.015°. The samples were then cut in half and polished without etching. Surface microstructures were examined using the secondary electron detector of a scanning electron microscope (SEM, Hitachi S-800). Elemental compositions were analyzed using an energy dispersive spectrometer (EDS, Kevex 3600-0398).

RESULTS AND DISCUSSION

Thermodynamic Modeling

The products of simulated stoichiometric combustion at 1600°C are 17.8 mol% H_2O, 8.7 mol% CO_2, 0.3 mol% H_2, and 0.6 mol% CO. The calculated equilibria for a rich mixture is 15.6 mol% H_2O, 3.9 mol% CO_2, 0.8 mol% H_2, and 8.6 mol% CO. The rich mixture favors limited H_2 and CO partial pressures at the expense of H_2O and CO_2. Figure 1 shows the calculated product phases as a function of temperature when $MoSi_2$ is exposed to rich combustion products. $Mo_{(s)}$ is predicted to form above 1322°C and $MoO_{2(s)}$ is no longer present above 1395°C. The amount of $SiO_{(g)}$ and $MoO_{3(g)}$ formed is everywhere negligible. This indicates that the weight loss due to MoO_3 gas release would not be expected.

Figure 2 shows the reaction products for various natural gas to air ratios at 1600°C. The following groups of oxidation products of $MoSi_2$ in combustion gas are calculated to form with increasing input air: (1) Mo_5Si_3 + SiC + $SiO_{(g)}$ at ratios of 1:1 to 1:2, (2) Mo + $SiO_{2(s)}$ at ratios of 1:3 to 1:6.7, (3) MoO_2 + $SiO_{2(s)}$ at ratios of 1:9 to 1:10, and (4) $MoO_{3(g)}$ + $SiO_{2(s)}$ at ratios of 1:10 to 1:19. $SiO_{(g)}$ plays an important role in the $MoSi_2$-natural gas-air system only when the gas-air ratio is between 1:1 and 1:3; at other ratios, the

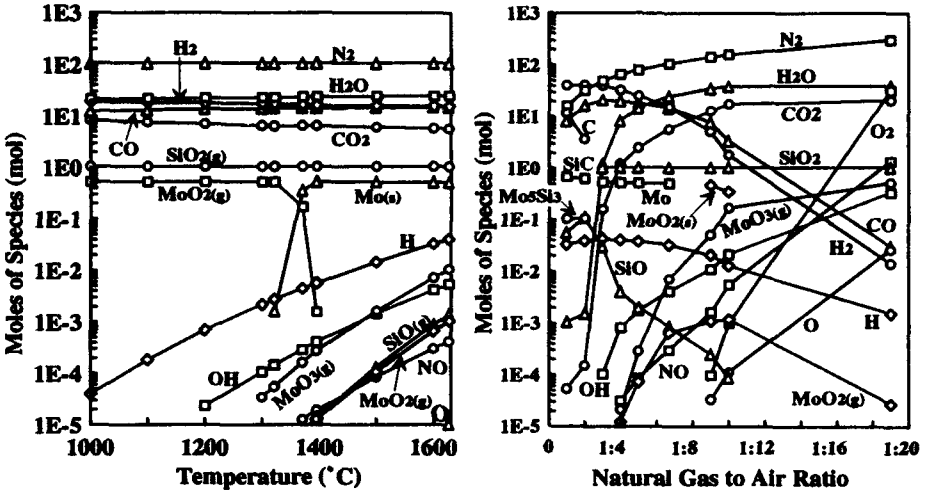


Figure 1: (left) Simulated phase equilibria between $MoSi_2$ and combustion products at a natural gas to air ratio of 1:6.7.

Figure 2: (right) The equilibrium phases in the $MoSi_2$-natural gas-air system at 1600°C with varying gas-air ratios.

amount of $SiO_{(g)}$ is negligible. The above was based on theoretical calculations; however, for practical combustion, only gas-air ratios between 1:4.3 and 1:15 are important, since this range represents the flammability limit of natural gas and air[12].

Combustion Gas Corrosion

The changing percentages of combustion products can be inferred from the mass spectra shown in Figure 3. The peak corresponding to molecular oxygen appears in the spectrum of 1:10 ratio. At a gas to air ratio of 1:6.7, a H_2^+ peak is [illegible]y observed. A clear trend of decreasing H_2 concentration and increasing CO_2 conce[illegible] is apparent with increasing air content in the combustible mixture. Trends in CO [illegible]tration are less certain and direct because of peak overlap with molecular nitrogen. Analysis of gas mixtures with excess natural gas to the point of being below the flammability limit showed spurious spectra due to incomplete reaction.

XRD traces of specimens after exposure for various times were taken (not shown). Based on relative peak heights, amorphous silica (indicated by the vitreous hump), and the Mo_5Si_3 to $MoSi_2$ ratio, increased with exposure time, while the Mo_5Si_3, $MoSi_2$, and cristobalite peak intensity decreased. After 66.5 hours of exposure, the amorphous layer coarsened to the point where the cristobalite peak could not be seen above the amorphous hump in the XRD pattern. No Mo, Mo_3Si, or MoO_2 were detected.

As shown in Figure 4, after 3.8 hours of exposure, a uniform and continuous surface layer (~8.4 μm) of glassy silica was observed. Dispersed cristobalite islands are expected to reside within the amorphous silica surface layer. A discontinuous layer of Mo_5Si_3 formed at the edge of the bulk in contact with the surface layer. After an exposure for 6 hours, the silica surface layer thickness increased to 10.7 μm. After 66.5 hours of exposure, the silica

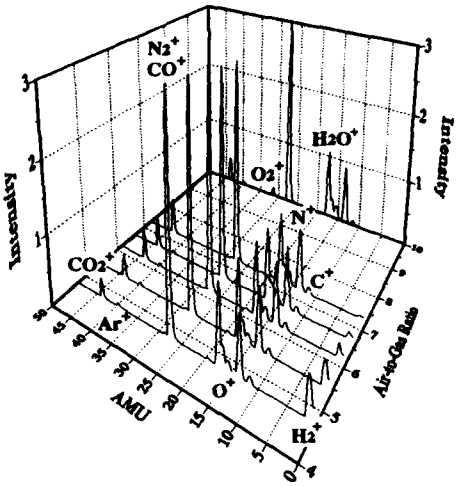




Figure 3: (left) Mass spectra of combustion products at various gas/air ratios.

Figure 4: (right) The microstructure of $MoSi_2$ in a rich environment at 1600°C for 3.8 hours.

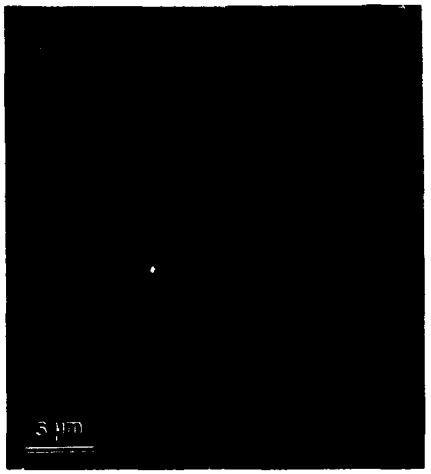
coating thickness increased to 15.5 μm and the interfacial layer of Mo_5Si_3 also coarsened and became nearly continuous, as shown in Figure 5. Comparison of Figures 4 and 5 shows that aluminosilicate pockets had consolidated with increasing exposure time.

Figure 6 shows that $MoSi_2$ gained weight with a corresponding coarsening of the silica coating with exposure. However, the slopes of both curves decreased with exposure time. By comparison, a retarded weight gain for $MoSi_2$ exposed to stoichiometric combustion gas can be seen. In previous work[8], the weight change curve for $MoSi_2$ exposed to stoichiometric combustion products consisted of a very rapid weight loss, followed by a gradual weight gain. Since the net weight gain portion initiated after less than one minute, it could not be shown in the curve in Figure 6. It was demonstrated that the weight loss portion corresponded to the formation of $MoO_{3(g)}$ as well as SiO_2. The loss of molybdenum in the form of oxide gas was the cause of initial net weight loss. As a result, as compared to the rich mixture, a given weight gain for the stoichiometric mixture corresponded to a coarser amorphous coating. For example, after 60 hours in stoichiometric combustion products, the coating thickness was measured to be ~19 μm, whereas after 60 hours in rich products, the coating thickness was only ~15.3 μm. SOLGASMIX-PV modeling shows that $MoO_{3(g)}$ forms only in presence of O_2. Molecular oxygen would not be expected for perfect stoichiometric combustion; however, Figure 3 indicates the presence of O_2 in the gas-air mixture intended to form the products of stoichiometric combustion. This oxygen was undoubtedly present as a result of outside air flow into the testing chamber.

The presence of the Mo_5Si_3 interface contrasted with the thermodynamic simulations predicting the formation of $Mo_{(s)}$ as a reaction product, i.e.,

$$MoSi_2 + 4H_2O \text{ (or } 4CO_2) \longrightarrow Mo + 2SiO_2 + 4H_2 \text{ (or } 4CO). \quad (1)$$

In reality, only local equilibria were achieved. The formation of the silica layer provided a kinetic diffusion barrier for soluble molecular gases such that the molecular water vapor and



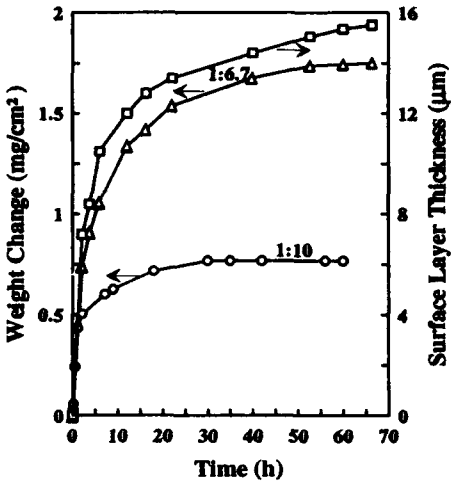


Figure 5: (left) After 66.5 hours of exposure at 1600°C to rich combustion products, an interfacial layer Mo_5Si_3 formed between $MoSi_2$ and SiO_2.

Figure 6: (right) Variation in weight per unit exposed area and silica coating thickness of $MoSi_2$ specimens exposed at 1600°C to rich combustion products (denoted by 1:6.7). The 1:10 annotation indicates the weight gain curve for $MoSi_2$ exposed to stoichiometric combustion products at 1600°C.

carbon dioxide activity at the $MoSi_2/SiO_2$ interface continued to be lowered. The thermodynamic modeling assumed access of a near-infinite quantity of gaseous oxidizing species to come in contact with $MoSi_2$, resulting in complete oxidation of the silicon component of the compound. When the oxygen contributing gas activity is very low, the reaction most conservative in the use of oxygen is favored[8], e.g.

$$5MoSi_2 + 7H_2O \text{ (or } 7CO_2) \longrightarrow 7Mo_5Si_3 + 7SiO_2 + 7H_2 \text{ (or } 7CO). \quad (2)$$

As the silica coating coarsened, consuming silicon at the Mo_5Si_3/SiO_2 interface, no Mo_3Si was detected using XRD. Due to the high mobility of silicon, the Mo_5Si_3 interface coarsened by conversion of $MoSi_2$ to Mo_5Si_3, providing diffusing silicon to the Mo_5Si_3/SiO_2 interface to form SiO_2. Until oxidation could occur to the point where all $MoSi_2$ would be converted to Mo_5Si_3, the formation of Mo_3Si would not be expected.

From the surface layer thickness of $MoSi_2$ exposed in a rich combustion environment for 3.8 hours and given an amorphous silica density of 2.2 g/cm^2, a weight gain of 0.99 mg/cm^2 as a result of oxygen uptake in the form of silica is calculated. This agrees with the measured weight increase 0.91 mg/cm^2 of the specimen in Figure 6 (within measurement variation in coating thickness). Similar calculations of weight gain from silica coating thickness after various exposure times showed a good agreement with the measured value. This implies that the oxygen uptake to form silica and Mo_5Si_3 was the only mechanism of silica layer formation.

The presence of Mo_5Si_3 between $MoSi_2$ and SiO_2 throughout the evaluated exposure period contrasts with the microstructures of $MoSi_2$ specimens exposed in a stoichiometric combustion environment at 1600°C for 60 hours[8]. Under stoichiometric combustion products, Mo_5Si_3 which initially resided at the interface (after $\sim$1 hour) was converted

back to $MoSi_2$ after exposure for 60 hours. In that work, it was interpreted that mobile silicon caused the interfacial Mo_5Si_3 to shrink in favor of the growth of large Mo_5Si_3 islands in the bulk, based on minimization of surface energy arguments. This would occur after the Mo_5Si_3-SiO_2 interface was no longer a sink for silicon (e.g. oxidation to coarsen the silica layer became negligible). Exposed to rich combustion products, after 60 hours, the coarsening of the silica layer continued (weight gain did not yet flatten out for the 1:6.7 curve in Figure 6). Thus, the microstructure after 60 hours of exposure to rich combustion products is considered to be commensurate to one hour of exposure to stoichiometric combustion products insofar as microstructural evolution is concerned.

CONCLUSION

Notwithstanding the presence of molecular hydrogen in the rich combustion products, $MoSi_2$ was still oxidized at 1600°C. The oxidation mechanism differed from that in stoichiometric combustion products in that an initial stage of surface oxidation to form $MoO_{3(g)}$ and SiO_2 did not occur. This passive oxidation revealed that the oxygen affinity of $MoSi_2$ was high enough to compete with H_2 and CO for oxygen. The diminishing oxidation rate with exposure time suggests that $MoSi_2$ may be used for a variety of high-temperature industrial applications involving combustion products of gas and air at a ratio of 1:6.7.

ACKNOWLEDGEMENT

This work was supported by The Gas Research Institute. Contract No. 5090-298-2073.

References

[1] A.K. Vasudévan and J. J. Petrovic, Mater. Sci. Eng. **A155,** 1 (1992).

[2] J.Y. Hsu, S.K. Sundaram, W.-Y. Lin, and R.F. Speyer, in Advances in Fusion and Processing of Glass, edited by A.K. Varshneya, D. Bickford, and P.P. Bihuniak (American Ceramic Society, Ohio, 1993) p. 73.

[3] W.-Y. Lin, J.Y. Hsu, Y.B. Berta and R. F. Speyer, Part I, accepted for publication in Am. Ceram. Soc. Bull., 1994.

[4] J.B. Berkowitz-Mattuck, M. Rossetti, and D.W. Lee, Metall. Trans. **1,** 479 (1970).

[5] R.W. Bartlett, J.W. McCamont, and P.R. Gage, J. Am. Ceram. Soc. **48,** 551 (1965).

[6] E. Fitzer, in Corrosion and Corrosive Degradation of Ceramics, edited by R.E. Tressler and M. McNallan (American Ceramic Society, Ohio, 1990) p. 19.

[7] J.B. Berkowitz-Mattuck, J. Electrochem. Soc. **112,** 583 (1965).

[8] W.-Y. Lin, J.Y. Hsu, and R. F. Speyer, submitted to J. Am. Ceram. Soc. for publication, 1993.

[9] G. Eriksson, Chem. Scr. **8,** 100 (1975).

[10] M.W. Chase, Jr., C.A. Davies, J.R. Downey, Jr., D.J. Frurip, R. A. McDonald, and A.N. Syverud, JANAF Thermochemical Tables, 3rd ed. Parts I and II, (American Chemical Society, Washington DC, 1985).

[11] W.T. Thompson, A.D. Pelton, and C.W. Bale, Calphad. **7,** 113 (1983).

[12] R.J. Reed, North American Combustion Handbook, Vol. I, 3rd ed. (North American Mfg. Co., Ohio, 1986) p. 12.

ELECTROCHEMICAL PROTECTION OF MOLYBDENUM AND MOLYBDENUM DISILICIDE IN MOLTEN SODA-LIME-SILICATE GLASS ENVIRONMENT

S. KAMAKSHI SUNDARAM AND ROBERT F. SPEYER
School of Materials Science and Engineering, Georgia Institute of Technology, Atlanta, GA 30332-0245, USA

ABSTRACT

Electrochemical corrosion of Mo and $MoSi_2$ in a molten soda-lime-silicate glass environment was studied using a two electrode cell with Pt as the counter electrode. XRD, SEM, and EDS were used to characterize the corroded specimens. When Mo was given a cathodic bias ($\sim$ 0.8V), the specimen surface oxidized to $MoO_{2(s)}$. With reverse bias, Mo ions were interpreted to have been removed into the glass melt. For $MoSi_2$, Mo_5Si_3 interfacial layers were observed for both cathodic and anodic corrosion. Mo_5Si_3 debris particles ($\sim$4 μm) were seen floating into the glass en masse under a cathodic bias, but not when the bias was reversed. This was interpreted to be a result of an inherent negative charge of debris particles.

INTRODUCTION

Molybdenum and less commonly molybdenum disilicide have been used as electrode materials for electric melting of glass[1]. A functional gradient of these materials is under development for gas-fired immersed combustion tubes for glass melting[2]. In previous work, the surfaces of immersed molybdenum were found to react sluggishly with molecularly soluble oxygen to form $MoO_{2(s)}$, while molybdenum disilicide reacted somewhat more rapidly with molecularly soluble oxygen to form Mo_5Si_3 and SiO_2[3]. The electrolytic nature[4] of molten glass and its effects on redox ions[5], oxygen reboil[6], its ionic behavior[7] and the electrodics of glass[8] have been previously studied.

Balazs and Russel[9] studied the corrosion rate of molybdenum electrodes in soda-lime-silicate glass melts using an electrochemical cell with three electrodes, viz., molybdenum, platinum, and ZrO_2/air reference electrode. Current-potential curves showed active and passive potential regions. Under an extremely cathodic potential (-1 to -2 V), the glass melt was claimed to have decomposed, and a $MoSi_x$ layer was formed on the Mo surface. The formation of $MoSi_x$ was experimentally supported by EDS/WDS data only. There is no literature regarding electrochemical studies of molybdenum disilicide corrosion in a molten glass environment. In the present paper, the effects of bias potential on the mechanism of glass corrosion of these materials are presented.

EXPERIMENTAL PROCEDURE

Molybdenum (Johnson Matthey/AESAR) specimens (semi-cylindrical) were of 12.5 mm diameter by 6.25 mm length for the purpose of complete immersion, to avoid oxidation of molybdenum in air. Chemical analyses for trace elements in as-received molybdenum showed less than 1 ppm of Al, Ca, Cr, Cu, Mg, Mn, Ni, Pb, Si, Sn, and Ti, less than 2 ppm of C and O, and less than 14 ppm of Fe. Cylindrical specimens of $MoSi_2$ (Kanthal Super 33) of 3 mm diameter by 420 mm length (U-shaped heating element cut in half) were used. The as-received $MoSi_2$ contained a $\sim$7.5μm thick fused silica surface layer. In the specimen bulk, 1.7 vol% Mo_5Si_3 grains were generally in contact with amorphous aluminosilicate glassy pockets, which in turn, comprised 18.6 vol% of the specimen[10].

Mat. Res. Soc. Symp. Proc. Vol. 322. ©1994 Materials Research Society

Soda-lime-silicate glass was prepared starting from analytical grade chemicals. The glass composition (in wt%) consisted of 73.3% SiO_2, 13.3% Na_2O, 11.0% CaO, 1.5% Al_2O_3, 0.3% K_2O, 0.2% MgO, and 0.2% ZrO_2. The starting materials, SiO_2, Na_2CO_3, Al_2O_3, K_2CO_3, $MgCO_3$ (Analytical Reagent Grade, Fisher Scientific Chemicals), CaO (Analytical Reagent Grade, J. T. Baker Chemical Co.), and ZrO_2 (High Purity Grade, Zirconia Sales Inc.), were mixed in a suitable ratio using a clean mortar and pestle. The mixed powder was transferred to a platinum crucible maintained at 1550°C in an electric furnace. The melt was allowed to equilibrate first at that temperature for 4 hours and then at 1600°C for 1 hour before it was poured into a graphite mold for quenching. The quenched glass was crushed (mortar and pestle) into -40 mesh powder and 48.5 grams of the glass powder was put into a fused-cast AZS (alumina-zirconia-silica) crucible (UNICOR51, Corhart Refractories Corp.). The AZS crucible was chosen since Si from the $MoSi_2$ would otherwise dissolve into the glass melt and alloy with a platinum crucible. The experiments were completed within 12 hours to avoid any contamination of the melt due to interaction with corrosion products of the AZS[3]. The molybdenum specimens were suspended into the melt using a Pt wire. Molybdenum disilicide specimens were introduced into the melt from the top of the furnace so that the electroded end was outside the furnace for connecting to leads. Pt wire was used as counter electrode and was protected by mullite sleeves.

The electrode leads were connected to an operational amplifier (1 A max., LH0021C, National Semiconductor Corp.) powered by a dual voltage dc power supply ($\pm$ 15 V, 700 mA, Sola Inc.). The opamp received dc voltage instructions from a personal computer through a 16 bit A/D–12 bit D/A plug-in board (CIO-DAS1600, Computer Boards, Inc.). The open circuit voltage (OCV) between the two electrodes was first measured. A known potential was then applied between the specimen and the Pt counter electrodes. The potential was ramped to the maximum value over a 1 hour period, and held at that potential for 4 hours. This procedure was repeated with the applied potential reversed. The potential and current were measured using the computer A/D as voltmeter and an external high precision microammeter (Keithley 196DMM), respectively.

The cross-section of the glass-coated corroded specimens were ground progressively on 120, 240, 320, 400, and 600μm abrasive papers and polished using 1μm diamond paste. The polished surface was etched using a 1% HF solution for 30 seconds for topographic contrast. The specimen-glass interfaces were characterized using scanning electron microscopy (SEM, Hitachi S-800). Energy dispersive spectroscopy (EDS Kevex 3600-0398) was used to determine the chemistry at and around the interfacial regions. A flat corroded surface of Mo was characterized using x-ray diffraction (XRD, Philips PW1800). The XRD pattern was matched with patterns available in JCPDS database, and the corrosion products were identified.

RESULTS AND DISCUSSION

Molybdenum

The open circuit rest potential of Mo/soda-lime-silicate glass/Pt cell was 762 mV in one case and 628 mV in another (Mo acting as anode). Figure 1 shows the I-V characteristics of the cell. The measured cell voltages and currents saturate at applied voltages of +0.377 V and -0.339 V.

Under a cathodic potential, a discontinuous interfacial layer was observed on molybdenum as shown in Figure 2a. This layer was identified using XRD as MoO_2. The lattice mismatch between Mo and MoO_2 causes the MoO_2 to crack away, allowing glass to attack

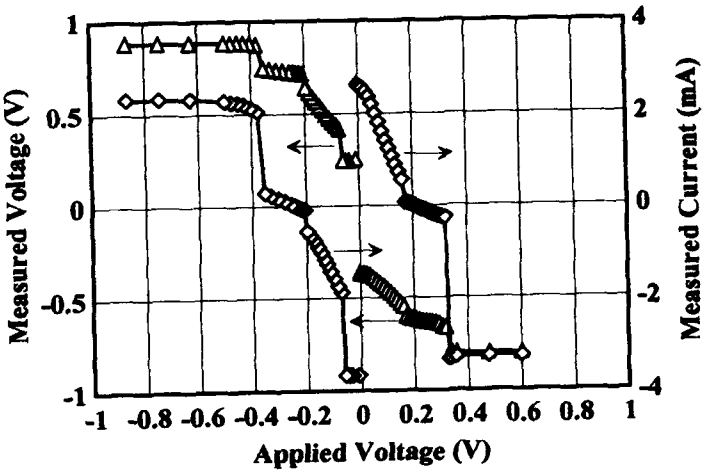


Figure 1: I-V characteristics of Mo/soda-lime-silicate glass/Pt cell. Positive applied voltage indicates positive potential applied to Mo.

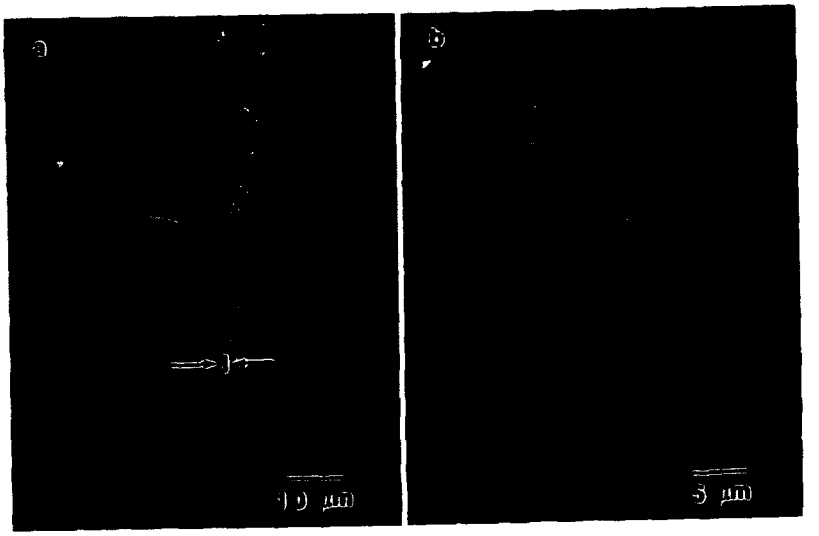


Figure 2: Mo-glass interface under (a) cathodic potential and (b) anodic potential. I: MoO_2 interface.

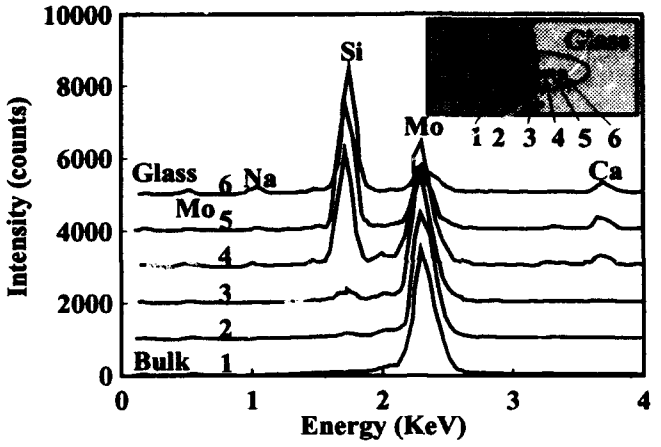


Figure 3: EDS spectra of Mo specimen corroded under anodic potential

freshly exposed Mo[3]. When the potential was reversed, a serrated Mo surface is apparent, as shown in Figure 2b. XRD showed only Mo peaks from the interface. Multiple EDS scans, analyzing in steps from the Mo bulk, through to the adjacent glass, are shown in Figure 3. Approaching the Mo/glass interface from the Mo bulk, an increase in silicon content is indicated. Considering the electron interaction volume, these Si peaks cannot be argued to be due to formation of a silicide phase, since contributions from the glass are expected. Since the Mo surface texture implies removal of material rather than plating out, and there was no XRD evidence of a Mo-Si compound on the surface, the conclusion of Balazs and Russel[9] cannot be supported.

It is interpreted that under anodic potential, Mo surface metal was converted to molybdenum ions which dissolve into the glass. Under a cathodic potential, there is a tendency against ionization of Mo. The current measured under these conditions is interpreted to be a result of forming molecular oxygen from dissolved oxygen ions at the anode and dissolving molecular oxygen into ions at the cathode. In this case, soluble molecular oxygen coming in contact with the cathode has the option of reacting with neutral Mo, or being converted to O^{2-}. This may be a viable mechanism of corrosion protection for molybdenum.

Molybdenum Disilicide

The open circuit rest potential of $MoSi_2$/soda-lime-silicate glass/Pt cell was -894 mV in one case and -970 mV in another ($MoSi_2$ acting as anode). $MoSi_2$/soda-lime-silicate glass/Pt cell. Similar to molybdenum, the voltage and the current flatten out indicating polarization of these electrodes.

Figures 5a and 5b show the $MoSi_2$-glass interfaces under cathodic and anodic bias, respectively. In both cases, $MoSi_2$ near the surface converted to Mo_5Si_3. The Mo_5Si_3 interfacial layer observed in both cases was confirmed by XRD and SEM-EDS. In other work[3] where no potential was applied, it was shown that molecularly dissolved oxygen in the glass melt reacted with $MoSi_2$ to form Mo_5Si_3 and SiO_2. The formation of Mo_5Si_3 in this work is taken to be impassive to the bias potential, since it is a reaction product of

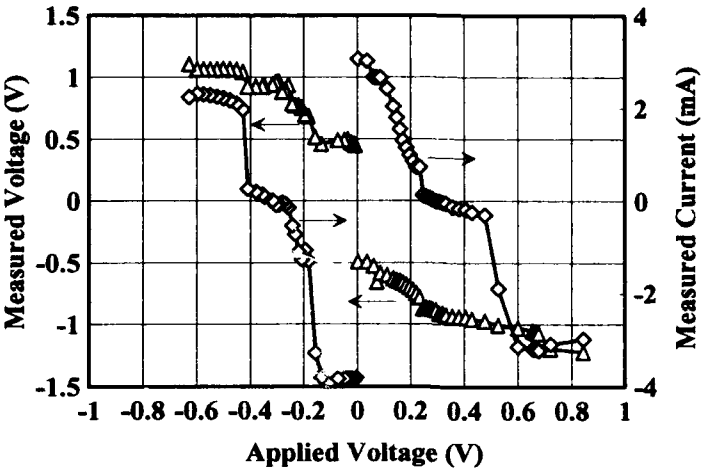


Figure 4: I-V characteristics of $MoSi_2$/soda-lime-silicate glass/Pt cell. Positive applied voltage indicates positive potential applied to $MoSi_2$.

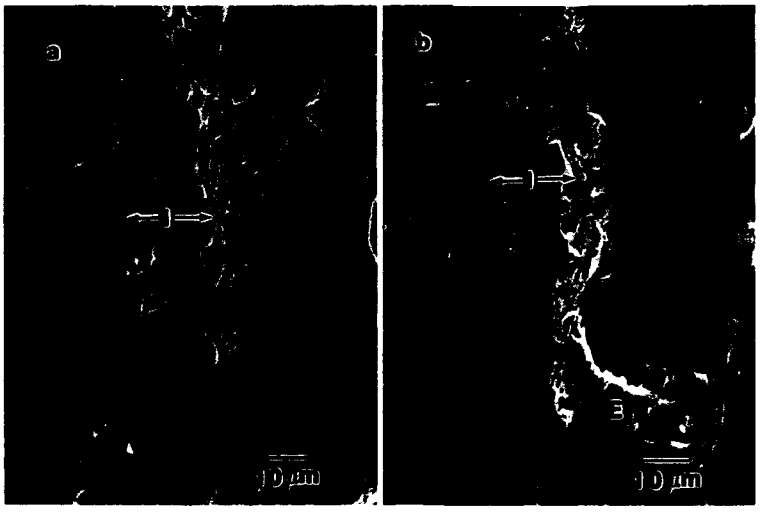


Figure 5: $MoSi_2$-glass interface under (a) cathodic potential and (b) anodic potential; I: interface, E: Mo-Si extension (see text).

molybdenum disilicide and molecular oxygen, rather than ions in solution. The saturation current and voltages in Figure 4 (as well as Figure 1) represent the maximum rate of ionization of molecular oxygen or rate of combination of dissolved oxygen ions. In the case of the anodically corroded specimen, the interfacial layer appeared to remain intact to the electrode. Extensions of Mo-Si compounds were seen (by EDS) protruding periodically from the specimen surface (see marker "E" in Figure 5b). By contrast, under cathodic bias, a significant density of $\sim$4 μm Mo-Si particles (interpreted as Mo_5Si_3) are seen floating into the glass as debris. Based on the available evidence, it is interpreted that these Mo_5Si_3 particles adopted a negative surface charge in glass, wherein they would be attracted to the $MoSi_2$ electrode if anodically biased, and repelled if it were cathodically biased. On this basis, although $MoSi_2$ in molten glass may not be protected from oxidation (by molecular oxygen) by a bias in the traditional sense, protection in the form of debris control is feasible. By attracting Mo_5Si_3 debris back to the corroding material, further corrosion by molecular oxygen may be slowed. Confirmation of this conjecture is in progress in our laboratory.

CONCLUSIONS

The application of a bias potential to Mo or $MoSi_2$ in molten glass does not halt their corrosion, since the mechanism of neutral corrosion does not involve ions in glass. Rather, both involve oxidation of the metal by molecularly soluble oxygen. Further, protection by applying an anodic bias to $MoSi_2$ may be feasible based on attraction of charged debris to the electrode which would slow further oxidation. Protection by applying a cathodic potential may nonetheless be feasible by conversion of local soluble molecular oxygen to oxygen ions, rather than reaction between molecular oxygen and Mo to form a MoO_2 scale.

ACKNOWLEDGEMENT

The financial support by Gas Research Institute (Contract No. 5090-298-2073) is acknowledged.

References

[1] W. Trier, Glass Furnaces, (Society of Glass Technology, Sheffield, 1987), p. 207.

[2] J.-Y. Hsu, S. K. Sundaram, W.-Y. Lin, and R. F. Speyer, in Advances in Fusion and Processing of Glass, edited by A. K. Varshneya, D. Bickford, and P. P. Bihuniak (American Ceramic Society, Ohio, 1993) p. 73.

[3] S. K. Sundaram, J.-Y. Hsu, and R. F. Speyer, accepted for publication in J. Am. Ceram. Soc., October, 1993.

[4] Information circular of the Institute of Silicate Research, The Glass Industry, **35**, 433 (1954).

[5] G. E. Rindone, E. C. Marboe, and W. A. Weyl, J. Am. Ceram. Soc., **30**, 314 (1947).

[6] J. H. Cowan, W. M. Buehl, and J. R. Hutchins, III, J. Am. Ceram. Soc., **49**, 559 (1966).

[7] K. Takahashi and Y. Miura, J. Non-Crystalline Solids, **80**, 11 (1986).

[8] K. Takahashi and Y. Miura, J. Non-Crystalline Solids, **38-39**, 527 (1980).

[9] G. B. Balazs and C. Russel, J. Non-Crystalline Solids, **105**, 1 (1988).

[10] W.-Y. Lin, J.-Y. Hsu, and R. F. Speyer, submitted to the J. Am. Ceram. Soc., 1993.

MICROSTRUCTURE AND MECHANICAL PROPERTIES OF NITRIDED MOLYBDENUM SILICIDE COATINGS.

J-P. Hirvonen, I. Suni, and H. Kattelus, Technical Research Centre of Finland, FIN-02151 Espoo, Finland; *R. Lappalainen and P. Torri,* FIN-00014 University of Helsinki, Finland, *H. Kung, T.R. Jervis, and M. Nastasi,* Los Alamos National Laboratory, Los Alamos, NM 87545, USA.

ABSTRACT

Mo-Si-N films with a high nitrogen concentration were produced by sputter-deposition in the presence of nitrogen plasma. The chemical composition was determined with Rutherford backscattering and nuclear reaction analysis. The ratio of Mo to Si was 1:2 in the coatings with a nitrogen concentration of 50 %. The microstructure of the as-deposited coatings on a silicon substrate was amorphous and no crystallization was found after annealing up to 1000 °C, although some relaxation was observed in X-ray diffraction. This was confirmed in high-resolution transmission electron microscope examination. The hardness of the Mo-Si-N films was 18.8 GPa as determined with a nanoindenter. This is significantly higher than that of $MoSi_2$ films, 11.2 GPa. The hardness of the Mo-Si-N films increased to 24.4 GPa after annealing at 800 °C, which is approximately the same as the hardness of the high-temperature tetragonal phase of $MoSi_2$, 25.5 GPa. Similarly, the modulus of the as-deposited Mo-Si-N film was higher (257 GPa) than that of the $MoSi_2$ film (222 GPa). However, only a slight increase in the modulus of the Mo-Si-N film was found after annealing at 800 °C, whereas the modulus of the crystallized tetragonal $MoSi_2$ was 382 GPa. No cracking was found in the Mo-Si-N films even after annealing at 1000 °C.

INTRODUCTION

The excellent oxidation resistance of molybdenum disilicide ($MoSi_2$) is widely known, as is its lack of ductility at low temperatures [1]. This disadvantage restricts the extensive use of $MoSi_2$ as a structural material. When applied as a coating, a more ductile base material can be used, and in this way the problem may be partly avoided. However, thermal stresses due to a mismatch of thermal expansion coefficients may result in cracking which will eventually degrade the good protective properties. In addition, possible transformation stresses in a coating can also result in cracking.

Reinforcement with particulates or fibers, such as TiB_2, Al_2O_3, and SiC [2,3], or combination with a ductile phase such as tantalum [4] have been used to reduce the low-temperature brittleness of $MoSi_2$. In these cases, at best an improvement in the fracture toughness from 2.7 to 4.9 $MPa/m^{1/2}$ was reported [4]. Recently a new approach, refinement of the microstructure down to the nanometer scale, has been used to enhance the mechanical performance of materials. In our previous work, we have reported the deposition and characterization of $MoSi_2$/SiC composite coatings [5]. Layered nanostructures were produced by sputter deposition. The main purpose of the SiC layers was to prevent a crystal growth of $MoSi_2$. Silicon carbide was chosen as a constituent because of the thermodynamic stability of a $MoSi_2$/SiC pair [6]. However, no improvement in room temperature toughness was observed, although indentation fracture measurements indicated different fracture behavior when compared to that of a single $MoSi_2$ layer.

Cracking of the $MoSi_2$/SiC composite coatings was, however, reduced during oxidation at relatively low temperatures. In fact a reduction of 66% in the crack line density was observed as compared to the cracking of a single $MoSi_2$ coating with approximately identical thickness. The

Mat. Res. Soc. Symp. Proc. Vol. 322. ©1994 Materials Research Society

composite coating still possessed good oxidation resistance, but differences were detected in the oxidation mechanism [7].

Previous experience suggests the possibility of cracking can be reduced by improving the ductility of the coating, by attaining an enhanced compatibility of elastic and thermal expansion properties between the base material and the coating, or by avoiding phase transformations. In this work we have successfully applied most of these principles by producing amorphous molybdenum silicide with a significantly higher crystallization temperature than usual. This was obtained by nitrogen alloying simultaneously during the sputter deposition.

EXPERIMENTAL PROCEDURE AND MEASUREMENTS

Single crystal silicon wafers and unalloyed carbon steel were employed as substrates. Prior to deposition the steel samples were mechanically polished, degreased in TCE, acetone and isopropanol, and finally sputter cleaned. A 1:50 HF:H_2O solution was used to remove the native oxide of the silicon wafers. Depositions on the silicon substrates were used to determine the chemical composition of the coatings (using Rutherford backscattering (RBS) spectroscopy and the 429 KeV resonance of the reaction $^{15}N(p,\alpha\text{-}\gamma)^{12}C$ [8] (NRA)), in nanoindentation measurements, in transmission electron microscopy (TEM), and in x-ray diffraction (XRD) examinations. Oxidation, corrosion, and thermal cracking measurements were performed on the steel samples. In this paper we report on the results obtained concerning the coatings on the silicon substrates.

Sputter deposition was carried out at a pressure of 1 Pa with an argon and nitrogen flow of 10 sccm/min. The nitrogen gas concentration in the flow was 50 %. Prior to deposition the chamber was evacuated down to a pressure of 10^{-4} Pa. Molybdenum silicide was sputtered from a planar magnetron $MoSi_2$ target with a diameter of 100 mm at a DC power of 200 W. The deposition rate was 27 nm/min. $MoSi_2$ coatings without nitrogen were also deposited onto the same substrate materials for reference. The thickness of the coatings varied from 1.2 μm to more than 3 μm.

In order to investigate the effect of heat treatment on the microstructure, the hardness and elastic properties, and the cracking of the coatings, annealing was performed in a quartz tube furnace at a temperature range of 450 - 1000 °C. Both the as-sputtered and annealed (1 h at 800 °C) Mo-Si-N coatings were made into cross-section TEM (XTEM) specimens using M-bond 610 for structural characterization. The specimens were examined using conventional and high-resolution transmission electron microscopy (HRTEM) on a Phillips CM30ST microscope operating at 300 kV. Thermal cracking was examined with a scanning electron microscope (SEM). The hardness and elastic properties were determined with a commercially available nanoindentation instrument.

RESULTS AND DISCUSSION

In Fig. 1 RBS spectra from as-deposited Mo-Si-N films are shown. The molybdenum to silicon ratio corresponds well to that of the sputtering target, [Mo]:[Si] = 1:2. The nitrogen concentration, determined from NRA, was 50 at. % and the concentration profile very uniform, as can also be seen in Fig. 1.

An isothermal section of the Mo-Si-N ternary phase diagram at 1400 °C is given in reference [9]. In the Mo-Si-N system silicon nitride Si_3N_4 can coexist with both $MoSi_2$ and $MoSi_3$ but no molybdenum nitride is stable without excess nitrogen at temperatures above 1000 °C. The third silicide of the Mo-Si system is Mo_3Si. Nitrogen is considered as practically insoluble in $MoSi_2$. The composition of our coatings is located quite close to silicon nitride

(Si_3N_4) on the isothermal section of the Mo-Si-N phase diagram. In fact, in ESCA measurements, a strong chemical interaction between silicon and nitrogen was observed, whereas in the $MoSi_2$ films the only bond type was the silicide type between silicon and molybdenum. It should be noted that chemical interaction between silicon and nitrogen is much stronger (heat of formation -25.6 kcal/g-at. [10]) than that between silicon and molybdenum (heat of formation-9.3, -8.5, and -5.8 Kcal/g-at for $MoSi_2$, Mo_5Si_3, and Mo_3Si respectively [11]).

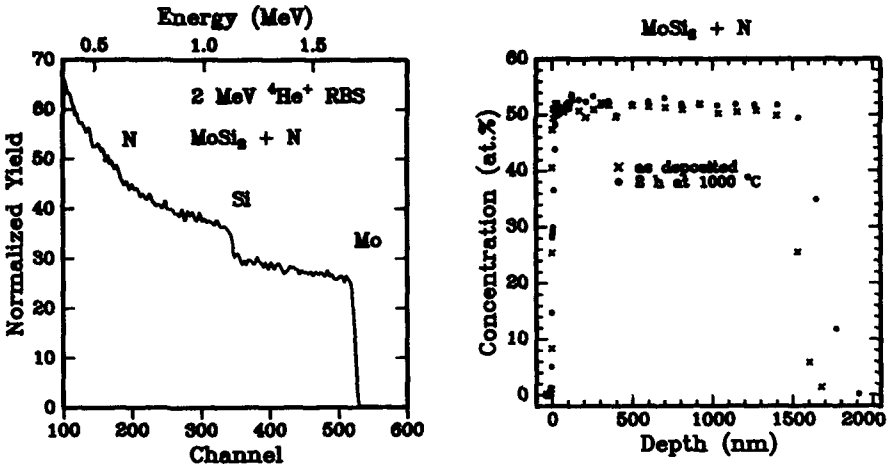


Fig. 1. *RBS spectrum and nitrogen distribution of the Mo-Si-N coating.*

The microstructure of both the as-deposited $MoSi_2$ and Mo-Si-N films was amorphous as determined by XRD. After annealing at 500 °C in a vacuum furnace, $MoSi_2$ films crystallize to a hexagonal structure, which is the stable phase of molybdenum disilicide at low temperatures. Nitrided Mo-Si-N films are still amorphous after annealing, as indicated by the broad diffuse feature in the spectrum. Even after annealing at 1000 °C the microstructure of these films remains amorphous. However, changes in the shape of the amorphous feature of the Mo-Si-N after annealing at high temperatures can be observed, which relate to a relaxation of the structure. This was also confirmed by TEM results. HRTEM observation of the as-deposited films revealed the amorphous structure as shown in Fig. 2(a). Fig. 2(b) shows the corresponding selected area diffraction (SAD) pattern. The diffuse rings indicate the presence of an amorphous structure which is consistent with the observation in (a). By measuring the diameter of the innermost ring and converted to the real space spacing using the known camera constant, the nearest neighbor distance was estimated to be 2.30 Å.

As discussed above, annealing the Mo-Si-N films at 800 °C for 1 h failed to crystallize the amorphous structure, as shown in Fig. 3(a). Fig. 3(b) shows the corresponding SAD pattern which confirms the amorphous nature of the structure. Even though Fig. 3 shows the amorphous structure, careful examination of the two structures reveals the difference in their detailed microstructure. After the 800 °C anneal, the amorphous structure seems to have a coarser microstructure and a different nearest neighbor spacing than the as-sputtered film. The latter difference is confirmed by comparing the diameters of the innermost ring on the SAD patterns. The ring diameter of the annealed film is 2.5% larger than the as-sputtered one, and corresponds to a nearest neighbor spacing of 2.25 Å. The decrease in the nearest neighbor spacing from 2.30 to 2.25 Å suggests that the annealing may have reduced the free volume in the as sputtered films and caused the densification of the coatings.



Fig. 2. *(a) Cross-section TEM micrograph of an as-deposited Mo-Si-N coating. (b) Corresponding SAD pattern.*

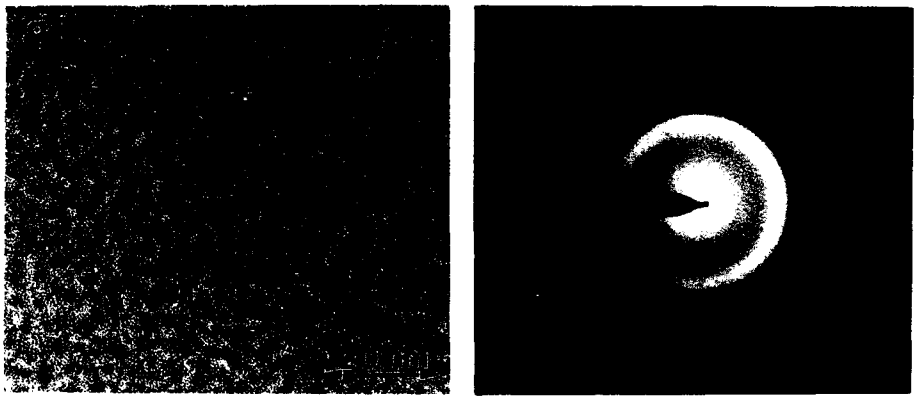


Fig. 3. *(a) Cross-section TEM micrograph of the Mo-Si-N coating annealed at 800 °C for 1 h (b) Corresponding SAD pattern.*

In Table 1, the mechanical properties of the as-deposited and heat treated Mo-Si-N films are shown. For comparison, the modulus and hardness of $MoSi_2$ films with different microstructures are given. The modulus of the as-deposited Mo-Si-N films is somewhat higher than that of the as-deposited $MoSi_2$ films. However, tetragonal $MoSi_2$ films have a significantly higher modulus, 382 GPa, reflecting the transformation to a crystalline phase. The fact that the modulus of the Mo-Si-N films remains fairly low may result in much lower residual and thermal stresses in these films. The value of the modulus of the Mo-Si-N coatings is, in fact, quite close to that of the most common steels, about 210 GPa.

Table 1. Mechanical properties of Mo-Si-N and $MoSi_2$ thin films.

Sample	Modulus [GPa]	Hardness [GPa]
As-deposited Mo-Si-N (amorphous)	257	18.8
Annealed 1 h @800 °C (amorphous)	273	24.4
As-deposited MoSi2 (amorphous)	222	11.2
Annealed 1 h @500 °C (hexagonal)	278	22.0
Annealed 1 h @900 °C (tetragonal)	382	25.5

Indentation measurements show that after annealing at 800 °C, the hardness of the Mo-Si-N films has increased from 18.8 to 24.4 GPa, while little difference in modulus was observed. The increase in hardness could be the result of the densification process discussed above. In any case, the hardness of the Mo-Si-N films is much higher than that of the amorphous $MoSi_2$ films. However, since no crystallization process is involved, one would not expect the elastic properties of the materials to change much, which is consistent with the small change in modulus observed in this case.

Thermal cracking was examined by annealing the samples at different temperatures in vacuum and viewing the possible cracking in a scanning electron microscope. In Fig. 4 SEM micrographs of the samples annealed at different temperatures are shown. Cracking is seen in the $MoSi_2$ coatings even after annealing at relatively low temperatures. In contrast, no cracking is observed on the Mo-Si-N coatings, even after annealing at 1000 °C. This absence of cracking may be due to several reasons. The modulus of the Mo-Si-N coating is closer to that of the substrate. There is no phase transformation (which could cause transformation stresses) in the temperature range investigated. Finally, the fracture toughness of amorphous material may be higher than that of crystalline material, although no direct evidence of this was obtained in the current experiments. This resistance to thermal cracking makes Mo-Si-N coatings very attractive for protective coatings in corrosive and hostile environments at elevated temperatures.

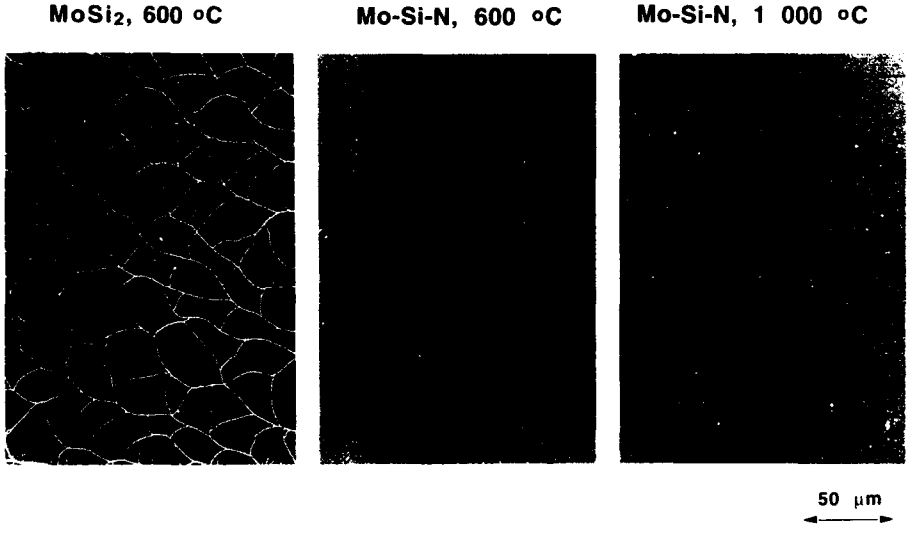


Fig. 4. *SEM micrographs of $MoSi_2$ coating annealed at 600 °C and Mo-Si-N coatings annealed at 600 and 1000 °C.*

CONCLUSIONS

Based on our observations, we can conclude that: i) molybdenum-silicon films with high nitrogen concentrations can be deposited by DC sputtering in the presence of a nitrogen plasma, ii) nitrogen significantly increases the crystallization temperature of molybdenum-silicon films, iii) the hardness and modulus of Mo-Si-N films are higher than those of amorphous $MoSi_2$ films; (after recrystallization into a tetragonal structure, the modulus of $MoSi_2$ films is greater than that of amorphous Mo-Si-N films), iv) thermal cracking of Mo-Si-N films is almost completely prevented at temperatures below 1000 °C.

ACKNOWLEDGMENTS

This work at the Metallurgy Laboratory of the Technical Research Centre of Finland (VTT) is supported jointly by The Academy of Finland and VTT through the project on "Nanocrystalline Thin Films and Multilayered Structures", and at the Los Alamos National Laboratory by the Department of Energy, Office of Basic Energy Science, Division of Advanced Energy Projects.

REFERENCES

[1] J. Schlichting, *High Temperatures - High Pressures* **10** 241 (1978).
[2] P.J. Meschter, *Scripta Met.* **25** 1065 (1991).
[3] C.H. Henager, J.L. Brinhall, and J.P. Hirth, *Scripta Met.* **26** 585 (1992).
[4] R.G. Castro, R.W. Smith, A.D. Rollett, and P.W. Stanek, *Scripta Met.* **26** 207 (1992).
[5] J-P. Hirvonen, H. Kattelus, I. Suni, J. Likonen, T.R. Jervis, and M. Nastasi, in *Mechanical Properties and Deformation Behavior of Materials Having Ultra-Fine Microstructure,* eds. M. Nastasi et. al. (Kluwer Academic Publishers, the Netherlands, 1993) p. 469.
[6] H.J. Goldschmidt, *Interstitial Alloys* (Butterworth and Co., Great Britain, 1967) p 560.
[7] J-P. Hirvonen, R. Lappalainen, H. Kattelus, J. Likonen, I. Suni, H. Kung, T.R. Jervis, and M. Nastasi, Mat. Res. Soc. Symp. Soc. **286** 373 (1993).
[8] R. Lappalainen, *Phys. Rev.* **B34** 3076 (1986).
[9] *Phase Diagrams of Ternary Boron Nitride and Silicon Nitride Systems,* eds. P. Rogl and J.C. Schuster (ASM International, Materials Park, OH, 1992) p. 169.
[10] *CRC Handbook of Chemistry and Physics,* 63rd edition (CRC Press, Boca Raton, FL, 1984).
[11] M-A. Nicolet and S.S. Lau, in *VLSI Electronics: Microstructures Science* ed. by N. G. Einspruch, Vol. 6 (Academic Press, Orlando FL, 1983) p. 330.

HIGH TEMPERATURE SILICIDE THIN-FILM THERMOCOUPLES

KENNETH G. KREIDER
National Institute of Standards and Technology, Chemical Science and Technical Laboratory, Gaithersburg, MD 20899

ABSTRACT

High-temperature silicides have been used in mechanical structures, heating elements, and electronic, CMOS applications. Their stability in high temperature oxidizing environments and excellent electrical conductivity may also make them useful as high temperature thin-film sensors in harsh environments. We have investigated sputter deposited $MoSi_2$, $ReSi_2$, $TaSi_2$, $TiSi_2$, and WSi_2 thin films and characterized their performance as thermoelements and stability up to 1200 °C. A multilayer technique was developed to ensure constant silicide stoichiometry during oxidation thereby maintaining a constant Seebeck coefficient. In addition techniques were developed to suppress the formation of metal oxides from the silicides. The results indicated excellent stability of Seebeck coefficient up to 1200 °C. These results are compared with the problems of thin film instability in the Seebeck coefficient found in noble metal thermocouples. Potential applications for temperature and heat transfer measurements will be discussed.

INTRODUCTION

Thin-film thermocouples have numerous advantages in measuring temperature. These advantages stem primarily from their small size, typically 1 μm thick and less than 1 mm wide. This small size permits extremely fast response (1 μs)[1], excellent spatial resolution (< 1 mm^2), low cost in high volume production, and compatibility with integrated circuit fabrication for instrumentation. Because they are thermocouples they have strong voltage outputs and have simple power and readout instrumentation requirements. These assets have led to numerous applications in gas turbine engines [2], diesel engines [3], thermopiles, AC-DC convertors, thermoelectric devices, and miniature temperature controllers. The materials that have been used to date for the thermoelements, however, have been primarily the same as those used in wire thermocouples and are limited in certain oxidative and corrosive aqueous environments. Because metal silicides have outstanding corrosion resistance, it was decided to explore certain highly stable thin-film metal silicides.

Many of the applications in aerospace industries involve high temperature environments where stability and reliability under harsh conditions are principal design considerations. The demanding requirements have led to the use of platinum-rhodium alloy thermocouples for their outstanding resistance to oxidation at high temperatures. Recent studies of thin-film platinum/platinum rhodium thermocouples have indicated serious oxidation problems related to rhodium oxidation in the 700-900 °C range [4] and substrate reactions at temperatures above 1250 °C. [5]. The reactivity of the thermoelements is a more profound problem with thin films compared to wires because of the very short (<1 μm) diffusion distances. What might be a

Mat. Res. Soc. Symp. Proc. Vol. 322. ©1994 Materials Research Society

small surface reaction layer on a 0.5 mm (500 μm) wire can consume a 1 μm thick film. In alloy thermocouples the alloying element, for example-Rh, has different reactivities with environmental factors, such as oxygen, sulphur, or silicon, than the platinum and a change in the solute levels leads to changes in the Seebeck coefficient. A review of candidates for surface temperature measurements up to 1650 °C (3002 °F) was made by Bennethum [6]. He presents a detailed analysis of potential materials and techniques for the measurements together with discussions of some of the compatibility problems.

One of the most desirable materials for high temperature measurements and heaters in oxidizing environments is molybdenum disilicide ($MoSi_2$). This compound is presently used in the highest temperature commercial electrical heater elements. Although $MoSi_2$ oxidizes in air the surface can be protected with a self-healing silicon dioxide, (SiO_2) diffusion barrier which limits oxygen diffusion to the silicide. The heating elements are commonly used to 1600 °C in air. Since $MoSi_2$ is a line compound with very small solubilities for impurities, we expected a stable Seebeck coefficient unaffected by compositional changes. The melting point of 1980 °C is very high and the thermal expansion coefficient is similar to aluminum oxide Al_2O_3. Because of these attributes, $MoSi_2$ was chosen for these studies as a high temperature thin film thermocouple element.

Metal silicides also have been studied in depth as electrical conductors in integrated circuits. Their advantages include high temperature stability during processing, compatibility with silicon, and good electrical conductivity. S.P. Murarka has reviewed a wide range of silicides [7] including properties, thermodynamics, formation, and oxidation. In fact, silicide characteristics and mechanisms have been described in detail [8-17] in the literature in connection with silicide conductors on silicon. It is evident from this body of work that titanium disilicide $TiSi_2$ and tantalum disilicide $TaSi_2$ have comparable or slower oxidation rates than $MoSi_2$ and may be promising as thin film thermoelements. $TiSi_2$ has been produced with less than 20 $\mu\ \Omega$ cm resistivity compared with $MoSi_2$ (100 $\mu\ \Omega$ cm) and $TaSi_2$ (50 $\mu\ \Omega$ cm). Other high conductivity metal silicides that appeared attractive include WSi_2 and $ReSi_2$ and thin-films of these silicides were fabricated for this study. The high conductivities are useful in thin films to avoid high impedances in the thermoelements. In contrast, silicon carbide SiC typically has $10^6\ \mu\ \Omega$ cm and has to be heavily doped to be useful as a thin film conductor. In our work we chose to investigate these silicides for use as thermoelements.

EXPERIMENTAL PROCEDURE

In order to study the feasibility of these high temperature thin-film silicide thermocouples, it was decided to sputter deposit 1-2 μm films on Al_2O_3 circuit board substrates. In addition, in order to supply silicon to grow the protective SiO_2 outer layer on the silicides, a sputtered layer of silicon was deposited on the alumina prior to the silicide deposition. After fabrication and suitable heat treatments, the samples were tested for thermoelectric output and changes in resistivity.

Silicide films 1-2 μm thick were sputtered from stoichiometric targets 99.5% $TaSi_2$, 99.5% $TiSi_2$ and 99.5% $MoSi_2$. Principal impurities are oxygen and metals, and alkali and alkaline earth elements are in the 2-5 ppm range. Sputtering was performed with RF planar magnetrons at 100 W on a 5 cm target, 8-10 cm from the substrate. Sputtering pressures were held to 0.3 Pa of argon to minimize the tensile stresses on the films which are probably due to compound

formation in the growing film. Substrate temperature was held at 120 °C to minimize incorporation of adsorbed gases (H_2O, etc) in the film. Before silicide film deposition, a 0.4 μm silicon film was sputtered deposited on the Al_2O_3 substrate film. The Si target was 99.9999% pure and sputtered under the same conditions.

Heat treatments were performed in a tube furnace in Ar (4%H_2), Ar, and in air. In growing the SiO_2 surface layer, the silicide was heated to 900 °C in argon before exposing it to air to suppress metal oxide formation. Resistivity measurements of the films were made with an osmium (Os) 4-point probe and thermoelectric measurements were made in a specially designed furnace [3] with a comparison to a reference grade ANSI Type S (platinum, platinum-10% rhodium) thermocouple. The specimen on the alumina substrate was 12 cm long between the water cooled reference junction and the measuring junction.

RESULTS

Ten thermocouple test coupons were fabricated from the stoichiometric titanium disilicide ($TiSi_2$) target with a 0.4 μm silicon layer underneath. This test specimen was annealed in Ar (4% H_2) for one-half hour and shows no loss in Seebeck coefficient. A summary of the results in testing the thermoelectric output of the $TiSi_2$ samples is presented in Table 1. The results are presented both as coefficients to a least squares fit of second degree and as the Seebeck coefficient, S_{500}, calculated at 500 °C. Where E, the thermoelectric output, in volts can be expressed: $E = AT + B/1000\ T^2 + C$ and S, the Seebeck coefficient, in volts per °C: $S = A + B/500\ T$. Fig. 1 is typical of the excellent fit obtained using the second degree polynomial. The most interesting aspect of the $TiSi_2$ results is that the Seebeck coefficient is unaffected by heat treatments up to 1200 °C which is an indication of its stability during oxidation. Fig. 1 displays the results after 3 hrs at 1200 °C (in air). An expected variation of $\pm$10% is observed in the reported values.

From the previous results of measurements of $TiSi_2$ thin film oxidation by Strydom et al [19], the expected values of oxide thickness would be approximately 300-400 nm after 3 hours at temperatures up to 1100 °C in dry oxygen and 800-900 nm after 20 hours at 1100 °C. Using the activation energy of 1.3eV for the parabolic rate constant (measured in oxygen) which is similar to that of silicon, one can also calculate the thickness expected at 1200 °C, etc. This activation energy is related to the diffusion of oxygen through SiO_2 and limits the rate if metal oxidation is suppressed. The expected thickness generated in oxygen after 3 hrs at 1200 °C would be approximately 600 nm. After 20 hours at 1200 °C a major fraction of the silicon and silicide will have been converted to SiO_2. The silicide film resistivity at room temperature for this exposure is also reported in Table 1. These are average values and the errors in the 4 point measurement technique and thickness measurements are estimated at less than 20% of the reported value. Multiple samples and tests all fall within these limits. It is apparent that the final high conductivity phase of the $TiSi_2$ is not mature until heat treatments comparable to 3 hours at 1000 °C are performed. At the highest temperature and longest time, apparently the loss of material is severely affecting the resistivity. In order to determine the morphology of the oxide growth, the $TiSi_2$ was also deposited on silicon which indicated surface roughening after 20 hrs at 1200 °C.

$TiSi_2$ Thermoelectric Output
Table 1

Heat-Treatment (°C)	(Hr.)	Resistivity ($\mu\ \Omega$ cm)	A (μV/°C)	B/1000 (μV/°C^2)	S_{500} (μV/°C)
800	1/2*		11.5	10.8	22.3
900	1/2*	200	9.1	10.7	19.8
800	3	45	8.5	11.1	19.6
1000	3	20	9.9	11.8	21.7
1000	20	23	9.2	11.6	20.8
1100	3	20	10.1	10.8	21.9
1200	3	24	10.8	10.0	20.8
1200	20	100			

*In Ar4%H_2; others in air

The results of testing nine thin-film thermocouples of $MoSi_2$ are presented in Table 2 and Fig. 2. The Seebeck coefficients and resistivities for multiple samples are averaged for the table. The high output after 1/2 hr at 800 °C in Ar + 4% Hz (S_{500} = 69 μV/°C) indicates that the final stoichiometry and morphology are not achieved at that point (900 °C). Notice in Table 2 that the resistivity is also high. The performance of the $MoSi_2$ film after three hours at 1200 °C is displayed in Fig. 2. Because the Seebeck coefficient is so similar to that of $TiSi_2$, these two

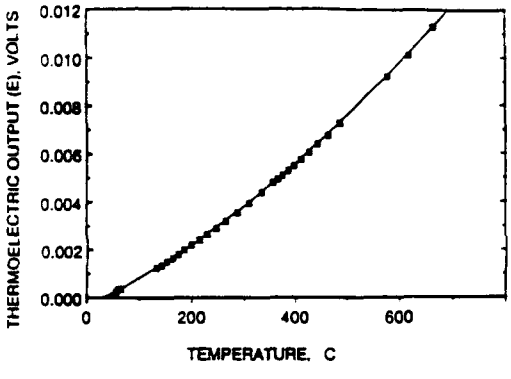


Fig. 1 Thermoelectric output of sputtered $TiSi_2$ 1.5 μm film after three hours at 1200 °C in air versus Pt.

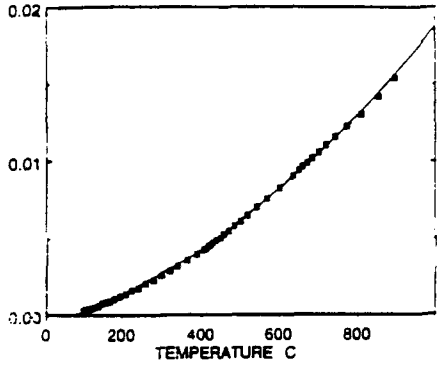


Fig. 2 Thermoelectric output of sputtered 1.6 μm $MoSi_2$ film after three hours at 1200 °C in air versus Pt.

silicides would not make a good couple. The resistivity measurements correspond to the thermoelectric measurements; it is apparent that the high conductivity phase is not completed until the sputtered compound is annealed above 800 °C and that brief annealing in a reducing atmosphere at 900 °C is not adequate. The $MoSi_2$ results are similar to those of the $TiSi_2$ and the thermoelectric output versus platinum is not modified by the development of the oxide even after three hours at 1200 °C. The oxide developed was found to be substantially SiO_2 by X-ray photoelectron spectroscopy (XPS) as the Mo signal was suppressed completely after a 900 °C anneal in air. The XPS results indicated small amounts of TiO_2 on the $TiSi_2$ after a similar heat treatment. These results correspond to earlier results [9][18] and relate to the refractive nature of TiO_2 which forms before the SiO_2 layer is complete and the volatile nature of molybdenum oxide MoO_3 which is lost as it forms. The oxidation treatment used with the silicide, using an $Ar(4\%H_2)$ below 900 °C, minimized low temperature, slow oxidation of the metal and favored the formation of SiO_2.

$TaSi_2$ was deposited using the same procedures as used with $MoSi_2$. The tantalum silicide yielded similar results to the $TiSi_2$ when annealed in argon plus 4% hydrogen, resulting in $S_{500} = 22\ \mu$ V/°C; however, the film lost electrical conductivity when annealed in air above 900 °C for 20 hours. A heavy oxide growth on the $TaSi_2$ may indicate the $TaSi_2$ film on the Al_2O_3 substrate was being damaged by a thermal expansion mismatch. Tungsten silicide was grown from a tungsten target 70% covered with a silicon wafer to deposit WSi_2 with a slight silicon excess. The 1 μm thick silicide had approximately 400 $\mu\ \Omega$-cm resistivity as deposited and 120 $\mu\ \Omega$-cm resistivity after annealing 2 hrs. at 900 °C in argon-4% hydrogen on an Al_2O_3 substrate. The silicide cracked and spalled from a silicon wafer with the same heat treatment. The tungsten silicide thin-film thermocouple had a Seebeck coefficient of 16.8 μ V/°C at 400 °C but changed rapidly above 500 °C in air and the film was lost at 760 °C. Apparently, the film formed the volatile oxide WO_2. Rhenium silicide was also deposited using both rhenium and silicon targets. The $ReSi_2$ was formed by reaction at 900 °C for 2 hrs in argon-4% hydrogen and yielded a film with 0.5 to 1.0 ohms resistance on the 4 point probe. It was found to be stable in the $Ar4H_2$ at 1050 °C but was oxidized significantly after 4 hours at 900 °C in air.

Table 2
$MoSi_2$ Thermoelectric Output

Heat-Treatment (°C) - (Hr.)		Resistivity ($\mu\ \Omega$ cm)	A (μV/°C)	B/1000 (μV/°C^2)	S_{500} (μV/°C)
800	1/2*	800	28.1	36.0	64.1
900	1/2*	500	38.8	29.3	68.6
800	3		36.6	29.6	66.2
900	3	100	10.3	11.1	21.4
1000	3	100	7.8	12.0	19.8
1000	20	100	8.3	12.0	20.3
1100	3	100	8.3	11.5	19.8
1200	3	120	8.0	11.4	19.4

*annealed in argon 4% H_2 others annealed in air.

CONCLUSIONS

Both $MoSi_2$ and $TiSi_2$ show promise as thermoelements in high temperature thin film thermocouples. Their resistance to oxidation damage is related to the slow parabolic rate of growth of the thickness of SiO_2 which is limited by oxygen diffusion. Research studies in the electronics industry on oxidation of these silicides has characterized the activation energy for the diffusion and the kinetics of oxide growth. Our results are in general agreement with their work and demonstrate the feasibility of using the $TiSi_2$ and $MoSi_2$ on Al_2O_3 substrates as TFTCs. We have investigated exposures of the silicides to air at temperatures as high as 1200 °C and found the thermoelectric output to be stable. This probably results from the fact that both silicides are "line" compounds and therefore have very little solubility for elements which would modify their thermoelectric potential. It is also implied that the Seebeck coefficient is not diminished by loss of material since in contrast to the electrical resistance, thermoelectric voltage is not a function of film thickness. Therefore, the outstanding corrosion resistance of $TiSi_2$ and $MoSi_2$ may lead to numerous applications where metal thermocouples are vulnerable to deterioration.

ACKNOWLEDGMENTS

The author wishes to acknowledge M. J. Tarlov and staff for the XPS analysis of the Process Measurements Division NIST.

REFERENCES

1. D. Burgess, M. Yust and K. G. Kreider, *Sensors and Actuators A 24, 155-161 (1990).*
2. R. R. Dils and P. S. Follansbee, "Superalloys: Metallurgy and Manufacture", ed. B.H. Kear, D.R. Muzyka and S. T. Wlodek, Claitor, *Baton Rouge, 37, (1976).*
3. T. Morrell, S. Wahiduzzaman, E. F. Fort, D.R. Tree, D.P. DeWitt and K.G. Kreider. *Congress of Society of Automotive Engineers Tech. Paper, Detroit, MI, Feb. 25, 1989.*
4. K. G. Kreider, *J. Vac. Sci and Tech.*, A 11(4), Jul/Aug 1993.
5. R. Hollanda in Temperature: *Its Measurement and Control in Science and Industry, p. 649 American Institute of Physics, New York, NY, 1992, Vol 1.* 1645.
6. W.H. Bennethum and L.T. Sherwood *"Sensors for Ceramic Components in Advanced Propulsion Systems"* NASA Contractor Report 180900 NASA, Lewis Research Center, Cleveland, OH Aug. 1988.
7. S. P. Murarka *"Silicides for VLSI Applications"* Academic Press, New York 1983.
8. B. E. Deal and A. S. Grove, *J. Appl. Phys., 36, 3770 (1965).*
9. J.R. Chen, M. P. Houng, S. K. Hsiung and Y. C. Liu, *Appl. Phys. Ltr., 37, 824 (1980).*
10. J. R. Chen, Y. C. Liu, and S. D. Chu, J. *Electron. Mater, 11, 355 (1982).*
11. M. Bartur and M-A. *Nicolet, Appl. Phys. A, 29, 69 (1982).*
12. M. Bartur and M-A. Nicolet, *Appl. Phys. Ltr., 40, 175 (1982).*
13. T. Mochizuki and M. Kashiwagi, J. *Electrochem. Soc. 127, 1128 (1980).*
14. J. E. E. Gaglin, F. M. d'heurle, and C. S. Peterson, *J. Appl. Phys., 54, 1849 (1983).*
15. S.P. Murarka, D.B. Fraser, W.S. Lindenberger & A.K. Sionha, *ibid., 512, 3241 (1980).*
16. R. R. Razouk, M. E. Thomas, and S. L. Pressacco, *ibid., 53, 5342 (1982).*
17. F. Mohammadi, K. C. Saraswat, and J. D. Meindl, *Appl. Phys. Letter, 35, 529 (1979).*
18. F. d'Heurle, E. A. Irene, and C. Y. Ting, *J. Appl. Phys., 54, 2716 (1983).*
19. W. J. Strydom and J. C. Lemband, Thin Solid Films, 131, 215-231 (1985).

CONCLUSIONS

Both $MoSi_2$ and $TiSi_2$ show promise as thermoelements in high temperature thin film thermocouples. Their resistance to oxidation damage is related to the slow parabolic rate of growth of the thickness of SiO_2 which is limited by oxygen diffusion. Research studies in the electronics industry on oxidation of these silicides has characterized the activation energy for the diffusion and the kinetics of oxide growth. Our results are in general agreement with their work and demonstrate the feasibility of using the $TiSi_2$ and $MoSi_2$ on Al_2O_3 substrates as TFTCs. We have investigated exposures of the silicides to air at temperatures as high as 1200 °C and found the thermoelectric output to be stable. This probably results from the fact that both silicides are "line" compounds and therefore have very little solubility for elements which would modify their thermoelectric potential. It is also implied that the Seebeck coefficient is not diminished by loss of material since in contrast to the electrical resistance, thermoelectric voltage is not a function of film thickness. Therefore, the outstanding corrosion resistance of $TiSi_2$ and $MoSi_2$ may lead to numerous applications where metal thermocouples are vulnerable to deterioration.

ACKNOWLEDGMENTS

The author wishes to acknowledge M. J. Tarlov and staff for the XPS analysis of the Process Measurements Division NIST.

REFERENCES

1. D. Burgess, M. Yust and K. G. Kreider, *Sensors and Actuators A 24, 155-161 (1990).*
2. R. R. Dils and P. S. Follansbee, "Superalloys: Metallurgy and Manufacture", ed. B.H. Kear, D.R. Muzyka and S. T. Wlodek, Claitor, *Baton Rouge, 37, (1976).*
3. T. Morrell, S. Wahiduzzaman, E. F. Fort, D.R. Tree, D.P. DeWitt and K.G. Kreider. *Congress of Society of Automotive Engineers Tech. Paper, Detroit, MI, Feb. 25, 1989.*
4. K. G. Kreider, *J. Vac. Sci and Tech.*, A 11(4), Jul/Aug 1993.
5. R. Hollanda in Temperature: *Its Measurement and Control in Science and Industry, p. 649 American Institute of Physics, New York, NY, 1992, Vol 1.* 1645.
6. W.H. Bennethum and L.T. Sherwood *"Sensors for Ceramic Components in Advanced Propulsion Systems"* NASA Contractor Report 180900 NASA, Lewis Research Center, Cleveland, OH Aug. 1988.
7. S. P. Murarka *"Silicides for VLSI Applications"* Academic Press, New York 1983.
8. B. E. Deal and A. S. Grove, *J. Appl. Phys., 36, 3770 (1965).*
9. J.R. Chen, M. P. Houng, S. K. Hsiung and Y. C. Liu, *Appl. Phys. Ltr., 37, 824 (1980).*
10. J. R. Chen, Y. C. Liu, and S. D. Chu, J. *Electron. Mater, 11, 355 (1982).*
11. M. Bartur and M-A. *Nicolet, Appl. Phys. A, 29, 69 (1982).*
12. M. Bartur and M-A. Nicolet, *Appl. Phys. Ltr., 40, 175 (1982).*
13. T. Mochizuki and M. Kashiwagi, J. *Electrochem. Soc. 127, 1128 (1980).*
14. J. E. E. Gaglin, F. M. d'heurle, and C. S. Peterson, *J. Appl. Phys., 54, 1849 (1983).*
15. S.P. Murarka, D.B. Fraser, W.S. Lindenberger & A.K. Sionha, *ibid., 512, 3241 (1980).*
16. R. R. Razouk, M. E. Thomas, and S. L. Pressacco, *ibid., 53, 5342 (1982).*
17. F. Mohammadi, K. C. Saraswat, and J. D. Meindl, *Appl. Phys. Letter, 35, 529 (1979).*
18. F. d'Heurle, E. A. Irene, and C. Y. Ting, *J. Appl. Phys., 54, 2716 (1983).*
19. W. J. Strydom and J. C. Lemband, Thin Solid Films, 131, 215-231 (1985).

MICROSTRUCTURAL EVOLUTION IN COMPOSITIONALLY TAILORED $MoSi_2$/SiC COMPOSITES

S.E. RIDDLE, S. JAYASHANKAR AND M.J. KAUFMAN
University of Florida, Department of Materials Science and Engineering, Gainesville, FL 32611

ABSTRACT

Compositionally tailored $MoSi_2$/SiC composites with silicon carbide content ranging from 0 to 60 volume percent were synthesized through a novel processing scheme involving the mechanical alloying of elemental molybdenum, silicon, and carbon. The effects of important processing parameters such as the nominal powder composition and the processing temperature on the microstructural evolution during mechanical alloying and subsequent heating are described based on the results obtained from DTA and XRD.

INTRODUCTION

The intermetallic $MoSi_2$ has long been considered as a potential material for high temperature structural applications [1] due to its high melting point and good oxidation resistance. However, it has low room temperature fracture toughness and limited strength at elevated temperatures. This may be partly due to the presence of grain boundary silica in powder-processed $MoSi_2$ and $MoSi_2$-based composites. Accordingly, various techniques have been implemented successfully to reduce the silica content in polycrystalline $MoSi_2$. They include silica reduction through suitable deoxidants including carbon [1-4], *in-situ* displacement reactions, ultra-clean processing, and hydrogen surface etching of the powders prior to consolidation.

Recently, a novel processing technique involving carbon additions, mechanical alloying, and *in-situ* displacement reactions has been used to synthesize silica-free $MoSi_2$-based composites [4] starting from elemental molybdenum, silicon, and carbon powders. Through the modification of the starting composition, it is possible, using this technique to synthesize $MoSi_2$/SiC composites with varying amounts of reinforcement.

The aim of this study was to characterize the microstructural evolution of the components during milling and subsequent heating as a function of the nominal SiC composition; such information should allow for better microstructural control during consolidation.

EXPERIMENTAL PROCEDURE

Based on the 1600°C isotherm of Nowotny and co-workers (Fig. 1) [5] and the 1727°C isotherm by Brewer and Krikorian [6], it is clear that ternary powder alloys within the composition limits established by the $MoSi_2 + C_{<1}Mo_{<5}Si_3 + SiC$ three-phase field should form thermally stable microstructures when consolidated at these temperatures. Further description of the processing rationale can be found elsewhere [4]. Accordingly, in the present study, ternary powder alloys were chosen for mechanical alloying in the $MoSi_2 + C_{<1}Mo_{<5}Si_3 + SiC$ three-phase field, with varying amounts of nominal silicon carbide, according to the Nowotny diagram (Fig. 1). The compositions are listed in Table I.

Table I. Nominal composition of ternary powders.

Alloy	Volume % SiC	Atomic Percent
MA 20	20	Si–25.1Mo–12.3C
MA 40	40	Si–17.8Mo–23.2C
MA 50	50	Si–14.4Mo–28.3C
MA 60	60	Si–11.3Mo–33.1C

MA (Mechanically Alloyed)

Mechanical alloying was performed in a water cooled Szegvari (planetary type) attrition mill using hardened steel balls as a milling media and a ball to charge ratio of 5:1. Elemental powders of commercial purity molybdenum (99.9 % purity, 3 - 7 μm),

Mat. Res. Soc. Symp. Proc. Vol. 322. ©1994 Materials Research Society

silicon (99.5% purity, -325mesh), and carbon (99% purity, -325 mesh, crystalline) were obtained from Johnson Matthey and used as starting materials. To minimize contamination during processing, a positive pressure of high purity titanium-gettered argon (oxygen content less than 4 ppm) was maintained in the attritor. The progress of the mechanical alloying process was monitored by withdrawing small amounts of powder after 0, 0.5, 1, 2, 5, 10, 15, 20, 30, 45, and 60 h of milling. The powders were then characterized for structure by XRD.

The transformation characteristics of the fully mechanically alloyed powders were monitored by differential thermal analysis (DTA), which was performed under flowing argon (1cc/min, oxygen content less than 4 ppm) on a Dupont 910-DSC system with heating and cooling rates of 10°C/min. For more detailed analysis, the fully mechanically alloyed powders of various compositions were heated at 10°C/min under flowing, titanium-gettered argon at 100°C intervals between 400°C and 1400°C and cooled rapidly for subsequent XRD analysis. Structural analysis of the as-alloyed and heat treated powders was carried out using a Phillips APD 3720 diffractometer operated at 40kV and 20mA with CuK_α radiation and digital data acquisition over 2θ ranges from 5-100°.

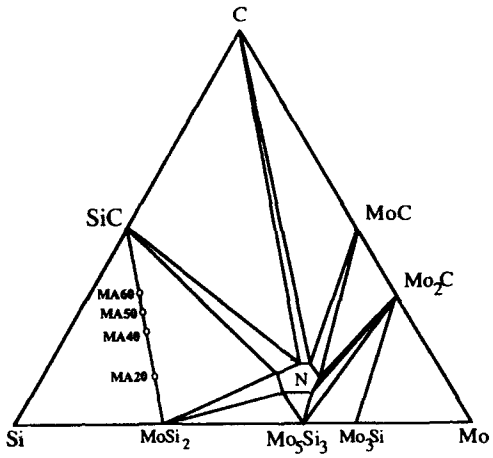


FIG. 1. Schematic of ternary isotherm @ 1600°C of the Mo-Si-C system proposed by Nowotny *et al* [5].

RESULTS AND DISCUSSION

Structural Evolution During Milling

Structural evolution studies of the higher carbon containing powders MA50 and MA60 as a function of milling time, shown in Fig. 2, indicate that only short milling times are required before all carbon goes into solution (0.5 h, see Fig. 2a), while the silicon peaks decrease significantly. Further milling results in a slow decrease in free silicon, probably because silicon is reaching its maximum metastable solubility in molybdenum. This occurs until between 5 and 10 h when the carbides Mo_2C (hexagonal) and SiC (cubic) as well as the intermetallic compounds α–$MoSi_2$ (tetragonal), Mo_5Si_3 (tetragonal), and $C_{<1}Mo_{<5}Si_3$ (hexagonal) are observed (see Fig. 2c). In previous studies, no evidence of carbide formation was observed during mechanical alloying [4], presumably because the compositions were lower in carbon content, in the middle of the $MoSi_2$ + $C_{<1}Mo_{<5}Si_3$ + SiC three-phase field, and away from the $MoSi_2$+SiC two phase field. Milling for 20 h results in the disappearance of Mo_2C and almost complete disappearance of the silicon peaks (Fig. 2d), along with considerable broadening of the α–$MoSi_2$ and SiC peaks; this is probably due to a decrease in the crystallite size rather than lattice strain [7] since α–$MoSi_2$ and SiC are brittle at the milling temperatures [4]. Continued milling through 60 h (Fig. 3c) resulted in a decrease in the molybdenum peaks and minimal increases in peak broadening. Comparing this to 20 h, Fig. 2d and 30 h (not shown) it can be concluded that milling is complete between 20 and 30 h. In order to ascertain the effects of compositional variations along the $MoSi_2$+SiC field, XRD patterns of all fully milled powder compositions were compared using previous work on mechanically alloyed $MoSi_2$ as a reference [4]. Increasing the nominal SiC content tends to suppress the formation and

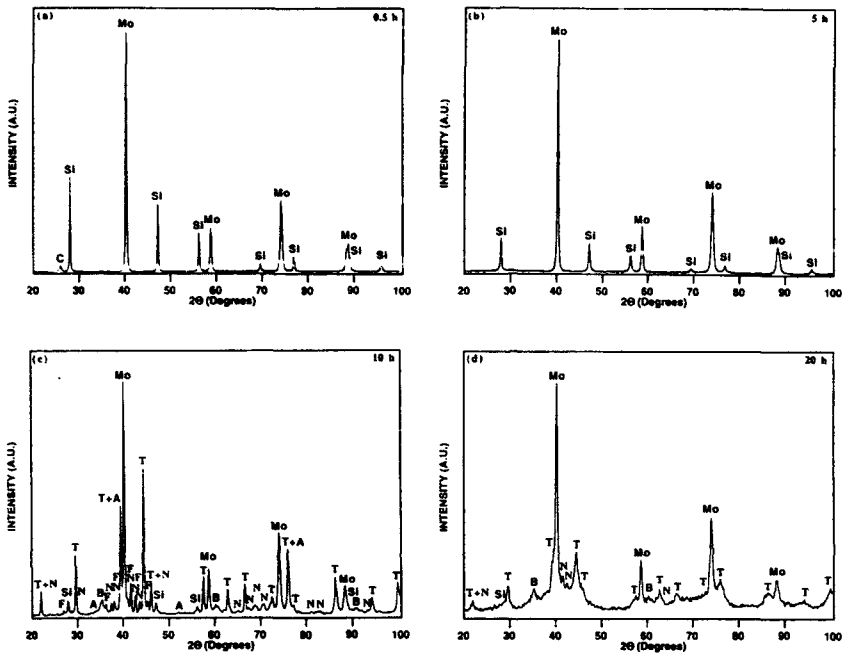


FIG. 2. Structural evolution of MA50 powders as a function of milling time. XRD patterns of the powders milled for the indicated times: (a) 0.5 h (b) 5 h (c) 10 h (d) 20 h (Mo is molybdenum, Si is silicon, C is carbon, A is hexagonal Mo_2C, B is cubic SiC, F is tetragonal Mo_5Si_3, T is tetragonal α–$MoSi_2$, and N is the hexagonal Nowotny phase).

stabilization of both α–$MoSi_2$ and β–$MoSi_2$ while simultaneously promoting the formation of SiC and $C_{<1}Mo_{<5}Si_3$ as seen by comparing the relative peak intensities of the aforementioned phases in Figs. 3a through 3d. It is also important to note that peak broadening increases with increasing nominal silicon carbide content.

Phase Evolution Upon Heating

The phase evolution of all compositions was studied by DTA. A typical heating trace of the MA20 ternary powder is shown in Fig. 4a, where strong exotherms at 480°C, 810°C, 960°C, and 1130°C (peak temperatures) are apparent. The transformations corresponding to these exotherms were studied by XRD analysis of powders heated to temperatures at the end of each exotherm using heating conditions similar to the DTA measurements (10°C/min.). Comparison of the room temperature and 700°C XRD patterns showed the 480°C exotherm is associated with the growth of β–$MoSi_2$ at the expense of molybdenum and dissolved silicon. Likewise, a comparison of the XRD patterns for 700°C and 900°C shows the 810°C exotherm corresponds to the growth of α–$MoSi_2$ and the Nowotny phase at the expense of molybdenum and dissolved silicon and carbon. The minor exotherm at 960°C appears to be associated with the transformation of molybdenum and

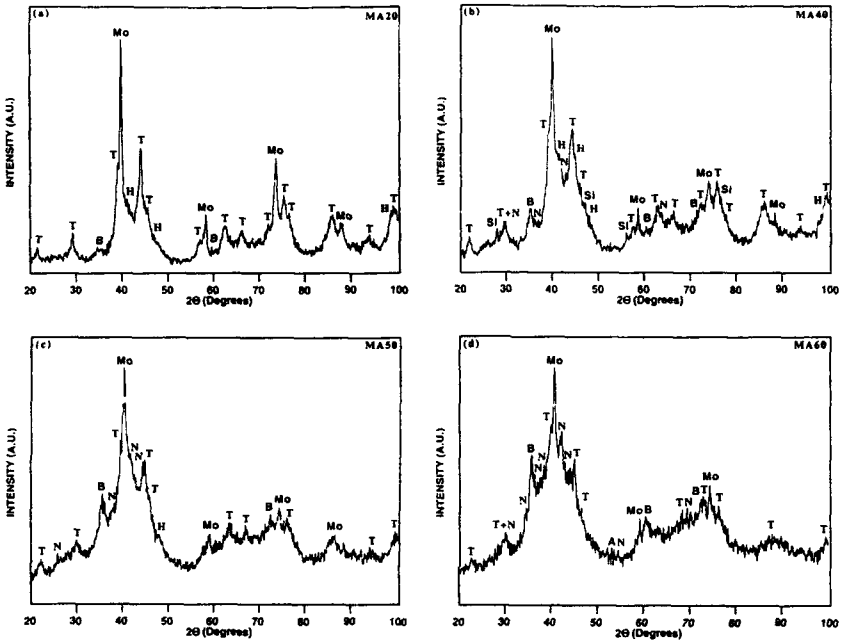


FIG. 3. XRD patterns of fully MA powders: (a) MA20, (b) MA40, (c) MA50, and (d) MA60. *Note the relative peak* intensities of the various phases present (Mo is molybdenum, Si is silicon, T is tetragonal α–$MoSi_2$, H is hexagonal β–$MoSi_2$, B is cubic SiC, and N is the hexagonal Nowotny phase).

β–$MoSi_2$ to α–$MoSi_2$. Further heating to 1400°C, resulted in a transformation of the Nowotny phase to α–$MoSi_2$ and SiC for the 1130°C isotherm.

Figure 4b shows the DTA trace of the MA60 ternary powder. The evolution is characterized by a weak exotherm at 440°C and strong exotherms at 760°C, 955°C, and 1270°C. The transformation sequences of these powders were monitored in the same manner as the MA20 powders. Comparison of the room temperature and 700°C XRD patterns showed the 440°C exotherm is associated with a partial transformation of molybdenum and the dissolved silicon and carbon into the Nowotny and α–$MoSi_2$ phases. Likewise, a comparison of the XRD patterns for 700°C and 900°C shows the 760°C exotherm corresponds to the growth of the Nowotny phase at the expense of molybdenum and α–$MoSi_2$. The minor exotherm at 955°C appears to be associated with the transformation of β–$MoSi_2$ and Mo_2C to α–$MoSi_2$, molybdenum and the Nowotny phase. This was apparent by the reappearance of the molybdenum peaks and the disappearance of the β–$MoSi_2$ peaks. Further heating to 1400°C resulted in a complete transformation of the Nowotny phase to α–$MoSi_2$ and SiC. This 1270°C exotherm is similar to that at 1130°C for the MA20 powders, indicating the greater stability of the Nowotny phase in the higher SiC containing powders. The other two compositions (MA40 and MA50) exhibited exotherms similar to the MA60 powders. XRD analysis between 400°C and 1400°C was performed at 100°C intervals to confirm these similarities and provide any indications of differences in phase stability/constitution. The stability range of β–$MoSi_2$ and the Nowotny phase show the most noticeable differences as a

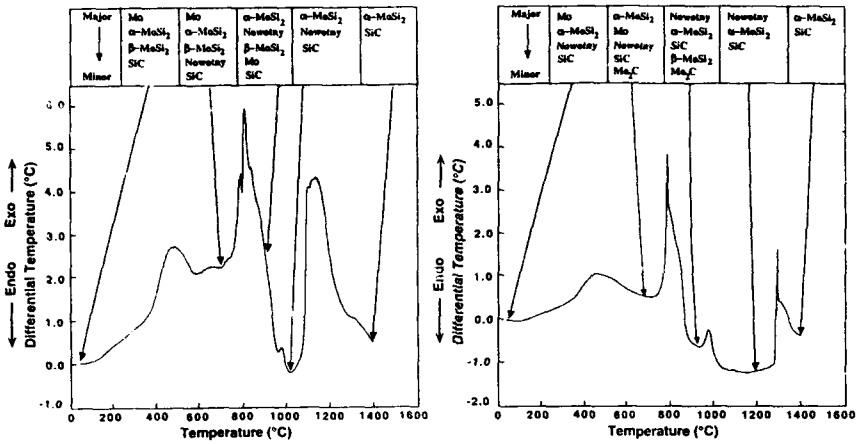


FIG. 4. DTA of MA powders under flowing argon at a heating rate of 10°C/min., along with the corresponding phases identified by XRD: (a)MA20 (b)MA60. ("Nowotny" refers to the Nowotny phase, $C_{<1}Mo_{<5}Si_3$)

function of silicon carbide content. For example, growth of the β–$MoSi_2$ peaks in the MA20 powders occurs up to 800°C and disappears around 1000°C while in the MA40 powders, β–$MoSi_2$ is absent in the as-milled powders but appears by 400°C and continues its growth until between 900°C and 1000°C before it eventually disappears by 1100°C. In the MA50 powders, β–$MoSi_2$ does not appear until 500°C and grows over a larger range to 1000°C before it disappears between 1100°C and 1200°C. Finally, in the MA60 powders, this phase appears only between 700°C and 1000°C. β–$MoSi_2$ has previously been reported to be stable up to 1030°C during mechanical alloying for an alloy with composition Si-28Mo-14C [4] and to 800°C for the isothermal annealing of Mo-Si multilayers [8, 9].

For all compositions, molybdenum is the predominant phase below 800°C while α–$MoSi_2$ becomes dominant above 800°C for both the monolithic $MoSi_2$ [4] and MA20 alloys. Increasing the nominal SiC content above 20% allows for the dominance of the Nowotny phase in the range 800°C–1000°C for MA40, 800°C–1100°C for MA50, and 800°C–1300°C for MA60. The temperature ranges over which the Nowotny phase is dominant was not the only difference observed as a function of silicon carbide content. The appearance, growth, and disappearance of the Nowotny phase are also affected. This phase does not appear until 700°C in MA20 and 400°C in MA40, while it is present in the as-milled MA50 and MA60 powders. The earlier this phase forms, as stated above, the larger is the temperature range over which it is stable. Even with the differences in appearance, growth and dominance, the Nowotny phase is always observed until 1300°C.

While the stability of β–$MoSi_2$ and the Nowotny phase are both affected by an increase in nominal SiC content, the stability of cubic SiC is not. This phase slowly grows to 1400°C with peak refinement above 800°C for all four of the compositions studied.

SUMMARY AND CONCLUSIONS

A novel processing strategy has been developed utilizing carbothermal reduction reactions, mechanical alloying, and carbon additions for the synthesis of $MoSi_2$ composites containing up to 60 volume percent silicon carbide particulate. The microstructural evolution during milling and consolidation has been studied. It has been shown that milling is complete after approximately 20 h. Structural evolution studies during milling have shown that an increase in the nominal SiC content along the narrow $MoSi_2$+SiC field tends to suppress the formation of α–$MoSi_2$ and β–$MoSi_2$ while increasing the formation of SiC and the Nowotny phase ($C_{<1}Mo_{<5}Si_3$) in the fully milled powders. While the milling studies showed the suppression of β–$MoSi_2$ in the fully milled powders, the phase evolution studies indicated an increase in the stability of β–$MoSi_2$ to between 1100°C and 1200°C in the MA50 powders, in contrast to 1020°C in previously reported studies [4] and 800°C reported for the isothermal annealing of Mo-Si multilayers [8, 9]. While the stability of the β–$MoSi_2$ phase increases with increasing nominal SiC content, the Nowotny phase becomes the dominant phase (instead of α–$MoSi_2$) to 1300°C in the MA60 powders.

ACKNOWLEDGMENTS

This work was supported through a Grant (No. MDA972-88-J-1006) from the Advanced Research Projects Agency. We would also like to thank G. LaTorre and J. Zhong for their assistance with the thermal analysis.

REFERENCES

1. W. A. Maxwell, *NACA RM E52B06* , (1952).
2. S. Jayashankar, M. J. Kaufman, *Scripta Metallurgica et Materialia* **26**, 1245-1250 (1992).
3. S. A. Maloy, A. H. Heuer, J. J. Lewandowski, J. J. Petrovic, *J. Am. Cer. Soc.* **10**, 2704-2706 (1991).
4. S. Jayashankar, M. J. Kaufman, *J. Mater. Res.* **8**, 1428-1441 (1993).
5. H. Nowotny, E. Parthe, R. Kieffer, F. Benesovsky, *Monatsh. Chemie* **65**, 255 (1954).
6. L. Brewer, O. Krikorian, *J. Electrochem. Soc.* **103**, 38 (1956).
7. B. D. Cullity, Eds., *Elements of X-Ray Diffraction* (Addison-Wesley, Menlo Park, California, (1978).
8. O. B. Loopstra, et al., *J. Appl. Phys.* **63**, 4960 (1988).
9. C. M. Doland, R. J. Nemanich, *J. Mater. Res.* **5**, 2854 (1990).

FABRICATION AND CHARACTERIZATION OF A FUNCTIONALLY GRADIENT Mo-$MoSi_2$ COMPOSITE

Gaurav Agarwal, Wen-yi Lin and Robert. F. Speyer, School of Materials Science and Engineering, Georgia Institute of Technology, Atlanta GA 30332-0245.

ABSTRACT

For the application of immersed combustion-radiant tubes in glass melters, a Mo-$MoSi_2$ functionally gradient composite was developed. A gradient profile mixture with varying amounts of powders of these two compounds was hot pressed at 1650°C and 17.4 MPa. Mo_5Si_3, and Mo_3Si reaction products were detected by XRD in the hot pressed composite. Limited cracking was apparent in regions where pure Mo regions applied tensile stresses to regions rich in Mo_3Si product. Cyclic heat treatments in a reducing atmosphere showed no signs of further CTE mismatch induced cracking, but did indicate a propensity to creep under load at $\sim$ 1400°C. A functionally gradient material with $MoSi_2$ on all exterior surfaces showed excellent oxidation protection to the Mo center.

INTRODUCTION

Currently, the favored source of energy input in industrial glass melters is via over the batch combustion of natural gas and air. To minimize particulate removal, convective heat transfer of the flame envelope on the batch/melt surface is discouraged, hence heat is predominantly transferred via radiation from a low emissivity flame, or secondarily from the crown. The Gas Research Institute has contracted our research group to develop materials for the application of immersed heating of molten glass, wherein a combustion process on the inside of the immersed tube would transfer more efficiently through the tube wall to the glass load.

The material issues of immersed heating remain a daunting problem; the tube would have to withstand the corrosive nature of high temperature (e.g. 1400°+) alkali-containing molten glass, as well as high temperature (e.g. 1700°C) combustion products. It would also need to have adequate mechanical strength and creep resistance to resist the gravitational, buoyant, and convective flow forces common in glass tanks, have an adequate effective thermal conductivity, and good thermal shock resistance against varying burner flow rates and initial insertion.

The results of materials investigations for these requirements have been reported elsewhere [1]-[4]. In summary, molybdenum showed the lowest recession rates during corrosion tests in soda-lime-silicate glass and E-glass (fiberglass) melts at ~1560°C. Molybdenum, unfortunately, oxidizes to $MoO_{3(g)}$ above ~600°C in a combustion product environment. A number of ceramic oxides (e.g. Al_2O_3), and silicon based materials (e.g. SiC, $MoSi_2$) showed good resistance against CO_2-H_2O corrosion at 1600°C. Silicon-based materials show good oxidation resistance by forming a continuous silica surface layer which prohibits oxidation of the material interior. Glass manufacturers, however, abhor the prospect of allowing SiC coming in contact with glass melts, since soluble molecular oxygen reacts with it to form CO (or CO_2) seeds and blisters.

An inner coating of $MoSi_2$ on a Mo tube (by vapor deposition or plasma spraying) was considered, but rejected, given the linear coefficient of thermal expansion (CTE) mismatch between coating and substrate. It was therefore concluded that an optimum

Mat. Res. Soc. Symp. Proc. Vol. 322. ©1994 Materials Research Society

Table I: Mole percent of powder mixtures in each of five levels, each level was approximately 0.25 cm in depth.

Layer	Mo	$MoSi_2$
1	100	0
2	75	25
3	50	50
4	25	75
5	100	0

choice of tube material would be a functional gradient from Mo to $MoSi_2$, the former concentrated at the outermost regions of the immersed portions of the tube. Reported herein is an investigation of the thermal-mechanical integrity of a functional gradient of Mo and $MoSi_2$. Of interest was the reactions between end-members as well as the self-sealing ability of $MoSi_2$ to protect Mo from oxidation.

EXPERIMENTAL PROCEDURE

The powders used for this study were 99.9% pure molybdenum metal (-325 mesh) and 99.5% molybdenum disilicide (-325 mesh). A gradient of five layers of varying amounts of these two powders was prepared, as listed in Table I. With calculations based on the densities of the two powders (Mo - 10.2 g/cm^3, $MoSi_2$ - 6.3 g/cm^3), the mixtures were prepared so that each layer would be .25 cm thick after hot pressing (assuming attainment of 100% density). The individual mixtures were blended by vigorous shaking in a container using alumina grinding media for 5 minutes. After each layer was poured in place as evenly as feasible, a die pin was gently pressed onto the powder to compact and distribute it within the graphite die. The five layers of powder mixture were hot pressed under a pressure of 17.4 MPa, starting at room temperature, heating at ~25°C/min, and holding at 1650°C for 4 hours. The furnace power was then turned off and the sample was allowed to cool to room temperature overnight. The hot pressed sample was then retrieved from the die and sections containing all five layers were cut using a diamond-tipped wafering blade.

To investigate the morphology of the phases formed across the Mo-$MoSi_2$ gradient, a scanning electron microscope (SEM, Hitachi S-800), equipped with an energy dispersive spectrometer (EDS, Kevex 3600-0398 detector with Kevex Delta-Class analyzer)was used. The sectioned samples were then polished using 1 μm diamond media and mounted on an aluminum stub using a highly conductive carbon cement, followed by sputter-coating with a ~25 nm film of Au-Pd. Samples were observed using both secondary electron and back-scatter detectors.

Using a diamond saw, the sample was sectioned through the visual boundaries of different layers. The side-faces of each section were analyzed using X-ray diffraction (XRD, Philips PW1800 diffractometer) with a 2.0 sec time constant and 0.02° step size. The XRD patterns were compared to JCPDS data and individual phases were then identified. Expansion/contraction hysteresis during cyclic heat treatments was studied using a dilatometer (Orton/Innovative Thermal Systems) with the intent of studying fissure formation in the composite as a result of thermal cycling. Bars were prepared such that the

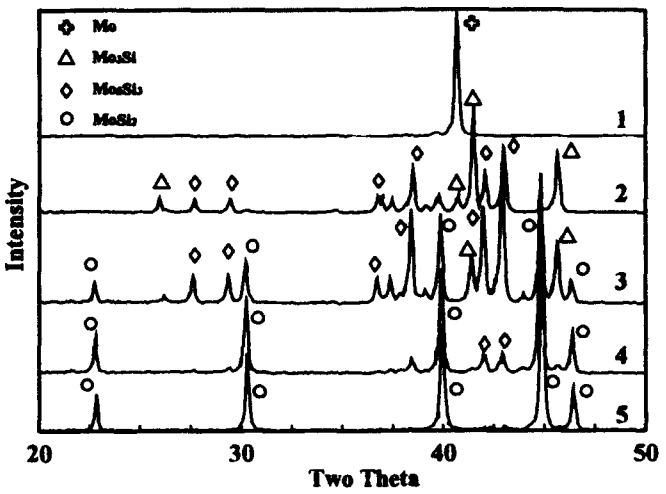


Figure 1: XRD traces of layer sections of functionally gradient material. Numbers on each trace correspond to original powder compositions shown in Table I.

direction of measured expansion would be parallel to the direction of the functional gradient. The sample was then heated to 1400°C at a rate of 5°C/min, cooled to 100°C/min and the cycle was repeated. Since Mo readily oxidizes in air, the dilatometer was run under a 95% argon - 5% hydrogen atmosphere. The dilation behavior was then analyzed, and the sample was examined for additional cracking.

In a separate investigation, a specimen was hot pressed (5.5 MPa at 1650°C for 6 hours) such that pure $MoSi_2$ was located at all exterior surfaces, and a functional gradient was formed toward a pure Mo center. This composite was then heat-treated in air at 1600°C for 24 hours to establish the oxidation protection imparted to Mo by the exterior $MoSi_2$.

RESULTS AND DISCUSSION

The XRD results are shown in Figure 1. Mo_5Si_3 and Mo_3Si formed as reaction products via:

$$3MoSi_2 + 7Mo \longrightarrow 2Mo_5Si_3$$

$$MoSi_2 + 5Mo \longrightarrow 2Mo_3Si$$

Mo_3Si was the major phase in layer 2, as would be expected given the above stoichiometry. The other phase present in this region was Mo_5Si_3; this would form since there would still be excess silicon if the two end-members reacted to form strictly Mo_3Si. The minute presence of $MoSi_2$ implies incomplete reaction amongst starting powders. In layer 3, Mo_5Si_3 and $MoSi_2$ were the dominant phases, with Mo_3Si being a minor phase. Layer 4 was predominantly $MoSi_2$ with Mo_5Si_3 as a minority phase. Layer 5 was strictly $MoSi_2$.



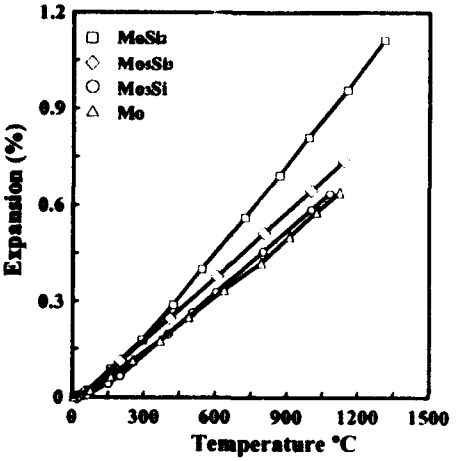


Figure 2: (left) Photograph of the functional gradient material. Top: layer 1, Bottom: layer 5.

Figure 3: (right) Expansion behavior of Mo[6], Mo_3Si[7], Mo_5Si_3[7] and $MoSi_2$[7].

These results indicate that reaction between powders occurred extensively, but protracted diffusion permitting annihilation of either Mo or $MoSi_2$ layers did not occur.

Visual observation showed cracking in layer 2, nucleating from the interface between layers 1 and 2 (Figure 2). Crack initiation in other layers was not apparent. The expansion behavior of these compounds is plotted in Figure 3. Since Mo has the lowest CTE, it (layer 1) would put the predominantly Mo_3Si layer (layer 2) in tension during cooling. The observed cracks, nucleating on layer 1, are the result of these tensile stresses.

Using the backscatter detector, compositional contrast permitted view of $MoSi_2$ and Mo_5Si_3 regions in the microstructure (Figure 4). Contrast between Mo and Mo_5Si_3 was inadequate, but these regions could be clearly delineated using SEM dot-mapping (Figure 5). The black oval-shaped regions in Figure 4 represent voids in the Mo_5Si_3 regions. While distributed somewhat throughout the Mo_5Si_3, the voids appear concentrated in fields just outside the $MoSi_2$ grains. The $MoSi_2$ regions represent the remains of unreacted original powder, while the Mo_5Si_3 regions represent reaction product between Mo and $MoSi_2$. Since $MoSi_2$ has the highest CTE, it is envisioned that during cooling, the contraction of the $MoSi_2$ grains put the surrounding Mo_5Si_3 grains in tension. Assuming that these Mo_5Si_3 regions are ductile at these temperatures, micro-fissures would form in regions near the $MoSi_2$ grains in response to the stress.

The sample hot pressed with $MoSi_2$ on all exterior surfaces and heat treated in air showed excellent oxidation resistance. Some cracking from the surface, possibly enhanced when attempting to remove the composite from the die, still did not allow oxygen to attack the Mo center (Figure 6). Apparently, amorphous silica reaction product filled in the cracks and sealed them.

The cyclic heat-treatments (Figure 7) were intended to show whether thermally induced fissures would form in the composite after cycling. SEM observation (not shown) showed

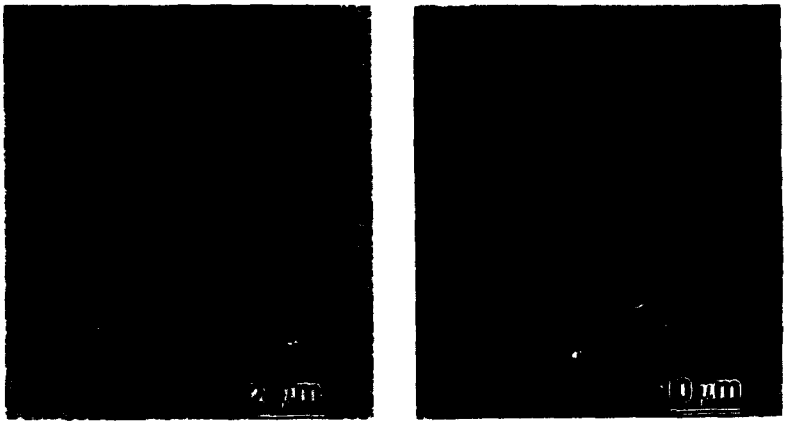


Figure 4: (left) Backscattered electron micrograph of $MoSi_2$ (dark regions) and Mo_5Si_3 (light regions) in layer 4.

Figure 5: (right) SEM/EDS dot-map of layer 2 where the dots represent silicon.

no indication of increased cracking due to thermal cycling. What was observed, however, was the onset of high temperature creep behavior near 1400°C. As shown by the dotted line in the figure, the specimen began contracting while it was still being heated near 1400°C. The maximum expansion was therefore lower during the second heating cycle when the specimen reached 1400°C. This creep behavior resulted from the appreciable force applied by the spring-loaded pushrod in the dilatometer. $MoSi_2$ has a demonstrated creep behavior above its brittle to ductile transformation temperature ($\sim$1000°C)[5].

For the present application, the load on the tube may in fact be nulled by varying the tube wall thickness so that the buoyant force on the immersed tube is matched by the gravitational force. Creep resistance has been reported to be improved by two orders of magnitude at 1200° by introducing second phase particulates/whiskers into a $MoSi_2$ matrix [5]. The introduction of these inclusions is under consideration for future work.

CONCLUSIONS

The five step functional gradient of Mo and $MoSi_2$ showed stress induced cracking only in Mo_3Si regions via tensile stresses applied by pure Mo. The introduction of a mediating layer of largely Mo with minute $MoSi_2$ (e.g. 5%) would be expected to minimize this cracking by forming a microstructure of mixed Mo and Mo_3Si grains, which would foster a less abrupt CTE gradient. These results form a basis for the design of powder composition as a function of depth for a continuous gradient. Such a functionally gradient material was shown to have promising thermal-mechanical behavior and good oxidation resistance when the $MoSi_2$ side is exposed to the atmosphere at elevated temperature.



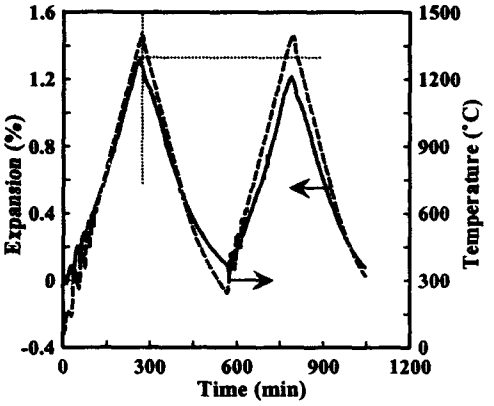


Figure 6: (left) Photograph of a functional gradient material, cut in half. The specimen, composed of pure $MoSi_2$ on all exterior surface, was exposed to an air atmosphere at 1600°C for 24 hours.

Figure 7: (right) Expansion/contraction behavior of the functionally gradient material with cyclic heat treatment. The temperature oscillations at low temperatures were from the gas flow tube obstructing feedback control communication between the heating element and the control thermocouple.

References

[1] W. Y. Lin, J.Y. Hsu, Y. Berta and R. F. Speyer, accepted for publication in Am. Ceram. Soc. Bull., 1994.

[2] W. Y. Lin, J.Y. Hsu, and R. F. Speyer, submitted for publication to J. Am. Ceram. Soc., 1993.

[3] W.Y. Lin, J.Y. Hsu, and R. F. Speyer, in Advances in Processing and Fusion of Glass, Ceramic Transactions; v 29, edited by A. K. Varshneya, Dennis F. Bickford and Peter P. Bihuniak (American Ceramic Society, Westerville, Ohio, 1993), p. 73.

[4] S. K. Sundaram, J.Y. Hsu, and R. F. Speyer, accepted for publication in J. Am. Ceram. Soc. for publication, 1993.

[5] A. K. Vasudevan and J. J. Petrovic in High Temperature Structural Silicides, edited by A. K. Vasudevan and J. J. Petrovic (Proceedings from the First High Temperature Structural Silicide Workshop, Gaithersburg, ML, 1991) pp. 1-17.

[6] L. Northcott, Molybdenum, (Butterworths Scientific Publications, London, 1956) p. 27.

[7] Y. S. Touloukian, Thermal Physical Properties of High Temperature Solid Materials, (The MacMillan Company, New York, 1967), pp. 441-443.

PART V

Recent Advances in Refractory Alloys and Processing

THE PROPERTIES AND USES OF REFRACTORY METALS AND THEIR ALLOYS

C.L. BRIANT
General Electric Company, Research and Development Center, P.O. Box 8
Schenectady, New York 12301

ABSTRACT

This paper reviews the problems that have limited the applications of refractory metals and their alloys. It also presents examples from recent work that has been done to overcome these problems. The work discussed concerns the refractory metals niobium, tantalum, molybdenum, and tungsten and alloys based on these elements. Recent results on intermetallic compounds that contain a refractory metal and composites that are made of refractory metals and their intermetallics are also presented.

INTRODUCTION

The primary purpose of this paper is to provide an introduction to the second half of this volume. The preceding papers dealt with research that concerned silicides, with a strong emphasis on $MoSi_2$. In the following papers the scope will be broadened to consider, more generally, refractory metals and their alloys. This introductory paper describes the background that has led to much of the research that is being done today and outlines the general directions that this research is taking. Results from this research will be discussed in much greater detail in the individual papers that follow.

REFRACTORY METALS

The first question that must be addressed when one considers refractory metals is what elements can be classed under this heading. Some classifications use the melting point as the only criterion and state that any metallic element with a melting point above 1925°C should be considered as a refractory.[1-3] If this definition is used, eleven metals would fall into this category. Other definitions are more restrictive and include the requirements that the metal have a body-centered-cubic crystal structure and that the ratio of the melting point of the oxide of the metal to that of the metal itself be less than one.[2] However, if one simply asks which of these very high melting point metals have received the greatest attention by researchers and which have the widest industrial applications, four elements clearly stand out. They are tantalum, niobium, molybdenum, and tungsten.

Table I gives some of the basic properties of these metals. They have high melting points and a body-centered-cubic crystal structure. If we plot the melting point as a function of density, as shown in Figure 1, we see that the densities of these four elements range from an intermediate value to a very high one. The figure also shows that for a given density range these elements have the highest melting points of the elements in that range.

The most attractive feature of these elements is their high melting points, and Table II shows that many applications of refractory metals and their alloys capitalize on this particular property. However, this list of applications is not as long as one might expect, because these elements also have certain features that limit their applications. Much of the

Mat. Res. Soc. Symp. Proc. Vol. 322. ©1994 Materials Research Society

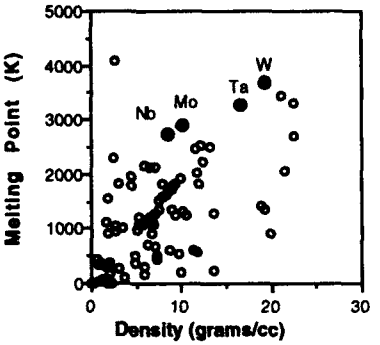


Figure 1 - The melting point of all elements plotted as a function of density. Note that the four refractory metals, niobium, tantalum, molybdenum, and tungsten, have among the highest melting points of the elements.

Table I
Refractory Metals and Their Properties

Element	Nb	Ta	Mo	W
Structure	BCC	BCC	BCC	BCC
Melting Point (^{o}C)	2468	2996	2617	3410
Density (g/cc)	8.58	16.7	10.3	19.3
Elastic Modulus (GPa) [1]	110.3	186.16	289.58	358.53
Thermal Conductivity cal/cm/^{o}C/s [2]	0.125	0.130	0.34	0.397
Method of Production	Melting (electric arc and electron beam) [4]	Melting (electric arc and electron beam) Powder metallurgy[5]	Powder metallurgy Melting (electric arc and electron beam)[6]	Powder metallurgy Chemical vapor deposition Liquid phase sintering[7]
Ore Source	(Fe,Mn) $(Ta,Nb)_2O_6$ (Tantalite)[4]	(Fe,Mn) $(Ta,Nb)_2O_6$ (Columbite)[5]		(Fe,Mn)WO_4 (Wolframite) $CaWO_4$ (Calcite)[7]

research in previous years and also much of that reported in this volume have been directed at overcoming these problems. Some of the most important issues are the following:

(1.) At elevated temperatures the tensile strength and creep strength of these materials is low. Figure 2 shows that at 1100°C, which is less than half of the melting point for tungsten and molybdenum, these element have tensile strengths below 300 MN/m^2.[3]

(2.) All of these metals oxidize very rapidly at elevated temperatures.[1,3,8] Figure 3 shows that even at 800°C oxidation is significant, and that at at temperatures above 1100°C the low oxidation resistance of these metals can completely preclude their use.

(3.) Because of the high melting points of these metals and their tendency to oxidize, their fabrication can be difficult. Table I shows that tantalum, niobium, and molybdenum are usually melted by electric arc or electron beam practices, and tungsten products are most commonly made by powder metallurgy methods. Tantalum and niobium are ductile at room temperature and can be mechanically processed at that temperature. Figure 4 shows that the ductile-to-brittle transition temperature of molybdenum is often close to room temperature and that of tungsten well above it. Consequently, these metals must be warm or hot worked.

Table II
Applications of Refractory Metals and Their Alloys

Element	Pure Element	Alloy
Ta[5,9]	Chemical industry Capacitors Weapons systems Alloying element	Aerospace systems Heat exchangers Furnace parts
Nb[10,11]	Alloying element	Aerospace industry Nozzle flaps for jet engines
Mo[6]	Lighting industry Alloying element	Aerospace industry Leads for incandescent lamps
W[7]	Heating elements Wall of plasma containment chamber Screens for photoetching Alloying element	Incandescent lamp filaments Cutting tools Propulsion systems Thermocouples Filaments for X-ray tubes

In a number of cases these difficulties have been surmounted, and it has been possible to use these refractory metals. A good example is the production of ductile tungsten for lamp filaments by the Coolidge process.[12] In this process tungsten is deformed at elevated temperatures by either swaging or wire drawing until a fibrous structure is produced. Once this structure is obtained, the ductile-to-brittle transition temperature of tungsten decreases to below room temperature and the material can be handled much more easily. It is the room temperature ductility of tungsten wire, which is achieved because of the fibrous structure produced by wire drawing, that allows lamp filaments to be coiled. However, in many cases it has not been possible to overcome these problems through process developments. Consequently, researchers have turned to alloying to try to improve the properties of these metals. The following section gives some examples of these improvements.

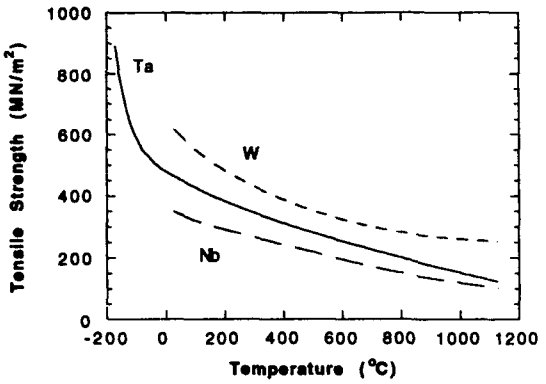


Figure 2 - The tensile strength of niobium, tantalum, and tungsten plotted as a function of temperature. Data taken from reference 3.

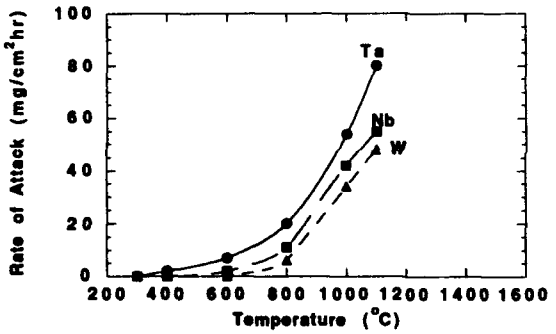


Figure 3 - The oxidation rate of tantalum, niobium, and tungsten plotted as a function of temperature. Data taken from reference 3.

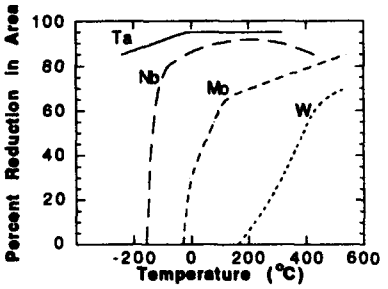


Figure 4 - The reduction in area in tensile tests plotted as a function of test temperature for tantalum, niobium, molybdenum, and tungsten. Note that the latter three metals show well defined ductile to brittle transition temperatures. Data taken from reference 2.

REFRACTORY METAL ALLOYS

Elevated Temperature Tensile Strength

Most work to improve the elevated temperature tensile strength of tantalum and niobium has relied on solid solution strengthening. Figure 5 shows the effect of tungsten, hafnium, and rhenium on the elevated temperature tensile strength of tantalum. Rhenium provides the greatest improvement, but the benefit it provides at elevated temperatures is offset by the fact that it makes tantalum very brittle at room temperature and hence difficult to process.[2,13] This fact, coupled with the expense of rhenium, has limited its use in tantalum-based alloys. Most commercial tantalum-based alloys available today are Ta-W alloys, with the tungsten compositions ranging between 2 and 10wt.%; higher levels of tungsten can lead to room temperature embrittlement.[14] In some cases hafnium is also added at levels up to approximately 2 wt.%.[2]

Figure 6 shows the effect of various alloying elements on the yield strength of niobium.[2,15] Again, rhenium would appear to be very beneficial at elevated temperatures, but for the same reasons described above for tantalum, its use as an alloying element in niobium has been very limited. Most commercial niobium-based alloys use hafnium, zirconium, and tungsten as their primary alloying elements.[2]

Unlike the situation in tantalum and niobium, rhenium additions provide improvements in the room temperature ductility of tungsten and molybdenum and thus it is used as an alloying element in these metals.[2,6,16-18] Rhenium, which has extensive solid solubility in both elements, also provides some improvement in the high temperature strength of tungsten and molybdenum. Data for tungsten are shown in Figure 7. However, it has been recognized that these alloys can be strengthened even more by using second phase particles such as ThO_2 and HfC. Therefore, particle strengthening has been used in W-Re and MoRe alloys in an attempt to provide exceptional high temperature strength.[6,19] Figure 7 shows the elevated temperature yield strength for W-Re-HfC and W-Re-ThO_2. The high temperature yield strength for the W-Re-HfC material is above 500 MN/m^2 at temperatures up to 1800°C and above 300 MN/m^2 at temperatures up to 2000°C. At temperatures between 1700 and 2100°C, these tensile strengths are some of the highest that have been recorded.[1] However, at temperatures above 2100°C coarsening of the HfC can lead to a rapid decrease in tensile strength.[19]

The final group of materials that exhibit high temperature tensile strength and creep strength are intermetallic compounds of which one element is a refractory metal.[20] Of these, the silicides and aluminides have received the most attention recently, since the addition of either element lowers the density of the compound relative to that of the refractory metal. One can thus achieve a high melting point and low density.[21] Although the creep strength of these compounds are often superior to those of the refractory metal[20,22], these compounds are also very brittle at room temperature with K_{IC} values of 1-3 $MPa\sqrt{m}$ [21,22]. This low fracture toughness greatly limits their applicability. However, as discussed below, they may be very useful as the strengthening phase when they are combined with a refractory metal or solid solution strengthened alloy in a composite.

Oxidation Resistance

Figure 3 shows that refractory metals oxidize very rapidly, and this drawback has limited their application. One approach to improving the oxidation resistance of refractory alloys has been to use coatings, and in some cases they are very effective[1,6,8,11, 23]. $MoSi_2$, whose oxidation resistance was discussed in papers earlier in this volume, has been used as a coating on molybdenum[6] and niobium.[8] Other silicides, such as niobium

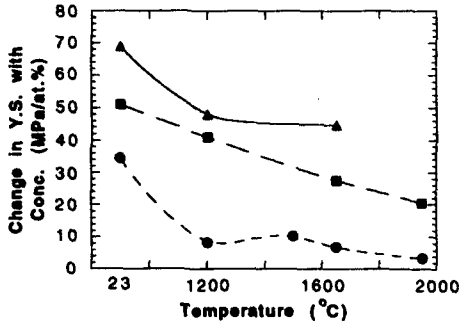


Figure 5 - The effect of alloying additions on the yield strenght of tantalum at room temperature and at elevated temperatures. The change in yield strength per increase in concentration is plotted as a function of test temperature. Data taken from reference 2.

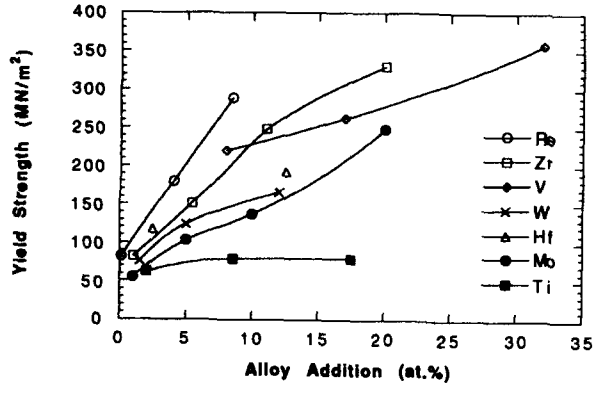


Figure 6 - The effect of various alloying addtions on the 0.2% yield strength of niobium at 1095°C. Data taken from reference 2.

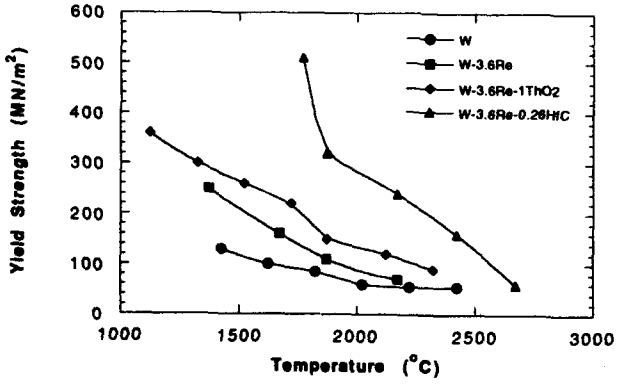


Figure 7 - The tensile strength of tungsten, W-3.6Re, W-3.6Re-1ThO2, and W-3.6Re-0.26HfC plotted as a function of test temperature. Data taken from reference 19.

silicide, both in its pure form and alloyed with iron and chromium[23], $(Mo,W)(Si,Ge)_2$ [8], and also aluminides[6] have been successfully applied. However, these coatings tend to be very brittle; some have ductile-to- brittle transition temperatures in excess of 1000°C [23]. Even a small mismatch in the thermal expansion coefficients between the base metal and the coating can lead to cracks. In some cases these cracks can heal, but often they expose the base metal which then rapidly oxidizes [23]. Consequently, the use of coatings to protect these metals is not always an adequate solution to the oxidation problem.

Significant improvements have been made in the oxidation resistance of niobium through alloying [24]. Figure 8 shows the oxidation rate of Nb-Ti-Al-Cr-Hf alloys and compares the results with conventional niobium alloys and nickel-based and cobalt-based superalloys. The results show that this combination of alloying elements provide a significant improvement in oxidation resistance over standard niobium alloys and that the oxidation rate of this alloy approaches that of the superalloys often used for high temperature applications.

COMPOSITES

One of the most interesting new types of refractory materials are those that have a composite structure. Most work to date has been done on a composite made of a refractory metal or alloy, most often niobium or niobium-based, and an intermetallic compound that contains a refractory element as one of its constituents. Figure 9a shows an example of a composite of a Nb-Cr solid solution and Cr_2Nb prepared by sputtering[20]; figure 9b shows a composite of prepared by directional solidification[25]. The goal of the development of these composites is to exploit the high temperature strength of the intermetallic compound and the room temperature ductility of the refractory metal. In this way, the room temperature toughness will be enhanced by ductile phase toughening.

Figure 10 shows room temperature fracture toughness for a Nb-10%Si alloy that consists of a composite of Nb and either Nb_3Si or Nb_5Si_3 and compares it with that of monolithic Nb_5Si_3. The results show that the room temperature toughness of the composite is considerably greater than that of the intermetallic and that the toughness of the composite can be affect by the way it is processed. Thus these composites appear to offer promise for many future applications.

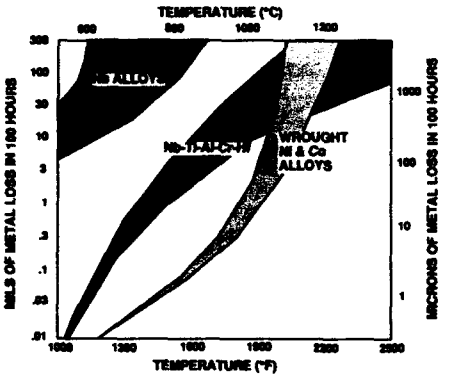


Figure 8 - The oxidation resistance of standard niobium alloys, a Nb-Ti-Al-Cr-Hf alloy, and wrought nickel-base and cobalt-base superalloys. Data taken from reference 24. Figure provided by M.R. Jackson, General Electric Research and Development Center, Schenectady, New York.

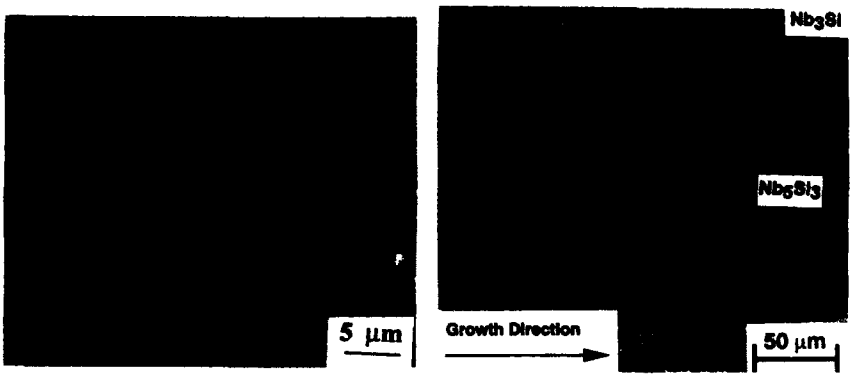


Figure 9 - Micrographs of refractory metal-based composites. (a.) A composite prepared by sputtering. The dark phase is Cr_2Nb containing Nb-Cr precipitates and the light phase is a Nb-Cr solid solution. The micrograph is courtesy of R.G. Rowe, General Electric Co., Research and Development Center, Schenectady, New York.[20] (b.) A Nb-Nb_3Si-Nb_5Si_3 composite prepared by directional solidification. The black phase is Nb_5Si_3 and the dark gray phase is Nb_3Si. The white phase is Nb. The photograph is courtesy of B.P. Bewlay, General Electric Research and Development Center, Schenectady, New York.[25]

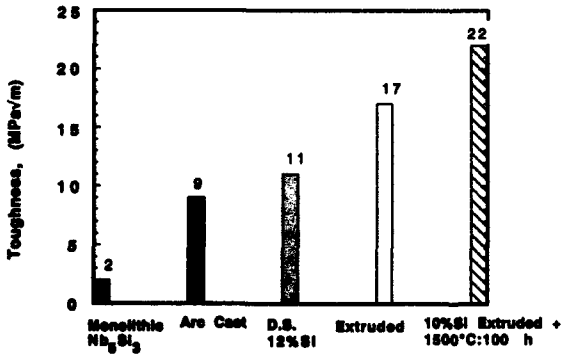


Figure 10 - The room temperature fracture toughness of monolithic Nb_5Si_3 compared to that of composites of niobium and either Nb_3Si (arc cast, directionally solidified, and extruded) or Nb_5Si_3 (extruded plus heat treated). Data taken from references 22 and 25. Figure supplied by B.P. Bewlay, General Electric Research and Development Center, Schenectady, New York.

SUMMARY

This paper has outlined some of the fundamental problems that in the past have prevented the use of refractory metals and their alloys in a number of applications. We have also shown that improvements in high temperature strength can be achieved with alloying and with particle strengthening agents and that oxidation resistance can be improved either with coatings or alloying additions. New techniques of alloy fabrication can provide optimization of a number of mechanical properties that should make these materials even more useful. In recent years the demands for new high temperature materials, primarily coming from the aerospace industry, has given a renewed interest to research on refractory metals and alloys, and interest in this area is approaching the level that it had in the 1950s and 1960s. Taken together, the papers that follow in this volume provide an excellent summary of the state-of-the-art of research in this field.

ACKNOWLEDGMENTS

The author would like to thanks Drs. B.P. Bewlay, M.R. Jackson, and R.G. Rowe of the General Electric Company Research and Development Center, Schenectady, New York, for supplying figures for this paper. He would especially like to thank Dr. Bewlay for many helpful discussions regarding this paper and for critically reading the manuscript.

REFERENCES

1. Jerry Wittenauer, JOM, **42**, 7 (August, 1990).
2. R.W. Buckman, Jr., in Alloying, edited by John L. Walter, Melvin R. Jackson, and Chester T. Sims, (ASM International, Metals Park, 1988) p. 419.
3. John Pugh, Journal of Metals, **212**, 335 (1958)
4. Chester T. Sims, Journal of Metals, **212**, 340 (May, 1958).
5. W. Kock and P. Paschen, JOM, **41**, 33 (October, 1989).
6. J. Wadsworth, T.G. Nieh, and J.J. Stephens, International Metals Review, **33**, 131 (1988).
7. Jerry P. Wittenauer, T.G. Nieh, and Jeffrey Wadsworth, Advanced Materials and Processes, **142**, 28 (September, 1992).
8. Mehmet Uz and Jerry P. Wittenauer, JOM, **44**, 25 (August, 1992).
9. Stacey M. Cardonne, P. Kumar, Christopher A. Michaluk, and H. Don Schwartz, Advanced Materials and Processes, **142**, 16 (September, 1992).
10. R.H. Titran and Toni L. Grobstein, JOM, **42**, 8 (1990).
11. J.J. Stephens, JOM, **42**, 22 (August, 1990)
12. W.D. Coolidge, J. Am. Inst. Elec. Eng., **29**, 253 (1910).
13. R.T. Begley, W.N. Platte, A.I. Lewis, and R.L. Ammon, EADC Technical Report 57-344, Part V, January, 1961
14. F.F. Schmidt, E.S. Bartlett, and H.R. Ogden, Technical Documentary Report No. ASD-TDR-62-594, Part II, May, 1963.
15. G.D. Gemmel, Trans. AIME, **215**, 898 (1959).
16. P.L. Raffo and W.D. Klopp, NASA-TND-2561, January, 1965.
17. W.D. Klopp, Transactions of Fourth Symposium on Space Nuclear Power Systems, Albuquerque, NM, 1987.
18. W.D. Klopp, W.R. Witzke, and P.L. Raffo, NASA TN D-3483, Cleveland Ohio, NASA Lewis Research Center, 1966.
19. Kwang S. Shin, Anhua Luo, Bor-Liang Chen, and Dean I. Jacobson, JOM, **42**, 12, (August, 1990).

20. R.G. Rowe, D.W. Skelly, M. Larsen, J. Heathcote, G. Lucas, and G.R. Odette, GE CRD Report 93CRD229, Schenectady, New York, December, 1993
21. Joseph D. Rigney, Preet M. Singh, and John J. Lewandowski, JOM, **44**, 36 (August, 1992).
22. D.M. Dimiduk, M.G. Mendiratta, and P.R. Subramanian, in "Structural Intermetallics," edited by R. Darolia, J.J. Lewandowski, C.T. Liu, P.L. Martin, D.B. Miracle, and M.V. Nathal, TMS Publications, (Warrendale, PA, 1993), pp.619-630.
23. Roger A. Perkins and Gerald H. Meier, JOM, **42**, 17 (1990).
24. M.R. Jackson, K.D. Jones, S.C. Huang, and L.A. Peluso, GE CRD Class I Report 90CRD182, September, 1992, Schenectady, NY.
25. B.P. Bewlay , H.A. Lipsitt , W.J. Reeder , M.R. Jackson and J.A. Sutliff , in Processing and Fabrication of Advanced Materials for High Temperature Applications III, edited by V.A. Ravi and T.S. Srivatsan (Warrendale, PA, TMS Publications, 1994).

RECENT ADVANCES AND DEVELOPMENTS IN REFRACTORY ALLOYS

T.G. NIEH AND J. WADSWORTH
Lawrence Livermore National Laboratory, L-350, P.O. Box 808, Livermore, CA 94551-9900

ABSTRACT

Refractory metal alloys based on Mo, W, Re, Ta, and Nb (Cb) find applications in a wide range of aerospace applications because of their high melting points and high-temperature strength. In this paper, we present recent progress in the understanding and applications of these alloys. Recent studies to improve the oxidation and mechanical behavior of refractory metal alloys, and particularly Nb alloys, will also be discussed. Some Re structures, for extremely high temperature applications (> 2000°C), made by CVD and P/M processes, are also illustrated. Interesting work on the development of new W alloys (W-HfC-X) and the characterization of some commercial refractory metals, e.g., K-doped W, TZM, and Nb-1%Zr, continues. Finally, recent developments in high temperature composites reinforced with refractory metal filaments, and refractory metal-based intermetallics, e.g., Nb_3Al, Nb_2Be_{17}, and $MoSi_2$, are briefly described.

INTRODUCTION

Although refractory metals have been used since the early 1900s for special applications in the chemical and electronic industries, it was not until the late 1950s that tonnage quantities of mill products were produced. At that time, the spectrum and range of quality of refractory alloys were comparable to those of stainless steels and superalloys. The production of molybdenum, tungsten, niobium, and tantalum alloy sheet was supported by most of the major US agencies, including the Department of Defense (DoD), the National Aeronautical and Space Administration (NASA), the Air Force Materials Laboratory (AFML), the Atomic Energy Commission (AEC), and the Bureau of Naval Weapons. As a result, a superb technical base for supporting major refractory metal use in nuclear and aerospace applications was developed. Two decisions in the early 1970's altered this picture dramatically. One was that work on nuclear space power systems was terminated in 1973 for an indefinite period. The second was the selection of reusable surface insulation (i.e., ceramic tiles) instead of coated refractory metals for thermal protection of the Space Shuttle.

In a report issued by Klopp [1] in 1974, work on refractory metal alloys before and after these decisions was well documented for one major facility specializing in this area, i.e., NASA's Lewis Research Center. The key issues described by Klopp are the dramatic decreases in funding, professional staff, and specialized facilities for refractory metals that occurred after about 1971-72. In fact, in 1974, the above NASA study was unable to identify any near term missions that would require refractory metal technology beyond the state-of-the-art that existed in 1974. This prediction has turned out to be rather accurate for at least a decade; the continuing work on refractory metals since about 1974 has largely been centered on the use of refractory metals for missile and spacecraft propulsion systems, selected jet engine components, and certain industrial applications.

In the mid 1980's, the above situation changed suddenly for two reasons. First, advanced compact nuclear systems, SP-100, were reconsidered as portable thermal and electrical power sources for possible aerospace applications [2]. Second, the advent of exotic vehicle designs such as the National Aerospace Plane (or derivatives of this concept) demanded the use of very high temperature materials that did not exist. The renewed interest in refractory metals for these applications resulted in advances in refractory metals for structural applications.

For many high-temperature structural applications, refractory alloys based on niobium (Nb), molybdenum (Mo), tantalum (Ta), tungsten (W), and even rhenium (Re) are the materials of choice. This is because, for applications requiring very high operating temperatures, strength levels are required that exceed the capabilities of conventional high temperature alloys such as stainless steels and superalloys. Figure 1 shows some comparative selected data for a number of

Mat. Res. Soc. Symp. Proc. Vol. 322. ©1994 Materials Research Society

competing high-temperature materials - including carbon, ceramics, and intermetallics. Each class of materials has inherent limitations which govern its application. In some cases, materials limitations are being solved through the use of engineered materials hybrids such as ceramic-coated refractory metals or ceramics toughened with a ductile refractory metal phase. For many applications, the use of ceramics and intermetallics is limited by technological immaturity. By way of contrast, current understanding and application of refractory metals is based upon nearly 40 years of application experience in high-temperature structures.

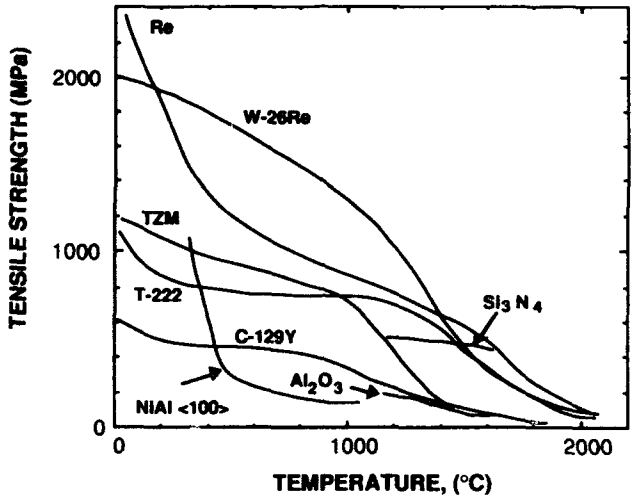


Fig.1 Strength as a function of temperature for selected refractory metals, ceramics, and intermetallics.

Selected data for the principal refractory metals are listed in Table I. As shown the favorable high-temperature strength properties of the refractory metals are often offset by poor room temperature ductility and fabricability (for Mo and W), embrittlement after welding or joining, and in some cases inadequate oxidation resistance. Despite these limitations, refractory metals have been used successfully in a number of demanding high-temperature structural applications — principally in areas of propulsion and energy conversion, such as rockets and re-entry systems [3]. Several refractory materials have also been supplanted in recent years by the demands of aerothermally-heated hypersonic vehicles, proposed high-Mach jet propulsion, and the development of thrust vector controls in advanced fighters.

Table I Selected Data for the Principal Refractory Metals

	Nb	Ta	Mo	W	Re
Melting Point (°C)	2468	2996	2617	3410	3180
Oxide Melting Point (°C)	1490	1772	795	1500	600
Density (g/cm^3)	8.6	16.7	10.2	19.3	21.00
Ductile-Brittle Transition (°C)	-125	-273	30	300	-273
Elastic Modulus (GPa)	110	186	324	405	460

By comparison, the production of alternative high-temperature structural materials (ceramics and intermetallics) has occurred over a much shorter time scale. Although ceramic "mill products" have been available for many years, it is only recently that the purity, density, and microstructural homogeneity of ceramics have allowed their consideration as useful high-

temperature engineering structural materials. Key technological advances have included improved toughness, greater availability of product forms, the introduction of ceramic-matrix composites, and gains in the area of superplastic forming. Intermetallic systems are at varying levels of technological maturity. Aluminides of Fe, Ni, and Ti, in particular, are presently under consideration for high-temperature application while a host of other intermetallic systems (e.g. silicides and beryllides) remain at the stage of laboratory examination. Practically all intermetallic systems under investigation today are seen as potential replacements for superalloys. Thus far, no intermetallic materials have emerged to challenge the refractory metals and ceramics for high-temperature (>1350°C) service.

The most recent review on refractory metals was conducted in 1988 [4]. Over the last few years, research has continued in all the major refractory metal groups. Symposia dedicated to the development of tungsten [5] and niobium [6] alloys have been held in the recent past. A special symposium was also organized in 1992 to address the evolution and history of refractory metals [7]. Another special symposium was also organized by the Engineering Foundation in 1993 to address specially on the recent advances in high temperature materials, including refractory metals [8]. In the present paper, we review the recent progress in the development of refractory metal alloys, including those based on tungsten, tantalum, molybdenum, niobium, and rhenium. Intermetallics and composites based on these metals will also be briefly described.

NIOBIUM

Alloys

The most significant technical effort in the field of structural refractory metals was probably the development of rapidly-solidified niobium alloys. This work was primarily triggered by an ARPA (formerly DARPA)-sponsored program on "Development of High-Temperature Metallics for Structural Aerospace Applications" in 1988 [9]. The goal of the program was to develop an intrinsically oxidation-resistant niobium alloy for use at 1537°C (2800°F). In 1991, a special symposium was dedicated to the modern development of high temperature niobium alloys [6]. Various topics related to the application of niobium, including oxidation, strengthening, and niobium-based composites, were addressed in the symposium.

As mentioned previously, the favorable high-temperature strength properties of the refractory metals are often offset by poor oxidation resistance. Traditionally, Nb alloys have to be protected by silicide coatings at high temperatures. An intrinsically oxidation-resistant Nb alloy would be extremely attractive, since niobium is less dense, but stronger, than Ni-base superalloys at high temperatures. The thermodynamic stability of various passivated oxide films are shown in Fig.2.. From an oxidation resistance point of view, passive oxides, such as a passive alumina (Al_2O_3) or silica (SiO_2) layer on Nb is desirable for temperatures above 2600°F (1700K). From Wagner's equation [10], in order to form an alumina scale, the critical aluminum content $N_{Al}^{crit.}$ must be

$$N_{Al}^{crit.} = \left(\frac{\pi g^*}{3} N_o^{(s)} \frac{D_o V_m}{D_{Al} V_{ox}}\right)^{1/2} \qquad (1)$$

where $N_o^{(s)}$ is the oxygen solubility in the alloy; D_o and D_{Al} are the diffusivity of O and Al in the alloy, V_m and V_{ox} are the molar volume of the alloy and oxide, and g^* is the critical volume fraction of oxide formed by internal oxidation. In order to develop protective scales therefore, one must increase D_{Al} and decrease $N_o^{(s)}$ and D_o in the alloy. For Nb, the addition of Ti, V, and Cr can produce these effects. Also, V and Cr can stabilize Al_2O_3 at low temperatures. (At low temperatures, Nb-Ti-Al alloys do not form Al_2O_3, but mixed transient oxides.) In fact, an alloy of composition Nb-44%Al-20%Ti-6%V-8%Cr was found to form an Al_2O_3 film at temperatures above 1000°C. Interestingly, similar results were obtained by Wukusick [11] about 30 years ago. The melting point of the new alloy was, however, low (about 1600°C). The low melting point resulted in poor mechanical strengths at high temperatures. Attempts to raise the melting point were made by replacing Nb (melting point ~2500°C) with much higher melting point Ta (melting point ~3000°C). This approach did lead to an increase in melting point, by approximately 300°C. The microstructures of the new Ta-Al-Ti-V-Cr alloys were, however,

thermally unstable. By comparison, their Nb counterparts had a relatively stable, two-phase structure.

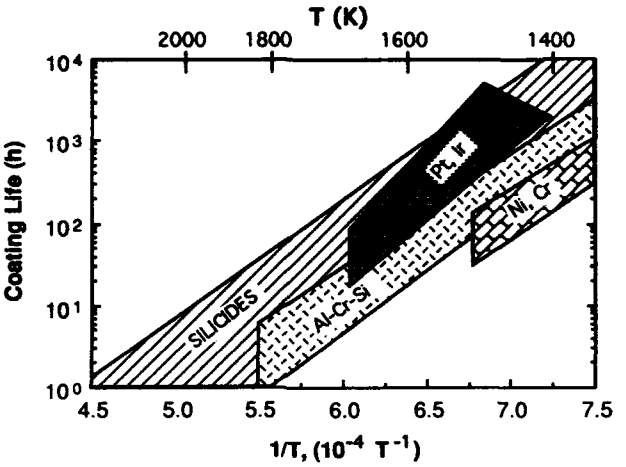


Fig.2 Formation of various oxide films as a function of temperature.

Technical efforts were also made to improve the strength and oxidation resistance of the above Nb-Al-Ti-V-Cr alloys via reinforcements [12]. Reinforcements such as Al_2O_3 and Y_2O_3 were found to be thermally and chemically stable with respect to Nb alloys (composition Nb-(23-25)at%Ti-(38-42)at%Al-3at%Cr-4at%V). In contrast, SiC, Nb_5Si_3, and AlN were found to react extensively with the Nb alloys at high temperatures. The reactions between SiC and Nb_5Si_3, and the Nb alloys resulted in Si formation and, thus, improvement in the oxidation properties of the Nb alloys. These reactions, however, also caused severe detrimental effect on the mechanical properties of these composites. Thermal and chemical instabilities eventually prevented the alloy from insertion into structural applications. Although the ARPA program did not directly result in an application product, the technical progress of the program greatly improved the basic understanding of Nb metallurgy.

Under the sponsorship of the U.S. Air Force, the dispersion strengthening behavior of niobium alloys has been investigated [13]. Dispersions were introduced through either alloying additions, or the additions of carbide, nitrides, and borides. Additions of up to 0.6 at% of refractory metals were found to be necessary to result in a uniform precipitate dispersion of refractory metal compounds. Nonetheless, blocky precipitates were still often observed to segregate preferentially at grain boundaries. The strongest alloys at 1400°C were those with precipitates (nitrides or borides) of the refractory metals Zr and Hf; the commercial alloys with large additions of Mo, Ta, and Zr; and the alloy containing TiN.

Some studies have been carried out to investigate the high-temperature deformation of conventional Nb alloys, and in particular Nb-1%Zr (one of the baseline materials for SP-100) [14]. Systematic investigation of the high-temperature deformation of Nb alloys has been conducted by Wadsworth *et al* [15]. Evidence was presented to indicate that many conventional Nb alloys are Class I solid solutions under creep conditions, as shown in Fig.3. In Class I solid solutions, creep behavior is believed to be controlled by solute drag on gliding dislocations. The law describing creep deformation can be written, in its simplest form, as $\dot{\varepsilon} = K \cdot \sigma^n$ where σ is the true flow stress, $\dot{\varepsilon}$ is the true strain rate, K is a material constant at a given temperature, and n is the stress exponent. In Class I solid solutions, n has a value of 3; this leads to an inherent high strain rate sensitivity of m = 0.33 in the equation $\sigma = k \cdot \dot{\varepsilon}^m$ where m = 1/n and k = 1/K. The strain rate sensitivity is known to control the rate of neck formation in tensile tests at elevated

temperatures. Most ordinary metals and alloys have values of $m \leq 0.2$ and, as a result, show modest tensile ductilities (from 50 to 100%) even at very elevated temperatures. Superplastic alloys have values of m between about 0.4 to 0.6. The high values of m in superplastic metals account for their high tensile elongations. The strain rate sensitivity of $m = 0.33$ found in Class I solid solutions is intermediate between that for pure metals and superplastic alloys, and therefore extended ductility (150 to 600%) is predicted for these alloys. This property is of potential importance to forming of these alloys.

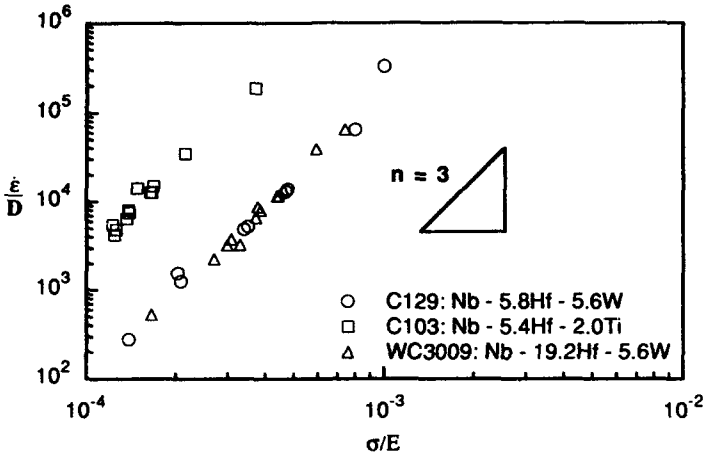


Fig.3 Diffusion-compensated strain rate versus modulus-compensated stress for niobium alloys C103, C129, and WC3009.

Niobium-base and niobium fiber reinforced composites

In seeking high temperature materials, NASA Lewis Research Center has made tungsten fiber reinforced niobium composites using an arc-spray process [16-18]. The mechanical properties (from 1300 to 1600K) of these composites were found to depend upon the W fiber; ThO_2 doped W fiber is more effective than K-doped lamp fiber. The strength difference between the two types of composites was suggested to be attributed to the fiber-matrix interface zone for the two fibers.

Several studies have been performed with the *in situ* 20% Nb-fiber reinforced Cu composites [19-21]. The composite was fabricated via a heavy drawing process; the reduction in area for the drawing process can, sometimes, be as high as 99.7%. Niobium was selected (versus W or Mo) because of its low ductile-to-brittle transition temperature. Experimental results showed that the *in situ* Nb-Cu composites generally exhibit good thermal conductivity and erosion resistance at elevated temperatures. The composites have been suggested for use as combustion chamber liners to replace conventional Cu. The *in situ* processing for Nb-fiber reinforced Cu composites involves spray deposition and subsequent consolidation by vacuum hot pressing or hot isostatic pressing. It is worth mentioning that two-dimensional Nb/Cu composites (laminates) have also been fabricated using a roll-bonding technique [22,23].

The recent interest in the development of structural intermetallics has extended to the niobium-based intermetallics [24-28]. Low-density niobium beryllides, e.g., $NbBe_{12}$ [27] and Nb_2Be_{17} [28,29], have been the emphasis of study in the US. The microstructure of these alloys is quite stable; these niobium beryllides exhibit good creep resistance at elevated temperatures. It has been suggested that creep deformation of these beryllides is controlled by dislocation glide.

Although these beryllides are lightweight and creep resistant at elevated temperature, the room temperature brittleness, as indicated by the DBTT behavior in Fig.4, and the handling problems associated with the toxicity of Be-containing compounds would prevent the alloys from a broad structural application.

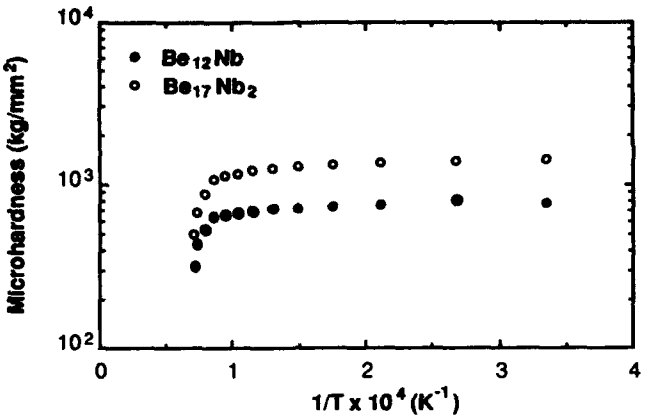


Fig.4 Hardness as function of temperature for various Nb beryllides.

Another Nb-base intermetallic, Nb_3Al (melting point~1960°C), is also currently being studied, particularly in Japan, as a potential extremely-high temperature material [24,30]. Many technical problems (such as extreme difficulty in material preparation, brittleness at ambient temperature, and expected poor oxidation resistance) are associated with using this material for structural applications. Nonetheless, it is important to point out that Nb_3Al is also a superconducting material. Hanada and Saito of Tohoku University [30] have successfully fabricated Nb_3Al by the so-called "Clad-Chop-Extrusion (CCE) Method," which involves cold rolling of clad Nb-Al sheets, followed by chopping and cold extrusion. They have produced good quality Nb_3Al wires by heat treatment of CCE materials at 1000°C. The work was performed under the Japanese MITI project on High-Temperature Ordered Intermetallics.

MOLYBDENUM

Alloys

Luo *et al* [31] investigated the effect of HfC additions (0.5 at.%) on the high-temperature microstructural stability and strength of Mo alloys. The dispersion of HfC in Mo was found to be effective in strengthening Mo; the tensile strength of Mo-HfC is approximately three times greater than that of commercially-pure Mo at 1830°C. The deformation mechanism in Mo-HfC was apparently dislocation glide up to 1530°C, and changed to grain boundary sliding at higher temperatures. In contrast, substructures such as subgrains, dislocation density, texture, and twin boundaries, were all found to be contributing factors to the strengthening of Mo-33 at.%Re at large deformation strains (i.e., various strains) [32].

In another study, potassium doping of molybdenum was carried out to improve high temperature strength; this is a similar approach to that used in K-doped W [33]. Experimental results indicate that doped Mo does offer a better creep strength than undoped Mo. This improved creep strength, together with the fact that Mo has a good thermal conductivity and low expansivity, makes K-doped Mo an attractive material for traveling wave tubes application [34].

There is considerable interest in the production of large-scale molybdenum single crystal sheets for electric components, and as blanket materials for controlled thermonuclear reactors

[35-38]. Secondary recrystallization processing has been used to produce single crystal sheets. The process involves the initial doping of sintered Mo with CaO and MgO and then hot rolling of sheet (~80% reduction in thickness). The rolled sheet is annealed above 2100°C to induce secondary recrystallization. Using the above technique, single-crystal Mo sheets of dimensions 2 mm x 40 mm x 180 mm have been made successfully [36].

In the case of joining, both electron beam welding [39-41] and friction welding [41] of Mo alloys (Mo, TZM, Mo-Nb) have been performed. The effects of impurity contents and their segregation at grain boundaries upon the properties of joints have been examined.

Intermetallics

Recent developments in intermetallics and intermetallic-matrix composites have led to an interest in developing $MoSi_2$ and $MoSi_2$-matrix composites for high-temperature structural applications [42,43]. The major problems associated with using $MoSi_2$ include low-temperature brittleness, dramatic loss of strength at temperatures >1200°C, and low-temperature pest. Many reinforcements have been added to $MoSi_2$ to improve its toughness and strength; reinforcements include ductile refractory metals (e.g., Nb and Ta [44,45]) and ceramic reinforcements, and in particular, SiC [46]. Although there are distinct advantages because of its excellent oxidation and corrosion resistance at high temperatures, molybdenum disilicide ($MoSi_2$) suffers from the "pest" phenomenon during low temperature (400-600°C) oxidation [47-49], as shown in Fig.5. This problem must be overcome before $MoSi_2$ can be widely accepted as a structural material. The development of $MoSi_2$ is extensively discussed in this symposium.

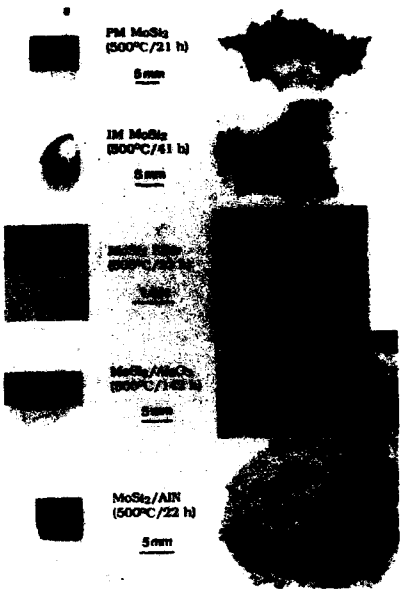


Fig.5 SEM micrographs showing the morphological characteristics of various $MoSi_2$-base materials before and after oxidation at 500°C.

TANTALUM

In contrast to other refractory metals, there has existed only a limited interest in using Ta alloys as structural materials in recent times. Tantalum has been treated as a model material for the evaluation of the performance of shaped charge liners. There was considerable experimental evidence to suggest that the crystallographic texture of the liners played an important role in jet formation and stability [50]. Efforts have been therefore made toward the characterization of the microstructural and textural development in pure tantalum [51,52] and Molybdenum [53] (both have a bcc structure) via thermomechanical processing.

It is of interest to note that the mechanical and structural properties of some Ru-Ta base intermetallic alloys ($L1_0$ structure) also have been investigated [54]. These research alloys were found to have good high-temperature specific strength and a reasonable room-temperature impact resistance. This is part of the technical effort by the US Air Force in seeking alloys for extremely high temperature applications [25,55].

TUNGSTEN

Alloys

There exists continued interest in the microstructure of tungsten rods [56,57] and the growth of creep voids in tungsten wire [58-61], as well as the effect of oxygen on tungsten filament sag kinetics [62]. In the area of alloy development, the Air Force remains interested in improving the room temperature fabricability and high temperature strength of tungsten via alloying. For example, rhenium has been added to thoria-doped tungsten and the alloy exhibits improved high temperature strength up to 2200K [63,64]. In contrast, W-Ir alloys were found to exhibit only a moderate strengthening effect, despite the fact that Ir and Re have a similar electronic structures [65]. In studying dispersion strengthening in W-base alloys, both HfC [64] and ThO_2 [66] have been alloyed to W-Re alloys. In the case of a W-26wt.%Re-1wt%ThO_2 alloy, ThO_2 was found to be effective up to about 2200K. In the case of W-3.6wt%Re-0.26wt%HfC, HfC particles were found to be even more thermally stable; in fact, the effectiveness of HfC extends to a temperature above 2600K [67]. The effectiveness of HfC can be understood according to an early description of carbide precipitation by Wadsworth [68].

Tungsten heavy alloys are penetrator materials which have a high toughness and a high kinetic energy. The uses include armor piercing projectiles as well as perforation devices for rejuvenation of stagnant oil and gas wells. Several recent studies have been performed to characterize the strength and ductility of W alloys as functions of alloy composition, microstructure, strain rate, and temperature [69-75]. The alloys were mainly based on W-Fe-Ni compositions, with various tungsten contents. Work softening effects, resulting from adiabatic heating, were observed to occur at strain rates higher than about 10 s^{-1} [69]. Cracking, and thus fracture, of the W heavy alloys was found to be mainly associated with the presence of a brittle phase at the W/Fe-Ni matrix interface.

Experimental evidence indicated that the performance of metals at high strain rates can be improved by refinement of grain size [76]. As a result, efforts have been made to produce W alloys with grain sizes finer than those of conventional W-Fe-Ni alloys. The approach taken was to minimize tungsten transport during liquid phase sintering. This was attempted by using an alloy matrix, such as Re- or Mo-modified Fe-Ni [77] or Cu [78], which has a reduced solubility for W during liquid phase sintering. Some progress was made, and the grain size of W alloys can now be reduced to the range of 5 μm (compared to 40-50 μm for W-Fe-Ni). Kim and Whang [79] have used a rapid solidification technique to examine the effect of cooling rate on grain refinement of W-Si alloys. The technique is interesting but may be impractical because of the extremely high melting point of W.

Tungsten alloys are conventionally manufactured using powder metallurgy techniques. Although chemical vapor deposition (CVD) has been used to process refractory metals, it has had only limited success in producing structural refractory metals with good mechanical properties. With the great improvement in CVD techniques in recent years, it is now possible to produce very fine-grained (~5 μm) W, as illustrated in Fig.6. The mechanical properties of the CVD W were observed to be similar to those of conventional powder metallurgy tungsten [80]. It is particularly noted that the technique has been used to produce net cone-shape charged liners [81].

Tungsten fiber reinforced composites

It is interesting to point out that W, because of its high modulus (~420 GPa) and excellent high temperature strength, has been investigated in wire form as a reinforcement for Cu and Ni superalloys [16,58]. In the case of W/Ni metal matrix composites, property improvements in the composites were found to be limited, as a result of extensive reaction between Ni and W at elevated temperatures [17]. In the case of W fiber-reinforced Cu composites (W/Cu), the composites were observed to have good thermal conductivity and exhibit excellent erosion properties at elevated temperatures [16,82]. Both W/Cu and Nb/Cu have been suggested as candidates for combustion chamber liners [83]. Although W/Cu possesses better properties than Nb/Cu, the fabrication processes of W/Cu are, however, quite elaborate and therefore expensive.

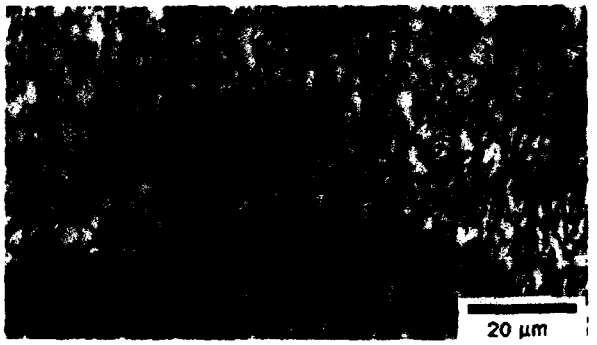


Fig.6 Microstructure of CVD tungsten showing fine grain size.

RHENIUM

Rhenium is the second highest melting point metal (3180°C), only lower than W (3400°C). It is more creep resistant than W and W-Re alloys at temperatures above 1600°C [84]. Also, Re is the only refractory metal that does not form a metal carbide. In fact, it has an extensive solid solubility (12 at.%) for carbon [85]. As a result, Re is expected to be compatible with carbon/carbon composites. These attractive mechanical and chemical characteristics have generated great interest in using Re for extremely high temperature applications, such as rocket thrusters and hot gas valves [81,86]. For instance, Re has been successfully tested for gas valve structures operating at 2200°C under the Lightweight Exoatmospheric Projectile (LEAP) Program, sponsored by the US Air Force. An artistic drawing of the LEAP is presented in Fig.7. To the authors knowledge, this may be the highest operating temperature for an engineering structure. The integrated gas valves of the structure require extensive joining. Brazing was considered impractical because it would reduce the service temperature of the valves. Rhenium can be joined by either electron-beam welding or diffusion bonding techniques, provided the bonding surfaces are properly cleaned. A cross sectional micrograph of a Re joint diffusion bonded at 2300°C with an applied stress of 10 MPa is shown in Fig.8. This joint has a strength of about 130 MPa at 2000°C. As shown in Fig.8, cracks do not propagate along bond interface.

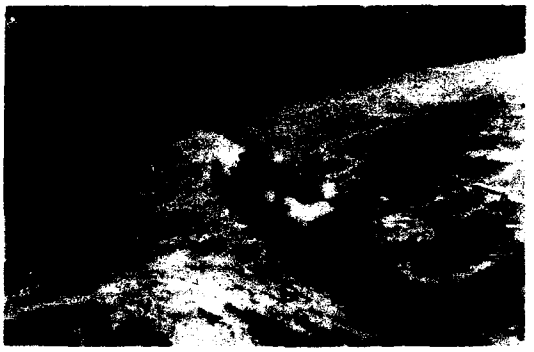


Fig.7 Artistic drawing of Lightweight Exoatmospheric Projectile (LEAP). The hot gas valves (indicated by arrows) operate at 4000°F (~2200°C).

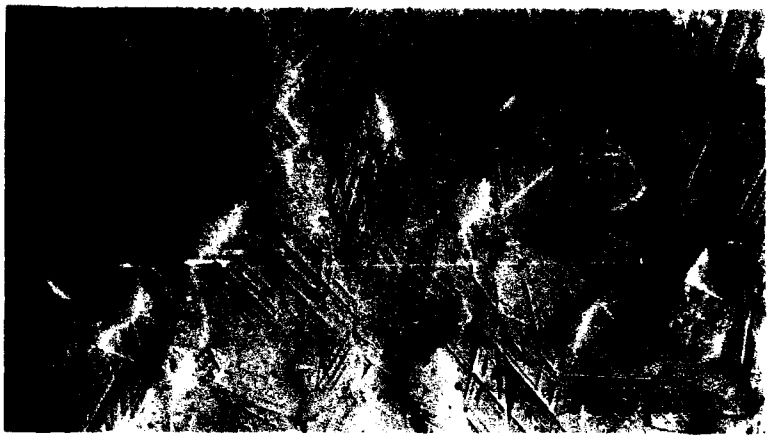


Fig.8 Cross sectional microstructure of a Re joint (indicated by arrows) diffusion bonded at 2300°C with an applied stress of 10 MPa.

Despite the above technological successes, the understanding of Re metallurgy is quite limited. Technical issues, such as oxidation protection, thermomechanical processing, and material availability are just some of the challenges. For instance, oxidation properties of Re are poor, as in the case of other refractory metals [87], although iridium coatings have been used to protect Re from excessive oxidation [86]. Rhenium has good room temperature ductility, but it has a relatively high strain hardening exponent [88]. As a result, Re is difficult to cold work into different shapes. Rhenium can be produced by halide reduction, but it is available only in limited quantity [89]. The cost of Re is, therefore, still high. In view of these technical and economic challenges, Re is not expected to be widely used, except in some special structures.

SUMMARY

The renewed interest in refractory metals for some major aerospace applications has resulted in advances in refractory metals for some structural applications. The major activities are summarized as follows.

1. Niobium - Emphases were on the development of intrinsically oxidation-resistant alloys and their composites. Some interest has been placed on the deformation and thus, the forming characteristics of these alloys.
2. Molybdenum - Thermal stability as well as the mechanical strength of Mo alloys (HfC- or K-doped) have been investigated. The major activity was, however, in the development of $MoSi_2$ and its composites for structural applications.
3. Tantalum - There is only limited interest in using Ta as a structural material; there has been some research work on texture development.
4. Tungsten - Hafnium carbide was found to be the most effective strengthener in W up to temperatures of ~2400°C. In addition, tungsten (and niobium) fiber reinforced copper was investigated as a high-strength, high-conductivity combustion chamber liner material to replace conventional copper.
5. Rhenium - Significant progress has been made in the understanding of Re metallurgy. Some special rocket thrusters and hot gas valves have been manufactured from Re and tested successfully at extremely high temperatures (~2200°C).

The development of other high-temperature structural materials (e.g., ceramics and intermetallics) has also taken place in the recent past. These new materials are, however, lacking

technological maturity. By comparison, refractory metals have been available for engineering use for over 100 years and have been used for aerospace hardware for at least 30 years. Some of the refractory metal structures may be gradually replaced by new materials, but certainly not in the immediate future.

ACKNOWLEDGMENT

This work was supported by the Department of Energy Contract No. W-7405-Eng-48 at Lawrence Livermore National Laboratory.

REFERENCE

1. W.D. Klopp, *Summary of NASA-Lewis Research Center Program on Refractory Metals for 1963-11974*, NASA-Lewis Research Center, 1974.
2. A.J. Bryhan and R.C. Chan, JOM, **45**(6) (1993), 50.
3. C.C. Wojcik, private communication, Teledyne Wah Chang, Albany, OR, 1991.
4. J. Wadsworth, T.G. Nieh, and J.J. Stephens, Inter. Mater. Rev., **33**(3) (1988), 131.
5. E. Chen, I. Ahmad, R. Ammon, and A. Crowson, *Tungsten and Tungsten Alloys- Recent Advances*, The Minerals, Metals & Materials Society, Warrendale, PA, (1991),.
6. J.J. Stephens and I. Ahmad eds. *High Temperature Niobium Alloys*, The Minerals, Metals & Materials Society, Warrendale, PA, (1991).
7. C.S. Olsen, E.N.C. Dalder, and T. Grobstein eds. *Evolution of Refractory Metal Alloys*, The Minerals, Metals & Materials Society, Warrendale, PA, (1993).
8. J. Wadsworth, J. Wittenauer, and T.G. Nieh, in *Critical Issues in High Temperature Materials*,. ed. N. Stoloff, Engineering Foundation, Washington, DC, (1993). (in press)
9. D. Alexander, D. Berczik, R. Bourdeau, R. Perkins, R. Svedberg, and J. Stephens, *Development of High-Temperature Metallics for Structural Aerospace Applications*, FR-20756, United Technologies, 1989.
10. R.A. Perkins, K.T. Chiang, and G.H. Meier, Scripta Metall., **22** (1988), 419.
11. C.S. Wukusick, *Oxidation Behavior of Intermetallic Compounds in the Nb-Ti-Al System*, GEMP-218, General Electric, 1963.
12. J.S. Lee, J.J. Stephens, and T.G. Nieh, in *High Temperature Niobium Alloys*,. ed. J.J. Stephens and I. Ahmad, The Minerals, Metals & Materials Society, Warrendale, PA, (1991), p. 143.
13. D.L. Anton, D.B. Snow, L.H. Favrow, and A.F. Giamei, *Dispersion Strengthening of High Temperature Niobium Alloys*, R89-917437-3, United Technologies Research Center, 1989.
14. M. Biberger, M.J. Davidson, and A.K. Mukherjee, Mater. Sci. Eng., **A159** (1992), 181.
15. J. Wadsworth, P.A. Kramer, S.E. Dougherty, and T.G. Nieh, Scr. Metall. Mater., **27** (1992), 71.
16. H.M. Yun and R.H. Titran, Metall. Trans., **23A** (1992), 3121.
17. T.L. Grobstein, *The Interface in Tungsten Fiber Reinforced Niobium Metal-Matrix Composites*, TM-102122, NASA, 1989.
18. T.L. Grobstein, *Creep Behavior of Tungsten Fiber Reinforced Niobium Metal-Matrix Composites*, TM-102307, NASA, 1989.
19. J.D. Verhoeven, W.A. Spitzig, F.A. Schmidt, P.D. Krotz, and E.D. Gibson, J. Mater. Sci., **24** (1989), 1015.
20. W.A. Spitzig, H.L. Downing, F.C. Laabs, E.D. Gibson, and J.D. Verhoeven, Metall. Trans., **24A** (1993), 7.
21. T.W. Ellis, I.E. Anderson, H.L. Downing, and J.D. Verhoeven, Metall. Trans., **24A** (1993), 21.
22. S.C. Jha, R.G. Delagi, J.A. Forster, and P.D. Krotz, Metall. Trans., **24A** (1993), 15.
23. P.D. Krotz, W.A. Spitzig, and F.C. Labbs, Mater. Sci. Eng., **A110** (1989), 37.
24. Y. Murayama, S. Hanada, and K. Obara, Mater. Sci. Eng., **A159** (1992), 173.
25. R.L. Fleischer, R.D. Field, K.K. Denike, and R.J. Zabala, Metall. Trans., **21A** (1990), 3063.

26. D.L. Anton and D.M. Shah, in *Intermetallic Matrix Composites, MRS Symp. Vol 194*,. ed. D.L. Anton, P.L. Martin, and D.B. Miracle, Materials Research Society, Pittsburgh, PA, (1990), p. 45.
27. C.H. Henager Jr., R.E. Jacobson, and S.M. Brummer, Mater. Sci. Eng., **A152** (1992), 416.
28. T.G. Nieh, T.C. Chou, J. Wadsworth, D. Owen, and A.H. Chokshi, J. Mater. Res., **8**(4) (1993), 757.
29. T.G. Nieh and J. Wadsworth, Scr. Metall. Mater., **24** (1990), 1489.
30. S. Hanada, private communication, Tohoku University, Japan, 1993.
31. A. Luo, J.J. Park, D.L. Jacobson, B.H. Tsao, and M.L. Ramalingam, Scr. Metall. Mater., **29** (1993), 729.
32. R.N. Wright, J.A. Brusso, and D.E. Mikkola, Mater. Sci. Eng., **A104** (1988), 85.
33. J. Choi, J.-H. Lee, I.-H. Moon, and H.S. Choi, Metall. Trans., **20A** (1990), 919.
34. C.M. McNally, T.G. Nieh, and W.H. Kao, Scr. Metall., **22** (1988), 1847.
35. T. Fujii, R. Watanabe, Y. Hiraoka, and M. Okada, Mater. Sci. Eng., **68** (1984), 45.
36. T. Fujii, R. Watanabe, Y. Hiraoka, and M. Okada, J. Less-Comm. Metals, **96** (1984), 297.
37. T. Fujii, R. Watanabe, Y. Hiraoka, and M. Okada, J. Less-Comm. Metals, **97** (1984), 163.
38. J. Xianlian and J. Pingan, J. Mater. Sci. Lett., **9** (1990), 763.
39. F. Morito, J. Mater. Sci., **24** (1989), 3403.
40. F. Morito, JOM, **45**(6) (1993), 54.
41. H.A. Calderon, G. Kostorz, and G. Ullrich, Mater. Sci. Eng., **A160** (1993), 189.
42. J.J. Petrovic, R.E. Honnell, and A.K. Vasudevan, in *Intermetallic Matrix Composites, MRS Symp. Vol 194*,. ed. D.L. Anton, P.L. Martin, and D.B. Miracle, Materials Research Society, Pittsburgh, PA, (1990), p. 123.
43. A.K. Vasudevan and J.J. Petrovic, Mater. Sci. Eng., **A155** (1992), 1.
44. T.C. Lu, A.G. Evans, R.J. Hecht, and R. Mehrabian, Acta Metall. Mater., **39** (1991), 1853.
45. K.T.V. Rao, W.O. Soboyejo, and R.O. Ritchie, Metall. Trans., **23A** (1992), 2249.
46. D.H. Carter, *SiC Whisker-Reinforced $MoSi_2$*, LA-11411-T, Los Alamos National Laboratory, New Mexico, 1988.
47. T.C. Chou and T.G. Nieh, J. Mater. Res., **8**(1) (1993), 214.
48. T.C. Chou and T.G. Nieh, J. Mater. Res., **8**(7) (1993), 1605.
49. T.C. Chou and T.G. Nieh, Scr. Metall. Mater., **26** (1992), 1637.
50. J. Jamet, in *8th International Symposium on Ballistics*,. ed. W.G. Reinecke, AVCO System Division, Wilmington, MA, (1984), p. v1.
51. J.B. Clark, J. R.K. Garrett, T.L. Jungling, R.A. Vandermeer, and C.L. Vold, Metall. Trans., **22A** (1991), 2039.
52. J.B. Clark, J. R.K. Garrett, T.L. Jungling, and R.I. Asfahani, Metall. Trans., **22A** (1991), 2959.
53. C.S. Choi, H.J. Prask, J. Orosz, and E.L. Baker, J. Mater. Sci., **28** (1993), 3557.
54. R.L. Fleischer, R.D. Field, and C.L. Briant, Metall. Trans., **22A** (1991), 129.
55. R.L. Fleischer, J. Metals, **37** (1985), 16.
56. C.L. Briant and E.L. Hall, Metall. Trans., **20A** (1989), 1669.
57. C.L. Briant, Mater. Sci. Technol., **7** (1991), 739.
58. H.M. Yun, Mater. Sci. Eng., **A165** (1993), 65.
59. J.L. Walter and E.F. Koch, J. Mater. Sci., **26** (1991), 505.
60. C.L. Briant, Metall. Trans., **24A** (1993), 1073.
61. C.L. Briant, Scr. Metall., **22** (1988), 1665.
62. J.W. Pugh, Metall. Trans., **20A** (1989), 1144.
63. A. Luo, D.L. Jacobson, and K.S. Shin, Scr. Metall. Mater., **25** (1991), 1811.
64. A. Luo, K.S. Shin, and D.L. Jacobson, Acta Metall. Mater., **40** (1992), 2225.
65. A. Luo, K.S. Shin, and D.L. Jacobson, Scr. Metall. Mater., **25** (1991), 2411.
66. A. Luo, K.S. Shin, and D.L. Jacobson, Mater. Sci. Eng., **A150** (1992), 67.
67. M. Liu and J. Cowley, Mater. Sci. Eng., **A160** (1993), 159.
68. J. Wadsworth, Metall. Trans., **14A** (1983), 285.
69. A. Bose, D. Sims, and R.M. German, Metall. Trans., **19A** (1988), 487.
70. A. Bose and R.M. German, Metall. Trans., **21A** (1990), 1325.
71. U. Gerlach, Metall. Trans., **17A** (1986), 435.
72. R.G. O'Donnell and R.L. Woodard, Metall. Trans., **21A** (1990), 744.

73. K.M.O. Zamora, J.G. Sevillano, and M.F. Perez, Mater. Sci. Eng., **A157** (1992), 151.
74. K.T. Ramesh and R.S. Coates, Metall. Trans., **23A** (1992), 2625.
75. R.S.A. Coates and K.T. Ramesh, Mater. Sci. Eng., **A145** (1991), 159.
76. C.G. Schmidt, R.D. Caligiuri, J.H. Giovanova, and D.C. Erlich, Metall. Trans., **22A** (1991), 2349.
77. A. Bose and R.M. German, Metall. Trans., **19A** (1988), 3100.
78. J.P. Wittenauer and T.G. Nieh, in *Tungsten and Tungsten Alloys- Recent Advances*,. ed. E. Chen, I. Ahmad, R. Ammon, and A. Crowson, The Minerals, Metals & Materials Society, Warrendale, PA, (1991), p. 21.
79. S.-G. Kim and S.H. Whang, J. Mater. Sci., **26** (1991), 5911.
80. J.P. Wittenauer and T.G. Nieh, in *Tungsten and Tungsten Alloys- Recent Advances*,. ed. E. Chen, I. Ahmad, R. Ammon, and A. Crowson, The Minerals, Metals & Materials Society, Warrendale, PA, (1991), p. 169.
81. T.G. Nieh, unpublished research, Lawrence Livermore National Laboratory, CA., 1993.
82. D.L. McDanels, *Tungsten Fiber Reinforced Copper Matrix Composites- A Review*, Technical Paper 2924, NASA, 1989.
83. L.J. Westfall and D.W. Petrasek, *Fabrication and Preliminary Evaluation of Tungsten Fiber Reinforced Copper Composites Combustion Chamber Liners*, TM-100845, NASA, 1988.
84. P.N. Flagella and C.O. Tarr, in *Refractory Metals and Alloys IV*, ed. R.I. Jaffee, G.M. Ault, J. Maltz, and M. Semchyshen, Gordon and Breach, Science Publisher, New York, (1967), p. 823.
85. B.W. Gonser ed., *Rhenium*, Elsevier Publishing Company, Amsterdam, (1962), p. 27.
86. J.C. Hamilton, N.Y.C. Yang, W.M. Clift, D.R. Boehme, K.F. McCarty, and J.E. Franklin, Metall. Trans., **23A** (1992), 851.
87. T.C. Chou, A. Joshi, and C.M. Packer, Scr. Metall. Mater., **28** (1993), 1565.
88. B.W. Gonser, editor, *Rhenium*, Elsevier Publishing Company, Amsterdam, (1962), p. 94.
89. A. Sherman, private communication, ULTRAMET Corp., Paloma, CA, 1993.

DEVELOPMENT OF HIGH-STRENGTH-FABRICABLE TANTALUM-BASE ALLOYS

R. W. Buckman, Jr.
Refractory Metals Technology
Pittsburgh, PA 15236

ABSTRACT

In the 1950s, Ta-7.5%W and the Ta-2.5%W were the only tantalum alloys of commercial significance. An intensive alloy development effort occurred between 1958 and 1968 in response to Air Force and Navy aerospace needs for high-temperature, oxidation-resistant alloys for rocket and air-breathing engines and airframe applications. Compatibility with oxidation-resistant coatings, high-temperature short-time strength, fabricability and weldability were of prime importance. These programs led to the development of Ta-10w%W, Ta-30w%Nb-7.5w%V, T-111(Ta-8w%W-2w%Hf), and T-222(Ta-10w%W-2.5w%Hf-0.01w%C). T-111, with its demonstrated compatibility with liquid alkali metals, and combination of strength, fabricability and weldability, was selected by NASA as the baseline reference alloy for space nuclear power systems studies. Significant quantities of T-111 and T-222 were produced in the 1960s. Today, however, production is limited to unalloyed tantalum and the tantalum-tungsten binaries because of the demand of the chemical industry for materials with outstanding acid corrosion resistance. To again produce T-111 and T-222 on a commercial basis will require relearning by the refractory metal alloy producers. The current lack of experience in the refractory metal industry with these high temperature alloys will necessitate recovery of the expertise needed for the United States to effectively compete in this technology arena.

INTRODUCTION

The evolution of tantalum alloy development was the subject of a recent paper presented at the 122nd National TMS Symposium. The basis and rationale for tantalum alloy development which started in the late 1950s and continued until 1972 is comprehensively covered by the authors [1]. This paper will present and discuss the characteristics and properties of the high-strength-fabricable tantalum-base alloys developed under Air Force and Navy sponsorship between 1958 and 1968. The sensitivity of hafnium containing tantalum alloys to contamination by copper and nickel, and the consequences of inadvertent exposure to copper during consolidation and processing, will also be discussed.

BACKGROUND

In the 1950s, the only tantalum alloys of commercial significance were the Ta-7.5%W (all compositions are given in weight percent unless otherwise noted) and the Ta-2.5%W which were used in the electronic and chemical industries [2-5]. An intensive alloy development effort occurred between 1958 and 1968 in response to Air Force and Navy aerospace needs for high-temperature, oxidation-resistant alloys for rocket and air-breathing engines and airframe applications. Compatibility with oxidation-resistant coatings, high-temperature short-time strength, fabricability and weldability were of prime importance. These programs led to the

Mat. Res. Soc. Symp. Proc. Vol. 322. ©1994 Materials Research Society

development of Ta-10%W [6], T-111 (Ta-8%W-2%Hf) [7], and T-222 (Ta-10%W-2.5%Hf-0.01%C) [8], under Navy sponsorship and the Ta-30%Nb-7.5%V [9,10] alloy under Air Force sponsorship. The chronology of development of these alloys is presented in Table I.

Table I. Tantalum Alloy Development Chronology

DEVELOPMENT PERIOD	ALLOY DESIGNATION	COMPOSITION, WEIGHT%
1950-1964	Ta-10W	Ta-10W
1958-1963	Ta-30Nb-7.5V	Ta-30Nb-7.5V
1958-1961	T-111	Ta-8W-2Hf
1961-1968	T-222	Ta-10W-2.5Hf-0.01C

TANTALUM ALLOY DEVELOPMENTS

The Navy and the Air Force, the initial sponsors of tantalum alloy development activity, had as their objective, achieving the highest elevated-temperature-strength tantalum-base alloy(s) as determined by tensile and short time rupture properties with minimal degradation of the room and low temperature ductility characteristics of tantalum. Four alloy compositions exhibited good room temperature and cryogenic ductility, as illustrated by the data in Table II. The density of the Ta-30Nb-7.5V alloy was also significantly less (~30%) than the other tantalum alloys and this feature was attractive to the Air Force.

Table II. Room Temperature Tensile Properties, Density, and Cryogenic Bend Ductility for Tantalum Base Alloys [6,11-18].

PROPERTY	Ta-10W	T-111	T-222	Ta-30Nb-7.5V
Density, g/cc	16.9	16.7	16.8	11.9
UTS-MPa	620	620	827	882
YS-MPa	448	517	758	653
% Elong.	30	30	25	28
90° Bend* DBTT, °C, for:				
R_a**Base Metal	<-196	<-196	<-196	<-196
As-GTA Welded	-171	-129	-73	<-196

* - Bend radius = 1t where t = sheet thickness

** - 1 hour at 1650°C

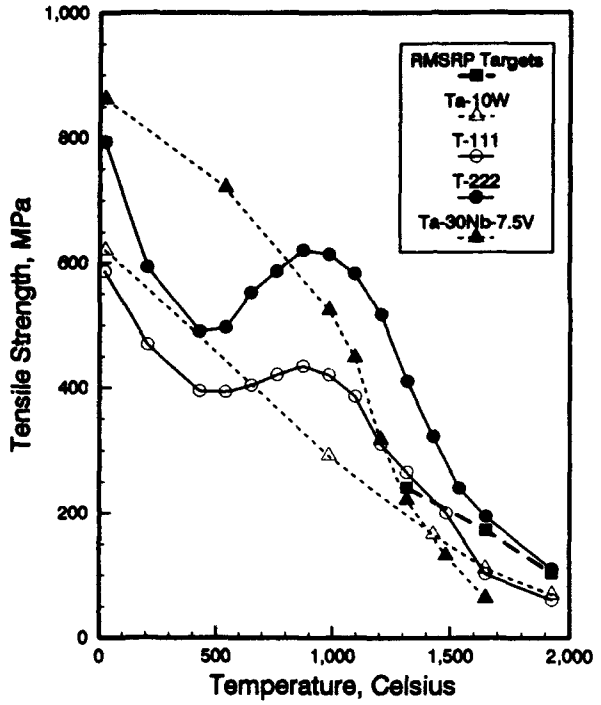


Figure 1. Tensile Strength of Tantalum Base Alloys [6,8,12,18,20].

Refractory Metal Sheet Rolling Panel (RMSRP)

In 1958, very few refractory-metal alloys were commercially available. Surface and dimensional control was poor and product quality extremely variable. There were no commercial tantalum sheet alloys available. Upon the recommendation of the Bureau of Naval Weapons, the Department of Defense asked the National Academy of Science to form a panel under the Materials Advisory Board to coordinate development activities aimed at providing high-quality sheet of the needed alloys. The RMSRP was formed in 1960. The decision as to which refractory metals or alloys would be supported was the responsibility of the sub-panel on Alloy Requirements and Selection. This panel set target properties for the specific classes of refractory metal alloys. The targets were submitted to the industry and candidate alloys were screened using the target properties as the criteria. T-222 was the only tantalum base alloy at that time which met or exceeded the target properties established by the RMSRP, and is illustrated by the data plotted in Figure 1. The short time stress-rupture properties for these alloys were in the same order. The stress for 10 hour rupture life at 1316°C for T-222, T-111, and Ta-10%W was 245, 70, and 160 MPa respectively [6,8,12,13-15]. In contrast, the Ta-30%Nb-7.5%V alloy could only sustain a stress of 110 MPa for a 10 hour rupture life at 1204°C [12].

In 1965, as one of the final actions prior to its dissolution, the RMSRP recommended no additional support for the Ta-30%Nb-7.5%V alloy, but urged continued effort on the T-222 alloy. The conclusions of the RMSRP were that tantalum alloys being developed should have a higher use temperature than niobium alloys and with better ductility. These objectives were met. One of the prime achievements of the RMSRP was to force a coordinated effort between the military user, the fabricator, and the producer. A detailed accounting of the activities and accomplishments of the RMSRP has been provided by Lane and Ault [19,20].

Alloy Design

The mechanism used initially to increase the high-temperature strength of the tantalum matrix was solid solution strengthening. The Ta-30%Nb-7.5%V, Ta-10%W, and T-111 alloys are generally referred to as solid solution strengthened alloys. However, T-111 has an uncontrolled increment of dispersed phase strengthening components which occur as the hafnium addition reacts with the residual interstitial impurities (C, O, and N) to form hafnium carbides, oxides, and/or nitrides [14,21]. The dispersed second phase particles which are most beneficial for increasing the elevated temperature strength are primarily the carbides. To take advantage of dispersed phase strengthening, intentional additions of carbon plus increased levels of hafnium and tungsten were added to T-111 to give the T-222 composition [8,13]. The alloy design of the tantalum base alloys closely paralleled the design of the high strength niobium base alloys described by Begley et al. [22].

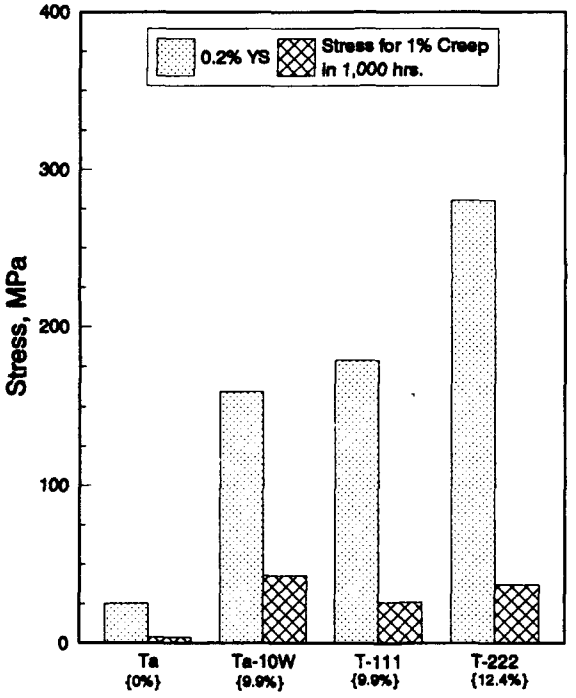


Figure 2. 0.2% Yield Strength and Stress to give 1% creep in 1000 hours at 1316°C [12,31]. {Atom % W + Hf}

Although the RMSRP focused on short time strength, there were developing in the 1960's long time applications associated with space nuclear power systems [23]. For these applications, creep or time dependent deformation was the primary strength criteria. When time dependent deformation is used as the strength criteria, the alloy ranking changes. For example, T-222 was the strongest tantalum base alloy when the tensile strength and 10 hour rupture life properties were the basis for comparison. However when the stress to give 1% creep in a 1000 hours is the criterion, both T-111 and T-222 are inferior to Ta-10%W as illustrated by the data plotted in Figure 2. This behavior can be explained by the observations of Sherby [24]. Two factors Sherby identified as controlling the time dependent deformation properties of a pure metal at and above $0.5T_m$ are its elastic modulus and the self diffusivity of the matrix. Adding hafnium to the Ta-W alloy matrix lowers the alloy melting temperature, thereby increasing the self diffusivity of the

matrix, and, hafnium will also lower the elastic modulus of the alloy matrix. Thus, T-111 and T-222 exhibit inferior long time creep strength at 1316°C (~0.5Tm) relative to Ta-10%W. The elevated temperature property characteristics of the Ta-30%Nb-7.5%V alloy can certainly be explained by the observations of Sherby [24].

TANTALUM ALLOY DESCRIPTION

Ta-30Nb-7.5V

The Air Force sponsored programs, carried out primarily at the Battelle Memorial Institute (BMI), Columbus, Ohio, focused on developing tantalum alloys with high specific tensile strength in the 1650-1927°C temperature range. Using high specific tensile strength, the Ta-30%Nb-7.5%V was identified by the BMI investigators as an optimum alloy composition and this composition was scaled up to production size quantities by The Wah Chang Corporation [11,12]. Although this alloy composition met some of the Air Force requirements, particularly lower density and compatibility with oxidation resistant coatings, the vanadium in this alloy presented difficulties, particularly during ingot consolidation by vacuum melting. Because of the high vapor pressure of vanadium, composition control during vacuum melting operations was difficult and welding by the electron beam process was not recommended [12].

Ta-10W

The Ta-10%W alloy was developed, under Navy sponsorship, at the National Research Corporation (NRC) (now known as the H. C. Starck Co.), in 1959-1960. During this time period the use of the electron beam melting in conjunction with consumable electrode vacuum arc melting produced ingots at the 115 mm diameter size [6,18]. The initial working of the as-cast ingot was by forging at 1100°C to sheet bar or round bar. After an in-process annealing heat treatment at 1650°C, final working to sheet or rod was done at room temperature. Ta-10W has been used as rocket nozzle inserts and piping for gas control systems for missiles. Ta-10%W is still being produced today, although the applications for this alloy are limited. Ta-10%W is generally melted as 200 - 250 mm diameter ingot and processed to rod or flat rolled product by a combination of forging for initial ingot breakdown, followed by swaging to produce a circular cross-section, and rolling to produce sheet and strip product [25].

T-111 and T-222

The research program, sponsored by the Navy Bureau of Weapons, initiated at the Westinghouse Electric Corporation Central Research Laboratory and continued at the Westinghouse Astronuclear Laboratory, focused primarily on investigating alloying additions and their effect on strength, ductility and weldability of tantalum. From a series of screening compositions, it was apparent that the best combination of strength and ductility with minimal effect on weldability was to be found in the Ta-W-Hf system. This alloy development program resulted in the development of the T-111 (Ta-8%W-2%Hf) alloy, which was subsequently optimized to the T-222 (Ta-10%W-2.5%Hf-0.01%C) composition [7,8].

The T-111 composition was developed under the initial Navy sponsored program [7]. Scale-up development of T-111 to 75 and 105 mm diameter ingot was demonstrated under Navy sponsorship [8]. Scale-up to commercial size ingots of T-111 was undertaken by Westinghouse

and 205 mm diameter ingots were produced and processed to sheet, rod, and tubular product. About this same time, commercial production of T-111 was undertaken, and one of the primary applications was for liquid alkali metal loops for space nuclear power studies being conducted under NASA sponsorship at the General Electric Company plant in Evendale, Ohio [26]. Although the hafnium addition to T-111 was to interact with residual interstitial impurities in the tantalum base, the hafnium addition was later discovered to provide resistance to corrosion by liquid alkali metals, particularly lithium [27,28]. Many hundreds of kilograms of T-111 material were produced in all mill forms for producing components for testing under the NASA sponsored program [26].

During the T-111 composition optimization studies, it was discovered that the weld ductile-brittle-transition temperature (DBTT) was sensitive to the W/Hf ratio. A minimum in the DBTT for as-GTA welded material occurred at a value of 4 and this effect was observed at W+Hf contents up to 14 weight percent [8].

Scale-up activities on T-222 culminated in a final Navy sponsored program to scale this alloy under the Phase I of the RMSRP program [15]. Under this program, a 229 mm diameter ingot weighing 454 kg was consumable-electrode-vacuum-arc melted into a water-cooled copper crucible. The ingot was processed to give fourteen sheets, each 610 mm wide x 1,220 mm long x 0.76 mm thick, which were thoroughly evaluated. The ingot was processed by a combination of extrusion, forging and sheet rolling using available metal working facilities. The yield of sheet from the as-melted ingot was 29.3%, from the conditioned ingot 34.6%, and from the conditioned extrusion 40.7%. The detailed evaluation of the sheet indicated excellent product uniformity within individual sheets, and from sheet to sheet within and between lots [15].

Silicide Coated T-222

Filippi [29] evaluated a (50%W-20%Mo-15%Ti-15%V)-disilicide coated T-222 sheet material product described in the preceding paragraph. The silicide coating was applied to the T-222 sheet specimens by a slurry-diffusion anneal process. The silicide coating provided excellent protection for times up to 500 hours of air isothermal exposure at 1316°C. Cyclic exposure reduced coating lifetime to about 300 hours. The coating was also susceptible to "pest" failure when exposed at 760°C. The silicide coating had minimal impact on the room temperature and 1316°C tensile strength as shown by Figure 3. The coating diffusion thermal treatment results in reduction of the creep resistance of T-222 as illustrated

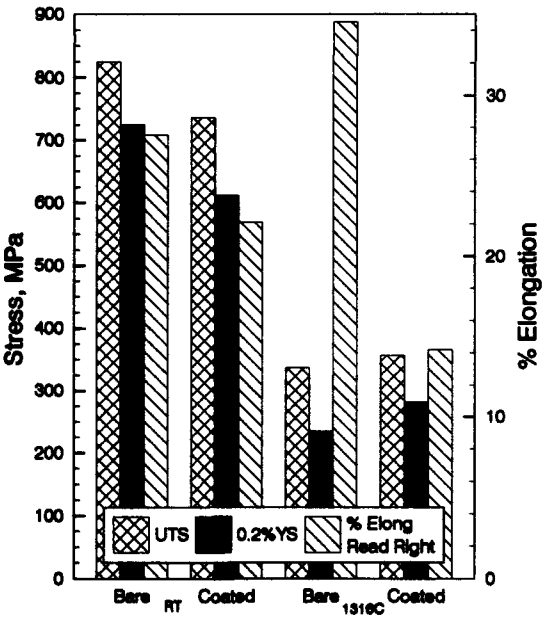


Figure 3. Tensile Properties of Bare and Coated T-222 at RT and 1316°C [29].

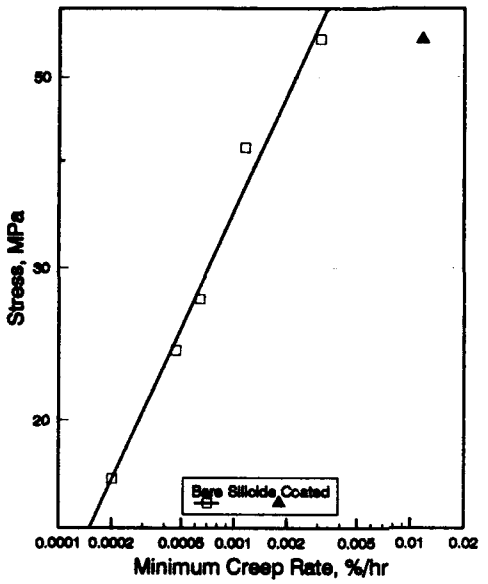


Figure 4. Creep Rate for Bare and Silicide Coated T-222 at 1316°C [29,32].

by the data plotted in Figure 4. It has been observed by a number of investigators that the carbide precipitate is a more effective strengthener when the precipitate reaction occurs under stress [22,30,31]. The carbide precipitates occurring without application of stress results in a carbide morphology that is not as effective a barrier to dislocation movement. This is the explanation for the increase in creep rate for the coated T-222 tested at 1316°C. However, the coated T-222 could sustain a creep rate of 0.018% per hour for up to 500 hours without coating failure. The ability to accommodate extension at this creep rate is attributed to a "self-healing" characteristic of this particular disilicide coating [29].

Accomplishments from Tantalum Alloy Developments

Out of the tantalum alloy development programs, came several significant accomplishments. These included the efficacy of the cold mold process for refractory-metal alloy development from non-consumable electrode melts of 50 grams to ingots weighing 500 kg with minimal differences in properties. One of the key developments contributing to the consistency of the tantalum alloy base was the introduction of electron beam melting capability in the 1958-1959 time frame [33,34]. The use of electron beam melting, coupled with the high melting temperature and low vapor pressure of tantalum, assured a high-purity product that was consistently reproduced [25,26]. Another key development was the use of the "sandwich" electrode design coupled with the use of single-phase AC power for consumable-electrode-vacuum-arc melting [8]. The sandwich "first melt" electrode design pioneered by the Westinghouse investigators was used to repeatedly melt complex compositions and control both substitutional and interstitial alloying additions to very close tolerances [8]. Early on in the developmental studies, it was recognized that low-density electrodes, fabricated from tantalum powders or tungsten powders could not be readily melted using a straight polarity DC arc due to the high electrical resistivity of the electrode [7]. This problem was overcome by the use of single-phase AC power supplies, which overcame the electrode resistance. The use of single-phase AC power for consumable-electrode-vacuum-arc melting was pioneered by Climax for melting molybdenum and molybdenum alloys. The reason for the selection of single-phase AC power for melting molybdenum by Climax was not from a technical consideration but was based on availability [35].

Copper Contamination

One issue which was recognized during the fabrication of T-111 components was the sensitivity of the hafnium bearing tantalum alloys to contamination by copper and nickel [36]. Both copper and nickel form eutectics with hafnium which form at 980 and 1150 °C respectively. Great care was taken in the 1960s to establish processing and handling procedures which minimized exposure to these elements. The issue of copper contamination is of particular significance since all vacuum melting operations, both by the electron beam and consumable electrode arc remelting is done using water cooled copper molds. When conditions are closely controlled, copper contamination during melting has only rarely been observed and when it occurred, it was generally with a major burn through and subsequent scrapping of the ingot being melted.

Recently, T-222 material was produced for the first time in about 20 years. During the consumable electrode vacuum arc melting operation, copper contamination occurred [37]. Improper stirring coil design and lack of adequate water cooling were the reasons attributed to the copper transfer from the mold to the ingot sidewall during melting. Attempts were made to mechanically and chemically remove all traces of the copper contamination and it was assumed that the procedures used were successful. A section of the ingot was coated with a silicide and heated to 1450°C(2600°F) for forging. Although significant losses occurred during the hot forging operation, a sizeable section of billet was recovered and conditioned to produce what was assumed to be sound sheet bar. The conditioned bar was vacuum annealed and then cold rolled to thin strip at room temperature. The strip was recrystallized and the room temperature tensile properties (803 MPa UTS, 753 MPa YS, and 27% elongation) were essentially equivalent to normal T-222. However when this same material was tested at 1200°C, the tensile elongation was essentially zero as failure was by intergranular separation, and the tensile strength measured was less than 34 MPa whereas T-222 normally exhibits a tensile strength of 414 MPa at 1200°C [37].

This "liquid metal embrittlement" failure is characteristic of tantalum or niobium alloys containing Group IVa Hf or Zr additions. Because of this sensitivity, it is of paramount importance that controlled processing procedures be in place to allow production of uncontaminated tantalum alloys, particularly those that contain hafnium such as T-111 and T-222. That this incident occurred is an indication of the loss of short term memory in the industry with respect to proper procedures for consolidation of the high strength tantalum alloys.

SUMMARY

Significant quantities of high strength-fabricable tantalum-base alloys were produced in the 1960s. Today, however, tantalum alloy production is limited to unalloyed tantalum and the tantalum-tungsten binaries because of the demand of the chemical industry for materials with outstanding acid corrosion resistance, and some minor requirements of the defense programs for the Ta-10W alloy. The market for high-strength fabricable tantalum-base alloys is small, and the government is still the primary customer as it was in the 1960s. If there is a resurgence in the demand for the high strength T-111 and T-222 alloys, there will be, more than likely, a painful relearning experience in applying the proper processing procedures for consolidating these alloys.

ACKNOWLEDGEMENTS

The author acknowledges the support and association with many colleagues during this era of concentrated refractory metal alloy development. Particularly, I would like to acknowledge T. A. Moss, R. L. Davies, R. T. Begley, R. L. Ammon, G. G. Lessmann, R. C. Goodspeed, J. L. Godshall, J. Cornie, D. E. Thomas and numerous support personnel whose dedication and professionalism made this work possible.

REFERENCES

1. R. W. Buckman, Jr. and R. L. Ammon "Evolution of Tantalum Alloy Development" Presented at 1993 TMS Annual Meeting, Denver, CO, February 21, To be Published.

2. A.B. Michael, in Refractory Metals and Alloys, 11, ed. M. Semchyshen and J.J. Harwood, Interscience Publishers, New York, Metallurgical Society Conferences, 1961, pp. 357-381.

3. L.D. Cunningham, "Columbium (Niobium) and Tantalum" (Annual Report, U.S. Department of the Interior Bureau of Mines, 1991).

4. Fansteel Metallurgical Corp., (U.S. Patents 1,701,299 and 2,015,509).

5. Fansteel Metals Brochure, "Tantaloy 61 Metal", (Published by Fansteel Inc. 1972).

6. M.L. Torti, "Development of Tantalum-Tungsten Alloys for High Performance Propulsion System Components" (Second Quarterly Report, Contract NOrd-18787, November 1958).

7. A.L. Feild, et al., "Research and Development of Tantalum and Tungsten-Base Alloys" (Contract NOas 58-852-C, Westinghouse Research Laboratories, May 26, 1961).

8. R.L. Ammon and R.T. Begley, "Pilot Production and Evaluation of Tantalum Alloy Sheet" (WANL-PR-M-004, Contract NOw-62-0656-d, Westinghouse Astronuclear Laboratory,15 June 1963).

9. F.F. Schmidt, et al., "Investigation of the Properties of Tantalum and Its Alloys" (Report WADD-TR-59-13, Battelle Memorial Institute, 1959).

10. F.F. Schmidt, et al., "Investigation of the Properties of Tantalum and Its Alloys" (WADD Technical Report 61-106, Battelle Memorial Institute, 1961).

11. D.J. Maykuth, A.G. Imgram, and H.R. Ogden, "Development of Techniques for the Production of Tantalum Alloy Sheet" (AF 33(657)-7015, Wah Chang Corporation, 1961).

12. Anon, Columbium, Tantalum and Tungsten Alloys Technical Information, vol. 3 (Wah Chang, Albany, A. Teledyne Co., Albany, Oregon 1968.

13. R.L. Ammon and R.T. Begley, "Pilot Production and Evaluation of Tantalum Alloy Sheet" (Part II, WANL-PR-M-009, July 1, 1964).

14. R.L. Ammon, A.M. Filippi and D.L. Harrod, "Pilot Production and Evaluation of Tantalum Alloy Sheet" (WANL-PR-M-014,Part III, Contract NOw-64-0394-d, Westinghouse Astronuclear Laboratory, October 1965).

15. A.M. Filippi, "Production and Quality Evaluation of T-222 Tantalum Alloy Sheet" (WANL-PR-9KK0-003, Westinghouse Astronuclear Laboratory, 1968).

16. H.R. Ogden, et al., "Scale-Up Development of Tantalum-Base Alloys" (Report No. ASD TR 61-684, Battelle Memorial Institute, 1962).

17. D.J. Maykuth, et al., "Development of Techniques for The Production of Tantalum Alloy Sheet"(AF33(657)-7015-Wah Chang Corporation, November 1961)

18. M.L. Torti, in High Temperature Materials II, (Met. Soc. Conf. 18, 1963), pp. 161-169.

19. G.M. Ault, "A Decade of Progress in Refractory Metals" (Presented at the 68th ASTM Annual Meeting, Lafayette, Ind., 13-18 June 1965).

20. J.R. Lane and G.M. Ault, in Metals Engineering Quarterly (American Society for Metals, August 1965), pp. 23-29.

21. R.L. Ammon and D.L. Harrod, in Refractory Metals and Alloys IV-Research and Development, ed. R.I. Jaffee, et al., (French Lick, IN, 3-5 October 1965), pp. 423-442.

22. R.T. Begley, et al., in Refractory Metal Alloys, ed. I. Machlin, R.T. Begley, and E.D. Weisert (Plenum Press, New York, 1961), pp. 41-84.

23. T.A. Moss, R.L. Davies, and G.J. Barna, in Recent Advances in Refractory Alloys for Space Power Systems,(Report NASA SP-245, 1969), pp. 1-18.

24. O.D. Sherby, "Factors Affecting the High Temperature Strength of Polycrystalline Solids", (Acta Met. vol. 10, 1962), pp. 135-147.

25. R.W. Buckman, Jr. in Proceedings of Refractory Alloy Technology for Space Nuclear Power Applications (CONF-8308130, January 1984), pp. 86-97.

26. E.E. Hoffman in Proceedings of Refractory Alloy Technology for Space Nuclear Power Applications (CONF-8308130, January 1984), pp. 18-33.

27. J.H. DeVan, et al. in Proceedings of Refractory Alloy Technology for Space Nuclear Power Applications (CONF-8308130, January 1984), pp. 34-85.

28. J.R. DiStefano and E.E. Hoffman in The Science and Technology of Tungsten, Tantalum, Molybdenum, Niobium and Their Alloys, ed. N. E. Promisel, (The MacMillan Company, New York, 1964), pp. 257-289.

29. A.M. Filippi "Evaluation of Mechanical Properties, Oxidation Resistance, and Structure of Slurry Silicide Coated T-222" NASA-CR-72713, December 1969.

30. A.L. Hoffmanner in Refractory Metals and Alloys IV-Research and Development, ed. R.I. Jaffee, et al. (French Lick, IN, 3-5 October 1965), pp. 639-657.

31. R.W. Buckman, Jr. in Alloying, ed. J.L. Walter, M.R. Jackson, and C.T. Sims (ASM International, 1988), pp. 419-446.

32. R.H. Titran, "Creep Behavior of Tantalum Alloy T-222 at 1365 to 1700 K" (NASA TN D-7673) June 1974.

33. H.R. Smith, in Transactions of The Vacuum Metallurgy Conference-1960 (Interscience Publishers, New York, 1961), pp. 255-266.

34. H.R. Smith, in Transactions of The Vacuum Metallurgy Conference-1962 (Publisher American Vacuum Society, Boston MA, 1963), pp. 95-102.

35. G.C. Timmons, Climax Metals-Private communication January 1992.

36. R.A. Ekvall, et al. in Recent Advances in Refractory Alloys for Space Power Systems, (NASA SP-245, 1970, pp. 221-261.

37. R.W. Buckman, Jr., Unpublished Data.

POWDER PROCESSING OF REFRACTORY METALS AND ALLOYS

RANDALL M. GERMAN
Engineering Science and Mechanics Dept., P/M Lab, 118 Research West, The Pennsylvania State University, University Park, PA 16802-6809, USA

ABSTRACT

For the past century the processing of refractory metals and alloys has been linked to powder metallurgy (P/M). A firm understanding of processing has been critical to attaining the desired performance levels. Although the consolidation science is in good shape, the availability of tailored powders with appropriate attributes is a limitation. This presentation reviews the key issues related to refractory metal and alloy processing, with particular emphasis on tungsten and its alloys. An exciting growth area is in liquid phase sintering microelectronic systems where the concern is with thermal properties, specifically for W-Cu and Mo-Cu.

HISTORICAL OVERVIEW

Powder metallurgy originated as a means of fabricating refractory metals in a nonfusion manner. Tungsten has been the pacing material and all other P/M refractory metal activities are small by comparison. By the late 18th century W was obtained by reducing Wolframite, an oxide of tungsten. The origin of the name tungsten came from the Swedish name meaning "Heavy Stone" [1]. Industrial applications emerged half a century later with early interest in incandescent lamp filaments. In 1910, Coolidge [2] successfully produced ductile filaments from sintered W powder mechanically worked and then drawn at room temperature. Similar work was carried by mixing W and Ni powders which were processed by liquid phase sintering. Subsequent work on W was performed by Smithells *et al.* [3] who investigated grain growth and its relation to powder particle size, compaction pressure, and sintering temperature. In 1938, Price *et al.* [4] prepared alloys of W-Ni-Cu with W contents from 80 to 97 wt% and achieved full density through liquid phase sintering. Because of the high density, these materials were used as shields for radium beam therapy. In recent years much emphasis has been on the W alloy systems [5-8].

POWDER FABRICATION

The conventional process of reducing ammonium paratungstate or tungsten oxide WO_3 in a hydrogen atmosphere is still the most widely used technique for producing pure tungsten powders. The particle size distribution is mainly affected by reduction conditions; temperature, time, hydrogen flow rate, and depth of the oxide layer [9]. The resulting powder has a cubic or an octahedral shape and a small particle size. Small particles require fine oxides, low reduction temperatures, high hydrogen flow rates, and short times. Electrochemical reduction processes are also employed where tungsten oxide WO_3 is fed into an electrolyte mixture of $Na_4P_2O_7$, NaCl, and $Na_2B_4O_7$ in a carbon cell with the cathode maintained at 1000°C. Powder size distribution is controlled by varying the current density. Chemical vapor deposition is also employed in the production of powder, where metal-halide gases are reacted in a hydrogen mixture. Submicron powders are obtained from tungsten chloride, but coarse powders result from fluoride-tungsten mixtures at temperatures up to 3000°C. Heavy alloy powders have been prepared from aqueous

Mat. Res. Soc. Symp. Proc. Vol. 322. ©1994 Materials Research Society

solutions. Ammonium metatungstate and sulfates or metal nitrates are freeze dried followed by calcination and hydrogen reduction [10]. Recently, plasma rapid solidification has been applied in the preparation of heavy alloy powders [11] with spherical shapes as shown in Figure 1.

Most P/M techniques are used in the compaction of the refractory metals, including conventional die compaction, hot or cold isostatic pressing, powder rolling (for sheets), extrusion (for rods), and injection molding. For some alloys, novel consolidation techniques have emerged, such as co-milling oxides so that reduction and densification are combined in a single sintering cycle [12].

POWDER INJECTION MOLDING

Powder injection molding (PIM) is a technique for producing complex shapes at low cost with high performance levels. The application of PIM to the refractory metals is a natural development since small powders are available from most of the candidate compositions [13-17]. One of the first commercial successes for PIM was a Nb rocket nozzle. The powders need to be equiaxed and deagglomerated with a smooth particle surface and wide size distribution (small mean size) to enhance the packing of the particles. Typically, the binder used is a thermoplastic. The removal of the binder from the powder compact is performed prior to sintering in a debinding step using thermal, solvent, or capillary extraction. Table I summarizes the mechanical properties of injection molded compacts as compared to die compacted materials; the PIM compacts exhibit competitive mechanical properties.

SOLID STATE SINTERING

Refractory metals can be densified by sintering at high temperatures without additives. For W powders formed by oxide reduction the typical sintering temperature ranges up to 3000° C for times between 15 and 30 min in hydrogen [18]. Heating is by direct current passage through the powder compact, giving sintered densities near 18 g/cm^3 (93% of theoretical). For fabrication of net-shapes, it is necessary to radiantly heat the compact in a refractory metal furnace. As an example, 4 μm W sinters to 84 to 94% of theoretical density using 2200° C for 4 h [19]. Longer times are required at lower sintering temperatures, namely 20 h at 1800° C for the same final density. Particle size is very important to densification. To attain 92% dense W at 1800° C, the following times are required for 1.7, 3.4, and 4.4 μm powders: 3, 22, and 50 h. Subsequent densification can be induced by post-sintering deformation. Dopants control the microstructure in sintering, especially in fabricating lamp filaments [20].

The fundamental sintering behavior is well understood and can be accurately predicted using multiple mechanism computer simulations [21]. The initial solid-state sintering is dominated by surface diffusion, particularly at lower temperatures. For tungsten, initial neck growth occurs between 600 and 1000° C without densification, because sintering is dominated by surface diffusion. Densification does not initiate until approximately 1000° C where grain boundary diffusion becomes active. Example input data for computer simulation of sintering are contained in Table II. Surface smoothing occurs and pores enlarge during heating [22], since neck growth by surface diffusion does not give densification. Hence, at higher temperatures there is a greater contribution from grain boundary diffusion. Such a mixture of sintering mechanisms (surface and grain boundary diffusion) was observed by Kothari [23] using powders between 0.5 and 15 μm and temperatures between 1100 and 1500° C. Grain boundary diffusion is dominant so there is great sensitivity to grain growth during sintering.

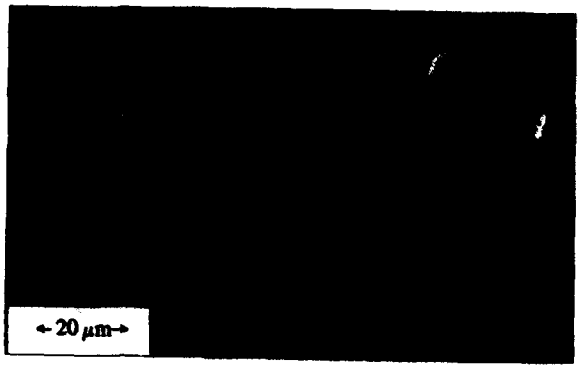


Figure 1. A scanning electron micrograph of a plasma microatomized tungsten alloy powder.

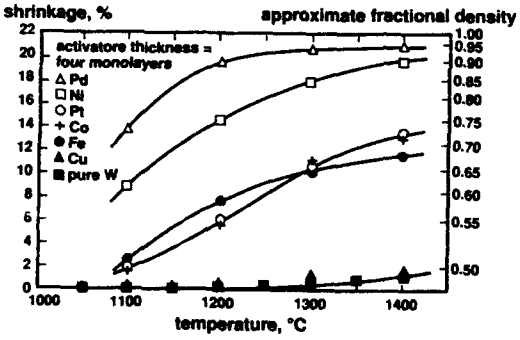


Figure 2. Shrinkage in isothermal sintering of tungsten showing the relative activator effect for various transition metals versus pure tungsten which gives minimal sintering response.

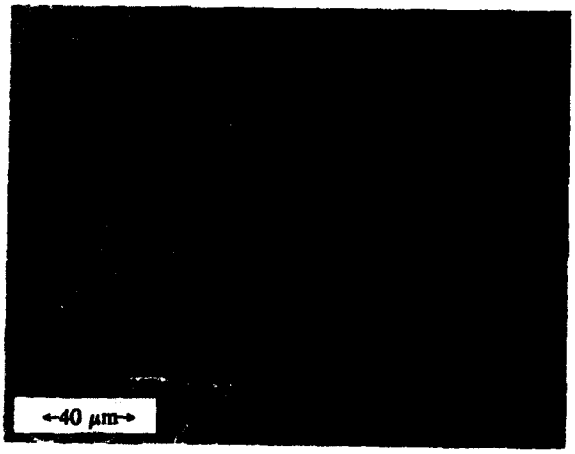


Figure 3. The microstructure of a liquid phase sintered 95% W heavy alloy, sintered 1480°C, 2 h.

Table I
Mechanical Properties of Tungsten Heavy Alloys

alloy and process	sintering temperature °C	yield strength MPa	tensile strength MPa	elongation %	hardness HRA
90W-8Ni-2Fe, P+S	1500	551	918	36	64
93W-5Ni-2Fe, P+S	1500	593	914	31	64
93W-5Ni-2Fe, PIM	1480	590	931	30	64
82W-8Mo-8Ni-2Fe, P+S	1500	688	1048	24	66
82W-8Mo-8Ni-2Fe, PIM	1500	700	1115	20	64
82W-8Mo-8Ni-2Fe, PIM	1530	688	1067	27	64

P+S = press and sinter, PIM = powder injection mold

Table II
Properties of Tungsten

Atomic number = 74
Atomic weight = 0.1839 kg/mol
Density = 19.3 Mg/m^3
Crystal structure = BCC
Melting temperature = 3410°C
Boiling temperature = 5900°C
Atomic volume = 1.59×10^{29} m^3
Burgers vector = 2.74×10^{-10} m
Thermal conductivity = 166 W/m/°C
Heat capacity (20°C) = 25 J/mol/°C
Thermal expansion coefficient (20°C) = 4.4 ppm/°C
Electrical resistivity (20°C) = 5.5 microhm-cm
Surface energy = 2.65 J/m^2
Elastic modulus (20°C) = 280 to 400 GPa
Shear modulus (20°C) = 160 GPa
Hardness (recrystallized) = 360 DPH
Yield strength (20°C) = 300 MPa
(annealed)
Yield strength (20°C) = 700 MPa (recrystallized)
Ductile to brittle transition temperature = 200 to 500°C
Catastrophic oxidation temperature = 600°C
Recrystallization temperature (90% CW) = 1420°C

Lattice diffusion	Frequency factor = 5.6×10^{-4} m^2/s	Activation energy = 585 kJ/mol
Boundary diffusion	Frequency factor = 5.5×10^{-13} m^3/s	Activation energy = 378 kJ/mol
Surface diffusion	Frequency factor = 2.6×10^{-13} m^3/s	Activation energy = 326 kJ/mol

Vapor pressure at 2000°C = 6.6×10^{-12} bar
Evaporation activation energy = 848 kJ/mol

PRESSURE ASSISTED SINTERING

Sintering densification can be enhanced by the application of a stress. Since strength drops with temperature, an external stress supplements the basic diffusional flow with plastic

deformation and creep processes. Hot isostatic pressing (HIP) densification is accurately computer simulated, giving plots of density versus pressure for various times and temperatures. For W densification is largely controlled by Nabarro-Herring creep. At 1500°C, full density is attainable with a 6 μm W powder at pressures of 200 MPa and times near 4 h. The other refractory metals prove equally responsive to high temperature HIP [24].

Hot isostatic compaction has been employed in the consolidation of W with the presence of a liquid phase [25,26]. Pressure induced preferential flow of the liquid into the pores creates inhomogeneities in the final microstructure. Thus the greatest promise for HIP is in healing defects. The benefits of such treatments are widely recognized in the cemented carbides [27]. The use of a post-HIP liquid phase sintering treatment eliminates agglomeration and inhomogeneity. This confirms a finding in many studies; solid-state processing of heavy alloys fails to give the homogeneity and properties obtainable with liquid phase sintering.

ACTIVATED SINTERING

The addition of small amounts of transition metals to a refractory powder results in an increased densification due to activated sintering [28-33]. This process is used in systems where processing at lower temperatures is desirable. The role of the additive is to lower the activation energy for bulk transport by providing a high diffusivity path. The W-Ni system is the best documented example. Figure 2 illustrates the dramatic sintering enhancement at relatively low temperatures for W due to four atomic monolayer coatings (approximately 0.2 wt.%) on the powder. In the 1100 to 1400°C temperature range the untreated W shows negligible sintering shrinkage. Gessinger and Fischmeister [31] suggested Ni segregation to the W grain boundary and successfully constructed a model for activated sintering assuming a diffusion controlled process. German and Munir [32] studied the effects of different dopants on the activated sintering of various refractory metals. They found the activation energies for shrinkage agree with activation energies calculated for heterodiffusion at the grain boundaries. Parameters that enhance activated sintering are a small particle size, high green density, and homogeneous activator distribution.

Activated sintering has been coupled with liquid phase sintering to promote densification. In the two step case, activated sintering is used to form a W skeleton and subsequently infiltrated by a liquid phase. Lee *et al.* [34] investigated the effects of Ni-P additions on the formation of a skeleton which enhanced the infiltration of Cu into the preform. The coupling of both processes has been demonstrated by Co additions to W-Cu [35]. Cobalt acts through activated sintering at low Cu contents, but gives a brittle W_6Co_7 intermetallic at the interface between the W and Cu.

LIQUID PHASE SINTERING

Sintering in the presence of a liquid can further accelerate densification and is widely employed for refractory metals. In the case of tungsten heavy alloys, a typical microstructure consists of solid grains in a solidified liquid matrix as shown in Figure 3. Wetting enhances densification since it promotes penetration along the particle contacts and grain boundaries. Further a wetting liquid exerts a strong attractive force that aids densification [5]. An additional effect is solubility. The best understood liquid phase sintered systems are the tungsten heavy alloys. However, they prove difficult to process into close final tolerances because of significant gravity effects [36,37].

During the first stage of liquid phase sintering, capillary forces due to the wetting liquid

act on the particles and pull them into close proximity by viscous flow. The liquid phase lubricates particle rearrangement and disintegrates particle clusters to allow repacking [38]. Pore growth occurs due to inhomogeneous liquid flow, resulting in a lower pore density but a larger pore size [39]. The uniformity of particle packing and mixing are major parameters in the rearrangement stage [40]. Shatt *et al.* [41] suggests dislocation pile-up at the grain boundary during compaction results in an increase of the grain boundary energy which favors the penetration of the melt. Particle shape accommodation brought about by solution-reprecipitation releases liquid to fill remaining pores [42]. Particle coalescence and neck growth proceed by mass transfer from small particles in the surrounding matrix [43]. Grain growth in systems with little or no solid solubility in the liquid, such as W-Cu and W-Au, is attributed to coalescence [44].

Grain growth, grain shape accommodation, and final pore removal occur during solution-reprecipitation [45]. Because a solid skeleton forms between the solid grains, any remaining pore elimination is dependent on diffusional relaxation of the skeleton. During the final stage of liquid phase sintering, grain coalescence contributes to grain growth. Yang *et al.* [46] incorporated the effect of contiguity on the growth kinetics of liquid phase sintered W-Ni-Fe heavy alloys, and observed good agreement with experimental results.

SINTERING ATMOSPHERE

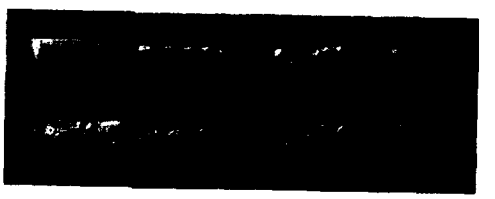
The sintering atmosphere has a direct effect on the residual porosity. Insoluble or low diffusivity gases such as argon or nitrogen result in entrapped pores in the microstructure. These pores persist during final stage sintering. The use of vacuum or high diffusivity gases inhibits the formation of such pores [47,48]. Residual porosity can also result from the reaction of hydrogen with dissolved oxygen in the refractory metals, forming water bubbles which cause swelling [49]. Figure 4 is an example of such surface blistering. Alternatively, in Ta the hydride reaction inhibits the use of a reducing atmosphere. For Nb, rapid heating gives liquid phase sintering from remaining surface oxides that are not evaporated [50]. Thus, atmosphere control during heating proves most important with the refractory metals.

The use of hydrogen in heavy alloy systems results in embrittlement leading to a decrease in ductility. The hydrogen preferentially concentrates in the matrix. The result is an apparent embrittlement because under deformation the hydrogen accumulates (via dislocation transport) at the interface, resulting in a decreased interfacial cohesion. Hence, an annealing cycle in an inert gas or vacuum after sintering is needed for high ductility alloys [47,51-53]. Impurity segregation is avoided with rapid cooling, leading to superior mechanical properties.

NOVEL CONSOLIDATION TECHNIQUES

Several new consolidation techniques have been applied to refractory metal powders. These include explosive and shock wave consolidation, plasma activated sintering, and various exothermic reactions for compounds. The explosive techniques are effective in delivering the heat and pressure pulses needed for densification [54]. However, the time at temperature is short and homogenization is poor, so post-consolidation heat treatments are needed. The milling of oxides or other mechanical alloying routes are under intense investigation, but the most successful results have been in systems such as Mo-W-Cu, where the fine scale of the milled oxides improves sintering. Plasma techniques are being explored for the atomization and alloying of refractory metals. One novel approach is to use a plasma inside the compact to activate the powder surface for subsequent low temperature

Figure 4. Surface blisters due to water vapor generation in closed pores during hydrogen sintering.



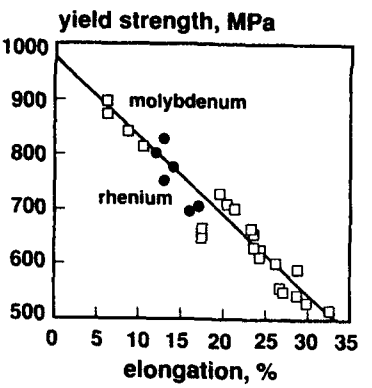


Figure 5. The relation between yield strength and fracture elongation for various heavy alloys.

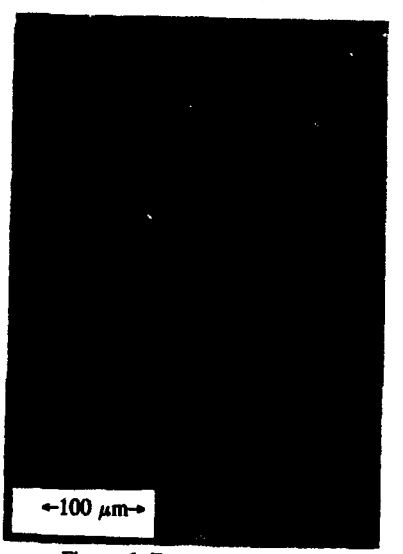


Figure 6. Fracture crack initiation at W-W contacts during tensile testing of a heavy alloy.



Figure 7. An example of the grain refinement possible in a sintered heavy alloy doped with Mo.

consolidation [55]. Finally, several self-propagating high-temperature synthesis reactions under study for various refractory compounds, including silicides, borides, carbides, and aluminides. A mixture of elemental powders is initiated and the resulting heat of reaction sustains the reaction. In a few instances the process has been controlled to generate intermetallics and non-oxide ceramics with attractive properties [56,57].

MECHANICAL PROPERTIES

The mechanical properties of the refractory metals processed by P/M are well documented in standard tabulations. Much attention has been directed to heavy alloys which benefit from the high strength tungsten combined with the high ductility matrix. Tensile strengths of 1000 MPa are usually obtained from liquid phase sintered composites with W compositions from 90 to 98 wt%. An elongation to failure of 30% is typical. A compromise between strength and ductility, as illustrated in Figure 5, is achieved through selection of intermediate compositions. Initial deformation initiates at the matrix which work hardens until a critical stress level around the W grains is reached [58]. At this point deformation of the W grains starts. Grain deformation is enhanced by the solid solution Ni and Fe in the W grains, but total ductility is dependent on the interfacial cohesion [53]. Fracture initiates at the W-W contacts as evident in the micrograph shown as Figure 6. These cracks link to eventually cause failure.

The mechanical properties of these composites are dependent on several factors [53,59,60]. Impurities can be detrimental to the properties of tungsten alloys. Phosphorus is often identified as a major actor in degraded properties [59,61]. A consequence of phosphorous contamination is a sensitivity to post-sintering heat treatment, alloying, and cooling rate [62].

As the tungsten content increases, strength increases with decreasing ductility. In the case of W-Ni-Fe, maximum tensile strength values are observed at 93 wt% W and approximately 7/3 Ni to Fe ratio. At higher tungsten levels, contiguity and connectivity increase, changing the fracture mode to intergranular failure. The mechanical properties at high tungsten contents are limited by the W-W contiguity [51,52,58,59,63]. During deformation the dislocation density increases up to 10^{15} per m^2 at the tungsten grain contacts, even under moderate levels of deformation [63]. These regions are then preferred for recrystallization during post-deformation anneals, and exhibit liquid film penetration on reheating to the liquid phase sintering temperature.

Alloying additions further improve the mechanical properties without a subsequent decrease in the density. Additions of Mo, Ta, or Re [64-66] are soluble in both W and the matrix, thus they result in grain refinement by limiting the solution-reprecipitation during liquid phase sintering. The improved tensile strength is attributed to solid solution strengthening and grain refinement. Figure 7 shows an example of the refined microstructure from Mo additions to a W-Ni-Fe heavy alloy.

The effects of test temperature and strain rate on the mechanical properties of tungsten heavy alloys have not been studied extensively. In oxidizing atmospheres, W is rapidly attacked at temperatures over 600°C. Further, in protective atmospheres there is considerable strength loss by 800°C, while at temperatures below room temperature there is a gradual transition from ductile to brittle fracture [53,67]. Accordingly, use of heavy alloys is generally restricted to 600°C or less. At the lower temperatures, an increase in strain rate results in an increase in strength and a lower ductility. By 600°C, the properties are approximately half those at room temperature and the properties are relatively insensitive to strain rate [67].

APPLICATIONS

The melting temperatures of the refractory metals are difficult to reach by fusion techniques. Thus, nonfusion P/M approaches are used in fabricating W, Mo, Nb, Re, Ta, Hf, Os, Ir, and Ru. The applications for refractory metals rely on the unique properties including the high density, high elastic modulus, low thermal expansion coefficient, low creep rate, low vapor pressure, and high melting temperature. These properties are useful for applications that include furnace heating elements, heat shields, radiation adsorption containers, x-ray targets, electrical contacts, lamp filaments, capacitors, heat sinks, and thermocouples. Many specific applications in the microelectronics industry are growing, including sputtering targets fabricated by HIP, microelectronic packages by PIM, heat sinks by sintering and infiltration, and capacitors by pressing and sintering high surface area powder [68].

Advances in high speed computers have created a major new technology in the management of heat around semiconductor devices. A high thermal conductivity package is used to remove the heat, but that package must have a thermal expansion coefficient compatible with the semiconductor. Silicon has a thermal expansion coefficient of approximately 5 ppm/°C near room temperature, which proves to be the major difficulty because the high thermal conductivity materials like Cu and Al have high thermal expansion coefficients. An expansion mismatch results in rapid failure by thermal fatigue. Several composite P/M materials have been developed with tailored thermal expansion coefficients and high thermal conductivities [69]. They are metal-metal composites, including W-Cu and Mo-Cu [70]. The precision and shape complexity dictate the fabrication of the composites. Powder metallurgy is effective in satisfying the shape, performance, and cost needs for many microelectronic packages. Table III summarizes the properties available from some of the P/M products for microelectronics. The W-Cu compositions are widely employed in situations where weight is not a major consideration, while the lower density Mo-Cu alloys find use in heat sinks and printed circuit boards. These material systems present unique fabrication problems. The W-Cu and Mo-Cu systems can be liquid phase sintered from micrometer sized particles. Billions of microelectronic devices are fabricated every year, making this a large application area.

High density alloys based on tungsten are used for radiation absorption, gyroscope weights, kinetic energy penetrators, sporting equipment, and aircraft wing weights. They are alloys with tungsten contents in the 85 to 98% range, giving densities in the 15 to 19 g/cm^3 range. A common use is in kinetic energy penetrators. The projectiles are accelerated to high velocities by an explosive, cannon, or rocket. The military application is in defeating armor, where projectile velocities for long rod penetrators are over 2 km/s and for shape charge penetrators can exceed 10 km/s at impact. The intense kinetic energy (over 5 MJ energy impacting on a target cross-sectional area of 7 cm^2) penetrates deeply. For that application, high density and toughness are required. Besides military, other applications of the technology are mining and oil well drilling, where the penetrator is used to open new fissures and cracks. In addition, the high density structure proves useful in biomedical, aerospace, and sporting devices.

SUMMARY

The refractory metals and P/M have been intimately interlinked throughout the past century. The high temperature properties are useful in many applications, but at the same time the high melting temperatures make P/M processing the only commercially viable

Table III
Properties of P/M Thermal Management Materials

property\composition	W-10Cu	W-20Cu	Mo-30Cu	Mo-50Cu
thermal expansion, ppm/°C	6.0	7.0	7.5	8.5
thermal conductivity, W/(°C m)	209	247	183	234
density, g/cm^3	17.0	15.1	9.7	9.5
strength, MPa	500	570	---	---
elastic modulus, GPa	340	290	220	215

option. New powder fabrication techniques that rely on plasmas and novel reactions are on the horizon, but largely the small refractory powders formed by chemical techniques dominate P/M. These small powders are responsive to compaction and sintering, however easier processing can be achieved for certain applications via techniques such as HIP, activated sintering, and liquid phase sintering. By far, sintering is the most widespread consolidation route. A properly designed liquid phase sintering system provides a means for full densification, and the resulting composite microstructure provides a novel combination of strength and ductility. Much processing knowledge has been gained on the liquid phase sintering of tungsten heavy alloys, allowing appropriate decisions on composition, compaction, sintering, and post-sintering heat treatment. For the other refractory metals there is much less knowledge.

The emerging challenges include several novel powder fabrication and processing techniques. For example, there are needs for higher purity prealloyed powders that cannot be satisfied by oxide reduction. Also, there is a desire for micrometer sized spherical particles for injection molding. New mechanical property levels are being achieved via modification in composition and processing. Consequently, there are many new opportunities for the refractory metals. This review has highlighted the current P/M techniques and indicated where the emerging techniques will intermesh with this base. It is realistic to expect that the close linkage between refractory metals and P/M will persist, and this situation will provide some exciting engineering challenges.

ACKNOWLEDGEMENT

The research on tailored microstructures in refractory metals using P/M techniques has been supported by the U.S. Army Research Office under the guidance of Dr. Edward Chen.

REFERENCES

1. C. J. Smithells, Tungsten: A Treatise on its Metallurgy, Properties, and Applications (Van Nostrand Company, New York, 1927).
2. W. D. Coolidge, Trans Amer. Inst. Elect. Eng. **29**, 961-965 (1910).
3. C. J. Smithells, W. R. Pitkins, and J. W. Avery, J. Inst. Metals **38**, 88-102 (1927).
4. G. H. S. Price, C.J. Smithells and S. V. Williams, J. Inst. Metals **62**, 239-264 (1938).
5. R. M. German, Liquid Phase Sintering (Plenum Press, New York, 1985).
6. A. Bose and R. J. Dowding (eds.), Tungsten and Tungsten Alloys (Metal Powder Industries Federation, Princeton, 1993).

7. A. Crowson and E. S. Chen (eds.), Tungsten and Tungsten Alloys, Recent Advances (Minerals, Metals and Materials Society, Warrendale, 1991).
8. R. Eck, Inter. J. Powder Met. Powder Tech. 17, 201-211 (1981).
9. H. G. Sell, in Refractory Metal Alloys, ed. I. Machlin, R. T. Begley and E. D. Weisert (Plenum Press, New York, 1968), pp. 395-439.
10. G. D. White and W. E. Gurwell, Adv. Powder Met. 2, 355-369 (1989).
11. R. F. Cheney, R. L. Daga, R. M. German, A. Bose and J. W. Burlingame, in Modern Developments in Powder Metallurgy, ed. P. U. Gummeson and D. A. Gustafson (Metal Powder Industries Federation, Princeton, 1988), pp. 155-169.
12. V. V. Skorokhod, Y. M. Solonin and N. I. Filippov, Soviet Powder Met. Metal Ceram. 23, 19-24 (1984)
13. R. M. German, Powder Injection Molding Symposium -1991, ed. P. Booker, J. Gaspervich and R. M. German (Metal Powder Industries Federation, Princeton, NJ, 1992), p. 1-17.
14. Tai-Shing Wei and R. M. German, Inter. J. Powder Met. 24, 327-335 (1988).
15. A. Bose, H. Zhang, P. Kemp and R. M. German, Adv. Powder Met. 3, 401-413 (1990).
16. I. H. Moon, K. M. Lee, J. Choi and Y. S. Kwon, Inter. J. Refract. Met. Hard Mater. 8, 244-248 (1989)
17. A. Bose, R. J. Dowding and G. M. Allen, in Powder Injection Molding Symposium 1992, ed. P. H. Booker, J. Gaspervich and R. M. German (Metal Powder Industries Federation, Princeton, NJ, 1992), pp. 261-274.
18. R. F. Cheney, in Metals Handbook 9th ed., vol. 7, (American Society for Metals, Metals Park, OH, 1984) pp. 389-393.
19. V. D. Barth and H. O. McIntire, Tungsten Powder Metallurgy NASA SP-5035. National Aeronautics and Space Administration, Washington, DC, 1965.
20. J. L. Walter and C. L. Briant, J. Mater. Res. 5 (9), 2004-2022 (1990).
21. F. B. Swinkels and M. F. Ashby, Acta Met. 29, 259-281 (1981).
22. L. A. Vermenko, O. I. Getman, S. P. Rakitin and V. V. Skorokhod, Soviet Po Met. Metal Ceram. 20, 766-771 (1981).
23. N. C. Kothari, Powder Met. 7, 251-260 (1964).
24. M. Boncoeur, F. Valin, G. Raisson and H. Michaud, in Hot Isostatic Pressing Theory and Applications, ed. M. Koizumi (Elsevier Applied Science, London, UK, 1992), pp. 247-252.
25. M. C. Cheynet, Inter. J. Refractory Met. Hard Mat. 5, 55-60 (1986).
26. A. Frisch, W. A. Kaysser and G. Petzow, Advances in Powder Metallurgy 2 (Metal Powder Industries Federation, Princeton, NJ, 1989), pp. 431-444.
27. U. Engel and H. Hueber, J. Mater. Sci. 13, 2003-2012 (1978).
28. P. E. Zovas, R. M. German, K. S. Hwang and C. J. Li, J. Metals 35 (1) 28-33 (1983).
29. G. V. Samsanov and W. I. Yakovlev, Z. Metallkde. 62, 621-626 (1971).
30. J. H. Brophy, H. W. Hayden and J. Wulff, Trans. TMS-AIME 224, 797-803 (1962).
31. G. H. Gessinger and H. F. Fishmeister, J. Less-Common Metals 27, 129-141 (1972).
32. R. M. German and Z. A. Munir, Rev. Powder Met. Phys. Ceram. 2, 9-43 (1982).
33. R. M. German, Sci. Sintering 15, 27-42 (1983).
34. J. S. Lee, H. H. Hwang and H. Shin, Inter. J. Refract. Met. Hard Mat. 9, 46-49 (1990).
35. J. L. Johnson and R. M. German, Metall. Trans. 24A, 2369-2377 (1993).
36. R. M. German, in Advances in Powder Metallurgy vol. 4, (Metal Powder Industries Federation, Princeton, NJ, 1991), pp. 183-194.
37. A. B. Rodriguez and J. G. Sevillano, in Tungsten and Tungsten Alloys - 1992, ed. A. Bose and R. Dowding (Metal Powder Industries Federation, Princeton, 1993), pp. 61-68.
38. V. Smolej, S. Pejovnic and W. A. Kaysser, Powder Met. Inter. 14, 34-36 (1982).

39. W. A. Kaysser, O. J. Kwon and G. Petzow, Proceedings P/M-82 (Associazione Italiana di Metallurgia, Florence, Italy, 1982), pp. 23-30.
40. R. M. German and S. Farooq, Sintering 87 (Applied Science, London, UK, 1988), pp. 459-464.
41. W. Shatt, S. Rolle, A. Sibilla and E. Friedrich, Sci. Sintering **18**, 3-20 (1986).
42. W. H. Huppmann, Z. Metalldke. **70**, 792-797 (1979).
43. W. J. Huppmann and G. Petzow, Ber. Bunsenges. Phys. Chem. **82**, 308-312 (1978).
44. E. G. Zukas, P. S. Z. Rogers and R. S. Rogers, Z. Metalldke. **67**, 591-595 (1976).
45. W. A. Kaysser, M. Zivcovic and G. Petzow, J. Mater. Sci. **20**, 578-584 (1985).
46. S. C. Yang, S. S. Mani and R. M. German, JOM **42**, 16-19 (1990).
47. R. M. German and K. S. Churn, Metall. Trans. **15A**, 747-754 (1984).
48. T. Kishi and R. M. German, Inter. J. Refractory Met. Hard Mat. **9**, 40-45 (1990).
49. A. Bose and R. M. German, Metall. Trans. **21A**, 1325-1327 (1990).
50. M. Krehl, K. Schulze and G. Petzow, Metall. Trans. **15A**, 1111-1116 (1984).
51. B. H. Rabin and R. M. German, Metall. Trans. **19A**, 1523-1532 (1988).
52. T. Kaneko, J. Japan Soc. Powder Powder Met. **37**, 885-892 (1990).
53. R. M. German, J. E. Hanafee and S. L. DiGiallonardo, Metall. Trans. **15A**, 121-128 (1984).
54. L. J. Kecskes and I. W. Hall, in Tungsten and Tungsten Alloys - 1992, ed. A. Bose and R. Dowding (Metal Powder Industries Federation, Princeton, 1993), pp. 155-165.
55. M. J. Tracy and J. R. Groza, Nanostr. Mater. **2**, 441-449 (1993).
56. J. C. Murray and R. M. German, in Advances in Powder Metallurgy and Particulate Materials vol. 9, ed. J. M. Capus and R. M. German (Metal Powder Industries Federation, Princeton, NJ, 1992), pp. 295-308.
57. Z. A. Munir, Ceramic Bull. **67**, 342-349 (1988).
58. L. Ekbom, Modern Developments in Powder Metallurgy vol. 14, ed. H. H. Hausner, H. W. Antes and G. D. Smith (Metal Powder Industries Federation, Princeton, NJ, 1981), pp. 177-188.
59. H. Danninger, W. Pisan, G. Jangg, B. Lux and W. J. Huppmann, Inter. J. Refractory Hard Met. **5**, 144-152 (1986).
60. A. Belhadjhamida and R. M. German, in Tungsten and Tungsten Alloys - 1992, ed. A. Bose and R. Dowding (Metal Powder Industries Federation, Princeton, 1993), pp. 195-204.
61. S. H. Hong, D. N. Yoon, S. J. L. Kang and W. H. Baek, Powder Met. Inter. **22** (6) 24-26 (1990).
62. S. H. Hong, S. J. L. Kang, D. N. Yoon and W. H. Baek, Metall. Trans. **22A**, 2969-2974 (1991).
63. M. Mitkov and W. A. Kaysser, Science of Sintering, ed. D. P. Uskokovic, H. Palmour and R. Sprigs (Plenum Press, New York, 1989), pp. 243-254.
64. A. Bose and R. M. German, Metall. Trans., **21A**, 1325-1327 (1990).
65. A. Bose, D. M. Sims and R. M. German, Prog. Powder Met. **43**, 79-92 (1987).
66. P. B. Kemp and R. M. German, J. Less-Common Met. **175**, 353-368 (1991)
67. A. Bose, D. Sims and R. M. German, Metall. Trans. **19A**, 487-494 (1988).
68. J. C. Wang, Prog. Powder Met. **43**, 281-301 (1987).
69. R. M. German, Metall. Trans. **24A**, 1745-1752 (1993).
70. E. Kny, in Proceedings of the Twelfth Plansee Seminar (Metallwerk Plansee, Reutte, Austria, 1989), pp. 763-772.

DIRECTIONAL SOLIDIFICATION OF REFRACTORY INTERMETALLICS: SINGLE CRYSTALS AND COMPOSITES

DAVID P. POPE*, DILIP M. SHAH**, WILLIAM ROMANOW* AND MARK HUNTLEY
*University of Pennsylvania, MSE Department, 3231 Walnut St., Philadelphia, PA 19104, USA
**Pratt and Whitney, Mail Stop 114-45, 400 E. Main St., E. Hartford, CT 06108, USA

ABSTRACT

Directional solidification of intermetallic compounds using the optical imaging floating zone technique is discussed. The advantages and disadvantages of the technique are described, and the systems to which this technique has been applied are listed. Finally, application of the technique to growing *in situ* Cr_2Nb/Nb composites is described. It is shown that well aligned, fine microstructures can be obtained using the technique. The aspect ratio of the Cr_2Nb platelets is 200:1, or better, and are a few microns thick. The Cr_2Nb has a strong <220> texture along the growth axis but the Nb is nearly random.

INTRODUCTION

In situ composites produced by the directional solidification of eutectic mixtures form the basis for the work discussed here Since the study concentrates on composites for high temperature use, only materials with eutectic temperatures of 1600°C or higher have been considered.

Processing Methods

Even though there are many ceramic and intermetallic-based eutectic systems that satisfy the above requirement on melting temperature, previous studies have been hampered by processing difficulties, particularly, the lack of containment vessels in which to melt and solidify the material. Current Ni superalloy single crystals, as well as directionally-solidified (DS) and equiaxed alloys, are solidified in alumina-based ceramic molds. Since so much effort has been invested in these kinds of molds, any new material which can be processed using the same or similar molds is extremely attractive. This is the case, for example, with NiAl and is one reason why this material is receiving so much attention.

For the production of ceramic-based eutectics, there are very few mold materials available. A Mo crucible has been used for MgO-$MgAl_2O_4$ [1] and Al_2O_3-ZrO_2 + Y_2O_3 [2], for example. In other cases, a floating zone technique has been used (more about this technique later). For oxide eutectics, an induction-heated graphite susceptor has served as a radiant heat source [3], and, for carbide and boride eutectics, direct induction heating has been employed [4]. In each case, well-defined eutectic microstructures have been produced, thereby demonstrating the feasibility of the DS technique for such materials.

There has been rather little work on the production of refractory intermetallic eutectic composites. Again, there is a severe limitation of available mold materials, and furthermore, since many of the attractive intermetallics contain reactive elements, such as Al and Si, the problems with containers are even more severe. Consequently, we have concentrated our attention on "containerless" processing, i.e., processing techniques in which the hot liquid is not in contact with a mold, as in the floating zone technique.

Mat. Res. Soc. Symp. Proc. Vol. 322. ©1994 Materials Research Society

Floating Zone Processing

The floating zone technique [5] is derived from the zone melting technique of Pfann [6]. The technique is based on the principle of melting a small amount of material in a relatively long charge, and allowing this molten zone to traverse through the charge, thereby either purifying the material and/or growing a single crystal or DS structure. In the float zone method, the molten zone is held in place by surface tension between the two colinear solid rods, thereby obviating a crucible. Single crystals or aligned composites are frequently produced after the passage of one zone. Two unique features of the float zone melting technique should be noted: first, as stated above, no crucible is used, so that contamination of the specimen by contact with other materials is minimized and, secondly, the growth process is essentially a progressive freezing of the specimen from a seed or a single nucleation event. It is the only technique generally used for solidification processing which combines these two features and it is, therefore, of particular value for use with reactive metals.

Almost any form of heating may be employed in the float zone method. Historically, the most commonly used were electron beam and RF induction heating. The electron beam method has the advantage of being very efficient; however, the process requires a good vacuum and this precludes application to high vapor pressure or dissociating materials, in addition to requiring electrical conductivity. The direct induction heating method requires the specimen to be a good conductor. The resulting levitation forces may be used to contain the molten zone and thereby allow large diameter crystals to be grown [7]. However, the coil design and the coupling between the electromagnetic field and the charge require extensive experimentation to obtain optimum conditions. If the material being processed is not an electrical conductor, the sample can be heated by radiation from a graphite susceptor placed between the sample and the RF coil, as was used by Hulse and Batt [3].

Optical Imaging Floating Zone Technique

In recent years, optical imaging systems have been used as heat sources. Various radiation sources have since been used, including carbon arc, xenon or mercury arcs, lasers and tungsten halogen lamps. Now that high power, reliable halogen lamps have become available, along with improved imaging systems that drastically improve the heating efficiency, the reliability of this optical imaging floating zone (OIFZ) technique has now been established.

Single crystals of a large number of high temperature materials have been grown using the OIFZ technique [8]. A closed ellipsoidal mirror, first introduced by Costello [9] with the heat source at one focal point and the sample at the other, focuses almost all the radiant energy on the specimen and refocuses the energy reflected from the specimen back to the specimen again. In a computer simulation, Eyer *et al.* [10] showed that the maximum attainable temperature in a closed ellipsoid imaging system is limited primarily by the quality of the mirror surface, rather than by the absorption and reflection properties of the samples. In Fig. 1 sketches of two commonly used optical imaging systems are shown for comparison. Compared with the single ellipsoidal imaging system, the double ellipsoidal system has the advantage of better thermal symmetry and higher total radiant energy.

The first published work on the use of the closed ellipsoidal, OIFZ technique was on the growth of ferrite single crystals by Akashi *et al.* [11]. Since then, the technique has been used mostly for growing single crystals of oxides [12] and only rarely for metallic systems. This is not surprising, since the non-conducting nature of most oxides prevents the application of other heating methods. It was not until the 1980's that the optical imaging technique was applied to growth of Be crystals [13], and applications to intermetallic compounds are more recent.

To summarize, the OIFZ crystal growth technique offers many attractive features:

- The ability to work in various environments, including reducing, oxidizing, vacuum, and pressurized atmospheres.
- It can be applied to both electrically insulating and conducting materials.
- The closed mirror geometry ensures that the maximum attainable temperature is independent of the sample surface.

- It allows a very high heating rate, so a large number of experiments can be carried out in a short period of time.
- The process can be monitored visually and allows in-process fine tuning.
- The small heating area usually associated with the imaging system is particularly suitable for the float zone technique.
- The process is clean since there is no crucible involved and the whole crystal growth assembly is enclosed in a quartz chamber.

The major disadvantage of OIFZ technique is that the specimen size is limited by a compromise between the liquid surface tension and the hot zone dimension.

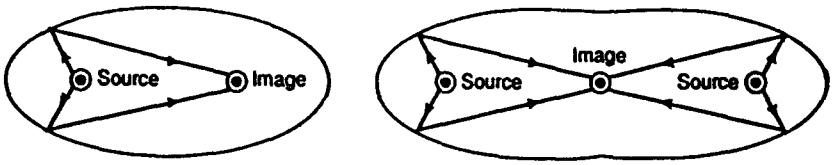


Fig.1 Commonly used optical imaging systems. The double ellipsoidal system is used in the University of Pennsylvania system.

A sketch of the OIFZ furnace at the University of Pennsylvania is shown in Fig. 2. The main features of this Asgal FZ-SS35W furnace are the two 3.5 kW tungsten halogen lamps enclosed in a double ellipsoidal gold plated water cooled chamber. The feed rod and the seed rod are aligned perpendicular to the long axis of the double ellipsoid, while the molten zone is produced at the overlapping focal point. The growth process is visually monitored through an opening in the chamber using an optical system which projects the image of the molten zone and its surroundings on the ground glass in the viewing port. The manual controls located below the viewing port give the operator the ability to adjust the crystal diameter instantaneously by either squeezing or stretching the molten zone. The growth conditions, e.g. growth rate, power level, and rotation rates can then be varied according to the image seen on the screen. A vacuum system equipped with mechanical and diffusion pumps is attached to the furnace for chamber purging. A thick walled quartz tube is used to separate the single crystal growth process from the surroundings and to maintain the protective atmospheres. For our investigations, we usually use a flowing Ti-gettered Ar atmosphere. Our system has been retrofitted with Ferrofluidic seals, replacing the O-ring seals between the vacuum chamber and the feed and seed rods, thereby making it possible to control the environment better and to operate without rotation of the rods, if desired.

Charge rods of the materials we studied were prepared using various techniques including powder reaction sintering, induction melting, arc melting, and drop casting. One large advantage of this technique is that feed rods with non-circular and non-uniform cross-sections can be utilized. For example, in many cases it is most convenient to produce the starting material by arc melting a pancake-shaped plate on a cold copper crucible. This plate is then EDM-cut into a polygonal cross-section of the correct area, then rapidly melted and resolidified in the crystal-grower to produce a more-or-less uniform rod for subsequent growth. The optimal sample conditions for growing single crystals are: rods of approximately 10 mm diameter having less than 15% porosity and a uniform composition along the length.

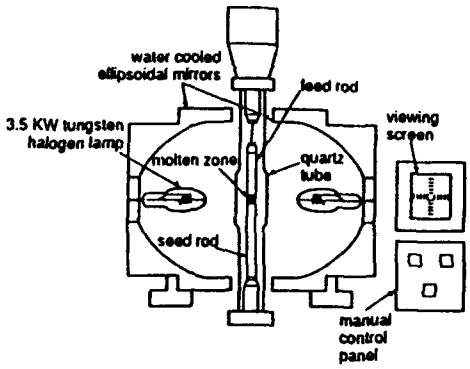


Fig. 2 A schematic diagram of the Optical Imaging Floating Zone Furnace at the University of Pennsylvania.

The feed rod is suspended by a molybdenum wire from the top shaft. When single crystals were not available for a seed, polycrystalline seeds and the following "necking" process were used. A stable molten zone is first established between the polycrystalline "feed" and "seed" rod, then the rods are moved at a high growth rate (about ten times of the normal growth rate) through the hot zone, meanwhile the feed rod was pulled up thereby reducing the float zone diameter (necking). Differential growth rates between different crystal orientations result in the selection of a single seed which then is used to grow the entire crystal. We have found using this necking process for producing single crystals to be very reliable. By using suitable feed rods, single crystals usually are grown at the first run.

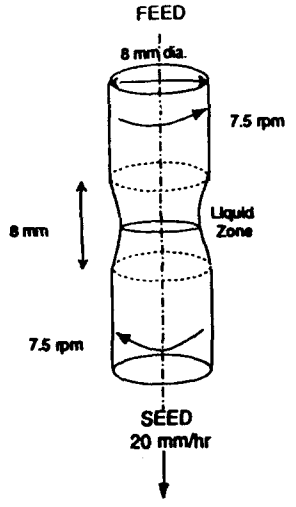


Fig. 3 The "feed" and "seed" rods and molten zone.

The quartz chamber is first evacuated to a 1μm vacuum and back filled several times with purified argon. The feed and seed rods are counter-rotated, each at about 10 rpm, while the lamp power is increased using a programmable controller connected to a regulated DC power supply. The molten zone is then produced by bringing the seed rod into contact with the melt on the bottom end of the feed rod. After the molten zone is stabilized for a few minutes the growth process then proceeds. A sketch of a typical configuration is shown in Figure 3. At completion, the power level is gradually reduced while the feed and crystal rods are slowly pulled apart so that the conditions in the molten zone can be preserved and investigated later.

In addition to the size limitations mentioned above, this method has two major limitations. First, it requires starting material with a high level of homogeneity. For example, if a sample contains two phases with dramatically different melting temperatures, then the material with the lower melting temperature will melt first and run down the rod. We have worked with systems in which it appeared from all preliminary work that the samples were totally homogeneous, but the above-mentioned differential melting was observed. This was a particular problem when growing Cr_3Si crystals. The ability to observe the sample during crystal growth is, of course, a great help in diagnosing these kinds of problems. Second, since the heat for melting passes through the walls of the quartz tube, any evaporation from the sample and condensation on the tube leads to substantial reductions in heat input to the sample and devitrification of the tube. Evaporation of Cr has been a problem when growing Cr_2Nb/Nb.

The DS samples have been inspected using various techniques to assure their quality. Visual examination is very useful since thermal etching and growth facets usually indicate when polycrystalline rods have been produced. The rods are then sectioned and examined by standard metallographic techniques including optical and scanning electron microscopy. X-ray powder diffraction was used to identify the phases, and the composition of the crystal was usually checked by EDAX and chemical analysis.

We have grown single crystals and DS composites of a number of intermetallic compounds using our OFIZ furnace at the University of Pennsylvania. They are (along with their melting temperatures): Al_3Ti (1390°C), Cr_3Si (1770°C), NiAl (1650°C), TiAl (1435°C), Ti_3Al (1600°C), $MoSi_2$ (2050°C), Cr_2Nb/Nb (1620°C) and Cr_3Si/Cr_5Si_3 (1660°C). A large number of ceramic single crystals have also been grown at other laboratories, including Al_2O_3, $LaFeO_3$, and $MgTiO_3$, e.g., see Mizutani *et al.* [14] and Kimura and Shindo [15], in addition to the DS eutectic ceramics mentioned earlier in this section. In a previous paper [16] we discussed the application of this technique to the growth of single crystals. In this paper we concentrate on the growth of *in situ* intermetallic-based composites with emphasis on the Cr_2Nb/Nb system.

APPLICATION TO THE Cr_2Nb/Nb SYSTEM

The Cr_2Nb/Nb is, in many ways, an ideal system to study the production of *in situ* composites (see Fig. 4 [17] for the phase diagram), as described in more detail elsewhere [18]. The material can be readily arc-melted into the previously-mentioned 7x7x1 cm "pancakes" from which several samples can be produced by EDM for directional solidification. Since homogeneity of the starting material is so important, we were especially concerned about simple methods for deciding beforehand if a given pancake is suitable for DS. The most dependable method relates to the fluidity of the melt during arc melting. If the melt is very fluid, the resulting material is usually easily-processed, but if the melt is very viscous, probably indicating the presence of solid, high-melting point phases, then subsequent DS processing is usually unsuccessful.

Composition

Based on the fact that some Cr loss during processing is inevitable and on the practical result that the best aligned microstructures were obtained for Cr-rich materials, most of this work is centered on approximately 44 a/o Nb — 55 a/o Cr starting materials; although higher Nb concentrations were also used (all compositions those of the starting materials and are given in a/o). However, coupled growth was found to be easier in Cr-rich samples.

Very well aligned microstructures can be produced in 44 Nb/54 Cr material at growth speeds of 20 mm/hr and rotational rates of 7.5 rpm of both the feed and seed rods (in opposite directions). Longitudinal and transverse cross-sectional views of such a sample are shown in Figure 5. In these SEM micrographs Nb is the lighter-colored phase and is a few microns thick and many microns long, giving an aspect ratio of 200 or better.

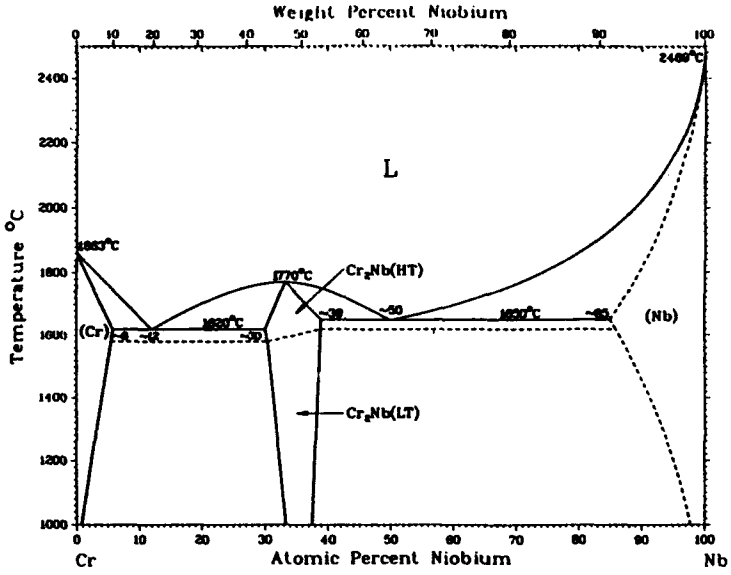


Fig. 4 The Cr-Nb phase diagram [17].

Variation of Growth Parameters

The number of parameters to be varied on the optical imaging system is small: only the growth rate and the rate(s) of relative rotation of the feed and seed rods. A growth rate of 20 mm/hr was found to be best for this system since it provided a well-aligned, fine scale microstructure without excessive loss of Cr. At 5mm/hr excessive Cr losses were observed which resulted in proeutectic Nb islands and a general coarsening of the microstructure — especially on the surface of the sample. Growth rates exceeding 20 mm/hr resulted in a lack of long range alignment. Energy dispersive x-ray analysis of the outer regions of the sample confirmed the loss of Cr, although there was no loss in the central regions. As the rotational speeds are increased above 10 rpm the microstructural alignment becomes increasingly disturbed. (Rotational speeds below 7.5 rpm have not yet been investigated because the o-ring seals on the rods required this rotational speed and we have not yet had the opportunity to attempt lower rates with our new Ferrofluidic seals).

When a transverse section of a sample is viewed in cross-section at low magnifications, Figure 6, a "tree-ring" structure is seen that results from periodic variations in the lamellar thickness between 2.5 to 5 microns. The source of this structure is not known, although similar structures have been seen in other DS material and even in ingot castings [19, 20].

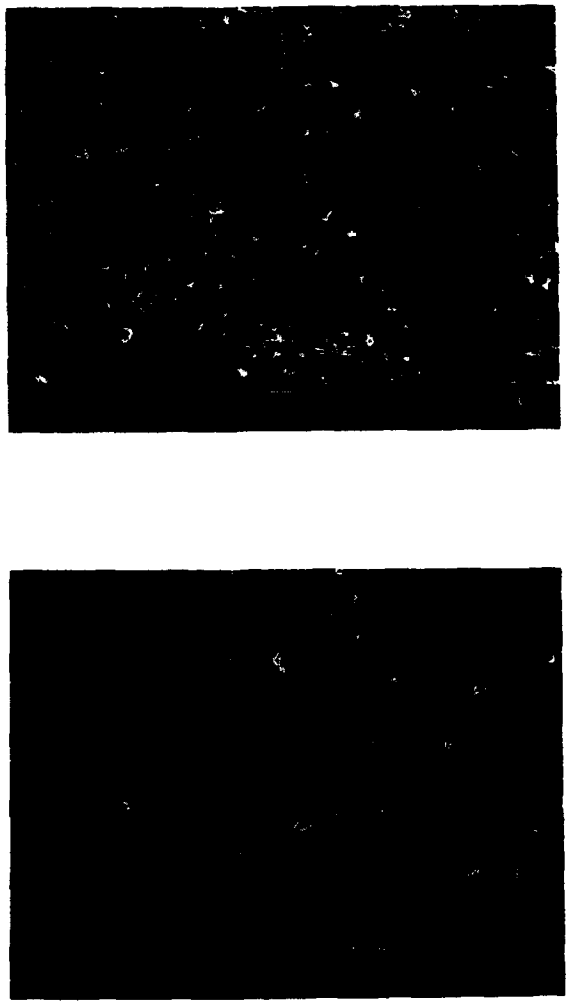


Fig. 5 Longitudinal (top) and transverse (bottom) sections of a 44Nb/56 Cr sample.

Alignment of the Phases

X-ray textural analysis was performed on sections of one sample (composition is 43.6 Nb, 56.4 Cr, 20 mm/hr and 10 rpm). The Cr_2Nb has a fairly sharp texture with most of the <220> poles within 30° of the DS direction, but the Nb appears to be nearly random. The intensity of some of the Cr_2Nb grains exceeds 47 times the random value. These results were confirmed by checking <222> and <422> pole figures. In contrast, the maximum intensity from the Nb grains did not exceed four times the random value.



Fig. 6 "Tree-ring" structure seen in low magnification views of the cross-sections of Cr_2Nb/Nb composites.

CONCLUSIONS

The optical imaging floating zone technique can be used to produce a wide range of intermetallic single crystals and intermetallic-based *in situ* composites. The system is unusually simple to use and offers great freedom from contamination. However, it suffers from requiring a small sample size and very homogeneous starting material, as well as allowing loss of volatile species. On balance, however, it is extremely useful for quickly producing small quantities of material for laboratory-scale uses.

ACKNOWLEDGMENTS

Part of this work was supported by Air Force Contract F33615-90-C-5957. Research facilities were supplied by the LRSM at the University of Pennsylvania supported by the NSF MRL program under grant DMR91-20668.

REFERENCES

1. F.L. Kennard, R.C. Bradt and V.S. Stubican, *J. Amer. Cer. Soc.*, **56** (1973) 566.
2. J. Echigoya, Y. Takabayashi, K. Sasaki, S. Hayashi and H. Suto, *Trans. Jap. Inst. Met.*, **27** (1986) 102.

3. C. Hulse and J. Batt, United Aircraft Technical Rep. L910803-7 (1972).
4. C.C. Sorrell, H.R. Beratan, R.C. Bradt and V.S. Stubican, *J. Amer. Cer. Soc.*, **67** (1984) 190.
5. P.H. Keck and M.J.E. Golay, *Phys. Rev.* **89** (1953) 1297.
6. W.G. Pfann, *Trans AIME*, **194** (1952) 474.
7. J.W. Rutter in *Techniques to Electron Beam Technology*, ed. R. Bakish (Wiley, New York, 1962), p. 184.
8. T.S. Laszlo in *Technique of Inorganic Chemistry*, Vol. V, ed. H.B. Jonassen and A. Weissberger (Wiley, NY, 1965).
9. B.J. Costello, *Western Elec. Eng.*, **7** (1963) 40.
10. A. Eyer, R. Nitsche and H. Zimmermann. *J. Crystal Growth*, **47** (1979) 219.
11. T. Akashi, . Matsumi, T. Okada and T. Mizutani, *IEEE Trans. MAG-5* (1969) 285.
12. Z.K. Kun, W.E. Kramer and G.W. Roland, *J. Crystal Growth*, **58** (1982) 122.
13. S. Stiltz and S. Jonsson, *Metall.* **38** (1984) 748.
14. T. Mitzutani *et al.*, *NEC Res. & Devel.* **86** (1974).
15. S. Kimura and I. Shindo, *J. Crystal Growth*, **41** (1977) 192.
16. C.S. Chang, Z.L. Wu and D.P. Pope in *Containerless Processing Techniques*, ed. W. Hofmeister, TMS, Warrendale, PA (1993).
17. T. Massalski, *Binary Alloy Phase Diagrams*, ASM Intl., Metals Park, OH (1990).
18. D.M. Shah and D.L. Anton in *Intermetallic Matrix Composites II*, ed. D.B. Miracle, D.L. Anton and J.A. Graves, MRS, Pittsburgh, PA (1992), p. 385.
19. G.E. Maurer, "Primary and Secondary Melt Processing — Superalloys", in *Superalloys, Supercomposites and Superceramics*, edited by J.K. Tien and T. Caulfield, Academic Press Inc., Boston, 1989, p. 58.
20. B. Toloui *et al.*, "Microstructural Perturbation in Directionally Solidified Al-In, Al-Bi and Zn-Bi Monotectic Alloys", in *In Situ Composites IV*, edited by F.D. Lemkey, H.E. Cline and M. McLean, MRS Proceed., Vol.12, Elsevier, 1982, p. 262.

MECHANICAL WORKING OF REFRACTORY ALLOYS PRODUCED BY MELTING PROCESSES

JOHN R. HUGHES
General Electric Corporate Research and Development, P.O. Box 8, Schenectady, NY 12301

ABSTRACT

The elements generally considered to be the "major" refractory metals are niobium (Nb) and tantalum (Ta) from group VA of the periodic table, and molybdenum (Mo) and tungsten (W) from group VIA. By virtue of their high melting points, these metals and their alloys constitute an important class of materials. When they are produced by melting processes, the resulting ingots usually have large grain sizes, which need to be refined during mechanical working. While the unalloyed refractory metals have varied room-or-low-temperature applications, they require alloy additions, in many cases substantial, to meet the requirements of most of their high-temperature applications. This often results in high flow stresses at elevated working temperatures, and a concomitant decrease in low-temperature ductility. As BCC materials, the refractory metals have ductile-to-brittle transition temperatures, which vary widely from one metal to another and with other metallurgical variables. All of these factors must be taken into account in order to develop successful processing schedules for the refractory metals.

INTRODUCTION

Disregarding boron and carbon, there are eleven elements with melting points above 1925°C (3500°F). They form a rather diverse group of materials with respect to crystal structure, deformation characteristics, and alloying behavior. This paper will be concerned with only the four "major" refractory metals, those which have been used as bases for alloy systems, i.e., tungsten (W), molybdenum (Mo), tantalum (Ta), and niobium (Nb). Further, it will discuss only those metals and alloys made by the various melting processes employed for high melting point materials, namely, vacuum arc melting, electron beam melting, and plasma melting. All four of the refractory metals have in common, of course high melting points, although there is a nearly 1000°C difference between the highest and lowest. They also share the characteristic of poor oxidation resistance. As Table I shows, however, in certain other properties they divide sharply

Table I. Physical Properties of the Refractory Metals [ref. 1]

Property	Nb	Ta	Mo	W
Melting point, °C	2470	3000	2610	3410
Density, gm/cm^3	8.57	16.6	10.2	19.3
Elastic modulus, 10^{-6} psi (at RT)	16	27	42	52
Linear thermal expansion, 10^{-6}/°C	7.1	5.9	5.4	4.5
Thermal conductivity, cal/cm/°C/s (near RT)	0.125	0.130	0.34	0.397
Thermal neutron cross section, barns/atom	1.1	21.3	2.4	19.2
Superconducting transition temperature, K	9.46	...	...	...
Interstitial solubility, ppm by weight(a):				
Oxygen	1000	300	1.0	1.0
Nitrogen	300	1000	1.0	<0.1
Carbon	100	70	<1.0	<0.1
Hydrogen	9000	4000	0.1	N.D.

(a) Based on estimates of the equilibrium solubility at the temperature where diffusion $D = 10^{-11}$ cm^2/s.

Mat. Res. Soc. Symp. Proc. Vol. 322. ©1994 Materials Research Society

into two sub-groups, the VA metals Nb and Ta, and the VIA group metals Mo and W. For example, Mo and W have lower coefficients of linear thermal expansion, but higher thermal conductivities and elastic moduli than do Nb and Ta. This pattern extends to solubilities for the interstitial elements C, O, N, and H. While Nb and Ta exhibit solubilities for the interstitials in the hundreds or even thousands of parts per million (PPM), Mo and W have very limited solubilities, in the range of 1.0 PPM or less. Some investigators [2, 3] have ascribed these low solubilities in Mo and W to the electronically stable configurations of the VIA elements. The high solubilities of Nb and Ta for interstitial elements are of practical significance because of the profound effects the interstitials can have on their low-temperature tensile properties and elevated temperature creep properties. Raw materials are available in higher purities now, and today's more efficient vacuum systems remove more of the interstitial elements, as well as some trace metallic impurities during melting. Thus, much of the mechanical property data generated on lower-purity Nb and Ta alloys during the 1960s and 1970s is probably not directly applicable today [4].

Another group VA/group VIA distinction in mechanical behavior is in the area of creep strength. Fig. 1 (data generated on melted material only) illustrates an approximately 3/1 advantage of Mo and W over Ta and Nb in load-bearing capacity at a given creep rate, when

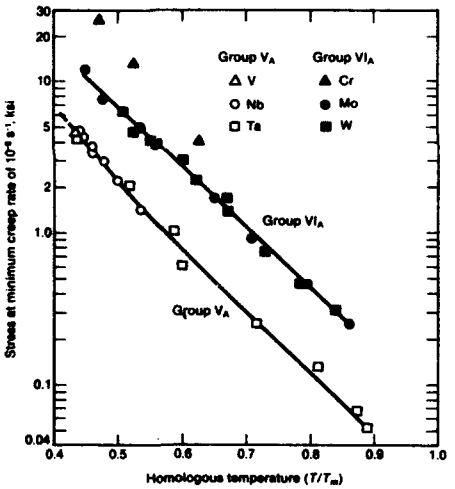


Fig 1. Creep strength of refractory metal elements as a function of homologous temperature [ref. 1].

compared at equivalent homologous temperatures. This difference has been rationalized on the basis that Mo and W have higher moduli and lower self-diffusivities than Nb and Ta [5, 6].

All four of the refractory metals have the body-centered cubic (BCC) crystal structure, and are isomorphic from absolute zero to their melting points. As BCC materials, they all exhibit a transition from ductile to brittle fracture behavior as ambient temperature decreases, although there is a wide variation in transition temperature from one metal to another (Fig. 2).

Again, there is a major difference between Nb and Ta, which have ductile-brittle transition temperature (DBTT's) well below room temperature, and Mo and W, which have DBTT's near room temperature. There is no singular DBTT for a given material since, in addition to composition, the specific transition temperature depends on numerous metallurgical factors such as purity (with respect to the interstitial elements), degree of cold work, grain size, and grain shape (equiaxed vs. elongated or fibrous, translating to metallurgical condition, i.e., recrystallized vs. stress relieved or wrought).

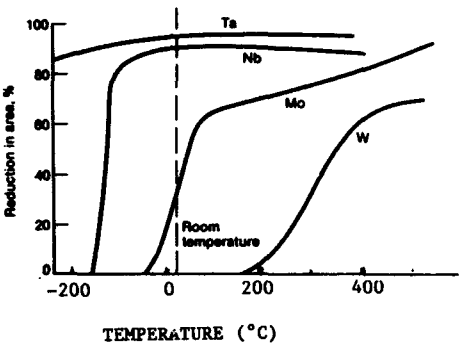


Fig. 2. Ductile-to-brittle transition temperatures for recrystallized polycrystalline refractory metals [ref. 1].

Figure 3 illustrates this latter point for commercial unalloyed Mo sheet. The amount of total strain in the "Luders strained" condition was 3-5%. The same general results are obtained for stress-relieved and recrystallized Mo sheet materials if tested in bending. Additionally, certain test conditions such as strain rate, surface condition, and direction of testing relative to the direction in which the test piece was worked will affect the DBTT.

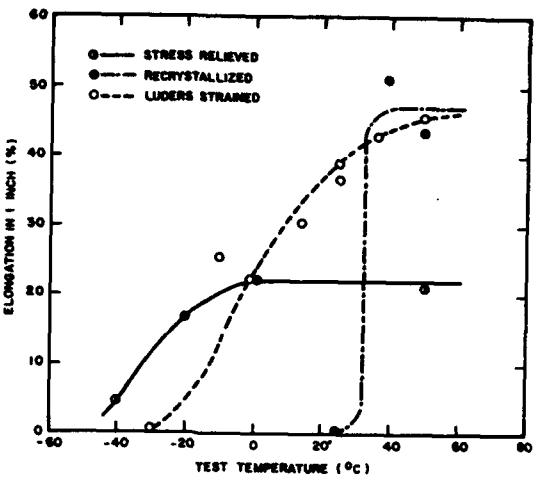


Fig. 3. Control of the ductile-to-brittle transition in Mo by thermal - mechanical treatments [ref. 7].

Strengthening

Despite their high melting points, the unalloyed refractory metals do not have sufficient strength for most elevated-temperature engineering applications. Several excellent reviews have been published on the strengthening mechanisms which operate in the refractory metals [8,9,10,11]. For the purpose of this paper, the pertinent mechanisms identified by Wilcox [8] are strengthening by (a) solid solution alloying, (b) second-phase particles, (c) strain hardening and grain size refinement, and (d) retaining worked structures at high temperatures. Table II lists those alloy additions which are present in the various commercial and/or developmental refractory alloys.

Table II. Additions to Refractory Metal Alloys made by Melting Processes [ref. 1].

Alloy Base	Substitutional solutes	Reactive elements	Interstitial elements
Nb	W, Mo, Ta, Hf, Zr, Ti	Hf, Zr, Ti	C
Ta	W, Re, Hf	Hf	C
Mo	W, Ti, Zr	Ti, Zr	C
W	Re, Hf	Hf	C

The substitutional solutes account for strengthening mechanism (a), and some also contribute to (d) in that those solutes which raise the solidus temperature often decrease self-diffusivity and thereby raise the recrystallization temperature. The reactive elements contribute directly to mechanism (b) by forming carbide and oxide (by scavenging oxygen from the base metal and/or other additions) dispersoids which impede dislocation motion during deformation, and indirectly to mechanism (d) by raising the temperature required for recrystallization. All three categories of additions contribute to mechanism (c). Those substitutional solutes which raise the recrystallization temperature raise the maximum temperature at which a worked microstructure can be produced and maintained. The reactive and interstitial elements contribute indirectly to mechanism (c) because the compounds they form help to develop and stabilize a worked microstructure.

Alloy Compositions

Various combinations of the additives listed in Table II have produced the compositions shown in Tables III and IV. In some instances, certain additions are incorporated into an alloy for purposes other than increasing elevated-temperature strength, e.g., to improve low-temperature toughness and ductility, oxidation resistance, or superconducting characteristics.

Table III. Commercial Refractory Metals and Alloys and Associated Melting Processes

Base Metal	Alloy Additions, wt. %	How Made
Nb		EBM
Nb	1Zr	EBM; EBM+VAM; PHM
Nb	7.5Ta	EBM+VAM
Nb	45-48Ti	EBM+VAM; PHM.
Nb	44Ti-25Ta	PHM
Nb	55Ti	PHM
Ta		EBM
Ta	2.5W	EBM+VAM
Ta	10W	EBM+VAM
Ta	40Nb	EBM+VAM
Mo(Low-carbon)	(<100PPMC)	VAM
Mo(Regular)	(≥100PPM C)	VAM
Mo	0.5Ti-0.08Zr-0.03C	VAM
Mo	30W	VAM

EBM = electron beam melted
VAM = vacuum arc melted
PHM = plasma hearth melted

Table IV. Typical Developmental Refractory Metal Alloys Made by Melting Processes

Alloy Designation	Nominal Composition, wt.%
PWC-11	Nb-1Zr-0.1C
C-103	Nb-10Hf-1Ti
FS-85	Nb-27Ta-10W-1Zr
SCb-291	Nb-10W-10Ta
B-88	Nb-28W-2Hf-0.07C
C-129Y	Nb-10W-10Hf-0.24Y
D-43	Nb-10W-1Zr-0.1C
F-48	NB-15W-5Mo-1Zr-0.035C
T-111	Ta-8W-2Hf
T-222	Ta-10W-2.5Hf-0.01C
ASTAR 811C	Ta-8W-1Hf-1Re-0.025C
TZC Mo	Mo-1.2Ti-0.3Zr-0.1C
W-Re-Hf-C	W-4Re-0.3Hf-0.025C

Table III lists the refractory metals and alloys that are presently being produced commercially by melting processes. W and its alloys are absent from this group. Currently, no unalloyed W or W alloy is being produced commercially via a melting process. With the exception of the Nb -lZr and the Mo-Ti-Zr-C (TZM) alloys, the list is comprised of unalloyed Nb, Ta, and Mo, and straightforward solid solution alloys. The right-hand column shows that any or all of three different melting processes may be employed for a given composition. When no alloy addition is to be made, Nb and Ta are produced by electron beam (EB) melting. This results in a high-purity ingot with a very coarse but basically equiaxed grain structure. When alloy additions are to be made, the unalloyed Nb or Ta is first EB melted to yield an ingot of high-purity base metal. This ingot is re-melted by vacuum arc melting (VAM), during which any alloy additions are made, to produce a compositionally homogenous ingot. After VAM, the ingot will have a mixed microstructure consisting of a central region of columnar grains which curve down and outward toward the ingot surface, surrounded by a region of equiaxed grains. The grain size of the ingot will be a function of its composition. In general, the lower the alloy content, the larger the grain size. VAM ingots of dilute alloys can be very coarse-grained, although not as coarse as an EB-melted ingot.

Mo and its alloys, and any developmental W alloys, would be made in a single vacuum arc melt which, for these materials, is sufficient to achieve the required purity (very low interstitial level) and alloy homogeneity. Ingots of unalloyed Mo or W made by this process, however, will have a very coarse-grained mixture of columnar and equiaxed grains as previously described. Figure 4 shows a montage of nine Mo, W, and Mo-W alloy wedges, all oriented transversely to the long axis of the ingot, etched to illustrate the as-cast macrostructure of each of the nine compositions represented. The photograph reveals the very strong influence of alloy content on the as-cast grain size. Figure 5 shows a surface produced by a vertical cut through the mid-plane of an experimental arc-melted ingot of a Nb-10Mo-10Ti-0.1C alloy. The previously described macrostructure of columnar grains running from the central portion down and out toward the ingot surface is quite fine - grained due to the high alloy content, but is still visible. In a similar section cut from a VAM ingot of unalloyed Nb or a dilute alloy, the columnar grains would be on the order of 1/4" wide by 2" long.

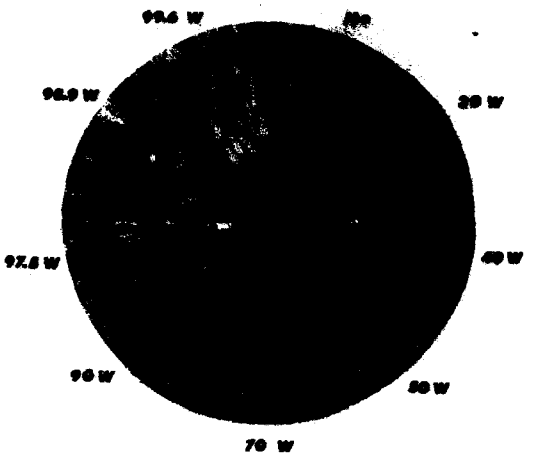


Fig. 4. Wedges cut from transverse slices of nine different Mo-W arc melted compositions, pieced together [ref.12].

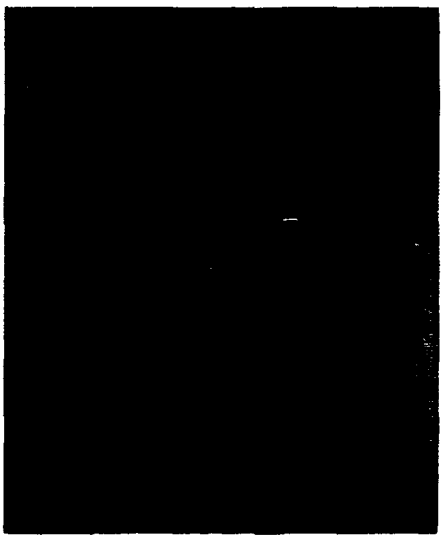


Fig. 5. Macrostructure of the vertical (longitudinal) mid-plane of an experimental arc melted ingot of a Nb-10Mo-10Ti-0.1C alloy [ref.13].

The remaining alloys in Table III all consist of a Nb base with additions of Ti and/or Zr and Ta. They are used to make aircraft fasteners and superconductor wire, two applications where microstructural cleanliness is very important. The alloys are currently made by a third process called plasma hearth melting (PHM), which utilizes a plasma gas to help stir the melt and to remove inclusions. This factor, plus a characteristically shallow molten pool and a low degree of superheat reportedly result in a relatively homogeneous ingot with a low inclusion count, and a grain size more than an order of magnitude finer than that found in EBM or VAM ingots [14].

Table IV shows the compositions of a number of typical "developmental" refractory alloy compositions. These are alloys which were developed years ago, but never reached commercial status because of a lack of demand, or because of the difficulty and the cost of processing them, or both. However, in at least one case (Nb alloy C-103), the alloy had achieved commercial status, but has recently been taken out of production due to a decreased demand for it. Figure 6 compares the high-temperature flow stress of some of the stronger alloys with those of the unalloyed refractory metals, and illustrates how effective some of the additives are in raising the elevated temperature strength of the base metals.

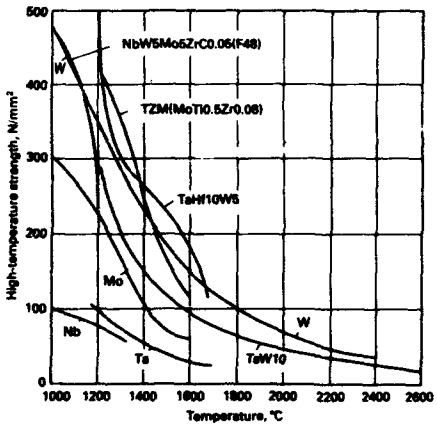


Fig. 6. Flow stress vs. temperature for the refractory metals and some refractory alloys [ref. 15].

MECHANICAL WORKING

In view of the previous discussions concerning certain similarities and differences in characteristics of the VA metals (Nb and Ta) vs. the group VIA metals (Mo and W) it should not be surprising that some of these factors influence the ways in which the two groups of metals are processed from ingot to the various product forms. Similarities such as high strengths at elevated temperatures, and differences such as in DBTT temperature ranges and in the solubilities of the interstitial elements, govern to a large extent the mechanical working of both groups. Regardless

of whether the initial operation is forging or extrusion, breakdown temperatures are high in order to insure adequate plasticity in the workpiece and to keep the force requirements within the capacity of the available equipment. The approximately 13" diameter Mo ingot shown in Figure 7 is representative of the upper end of initial cross-section size for the refractory metals.

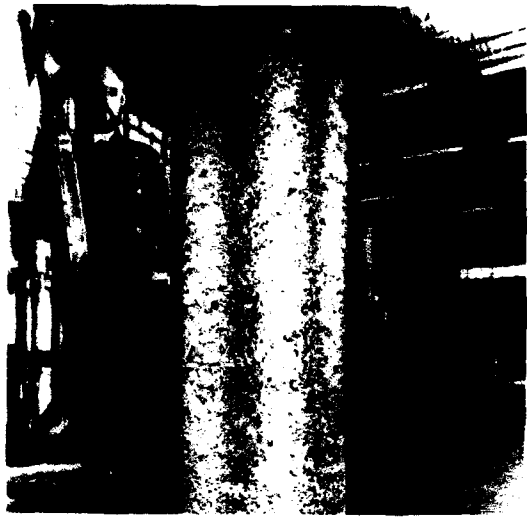


Fig. 7. Approximately 13" - diameter ingot of vacuum arc-melted Mo [ref. 12].

Breakdown temperatures are selected to be in the upper end of the warm-working range, and thus result in a wrought microstructure. Figure 8 depicts such a microstructure, in both the longitudinal and transverse direction, of a sheet bar of unalloyed Mo extruded below the hot-working temperature range. It can be seen that the type of as-cast structure depicted in Figure 4 was elongated by the deformation, but not broken up. Typically a recrystallization anneal would be employed here to establish an equiaxed, but fine-grained, microstructure prior to further working. Virtually all Nb and Ta alloys can be broken down directly from the ingot by either side - or upset -forging. Only the very high strength alloys such as F-48 require the benefit of an initial deformation by the highly-compressive stresses of extrusion. In contrast, unalloyed Mo, all Mo alloys, and any W or developmental W alloys made by a melting process require an initial working via extrusion before further deformation by forging or rolling can be safely undertaken.

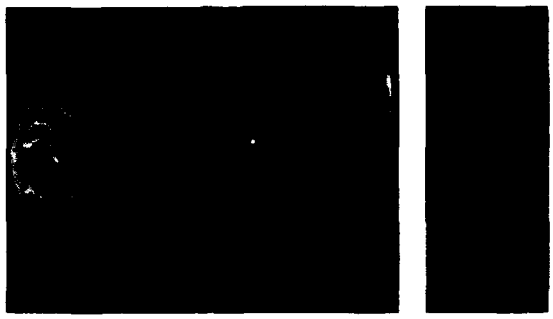


Fig. 8. Transverse (left) and longitudinal (right) cross-sections of an extruded sheet bar of unalloyed Mo, extruded in the warm-working temperature range [ref. 16].

For Mo, an area reduction of 67-80%, corresponding to an extrusion ratio of a minimum of 3/1, is sufficient to permit further deformation. For W, an area reduction of at least 75% (extrusion ratio of 4/1) is preferred. Once through the breakdown step and a subsequent anneal, further deformation can be carried out by whatever operation is appropriate for the product required. Cogging, rotary forging, and flat and rod rolling are typically employed at this point. Table V offers general guidelines with respect to mill processing temperatures. Secondary operations for the Nb or Ta alloys are generally performed at very modestly elevated temperatures in order to minimize pickup of oxygen and nitrogen, both of which harden those alloys and greatly reduce ductility at room and slightly elevated temperatures. Secondary processing temperatures for Mo and W and their alloys are considerably higher than for Nb and Ta, but they must never be high enough to cause the alloy to recrystallize. Rather, a wrought, fibrous microstructure, such as that shown in Figure 9 for W-Re-Hf-C wire, must be developed and maintained. Such a microstructure will result in a mill product with an acceptably low DBTT, whereas a product with a recrystallized microstructure may not.



Fig. 9. Longitudinal microstructure of a 0.14" - diameter rod, swaged to approximately 87% reduction at 1600° - 1400°C [ref. 18].

Table V. Mill Processing Temperatures for Refractory Metals [ref.17]

Metal or alloy	Forging			Extrusion			Rolling		
	Temperature(a)		Typical total reduction, %	Temperature(a)		Typical reduction ratio	Temperature(a)		Typical total reduction between anneals, %
	°C	°F		°C	°F		°C	°F	
Niobium and niobium alloys									
Niobium	980–650	1800–1200	50–80	1095–650	2000–1200	10:1	315–205	600–400	50 breakdown
							20	70	90 finish
Nb-1Zr	1205–980	2200–1800	50–80	1205–980	2200–1800	10:1	315–205	600–400	50 breakdown
							20	70	80 finish
FS-85	1315–980	2400–1800	50	1315–980	2400–1800	4:1	370–205	700–400	40 breakdown
							20	70	50–65 finish
Cb-752	1205–980	2200–1800	30	1315–980	2400–1800	4:1	370–260	700–500	50 breakdown
							20	70	60–75 finish
C-103	1315–980	2400–1800	50	1315–980	2400–1800	8:1	205	400	50 breakdown
							20	70	60–70 finish
C-129Y	1315–980	2400–1800	50	1315–980	2400–1800	4:1	425	800	50 breakdown
							20	70	60–70 finish
Tantalum and tantalum alloys									
Tantalum	<500	<930	50–80	1095	2000	10:1	370–260	700–500	80 breakdown
	20	70	Finish				20	70	90 finish
Ta-10W	1260–980	2300–1800	50	1650–1425	3000–2600	10:1	370–260	700–500	80 breakdown
	1095–815	2000–1500	Finish				20	70	90 finish
T-222	1260–1205	2300–2200	50	2040–1650	3700–3000	10:1	370–260	700–500	75 breakdown
							20	70	50–75 finish
Molybdenum and molybdenum alloys									
Molybdenum	1315–1150	2400–2100	50	1760–1370	3200–2500	8:1	1205	2200	50 breakdown
	925–815	1700–1500	Finish				870	1600	90–75 finish
Mo-0.5Ti	1425–1260	2600–2300	50	1815–1480	3300–2700	8:1	1205	2200	50 breakdown
	1315–1150	2400–2100	Finish				870	1600	75 finish
TZM	1480–1315	2700–2400	50	1815–1540	3300–2800	8:1	1350–1205	2460–2200	50 breakdown
	1370–1205	2500–2200	Finish				1000–980	1830–1800	60
							315	600	10 finish
Tungsten									
Tungsten	1815–1595	3300–2900	20	1925–1650	3500–3000	9:1	1450–1400	2640–2550	50 breakdown
	1315–1010	2400–1850	Finish				1370–980	2500–1800	90 finish

(a) Where a range is given, the higher temperature is the typical starting temperature and the lower temperature is the minimum working temperature for that process.

Finishing operations for Nb and Ta alloys can be carried out at room temperature, with some alloys able to undergo area reductions of as much as 80 or 90% between anneals. In the case of Mo, W and their alloys, processing temperatures are still moderately elevated at the finish of sheet rolling and for the drawing of small diameter rod.

SUMMARY

Typical processing schedules for ingots of Nb or Ta and their alloys, and for ingots of Mo or W and their alloys, are summarized in Tables VI and VII.

Table VI. Summary of Mechanical Working of Nb, Ta, and Alloys

Breakdown
Usually by forging
Sometimes by extrusion
(in hot or warm working temperature range)

Recrystallize (preferably in vacuum)

Warm work to minimize contamination by O_2 and N_2

Recrystallize to fine grain size (in vacuum)

Cold work (room Temp.) to finish size
with intermediate vacuum anneals

Recrystallize to fine grain size (in vacuum)

Table VII. Summary of Mechanical Working of Mo, W, and Alloys

Breakdown
By extrusion (in warm-working temperature range)
67-80% RA (corresponds to extrusion ratio of 3/1 to 5/1)

Recrystallize

Warm work (cog, side forge, roll)

Recrystallize to fine grain size

Warm work at decreasing temperatures to avoid subsequent
recrystallization (To control DBTT)

Use in wrought or stress-relieved condition
(to maintain low DBTT)

ACKNOWLEDGEMENTS

The author wishes to thank the following for helpful discussions: John A. Shields, Jr., and James Wodyca (Climax Specialty Metals), Craig Wojcik (Teledyne Wah Chang, Albany), P. Kumar, Don Schwartz, and Chris Triolo (Cabot Corp.), Tom Ramlow and Paul Forde (H.C. Starck, Inc.), Robert H. Titran (Nasa-Lewis), James Anderson (Philips Elmet Corp.), Boris Bryskin (Sandvik Rhenium alloys, Inc.), and George McClary (H. Cross, Inc.). Sincere thanks are due to Phyllis Liu, Karen Keevern, and Yvonne Mastracchio for preparation of the manuscript.

References

1. R.W. Buckman, Jr., in Alloying, edited by J.L. Walter, M.R. Jackson, and C.T. Sims (ASM International, Metals Park, Ohio, 1988), p.421.

2. D.A. Robins, J. Less-Common Metals 1, 396 (1959).

3. G.T. Hahn, A. Gilbert, and R.I. Jaffee, in Refractory Metals and Alloys II, edited by M. Semchyshen and I. Perlmutter (Interscience Publishers, New York, 1963), pp. 23-63.

4. R.H. Titran, Advanced Materials and Processes 142 (5) 38 (1992).

5. R.T. Begley, D.L. Harrod, and R.E. Gold, in Refractory Metal Alloys, edited by I. Machlin, R.T. Begley, and E.D. Weisert (Plenum Press, New York, 1968), pp. 41-84.

6. O.D. Sherby, Acta Met. 10, 135-147 (1962).

7. R.A. Perkins, in Refractory Metal Alloys, edited by I. Machlin, R.T. Begley, and E.D. Weisert (Plenum Press, New York, 1968), p. 106.

8. B.A. Wilcox, in Refractory Metal Alloys, edited by I. Machlin, R.T. Begley, and E.D. Weisert (Plenum Press, New York, 1968), pp. 1-34.

9. W.H. Chang, in Refractory Metals and Alloys, edited by M. Semchyshen and J.J. Harwood, AIME Met. Soc. Conf. 11 (Interscience, New York, 1961), p. 83.

10. R.W. Armstrong, J.H. Bechtold, and R.T. Begley, in Refractory Metals and Alloys, edited by Semchyshen and I. Perlmutter, AIME Met. Soc. Conf. 17 (Interscience, New York, 1963), p. 159

11. J.H. Bechtold, E.T. Wessel, and L.L. France, in Refractory Metals and Alloys, edited by M. Semchyshen and J.J. Harwood, Vol. 11 (Interscience, New York, 1961), pp. 25-81.

12. J.A. Shields, Jr. (Private Communication).

13. R.O. Carson, Interim Report 7-782(V) to Aeronautical System Division, Contract No. AF33(600)-39944. August 1961.

14. T. Ramlow (Private Communicaiton).

15. K. Laue and H. Stenger, Strangpressen (Aluminium-Verlag GmbH, Düsseldorf, 1976) [Extrusion: Processes, Machinery, Tooling] (American Society for Metals, Metals Park, Ohio, 1981).

16. J.R. Hughes (Unpublished).

17. J.B. Lambert and J.J. Rausch, in Metals Handbook, 10th ed., vol. 2 (ASM International, Metals Park, Ohio, 1991), P.561.

18. Y.J. Park and J.K. Anderson, in Tungsten and Tungsten Alloys - Recent Advances, edited by Andrew Crowson and Edward S. Chen (The Minerals, Metals, and Materials Society, Warrendale, PA, 1991), pp. 177-183.

EFFECT OF DEFORMATION PROCESSING ON MECHANICAL PROPERTIES OF Nb-10 a/o Si IN-SITU COMPOSITE

I. WEISS, M. THIRUKKONDA*, AND R. SRINIVASAN
Mechanical and Materials Engineering Dept., Wright State University, Dayton, Ohio 45435-0002.
* now at Concurrent Technologies Corp., Johnstown, Pennsylvania, 15904.

ABSTRACT

Nb-10 a/o Si alloy is an in-situ composite. The microstructure of the cast alloy consists of pro-eutectic Nb dendrites distributed in a matrix of eutectic Nb_3Si + Nb phases. The microstructure of the as-cast alloy was modified by multiple hot extrusions producing an oriented composite. Extensive grain size refinement occurred in both the Nb and Nb_3Si phases. The ductile primary (pro-eutectic) Nb particles were aligned along the extrusion direction. Bend strength and fracture toughness measured by three point bend and four point bend tests, respectively, showed that both the yield strength and fracture toughness of the alloy increases considerably following this thermomechanical processing. These improvements have been attributed to the changes in size, morphology and spacing of the constituent phases and their microstructural refinement.

MATERIALS AND EXPERIMENTAL PROCEDURE

Nb-10 a/o Si ingots were prepared by arc melting a master alloy in a water cooled copper crucible. The master alloy was prepared from double arc melted high purity Nb and electronic grade Si. The silicon content was measured to be 9.08 a/o, about 1 a/o less than the desired Si level. The wet chemical analysis was also carried out to verify the amounts of interstitial and trace elements and it was found that the carbon content varied from 0.10 to 0.2 a/o. A LECO TC-136 Oxygen/nitrogen analyzer was used to measure the O and N levels and they were found to be about 0.081 and 0.0465 a/o respectively. The ingots were canned in Mo and hot extruded at 1800°C to a 4:1 reduction in cross sectional area. Some samples were re-canned and re-extruded at 1750°C with the same extrusion ratio. A slow cooling rate was adopted after all extrusions.

Notched specimens of nominal dimensions 5 mm (t) x 10 mm (w) x 45 mm (L) were made by EDM from the as-cast and extruded materials to evaluate the fracture toughness by four-point bend tests. A notch of 5 mm in length and 0.2 mm in thickness was machined by wire EDM. Smooth specimens of nominal dimension, 3 mm (t) X 4 mm (h) X 45 mm (L) were also made by EDM for evaluation of strength by three-point bend tests. In order to transform the metastable Nb_3Si to the stable Nb_5Si_3 phase, the extruded and re-extruded bend test samples were heat treated at 1450°C for 25 hours in a vacuum of 10^{-6} torr.

Fracture surfaces were examined by SEM to study the mechanism of fracture, the role of micro-constituents in fracture, and in particular the role of primary Nb particles in toughening the composite. Energy Dispersive Spectroscopy (EDS) was also performed on the fracture surfaces to identify the phases.

RESULTS AND DISCUSSION

Microstructure of the Nb-10 a/o Si in-situ Composite

Figure 1 shows the microstructure of the Nb-10 a/o Si alloy in the as-cast (AC), once extruded (E1) and twice extruded (E2) conditions. In the as-cast condition, the primary (pro-

Mat. Res. Soc. Symp. Proc. Vol. 322. ©1994 Materials Research Society



Figure 1: Microstructure of Nb-10 a/o Si in-situ composite

(a) As-cast (AC) condition



(b) Extruded (E1) condition



(c) Re-extruded (E2) condition

eutectic) Nb dendrites are essentially single grains, while the Nb_3Si matrix is polycrystalline. Secondary (eutectic) Nb particles are distributed within the Nb_3Si matrix. Based on line intercept measurements in several orientations an average Nb particle size was found to be approximately 20 μm. The average spacing between primary Nb particles was calculated to be 14 μm. The grain size measurements in the Nb_3Si phase yielded an average value of 18 μm. The Nb_3Si phase does not undergo eutectoid decomposition to Nb and Nb_5Si_3 after hot extrusion. After extrusion, both the Nb and Nb_3Si phases are elongated and aligned in the extrusion direction. In addition, recrystallization of both phases following extrusion reduces the average grain size of the primary Nb particles to about 11 μm and that of the Nb_3Si matrix to about 5 μm, and the spacing between the primary Nb particles to 11 μm. The aspect ratio of the primary Nb particles was determined to be 4 in the extruded condition. Re-extrusion further elongates, orients, and aligns the primary Nb particles in the extrusion direction. The average grain size in this condition is about 6 μm and 2 μm in the Nb and Nb_3Si phases, respectively. The spacing between primary Nb particles reduces to around 6 μm. In addition, the aspect ratio of the primary Nb particles increases to approximately 14. Fractographs taken from bend test specimens of the re-extruded material reveal that the secondary Nb particles are present along the grain boundaries of the Nb_3Si matrix.

Bend Strength of the Nb-10 a/o Si in-situ Composite

Smooth bend bars of the Nb-10 a/o Si alloy in the AC, E1 and E2 conditions were tested by three point bending over the temperature range from 25°C to 1200°C. Figure 2 shows the bend strength of Nb-Nb_3Si composite as a function of temperature. Fracture stress values are reported at room temperature since all three conditions (AC, E1 and E2) of Nb-10 a/o Si alloy with the Nb_3Si matrix phase failed in a brittle manner. Yield stress values are plotted at all other temperatures. The yield strength of the alloy decreases with increasing temperature. The Nb + Nb_3Si composite in all conditions exhibits appreciable plastic deformation at 1000°C and 1200°C. The as-cast specimens at these temperatures yielded and then fractured, whereas specimens in the E1 and E2 conditions continued to bend without fracture and bottomed out in the test jig. At all temperatures, the Nb-10 a/o Si alloy in the extruded (E1) condition showed higher bending strength than the as-cast (AC) material, and the material in the twice extruded (E2) condition showed the highest bending strength.

The Nb-10 a/o Si alloy with Nb_5Si_3 matrix shows similar results, with the re-extruded and heat treated (E2+HT) material exhibiting the highest strength at all temperatures (Figure 3). Bend strength data obtained from an earlier study on as-cast and heat treated (AC+HT) and extruded and heat treated (E1+HT) of Nb-10 a/o Si alloy have been plotted for comparison [1]. Figures 2 and 3 show that the composite with the metastable Nb_3Si phase matrix has higher bending strength than the composite with the stable Nb_5Si_3 phase matrix.

Fracture Toughness of the Nb-10 a/o Si Composite

Fracture toughness of the alloy thermomechanically processed to the various conditions was evaluated over the temperatures range of 25°C to 1200°C by four-point bending of notched specimens. The specimens had round tipped notches made by wire EDM, and did not conform to the ASTM standard which requires a V-shaped notch which has been pre-cracked by fatigue. Therefore, the results presented in Figures 4 and 5 for the Nb_3Si and Nb_5Si_3 matrix composites, respectively, are K_Q and not K_{IC}. The fracture toughness K_Q was calculated using the following

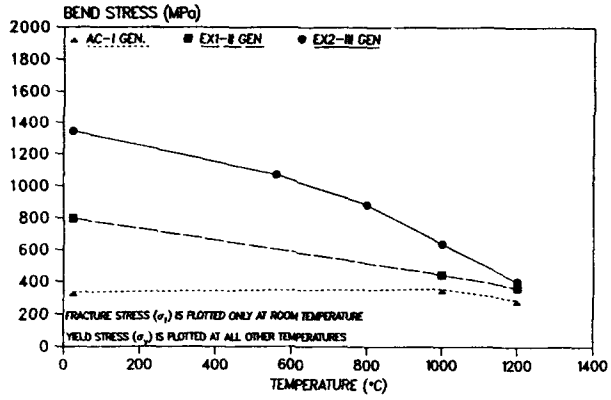


Figure 2: Bending strength of Nb-10 a/o Si composite (Nb + Nb_3Si) in different thermomechanical conditions

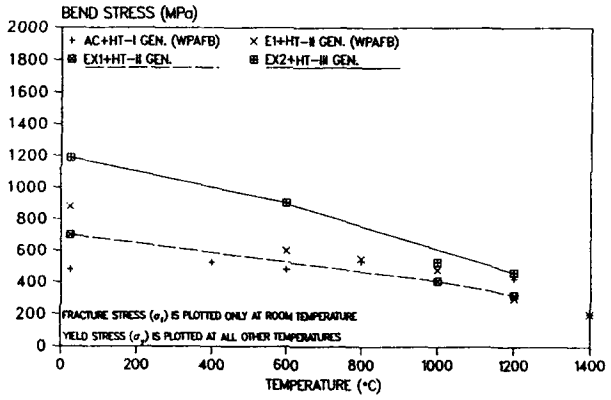


Figure 3: Bending strength of Nb-10 a/o *Si composite (Nb +* Nb_5Si_3) in different thermomechanical conditions

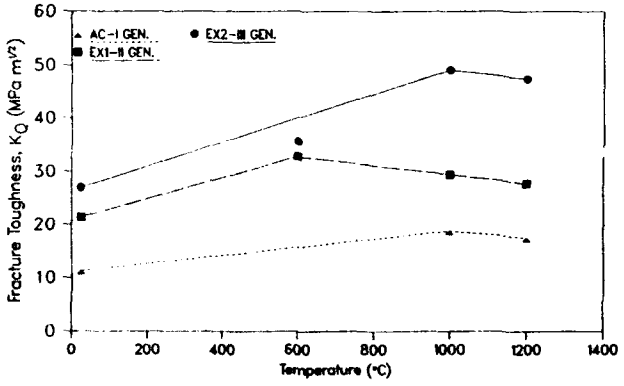


Figure 4: Fracture toughness (K_Q) of Nb-10 a/o Si composite (Nb + Nb_3Si) in different thermomechanical conditions

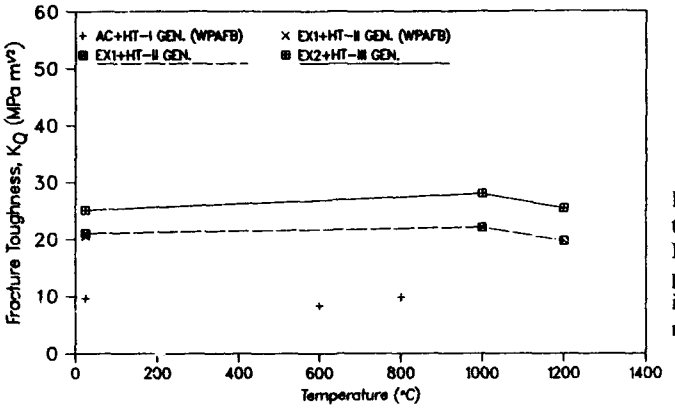


Figure 5: Fracture toughness (K_Q) of Nb-10 a/o Si composite (Nb + Nb_5Si_3) in different thermomechanical conditions

equation [2].

$$K_Q = \frac{6Ma^{1/2}}{bw^2} f\left(\frac{a}{w}\right) \qquad (1)$$

where, **M** (= **PL**/2) is the applied bending moment at fracture, **P** is the load at fracture, **L** is the span, **a** is the notch length, **b** is the specimen thickness, **w** is the specimen width, and **f** (**a**/**w**) is a geometry parameter given by:

$$f\left(\frac{a}{w}\right) = 1.99 - 2.47\left(\frac{a}{w}\right) + 12.97\left(\frac{a}{w}\right)^2 - 23.17\left(\frac{a}{w}\right)^3 + 24.8\left(\frac{a}{w}\right)^4 \qquad (2)$$

At room temperature, where fracture toughness is critical, Nb-10 a/o Si alloy in the as-cast condition with the Nb_3Si matrix shows a K_Q of 11.3 MPa$\sqrt{m}$. Upon extrusion this value increases to 21.4 MPa$\sqrt{m}$ for the E1 material, and with further extrusion the fracture toughness increases by a factor of two-and-a-half to 27.0 MPa$\sqrt{m}$ for the E2 material also with Nb_3Si matrix, when compared to the as-cast material. Such an improvement in the fracture toughness can be attributed to the alignment and stretching of Nb particles along the length of the specimen by hot extrusion and to grain refinement of both the Nb_3Si matrix and the ductile Nb phase. With increasing temperature, the fracture toughness increases up to 1000°C due to increased ductility of the material. At 1200°C the slight drop in fracture toughness is due to a significant loss of strength of the composite at this temperature.

Figure 6 summarizes the effect of thermomechanical processing on the strength and toughness of the Nb-10 a/o Si alloy. At all temperatures, increases in toughness of the alloy is associated with increased in the bending strength for all conditions of the alloy (AC, E1, E2, E1+HT, E2+HT). This is to be expected in ceramic-base materials since increases in toughness directly translate to improvements in strength [3]. At room temperature the strength of the Nb + Nb_3Si composite increases from 334 MPa to 1344 MPa, a change of approximately 300%. The fracture toughness K_Q improves from 11.3 to 27.0 MPa$\sqrt{m}$, an increase of about 140%. The bend strength and fracture toughness of the composite in the heat treated condition with the stable Nb_5Si_3 matrix are somewhat less than those of the composite with the metastable Nb_3Si matrix

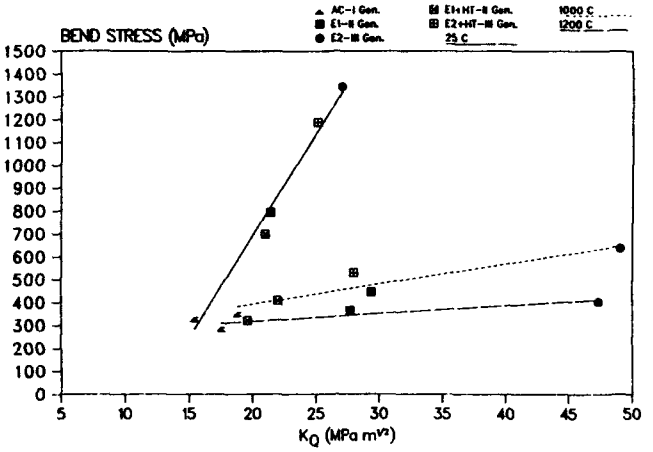


Figure 6: Bend strength and fracture toughness (K_Q) of Nb-10 a/o Si in-situ composite.

phase. At the higher temperatures, there is a considerable increase in the ductility of the composite. As a result, the fracture toughness of the alloy shows very large increases for smaller increases in the strength of the composite. Fractographs reveal that the morphological changes of both the phases following thermomechanical processing play a major role in improving the toughness of the composites.

Fractography

Figure 7 shows a small area of the fracture surface of the as-cast material. The fracture surface is essentially flat, and the crack front appears to have swept through this area causing brittle fracture of most of the large primary Nb particles and of the Nb_3Si matrix by cleavage. Only a few primary Nb particles exhibited ductile fracture, as shown in Figure 8. Extensive shallow "river" patterns or ridge markings are observed in the primary Nb particles which have



Figure 7: Brittle fracture of primary Nb particles in the as-cast Nb-10 a/o Si in-situ composite.



Figure 8 : A debonded interface between an Nb particle and the Nb_3Si matrix showing brittle fracture of the silicide and dimpled failure of the Nb phase

fractured by cleavage (Figure 7). The Nb_3Si matrix does not show similar river patterns on the fracture surfaces, but microcracks are observed especially where the Nb_3Si matrix around the primary Nb particle had cracked and facilitated debonding (Figure 8). Figure 9 shows microcracking of the Nb_3Si matrix along with a large cleaved Nb particle, even after that particle had debonded from the matrix.

Figure 10 shows a small area of the fracture surface of the twice extruded (E2) material tested at room temperature. The fracture surface is not flat, and the crack appears to have changed path many times. Also, more microcracks are observed in the Nb_3Si matrix. A large number of the recrystallized primary Nb particles undergo ductile fracture after being debonded from the matrix by interface cracking, as shown in Figure 11. An interesting feature observed

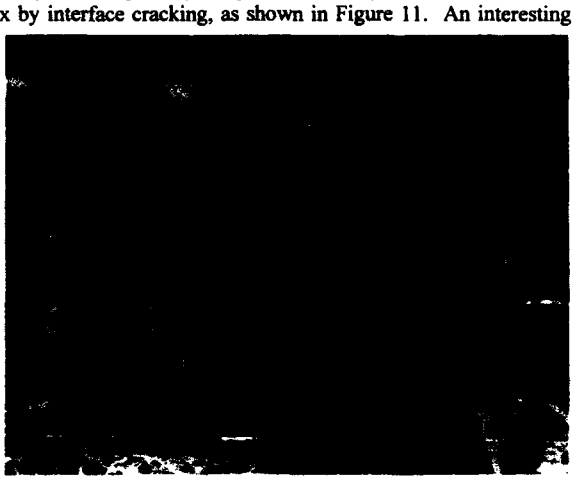


Figure 9: Micro-cracking of the Nb_3Si phase, debonding and brittle failure of an Nb phase.



Figure 10: Fracture surface of re-extruded (E2) Nb-10 a/o Si alloy showing ductile failure of the Nb particles and extensive micro-cracking of the Nb_3Si matrix.

was that, unlike in the as-cast material, the crack front in the E2 material forms steps while moving through a recrystallized Nb particle (Figure 12). These steps at the Nb/Nb boundaries exhibit a ductile (dimpled) fracture appearance. This is an additional energy absorption mechanism during fracture, resulting in a more ductile product during the fracture of the re-extruded material as compared to the fracture of the as-cast material. Recrystallization of both Nb and Nb_3Si phases changes the nature of the Nb/Nb_3Si interface [4], which debonds under stress. Subsequently, ductile ridges form at the interfaces between small grains in the recrystallized Nb particles. This is in contrast to the as-cast material which contains primary Nb particles which are essentially single grains.



Figure 11: Ductile failure of primary Nb particles and micro-cracking of the Nb_3Si matrix in the re-extruded (E2) Nb-10 a/o Si alloy.



Figure 12: Ductile steps within a recrystallized primary Nb particle.

Features observed on the fractured Nb_3Si matrix are shown in Figure 13. A large number of microcracks are observed in the Nb_3Si matrix of the re-extruded material, indicating that microcrack toughening is a mechanism that increases the toughness of Nb_3Si matrix. Figure 14 shows that the secondary Nb particles, which are present mainly along the Nb_3Si grain boundaries, have clearly undergone ductile fracture and have been pulled to a "knife-edge" geometry upon failure. The fracture surface of the Nb_3Si also appears facetted, indicating that there is considerable crack branching and meandering before failure.



Figure 13: Micro-cracks in the silicide matrix of the re-extruded (E2) Nb-10 a/o Si alloy.

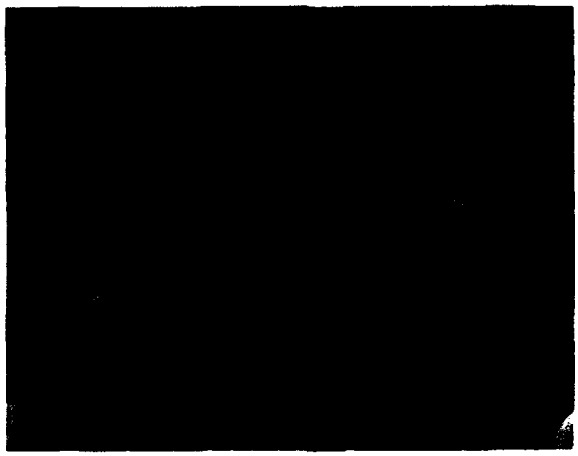


Figure 14: Ductile failure of secondary Nb particle located along grain boundaries of the Nb_3Si matrix and facetted fracture of the Nb_3Si matrix in the re-extruded (E2) Nb-10 a/o Si alloy.

SUMMARY AND CONCLUSIONS

(1) Multiple hot extrusion of Nb-10 a/o Si alloy results in morphological alignment and microstructural refinement of the ductile Nb and brittle Nb_3Si matrix phases of this ductile phase toughened in-situ composite.

(2) The room temperature strength of the composite increases from 334 MPa for the as-cast (AC) material to 1344 MPa for the twice extruded (E2) material.

(3) The fracture toughness of the composite increases from 11 MPa$\sqrt{m}$ for the as-cast (AC) material to 27 MPa$\sqrt{m}$ for the twice extruded (E2) material.

(4) The volume fraction of primary Nb particles undergoing ductile failure increases considerably from the as-cast (AC) to the twice extruded (E2) material due to changes in the primary Nb/Nb_3Si interface, which debonds under stress, and the formation of ductile ridges at the interfaces between small Nb grains.

REFERENCES

1. M.G. Mendiratta, J.J. Lewandowski and D.M. Dimiduk, Met. Trans., **22A**, 1573, (1991).
2. G.K. Bansal and W.H. Duckworth, Fracture Mechanics Applied to Brittle Materials, edited by S.W. Freiman, (ASTM, Philadelphia 1979), pp. 38.
4. G. Petzow, R. Telle, and R. Danzer, Materials Characterization, **26**, 289, (1991).
3. B. Cockeram, H.A. Lipsitt, R. Srinivasan, and I. Weiss, Scripta Metallurgica and Materialia, **25**, 2109, (1991).

ACKNOWLEDGEMENT

Support from AFOSR under Grant No. AFOSR-90-0205, Dr. A.H. Rosenstein, Program Manager is gratefully acknowledged.

EFFECT OF COOLING RATE ON THE TENSILE YIELD STRENGTH AND DUCTILITY OF B2 COMPOUND IN Nb-40at.%Ti-15at.%Al ALLOY

D.-H. Hou and H.L.Fraser
Dept. of Materials Science and Engineering, The Ohio State University,
2041 College Road, Columbus, OH 43210, USA

ABSTRACT

The effect of cooling rate on the tensile properties of specimens of the Nb-40Ti-15Al alloy (in at.%) subjected to various heat treatments has been studied. This alloy has the B2 crystal structure and an order-disorder transition temperature between 1020°C and 1100°C. Two heat treatments have been carried out; the first one involves an 1100°C/1hr heat treatment followed by furnace cooling, air cooling or water quenching. The second type of heat treatment involves re-heating the furnace-cooled and water-quenched specimens at 400°C for 10 minutes or 900°C for 30 minutes, followed by either furnace cooling or water quenching. Tensile properties, SEM fractographs and microstructures of these specimens have been assessed. It is shown that specimens furnace-cooled from 1100°C have higher strength and less ductility than the water quenched ones. An observed microstructural feature associated with cooling rates is the difference in anti-phase domain (APD) size. Discussions are focused on possible cooling rate related phenomena that could affect the tensile properties. It is proposed that the degree of long range ordering, not the APD size, is the dominant factor for the observed cooling rate effect on the tensile properties.

INTRODUCTION

A niobium based alloy with a nominal composition of Nb-40Ti-15Al (in at.%) has been developed for high temperature structural applications[1-3]. This alloy has the B2 crystal structure in the as-cast condition and transforms to a disordered bcc structure at higher temperature[1]. The transformation temperature (T_c) determined by quenching experiments is between 1020°C and 1120°C[1]. An orthorhombic phase (o-phase) forms in the B2 matrix after an 800°C/20hr heat treatment [1] and redissolves at 1000°C or higher [3, 4]. A room temperature tensile ductility of 20% has been observed in this B2 alloy [2, 5], indicating that it is a "ductile" intermetallic compound. However, it has been shown that specimens furnace cooled from 1100°C were less ductile than the water quenched ones [3]. The factors responsible for this cooling rate effect have been correlated to the anti-phase domain (APD) size, but no satisfactory conclusion could be made [3]. In the present work, other mechanisms related to cooling rates are studied. Tension tests were performed on specimens subjected to two types of heat treatments followed by various cooling rates. The Young's modulus of some of these specimens was also measured. The test results, together with the fractographs, microstructures and deformation mechanisms of these specimens, are presented and discussed in light of possible embrittlement mechanisms.

EXPERIMENTAL PROCEDURE

The Nb-15Al-40Ti alloy was prepared by plasma arc melting in an Ar atmosphere on a water cooled copper hearth. Heat treatments were performed by encapsulating the specimens quartz tubes which were back-filled with Ar and subquently sealed, and then heated in a conventional resistance furnace. Tension test specimens with a 30mm gauge length and a 5mm gauge width were made from plates of 2mm thickness, which were cold rolled to ≈ 60% reduction in thickness. Various heat treatments were applied to the specimens as designated in Table I. Tension tests were carried out at a strain rate of 10^{-4} sec^{-1} at the room temperature. Tensile strains were recorded using an extensometer with 0.5" gauge length. Sonic resonance measurements (ASTM C1198-91) were used to measure the elastic modulus of a specimen of 58x4x20mm in size; these measurements were repeated on the same specimen after heat treatment at 1100°C/7hr followed by furnace cooling, and heat treated again at 1100°C/1hr followed by water quenching. The fracture surfaces of samples tested in tension were examined in a Hitachi S4000 SEM. Thin foils for transmission electron microscopy (TEM) were prepared by twin jet electropolishing using 7.5 vol.% H_2SO_4 in methanol at -40°C. The foils were examined in a JEOL 200CX TEM operating at 200kV.

Mat. Res. Soc. Symp. Proc. Vol. 322. ©1994 Materials Research Society

Table I. Heat treatments of tension test specimens

Mechanical Processing	Specimens	Stage 1	Stage 2
	TW	1100°C / 1hr / WQ	-
	TA	1100°C / 1hr / AC	-
* (cold rolled to 60%	TF	1100°C / 1hr / FC	-
reduction is thickness	TW9W	1100°C / 1hr / WQ	900°C / 30min /WQ
before heat treating)	TW9F	1100°C / 1hr /WQ	900°C / 30min /FC
	TW4F	1100°C / 1hr /WQ	400°C / 10min /WQ
	TF4W	1100°C / 1hr / FC	400°C / 10min / FC

WQ= water quenched
FC= furnace cooled, cooling rate ≈ 10^1 °C/min.
AC= air cooled, cooling rate ≈ 10^2 °C/min.

RESULTS

The tension stress-strain curves of TA, TF and TW specimens and the tested specimens are shown in Fig. 1. The tension test results are summarized in Table II. For the TW and TA specimens, a yield point phenomenon was observed and no apparent strain hardening occurred after yielding. Both specimens have an engineering strain at fracture (e_f) of ≈20% and a reduction in area at fracture (RA) of ≈40%. Necking of the TA specimen has occurred outside the gauge length of the extensometer, so the e_f (≈ 5%) reported in Fig. 1a is much lower than the real e_f and can be viewed as an indication of the uniform elongation (e_u). It is noted that a crack formed in the TF specimen after it reached a ultimate tensile stress (σ_u) of 750MPa, but this crack did not propagate through the specimen immediately and some deformation was observed in the remaining section. Since no yielding or deviation of linearity in the stress-strain curve was observed, the yield stress of the TF specimen should be higher than or equal to the σ_u. The effect of cooling rate on the elastic modulus

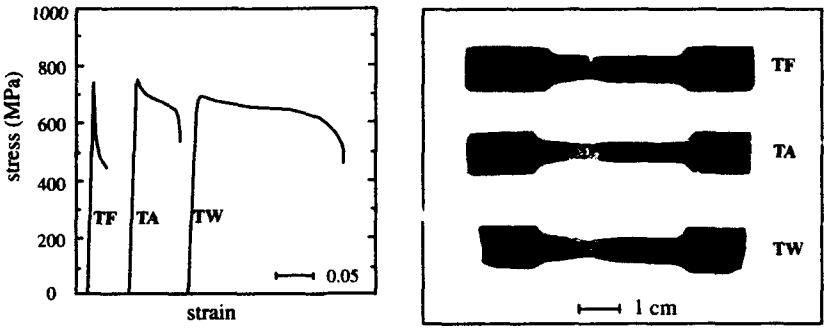


Fig. 1 (a) stress-strain curves of various tension tests. (b)tested and fractured tension specimens

Table II. Yield stress, elongation at frature (e_f), reduction in area at fracture (RA) and APD size of tension test specimens.

Specimen	Y.S.	e_f	RA	APD size
TW	690 MPa	≈ 20 %	40 %	0.05 μm
TA	750 MPa	≈ 20 %	40 %	0.2 μm
TF	750 MPa	≈ 10 %	35 %	2.0 μm

Table III. Effect of cooling rate on Young's Modulus (E)

Heat treatment	E
as cast	100 GPa
(as cast) + 1100°C/7hr/FC	105 GPa
(as cast + 1100°C/7hr/FC) + 1100°C/1hr/WQ	100 GPa

is summarized in Table III. Since all the measurements were made on the same specimen, there will be no error caused by variations in specimen size and geometry. It is seen that the specimen has a lower Young's modulus in the as-cast and water-quenched conditions compared with the furnace cooled conditions.

The fracture mode of the tension test specimens were studied by SEM fractography. Dimpled rupture surfaces (Fig. 2a) were observed for both the TA and TW specimens, denoting a ductile fracture. For the TF specimen, a mixed mode fracture consisting of cleavage, ductile and intergranular fracture was observed (Fig. 2b). It is noted that the section in which the cracks have initiated failed primarily in the intergranular or cleavage mode, while the rest failed primarily in the ductile mode. The microstructures of samples tested in tension were studied by optical microscopy (OM) and TEM. All the specimens have a similar grain size ($d_n \approx 200\mu m$) and have no second phase (o-phase) precipitates. The only apparent microstructural difference observed is the APD size, as shown in Fig. 3. Transverse sections of the tested tension specimens were examined by OM to find the extent of the deformation zone. The TA and TW specimens have a similar deformation zone which extends through the necking section, as shown in Fig. 4a. Conversely, the deformation zone of the TF specimen is localized near the fracture surface, as shown in Fig. 4b.

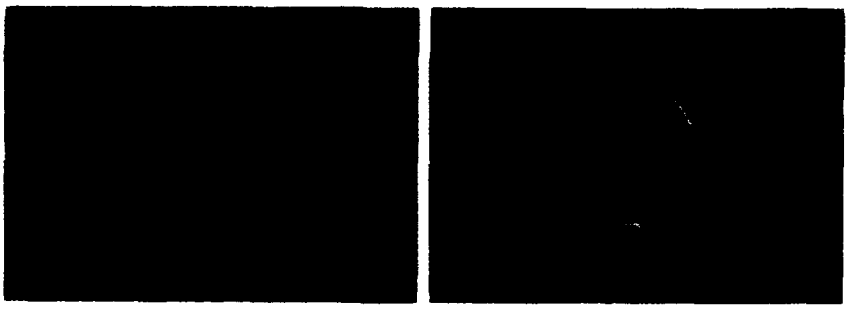


Fig. 2 SEM fractographs of (a) the TW specimen, and (b) the TF specimen.

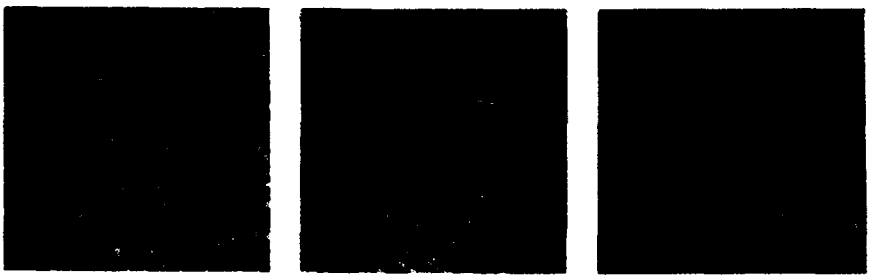


Fig. 3 Dark field TEM micrographs showing the APD's of (a) the TW specimen, (b) the TA specimen, and (c) the TF specimen.



Fig. 4 Transverse sections of the tension tested (a) TW and (b) TF specimens.

The deformation mechanism of both compression and tension tested specimens were studied by TEM. It has been shown [2, 5, 6] that these B2 compounds deform by the glide of coupled super-dislocation pairs each with **b**=1/2<111> on {110}, {112} and {123} planes, and the deformation is fairly localized, as evidenced by the observation that dislocations tend to appear in bands[6]. The same deformation mechanisms and heterogeneous plasticity were observed in the present specimens. The details of the deformation mechanism study will be given elsewhere [7]. Special attention has been paid to the dislocation-APB interactions, but no evidence of possible dislocation pinning by APB's was found[3].

Table IV summarizes the tension test results of specimens which underwent a two-stage heat treatment. Similar to the TW and TA specimens, the stress-strain tensile curves of the TW4F and TW9W specimens show a yield point and no work hardening. The TW4F specimen has the highest e_f (≈35%) and RA (≈65%) among all the specimens in this study. The TW9W specimen has similar e_f and RA as the TA and TW specimens. No tensile ductility was observed for the TF4W and TW9F specimens, which failed at the stress of 600MPa and 580 MPa, respectively. Dimpled fracture surfaces were observed for the TW4F and TW9W specimens, which are similar to the TW and TA specimens. A mixed fracture mode was observed for the TF4W and TW9F specimens. Unlike the TF specimens, they failed catastrophically and only a small portion of the fracture surface (< 5%) shows a dimpled morphology.

Table IV. Yield stress, elongation at frature (e_f), reduction in area at fracture (RA) and APD size of tension test specimens subjected to two-stage heat treatments.

Specimen	Y.S.	e_f	RA	APD size
TW4F	690 MPa	≈ 35 %	≈ 65 %	0.05 μm
TF4W	600 MPa†	-	-	2.0 μm
TW9F	580 MPa†	-	-	2.0 μm
TW9W	690 MPa	≈ 20 %	≈ 40 %	2.0 μm

† UTS, failed before yielding

DISCUSSION

All the tension specimens have a similar grain size of about 200μm, thus the grain size effect should not be a factor in the following discussion. Considering first the TF and the TW specimens, where the former has higher yield stress[‡] and lower ductility than those of the latter, the difference is that they experienced different cooling rates after 1100°C/1hr heat treatment. An important microstructural feature associated with different cooling rates in this B2 alloy is the difference in APD

‡ The higher yield stress observed in the TF specimen compared with the TW specimen is further noted by the compression test results, where the furnace-cooled specimen has a higher yield stress of 770MPa compared with that (690MPa) of the water-quenched specimen [7].

size, which can be rationalized as follows. As the temperature of the TF specimen decreased from 1100°C through the T_c during the furnace cooling process, the slow cooling rate ($\approx 10^2$°C/min.) will allow the newly formed APD's to grow and result in a large APD ($\approx 2\mu m$) microstructure. On the contrary, the TW specimen water-quenched from a temperature higher than T_c has a fine APD ($\approx 0.05\mu m$) structure due to the limited time allowed for the APD growth during the cooling process. Despite the large difference in APD size, there is no direct evidence of the effect of APD size on the yield stress and ductility, such as a change of deformation mechanisms and dislocation-APD interaction, can be found. To further test the APD size effect, the tension test results of the TW9F and TW9W specimens, which both have large APD microstructures¶, were compared. It was found that the TW9W specimen has a similar yield stress and ductility as the TW specimen while the TW9F specimen is brittle and no yielding was observed. It is then suggested that the large scale of APD microstructure alone does not necessarily cause the high strength and brittleness of the TF specimens.

The second phenomenon which can be related to the cooling rate is dislocation locking by interstitial solute atoms like carbon, nitrogen and oxygen. The higher yield stress of the TF specimen compared with the TW specimen might be related to the formation of a condensed solute atmosphere (Cottrel atmosphere) along the dislocations during the slow cooling process. If this is the case, the yield stress of the TF specimen can be lowered by dissolving the locking solute atmosphere, and the yield stress of the TW specimens can be increased by condensing the locking solute atmosphere. These experiments were attempted by carrying out the TF4W and TW4F heat treatments†. The TF4W specimen failed prematurely in a mostly brittle mode and no yielding was observed. The yield stress of the TW4F specimen was not increased but remained the same as the TW specimen. This indicates that the solute-locking phenomenon should not contribute to the high yield stress and low ductility of the TF specimen.

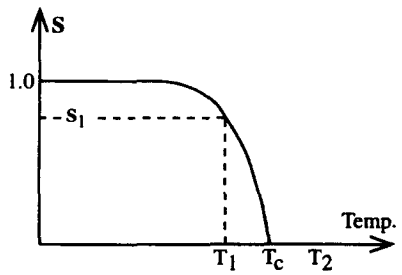


Fig. 5 The effect of temperature on the degree of long range ordering (S)

Another phenomenon associated with the cooling rates is the degree of long range ordering (LRO) in this B2 alloy. Generally, the degree of LRO can be described by the long range ordering parameter (S) based on a stoichiometrical state[8]. A typical S dependence on temperature is shown in Fig. 5. The TW and TF specimens can be envisaged as specimens quenched and slowly cooled, respectively, from a temperature (T_2) higher than the T_c. The latter may have a higher value of S than the former because the slow cooling process may allow the ordering to develop. Thus the S of the TA specimen should be higher than that of the TW specimen but lower than that of the TF specimen. Similarly, the TW9W and TW9F specimens can be envisaged as specimens quenched and slowly cooled, respectively, from a temperature (T_1) slightly lower than the T_c. Again, the slowly cooled TW9F specimen will have a higher value of S than that of the quenched TW9W specimen ($\approx S_1$), despite both the specimens having similar APD size. The ability to control the APD size and S separately has also been shown in the Cu_3Au system [9]. Based on the argument given above, the TF and TW9F specimens are expected to have a more "ordered" structure than the TW and TW9W specimens. Therefore, it is proposed that the higher yield strength of the TF and TA specimens is due to the higher degree of LRO associated with the slow cooling process. This postulate is further supported by the results of Young's modulus measurements, where the furnace cooling results in higher Young's modulus than that from the water quenching. In order to verify this postulate, the S values in this ternary B2 alloy must be determined for specimens with different cooling rates and APD sizes.

¶ The first-stage heat treatment (1100°C/1hr/WQ) gives both specimens a fine APD microstructure and the second-stage heat treatment (900°C/30min/WQ or FC) leads to the APD growth and then a large APD microstructure.

† The detail calculations to determined the heat treating temperature and time to dissolve the solute atomsphere will be given elsewhere [7].

Although LRO phenomenon has been used to rationalize the higher yield stress of the TF and TA specimens compared with that of the TW specimen, it can not explain the low fracture stress and lack of ductility of the TF4W and TW9F specimens. A low fracture stress generally implies that a fracture mechanism becomes active at a stress lower than the yield stress. The observed intergranular fracture suggests that solute segregation or formation of second phase precipitates along grain boundaries may be the possible fracture mechanism associated with the cooling rate. It is noted that the TA specimen has a combination of high yield stress and ductility compared with the TF and TW specimens. This suggested that air cooling rate is slow enough to allow the development of LRO but not too slow to cause embrittlement. Investigation of the fracture mechanisms which can cause the low ductility and the change of fracture mode, i.e. from the dimpled rupture to the mixed mode fracture, will be the topics for future study. Nevertheless, it seems that the combined effect of the increasing flow stress and activation of brittle fracture mechanisms, both of which are associated with slow cooling rates, causes the low fracture stress and ductility.

SUMMARY

The tensile yield stress and ductility are related to the cooling rates of the specimens after being heat treated at 1100°C, which is above T_c. The TF specimen has higher yield stress and lower ductility than those of the TW specimen. A difference in APD size was observed for these specimens. It was shown that neither the APD size nor the phenomenon of dislocation pinning by solute atoms cause the difference in yield stress. It is suggested that the high degree of LRO gives rise to the high yield stress. The lower ductility and mixed fracture mode of the TF, TW9F and TF4W specimens are tentatively explained as a combined effect of increasing yield stress and other embrittling mechanisms associated with a slow cooling rate.

ACKNOWLEDGMENTS

This research has been supported by the Office of Naval Research, with Dr. George Yoder as Program Manager.

REFERENCES

1. J. Shyue, D.-H. Hou, S.C. Johnson, M. Aindow and H.L. Fraser, in "High Temperature Ordered Intermetallic Alloy V", MRS Proceedings, **288**, edited by I. Baker et al., Pittsburgh, PA(1992)243.
2. J. Shyue, D.-H. Hou, S.C. Johnson, M. Aindow and H.L. Fraser, in "High Temperature Ordered Intermetallic Alloy V", MRS Proceedings, **288**, edited by I. Baker et al., Pittsburgh, PA(1992)573.
3. J. Shyue, D.-H. Hou, S.C. Johnson and H.L. Fraser, in "Structural Intermetallics", Eds. R. Darolia et al., Inter. Symp. Structural Intermetallics (Champion, PA, 1993), pp. 631.
4. D.-H. Hou, S.-S. Yang, J. Shyue and H.L. Fraser, in "High-Temperature Silicides and Refractory Alloys", MRS Proceedings, Pittsburgh, PA(1993)in press.
5. J. Shyue, D.-H. Hou, M. Aindow and H.L. Fraser, *Materials Sci. Eng. A* , **170**, (1993)1.
6. D.-H. Hou, J. Shyue, S.-S. Yang and H.L. Fraser, in "Alloy Phase Stability and Design", TMS Fall Meeting (Pittsburgh, PA, 1993), in press.
7. D.-H. Hou, Ph.D. Thesis (in preparation), The Ohio State University
8. R.A. Swalin, *Thermodynamics of Solids* (John Wiley & Sons, Inc., 1972),pp. 153-154.
9. D.G. Morris, F.M.C. Besag and R.E. Smallman, *Phil. Mag.* , **29**, (1974)43.

PART VI

Refractory Alloys: Physical and Mechanical Metallurgy

REFRACTORY AND SILICIDE LAVES PHASES

JAMES D. LIVINGSTON
Massachusetts Institute of Technology
Department of Materials Science and Engineering
Cambridge, MA 02139

ABSTRACT

Present knowledge and understanding of deformation mechanisms, mechanical properties, and dislocations in Laves phases are reviewed. Although the amount of study applied to alloys containing these compounds has been relatively limited, several systems with promising high-temperature properties have been identified, including alloys hardened by binary chromides, ternary aluminides, and ternary silicides. Studies of model alloy systems have suggested possible approaches to increase the room-temperature ductility and toughness of Laves phases. Fundamental studies of the effects of stoichiometry, alloying, atom sizes, electronic structures, stacking fault energy, and other variables on dislocation mobility are needed.

INTRODUCTION

The standard compilation of intermetallic compounds [1] lists approximately one thousand known binary and ternary Laves phases, many with high melting points. Yet recent conferences on intermetallics have typically consisted of a hundred or more papers on nickel and titanium aluminides, and only two or three papers on Laves phases, usually relegated to a session on "other", "exotic", or "advanced" materials. There has been, comparatively, so little fundamental study of the mechanical properties of Laves phases that understanding of this large class of intermetallics is far from "advanced". Nevertheless, understanding is growing, and further fundamental study will eventually make Laves phases more familiar and less "exotic" than they seem today.

Laves phases are topologically close-packed phases of approximately AB_2 composition, the B atoms being slightly smaller than the A atoms. Most Laves phases have either the cubic C15 ($MgCu_2$) or hexagonal C14 ($MgZn_2$) structures, and a relatively small number have the dihexagonal C36 ($MgNi_2$) structure. Several other structures are usually categorized among the Laves phases [2]. The $MgSnCu_4$ structure is related to C15, but with the A sites divided into two sublattices, one occupied by Mg and the other by Sn. Similarly, the $AuBe_5$ structure is related to C15, with the smaller B atoms occupying one of the two A sublattices. However, we limit this paper to a discussion of the common C15(cF24), C14(hP12), and C36(hP24) structures.

The highest known melting point of binary Laves phases is 3160°C for C14 $HfRe_2$. More than twenty others have melting points over 2000°C, including HfW_2 (2512°C), ZrW_2 (2210°C), $HfMo_2$ (2170°C), $MoBe_2$, (2027°C), and $TaCr_2$ (2020°C). Laves compounds rich in Cr or Al with melting points above 1500°C include $HfCr_2$ (1825°C). $NbCr_2$ (1770°C), $HfAl_2$ (1650°C), and $ZrAl_2$ (1645°C).

Mat. Res. Soc. Symp. Proc. Vol. 322. ©1994 Materials Research Society

There are no binary Laves phase silicides. However, silicon has been found to form ternary C14 phases in dozens of transition metal systems [3,4]. Examples include $Mo(Co,Si)_2$ and $W(Ni,Si)_2$. Although many of these ternary C14 silicides occur over a wide range of $AB_{2-x}Si_x$ compositions, the stoichiometries most often reported correspond to $x = 1$ or $x = 1/2$.

In addition to numerous binary Laves-phase aluminides, aluminum also forms several ternary Laves phases, including $Nb(Ni,Al)_2$ and $Ti(Cu,Al)_2$. Ternary aluminides with refractory metals have been reviewed by Kumar [5]. Most binary and ternary Laves phases can also incorporate substantial amounts of Cr, Al, or Si as substitutional alloying elements, usually on B-atom sites, if necessary for improved oxidation resistance.

We review below recent studies of plastic deformation of Laves phases and alloys containing Laves phases. The reader is referred also to an earlier review [6].

SLIP, TWINNING, AND TRANSFORMATIONS

Plastic deformation in single-phase samples of Laves compounds has been reported only at temperatures above about two-thirds of the melting point. Slip and twinning systems observed in C15 and C14 compounds are analogous to those observed in f.c.c. and h.c.p. structures, respectively. Cubic C15 compounds deform on {111} <110> slip systems [7,8] and by {111} <112> mechanical twinning [7,9]. Hexagonal C14 compounds deform by $\langle 11\bar{2}0 \rangle$ slip on both basal and prismatic planes [10], and several twinning systems have been reported [11]. One study of high-temperature compression of dihexagonal C36 compounds indicated that basal slip was the dominant deformation mechanism [12].

As with most intermetallics, brittleness at low temperatures is a major problem. However, plastic deformation in Laves phases at room temperature has been demonstrated in several two-phase alloys. The first alloys in which room-temperature deformability of Laves phases was demonstrated were V-Hf-Nb alloys being studied for their high-field superconducting properties [13,14]. The alloys contained a V-rich bcc solid solution and a HfV_2-based C15 phase. Transmission electron microscopy and accompanying electron diffraction showed that the major deformation mechanism of the C15 phase was {111} <112> mechanical twinning [9,15,16].

The elastic behavior of HfV_2 (and ZrV_2) is anomalous, in that both the Young's modulus and the shear modulus decrease with decreasing temperature [17,18]. This lattice instability is related to a martensitic transformation to an orthorhombic structure below about 120K [19]. If the room-temperature mechanical twinning in V-Hf-Nb alloys derives from this lattice instability, this mechanism for low-temperature toughness of Laves phases may be limited to only a few alloy systems. One approach to answer this question is further study of the temperature dependence of twinning and ductility in these alloys [15,16,20], including extension to cryogenic temperatures. More broadly, it would be of interest to determine whether control of stacking fault energy or other variables could be used to enhance mechanical twinning in other C15 phases.

There is some evidence that the presence of Nb alloying additions in the HfV_2 contributed to the ease of twinning in these alloys [9,15,16]. Intermediate in atomic size between Hf and V, the Nb apparently substituted both on Hf sites and V sites, possibly enhancing the mobility of twinning dislocations. Detailed study of the effect of Nb and

other alloying additions on twinning in HfV_2 would be a useful start to examining the various effects of ternary alloying elements on the deformability of Laves phases. Aside from limited information on solid-solution hardening of $MgCu_2$ [8], $ZrCr_2$ [21], and $NbCr_2$ [22] at elevated temperatures, this important question remains essentially unexplored.

Another low-temperature deformation mechanism recently reported in a Laves phase is stress-assisted phase transformation [23]. In an Fe-rich $ZrFe_2$ phase in a two-phase Fe-Zr alloy, compression at room temperature resulted in partial shear transformation of dihexagonal C36 phase to cubic C15 phase, as evidenced by X-ray diffraction and transmission electron microscopy (Fig. 1). As with the mechanical twinning in V-Hf-Nb, it is important to know whether such stress-assisted phase transformations may offer a general approach to toughening—in this case, "transformation toughening"—of Laves phases.

In further work, Liu [24] has deformed a two phase Ni-Mg in compression at room temperature, and observed, by TEM, evidence of both prismatic and pyramidal slip in the C36 $MgNi_2$ phase (Fig. 2). He has also applied TEM to study deformation-induced microstructure changes under microhardness impressions in two-phase Ni-Mg and Fe-Zr alloys. Complex deformation cells were observed in the C36 $ZrFe_2$ and $MgNi_2$ phases, indicative of substantial slip on both basal and nonbasal planes (Fig. 3). Limited plastic deformation by shear and twinning has also been observed in C15 $TiCr_2$ after room-temperature compression of a two-phase Ti-Cr alloy (Fig. 4) [25].

The above studies have shown that in compression or under microhardness impressions, some Laves phases in two-phase alloys are capable of room-temperature plastic deformation by mechanical twinning, by stress-assisted phase transformation, and by basal and nonbasal slip. Although plastic deformation in most cases was limited, and was often accompanied by some cracking in the Laves phase, it is encouraging to know that Laves phases are not as undeformable at room temperature as was earlier thought. We review next some of the more applied studies aimed at evaluating specific alloys for high-temperature structural applications.

BINARY CHROMIDES

As noted earlier, several chromium-rich Laves phases have high melting points. Since these phases also have promising oxidation resistance at elevated temperatures, mechanical properties of two-phase alloys hardened by chromium-rich Laves phases have been evaluated by several groups. Alloys containing $NbCr_2$ have received the most attention.

In a broad study of many intermetallics with high melting points, Anton and Shah [26] identified $NbCr_2$ and $NbCo_2$ (also a Laves phase) among a total of seven intermetallics with "excellent creep resistance at 1200°C." Cyclic oxidation tests between 1200°C and room temperature also showed that protective and continuous oxide films formed on $NbCr_2$, $HfCr_2$, $NbFe_2$, and $NbCo_2$, leading to low metal loss rates [27]. Takeyama and Liu [28] studied two-phase Cr-$NbCr_2$ alloys and found that the Cr-rich phase was very effective in stopping the propagation of cracks originating in the Laves phase, leading to ductilities of 5% - 11% in compression at room temperature. Liu et al [29] have studied the effects of alloying additions of Re, Al, Ni, Fe, and Co to Cr-$NbCr_2$ alloys, and found that Re is the most effective in improving the mechanical properties at



Fig. 1. High-resolution TEM of $ZrFe_2$ in which room-temperature compression induced C36→C15 phase transformation. From [23].



Fig. 2. Evidence of prismatic and pyramidal slip in compressed $MgNi_2$. From [24].



Fig. 3. Cell Structure in $ZrFe_2$ produced by microhardness indentation. From [24]

room and elevated temperatures. Limited fracture resistance in tension at room temperature remains a problem requiring both better control of microstructure and better understanding of the factors affecting deformability of $NbCr_2$. For the high-temperature structural applications for which these alloys are being considered, isothermal and cyclic oxidation resistance are also of great importance, and are under study by Tortorelli et al [30]. Mechanical properties and oxidation resistance of Nb-rich alloys hardened by $NbCr_2$ have also been studied [31].

The equilibrium structure of $NbCr_2$ and other binary Laves-phase chromides is believed to be C14 at high temperatures and C15 at low temperatures, perhaps with an intermediate regime where C36 is stable. The effect of the phase transformation on mechanical properties is unknown. The transformation involves little or no volume change (despite incorrect claims to the contrary by Vignoul et al. [32]), but does involve a 35% shear (like hcp $\rightarrow$fcc). This can lead to large internal stresses unless relieved by twinning in the cubic C15 phase. The large shear may also explain the frequent observation of C36 structure in $NbCr_2$ and similar compounds, since the C14$\rightarrow$C36 transformation can be accomplished with no net shear, and therefore has a lower activation energy than the C14$\rightarrow$C15 transformation [33].

In Fe-Zr alloys, some room-temperature deformability in $ZrFe_2$ was achieved via a stress-assisted C36$\rightarrow$C15 martensitic transformation [23]. This suggests the possibility that if rapid cooling of Cr-Nb alloys could produce $NbCr_2$ predominantly in the metastable C14 or C36 structures, a similar stress-assisted transformation could enhance room-temperature toughness. The extreme cooling rates associated with splat quenching Cr-Nb alloys [34] produce striking changes in phase compositions and microstructure, and effects of such treatments on mechanical properties also merit further study.

Effects of alloying additions on low-temperature mechanical properties may be related to their effects on phase equilibria and transformation kinetics. It is known, for example, that additions of Fe [33] and Ni [35] to $NbCr_2$ stabilize the hexagonal Laves phases, and Be and others may favor cubic C15. Another important variable is the stoichiometry of the Laves phase, which is known to affect the relative stability of the cubic and hexagonal polytypes. Studies of lattice parameter vs. composition [36] also suggest different defect structures for Cr-rich and Nb-rich compositions.

Eutectic alloys based on $NbCr_2$, $HfCr_2$, $TaCr_2$, or $ZrCr_2$ have been suggested as possible "in-situ composites" for high temperature applications [37]. Bewlay et al [38] have recently studied the microstructure of directionally-solidified Cr-$NbCr_2$ and Nb-$NbCr_2$ eutectics. Kumar and Miracle [39] have recently studied the microstructure and mechanical properties of a Cr - 6 at. % Hf alloy containing $HfCr_2$. Notched and unnotched specimens were tested in bending at various temperatures to estimate the ductile-brittle transition temperature and to measure toughness, which was about 7 MPa$\sqrt{m}$ at room temperature and 15 MPa$\sqrt{m}$ at 600°C. The Laves phase $TiCr_2$ was regarded as promising for high-temperature applications as early as 1953 [40], and alloys hardened by $TiCr_2$ have been studied by various investigators [25,41]. (The Ti-Cr system is rather different from the Nb-Cr, Hf-Cr, Ta-Cr, and Zr-Cr systems in that $TiCr_2$ forms by precipitation from a bcc solid solution rather than directly from the liquid.) There has been little study of alloys hardened by $TaCr_2$ or $ZrCr_2$, although there have been microstructural studies of $Zr(Cr,Fe)_2$ compounds in connection with their potential for hydrogen storage [42].

TERNARY ALUMINIDES AND SILICIDES

As noted earlier, there are many true ternary Laves phases, i.e., phases that are not formed simply by substitutional alloying of binary Laves phases. The C14 ternary aluminides have been employed by Sauthoff and co-workers [43,44] to increase the creep resistance of NiAl. Although commonly denoted as NbNiAl and TaNiAl, these phases actually occur over a range of compositions. These Laves phases substantially strengthen NiAl, but also increase the ductile-brittle transition temperature. Wunderlich et al. [45] have analyzed the slip systems activated in NiAl near NiAl - NbNiAl boundaries that slow the propagation of cracks from the Laves phase. The oxidation resistance of NbNiAl and alloys hardened by NbNiAl have been studied, and a three-phase alloy containing NiAl, NbNiAl, and $NbAl_3$ was found to have oxidation resistance comparable to pure NiAl [46]. Machon [47] has studied "NbNiAl" in detail, including measurements of thermal expansion and elastic modulus, TEM analysis of dislocation networks, and X-ray determination that Ni and Al are distributed randomly on B-atom sites.

The Mo-Co-Si and Mo-Ni-Si systems are among the many ternary systems that contain a ternary C14 silicide. The $Mo(Co,Si)_2$ and $Mo(Ni,Si)_2$ phases provide the hardening in the series of commercial wear-resistant alloys known as "Tribaloys" [48,49]. Directionally-solidified Co-rich and Ni-rich eutectics hardened by ternary Laves silicides have been studied by Sprenger et al. [50] and by Livingston [51]. In the latter study, the tensile strength of the Co-$Mo(Co,Si)_2$ eutectic was found to be 520 MPa at 1000°C and 1920 MPa at room temperature. Also tested, but weaker, were directionally-solidified Co-rich eutectics hardened with $W(Co,Si)_2$ and $Ti(Co,Si)_2$ C14 compounds. The cobalt-rich eutectics were disappointing in cyclic oxidation and hot-corrosion tests, but alloying with Cr and/or Al may improve these properties.

Despite a very limited number of studies, some two-phase alloys hardened with binary or ternary Laves phases have shown promising high-temperature properties, in some cases with tolerable room-temperature ductility or toughness. To guide further alloy development, it would be helpful to improve our current understanding of the fundamental mechanisms of plastic deformation and dislocation behavior in C15, C14, and C36 structures. We review next the atomic structure of Laves phases and current understanding of dislocation structures and mobilities.

STRUCTURES AND DISLOCATIONS

The crystallographic literature on Laves phases is extensive. In 1981, Pearson wrote, "So much has been written about Laves phases that it seems inconceivable that there is anything significant still to be said." [52] Nevertheless, he went on to discuss "their elegant geometry" in a series of papers [52-54] focussed on the effects of atom sizes and valencies on Laves lattice parameters, and many other papers have since appeared on these and related structural issues.

One question that has drawn considerable interest over the years is the relative stability of the C15 and C14 structures and its connection to electron structure. Johnston and Hoffmann [55] have recently applied Huckel band calculations to this problem with results in some accord with experiment. Their bibliography includes much of the earlier theoretical literature. More detailed understanding of the various factors affecting relative phase stability and stacking fault energy, including effects of stoichiometry, alloying, and temperature, may lead to approaches to enhance mechanical twinning and/or transformation toughening in Laves phases. Ohta and Pettifor [56] have applied a simple tight-binding model to determine the effects of atom size and electronic

factors on the relative stability of Laves phases and two competing phases of AB_2 stoichiometry. The effects of magnetic and antiferromagnetic interactions on relative phase stability in Laves phases have been treated in detail by Asano and Ishida [57].

The Laves phases are closely related to other topologically close-packed (sometimes called tetrahedrally close-packed) phases—such as A-15, sigma phase, and mu phase. Sinha [58] has discussed in detail the relations between the structures and properties of the various TCP phases. These connections raise the hope that improved understanding of the mechanical properties of Laves phases may open the door to improved understanding of these related phases.

The structures of Laves phases are most easily described in terms of the stacking of four-layer units, in close analogy to the familiar description of fcc and hcp structures in terms of stacking sequences of single close-packed layers. (We remind you that slip and twinning systems in C15 and C14 are analogous to those in fcc and hcp, respectively.) Each basic Laves stacking unit contains a Kagome network layer of the smaller B atoms with pairs of the larger A atoms imbedded in the gaps (Fig. 5). These three layers of the four-layer stacking unit are believed to remain intact during any shear processes between the stacking units that may take place during slip, twinning, or phase transformations.

Between neighboring three-layer "sandwiches", say X and Y, is a layer of B atoms that occupy the sites not occupied by neighboring sandwiches. Labelling these intermediate layers with lower-case x, y, and z, the C14 structure can be represented by XzYzXzYz stacking and the C15 by XzYxZy stacking. (The intermediate C36 stacking is XzYzXyZy. Many longer-period stacking sequences are possible.)

In fcc, passage of a standard Shockley partial between X and Y layers changes X|YZ ... into X|ZX ..., all layers to the right being shifted in the pattern Y→Z, Z→X, X→Y. The Burgers vector of this standard partial is 1/6 <211>. The corresponding shear between X and Y layers in C15, however, also requires the synchronized shear of the intermediate z layer in a different direction. XzYxZy... is thereby changed to X|yZyXz... . While all layers to the right are sheared in the pattern Y→Z, Z→X, X→Y, the intermediate layer is sheared z→y, i.e., in a direction at 60° to the dominant shear.

This "synchroshear" (a term coined by Kronberg [59]) in Laves phases was first described in 1968 by Kramer and Schulze [60]. It was subsequently discussed by Allen et al. [61], Livingston and Hall [9], Chu and Pope [15,16], and Hazzledine et al. [62,63]. The descriptions differ in detailed terminology, but all are equivalent, including the above simplified description.

It was pointed out by Amelinckx [64] that only in glide on simple planes in simple structures can dislocation glide be considered as occurring on a single "slip plane" between two rigid blocks of crystal (Fig. 6a). In slip between stacking layers in Laves phases, as discussed above, one layer of atoms moves neither with one block nor the other, but performs a synchronized movement differing from that of either block. This can be represented (Fig. 6b) by a standard Shockley dislocation that describes the net shear, plus a coupled partial dislocation dipole that accounts for the synchroshear of the intermediate atom layer. More complex structures and/or more complex planes may require differing shears in several interpenetrating atomic layers, a "zonal glide" involving "zonal dislocations" (Fig. 6c). Even description of slip on pyramidal planes in hcp Zn requires complex zonal dislocations [65].



Fig. 4. Faults in C15 $TiCr_2$ displaced about 20 nm by shear band produced by room-temperature compression. From [25].

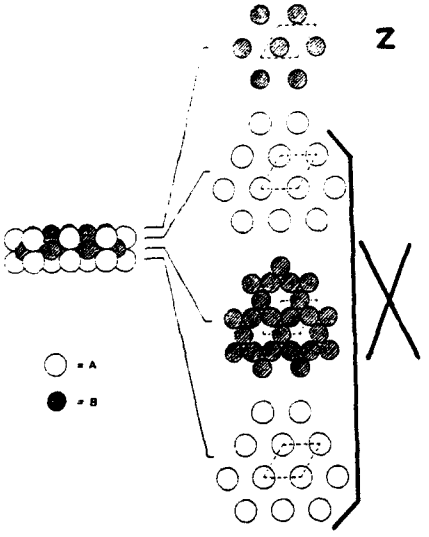


Fig. 5. Basic four-layer stacking unit of Laves phases, with three-layer sandwich X and synchroshear layer z.

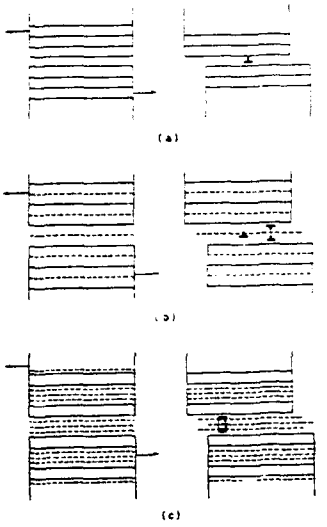


Fig. 6. (a) Simple slip. (b) Synchroshear: One atom layer shears in direction different from dominant shear. (c) Zonal glide. From [64].

Recently, an alternative dislocation description of synchroshear in Laves phases has been introduced [63]. Synchroshear is instead represented by the motion of two coupled Shockley partials, the vector sum of their two Burgers vectors equaling the net shear. The coupled pair of Schockley partials was called a "synchroshockley," a term that could also be applied to the Shockley partial plus dipole in the equivalent but older model of Amelinckx. The advantage of the original description is that, for most purposes, the dipole can be ignored and the separate Shockley partial is analogous to the familiar Shockley partial in fcc or hcp.

Employing the Amelinckx description and ignoring the dipole, twinning of C15 can be described by a sequence of gliding 1/6 <211> partials in precisely the same way that twinning in fcc is described. Shear transformation between C15 and C14 can be described by a sequence of gliding 1/6 <211> partials in the same way that shear transformation between fcc and hcp is described. Phase transformations between other Laves variants can also be described with the standard Shockley partials [66]. Slip on {111} planes in C15 and the (0001) plane in C14 or C36 can be described by the glide of two partials, separated by a stacking fault, in the same way that slip on the same planes in fcc and hcp is described.

Although slip, twinning, and transformations in Laves phases can thus be described without specifically considering the intermediate atomic layer that synchroshears, it is presumably the cooperative atomic motions of synchroshear that actually determine the mobility of the synchroshockleys. The "zig" (z→y) of the intermediate layer while the moving block "zags" (Y→Z) results in A atoms exchanging places with B atoms along the shearing interface. It seems likely that the motion of the larger A atoms is the limiting feature of synchroshear, suggesting that alloying substitutions on A sites of atoms smaller than A (e.g., Nb on Hf sites in HfV_2) and/or B-rich compositions with antisite substitutions or A-site vacancies would enhance the mobility of synchroshockleys.

Splitting of individual dislocations in $MgCu_2$ into two partials with a spacing of about 10 nm was seen in weak-beam TEM images, and much larger separations were observed in extended nodes in dislocation networks [8]. High-resolution TEM of dislocation splitting on the basal plane of $MgNi_2$ (Fig. 7) shows a spacing of 34 nm, consistent with the low stacking fault energy expected for the C36 structure [24]. High-resolution TEM has also been used to characterize stacking faults on basal and non-basal planes in $MgNi_2$ [24]. Both extrinsic and intrinsic basal faults were observed before deformation. Although these faults were sessile, subsequent generation and motion of a series of standard glissile Shockley particles could transform them into the complex multi-layer faults observed in $MgNi_2$ after deformation at high temperatures [12].

SUMMARY AND CONCLUSIONS

Considering the prevalence of Laves phases among intermetallics with high melting temperatures, including many chromides, aluminides, and silicides, it seems likely that alloys strengthened with Laves phases will ultimately find use as high-temperature structural materials. However, despite extensive literature on the crystallographic, electronic, and magnetic properties of Laves phases, their mechanical properties have unfortunately received relatively little attention.

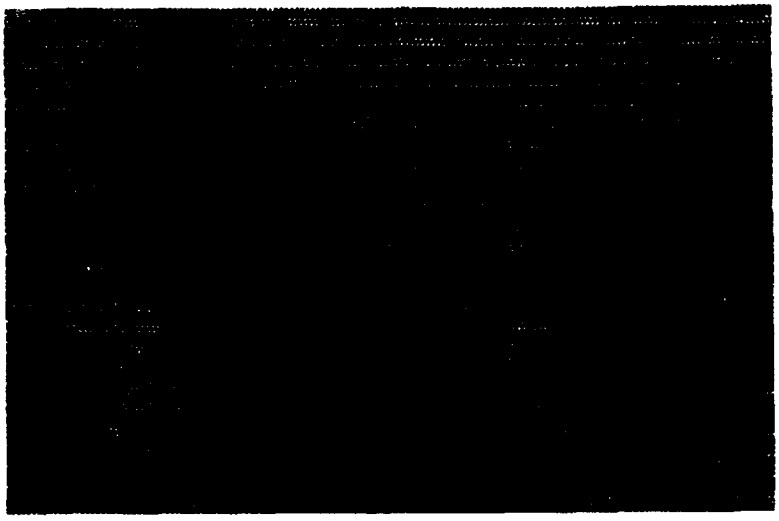


Fig. 7. High-resolution TEM of dislocation on basal plane of $MgNi_2$ split into two partials separated by a stacking fault. From [24].

As with most intermetallics and ceramics, limited fracture toughness at low temperatures is a major concern. Studies on model alloy systems have shown that some Laves phases are capable of room-temperature plastic deformation by mechanical twinning, by stress-assisted phase transformation, and by basal and non-basal slip. The crystallography of slip, twinning, and phase transformations in Laves phases can be understood by direct analogy to the same processes in fcc and hcp structures. However, the mobility of dislocations in Laves phases is controlled by the ease or difficulty of the detailed atomic motions required for synchroshear, which are more complex than those required for shear in the simpler structures. There is great need for fundamental study of the effects of factors such as stoichiometry, alloying, atom sizes, electronic structure, and stacking fault energy on dislocation mobility in Laves phases, at both low and high temperatures.

With regard to creep resistance, more data are needed on diffusion in Laves phases. A recent study on interdiffusion in $NbCo_2$ [67] reported a rapid increase in diffusion coefficients with departures from stoichiometry. More diffusion data are needed, as are accurate data on lattice parameters vs. composition, which can provide information on the nature of off-stoichiometry defects [36].

The limited alloy development studies to data have focused on binary chromides like $NbCr_2$ and ternary aluminides like $Nb(Ni,Al)_2$. In addition to further studies on these and related systems, studies of ternary silicides like $Mo(Co,Si)_2$ should be considered.

Various engineering developments have illuminated the need for structural materials with higher temperature capabilities than present-day superalloys. Among the materials that eventually fill this need will, most probably, be alloys strengthened by the "elegant geometry" of Laves phases. However, this may remain far in the future unless the pace of basic and applied research on these promising but still "exotic" materials is increased.

ACKNOWLEDGEMENTS

Many thanks are due Dr. Joseph Darby and the Division of Materials Science, Office of Basic Energy Sciences, United States Department of Energy, for their steadfast support of basic research on the mechanical properties of Laves phases, most recently under Grant # DE-FG02-90ER45426. Helpful discussions with Prof. S.M. Allen, Dr. Y. Liu, and K. Chen are gratefully acknowledged. Thanks also to C.T. Liu, K.S. Kumar, B.P. Bewlay, and G. Sauthoff for forwarding research reports prior to publication, and to Y. Liu for permission to use figures from his doctoral thesis.

REFERENCES

1. P. Villars and L.D. Calvert, Pearson's Handbook of Crystallographic Data for Intermetallic Phases, 2nd Ed., ASM International, Materials Park, Ohio (1991).
2. W.B. Pearson, The Crystal Chemistry and Physics of Metals and Alloys, Wiley-Interscience, New York (1972).
3. D.I. Bardos, K.P. Gupta, and P.A. Beck, Trans. Met. Soc. AIME 221, 1087 (1961).
4. R.C. Mittal, S.K.Si, and K.P. Gupta, J. Less-Common Metals 60, 75 (1978).
5. K.S. Kumar, Internat. Mater. Rev. 35 (6), 293 (1990).
6. J.D. Livingston, Phys. Stat. Sol. (a) 131, 415 (1992).
7. J.B. Moran, Trans. Met. Soc. AIME 233, 1473 (1965).
8. J.D. Livingston, E.L. Hall, and E.F. Koch, MRS Symp. Proc. 133, 243 (1989).
9. J.D. Livingston and E.L. Hall, J. Mater. Res. 5 (1), 5 (1990).
10. H. Kubsch, P. Paufler, and G.E.R. Schulze, Phys. Stat. Sol.(b) 56, 231 (1973); Phys. Stat. Sol. (a) 25, 269 (1974).
11. P. Paufler and G.E.R. Schulze, Naturwissenschaften 54, 69 (1967); Kristall and Technik 2, 231 (1967).
12. J.D. Livingston and E.L. Hall, MRS Symp. Proc. 213, 443 (1991).
13. K. Inoue, and K. Tachikawa, IEEE Trans. Magn. MAG-13, 840 (1977).
14. K. Inoue, T. Kuroda, and K. Tachikawa, IEEE Trans. Magn. MAG-15, 635 (1979).
15. F. Chu and D.P. Pope, Mat. Sci. Eng. A170, 39 (1993).
16. D.P. Pope and F. Chu, in Structural Intermetallics, R. Darolia, J.J. Lewandowski, C.T. Liu, P.L. Martin, D.P. Miracle, and M.V. Nathal, eds., TMS, Warendale, Pa. (1993) p. 637.
17. A.S. Balankin and D.M. Skorov, Sov. Phys. Solid State 24 (4), 681 (1982).
18. A.S. Balankin, Yu. F. Bychkov, and Ye. I. Yakovlev, Phys. Met. Metall. 56 (1), 119 (1983).
19. H.C. Jain, L. Freise, and M. Forker, J. Phys.: Condens, Matter 1, 2157 (1989).
20. F. Chu and D.P. Pope, Scripta Met. et Mater. 28, 331 (1993).
21. R.L. Fleischer, Scripta Met. et Mater. 27, 799 (1992).
22. D.L. Anton and D.M. Shah, Proc. Internat. Symp. on Intermetallic Compounds, JIMIS-6, O. Izumi, ed., Japan. Inst. of Metals, Sendai (1991) p. 379.
23. Y. Liu, J.D. Livingston, and S.M. Allen, Met. Trans. 23A, 3303 (1992).
24. Y. Liu, Ph.D. Thesis, Dept. Mat. Sci. and Eng., MIT (1993).

25. K.C. Chen, S.M. Allen, and J.D. Livingston, MRS Symp. Proc. 288, 373 (1992).
26. D.L. Anton and D.M. Shah, MRS Symp. Proc. 213, 733 (1991).
27. D.L. Anton and D.M. Shah, Mater. Sci. Eng. A153, 410 (1992).
28. M. Takeyama and C.T. Liu, Mater. Sci. Eng. A132, 61 (1991).
29. C.T. Liu, J.A. Horton, and C.A. Carmichael, Proc. 7th Ann. Conf. on Fossil Energy Materials, ORNL/FMP-93/1, Oak Ridge, Tenn. (1993) p. 297.
30. P.F. Torterelli, L.J. Carson, and J.H. DeVan, ibid, p. 309.
31. T. Takasugi, S. Hanada, and K. Miyamoto, J. Mater. Res. 8 (12) (1993).
32. G.E. Vignoul, J.M. Sanchez, and J.K. Tien, MRS Symp. Proc. 213, 739 (1991).
33. M. Grujicic, S. Tangrila, O.B. Cavin, W.D. Porter, and C.R. Hubbard, Mater. Sci. Eng. A160, 37 (1993).
34. D.J. Thoma and J.H. Perepezko, MRS Symp. Proc. 194, 105 (1990).
35. V.M. Pan, Phys. Met. Metallog. 12, 139 (1961).
36. D.J. Thoma and J.H. Perepezko, Mater. Sci. Eng. A156, 97 (1992).
37. S. Mazdiyasni and D.B. Miracle, MRS Symp. Proc. 194, 155 (1990).
38. B.P. Bewlay, J.A. Sutliff, M.R. Jackson, and H.A. Lipsitt, submitted to Acta Met. et Mater.
39. K.S. Kumar and D.B. Miracle, submitted to Intermetallics.
40. W. Arbiter, WADC Technical Report 53-190 (1953).
41. R.L. Fleischer and R.J. Zabala, Met. Trans. 21A, 2149 (1990).
42. X.M. Burany and D.O. Northwood, J. Less-Common Metals 170, 27 (1991).
43. G. Sauthoff, Z. Metallk. 80, 337 (1989); Z. Metallk. 81, 855 (1990).
44. G. Sauthoff, in Structural Intermetallics, R. Darolia et al, eds., TMS, Warrendale, Pa. (1993) p. 845.
45. W. Wunderlich, L. Machon, and G. Sauthoff, Z. Metallk. 83, 679 (1992).
46. H.J. Grabke, M. Brumm, and M. Steinhorst, Mater. Sci. and Technol. 8, 339 (1992).
47. L. Machon, Doctoral Thesis, Technische Hochschule Aachen (1992).
48. A. Halstead and R.D. Rawlings, J. Mater. Sci. 20, 11248, 1693 (1985).
49. S.E. Mason and R.D. Rawlings, Mater. Sci. and Technol. 5, 180 (1989).
50. H. Sprenger, H. Richter, and J.J. Nickl, Z. Metallk. 68, 241 (1977).
51. J.D. Livingston, J. Mater. Sci (Letters) 14, 1260 (1979).
52. W.B. Pearson, Acta Cryst. B37, 1174 (1981).
53. W.B. Pearson, Phil. Mag. A46, 379 (1982).
54. E. Hellner and W.B. Pearson, Z. Kristall. 163, 197 (1983).
55. R.L. Johnston and R. Hoffman, Z. anorg. allg. Chem. 616, 105 (1992).
56. Y. Ohta and D.G. Pettifor, J. Phys.: Condens. Matter 2, 8189 (1990).
57. S. Asano and S. Ishida, J. Phys.: Condensed Matter 1, 8501 (1989).
58. A.K. Sinha, Prog. Mater. Sci. 15, 79 (1970).
59. M.L. Kronberg, Acta Met. 5, 507 (1957); 9, 970 (1961); J. Nucl. Mater. 1, 85 (1959).
60. U. Kramer and G.E.. Schulze, Kristall und Technik 3, 417 (1968).
61. C.W. Allen, P. Delavignette, and S. Amelinckx, Phys. Stat. Sol. (a) 9, 237 (1972).
62. P.M. Hazzledine, K.S. Kumar, D.B. Miracle, and A.G. Jackson, MRS Symp. Proc. 288, 591 (1993).
63. P.M. Hazzledine and P. Pirouz, Scripta Met et Mater. 28, 1277 (1993).
64. S. Amelinckx, in Dislocations in Solids, Vol. 2, F.R.N. Nabarro, ed., North-Holland, Amsterdam (1979) p. 67.
65. H.S. Rosenbaum, in Deformation Twinning, R.F. Reed-Hill et al, eds., Gordon and Breach, New York (1964) p. 43.
66. C.W. Allen and K.C. Liao, Phys. Stat. Sol. (a) 74, 673 (1982).
67. H. Sprenger, M. Denkinger, and H. Mehrer, Proc. DIMAT, Kyoto (1992).

INFLUENCE OF TUNGSTEN ALLOYING ADDITIONS ON THE MECHANICAL PROPERTIES AND TEXTURE OF TANTALUM

G.T. GRAY III, S.R. BINGERT, S.I. WRIGHT, AND S.R. CHEN
Los Alamos National Laboratory, Los Alamos, New Mexico 87545

ABSTRACT

Tantalum, like all bcc metals, exhibits deformation behavior which is substantially influenced by alloying, temperature, and strain rate. Recently, the mechanical response, in particular the high-strain-rate response, of tantalum and tantalum alloys has received increased interest for ballistic applications. In this paper, recent results on the influence of tungsten alloying additions on the mechanical response and starting crystallographic texture of tantalum-tungsten alloys are presented. The stress-strain behavior of three tantalum alloys containing 2.5, 5, and 10 wt.% W has been investigated as a function of loading path, tension and compression, and strain rate, 10^{-3} to 8000 s^{-1}. The yield strength and work-hardening rate were found to increase with increasing tungsten alloying content compared to unalloyed-Ta. Based on measurements of the surface and centerline textures of the Ta-W alloys, no systematic effect of tungsten content on texture was documented. However, due to variations in mechanical behavior between through-thickness and in-plane properties the need for complete through-thickness texture measurements is indicated.

INTRODUCTION

The microstructure / property relationships of tantalum and tantalum-based alloys continue to attract scientific and engineering interest due to their high density, melting point, excellent formability, good heat conductivity, good fracture toughness (even at low temperatures), corrosion resistance, and their weldability[1]. Since 1950 numerous studies have probed the microstructure-chemistry/property response of a large number of tantalum and tantalum-based alloys, both in single-crystal and polycrystalline form[1-5]. Tantalum, like all bcc metals exhibits deformation behavior which is markedly influenced by impurities, alloying additions, crystallographic texture, temperature, and strain rate[2-5]. Recent efforts have been focused on the optimization of tailored and reproducible microstructure / property relationships for a given application of tantalum. This emphasis has led to changes in the chemistry and processing controls used to produce current tantalum mill products, including control of crystallographic texture to affect in-plane homogeneity. Concentrated studies of the influence of texture on the deformation response of tantalum alloys have been fostered by recent code simulations and experiments revealing an influence of anisotropy on material response in ballistic applications[6]. The purpose of this paper is to report recent findings on the influence of tungsten alloying additions on the mechanical properties, as a function of loading direction and strain rate, and starting texture of tantalum alloys representing current plate materials.

EXPERIMENTAL PROCEDURE

The materials used in this investigation were commercially-pure (triple electron-beam) annealed unalloyed-Ta, Ta-2.5W, Ta-5W, and Ta-10W supplied by Cabot Corporation with compositions as listed in Table I. The unalloyed-Ta, Ta-2.5W, and Ta-10W materials were prepared by melting 25.4 cm-dia. or greater ingots. The Ta-5W in contrast was cast in a smaller research scale electron beam melter, triple melted similar to the other ingots. All the ingots were forged into billets, the billets were annealed, and then cut prior to cross rolling. The plates were straight rolled in the final finishing passes. Each material was supplied in 6.35-mm-thick plate form; in addition the unalloyed-Ta was also studied in 10.2-mm-thick plate form. The as-tested microstructures of the 6.35-mm-thick unalloyed-Ta, Ta-2.5W, Ta-5W, and Ta-10W plates were

Mat. Res. Soc. Symp. Proc. Vol. 322. ©1994 Materials Research Society

all equiaxed grains with average grain sizes of 42 μm, 45 μm, 48 μm, and 42 μm, respectively. The 10.2-mm-thick unalloyed-Ta plate had an equiaxed 43 μm grain size.

Table I - Alloy Compositions (in ppm wt. %)

Metal (thickness)	C	O	N	H	W	Nb	Si	Ta
Ta (10.2 mm)	10	<50	<10	<5	<25	<25	<5	bal.
Ta (6.35 mm)	12	<50	<10	<5	60	250	5	bal.
Ta-2.5W (6.35 mm)	18	98	<10	<5	2.4%	330	<5	bal.
Ta-5W (6.35 mm)	15	<50	<10	<5	5.2%	65	<5	bal.
Ta-10W (6.35 mm)	11	63	<10	<5	9.6%	385	5	bal.

The mechanical responses of the tantalum materials were measured in compression using solid-cylindrical samples 6.35-mm in diameter by 6.35-mm long, lubricated with molybdenum grease. Compression samples were machined from the plates in both the through-thickness and in-plane longitudinal orientations. Sheet tensile samples were machined with square gage sections 5.56 mm by 5.56 mm by 25.4-mm gauge length from the alloys in the plane of the plates. The starting cross sectional area is comparable to that of specimens machined to ASTM E8-82[6.2-mm rounds]. Quasi-static compression and tension tests were conducted at a strain rate of 0.001 s^{-1}. Dynamic tests, strain rates of 1000-8000 s^{-1}, were conducted utilizing a Split-Hopkinson Pressure Bar. The inherent oscillations in the dynamic stress-strain curves and the lack of stress equilibrium in the specimens at low strains make the determination of yield inaccurate at high strain rates. The texture of the tantalum and tantalum alloys was characterized using X-ray diffraction. (110), (200) and (211) X-ray pole figures were measured at the surface and centerline of samples from each plate. The corresponding orientation distributions were determined from the experimental pole figures using the WIMV[7] algorithm as implemented in *popLA*[8], a texture analysis software package. Orthorhombic sample symmetry was enforced during the calculations. The orientation distribution was then used to generate (111) and (100) pole figures.

RESULTS AND DISCUSSION

The quasi-static compressive and tensile stress-strain responses of the 6.35-mm-thick plate tantalum materials as a function of Ta-alloying content are shown in Figure 1. The dynamic compressive stress-strain response is shown in Figure 2. The yield and flow stress levels in the tantalum and tantalum alloys beyond yield are seen to increase with increasing tungsten alloying additions. The quasi-static stress-strain response of the 6.35-mm thick Ta-2.5W, omitted from Figure 1 for visual clarity, was measured to lie roughly midway between the unalloyed-Ta and the Ta-5W response. Similar to the unalloyed-Ta and Ta-5W, both the longitudinal compressive and tensile response of the Ta-2.5W were measured to lie below the compressive through-thickness stress-strain behavior; the tensile curve exhibiting the lowest flow stress. Increasing the alloying content to 10 wt.% in the Ta-10W alloy results in a factor of 2 increase in the yield and flow stress levels attained compared to the unalloyed Ta. This observation is consistent with well established solute strengthening effects of tungsten alloying additions on Ta[2,3]. This strengthening effect is further observed to prevail under both quasi-static[Figure 1] and dynamic loading[Figure 2] conditions. Comparison of the flow strength levels between quasi-static and dynamic loading for all the tantalum materials reflects the pronounced temperature and rate sensitivity of Ta[3]. At 2% strain the flow stress increases from ~200 to 575 MPa for unalloyed-Ta and from ~520 to 820 MPa for Ta-10W with a increase in strain rate. In addition to the increase in yield response linked to tungsten content, the compressive stress-strain response is seen to exhibit a higher flow stress response than displayed under tensile deformation. This observation is also consistent for the unalloyed Ta, Ta-5W, and Ta-10W.

In addition to yield, flow strength, and strain-rate variations tungsten alloying is also seen to have a pronounced influence on work-hardening behavior in Ta alloys. Under quasi-static loading, the

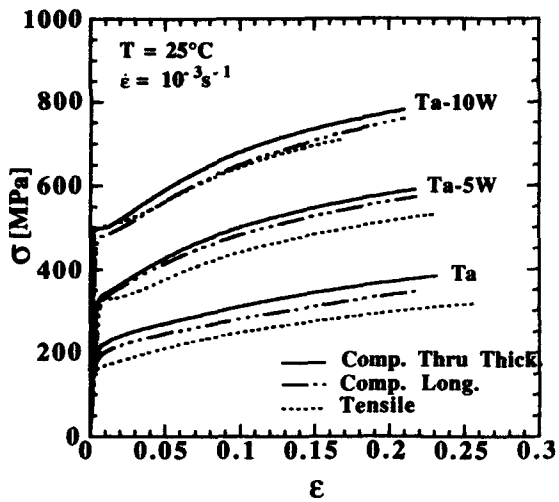


Figure 1: Compressive and tensile stress-strain response of Ta, Ta-2.5W, Ta-5W, and Ta-10W at a strain rate of 0.001 s^{-1} at 298K.

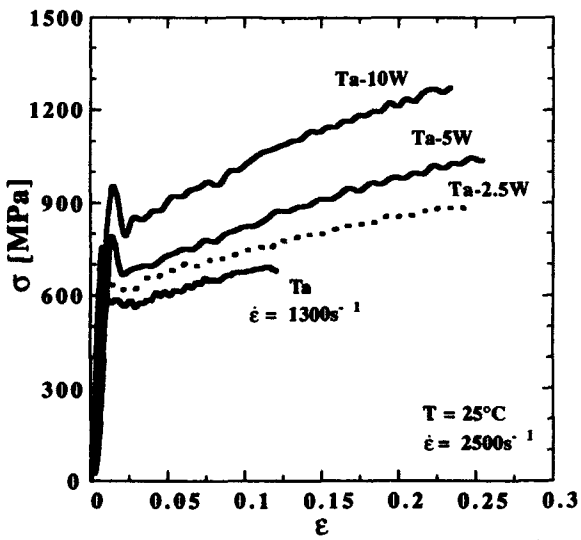


Figure 2: Compressive stress-strain response of Ta, Ta-2.5W, Ta-5W, and Ta-10W at a strain rate of ~2000 s^{-1} at 298K.

stress-strain curves measured in both compression and tension are seen to be parallel after ~2% plastic strain. The average strain-hardening rate is, however, seen to increase slightly in the quasi-static tests following the elastic-plastic transition as a function of increasing tungsten content; from nominally 830 MPa/ unit strain for unalloyed-Ta to 1330 MPa/ unit strain for Ta-10W calculated over the strain range of 0.05 to 0.2. This effect is more clearly evident under dynamic loading[Figure 2] where the average rate of strain hardening is seen to increase from nominally 1440 MPa/ unit strain for unalloyed-Ta to 2300 MPa/ unit strain for Ta-10W, calculated over the strain increment of 0.025 to 0.15. Comparison of these nominal hardening rates as a function of loading rate also reveals how increasing the strain rate to dynamic levels results in hardening rates in unalloyed-Ta equivalent to those exhibited during the quasi-static response of Ta-10W. Increasing levels of work-hardening with increasing strain rate or tungsten-alloying additions is consistent with the suppression of dynamic recovery processes, including reduced cross-slip during deformation[9, 10].

The textures of the tantalum materials were found to vary with tungsten alloy content and with plate thickness in the case of the pure tantalum plates as shown in Figure 3. The thicker pure tantalum plate exhibits very little texture gradient between the plate surface and centerline; whereas, the pure and alloyed tantalum 6.35-mm-thick plate samples exhibit pronounced through-thickness texture gradients. Texture gradients have been frequently observed in tantalum plate materials[6]. The results of the current study on 6.35-mm-thick plate suggests that there is no systematic effect of tungsten alloying on the texture of the tantalum plate, except that the alloying seems to reduce the propensity for (111) planes to lie normal to the through-thickness direction. However, no investigation of the distribution of the "surface" and "centerline" textures through the thickness of the plate has been made to see if the measured textures truly represent the real textures of significant volumes of material. The mechanical tests also suggest that the measured textures are not representative of the bulk of material in the plates studied.

For example, in the case of the Ta-10W, the longitudinal compression stress-strain curve falls below the through-thickness curve (see Figure 1). This behavior is consistent with a (111) fiber texture, however, it is not consistent with either the measured centerline texture or the measured surface texture. The effect of texture on the stress-strain response was modeled using a Taylor polycrystal plasticity model[11] where strain is assumed to be uniform throughout the polycrystal. Using this approach, the predicted through-thickness stress-strain curve fell below the predicted longitudinal curve, just opposite of the observed trend. Thus, it is likely that the texture of the bulk of the material is more (111) fiber-like than was captured from the measured planes. Prior work has shown that the spatial distribution of texture in tantalum is not always uniform and can have significant effects on the mechanical properties[12]. Thus, the texture of tantalum and Ta-W alloy plates should not be measured in the conventional manner where planes normal to the through-thickness are measured, but rather, textures should be measured from planes normal to either the longitudinal or the transverse directions.

Even though the mechanical tests do not appear to be at first completely consistent with the measured textures, the observation that the longitudinal compressive stress-strain responses of the unalloyed-Ta, Ta-2.5W and Ta-5W exhibited higher flow stress responses than those observed under tensile deformation is likely a direct result of texture effects. The tensile samples were prepared by machining away significant amounts of material from the surfaces of the plates. Since the 6.35-mm thick unalloyed-Ta, Ta-2.5W, and Ta-5W exhibited substantial texture gradients, this removal of material had a significant effect on the tensile stress-strain response. The Ta-10W did not display such a strong texture gradient and, thus, the tensile and longitudinal compressive stress-strain responses were quite similar.

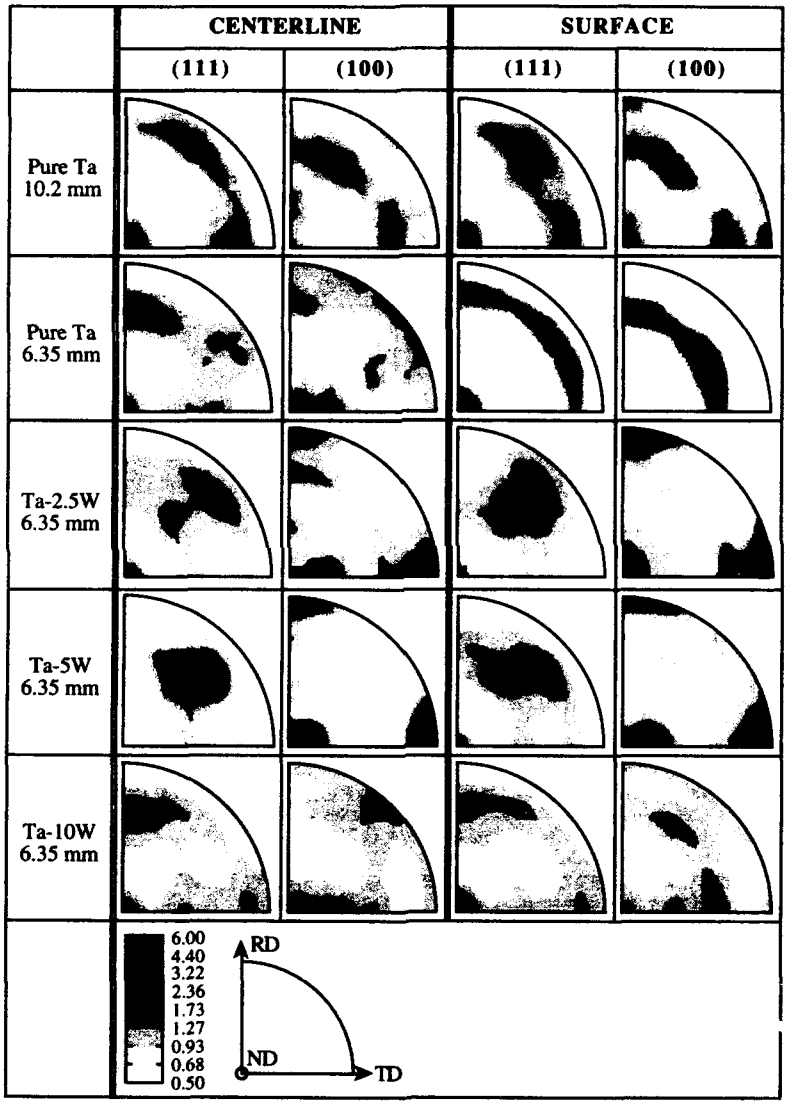


Figure 3: (111) and (100) pole figures of Tantalum alloys measured at the surface and centerline of the plates.

CONCLUSIONS

The current study of the influence of tungsten alloying additions on the mechanical properties and texture of tantalum plate indicates:

a) Tungsten alloy additions significantly increase the yield and flow stress levels attained and increase the rate of work-hardening compared to unalloyed tantalum, under both quasi-static and dynamic strain rates.

b) The results of the current study on 6.35-mm-thick plate suggests that there is no systematic effect of tungsten alloying on the texture of the tantalum plate, except to reduce the propensity for (111) fiber-type textures to form. However, the existence of strong texture gradients through the thickness of the plates and inconsistencies between the measured textures and the observed mechanical anisotropy suggest that the measured textures presented here are not completely representative of significant volumes of material. Textures should be measured from planes containing the through-thickness direction not planes normal to the through thickness direction.

ACKNOWLEDGEMENTS

This work was supported under the auspices of the United States Department of Energy. The authors acknowledge the assistance of R. Aiken, M.F. Lopez, W. Wright, and R.W. Carpenter II for conducting the mechanical tests and C. Necker for assisting with the texture studies. The authors acknowledge Cabot Corporation for providing some of the tantalum materials studied.

REFERENCES

1. W. Kock and P. Paschen, JOM **41**, 33 (1989).
2. R.J. Arsenault and A. Lawley, in Work Hardening, edited by. J.P. Hirth and J. Weertman (Gordon and Breach, New York, 1968), p. 283.
3. G.T. Gray III and A.D. Rollett, in High Strain Rate Behavior of Refractory Metals and Alloys, edited by. R. Asfhani, E. Chen and A. Crowson (TMS Society, PA, 1992) 303.
4. J.B. Clark, R.K. Garrett, Jr., T.L. Jungling, and R.I. Asfahani, Metall. Trans. A **23A**, 2183 (1992).
5. J.B. Clark, R.K. Garrett, Jr., T.L. Jungling, and R.I. Asfahani, Metall. Trans. A **22A**, 2959 (1991).
6. P.C. Chou and M.E. Grudza, in High Strain Rate Behavior of Refractory Metals and Alloys, edited by. R. Asfhani, E. Chen and A. Crowson (TMS Society, PA, 1992) 97.
7. S. Matthies and G. W. Vinel, Phys. Stat. Sol. (b) **112**, K111 (1982).
8. J.S. Kallend, U. F. Kocks, A. D. Rollett and H.-R. Wenk, Mat. Sci. Eng. **A132**, 1(1991).
9. G.T. Gray III, in Modeling the Deformation of Crystalline Solids, edited by T.C. Lowe, A.D. Rollett, P.S. Follansbee, and G.S. Daehn (TMS Society, PA, 1991) 145.
10. U.F. Kocks, in Proc. Conf. on Dislocations and Properties of Real Materials, (The Institute of Metals, London, Book 323, 1985) 125.
11. G.I. Taylor, J. Inst. Metals **62**, 307 (1934)
12. S.I. Wright, G. T. Gray III and A. D. Rollett, Metall. Trans. A, 1993, (submitted June 1993).

EFFECT OF INTERMETALLIC COMPOUNDS ON THE PROPERTIES OF TANTALUM

P. KUMAR, C.E. MOSHEIM AND C.A. MICHALUK
CPM Division, Cabot Corporation, County Line Road, Boyertown, PA 19512

SUMMARY:

While pure tantalum has excellent corrosion resistance and formability, its high temperature properties and thermal stability are marginal for some intended applications. Traditional approaches for improving these properties have been dispersion and solid solution strengthening. Modifications of properties via an intermetallic precipitation was not considered until recently.

Results of an on-going investigation on the processing and evaluation of silicide-strengthened tantalum are presented. Yttrium silicide-containing Tantalum samples were produced via the P/M method. Evaluation consisted of microstructural, mechanical, chemical and functional tests. Results were compared with those of commercially available tantalum. Intermetallics precipitates were found to be very potent in altering these properties.

While the preliminary results are encouraging, extensive functional testing is required to assure that there is no unexpected adverse effect.

BACKGROUND

Tantalum alloys have been recognized as preferred materials in the field of furnace equipment, such as trays and heating elements, and radiation shielding where the thermal stability of the alloy is maintained and the life span of the product is enhanced by reduced embrittlement (1,2). Tantalum alloys have also been employed in the manufacture of wire and more particularly as electric component leads where product characteristics such as ductility and high dielectric constant, as well as resistance to grain growth at elevated temperatures are required. The need for high temperature stability arises during assembly of the capacitors; the lead wires may either be pressed into the tantalum powder anode and subsequently sintered at high temperatures, or spot welded to sintered capacitor bodies.

In both electrical component and furnaces equipment products, contamination by oxygen contributes to embrittlement and piece failure. For example, in wire products, the area where a lead wire leaves an anode body is highly susceptible to embrittlement due to migration of oxygen from the sintered body to the wire. Lead wires which become embrittled will break, resulting in the loss of the entire piece.

Oxygen embrittlement occurs in tantalum base alloy products by several mechanisms. Tantalum acts as a getter for oxygen in addition to other gaseous impurities (such as carbon monoxide, carbon dioxide, and water vapor) which are present in sintering operations or during high temperature service. Attempts have been made to reduce tantalum oxide

Mat. Res. Soc. Symp. Proc. Vol. 322. ©1994 Materials Research Society

formation by doping tantalum with carbon or a carbonaceous material. Oxygen reacts with the carbon at the surface of the metal rather than diffusing into the tantalum, thereby minimizing embrittlement. While enhanced ductility levels may be achieved with carbon addition, the dopant may adversely effect the processability and electrical characteristics of the metal. Micro-alloying with silicon has been used to improve the oxygen-embrittlement-resistance of tantalum (3). However, silicon is volatilized in part during processing and therefore must be added in excess in the original master blend. While it is speculative that silicon functions as a getter similar to carbon, the addition of excess silicon may effect the electrical characteristics of the wire product.

Another mechanism for reducing the embrittlement of tantalum base alloy products involves the doping of tantalum powder with yttrium. Since yttria is more stable than tantalum oxide, yttrium oxidizes to yttria during processing. During the subsequent high temperature exposure, oxide particles pin the grain-boundaries and prevent grain-growth (4); improvement in embrittlement-resistance is primarily due to retaining a fine grain-size. Obviously, oxide particles become ineffective after extended high temperature exposure due to increase in their size and subsequent grain coarsening (5,6,7,8). Although the mechanism is not completely understood, one theory accounting for dopant particle growth or "dispersant coarsening" is that the coarsening occurs due to the high diffusion rate of oxygen and metal atoms of oxides in refractory metals which is driven by the interfacial energy of the dispersoids. Enlarged dispersant particles have lower surface energy and therefore cannot function to restrain grain boundary migration. Grain growth in turn, results in a loss of ductility.

A combination of yttria and silicon dopants in Ta has also shown promise. It is maintained that the mechanisms where silicon functions as an oxygen getter and where metal oxide functions as a grain boundary restraint explains the reported fine grain size and ductility in Ta-Si-Y alloys. These mechanisms, however, suffer from previously discussed problems of product quality due to silicon evaporation and grain growth after exposure to high temperatures.

Table 1 summarizes alloying elements normally used with Ta. In principle, both interstitial and substitutional alloying elements can be used. However, due to the relative ease of controlling the composition and processing, substitutional alloying is often preferred.

OBJECTIVE:

The objective of this on-going investigation is to provide a doped tantalum alloy which maintains a high level of processability and ductility and wherein the dopants resist coarsening after exposure to high temperatures (9). Intermetallic compounds, such as silicides, are expected to provide these desired results. Since these compounds are not inert to the tantalum matrix, they are not prone to coarsening after exposure to high temperature. At the same time, they exhibit adequate stability to pin the grain boundaries.

TABLE 1
ELEMENTS USED FOR MICROALLOYING TANTALUM

A. Alloying Element	Atomic Radius[1]	Substitutional/Interstitial[2]
O	0.6	I
N	0.71	I
C	0.77	I
Si	1.17	S
Mo	1.40	S
W	1.41	S
Nb	1.47	S
Y	1.81	S
[1]Atomic Radius of Ta=	1.47A	
[2]Solute/solvent <0.59 for	Interstitial	

B.
Effects of Alloying

- Strength
- Ductility
- Grain Size
- Grain Growth Kinetics

RESULTS AND DISCUSSION:

In-situ Silicide Formation:

Powder metallurgical processing was used for producing wrought tantalum samples having in-situ silicide precipitates. The first experiment was to establish that in-situ silicides could indeed be formed. A blend of Ta + 10wt%YN + 40% Si powder was heated at 1300°C for 2 hours and evaluated via x-ray diffraction. Another blend of Ta + 10wt%Y_2O_3 + 40% Si was also processed and evaluated for comparison. As illustrated in Table 2, the blend containing the composition of yttrium nitride and silicon showed the presence of yttrium silicide dispersed in the base metal matrix, while the yttrium oxide and silicon blend did not. Although the latter did have yttrium silicate, the thermodynamic stability of yttrium oxide apparently prohibits its decomposition. It is believed that yttrium oxide preempts the formation of yttrium silicide; silicide cannot be formed, and an oxide (yttrium silicate) is formed instead.

It should be noted that while a blend of YN + Si was used for the in-situ formation of yttrium silicide in this investigation, several other methods of producing YSi_x may also be equally feasible (10,11).

TABLE 2

Identification of Yttrium Silicide and Yttrium Silicate by X-ray Diffraction (XRD)

Composition Heated at	Ta + 10% YN + 40% Si 1300°C				Ti + 10% Y_2O_3 + 4% Si 1300°C			
	XRD of Sample		Known Pattern for Y Si_2		XRD of Sample		Known Pattern for Y_2SiO_5	
	din A	I	din A	I	din A	I	din A	I
	4.1315	14	4.13	18	6.11	1	6.11	0.77
	3.496	100	3.5	88	5.89	1	5.89	1.5
	2.568	46	2.57	53	3.891	3	3.90	6.9
	2.386	15	2.389	16	3.66	1	3.66	0.46
	2.243	85	2.246	84	3.504	100	3.55	6.2
	2.186	16	2.187	26	3.324	2	3.36	0.46
	2.068	39	2.07	31	3.132	62	3.14	7.3
	1.931	63	1.932	57	3.022	6	3.03	7.3
	1.613	7	1.615	8.8	2.94	2	2.945	5.4
	1.564	6	1.565	5.3	2.907	5	2.906	7.7
	1.522	26	1.525	18	2.806	1	2.806	0.46
	1.503	25	1.505	22	2.648	2	2.671	0.77
	1.411	17	1.413	16	2.592	10	2.599	0.46
	1.379	4	1.38	3.5	2.571	57	2.55	4.6
	1.351	34	1.353	18	2.429	5	2.43	1.9
	1.272	18	1.273	16	2.246	84	2.249	0.77
	1.252	7	1.252	5.3	2.188	29	2.203	2.7
					2.032	1	2.032	0.46
					1.987	1	1.987	0.46
					1.852	1	1.852	0.62
					1.523	29	1.517	1.2

Micro-alloyed Ta Wire:

Table 3 gives physical and chemical properties of starting tantalum powder. This powder was mixed with dopants to obtain the following nominal compositions (by weight):

Blend I. D.	
1	400 ppm Si + 100 ppm YN
2	DR-Ta[A]
3	400 ppm Si + 100 ppm Y_2O_3
4	400 ppm Si

The blended powder was cold isostatically pressed at 60,000 PSI into bars weighing about 22 pounds each. The cross-section of the bar was about 41mm x 41mm. The bars were sintered by direct resistance sintering in a vacuum furnace at a temperature of between about 2200 - 2400°C. The bars were maintained at the temperature for about 4 hours. Sintered bars were rolled to a 20mm x 20mm cross-section and annealed at a temperature of 1300°C for 2 hours. The bars were then rolled to 9mm x 9mm, reannealed at 1300°C for an additional 2 hours; bars were subsequently drawn through various dies and annealed at a temperature of about 1300°C. The final wire diameter was 0.25mm.

TABLE 3
Properties of Starting Tantalum Powder

Chemical Analysis

Element	Concentration (ppm)
C	10 ppm
O_2	840
H_2	<5
N_2	<25
Others	Not Detected

Sieve Analysis

Size	Wt%
+60 Mesh	0
60/100 Mesh	0
100/200 Mesh	18.8%
200/325 Mesh	31.6%
-325 Mesh	49.5%

A. Cabot Performance Material produces DR-Ta for capacitor can and lead wire applications.

Table 4 gives the grain-size, mechanical and chemical properties of wires from blends 1, 2, 3 and 4. An increase in strength, without a sacrifice in ductility, is obtained in wire produced from a YN+Si doped blend.

Wires 1 to 4 were pressed into tantalum capacitor anodes, sintered under vacuum, and tested for bend-ductility in accordance with the test procedure described below:

The bend-ductility of the sintered wire was determined by securing a sintered anode preformed with one inch wire embedded therein. A 54 gm dead weight was attached to the lead extremity. The anode was then pivoted through a 180 degree arc causing the wire to bend at the juncture with the anode. One bend was defined as the complete pivoting of the anode through a 90 degree arc and returning to the starting position. The number of bends were counted. Ten anodes were tested and the reported bend ductility is an average these of ten trials.

TABLE 4

Properties of Wire 0.25 mm Diameter Tantalum Wires

Blend No.	1 (YN + Si)	2 (DR-Ta)	3 (Y_2O_3 + Si)	4 (Si)
Grain Size in Micrometers	2.8	6	2[1]	6
Mechanical Strength				
Tensile Strength (KSI)	87.1	73.4	90.2	74.1
Yield Strength (KSI)	67.7	54.2	79.9	53.2
Elongation (%)	24.8	23.8	20	24.6
Chemical Composition (in ppm)				
Si	225	--	250	250
Y	30	--	40	--
C	45	45	65	50
N_2	45	35	30	10
O_2	190	145	120	75
Others	None	None	None	None

[1] Not Fully Recrystallized (NFR)

Three sintering cycles were studied. In the first cycle, the furnace was evacuated and the temperature was raised to 1670°C for 30 minutes and then shut-off. The second cycle was the same as the first cycle except that the furnace was back-filled with argon after the evacuation, reevacuated, and then the temperature was raised to 1670°C and, after 30 minutes, the furnace was shut off. The third cycle was the same as the first except that wire/powder assemblies were reheated for 2 minutes at 1670°C.

Table 5 compares the bend-ductility of wire formed by the procedures set forth in blends 1 to 4. The wire containing Si & YN exhibited 57% improvement in comparison with tantalum wire doped with silicon and yttrium oxide after 30 minutes of sintering followed by an additional two minutes.

TABLE 5

Bend-Ductility of 0.25mm Diameter of Tantalum Wire

Example	1	2	3	4
Blend Compositions (in ppm)	100 YN + 400 Si	DR-Ta	100 Y_2O_3 + 400 Si	400 Si
Thermal Cycle 1670°C/30 min.	4.2	0.5	4	4
1670°C/30 min after purging with Argon and Re-evacuation	3.5	0.1	2.9	2.2
1670°C/30 min + 2 min	2.2	0.1	1.4	0.9

Micro-alloyed Ta Sheet:

Composition of blends 1, 2, 3 and 4 were also processed into 9mm x 9mm annealed bars which were rolled into 0.38mm thick sheets. The sheets were annealed at various temperatures.

Table 6 compares the grain-sizes of sheets produced by the examples listed. Sheets of compositions 1 (400Si + 100YN) and 3 (400Si + 100Y_2O_3) were evaluated via electron microscopy after annealing at 1500°C. Discs were cut to about 250 micrometers in thickness using a slow speed diamond saw. The discs were then ion milled to a thickness of 50-100 micrometers and then electropolished in a 90% H_2SO_4 + 10% HF solution until they developed microperforations. Diffraction patterns of lattices of samples of compositions of Example 1 (400Si + 100YN) and Example 3 (400Si + 100 Y_2O_3) were also taken. The

electron microscopy was performed in the vicinity of the perforations. Scanning electron micrographs in the vicinity of micro-perforations demonstrate that the size of precipitate in the sample of composition 1 (400Si + 100YN) is about 0.7 x 0.9 micrometers and the size of precipitate in the sample of composition 3 (400Si + 100Y_2O_3) was about 1.2 x 3 micrometers. The diffraction patterns of lattices indicate a significant difference between the effects of oxide and nitride additions as dopants. It appears that lattice strains associated with oxides is substantially more than with nitrides. One theory accounting for the strained lattice is that the higher thermodynamic stability of oxides could prevent the interaction between oxides and the matrix. The higher stability will also prevent the dissolution of oxide particles into matrix. With the prolonged exposure to elevated temperature (as encountered during processing and application procedures), oxide particles might grow via mechanisms akin to Ostwald ripening.

TABLE 6

GRAIN-SIZES OF 0.38mm THICK TANTALUM SHEETS IN MICROMETERS

Example	1	2	3	4
Blend Composition (in ppm)	100 YN + 400 Si	DR-Ta	100Y_2O_3 400 Si	400 Si
Annealed at 1500°C/2 hr/Vac	11	22	14[1]	16
Annealed at 1650°C/2 hr/Vac	14	26	17	25
Annealed at 1800°C/2 hr/Vac	22	135	27	57

[1] NFR = Not Fully Recrystallized

CONCLUSION

Our investigation has been limited to the alloying with silicon and yttrium compounds. Although both in-situ intermetallic (YSi_2) and oxide (Y_2O_3) dispersoids are effective strengtheners, the former offers the advantage maintaining high ductility in Ta wire. We believe that it is primarily due to the interaction between dispersoid and matrix; a finer grain size can be maintained in Ta by doping with intermetallic disperoids.

The formation of intermetallic YSi_2 in tantalum from doping with YN + Si, but not from Y_2O_3 + Si, can be rationalized from thermodynamic principles. Yttrium nitride has a

Gibbs free energy of -52.4 Kcal/gAtom which is significantly greater than that reported for yttria of -145 kcal/gAtom (12,13). It is likely that the ΔG_f for YSi_2 lies between these two values. Therefore, it is energetically favorable for YN to read with Si to form YSi_2. The low free energy of the Y_2O_3 prevents the formation of an intermetallic yttrium compound; only Ostwald ripening of the Y_2O_3 is expected during high temperature exposure. This accounts for the greater lattice strains found in Y_2O_3 doped Ta.

ACKNOWLEDGEMENTS:

Authors acknowledge the assistance of Messrs. R. C. Engleman, R. J. Neider, M. A. Ferreri and R. W. Steele in the production and testing of samples. Mrs. C. M. Yoder's help in preparing the manuscript is also appreciated.

Bibliography:

1. S.M.Cardonne, P.Kumar, C.A. Michaluk and H.D. Schwartz, "Tantalum and Its Alloys", Advanced Materials and Processes, Sept. 1992

2. "Tantalum, Columbium and Their Alloys", Published by Cabot Corp., 1986

3. P. Kumar, K.D.Moser and T.K.Chatterjee, "The Effect of Microalloying with Silicon on the Properties of Tantalum", J.of Metals, Vol. 41, No. 10, October 1989, pp. 50-53.

4. G. E. Dieter, Mechanical Metallurgy, McGraw-Hill Book Co., 1987, pp. 188-220.

5. D. L. Anton, D. B. Snow, L. H. Favrow and A. F. Giamei, "Dispersion Strengthening of High Temperature Niobium Alloys", Report No. R89-917437-3, pp.2. Issued by United Technology Research Center, East Hartford, CT 06108. July 31, 1989 Final Report. Contract No. F49620-86-C-0053 for Air Force office of Scientific Research, Building 410, Bolling Air Force Base, Washington DC 20332.

6. K. Kusunoki, K. Sumino, Y. Kawasaki and Y. Yamazaki, "Effect of Amount of Y and Oxide content on the Secondary Recrystallization Temperature of Nickel - Base Superalloys" Metallurgical Transactions A, Vol. 21A, March 1990, pp. 547.

7. D. M. Williams and G. C. Smith, "A Study of Oxide Particles and Oxide-Matrix Interfaces in Copper" in Proceedings of a Symposium on "Oxide Dispersion Strengthening, Editors: G. S. Ansell, T. D. Copper and F. V.

Lenel. Publ. by Gordon and Breach, 1968, pp. 509-36.

8. C.A.Michaluk, G.T.Gray and T.Chatterjee, "The Effect of Oxygen, Grain Size and Strain Rate on the Mechancial Behavior of Forged P/M Tantalum", P/M in Aerospace Defense, and Demanding Applications-1993, Metal Powder Industries Federation, 1993, p. 195-204.

9. P.Kumar and C.E.Mosheim, U. S. Patent No. 5,171,379, "Tantalum Base Alloys"

10. O. D. McMasters, K. A. Gschneidner, E. Kaldis, and G. Sampietro, "High-temperature enthalpies and standard Gibbs free energies of formation of the europium cholcogenides: EuO, EuS, EuSe and EuTe." J. Chem. Thermodynamics, Vol. 6, 1974, P. 845-57.

11. K. C. Miller, "Thermodynamic Data for Inorganic Sulphides, Selenides & Tellurides" Butterworth and Co., 88 Kingsway, London WC2B6AB, 1974 publication. ISBN 0-408-70537X

12. K. A. Gschneidner, N. Kippenhan and O. D. McMasters, "Thermochemistry of the Rare Earth" Rare-Earth Information Center Institute for Atomic Research, Iowa State University, Ames, Iowa 50010, August 1973.

13. F. R. deBoer, R. Boom, W. C. M. Mattens, A. R. Miedema and A. K. Niessen, "Cohesion in Metals", North-Holland publication, 1988, pp. 545.

TERNARY $MoSi_2$ COMPOUNDS FOR HIGH TEMPERATURE STRUCTURAL APPLICATIONS

S. CHIN, D. L. ANTON AND A. F. GIAMEI
United Technologies Research Center, 411 Silver Lane, East Hartford, CT 06108

ABSTRACT

The microstructure and phase composition of $MoSi_2$ modified with Al, B, Ge, Hf, Nb, and Re have been investigated. B and Hf substitutions for Si and Mo, respectively, exhibited very low solubilities in $MoSi_2$. Al and Nb substitutions for Si and Mo, respectively, changed the crystal structure from tetragonal $C11_b$ to hexagonal C40. Phase boundaries and solubility limits were determined for Al and Nb substitutions. Ge and Re substitutions for Si and Mo, respectively, exhibited complete solubility and maintained the tetragonal $C11_b$ crystal structure. The mechanical properties evaluation as determined by four-point flexural testing indicate a ductile-to-brittle transition temperature (DBTT) of 1250-1350°C for all of the modifications evaluated. Isothermal oxidation testing at 1400°C indicates no significant debit in oxidation resistance of $MoSi_2$ that can be attributed to alloying, however, alloys containing higher concentrations of the ternary elements may exhibit reduced oxidation resistances.

INTRODUCTION

The performance of the next generation of military gas turbine engines will be largely determined by the temperature capabilities of structural materials. This is especially true in the case of the high pressure turbine where gas path temperatures already approach 1500°C and metal temperatures approach 1150°C. Programs such as the DoD IHPTET initiative are aimed at doubling the thrust-to-weight performance of military engines. To accomplish this objective, design calculations indicate that gas path temperatures of about 2100°C are required. The same goal can be accomplished utilizing advance cooling schemes (possible with conductive materials such as metals and intermetallics) that maintain a gas path temperature of 2100°C and a metal temperature of 1540°C. These temperature requirements are clearly beyond the capabilities of materials currently available. In addition to the temperature requirements, other critical materials properties cannot be compromised. These properties include environmental resistance (oxidation and hot corrosion), adequate low temperature fracture toughness or ductility, elevated temperature strength (tensile and creep), and thermal mechanical fatigue resistance.

The materials used exclusively in the high pressure turbine of all state-of-the-art military engines are nickel-based superalloys. These materials are unique in that they exhibit sufficient mechanical properties and environmental resistance to be used at temperatures up to about 85% of the melting point. This enhanced capability, relative to other alloy systems, can be attributed to the use of coherent precipitation strengthening, alloy modifications with rhenium additions for enhanced creep resistance and technologies such as directional solidification for enhanced thermal fatigue resistance. Since the melting points of these alloys are about 1350°C, close to that of pure nickel, significant further advancements in temperature capability will not be attainable.

Several classes of materials can potentially meet the aggressive goals stated above. They include ceramics and ceramic matrix composites (CMCs), refractory metals with protective coatings, and intermetallics and intermetallic matrix composites (IMCs). However, all of these materials will require major improvements in one or more critical property to attain the required blend of environmental resistance, low temperature ductility (or toughness) and high temperature strength.

Mat. Res. Soc. Symp. Proc. Vol. 322. ©1994 Materials Research Society

In general, the ceramics and CMCs suffer from a lack of ductility and fracture toughness throughout the temperature range. Additionally, their low thermal conductivity would have a negative impact on the ability to utilize advance cooling schemes. They have the advantage of low densities and good oxidation resistances. The shortcoming of available refractory metals is poor oxidation resistance. Although they can be improved with protective coatings (such as plasma sprayed $MoSi_2$ coatings or diffusion slurry silicide coatings for niobium alloys), failure of these coatings result in rapid deterioration of the substrate due to either internal oxidation (resulting in alloy embrittlement) or non-protective oxidation. Refractory metals have the advantages of having a mature metallurgical knowledge and experience base, good thermal conductivities, adequate ductility throughout the temperature range of interest, and can be strengthened by traditional solid solution and dispersion hardening techniques[1]. Intermetallics generally exhibit insufficient ductility at low temperatures (below the alloy ductile-to-brittle transition temperature) and inadequate strength at elevated temperatures. They have good thermal conductivities such that advanced cooling schemes can be used and they have lower densities than the refractory metals (but generally higher than the ceramic materials). Several of the intermetallic systems such as NiAl and $MoSi_2$ exhibit excellent oxidation resistances. Of all the intermetallics, $MoSi_2$ has the best combination of a high melting point, high temperature strength, and oxidation resistance.

EXPERIMENTAL PROCEDURES

Intermetallic alloys for this program were prepared by arc-melting. Purified argon gas, gettered by flowing standard bottled gas over heated titanium chips, was used to create a protective atmosphere which minimizes interstitial pick-up. Typical oxygen impurity levels in the argon gas, monitored continuously throughout the melting process, were below 10^{-7} ppm by weight (one part impurity in 10^{13} parts argon). Buttons were cast in water-cooled copper hearths using a minimum of three melting and resolidification sequences; to minimize macrosegregation, the cast buttons were "flipped" between melting operations.

Heat treatments were performed in an all-metal tungsten-element vacuum furnace. Purified helium or argon gas, also gettered by flowing standard bottled gas over heated titanium chips, was used to create the protective atmosphere.

Specimens prepared for mechanical testing were fabricated utilizing a powder metallurgy process. The procedure selected for specimen preparation consists of (1) arc-melting of materials to the desired composition (2) crushing, attriting and screening to fine powders (-325 mesh or ≤44μ) (3) consolidation by vacuum hot pressing and (4) EDM machining and mechanically polishing the surfaces to at least a 600 grit (≤27μ) surface finish. Comminution of the arc-melted buttons was accomplished using a standard ball mill with tungsten carbide balls under an inert (argon) environment.. Most of the compositions were prepared by vacuum hot pressing at 1600-1650°C/10-15ksi/1-2 hours. Lower VHP temperatures (1500°C) were utilized where necessary for the aluminum and germanium modifications.

Optical Microscopy (OM), electron probe microanalysis (EPMA), X-Ray Diffraction (XRD), and wet-chemistry by inductively coupled plasma/atomic emission spectroscopy (ICP) were used to characterize the structure and composition of $MoSi_2$ compositions. The microstructure of $MoSi_2$ with the $C11_b$ crystal structure was determined by optical means under polarized light. Grain structures are clearly evident in this imaging mode. Phase analyses of various $MoSi_2$ compositions were determined by EPMA. Phase contrast was provided by backscattered electron imaging. Compositions were determined by wavelength dispersive spectroscopy (WDS) using pure elemental standards and ZAF corrections. Crystal structures were determined by XRD.

Specimens prepared for four-point flexure testing exhibited dimensions of approximately 4mm (width) X 1mm (thickness) X 30mm (length). Testing was performed under argon in an all metal tungsten-element

heated vacuum furnace. The molybdenum fixture contains alumina contact rods with a geometry of major span = 25.4 mm; minor span = 12.7 mm. Displacement was measured using a center point contact extensometer. Measurements of stress, modulus, and ductility were determined from outputted load-displacement curves.

RESULTS AND DISCUSSION

Alloy Screening

Six elemental modifications were selected for evaluation. Aluminum, boron and germanium substitutions for silicon and hafnium, niobium and rhenium substitutions for molybdenum were selected for alloy screening. These modifications will serve to evaluate the effects of crystal structure, substitutional alloying, atomic radii size, and e/a ratio as well as clarification or confirmation of phase boundaries. The initial samples for evaluation contained substitutions of 50 percent (16.7 atomic percent when substituted for molybdenum and 33.3 atomic percent when substituted for silicon) and were prepared by arc-melting and homogenization heat treatment at 1400°C for 48 hours. Additional samples of other compositions to better define phase boundaries were also prepared by arc-melting. Phase analyses were performed by x-ray diffraction (XRD) and electron probe microanalysis (EPMA). The results are discussed below.

Aluminum Modifications

The composition of $Mo(Si_{0.5}Al_{0.5})_2$ exhibited the C40 hexagonal crystal structure and the lattice parameter is consistent with that found by Nowotny[2] (x-ray card 10-277). Additional compositions containing 5 and 40.5 atomic percent aluminum were also prepared to better define solubilities and phase boundaries. EPMA results generally confirm the phase diagram and solubility limits observed by previous investigators[3]. A backscatter electron images (BSE) along with the EPMA phase analyses is shown in Fig. 1. The phase boundaries bounded by the C40 phase occur at aluminum concentrations of 8.6 and 41.6 atomic percent at 1400°C. The solubility of aluminum in $MoSi_2$ is 3.1 atomic percent. Based on these results, two compositions (20 and 50% aluminum substitution for silicon) were selected for evaluation of properties. These compositions have the C40 crystal structure.

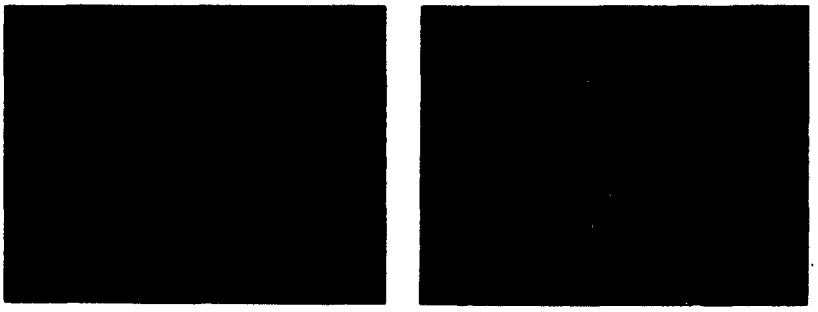


Fig. 1 Phase Compositions of (a) 33.3Mo-61.7Si-5.0Al and (b) 33.3Mo-26.2Si-40.5Al Alloys

Boron Modifications

The composition containing 50 percent substitution of boron for silicon (33.3 atomic percent B) exhibited a multiphase structure consisting of $MoSi_2$ (with the $C11_b$ structure) and borides approximating the compositions MoB and MoB_2. A BSE image along with the EPMA phase analysis is shown in Fig. 2. These results confirm previous studies[4] and indicate no solubility of B in $MoSi_2$ or Si in the molybdenum borides. Based on these results, boron modifications were not selected for further evaluation.



200μ

Phase X: 32.9Mo-67.1Si-0.0B Phase Y:32.9Mo-0.0Si-67.1B Phase Z:50.7Mo-0.0Si-49.3B

Fig. 2 Phase Composition of 33.3Mo-33.4Si-33.3B Alloy

Germanium Modifications

The compositions containing 10, 25, and 50 percent germanium substitutions for silicon (6.7, 16.7, and 33.3 atomic percent Ge) exhibited a single phase $C11_b$ crystal structure indicating complete solubility of germanium in $MoSi_2$ in the region of interest. The lattice parameters generally followed the rule of mixtures and increased with increasing germanium concentrations. These modifications have been selected for properties evaluation.

Hafnium Modifications

The composition containing 50 percent hafnium substitution for molybdenum (16.7 atomic percent Hf) in $MoSi_2$ exhibited a two phase structure of $MoSi_2$ (with the $C11_b$ structure) and $HfSi_2$ (with the C49 structure). This result verifies phase diagram results by other investigators[5] and indicates very low solubilities of Hf in $MoSi_2$ and Mo in $HfSi_2$. The hafnium system is different from the titanium system where a wide C40 phase field has been observed[6]. A BSE image along with the EPMA phase analysis is shown in Fig. 3. Based on these results, hafnium modifications were not selected for further evaluation.

Niobium Modifications

The composition containing 50 percent niobium substitution for molybdenum (16.7 atomic percent Nb) exhibited the C40 hexagonal crystal structure. An additional composition containing 6.3 atomic percent Nb was prepared to better define the solubility limits. The results of EPMA analyses indicate solubility limits that are different than that observed by other investigators[7]. A BSE image along with the EPMA phase analysis is shown in Figs. 4.



200μ

Phase A: 0.0Mo-39.2Hf-60.8Si; Phase B:33.1Mo-0.05Hf-66.9Si; Phase C:0.2Mo-57.4Hf-42.4Si

Fig. 3 Phase Composition of 16.7Mo-16.6Hf-66.7Si alloy



200μ

Phase a: 26.5Mo-6.7Nb-66.8Si; Phase b:31.5Mo-1.5Nb-67.0Si

Fig. 4 Phase Composition of 27.0Mo-63Nb-66.7Si Alloy

The solubility of niobium in $MoSi_2$ ($C11_b$ structure) is 1.5 atomic percent while the solubility of molybdenum in $NbSi_2$ (C40 structure) is 26.5 atomic percent. The lattice parameter of $MoSi_2$ (C40 structure) was found to increase linearly with increasing niobium concentrations. Based on these results, compositions with 9.7 and 16.7 atomic percent niobium substitutions for molybdenum in $MoSi_2$ were selected for further evaluation.

Rhenium Modifications

The compositions containing 10, 25, and 50 percent rhenium substitutions for molybdenum (3.3, 8.3, and 16.7 atomic percent Re) exhibited the $C11_b$ tetragonal structure. The results indicate complete solubility in the $ReSi_2$-$MoSi_2$ system. The lattice parameter decreased linearly with increasing rhenium concentrations. These compositions have been selected for further evaluation.

Mechanical Properties

The mechanical properties have been determined by four point flexural testing. The testing was performed at room temperature and at elevated temperatures to determine strength, ductility, and ductile-

to-brittle transition temperature (DBTT). These results are summarized in Table 1. In general, no ductility was observed below the DBTT. The strength of the alloys appear to increase with increasing temperatures while the elastic modulus decreases with increasing temperature. The DBTT was not altered significantly with the alloy compositions and crystal structures evaluated. The observed DBTT appears to be higher than that reported in the literature[8] and may be attributed to the processing techniques used. Higher purities with lower interstitial containing samples were evaluated under this program.

TABLE 1 FOUR-POINT FLEXURE TEST RESULTS

$MoSi_2$ Composition	Temp (°C)	UTS (MPa)	E (GPa)	ε (%)	Remarks
$Mo(Si_{0.5}Al_{0.5})_2$	1200	207	117	0	DBTT ~ 1250°C
C40 structure	1300	139	123	>1.0	
$(Mo_{0.5}Nb_{0.5})Si_2$	1300	346	169	0	DBTT ~ 1350°C
C40 structure	1400	244	147	>1.5	
$(Mo_{0.9}Re_{0.1})Si_2$	1200	275	207	0	
$C11_b$ Structure	1300	261	229	0.1	DBTT ~ 1350°C
	1400	241	104	>0.9	
$(Mo_{0.75}Re_{0.25})Si_2$	1200	189	165	0	
$C11_b$ Structure	1300	171	179	0	DBTT ~ 1350°C
	1400	192	205	0.4	
$(Mo_{0.5}Re_{0.5})Si_2$	1000	243	284	0	
$C11_b$ Structure	1200	231	235	0.1	DBTT ~ 1250°C
	1300	191	138	>1.1	

Oxidation Resistance

Samples for evaluation of oxidation resistance and mechanical properties were prepared. A procedure of arc-melting/powder comminution/VHP consolidation was utilized. Oxidation testing was performed at 1400°C for 22 hours and 124 hours under isothermal conditions. This test was a screening test to determine if the alloy modifications selected would degrade oxidation resistance. The weight change results shown in Table 2 indicate all the alloy modifications did not significantly debit the oxidation resistance of $MoSi_2$. However, the samples containing 50% aluminum substitutions exhibited spalling (apparently due to the formation of a mixed oxide scale) while the composition containing 50% substitution of rhenium for molybdenum exhibited large initial weight losses.

TABLE 2 ISOTHERMAL OXIDATION RESULTS (1400°C)

	Weight Change (mg/cm^2)	
$MoSi_2$ Composition	22 hours	124 hours
Baseline $MoSi_2$	+0.5	+1.2
$Mo(Si_{0.5}Al_{0.5})_2$	+1.5	+4.9
$Mo(Si_{0.9}Ge_{0.1})_2$	+1.7	+1.7
$Mo(Si_{0.75}Ge_{0.25})_2$	+1.0	+0.0
$(Mo_{0.5}Nb_{0.5})Si_2$	+1.5	+5.3
$(Mo_{0.9}Re_{0.1})Si_2$	+1.1	+4.3
$(Mo_{0.75}Re_{0.25})Si_2$	+1.3	+3.6
$(Mo_{0.5}Re_{0.5})Si_2$	- 6.6	- 5.6

CONCLUSIONS

Six elemental modifications of $MoSi_2$ have been evaluated. They are Al, B, and Ge substitutions for Si and Hf, Nb, and Re substitutions for Mo. B and Hf modifications exhibited two phase or multiphase structures indicating very little solubility in $MoSi_2$. Al and Nb substitutions for Si and Mo, respectively, in $MoSi_2$ resulted in alloys with the C40 hexagonal crystal structure. Ge and Re substitutions for Si and Mo, respectively, in $MoSi_2$ resulted in alloys with the $C11_b$ tetragonal crystal structure. Most of the analyses confirm the validity of available phase diagrams although the results presented here indicate a need to refine the solubility limits. Mechanical properties as determined by four-point flexural testing indicate DBTTs were in the temperature range 1250-1350°C for all of the modifications evaluated. Isothermal oxidation testing indicates no significant debit in oxidation resistance at 1400°C although alloys containing higher concentrations of ternary elements may exhibit reduced oxidation resistances.

ACKNOWLEDGMENT

Research sponsored by the Air Force Office of Scientific Research (AFSC) under contract F49620-92-C-0043. The United States Government is authorized to reproduce and distribute reprints for governmental purposes notwithstanding any copyright notation hereon.

REFERENCES

1. D. L. Anton, D. B. Snow, L. H. Favrow, and A. F. Giamei, Final Report R89-917437-3 on AFOSR Contract F49620-86-C-0053, 7/89.
2. H. Nowotny, Huschka, Monatsh. Chem., 88, (1957) 894
3. Ageev, N. V., Diagram Sostoyaniy Metallicheshikh Sistem, VINITI Press, Moscow, 1960, 100 and 1966, 143
4. Ageev, N. V., Diagram Sostoyaniy Metallicheshikh Sistem, VINITI Press, Moscow, 1957
5. Ageev, N.V., Diagram Sostoyaniy Metallicheshikh Sistem, VINITI Press, Moscow, 1971, 270
6. W. J. Boettinger, JJ. H. Perepezko, and P. S. Frankwicz, Mat. Sci. and Eng., A155 (1992), 33
7. Ageev, N. V., Diagram Sostoyaniy Metallicheshikh Sistem, VINITI Press, Moscow, 1965, 234
8. P.J. Meschter and D. S. Schwartz, "Silicide-Matrix Materials for High Temperature Applications", Journal of Metals, V.41 N11, 11/89, 52

MOLYBDENUM-RHENIUM DISILICIDE ALLOYS

D.L. Davidson* and A. Bose†
*Southwest Research Institute, San Antonio, TX
† Parmatech, Petaluma, CA

ABSTRACT

Rhenium was added to $MoSi_2$ in two concentrations and billets were made by hot pressing powders. The microstructures obtained are reviewed. Fracture toughness was measured at 20 and 800°C, hardness was measured at 20°C, and oxidation resistance was determined at 500°C. Toughness was not enhanced, but hardness and oxidation resistance were. However, the base alloy made for comparison had better properties than those given in published reports.

INTRODUCTION

Molybdenum disilicide is an extremely attractive compound for high temperature structural use because of its high melting point (2010°C), low density (6.3 gms/cc), and excellent oxidation resistance above 1000°C [1]. It is now being used for furnace heating elements to 1700°C. However, the poor mechanical strength at high temperature and low ductility at low temperature have thus far limited the use of this material as an advanced high temperature structural material. The research reported in this paper describes an effort aimed at increasing the ambient temperature toughness of molybdenum disilicide through alloying additions.

The most effective means of increasing fracture toughness is to increase the plastic response of material near a crack tip. Enhancing toughness sometimes may be accomplished in metals by microstructural manipulation, especially by suitable alloying additions. One example of the effect of alloying addition on toughness was the discovery in 1955 that the addition of rhenium to molybdenum resulted in an increase in room temperature ductility [2]. The simplest way to explain this effect is that rhenium adds electrons to the directionally bonding d-electrons and that causes the core structure of the dislocations to be more flexible allowing them to be activated at lower stress and to move on planes other than the one with the largest stress.

The "rhenium effect" in Mo lead us to hypothesize that a similar result might accrue to the addition of Re to $MoSi_2$. Re atoms were hypothesized to substitute for Mo atoms in the ordered $MoSi_2$ compound, thereby increasing the electron density per atom which would have the effect of decreasing the binding energy between atoms. This effect would decrease the temperature at which the transition from brittle to ductile behavior would occur, and this would impart increased room temperature ductility and fracture toughness to the alloyed compound,thereby partially solving one of the limitations to using this material in structural applications.

Rhenium additions were found, in 1955, to impart considerable additional ductility to molybdenum [2] and similar effects were subsequently found for other Group VI elements. Re is one of the few elements with substantial solubility in transition elements; up to 35 atomic % Re can be dissolved in Mo. The "rhenium effect" increased the tensile elongation of tungsten at 460°K from zero to 10 % with addtion of Re. Addition of 7 to 25 atomic % Re alters both the temperature of the ductile-to-brittle transition and the nature of the transition. At 20°C, softening occurs for Re additions less than 10 at.%, while solid solution hardening occurs at higher concentrations.

The reasons rhenium "ductilizes" molybdenum were investigated by Davidson and Brotzen in the 1960's [3-5]. Mo was alloyed with Re and the elastic constants [3] and mechanical properties of single crystals [4] were measured. Experimental measurements were combined with theory to gain an understanding of how Re additions changed the mechanical properties of the alloys. It was concluded that Re lowered the Peierls stress, particularly for screw dislocations. These effects were further explored [5] by calculating the energy required for atom movements in Mo and Mo-Re alloys as would occur during dislocation motion using interatomic potential functions. It was concluded from this work that dislocation core structures in the Zr-Nb-Mo-Re system were

Mat. Res. Soc. Symp. Proc. Vol. 322. ©1994 Materials Research Society

modified, and that the Peierls stress for screw dislocations was lowered when Mo was alloyed.

Some investigation of $Re_xMo_{1-x}Si_2$ has been done for possible use of these compounds as infrared detectors in the 3-14 μm bands [6] This work gave information on the crystallographic effects of Re additions. Using x-ray diffraction, it was determined that "the metal atoms may be freely substituted for one another over the entire compositional range with no fundamental alteration of crystal structure except that the lattice parameters change smoothly with composition."

MATERIAL SYNTHESIS

Two techniques were used to fabricate billets of material so that the hypothesis of rhenium increasing the toughness of $MoSi_2$ could be evaluated. For both of these fabrication routes, powders of $MoSi_2$ and $ReSi_2$ were purchased (Cerac, Inc., Milwaukee, WI). Also, elemental Mo and Re powders were purchased (Sandvik Rhenium, Inc., Elyria, OH). These powders were then blended in appropriate proportions in order to obtain the compositions of interest. Consolidation of the powder mixtures was accomplished using (1) hot pressing and (2) drop melt casting followed by hot isostatic pressing (HIP). All billets fabricated by melt casting/HIPing fractured into several pieces during handling or during cutting operations and were not evaluated.

Hot Pressing in cylindrical dies 64 mm in diameter by about 13 mm thick was used to consolidate blended mixtures of powders. Each billet was subjected to the following schedule of pressure and temperature: heat to 1000°C at 10°C/min; apply 35 MPa pressure after 50 min at 1000°C; heat to 1650°C at 10°C /min and hold for 3 hrs; cool to 1000°C at 10°C/min; remove load, then cool to ambient. Initial processing resulted in billets having considerable porosity and chemical inhomogeniety; thus, the billets were hot pressed a second time using the following parameters: heat to 1850°C at 10°C/min; apply 35 MPa pressure: hold at temperature and pressure for 8 hrs, then cool to ambient and release the pressure.

EVALUATION OF MECHANICAL PROPERTIES

For $MoSi_2$, K_c = 2.8 - 3.8 MPa$\sqrt{m}$ at 20°C and decreases to ≈ 3 at 1000°C [1], while Vickers hardness drops from ≈ 875 kg/mm^2 to ≈ 300 kg/mm^2. Various efforts to incease fracture toughness by composite technology have raised ambient toughness to as high as ≈ 8 MPa$\sqrt{m}$. Addition of carbon to $MoSi_2$ raised the hardness to 1300 kg/mm^2 at ambient temperature.

Hardness

A Vickers' four-sided diamond pyramid indentor was used to measure hardness. Loads of greater than 50 grams caused cracking of all the materials and were not used to determine hardness. Hardnesses determined for the alloys, using loads of 25 and 50 grams are shown in Table I. Each hardness (DPH) shown is the average of 6 indentations. Stress (GPa) = 9.8×10^{-3}DPH. Anisotropy, thought to be due to differences in grain orientation, was found in hardness between grains in all of the samples. The hardnesses obtained are greater than those reported for pure $MoSi_2$ (≈ 875 kg/mm^2) and for the alloys are in excess of those found for $MoSi_2$+2wt.%C.

Microstructures

Only twice hot pressed samples were evaluated in detail. Typical microstructures (backscattered electron images) are shown in Fig. 1. Grain sizes were found to be about 40μm for all the materials. The gray background is interspersed with other "regions;" these are labelled as "grey, white, and black" for description. Table II lists the composition of these regions as measured by energy dispersive x-ray analysis (EDS).

Table I
Hardness of
Hot Pressed Alloys

Alloy	Load	Vickers Hardness	
	grams	kg/mm^2	GPa
$MoSi_2$	25	1187	11.6
Material A	50	1071	10.5
$Mo_{30.5}Re_{2.5}Si_{67}$	25	1363	13.4
Material B	50	1189	11.7
$Mo_{28.0}Re_{5.0}Si_{67}$	25	1689	16.6
Material C	50	1284	12.6

Table II
Analysis of Microstructural Features

Material	Region	Average Size (μm^2)	Volume Percent	Composition (at. %) Mo	Si	Other
$Mo_{33}Si_{67}$	grey		97	31.9	68.1	
Material A	white	50	1.13	58.6	41.0	0.4 (Fe)
	black	5	1.35	4.2	95.3	0.8 (Al)
$Mo_{30.5}Re_{2.5}Si_{67}$	Lt. grey		37	27.5	66.7	5.8 (Re)
Material B	Dk. grey		61	31.7	68.0	0.34 (Re)
	white	65	1.1	51.0	38.2	10.2 (Re), 0.6 (Fe)
	black	6	1.0	6.6	85.5	4.8 (Re), 2.7 (Al)
$Mo_{28.0}Re_{5.0}Si_{67}$	Lt. grey		50	25.2	65.0	9.8 (Re)
Material C	Dk. grey		50	31.6	68.3	
	white	18	0.4	44.0	37.8	17.8 (Re), 0.4 (Fe)
	black	8	1.7	0.3	99.3	0.34 (Re)

These results indicate that Re was not distributed uniformly throughout the $MoSi_2$ matrix. In all cases, the Mo rich (white) phase held the bulk of the Re; the Si rich phase (black) also held Re, but much less. For both alloys, the matrix material contained Re-rich and non-Re regions. The volume percents shown in the table for light and dark grey (Re rich and non-Re regions, respectively) is based on a materials balance. These fractions very roughly agree with the contrast seen in the photographs of Figs. 1(b) and 1(c).

Bulk analysis for rhenium was made using atomic absorption (enhanced by Induction Plasma). The results are shown in Table III. Two sets of results are shown for $MoSi_2$ because Re was found unexpectedly and in a relatively large amount during the first analysis. No Re was detected by X-ray diffraction or microprobe.

With the various phases present, it was difficult to determine what was porosity and what was second phase, but measurements of porosity were made with the following results: Material A - 0.7%, Material B - 1.2%, and Material C - 2.0%. Likewise, the SiO_2 content was estimated using polarized light optical miroscopy to be not more than 2%.

Fracture Toughness

Fracture toughness of the alloys was evaluated at ambient temperature using straight cut and chevron notched beams loaded in 3-point bending. This method has been shown to be useful in evaluating brittle materials and has the advantage that specimens of small size may be obtained from limited amounts of mateial. Results of the fracture tests are given in **Table IV.**

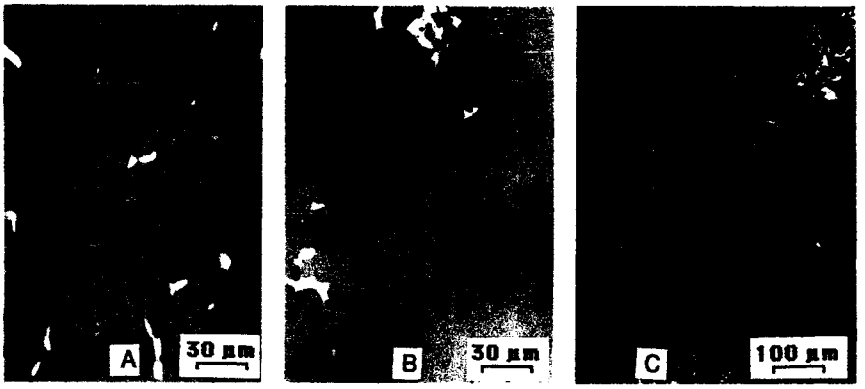


Fig. 1 Backscattered electron images of the microstructures of the three materials.

Table III
Bulk Chemical Analysis (Atomic Percent)

Material	Mo	Si	Re	O (wt.%)	C
$MoSi_2$	33.2	66.6	0.19	0.17	0.48
	31.6	67.6	0.22		
$Mo_{30.5}Re_{2.5}Si_{67}$	31.0	66.4	2.62	0.19	
$Mo_{28.0}Re_{5.0}Si_{67}$	29.0	65.4	5.57	0.22	

Table IV
Fracture Toughness

Material	Designation	Measured K_c (MPa$\sqrt{m}$)	
		20°C	800°C
$Mo_{33}Si_{67}$ ($MoSi_2$)	A	4.3, 5.6, 7.1	4.7
$Mo_{30.5}Re_{2.5}Si_{67}$	B	2.6, 4.7, 5.0	1.6
$Mo_{28.0}Re_{5.0}Si_{67}$	C	2.7, 3.8	0.5

Fractography

At ambient temperature, fractographs such as shown in **Fig. 2** show that Material A was very brittle and had a large fraction of transgranular, conchoidal fracture with few river lines. Material B ($Mo_{30.5}Re_{2.5}Si_{67}$) showed similar features. Material C ($Mo_{28.0}Re_{5.0}Si_{67}$) had conchoidal fracture features, a lack of river lines, and was mostly transgranular, but more

intergranular fracture than the other materials. It is concluded that fractographic features agree generally with the fracture toughness trends.

Evidence of a relationship was sought between the fracture surface features and regions of decreased Re content (evident in the backscattered electron images of Fig. 1 and microprobe data of Table III), but nothing was found. The fracture surface of Material C was cross sectioned, but the crack path did not appear to favor regions of more or less Re content. However, a number of secondary cracks were found in the material away from the fracture surface, but none of these were found to penetrate the regions of low Re content.

Only evidence of very brittle fracture was found on the fracture surfaces of materials broken at 800°C, Fig. 3. All the fractures were predominantly transgranular, although Material A did evidence some (≈ 20%) intergranular fracture. Conchoidal fracture without river lines was found on all fracture surfaces and there was no evidence of any plasticity associated with any of the secondary cracks. These fracture features coincide with the low toughness values measured. The intergranular fractures reported by previous investigators for $MoSi_2$ were much less prevalent in Material A, and the other materials exhibited only a small amount of intergranular cracking.

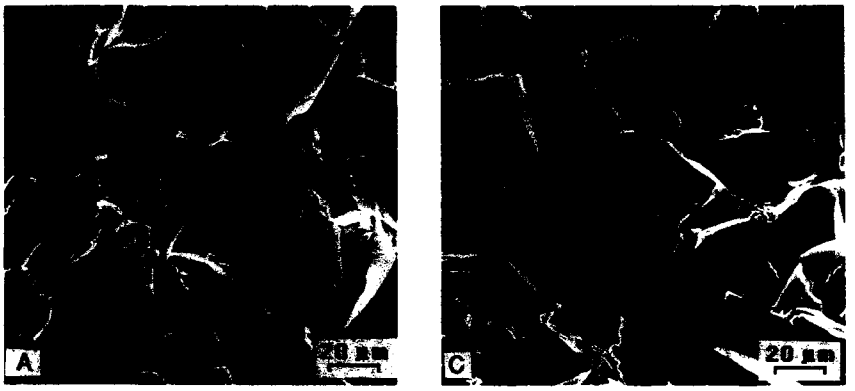


Fig. 2 Fracture toughness specimens broken at 25°C.

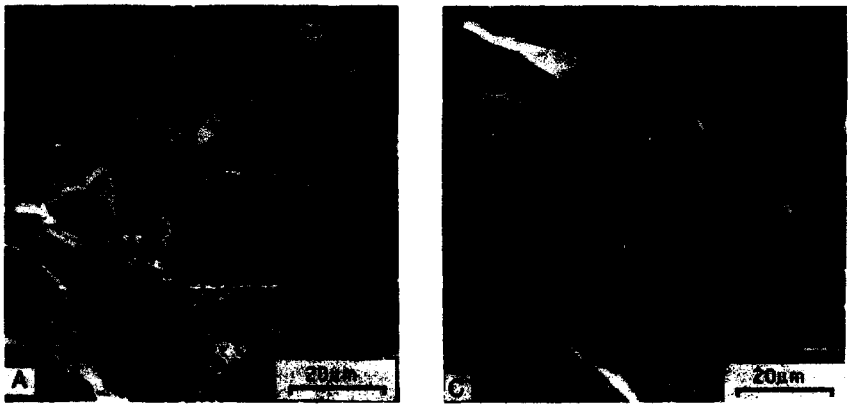


Fig. 3 Fracture toughness specimens broken at 800°C.

EVALUATION OF OXIDATION RESISTANCE

At temperatures between 400 and 600°C, $MoSi_2$ can exhibit an increased oxidation rate due to the formation of MoO_3 in the oxide, which inhibits the formation of the normally protective SiO_2 coating. This decreased oxidation resistance has been termed "pesting." When MoO_3 forms in cracks and pores within a material, it wedges open the flaw (MoO_3 occupies more space than SiO_2), cracking the material, and often reduces it to powder.

Samples of the hot pressed materials were held at 450-500°C for approximately 200 hours to observe any differences that the alloying might have on oxidation resistance of these materials. The qualitative results, shown in Fig. 4, suggest that alloying increases the resistance of $MoSi_2$ to "pesting," although the $MoSi_2$ base material was not nearly as susceptible to pesting as materials reported in the literature.

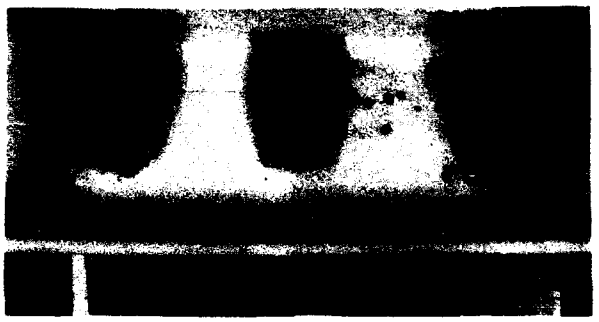


Fig. 4 Oxidation at 500°C for 200 hours.

SUMMARY AND CONCLUSIONS

The "baseline" $MoSi_2$ material had twice the toughness of room temperature tests reported in the literature and did not exhibit "pesting" at 500°C. It was discovered that the $MoSi_2$ did contain about 0.5 at. % Re and about an equal amount of C, which might account for the increased properties observed. Alloying with larger concentrations of Re decreased the toughness, but increased the hardness, and the environmental stability of the material at 500°C was slightly increased. At 800°C, the toughness of the base $MoSi_2$ alloy decreased 26% relative to ambient, but for the higher Re alloys, toughness decreased drastically. It is concluded from this study that small amounts of Re (<2.5 at. %), perhaps in synergism with C, increases the toughness and strength of $MoSi_2$ at ambient temperature and 800°C, and pesting resistance is also enhanced, while greater amounts of Re degrade toughness.

REFERENCES

1. Proceedings of the First High Temperature Structural Silicides Workshop, Nov. 4-6, 1991, published in Mat. Sci. and Eng., July 30, 1992, A155, Nos. 1-2.
2. G.A. Geach and J.R. Hughes in Proceedings of the Plansee Conference (Pergamon Press, Oxford, 1956), p. 253.
3. D.L. Davidson and F.R. Brotzen , J. App. Physics, 39, 5768-5775 (1968).
4. D.L. Davidson and F.R. Brotzen, Acta Metallurgica, 18, 463-470 (1970).
5. D.L. Davidson, Nuclear Metallurgy, 20, pt. 1, 286-297 (1976).
6. R.G. Long and J.E. Mahan, Appl. Phys.Lett., 56, 1655-1657 (1990).

INVESTIGATION OF B2 AND RELATED PHASES IN Ti-MODIFIED Nb-Al ALLOYS

D.-H. Hou, S.S. Yang, J. Shyue and H.L. Fraser
Dept. of Materials Science and Engineering, The Ohio State University
2041 College Road, Columbus, OH 43210, USA

ABSTRACT

The B2 ordering and phase stability of three ordered intermetallic alloys with compositions (in at.%) of Nb-15Al-10Ti (10Ti alloy), Nb-15Al-40Ti (40Ti alloy), and Nb-15Al-25Ti (25Ti alloy) have been studied. All three alloys have the B2 crystal structure in the as-cast form. The Atom Location by Channeling Enhanced Microanalysis (ALCHEMI) technique has been employed to assess the site occupancy of these B2 alloys. The results of site occupancy are represented as Ordering Tie Lines on a ternary composition diagram. Various second phases were observed in heat treated samples. An ω-type phase was found in the 10Ti alloy in samples heat treated for 10 minutes and 4 hours at 900°C. At 800°C, orthorhombic phase was found in the 40Ti alloy while a three phase microstructure of o-phase/B2/A15 was observed in both the 10Ti and 25Ti alloys. Annealing at 1100°C leads to the dissolution of the o-phase and the presence of A15 phase in the 10Ti and 25Ti alloys, but no other phase in the 40Ti alloy. The observed phase equilibria in these alloys are compared with those in the literature.

INTRODUCTION

Three Nb-based alloys with nominal compositions (in at.%) of Nb-15Al-10Ti (10Ti alloy), Nb-15Al-40Ti (40Ti alloy), and Nb-15Al-25Ti (25Ti alloy) have been developed for elevated temperature applications[1-4]. All these alloys exhibit the B2 crystal structure in the as-cast form[2] and show promising elevated temperature strength and ambient temperature ductility[3]. The B2 ordering implies the AB stoichiometry, but the the compositions of these ternary alloys are far off this stoichiometry. In this study, the site occupancies of these ternary B2 compounds are assessed by the ALCHEMI technique[5]. The B2 ordering phenomenon is then discussed based on the site occupancy results. It has been shown that the A15 phase of $(Nb,Ti)_3Al$ precipitates out from the matrix[2, 6] in the 10Ti alloy heat treated at high temperatures (>1000°C). The phase stabilities at intermediate temperatures (700°C - 900°C) of the Ti alloy, as well as the 40Ti and 25Ti alloys, are to be studied in this temperature range.

EXPERIMENTAL PROCEDURE

Alloys with nominal compositions of Nb-15Al-10Ti, Nb-15Al-25Ti, and Nb-15Al-40Ti were prepared by plasma arc melting in an Ar atmosphere on a water cooled copper hearth. Samples were encapsulated in Ar-backfilled quartz tubes and heat treated in a conventional resistance furnace. Samples were quenched by breaking the quartz tubes in water following heat treatment. For temperatures higher than 1150°C, samples were wrapped in Ta foils and heat treated in a vacuum furnace evacuated and backfilled with Ar. TEM foils were prepared by twin jet electropolishing using 7.5 vol.% H_2SO_4 in methanol at -40°C and 90mA and then examined on a JEOL 200CX TEM. ALCHEMI and micro-chemical analyses were performed on a HITACHI 9000NAR TEM equipped with a Noran Voyager EDS system operated at 300kV.

RESULTS

Site Occupancy (ALCHEMI)

The B2 phase was identified using selected area electron diffraction patterns (SADP). A typical set of SADP's taken from the 40Ti alloy are shown in Fig. 1. The site occupancy was deduced from the ALCHEMI experiments, and the detail algorithm will be given elsewhere[7]. The results for the 10Ti and 40Ti alloys are listed respectively as follows:

α sites: 30Nb-5Ti-15Al		α sites: 25Nb-10Ti-15Al
β sites: 45Nb-5Ti	and	β sites: 20Nb-30Ti

Mat. Res. Soc. Symp. Proc. Vol. 322. ©1994 Materials Research Society

The two sublattice sites of the B2 structure are designated as α and β. It is seen that Ti atoms show no preference taking either α or β site when a small amount of Ti is added. As the Ti atom content increases, the atoms tend to occupy a sublattice which does not contain Al atoms.

Phase Stability

10Ti Alloy

Samples were first homogenized at 1800°C for 5 hours and were subsequently heat treated at 700°C, 800°C and 900°C. No second phases were observed in samples heat treated at 700°C for 4 and 50 hours, but a slight growth of anti-phase domain (APD) in the B2 phase occurred (Fig. 2a,b). Fine second phase precipitates were found in samples heat treated for another 500 hours at this temperature (Fig. 3). Since these needle-like precipitates are very small in size (100Å in length), neither SADP's nor the composition from individual precipitate has been obtained. This new phase was identified by matching SADP's in Fig. 3 with superimposed SADP's of possible second phases and the B2 matrix. A match is found for the orthorhombic-phase (o-phase) bearing an orientation relationship (OR) of $[001]_o \| [101]_{B2}$ and $[\bar{1}10]_o \| [\bar{1}11]_{B2}$[8, 9]. The detailed analyses of the o-phase will be given elsewhere[10]. It was found that the o-phase redissolved and the A15 phase formed in a sample heat treated at 1100°C for 50 hours after 700°C/500hr heat treatment.

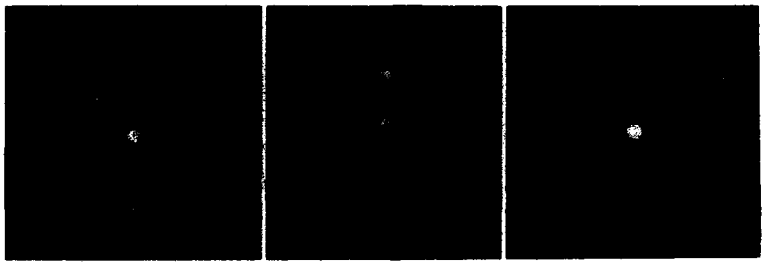


Fig. 1 SADP's of the 10Ti alloy in (a) [001], (b) [011], and (c) [111] zone axis.

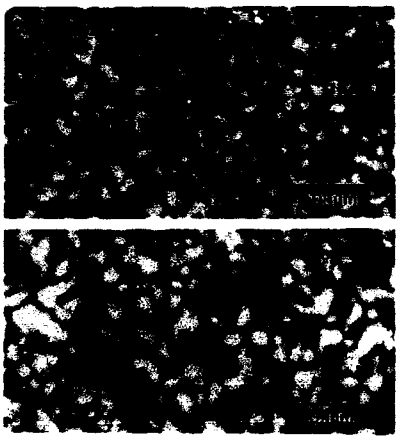


Fig. 2 Dark field TEM micrographs of the 10Ti alloy after being heat-treated at 700°C for (a) 4 hours and (b) 50 hours.

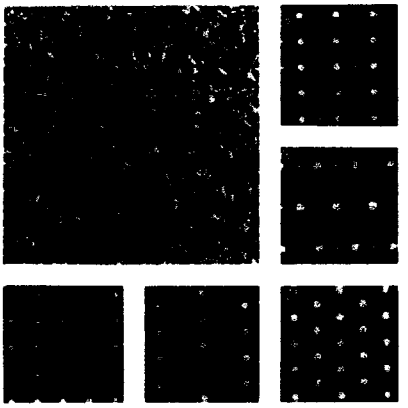


Fig. 3 (a). Dark field TEM micrograph of the 10Ti alloy heat treated at 700°C for 500 hours. (b-f) correspondingSADP's taken in $[011]_{B2}$, $[012]_{B2}$, $[\bar{1}11]_{B2}$, $[\bar{1}13]_{B2}$, and $[001]_{B2}$ zone axes, respectively.

Heat treating at 800°C for 500 hours led to the formation of two phases with different sizes and morphologies, as shown in Fig. 4. The thick plate-like phase and the fine needle-like phase were identified as the A15 phase and the o-phase, respectively. The compositions of these phases are Nb-21Al-8Ti, Nb-24Al-14Ti and Nb-12Al-7Ti for the A15, o-phase and matrix, respectively. It is noted that the compositions of the o-phase and matrix should be cited as an approximate value because of the unavoidable electron beam overlapping due to the fine size of the o-phase.

For samples heat treated at 900°C for 10 minutes and 4 hours followed by either water quenching or furnace cooling (10°C/min), very fine precipitates were found (Fig. 5a). The results of SADP matching(Fig. 5b-d) suggests that the fine precipitates are the "ω-type" phases, which are commonly observed in Ti-Nb[11] and Ti-Al-Nb[12] alloys, and have the OR of $(0001)_\omega \| (111)_{B2}$ and $[2\bar{1}\bar{1}0]_\omega \| [\bar{1}10]_{B2}$ [12]. Prolonged annealing at 900°C for 500 hours leads to the formation of the A15 phase at expense of ω-phases. This indicates that the ω-phase is a metastable phase.

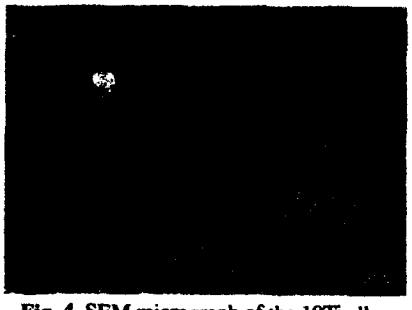


Fig. 4 SEM micrograph of the 10Ti alloy after 800°C/500hrs annealing

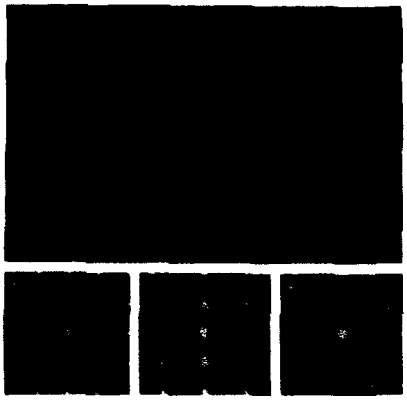


Fig. 5 (a). TEM micrograph showing the ω-phase in the 10Ti alloy heat treated at 900°C for 10 minutes (b-d). electron diffraction patterns of (a) taken from $[001]_{B2}$, $[011]_{B2}$ and $[\bar{1}11]_{B2}$ zone axes.

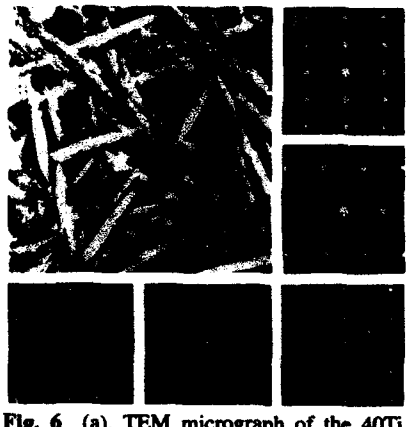


Fig. 6 (a). TEM micrograph of the 40Ti alloy heat treated at 800°C for 20 hours. (b-f) correspondingSADP's taken in $[011]_{B2}$, $[012]_{B2}$, $[\bar{1}11]_{B2}$, $[\bar{1}13]_{B2}$, and $[001]_{B2}$ zone axes, respectively.

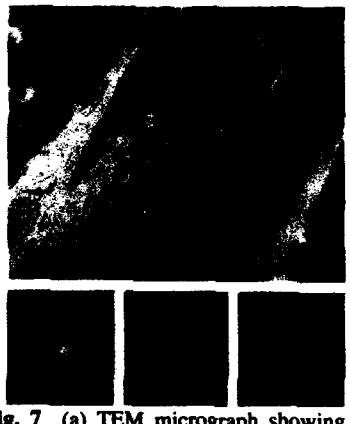


Fig. 7 (a) TEM micrograph showing the o-phase in a sample of the 40Ti alloy, which was heat treated at 800°C for 20hours and then at 900°C for 50hours. (b) SADP's of a precipitate labeled as "A" in $[\bar{1}02]_o$, $[012]_o$ and $[\bar{2}12]_o$ zone axes.

40Ti Alloy

Fine lenticular precipitates about 1-2μm in length, as shown in Fig. 6a, were found in samples heat treated at 800°C for 20 hour. The SADP's of the precipitates with the matrix are shown in Fig. 6b-f. They are also identified as the o-phase[2] and exhibit the same OR with the B2 matrix, as in the case of the 10Ti alloy. Further annealing at the same temperature for another 500 hours did not change the o-phase morphology but increased its size slightly to an average of 2-3μm in length. The o-phase coarsened to about 4-5μm in length after heat treating at 900°C for 50 hours (Fig. 7) and redissolved at temperatures higher than 1000°C. The compositions of the o-phase and the B2 matrix were measured by the thin film EDS technique. They are Nb-25Al-43Ti (o-phase) and Nb-10Al-34Ti (B2) at 800°C, and Nb-24Al-44Ti (o-phase) and Nb-15Al-39Ti (B2 matrix) at 900°C. It is noted that the measured compositions of the o-phase in 40Ti alloy are very close to Ti_2AlNb, which is considered the stoichiometrical composition of the o-phase[8, 9].

25Ti Alloy

In this alloy, heat treating at 1100°C for 50 hours leads to the formation of the A15 phase, which is similar to that of the 10Ti alloy. The compositions of A15 and the B2 matrix are of Nb-18Al-20Ti and Nb-12Al-27Ti, respectively. Heat treating at a lower temperature of 800°C for 500 hours gives a three-phase microstructure consisting of the B2, A15 and o-phases as shown in Fig. 8. The o-phase has the same OR with B2 matrix as mentioned previously. The compositions of these phase were determined to be Nb-11Al-21Ti, Nb-19Al-22Ti, and Nb-24Al-31Ti, for the B2, A15 and o-phase, respectively.



Fig. 8 TEM micrograph showing the o-phase (labeled as "o") and A15 phase (labeled as "A") in a sample of the 25Ti alloy after 800°C/500hrs heat treating

DISCUSSION

B2 Ordering Phenomenon

B2 ordering generally implies a binary stoichiometry of AB, it is interesting to find out the ordering states of these ternary B2 compounds with compositions far off this stoichiometry. In binary alloys, the ordering state is generally described by the long range ordering parameter (LRO) with the AB stoichiometry as the standard[13]. Similar LRO's can be defined in these ternary alloys if a stoichiometrical state is defined. However, such a state is very unlikely to exist in the present Nb-Al-Ti system because a wide range of compositions of B2 compounds have been reported[14-16]. The compositions of these B2 compounds are plotted as closed circles on a ternary composition diagram shown in Fig. 9a. Nonetheless, the LRO's can still be defined on a "hypothetical" stoichiometrical state, which is the virtue of any thermodynamical quantity.

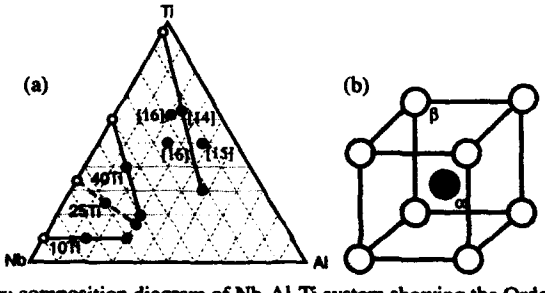


Fig. 9 (a). Ternary composition diagram of Nb-Al-Ti system showing the Ordering Tie Lines of some B2 compounds. (b). Schematic drawing showing the unit cell of the B2 structure. Two sublattice sites are denoted as a and b.

Instead of defining the LRO's on a hypothetical stoichiometrical state, a graphical method to represent the ordering state is proposed here. The B2 structure can be viewed as an ordered bcc structure with two sublattices of α and β, as shown in Fig. 9b. The "compositions", which are essentially defined by the site occupancies, of the two sublattices determine whether the structure is A2(bcc) or B2. If the "compositions" of the α sublattice (C^{α}) and the β sublattice (C^{β}) are different, the alloy is said to have the B2 structure. In this study, the B2 ordering state in these ternary alloys is proposed to be represented as a straight line designated as the Ordering Tie Line (OTL), with the original composition (C^{o}) in the middle and with C^{α} and C^{β} at two ends. For example, the C^{α}, C^{β} and C^{o} for the 40Ti alloy are Nb-30Al-10Ti, Nb-70Ti and Nb-15Al-40Ti, respectively. The corresponding OTL's for the 10Ti alloy, 40Ti alloy are plotted on the Nb-Al-Ti ternary composition diagram as shown in Fig. 9a. The OTL of Ti-24Al-14Nb alloy of which site occupancy was determined[14] is also shown in the same diagram for comparison. It is seen that the OTL of the 40Ti alloy is nearly parallel to that of Ti-24Al-14Nb but runs in a different orientation from that of the 10Ti alloy. This suggests that the ordering state of the 40Ti alloy should be different than that of the 10Ti alloy. It will be interesting to examine the site occupancy of the 25Ti alloy to find out if there is a gradual change of ordering state. Preliminary experimental results on the 25Ti alloy[17], which is represented by the dashed OTL in Fig. 10, seem to support this gradual change of ordering state.

Phase Equilibrium

It has been shown in previous sections that annealing at various temperatures leads to the formation of the o-phase, ω-phase and A15 phase in these ternary B2 alloys. The ω-phase will not be discussed here since it has been proven to be a metastable phase. To compare present results with those reported in the literature, the compositions of all the phases in these alloys at 800°C and 1100°C are plotted over two isothermal sections of Nb-Al-Ti phase diagram at 700°C[18] and 1200°C[19], respectively (Fig. 10a,b). The following discussion will focus mainly on the phase equilibria rather than the exact locations of phase boundaries. It is seen that at 1100°C both the 10Ti and 25Ti alloys have B2/A15 two-phase structure and B2/A15 tie lines follow the same trend as those in the experimentally determined 1200°C isotherm (Fig. 10b). For the 40Ti alloy, only a single phase B2 structure was observed for temperatures above 1000°C. The phase equilibria of these alloys at high temperatures (1000°C and 1100°C) agree well with the literature.

The phase equilibria at temperatures lower than 1000°C are more complicated. At 800°C, although the B2/o-phase two phase equilibrium can be predicted by the proposed 700°C isotherm, the B2/o-phase tie line in the 40Ti alloy run in a different direction from that in the 700°C isotherm. It may be argued that the results obtained in this study at 800°C should not be compared to the 700°C isotherm. However, the discrepancy is so marked that it is unlikely to expect such a change to occur between these two temperatures. Another intriguing result is the three phase equilibrium observed in both the 10Ti and 25Ti alloys. The three phase field determined by the EDS in the 10Ti alloy is different from that of the 25Ti alloy. This should not occur, according to the phase rule, if

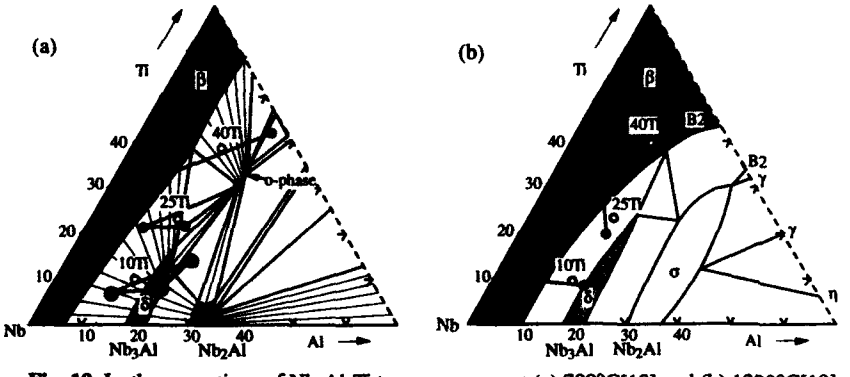


Fig. 10 *Isotherm sections of Nb-Al-Ti ternary system at (a) 700°C[18] and (b) 1200°C[19].*

the A15 phase and the o-phase observed in one alloy are the same as those observed in another alloy. However, there is no evidence supporting that the A15 phases and o-phases found in both alloys are different phases. Thus a possible explanation will be that one of the two three-phase equilibria is not a "true" equilibrium. The 25Ti alloy is more likely to have the true three-phase equilibrium since it has higher Ti content than the 10Ti alloy and its composition is very close to the proposed three phase field in Fig. 10a. This suggests that the o-phase observed in 10Ti alloy could be an intermediate phase which may redissolve during the formation of A15 phase.

SUMMARY

1. Three alloys with compositions of Nb-15Al-10Ti, Nb-15Al-40Ti and Nb-15Al-25Ti have single phase B2 structures in as-cast form.
2. A graphic method of describing the ordering state of ternary B2 compounds by the Ordering Tie Line (OTL) is introduced.
3. For the Nb-15Al-10Ti alloy, 800°C/500hr heat treatment leads to the formation of the o-phase and the A15 phase in the matrix. Heat treating at 900°C for less than 4 hours leads to the formation of metastable ω-phase, which will redissolve with the formation of the A15 phase after 500 hours heat treating.
4. The o-phase is the only second phase found in the Nb-15Al-40Ti alloy and is unstable at higher temperatures (>1000°C).
5. The Nb-15Al-25Ti alloy has B2/A15/o-phase three phase equilibrium at 800°C and B2/A15 two phase equilibrium at 1100°C.

ACKNOWLEDGMENTS

This work has been supported by the Office of Naval Research, Dr. George Yoder as Program Manager.

REFERENCES

1. J. Shyue, Ph.D. Thesis, The Ohio State University (1992).
2. J. Shyue, D.-H. Hou, S.C. Johnson, M. Aindow and H.L. Fraser, in "High Temperature Ordered Intermetallic Alloy V", MRS Proceedings, **288**, edited by I. Baker et al., Pittsburgh, PA(1992)243.
3. J. Shyue, D.-H. Hou, S.C. Johnson, M. Aindow and H.L. Fraser, in "High Temperature Ordered Intermetallic Alloy V", MRS Proceedings, **288**, edited by I. Baker et al., Pittsburgh, PA(1992)573.
4. J. Shyue, D.-H. Hou, M. Aindow and H.L. Fraser, *Materials Sci. Eng. A* ,**170**, (1993)1.
5. J.C.H. Spence and J. Taftø, *J. Microscopy* , **130**, (1983)147.
6. E.S.K. Menon, P.R. subaramaniam and D.M. Dimiduk, *Scripta Metall.* , **27**, (1992)265.
7. D.-H. Hou, I.P. Jones and H.L. Fraser (in preparation).
8. D. Banerjee, A.K. Gogia, T.K. Nandi and V.A. Joshi, *Acta metall.* , **36**, (1988)871.
9. L.A. Bendersky, W.J. Boettinger and A. Roytburd, *Acta metall.* , **39**, (1991)1959.
10. D.-H. Hou, Ph.D. Thesis (in preparation), The Ohio State University
11. D.L. Moffat and D.C. Larbalestier, *Met. Trans. A.* , **19A**, (1992)1677.
12. R. Strychor, J.C. Williams and W.A. Soffa, *Met. Trans. A* , **19A**, (1988)225.
13. R.A. Swalin, *Thermodynamics of Solids* (John Wiley & Sons, Inc., 1972),pp. 153-154.
14. D. Banerjee, T.K. Nandy and A.K. Gogia, *Scripta Metall.* , **21**, (1987)597.
15. L.A. Bendersky, W.J. Boettinger, B.P. Burton and F.S. Biancaniello, *Acta Metall.* , **38**, (1990)931.
16. S. Naka, M. Thomas, M. Marty, G. Lapasset and T. Khan, in "Structural Intermetallics", Eds. R. Darolia et al., Inter. Symp. Structural Intermetallics (Champion, PA, 1993), pp. 647.
17. S.-S. Yang, D.-H. Hou and H.L. Fraser, *unpublished work* , (1993)
18. U.R. Kattner and W.J. Boettinger, *Mat. Sci. Eng.* , **152**, (1992)9.
19. S. Das, T.J. Jewett and J.H. Perepezko, in "Structural Intermetallics", Eds. R. Darolia et al., Inter. Symp. Structural Intermetallics (Champion, PA, 1993), pp. 35.

EFFECTS OF PROCESSING AND PROLONGED HIGH TEMPERATURE EXPOSURE ON THE MICROSTRUCTURE OF Nb-1Zr-C SHEET

Mehmet Uz* and R. H. Titran**
*Chemical Engineering Department, Lafayette College, Easton, PA 18042
**NASA Lewis Research Center, MS 49-1, Cleveland, OH 44135

ABSTRACT

High temperature stability of the microstructure of Nb-1Zr sheet containing 0.1 and 0.06 wt.%C was studied as affected by processing and prolonged 1350-K exposure with and without applied stress. Sheets were fabricated by cold rolling bars that were single-, double- or triple-extruded at 1900 K. Creep samples were double-annealed (1 h @ 1755 K + 2 h @ 1475 K) prior to testing at 1350 K for 10,000 - 34,500 h. The microstructures of the as-cast, extruded, rolled, DA and crept samples were characterized using various metallographic and analytical methods. The precipitates were rather coarse Nb_2C initially, but transformed to finer (≤ 1 μm) carbides of (Zr,Nb)C with each subsequent high temperature process. The grain size, and the relative amount and morphology of (Zr,Nb)C were found to be affected by the number of extrusions and to some extent by C-content. However, the microstructures of all the crept samples were similar with (Zr,Nb)C distributed throughout the matrix indicating that prolonged exposure to 1350 K gave rise to complete transformation of Nb_2C to (Zr,Nb)C regardless of the processing history. These and other observations are presented with the emphasis on the correlation between processing, microstructure and creep properties.

INTRODUCTION AND BACKGROUND

Advanced power systems with a nuclear reactor as the primary heat source are being developed to provide electricity for future space missions. One of the critical concerns is the selection of the proper materials to meet the rather stringent design requirements of the reactor system. These include a full-power (100 kW) operating life of 7 years at 1350-1450 K and 5-25 MPa in a liquid alkali metal environment with total creep strain of less than 2%[1,2]. Nb-Zr alloys with and without C were selected over other refractory metal alloys primarily because of their resistance to liquid alkali metal corrosion, ease of fabrication and relatively low densities. In particular, Nb-1Zr (all compositions in wt.%) was chosen for ground demonstration of the power system[3] and Nb-1Zr-0.1C, an alloy developed in 1960s[4], was suggested to provide additional design margins[5]. Reactor test loops with components made from both alloys have been tested successfully in liquid lithium for up to 3200 hours[6]. However, recent work[7-10] showed that the creep resistance of the precipitate-hardened Nb-1Zr-C alloys is superior to that of the solid solution-strengthened Nb-1Zr. Based upon weight limits, it was also clear that a Nb-1Zr-C alloy must be used in the parts of the power system where the stresses are expected to approach or exceed 10 MPa at 1350 K when a service life of 7 years or more is required[10].

The strength and creep resistance of Nb-Zr-C alloys is due to the carbides of Nb and/or Zr; therefore, it is important to have a complete understanding of their precipitation sequence, morphology and high temperature stability. A number of studies have been reported on microstructural characterization of the Nb-Zr-C alloys[11-23], but only a few investigated the effects of processing and long-term exposure to elevated temperatures[10,22,23]. This paper deals with the characterization and long-term stability of the microstructure of Nb-1Zr sheets containing 0.06 and 0.1C as affected by processing and carbon content with the emphasis on precipitate composition and morphology.

Mat. Res. Soc. Symp. Proc. Vol. 322. ©1994 Materials Research Society

EXPERIMENTAL

Samples were taken from the materials before and after each process, and the condition of each as examined in this study is listed in Table I. Uniaxial creep tests were conducted on 1-mm thick sheets fabricated from vacuum arc-melted (VAM) ingots by a combination of hot extrusion and cold rolling operations as indicated. Two Nb-1Zr-0.06C samples were creep tested, one in double-annealed (DA) and the other in double-annealed and aged (DA/AGE) condition. A sample from each of the three Nb-1Zr-0.1C sheets was also creep tested after the double-anneal heat treatment. All the creep tests were carried out in vacuum (10^{-6} Pa or better pressure) at 1350 K for times ranging from about 10,000 h to 34,500 h. The ends (E) of each of the crept samples were assumed to be heat treated without applied stress, because the regions beyond the grips of the uniaxial creep samples underwent no measurable deformation. This allowed the assessment of the effect of stress on the microstructure during high temperature exposure.

The as-received samples were chemically analyzed to verify initial composition. Additionally, all the heat-treated and crept samples were analyzed to monitor the loss or pick up of interstitial impurities (O, N, C).

Table I. Processing history and condition of each sample from sheets of Nb-1Zr-0.06C (LC-samples) and Nb-1Zr-0.1C (064-samples).

SAMPLE	NUMBER OF EXTRUSIONS[a]	HEAT TREATMENT/CONDITION
LC	1	AS COLD ROLLED
LC-DA	1	DA[d]
LC-DA10(E)[b]	1	DA + 34,500 h @ 1350 K
LC-DA10(M)[c]	1	DA + 34,500 h @ 1350 K and 10 MPa
LC-DA/AGE	1	DA + AGE[e]
LC-DA/AGE10(E)	1	DA + AGE + 32,500 h @ 1350 K
LC-DA/AGE10(M)	1	DA + AGE + 32,500 h @ 1350 K and 10 MPa
064-INGOT		VACUUM ARC-MELTED INGOT
064A	1	AS COLD ROLLED (96%)
064A-DA	1	DA
064A-DA34(E)	1	DA + 18780 h @ 1350 K
064A-DA34(M)	1	DA + 18780 h @ 1350 K and 34.5 MPa
064B	2	AS COLD ROLLED (88%)
064B-DA	2	DA
064B-DA34(E)	2	DA + 15460 h @ 1350 K
064B-DA34(M)	2	DA + 15460 h @ 1350 K and 34.5 MPa
064C	3	AS COLD ROLLED (60%)
064C-DA	3	DA
064C-DA34(E)	3	DA + 9950 h @ 1350 K
064C-DA34(M)	3	DA + 9950 h @ 1350 K and 34.5 MPa

[a] Number of hot (1900 K) extrusions prior to cold rolling of the sheet bars.
[b] (E): Low-stress end portions of crept sample.
[c] (M): Stressed gage section of crept sample. Total strain was <0.3% in each.
[d] DA: Double-anneal, 1h @ 1755 K + 2h @ 1475 K, furnace-cooled after each step.
[e] AGE: Heat treatment of 1000 h @ 1350 K followed by furnace cooling.

The sheet samples were examined in the as-polished condition by light microscopy and scanning electron microscopy (SEM) for precipitate morphology and distribution. The polished specimens were also etched by a solution of 30 ml lactic-15 ml nitric-5 ml hydrofluoric acids and then examined by light microscopy for grain size. A lineal intercept method[24] was used to determine the grain size. Phase extraction was performed on each specimen listed in Table I using a solution of 900 ml methanol-100 ml bromine-10 g tartaric acid with platinum as the catalyst. The residue obtained from each was analyzed by (1) x-ray spectroscopy for precipitate identification and (2) an inductively-coupled plasma (ICP) method for Nb and Zr contents. The double-annealed samples from the Nb-1Zr-0.1C sheets were also examined by transmission electron microscopy (TEM) to verify the results from X-ray analysis of the residue. Energy-dispersive X-ray spectroscopy (XEDS) using SEM was also performed on various residue samples to verify the trends observed from the ICP results.

RESULTS AND DISCUSSION

Chemical Analysis and Metallography

The chemical composition and grain size of the samples are given in Table II. These together with the microstructural observations are discussed below.

Table II. Chemical analysis and grain size for Nb-1Zr-0.06C (LC-) and Nb-1Zr-0.1C (064-) sheet samples.

SAMPLE	CHEMICAL COMPOSITION (wt.%)				GRAIN SIZE	ASPECT
	O[a]	N[a]	C[b]	Zr[c]	(μM)	RATIO
LC	0.0078	0.0053	0.0630	0.90		
LC-DA	0.0034	0.0050	0.0500	0.90	25±4	1-3
LC-DA/AGE	0.0031	0.0030	0.0600	0.90	25±1	1-2
LC-DA10(E)	0.0080	0.0032	0.0640	0.90	21±3	1-2
LC-DA10(M)	0.0430	0.0026	0.0620	0.90	26±1	1-2
LC-DA/AGE10(E)	0.0120	0.0040	0.0640	0.90	27±2	1-2
LC-DA/AGE10(M)	0.0270	0.0035	0.0610	0.90	29±3	1-2
064-INGOT	0.0050	0.0025	0.0910	0.96		
064A	0.0035	0.0025	0.0900	0.93		
064A-DA	0.0028	0.0019	0.0921	0.95	110±14	1-2
064A-DA34(E)	0.0133	0.0026	0.0920	0.95	31±2	1-2
064A-DA34(M)	0.0220	0.0044	0.0980	0.95	32±4	1-2
064B-DA	0.0033	0.0022	0.0914	0.95	69±7	1-3
064B-DA34(E)	0.0176	0.0046	0.0890	0.95	39±4	1-2
064B-DA34(M)	0.0217	0.0040	0.0860	0.95	42±5	1-2
064C-DA	0.0022	0.0009	0.0944	0.95	32±3	1-10
064C-DA34(E)	0.0740	0.0079	0.0920	0.95	71±10	1-3
064C-DA34(M)	0.0420	0.0113	0.0870	0.95	79±7	1-3

[a] Inert gas fusion method.
[b] Combustion extraction method.
[c] Inductively-coupled plasma (ICP) method.

Chemical Analysis: Table II shows that there was some decrease in the O-content upon double-anneal of all the samples, and this was accompanied by a decrease in C-content in LC-DA. These losses may have been in the form of CO and/or CO_2 during the heat treatment. However, all the samples picked up O during the creep testing at 1350 K. In general, this contamination appeared to be higher in the middle regions as compared to the ends of the crept samples. The lack of oxides in phase-extracted residue indicates that O was in solid solution in the samples. There was no significant change in C or N contents during the tests. Given the long testing periods, the extent of contamination can be considered minimal.

As-Received Samples: The as-cast, as-extruded and as-rolled microstructures in Fig. 1 were typical of the other similar samples. Fig. 1(a) shows that the coarse precipitates were distributed throughout the matrix and somewhat continuously along the grain boundaries of the cast sample. Most of these precipitates were over 10 μm along their major axes. Fig. 1(b) shows that 4:1 extrusion at 1900 K caused the precipitates to break down, and align in the extrusion direction; however, needle-like precipitates, similar to those in the as-cast sample, were also present. The cold-rolled samples (Figs. 1(c,d)) had microstructures with highly-deformed grains and precipitates aligned in the rolling direction. The precipitates were more discrete and rounded , and varied in size from less than 1 μm to over 5 μm. It is evident that marked changes in precipitate morphology and distribution took place during the operations used in sheet fabrication.

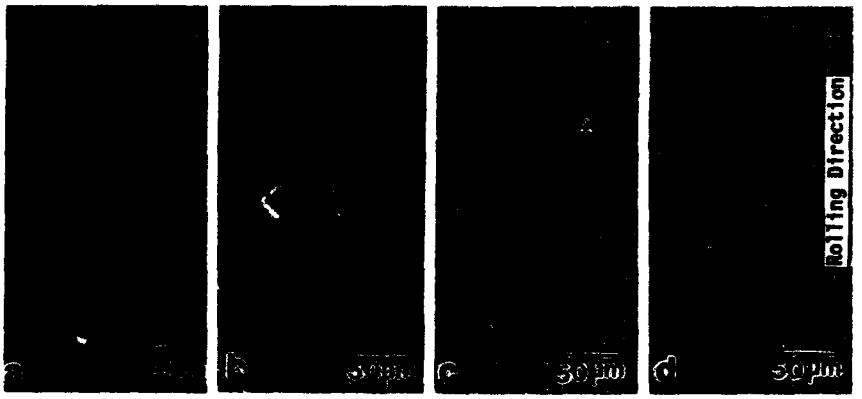


Figure 1. Microstructures of Nb-1Zr-0.1C alloy samples: (a) as-cast, secondary-electron SEM image, as-etched; (b) single-extruded bar, optical, differential interference contrast (DIC), as-polished, (c) 064A: as-rolled sheet from single-extruded bar, optical, DIC, as-polished; (d) the same as (c), but also etched.

Annealed Samples: Fig. 2(a) shows the microstructure of the double-annealed Nb-1Zr-0.06C sample (LC-DA) which appeared recrystallized. The grains were nominally equiaxed with an aspect ratio of less than 2 and an average grain size of about 25 μm (Table II). The double-annealed and aged sample (LC-DA/AGE) was very similar in appearance to Fig. 2(a) indicating ageing of LC-DA at 1350 K for 1000 h had no significant effect on its structure. However, there were noticeable differences among the microstructures of the double-annealed samples from the single-, double- and triple-extruded Nb-1Zr-0.1C sheets as are evident from Figs. 2(b-d) and Table II. Both 064A-DA and 064B-DA had relatively equiaxed grains with

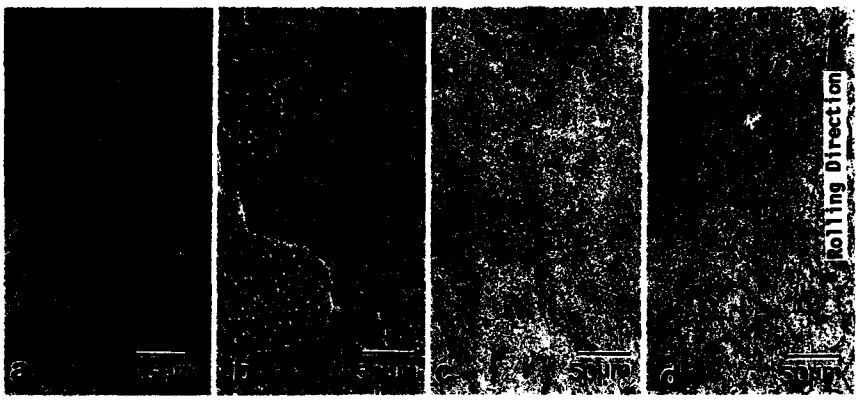


Figure 2. Double-annealed (DA: 1 h @ 1755 K and 2 h @ 1475 K) microstructures of samples from (a) Nb-1Zr-0.06C sheet LC-DA, (b) single-extruded Nb-1Zr-0.1C sheet 064A-DA, (c) double-extruded Nb-1Zr-0.1C sheet 064B-DA, and (d) triple-extruded sheet 064C-DA. All as-polished and etched, DIC.

an aspect ratio of less than 3 indicating full recystallization, but 064C-DA had mostly elongated grains with aspect ratios varying from 1 to nearly 10. The average grain size of these samples were approximately 112, 69 and 32 μm for 064A-DA, 064B-DA and 064C-DA, respectively. These observations indicate that the degree of recrystallization and average grain size decreased with increased number of extrusions. This may be due to the marked difference in the percent cold work (%CW) in the as-rolled sheets Nb-1Zr-0.1C (Table I). The %CW in 064C (66%) was much smaller than that in either of the 064A and 064B (96 and 88%, respectively). This would lead to lower stored energy and driving force for complete recrystallization. Another possible explanation for the highly elongated grains in 064C-DA may be that the precipitates stopped the growth in the transverse direction. However, this should have been, but was not, the case in other samples. Regardless of the apparent differences in their microstructures, the precipitates, varying in size (from 1 to about 5 μm), were finely distributed throughout the matrix and along the grain boundaries in all the samples. Also, the precipitates appeared to be more abundant in the 0.1-C samples than in the 0.06-C samples as expected.

Crept Samples: Fig. 3(a-d) show the microstructures of the gage sections of samples LC-DA10, 064A-DA34, 064B-DA34 and 064C-DA34. The microstructure of the gage and low-stress end sections of each sample were similar. This was not unexpected, because the total strain in each of the crept samples was negligibly small (< 0.3%). A comparison of Fig. 3(a) with Fig. 2(a) shows that the microstructure, including the grain size (Table II) of LC-DA did not change significantly during exposure at 1350 K for over 30,000 h with or without the applied stress. This was also the case for LC-DA/AGE indicating that ageing at 1350 K for 1000 h following the double-anneal did not deteriorate the excellent high-temperature stability of the microstructure of the Nb-1Zr-0.06C alloy.

In contrast to the 0.06-C sheets, changes during the creep testing of the samples from the 0.1-C sheets were more apparent as can be seen from a comparison of their respective microstructures in Figs. 2 and 3 and the grain size data in Table II. The grains of the crept samples from the single- and double-extruded



Figure 3. Microstructures of the gage sections of the samples after creep testing at 1350 K and (a) 10 MPa for 34,500 h (LC-DA10(M)), (b) 34.5 MPa for 18,780 h (064A-DA34(M)), (c) 34.5 MPa for 15,460 h (064B-DA34(M)), and (d) 34.5 MPa for 9950 h (064C-DA34(M)). All as-polished and etched, DIC.

sheets (064A-DA34 and 064B-DA34, respectively) were still relatively equiaxed, but appeared to have undergone noticeable refinement in size. The decrease in the grain size upon exposure to 1350 K and 34.5 MPa was from about 110 to 30 μm for 064A-DA after nearly 19,000 h, and from roughly 70 to 40 μm for 064B-DA after about 15,500 h. While a decrease in grain size during thermal exposure is unusual, it is possible that the low-angle boundaries were not revealed by etching in the double-annealed samples from these sheets. Subsequent long-time exposure to 1350 K, however, could have resulted in the exposure of such boundaries as a result of solute segregation and carbide precipitation. The changes in the microstructure of 064C-DA were more as expected upon creep testing for nearly 10,000 h at 1350 K. (Figs. 2(d) and 3(d)). The grains were highly-elongated with an average size of about 31 μm prior to the test, but became fairly equiaxed with over a 2-fold increase in size (Table II). This would indicate that grain growth, especially in the transverse direction, occurred in this sample during the prolonged exposure to 1350 K.

In order to verify that the protrusions and/or pits in the as- polished and/or etched samples were indeed precipitates rather than optical artifacts, the samples were also examined via an SEM. Representative results can be seen from Fig. 4 which shows the back-scattered electron images of samples from the single-extruded sheet before and after creep testing, (064A-DA and 064A-DA34(M), respectively). The precipitates, which are carbides of Nb and/or Zr, appear darker in these images, because they have a lower average atomic number than the Nb-Zr matrix. While the carbides varied in size, and were rather coarse and somewhat continuous along the grain boundaries of 064A-DA, they were a micrometer or less and finely-distributed throughout the matrix in 064A-DA34(M).

Work on Phase-Extracted Residue

The results of the analyses of the phase-extracted residues are tabulated in Table III. The precipitates in the as-rolled Nb-1Zr-0.06C (LC) sheet were orthorhombic Nb_2C, and the residue analyzed nearly all Nb. In the double-annealed sample LC-DA, some cubic phase, (Zr,Nb)C was detected together with Nb_2C,

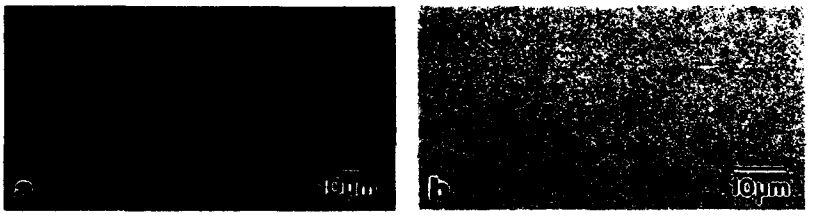


Figure 4. Back-scattered SEM images of samples from single-extruded Nb-1Zr-0.1C sheet (a) as double-annealed (064A-DA), and (b) after creep testing at 1350 K and 34.5 MPa for 18,780 h (064A-DA34(M)).

and this was accompanied with a very small increase in Zr/Nb ratio. The only phase detected in LC-DA/AGE was the cubic carbide with a_o of about 0.460 nm indicating that ageing of the double-annealed sample at 1350 K for 1000 h resulted in conversion of all Nb_2C to (Zr,Nb)C. This was also accompanied by a significant increase in Zr/Nb ratio from ~0.04 to ~0.6. The only phase detected in the crept samples from the Nb-1Zr-0.06C alloy was (Zr,Nb)C with a Zr/Nb ratio of greater than 1. This indicates that exposure to 1350 K for over 30,000 h did not change the phase make-up of LC-DA/AGE, while it resulted in complete transformation of Nb_2C to (Zr,Nb)C in LC-DA, possibly during the first 1000 h. The changes in the phase make up of Nb-1Zr-0.1C samples (064- in Table III) during high temperature exposure were similar to those of Nb-1Zr-0.06C. The only type of precipitate detected in the residue of the as-cast ingot was Nb_2C which again analyzed nearly all Nb indicating that Zr was in solid solution. High temperature extrusions prior to cold rolling, subsequent double-anneal heat treatment and prolonged exposure to 1350 K evidently resulted in increasing transformation of Nb_2C to (Zr,Nb)C. This is evident from the increased detection of the cubic phase and the accompanying increase in the Zr/Nb ratio along the process path of each of the samples in Table III. Again, the only phase detected in the residue from the crept samples was the cubic (Zr,Nb)C indicating complete transformation of Nb_2C to the more stable (Zr,Nb)C. Another noteworthy trend observed was that the Zr/Nb ratio, which is an indicator of the relative abundance of the cubic carbides, increased with increasing number of extrusions (Table III). This trend was reinforced by also analyzing the residue from the double-annealed Nb-1Zr-0.1C sheets by energy-dispersive x-ray spectroscopy using SEM as can be seen from the last column in Table III. Furthermore, the identification of the precipitates by x-ray and chemical analysis of the residue has been verified by TEM studies[23]. In 064A, the precipitates were determined to be orthorhombic Nb_2C regardless of size which varied from 1 to about 5 μm. In the double annealed samples, the coarser precipitates were again Nb_2C, but the finer precipitates (1 μm or less) were cubic (Zr,Nb)C. These cubic carbides were coherent with the matrix and were finely-distributed in the samples exposed to 1350 K for very long times.

The lattice parameters, a_o, of the cubic phase in Table III, 0.450-0.468 nm fall between the a_o values of NbC (≈0.447 nm) and ZrC (≈0.470 nm). As both carbides have FCC crystal structures, it is probable that the cubic precipitates are solid solutions of NbC and ZrC. As the phase transformation from Nb_2C to (Zr,Nb)C increased, the Zr/Nb ratio in the residue of a sample also increased and was generally accompanied by an increase in the a_o value of the cubic carbide. This would be expected, because a_o(Zr)>a_o(Nb) and a_o(ZrC)>a_o(NbC). Similar a_o values and Zr/Nb ratios for (Zr,Nb)C as those in Table III have also been reported in the literature[11,18-23]. It has also been suggested that the solid

Table III. Results of the analysis of phase-extracted residue from Nb-1Zr-0.06C (LC-) and Nb-1Zr-0.1C (064-) samples.

SAMPLE	X-RAY ANALYSIS				Zr/Nb RATIO	
	PHASES	LATTICE PARAMETERS (nm)			CHEM ANALYSIS	SEM[a] XEDS
		a_o	b_o	C_o		
LC	Nb_2C	1.09	0.492	0.311	1/99	
	(Zr,Nb)C	0.468				
LC-DA	Nb_2C				4/96	
	(Zr,Nb)C	0.458				
LC-DA10(E)	(Zr,Nb)C	0.465			72/27	
LC-DA10(M)	(Zr,Nb)C	0.464			63/37	
LC-DA/AGE10	(Zr,Nb)C	0.460			38/62	
LC-DA/AGE10(E)	(Zr,Nb)C	0.465			60/40	
LC-DA/AGE10(M)	(Zr,Nb)C	0.465			56/44	
064-INGOT	Nb_2C	1.092	0.498	0.310	2/98	
064A	Nb_2C	1.092	0.497	0.311	3/97	
	(Zr,Nb)C	0.453				
064A-DA	Nb_2C	1.09	0.48	0.29	10/90	
	(Zr,Nb)C	0.450				11/89
064A-DA34(E)	(Zr,Nb)C	0.454			58/42	
064A-DA34(M)	(Zr,Nb)C	0.454			54/46	
064B	Nb_2C	1.09	0.499	0.311	14/96	
	(Zr,Nb)C					
064B-DA	Nb_2C				37/63	
	(Zr,Nb)C	0.459				30/70
064B-DA34(E)	(Zr,Nb)C	0.456			63/37	
064B-DA34(M)	(Zr,Nb)C	0.454			57/44	
064C	Nb_2C	1.09	0.497	0.311	25/75	
	(Zr,Nb)C					
064C-DA	(Zr,Nb)C	0.459			63/37	71/29
064C-DA34(E)	(Zr,Nb)C	0.459			72/28	
064C-DA34(E)	(Zr,Nb)C	0.458			85/15	

[a] Average of analysis of 4 areas ranging in size 250x250 μm to 5x5 μm.

solutions of NbC and ZrC yield non-stoichiometric carbides of $(Zr,Nb)C_x$ or $Zr_xNb_{1-x}C_y$ with x and y varying between 0.8 and 0.98, but this could not be verified in this study. However, it is evident from the results of this study that the finely distributed cubic carbides of (Zr,Nb)C form as a result of transformation from Nb_2C during thermomechanical processing and/or exposure to elevated temperatures. This transformation has been reported to be complete from about 100 h[19] to over 10,000 h[18] of ageing at temperatures over 1300 K. The results in this study show that the transformation of Nb_2C to the stable monocarbide was complete within the first 1000 h of exposure to 1350 K in the Nb-1Zr-0.06C alloy. In the Nb-1Zr-0.1C sheets, it appeared to be completed during the double-anneal in the triple-extruded sheet, 064C-DA, and may have been completed in the others early during the exposure to 1350 K with or without applied stress.

CONCLUSIONS

The results presented in this paper clearly show that the rather coarse Nb_2C, which is orthorhombic and forms during casting of Nb-1Zr-C alloys, increasingly transforms to submicron-sized cubic (Zr,Nb)C during thermomechanical processing and/or high temperature exposure. The transformation of Nb_2C to (Zr,Nb)C was essentially complete in a Nb-1Zr-0.06C sheet within 1000 h at 1350 K following a double-anneal heat treatment (1 h @ 1755 K + 2 h @ 1475 K). The phase transformation was complete also during the double-anneal in the triple-extruded sheet and during the subsequent 1350-K exposure in the single- and double-extruded sheets from the Nb-1Zr-0.1C alloy. Once formed, the cubic carbides were extremely stable giving the alloy excellent microstructural stability during prolonged (10,000 - 34,500 h) exposure to 1350 K with or without applied stress.

Increasing the C-content from 0.06 to 0.1 wt.% resulted in an increase of the amount of precipitates as be expected. The multiple extrusion of Nb-1Zr-0.1C alloy at 1900 K affected the double-annealed microstructures, but appeared to have no end-benefit concerning high temperature stability. The microstructures of the samples from the single-, double - and triple-extruded sheets all appeared similar with the cubic phase finely-distributed throughout the matrix.

ACKNOWLEDGEMENTS

This work was performed by the NASA Lewis Research Center for the U.S. DOE Office of Nuclear Energy and the Strategic Defense Initiative Office under interagency agreement DE-a103-86SF16310.

REFERENCES

1. R.H. Cooper, Jr., in Refractory Alloy Technology for Space Nuclear Power Applications, edited by R. H. Cooper and E. E. Hoffman, (Technical Information Center, US Department of Energy, Oak Ridge, TN 1984) pp. 14-17.

2. R. H. Titran, Advanced Materials and Processes 142(5), 34-41(1992).

3. G. C. Kruger, S. Vaidyanathan, N. Deane, R. Protsik, R.E. Murata, in SP-100 Reactor Design, (22nd Intersociety Energy Conversion Engineering Conference Proc. 1, AIAA, New York, 1989) pp. 419-423.

4. E.J. DelGrosso, C.E. Carlson and J.J. Kaminsky, JLCM 12, 173-201(1967).

5. W. Dokko, JPL Report No. JPL D-1948, Jet Propulsion Lab., Pasadena, CA, 1984.

6. A. J. Bryhan and R. C. Chan, JOM 45(6), 50-53(1993).

7. R.H. Titran, NASA TM-100142, NASA LeRC, Cleveland, OH, 1986.

8. R.H. Titran, T.J. Moore and T.L. Grobstein, NASA TM-89834, NASA LeRC, Cleveland, OH, 1987.

9. R.H. Titran, NASA TM-102390, NASA LeRC, Cleveland, OH, 1990.

10. Mehmet Uz and R.H. Titran, NASA TM-106319, NASA LeRC, Cleveland, OH, 1993.

11. J.T. Norton and A.L. Mowry, J. Metals 1(2), 133-136(1949).

12. F. B. Cuff, Jr., Report ASD-TDR-62-7, PART I, Wright Patterson AFB, OH, 1962.

13. R.T. Begley, R.L. Ammon, and R.Sticker, Report WADC-TR-57-344, PART VI, Wright Patterson AFB, OH, 1963.

14. F. Ostermann and F. Bollenrath, AFML-TR-66-259, Wright Patterson AFB, 1966.

15. F. Ostermann, J. Less-Common Metals, 25, 243-256(1971).

16. A.E. Kissil, P.A. Khandarov, A.D. Rapp, L.P. Onisenko, L.Z. Polyak, A.G. Arakelov and I.I. Maximow, Sov. Mater. Sci., 12, 640-643(1976), (Engl. Transl.)

17. V.B. Arsomosov, and E.V. Vasil'eva, Met. Sci. Heat Treat., 20,291-293(1978),

18. P.A. Khandarov, A.N. Luk'yanov, A.G. Arakelov, O.S. Tsvikilevich, E.M. Lyutyi and G.G. Maximovich, Sov. Mater. Sci., 14, 431-435(1978), (Engl. Transl.)

19. A.D. Korotayev, A.N. Tyumentsev, M.G. Glazunov, L.M. Dizhar, A.I. Yakushina, S.P. Semkin and T.I. Vitkovskaya, Phys. Met. Metallogr., 52, 128-135(1981).

20. G.K. Moiseev, N.A. Vatolin and S.K. Popov, Izv. Akad. Nauk SSSR, Neorg. Mater., 19(9), 1478-1483(1983). (Engl. Transl.)

21. T.L. Grobstein and R.H. Titran, NASA TM-100848, NASA LeRC, Cleveland, OH, 1986.

22. Mehmet Uz and R.H. Titran, NASA TM-103647, NASA LeRC, Cleveland, OH, 1991.

23. Mehmet Uz and R.H. Titran, 10th Symp. Nuclear Power and Propulsion, AIP Conf. Proc. 271, edited by M.S. El-Genk and M.D. Hoover, Albuquerque, NM 1993, pp. 69-83.

24. ASTM Standard E112, Annual Book of ASTM Standards 03.03, ASTM, Philadelphia, 120(1984).

MICROSTRUCTURES, DEFECTS AND DEFORMATION MECHANISMS IN VANADIUM MODIFIED Nb_3Al

L.S. SMITH, M. AINDOW AND M.H. LORETTO
IRC in Materials for High Performance Applications, and School of Metallurgy and Materials, The University of Birmingham, Edgbaston, Birmingham, B15 2TT, UK.

ABSTRACT

A transmission electron microscope study of the microstructure and defect structure in vanadium modified Nb_3Al and its deformation mechanisms is presented. Two alloys are examined in which 20 and 40 atomic % V is substituted for Nb. The former alloy exhibits a microstructure containing a stable A15 phase and a metastable B2 phase which transforms to A15 upon heat treatment. The A15 grains contain defects similar to those observed previously in binary Nb_3Al: i.e. large growth faults with $R=1/4\langle 012\rangle$ and dissociated dislocations with a separation of ≈15nm and $b=1/2\langle 001\rangle$ bounding a stacking fault with $R=1/2\langle 001\rangle$. The alloy containing 40 atomic % V consists only of an equilibrium B2 phase and exhibits greatly enhanced ductility. Slip occurs by the glide of dislocations with $b=\langle 111\rangle$ on {011}.

INTRODUCTION

The compound Nb_3Al has the A15 structure and is perhaps best known for its superconducting properties at liquid helium temperatures. It also exhibits many properties which are desirable for high temperature structural applications but their exploitation has, however, been prevented by the limited ductility of this compound at temperatures <900°C. This brittleness is thought to arise from an inadequate number of available slip systems. The slip systems which have been proposed are $\langle 100\rangle\{001\}$ [1] and $\langle 100\rangle\{012\}$ [2] but the operation of either or indeed both still yields only three independent slip systems and thus the von-Mises criterion [3] for general polycrystalline plastic deformation is not satisfied.

Previous studies have shown that alloying Nb_3Al with titanium can stabilise the B2 crystal structure and leads to greatly enhanced ductility [4]. The defects responsible for deformation in this B2 phase were pairs of partial dislocations each with $b=1/2\langle 111\rangle$ bounding ribbons of antiphase boundary (APB). It was found that these defects glide on {110}, {112} and {123} giving many combinations of independent slip systems. There are several other transition elements which have a significant but limited solubility in Nb_3Al [5], and of these, vanadium lies closest to titanium in the Pettifor diagram for A_3B stoichiometry [6]; thus it might be expected to have a similar effect when alloyed with Nb_3Al. In this paper we present a study of the microstructures, defects and deformation mechanisms in V-modified Nb_3Al and compare the results obtained with those for Ti-modified alloys.

EXPERIMENTAL PROCEDURE

Two Nb-V-Al alloys, both containing 25 at. % Al, and with V contents of 20 and 40 at.%, were studied. For both compositions, 500g ingots were prepared by plasma melting under an argon plus helium atmosphere, using elemental starting materials. Portions of each ingot were heat treated for 50 hours at 1500°C. Compression specimens 3mm in diameter and ≈ 8mm in length were deformed under vacuum at a strain rate of approximately 10^{-4} s^{-1}.

Discs for TEM specimens were polished mechanically to a thickness of 200-150μm and final thinning was achieved by twin jet electropolishing in a Tenupol 3 using a solution of 10% H_2SO_4 in methanol at -40°C and a voltage of 10V. The foils were examined in a Philips CM20T transmission electron microscope operating at an accelerating voltage of 200kV.

Mat. Res. Soc. Symp. Proc. Vol. 322. ©1994 Materials Research Society

RESULTS

The alloy containing 40 at.% V exhibited a microstructure containing only B2 grains in the as-cast state which, after heat-treatment, transformed partially to A15 giving a mixed B2+A15 microstructure. The alloy with 20 at.% V consisted of A15 precipitates in a B2 matrix in the as-cast condition and this transformed to a microstructure consisting only of A15 grains upon heat-treatment. Microchemical analyses revealed that the B2 and A15 grains in the as-cast 20 at.% V alloy had approximately the same composition, i.e. $Nb_{2.2}V_{0.8}Al$. The B2 phase in the heat treated alloy with 40at.% V was richer in V and depleted in Nb and Al when compared with the nominal composition of the alloy. Similarly the A15 phase is richer in Nb and depleted in V.

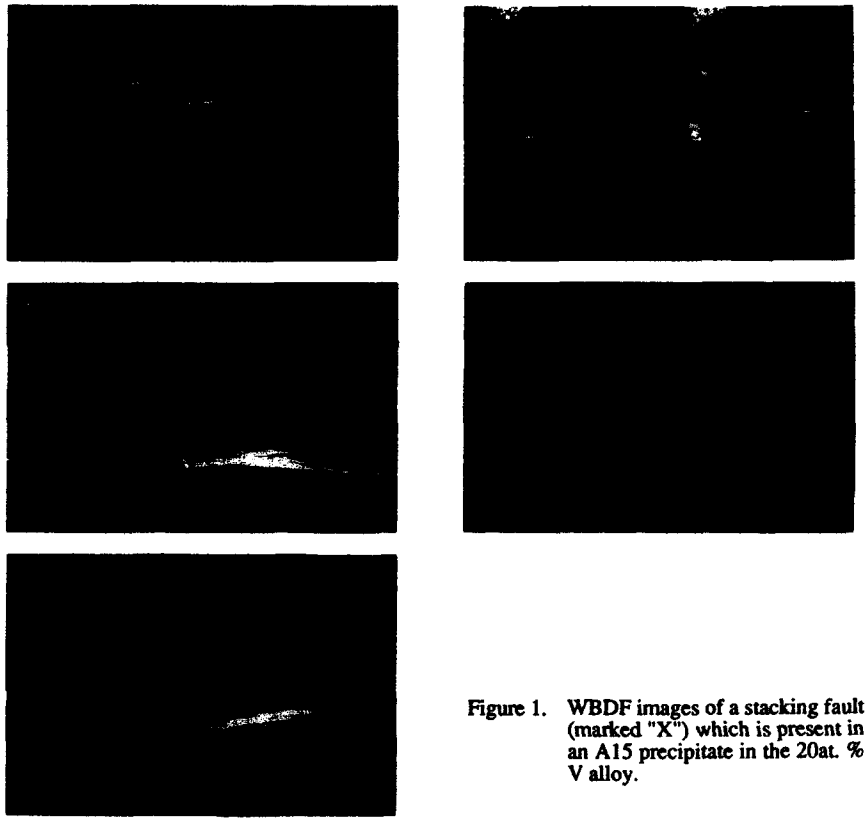


Figure 1. WBDF images of a stacking fault (marked "X") which is present in an A15 precipitate in the 20at. % V alloy.

Both alloys were compressed at a range of different temperatures in the as-cast and heat-treated states. The compressive yield stresses obtained are shown in Table 1. The as-cast 40 at.% V alloy contained precipitates with the A15 structure after deformation, whereas the 20 at.% V alloy consisted entirely of a fine grained (≈3μm) A15 phase. The 20 at.% V alloy compressed at 1000°C did not yield before the load limit of the deformation rig was reached and visible cracks were present after unloading.

Temperature	20 at.% V (as-cast)	20 at.% V (heat-treated)	40 at.% V (as-cast)	40 at.% V (heat-treated)
800°C	-	-	510 MPa	500 MPa
1000°C	>450 MPa	-	126 MPa	-
1200°C	147 MPa	151 MPa	61 MPa	-

Table 1. Compressive yield stresses of the two alloys in the as-cast and the heat-treated states.

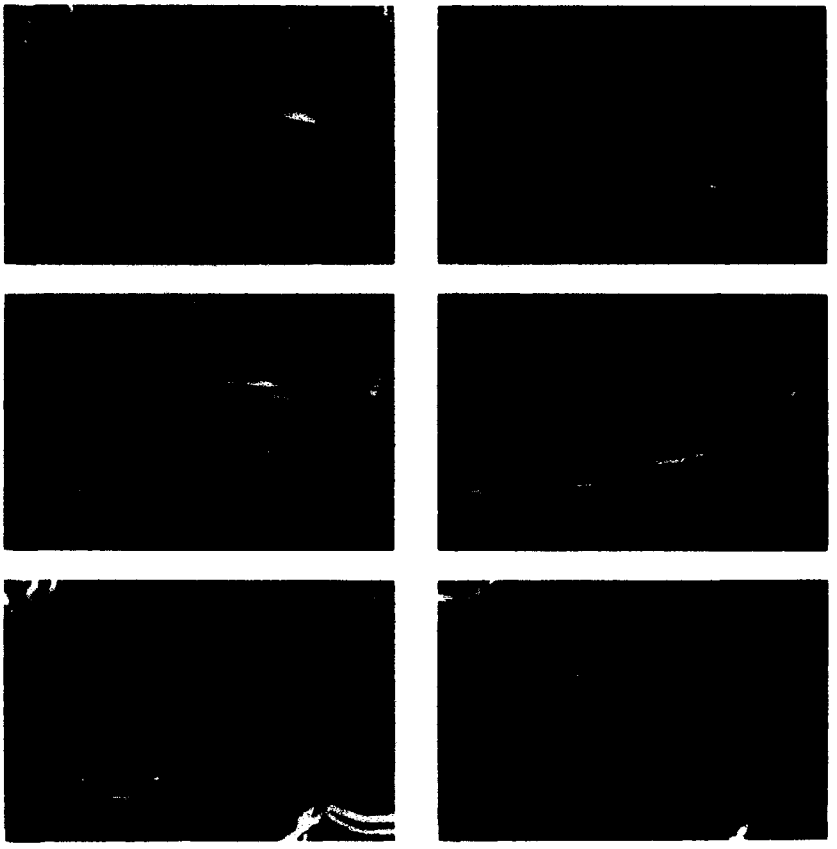


Figure 2. WBDF images of dissociated dislocations in the deformed 40at.% alloy.

The A15 grains in the 20 at.% V alloy, and the A15 precipitates in the heat-treated and the as-cast deformed 40 at.% V alloy contained a high density of stacking faults. Figs. 1(a-e) are a series of weak beam dark field (WBDF) micrographs from an A15 precipitate in the as-cast 20 at.% V alloy obtained with $\mathbf{g} = 210, 20\bar{1}, 0\bar{2}1, 020$ and 200, respectively. A single large fault lies on (001) and terminates at a partial dislocation (marked X in Fig. 1(a)). If the partial dislocation has a Burgers vector **b**, we assume that the displacement vector of the fault $\mathbf{R} = \mathbf{b} = [h\ k\ l]$. Both the dislocation and the fault are out of contrast for g=200 (Fig. 1(e)) so $\mathbf{g}.\mathbf{R} = 0$ and $h = 0$. For **g**

= 020 (Fig. 1(d)) only the fault is out of contrast indicating that g.R = integer. However, since both the fault and dislocation are in contrast for g=210 (Fig. 1(a)) then k=1/2. Similarly, both are again in contrast for g = 20$\bar{1}$ (Fig. 1(b)), so $l \neq$ integer. Analyses of faults in the alloy with 40 at.% V (both in the heat-treated and the as-cast deformed state) gave similar results.

Whilst the as-cast 20 at.% V alloy contains a very high density of the stacking faults described above, very few dislocations are present except in grain boundaries. In sharp contrast, when deformed this alloy contains no large stacking faults but a much higher density of dislocations. Figs. 2 (a-f) are a series of WBDF images of typical dislocations obtained with conditions g = 201, 120, 200, $\bar{2}00$, 0$\bar{2}$0 and 0$\bar{2}$1 respectively. The dislocations are present in pairs with a consistent separation of ≈15nm such as at position X marked in Fig. 2 (a). The dislocations are out of contrast for g = 0$\bar{2}$0 and 0$\bar{2}$1 (Figs. 2(e)&(f)) where g.b = 0 and hence the Burgers vectors of these dislocations are parallel to [100]. These dislocations are not part of a dipole since their apparent separation does not change on reversing the sign of g (Figs. 2(c)&(d)). Furthermore, for g = 120 weak stacking fault contrast is observed confirming that this feature is a pair of partial dislocations bounding a stacking fault. No stacking fault contrast is observed for g = 201 (Fig. 1(a)) indicating that g.R = 0. If we assume that b = R then both equal 1/2[100]. Stereographic analysis reveals that the partial dislocations lie within 5° of pure screw orientation. The cross product of the line direction with the direction of the line joining the points at which the partials terminate at the surface yields a habit plane of (0$\bar{1}$2). Many of the dislocations constrict at various points along their length and these correspond to positions where the habit plane changes from one {012} to another. One such feature is indicated by an arrow in Fig. 2(a).

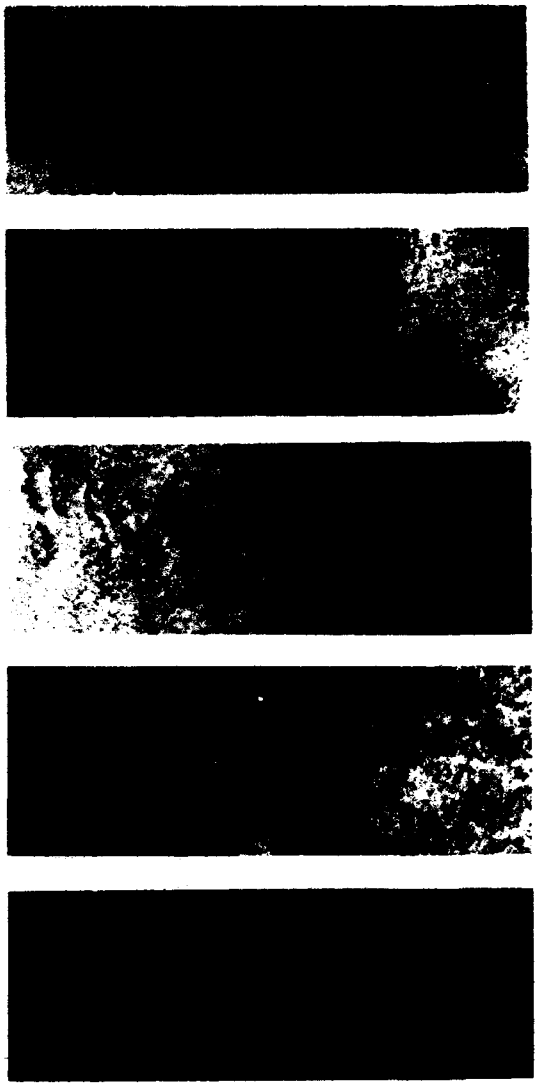


Figure 3. Images of a slip band in the 40at. % alloy (a-d) BF images; (e) DF (superlattice reflection)

Whilst the A15 grains in the deformed 40 at. % V alloy contain very few dislocations, the B2 grains contain a very high density of dislocations and these are present in pronounced slip bands. Figs. 3(a-d) are a series of bright field images obtained with $\mathbf{g} = 1\bar{1}0$, $\bar{1}10$, $10\bar{1}$, and $0\bar{1}1$, respectively, from a region containing part of a slip band in an as-cast specimen deformed at 800°C. The dislocations are out of contrast for $\mathbf{g} = \bar{1}10$ and $0\bar{1}1$ (Figs. 3(b)&(d)) and hence $\mathbf{b} // \bar{1}11$. A DF image obtained with a superlattice reflection with $\mathbf{g} = 100$ is shown in Fig. 3(e). Fine contrast is observed corresponding to thermal APB's but no additional contrast is revealed and thus no shear APB's are present between the dislocations. Furthermore, no splitting of the dislocations is apparent in WBDF images obtained with $\mathbf{g} = <110>$ and thus if these dislocations are partials, then the separation must be less than the ≈2nm resolution of this technique. The most likely Burgers vectors of these dislocations is thus $\mathbf{b} = [\bar{1}11]$. They are within 7° of screw orientation and stereographic analysis reveals that the slip plane is $(01\bar{1})$.

DISCUSSION

The B2 phase present in the 40 at.% V alloy appears to be stable indicating the existence of a B2 phase field at this composition. The B2 phase which is present in as-cast 20at.% V alloy transforms to A15 upon heat-treatment indicating that it is a 'quenched in' constituent. It has been suggested recently that, in binary Nb-Al alloys, the B2 phase exists as a metastable intermediate in the A2 to A15 transformation [7]. It therefore seems likely that this is also the case for Nb-V-Al alloys where there is an A2 to A15 transformation and thus the B2 phase at this composition could have been produced by a quench from either an A2 or a B2 phase field.

A high density of large stacking faults was observed in the A15 phases of the 20at.% V alloy and the deformed as-cast 40at.% V alloy. Although a complete analysis of these faults is not presented the displacement vector has been shown to be of the form $\mathbf{R}=<0\ 1/2\ l>$, where l is not an integer. It seems likely that these faults are simply *intrinsic growth* faults such as have been observed in binary Nb_3Al [8] with $\mathbf{R}=1/4<021>$. Such a fault could not be created by deformation and so those observed in the A15 precipitates of the deformed 40at.% V alloy must have formed during crystallisation. The defect microstructure present in the deformed 20at.% V alloy indicates that significant recovery has taken place. Many of the dissociated dislocations were observed to constrict and change their habit plane at various points along their length and thus they are effectively locked. Moreover, whilst no conclusions can be drawn as to the actual slip plane, it is clear that slip of dislocations with $\mathbf{b} // <100>$ on any plane $\{0\ k\ l\}$would give only three independent slip systems. This combination of dislocation locking and insufficient slip systems could help to account for the relatively high strength of this alloy and its brittle nature at <1000°C.

In contrast, the 40at.% V alloy deformed readily at lower temperatures although, in practice, deformation below 800°C was prevented by the limitations of the deformation apparatus. The alloy has a compressive yield stress at 800°C of ≈500 MPa and this is comparable with that of the B2 alloy Nb-40at.% Ti-15at.% Al (400-600MPa) and is much lower than that for binary Nb_3Al [4]. It is unusual for perfect dislocations to have a Burgers vector $\mathbf{b} = <111>$ in a compound with B2 structure. It would be expected that the elastic energy of these dislocations could be reduced by splitting into two partials with $\mathbf{b}=1/2<111>$ bounding an APB as has been observed in Ti modified Nb_3Al alloys [4]. That this is not the case implies that the ordering energy is high, preventing the formation of an APB. If this were the case in a conventional B2 alloy with stoichiometry AB it would be expected that slip would occur along <100> for which no A-B bonds are broken and thus order is not violated [9]. Indeed it is not clear why this should not occur in the 40at.% V alloy. It is worth noting that for the grain in Fig. 3 the compression axis was near [011] and thus the Schmidt factor would be favourable for the formation of slip bands with <010> dislocations. Thus the primary operating slip system is <111>{011} although further investigation is necessary to exclude the possibility of slip on {112} or {123}. We should note, however, that the observation of dislocation segments with screw character implies that it is the *edge* segments which are most mobile and therefore one would expect no cross-slip from one slip plane to another. Even if slip is restricted to {110}

only, there will still be many independent slip systems satisfying von Mises criterion and this could help to explain the greatly enhanced ductility observed in the 40at.% V alloy.

CONCLUSIONS

A microstructure consisting of an A15 plus a metastable B2 phase has been produced in Nb-20at.% V-25 at.% Al which transforms fully to A15 after heat-treatment. The compressive yield stress of this alloy is lower than that for Nb_3Al and it is expected that the as-cast structure exhibits improved toughness. An equilibrium B2 phase can be produced by increasing the V content to 40at.% and this greatly enhances ductility. Defects similar to those in Nb_3Al are observed in A15 phases. Large growth faults are present with a displacement vector of R=1/4<012>. Additionally ribbons of faults with R=1/2<100> are observed bounded by partial dislocations with b=1/2<100> with a separation of ≈15nm. Slip in the B2 phase occurs by the glide of perfect edge dislocations with **b** = <111> on {011}. This yields a sufficient number of slip systems to satisfy von Mises criterion explaining the enhanced ductility which is observed.

ACKNOWLEDGEMENTS

This work has been carried out with the support of SERC. The authors would like to thank Dr. J. Shyue and Prof. H. L. Fraser for many helpful discussions. Financial support for LSS to attend this meeting was provided by the Institute of Physics EMAG group, C. R. Barber Trust Fund and the Institute of Materials Andrew Carnegie Grant Scheme.

REFERENCES

[1] T.N. Marieb, A.D. Kaiser, S.R. Nutt, D.L. Anton and D.M. Shah, in High Temperature Intermetallic Alloys IV, edited by L.A. Johnson, D.P. Pope and J.O. Steigler (Mater. Res. Soc., 213, Pittsburgh, PA, 1991) p.141.
[2] M. Aindow, J. Shyue, T.A. Gaspar and H.L. Fraser, Phil. Mag. Lett., 64, 59 (1991).
[3] R. von Mises, Z. Angew. Math. Mech., 8, 161 (1928).
[4] J. Shyue, D-H Hou, S. Johnson, M. Aindow and H. Fraser, in High Temperature Intermetallic Alloys V, edited by I. Baker, R. Darolia, J.D. Whittenberger and M.H. Yoo (Mater. Res. Soc., 288, Pittsburgh, PA, 1993) p.573. J. Shyue, D-H. Hou, M. Aindow and H.L. Fraser, J. Mat. Sci. and Eng. 170: 1 (1993).
[5] D.L. Anton and D.M. Shah, in Intermetallic Compounds: Structure and Mechanical Properties, edited by O. Izumi (Sendai, Japan, 1991) p. 379.
[6] D.G. Pettifor, J. Phys. C, 19, 285 (1986).
[7] H. Kohmoto, J. Shyue, M. Aindow and H.L. Fraser, Scripta Met. 29, 1241, (1993)
[8] L.S. Smith, T-T. Cheng and M. Aindow, in High Temperature Intermetallic Alloys V, edited by I. Baker, R. Darolia, J.D. Whittenberger and M.H. Yoo (Mater. Res. Soc., 288, Pittsburgh, PA, 1993) p.263.
[9] W.A. Rachinger and A.H. Cottrell, Acta Met., 4, 109 (1956).

PART VII

Refractory Alloys: Multiphase Materials and Composites

PROPERTIES OF MICROLAMINATED INTERMETALLIC-REFRACTORY METAL COMPOSITES

R. G. ROWE*, D. W. SKELLY*, M. LARSEN*, J. HEATHCOTE**, G. LUCAS** AND G. R. ODETTE**
* GE Corporate Research and Development , Schenectady, NY 12309
** University of California at Santa Barbara, Materials Department, Santa Barbara, CA

ABSTRACT

Microlaminated composites of Nb_3Al-Nb and Cr_2Nb-Nb(Cr) were synthesized by high rate magnetron sputtering. Both composites were stable at elevated temperatures. A Cr_2Nb-Nb(Cr) composite with 2 μm metal and intermetallic layers had room temperature tensile fracture strength over 725 MPa and a fracture toughness of about 20 MPa√m. Composites with 2 μm and 6 μm thick refractory metal and intermetallic laminations were compared and it was found that layer thickness did not affect fracture toughness. Microlaminates with the thicker 6 μm laminations had lower fracture strength, however. Good fracture strength and high fracture toughness indicated that microlaminated high temperature composites synthesized by vapor phase deposition exhibit the properties predicted by ductile toughening models.

INTRODUCTION

The thrust to weight ratio of aircraft engines is limited by the density and elevated temperature capability of high temperature turbine materials. Single crystal superalloys, which are the current state-of-the-art in high temperature turbine blade materials, have limited potential for further increases in temperature capability. High temperature intermetallics offer the advantage of higher specific strength and higher temperature capability. For example, the specific strength of the very high temperature intermetallic compounds Cr_2Nb, Nb_2Al and Cr_3Si, estimated from published compression and microhardness data [1-5] , are plotted as a function of temperature in Figure 1 and compared to single crystal superalloys. The intermetallics lack ductility below 1000°C, however, and monolithic components lack the toughness to be used in most applications. By compositing these very high temperature intermetallics with ductile metals, their toughness may be improved to the point [6-9] where the composites have applicability in aircraft engine turbine sections.

Lamination of ductile metals with continuous intermetallic layers offers one means of producing metal-intermetallic composites. The lamellar thickness must be small because the thickness of the intermetallic lamellae will control the intrinsic defect size and hence the fracture strength of these materials. Intermetallic composites will require a refractory metal for toughening because of the need for metal strength at temperatures above 1100°C. Niobium-base alloys were selected as the toughening layer in this study because of their low density compared to superalloys, experience with oxidation-resistant niobium alloys [10] and the existence of metal-intermetallic systems in equilibrium at high temperatures [9, 11, 12]. Two microlaminated composite systems, Nb_3Al-Nb and Cr_2Nb-Nb(Cr) were chosen for microstructural and mechanical property evaluation. This choice of systems was based upon well established knowledge of phase relations between the metal and the intermetallic compositions.

COMPOSITE SYNTHESIS

Metal and intermetallic alloys were alternately vapor deposited with 2 and 6 μm thick metal and intermetallic layers by Magnetron® sputtering to produce microlaminated composite sheet approximately 0.15 mm thick [13]. The in-situ deposition process produced intermetallic

Mat. Res. Soc. Symp. Proc. Vol. 322. ©1994 Materials Research Society

composites with interstitial levels below 800 wppm [13]. The compositions and composite parameters of the two Nb_3Al-Nb and Cr_2Nb-Nb(Cr) microlaminated composites are shown in Table 1. Pure Nb was used as the metal layer in the Nb_3Al-Nb microlaminate to maximize room temperature ductility of the metal layer. The metal and intermetallic compositions of the Cr_2Nb-Nb(Cr) microlaminate were displaced to the Nb rich side of high temperature equilibrium compositions.

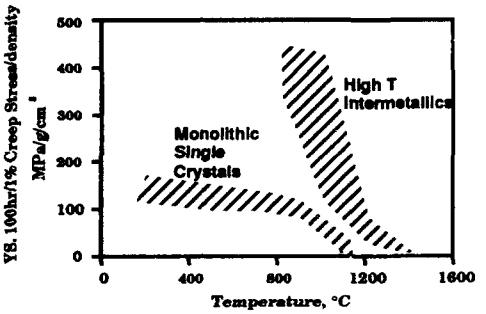


Figure 1. Specific strength of very high temperature intermetallic compounds compared to single crystal superalloy properties.



Figure 2. Backscattered electron (BSE) micrograph of as-deposited Nb_3Al-Nb microlaminate L8[1].

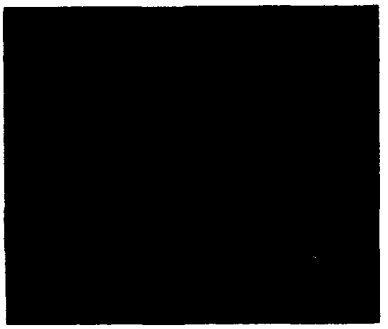


Figure 3. Backscattered electron (BSE) micrograph of as-deposited Cr_2Nb-Nb(Cr) microlaminate composite L17.

Nb3Al-Nb Microlaminated Composites

Figure 2 shows a backscattered electron (BSE) scanning electron microscope (SEM) image of the Nb_3Al-Nb microlaminated composite which consisted of 32 Nb_3Al and 33 Nb layers (Nb layers were imaged as the light layer). The laminated composite structure was flat with constant 2 μm metal and intermetallic lamellar thicknesses. Samples were annealed 2 hr. in argon at temperatures from 800°C to 1400°C and examined by X-ray diffraction to determine the effect of annealing on the relative contents of the two principal phases: metal (bcc) and Nb_3Al (A15). The as-deposited microlaminate had broadened diffraction peaks at $2\theta \approx 39°$, 55° 70°, and 83°

[1] Micron markers are not shown on micrographs which show the lamellar spacing as a dimensional reference.

which indexed only to bcc and indicated metastability of the intermetallic layer -- i.e., the as-deposited intermetallic layer was a metal solid solution. All annealed samples contained A15 (Nb_3Al) plus bcc diffraction peaks. There was evidence of a preferred growth texture in all samples.

Table 1 Laminated Composite Compositions and Layer Count[2]

ID No.	Intermetallic Composition at.%	Metal Composition at.%	Layer Thickness (μm)	Number of Intermet. Layers	Number of Metal. Layers
L8, L9	Nb-18.3Al	Nb	2	32	33
L17	Cr-40.5Nb	Nb-4.7Cr	2	32	33
L60	Cr-42.2Nb	Nb-3.3Cr	6	11	11

Table 2: Ratio Nb_3Al (222) to Nb (211) X-ray Peak Intensity for the Nb_3Al-Nb Microlaminated Composite

Sample Heat Treatment	Measured $I_{Nb_3Al(222)}/I_{Nb(211)}$	Estimated v/o Ratio Nb_3Al/Nb	Observed Nb_3Al/Nb layer thickness ratio t_{Nb_3Al}/t_{Nb}
As-Deposited	0	0	1.0
800°C/2 hr..	0.13	1.0	1.0
900°C/2 hr.	0.14	1.1	1.0
1000°C/2 hr.	0.13	1.0	0.7
1200°C/2 hr.	0.04	0.3	0.5
1400°C/2 hr.	0.02	0.16	.3

The X-ray intensity ratios $Nb_3Al(222)/Nb(211)$ were measured and corrected for absorption and atomic scattering factors[3] to obtain estimates of the ratio of Nb_3Al to Nb, Table 2. The volume fraction of Nb_3Al remained constant after annealing at 800°C to 1000°C, but dropped rapidly above 1000°C, indicating that the limit of stability of the Nb_3Al-Nb composite was 1000°C. Since the Nb_3Al diffraction peak intensities dropped faster than the layer thicknesses at 1200°C and 1400°C, we concluded that the intermetallic layers were two-phase. This was confirmed by BSE imaging; light imaging bcc particles were evident in the intermetallic layer at 1200 and 1400°C.

Columnar grain structure was observed in both layers at the lower temperatures, but dark imaging precipitates were observed along columnar grain boundaries of the Nb_3Al layers. These precipitates were identified as Al_2O_3 by TEM selected area diffraction. Chemical analysis of as-deposited microlaminate L8 indicated that it contained 750 wppm oxygen. Analysis of annealed specimens of other microlaminates showed that oxygen was not picked up in the annealing capsules, so that we conclude that 750 wppm O is a sufficient level for Al_2O_3 formation in Nb_3Al.

Characterization of Cr_2Nb-Nb(Cr) Microlaminated Composites

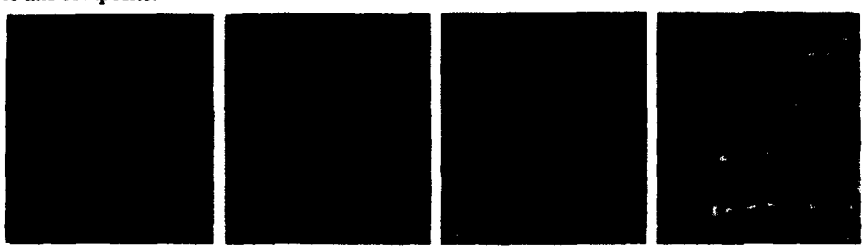
2 μm lamination thickness: The Cr_2Nb-Nb(Cr) microlaminate L17, which had 2 μm metal and 2 μm intermetallic layer thicknesses, had mirror-perfect flatness as-deposited, Figure 3. The smoothness contrasted with that of the Nb_3Al-Nb composite which had columnar grain growth in both metal and intermetallic layers. TEM of the as-deposited Cr_2Nb-Nb(Cr) metal layer revealed columnar grain structure, but the "intermetallic" Cr_2Nb layer had a microcrystalline bcc structure

[2] As noted later, the intermetallic layers are initially deposited as metastable solid solutions. Annealing at elevated temperatures transforms them to the stable intermetallic structure. For convenience, we will refer to them as the "intermetallic" layers throughout the text.

[3] Absorption of the incident and diffracted beams through each metal and intermetallic layer was summed over sufficient layers to determine the limiting absorption correction.

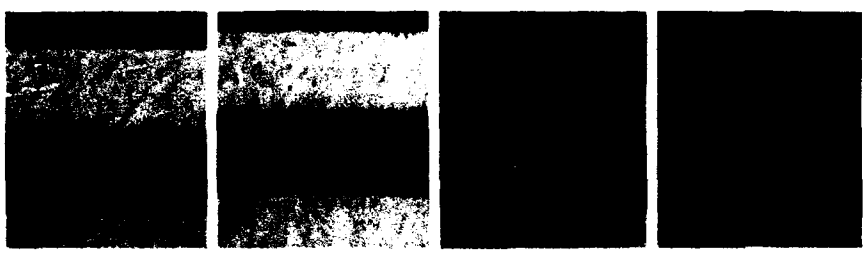
which suggested that it may have been amorphous as-deposited and which could account for the smoothness of the laminations. Partial crystallization of bcc particles occurred in the "intermetallic" layer during synthesis.

The Cr_2Nb(311)/bcc(211) X-ray intensity ratios and estimated Cr_2Nb/Nb(Cr) volume fraction ratios are given in Table 3. As-deposited samples and samples annealed at 800°C/2 hr. and 900°C/2 hr. had no discernible C15 Cr_2Nb diffraction peaks above background. Strong Cr_2Nb diffraction peaks were observed after the 1200°C/2 hr. anneal. The volume fraction of Cr_2Nb within the intermetallic layer of the 1200°C annealed sample was estimated by X-ray intensity measurements to be 75% which was confirmed by metallographic (BSE) imaging. Comparing the volume fraction ratios of Cr_2Nb/Nb(Cr) and the intermetallic to metal layer thicknesses measured from backscattered electron micrographs, with published binary phase diagram data [11, 12], we concluded that nucleation and growth of the C15 Cr_2Nb phase was kinetically limited below 1200°C. Above 1200°C, the Cr_2Nb fraction dropped to 17% of the total (Cr_2Nb/Nb(Cr) = 0.2) which indicated that 1200°C was the maximum stability temperature for this composite.



(a) (b) (c) (d)

Figure 4. BSE micrographs of Nb_3Al-Nb microlaminates annealed 2 hours at (a) 800°C, (b) 1000°C, (c) 1200°C and (d) 1400°C.



(a) (b) (c) (d)

Figure 5. BSE micrographs of Cr_2Nb-Nb(Cr) microlaminate L17 (2 μm layer thickness) annealed 2 hours at (a) 800°C, (b) 900°C, (c)1200°C and (d)1400°C.

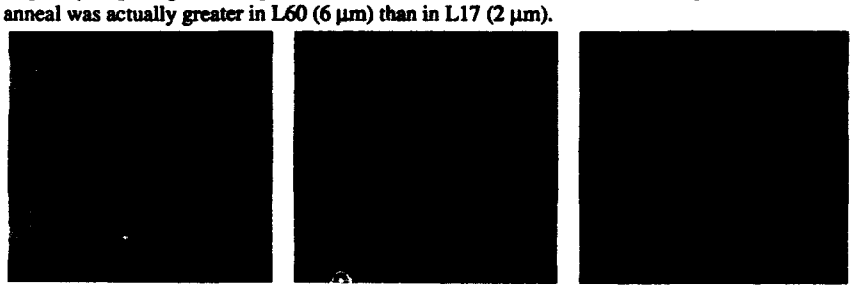
Figures 5(a-d) are backscattered electron micrographs of the annealed samples of the Cr_2Nb-Nb(Cr) microlaminate. The light bands of the micrograph are the metal layers. Precipitation of Nb-rich bcc particles in the Cr_2Nb layer was observed above 900°C. No oxide precipitation was observed at any temperature. Chemical analysis of the Cr_2Nb-Nb(Cr) microlaminates by the fusion technique indicated oxygen contents of 100 to 200 wppm; much lower than the 750 wppm oxygen content of the Nb_3Al-Nb composite. The difference suggested

that the Nb_3Al picture frame sputtering target may have been a source of oxygen in the Nb_3Al-Nb microlaminate.

Table 3. Cr_2Nb-Nb(Cr) Microlaminate L17 (2 μm) X-ray Diffraction Peak Intensity Comparisons

Sample Heat Treatment	$I_{Cr_2Nb(311)}/I_{bcc(211)}$	Estimated v/o Ratio Cr_2Nb/Nb	Measured Cr_2Nb/Nb layer thicknesses ratio, t_{Cr_2Nb}/t_{Nb}
As-Deposited	0	0	1.0
800°C/2 hr.	0	0	1.0
900°C/2 hr.	0	0	1.0
1000°C/2 hr.	0.006	0.08	1.0
1200°C/2 hr.	.038	0.52	0.8
1400°C/2 hr.	.015	0.20	0.6

6 μm lamination thickness: A Cr_2Nb-Nb(Cr) microlaminate with 6 μm thick metal and 6 μm thick intermetallic layers, L60, was synthesized to approximately the same total thickness as microlaminate L17. BSE images of annealed samples of L60 are shown in Figures 6(a-c). At 1000°C and 1200°C, microstructural features were the same in L60 and L17. There was little change in the thickness ratios of the metal or intermetallic layers of L60 at 1200 or 1400°C compared to L17. The smaller change in Cr_2Nb thickness ratio compared to L17 was due to its larger layer spacing. The displacement of the Cr_2Nb-Nb(Cr) interfaces during the 1400°C/2hr. anneal was actually greater in L60 (6 μm) than in L17 (2 μm).



(a) (b) (c)

Figure 6. BSE micrographs of Cr_2Nb-Nb(Cr) microlaminate L60 (6 μm layer thickness) heat treated 2 hours at (a) 1000°C, (b) 1200°C and (c)1400°C.

TEM:

Transmission electron microscopy (TEM) was used to examine sections across the metal and intermetallic layers of microlaminates L8, the 2 μm layered Nb_3Al-Nb microlaminate, and L17, the 2 μm layered Cr_2Nb-Nb(Cr) microlaminate, which were heat treated at 1000°C/2hr. and 1200°C/2 hr., respectively, Figures 7 and 8. The metal layers in both microlaminates retained columnar bcc microstructures and the intermetallic layers had two-phase fine equiaxed intermetallic plus bcc microstructures after annealing. Fine bubbles, presumably Ar-stabilized voids, were observed in the matrix and along grain boundaries in both layers.

COMPOSITE MECHANICAL PROPERTIES

Room Temperature Fracture Strength

Sheet tensile specimens, 0.15 mm thick with gage sections 4.2 mm wide and 12.5 mm long, Figure 9, were formed by EDM machining and were annealed in argon for 2 hours at 1000°C and

1200°C for the Nb_3Al-Nb and Cr_2Nb-Nb(Cr) composites, respectively. They were tested in tension at room temperature at a strain rate of $7x10^{-4}$/s. Most samples failed at the first cracking event, but a few exhibited microcracking before failure.



Figure 7. TEM micrograph of the Nb_3Al-Nb microlaminate L8 (2 µm).

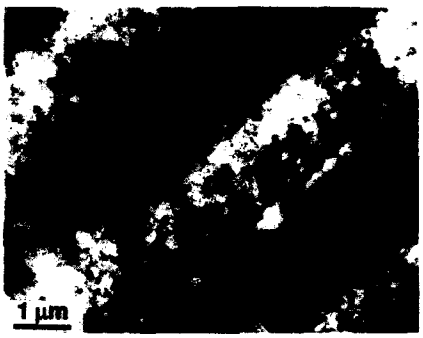


Figure 8. TEM micrograph of the Cr_2Nb-Nb(Cr) microlaminate L17 (2 µm).



Figure 9. Photograph of the microlaminated composite sheet tensile specimen.

Table 4 Room Temperature Fracture Strengths of Composite L8, Nb_3Al-Nb

Heat Treatment	Fracture Stress (MPa)
1000°C/2 hr.	501
1000°C/2 hr.	451
Average	476

Table 5. Room Temperature Fracture Strengths of Composite L17, 2 µm layers, Cr_2Nb-Nb(Cr)

Heat Treatment	Fracture Stress (MPa)
1200°C/2 hr.	750
1200°C/2 hr.	731[4]
1200°C/2 hr.	725
Average	735

Table 6. Room Temperature Fracture Strengths of Composite L60, 6 µm layers, Cr_2Nb-Nb(Cr)

Heat Treatment	Fracture Stress (MPa)
1200°C/2 hr.	500
1200°C/2 hr.	441
1200°C/2 hr.	484[5]
Average	475

The room temperature tensile strengths of the Nb_3Al-Nb and Cr_2Nb-Nb(Cr) microlaminates are listed in Tables 4-6. The average fracture strength of the Nb_3Al-Nb microlaminate L8 was 476 MPa (69 ksi). The 2 µm thick Cr_2Nb-Nb(Cr) microlaminate L17 had an average fracture strength of 735 MPa (107 ksi) and the 6 µm layer Cr_2Nb-Nb(Cr) composite

[4] Through crack 0.39 mm average width prior to final fracture.
[5] Cone growth defect halfway through thickness at fracture surface.

L60 had an average fracture strength of 475 MPa (69 ksi). The fracture surfaces of all samples revealed growth defects of various sizes. Because of this, fracture strength was a function of the product of the toughness of the composite and the distribution of defects in the sample.

The benefit of the toughening Nb layers in microlaminates L8 through L60 was demonstrated by measurement of the room temperature fracture strength of a brittle-brittle Nb_2Al-Nb_3Al microlaminate, which is compared to the fracture strengths of the ductile-brittle microlaminates Cr_2Nb-Nb(Cr) and Nb_3Al-Nb in Figure 10. The average tensile fracture strength of the 2 μm layer thicknesses brittle-brittle microlaminate Nb_2Al-Nb_3Al was less than one quarter of the average fracture strength of microlaminate L17.

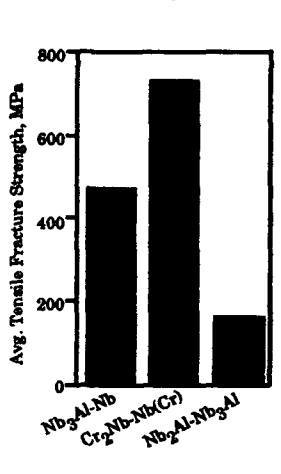


Figure 10. Comparison of 2 μm layer thickness brittle-ductile and brittle-brittle microlaminated composites.

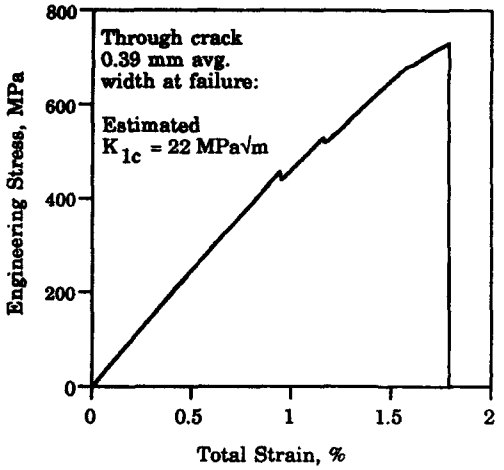


Figure 11. Engineering stress vs percent extension for Cr_2Nb-Nb(Cr) microlaminate L17 (2 μm).



Figure 12. SEM fractograph of the fracture initiation site for the Cr_2Nb-Nb(Cr) microlaminate corresponding to the data in Figure 11.

Fracture Toughness

One of the Cr_2Nb-Nb(Cr) L17 microlaminates (2 μm layer thickness) exhibited cracking and crack arrest prior to final fracture. The engineering stress versus strain curve for this sample, shown in Figure 11, was derived from the load-time curve (at constant crosshead speed) for the specimen. Arrested cracks, which initiated at stresses on the order of 40 MPa, were found by fractography to have initiated at a through thickness growth defect and to have grown to an average through thickness width of 0.39 mm. The shape and location of the crack is shown in Figure 12. Using a linear elastic fracture mechanics analysis for an off-center through crack in a

finite width sheet [14], the limiting room temperature fracture toughness of microlaminate L17 was estimated to be 22 MPa√m (19.5 ksi√in).

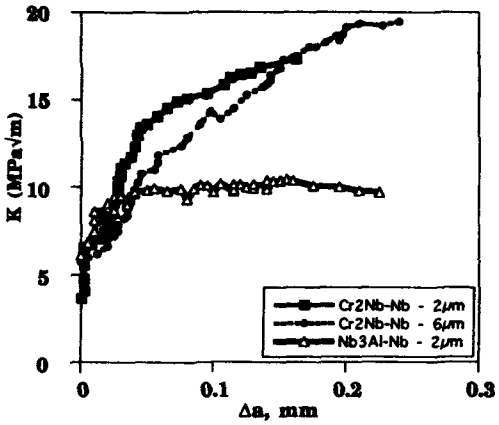


Figure 13. Fracture resistance curves: stress intensity vs crack length for the Nb_3Al-Nb, Cr_2Nb-Nb(Cr) (2 μm) and Cr_2Nb-Nb(Cr) (6 μm) microlaminates.

Fracture Resistance Curves

Fracture resistance curves were determined for Nb_3Al-Nb microlaminate L8 annealed at 1000°C and for Cr_2Nb-Nb(Cr) microlaminates L17 (2 μm) and L60 (6 μm) annealed at 1200°C. The samples were tested using a frame bending technique. A side notched 2.5 cm x 0.787 cm panel of the microlaminate was glued onto an aluminum support frame which provided a loading surface and prevented buckling. The compound specimen was tested in three-point bending with the direction of crack propagation within the plane of the sheet so that the crack cut across all lamellae simultaneously. The stiffness of the frame was taken into account in the calculation of stress intensity. The fracture resistance curves, stress intensity K vs crack length Δa for these microlaminates are plotted in Figure 13. All three microlaminates exhibited an initiation toughness of about 5 MPa√m and an increasing stress intensity with crack extension up to an approximate saturation value; tests were terminated by unstable crack propagation.

The Nb_3Al-Nb microlaminate L8 exhibited a rapid increase of K with crack extension, but had a maximum value of approximately 10 MPa√m after 0.05 mm of crack propagation. The stress intensity vs Δa curves of the Cr_2Nb-Nb(Cr) microlaminates rose to much higher stress intensities, approaching 20 MPa√m, before a limiting value was attained. The stress intensity rose slightly faster for the 2μm thick Cr_2Nb-Nb(Cr) microlaminate, but both the 2 and 6 μm microlaminates had the same approach to a limiting value after crack propagation distance of 0.2 mm (~4 times the crack extension to apparent saturation for the Nb_3Al-Nb microlaminate).

A combination of confocal microscopy, fracture surface reconstruction, and solid mechanics modeling of bridged cracks has been used to estimate the bridge lengths and critical (metal) ligament extensions to failure. Preliminary estimates suggest the bridge lengths are about 0.05 mm for the Nb_3Al-Nb microlaminate and 0.3 mm for the 6 μm layer thickness Cr_2Nb-Nb(Cr) microlaminate. These bridge lengths correspond to values of crack extension at which K approaches an apparent saturation value (Figure 13). Critical ligament extensions to failure are

estimated to be about 1-1.3 mm for Nb_3Al-Nb and about 5 mm for Cr_2Nb-Nb(Cr) (6 μm layers). Hence, the ligament extensions are 3-5 times larger in the Cr_2Nb-Nb(Cr) microlaminate than in the Nb_3Al-Nb microlaminate. This corresponds, to first order, to the greater extent of toughening in Cr_2Nb-Nb(Cr) where the difference between apparent saturation toughness and initiation toughness was about 15 MPa$\sqrt{m}$ versus about 5 MPa$\sqrt{m}$ for Nb_3Al-Nb. However, it should be noted that the greater extension observed in the 6 μm thick Nb(Cr) layer may be largely due to layer thickness. The relative strengths of the constrained Nb layers in the Nb_3Al-Nb microlaminate and the Nb(Cr) layer in the Cr_2Nb-Nb(Cr) microlaminate may also be different and this could contribute to differences in toughening as well. Evaluation of the critical extensions in the 2 μm layer Nb(Cr) and the entire stress-displacement functions for these ductile layers is still in progress.

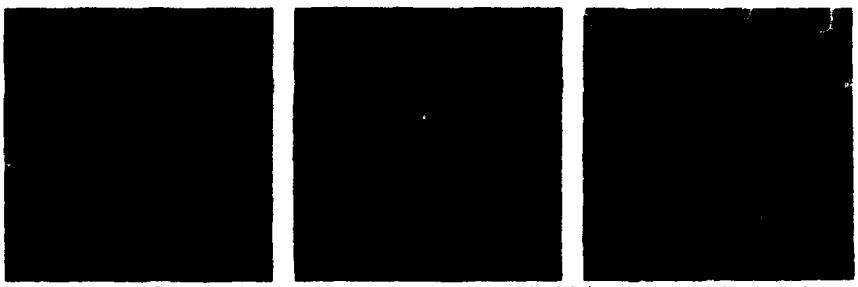


Figure 14. SEM fractographs of room temperature fractured (a) Nb_3Al-Nb microlaminated composite and Cr_2Nb-Nb(Cr) microlaminated composites (b) 2 μm thick and (c) 6 μm thick.

Fractography

SEM fractographs of the microlaminates of Tables 4-6 that were tensile tested at room temperature are shown in Figure 14. Chisel-point necking of the Nb layers such as that shown in Figure 14(a) was observed in all tensile fractures of the Nb_3Al-Nb microlaminate. The Nb layer fractured with the appearance of highly restrained metal failure [15] and little or no metal-intermetallic delamination was observed. Intermetallic Nb_3Al layers failed by brittle cleavage. Al_2O_3 particles that were observed in the intermetallic layers did not appear to have affected the fracture path.

The tensile fracture surfaces of the Cr_2Nb-Nb(Cr) microlaminates L17 (2 μm) and L60 (6 μm) are shown in Figures 14(b) and (c), respectively. Failure of the Nb layers in the fast fracture regions of the Cr_2Nb-Nb(Cr) tensile specimens was by very local fluted dimpling parallel to the columnar grain structure of the Nb layer. This was distinctly different from the failure appearance of the Nb_3Al-Nb metal layer. The Cr_2Nb intermetallic layer fractured by flat cleavage, but the angle of fracture and smoothness of the intermetallic fracture surface in L17 (2 μm) appeared to be related to features within the Nb layers. The intermetallic layers of L60 (6 μm) were flatter. Both L17 and L60 Cr_2Nb-Nb(Cr) microlaminate intermetallic layers showed evidence of the bcc second phase particles that were observed in metallographic sections.

The fracture surface of the Nb_3Al-Nb three-point bend fracture specimen was similar to the tensile specimens -- chisel point fracture in the Nb layer with voids along the necking ridge combined with cleavage in the Nb_3Al layers. The fracture surface of the Cr_2Nb-Nb(Cr) microlaminate L17 (2 μm) had different features in the regions of stable and unstable crack propagation. In the region of unstable crack propagation, the fracture surface was similar to the tensile specimen -- fluted dimpling parallel to the columnar grain structure in the Nb(Cr) layer

and cleavage in the Cr_2Nb layer. In the region of stable crack growth, however, the failure of the Nb(Cr) layer looked much more like the Nb_3Al-Nb microlaminate, with evidence of microvoid growth and coalescence along a chisel-point ridge formed by necking.

DISCUSSION OF RESULTS

Synthesis and Thermal Stability

The microstructures, low interstitial content and mechanical properties of microlaminates L8 through L60 demonstrate that vapor phase synthesis can be used successfully to produce composite sheet materials for the characterization of mechanical properties of very high temperature intermetallic composites. The synthesis process appeared to be contamination free, with little pickup of interstitial impurities. There was a large difference in oxygen content of the Nb_3Al-Nb and Cr_2Nb-Nb(Cr) microlaminates that may be attributable to the sputtering targets. The pure Nb layer in the Nb_3Al-Nb composite was assumed to have had the same low oxygen content as the Nb layer in the Cr_2Nb-Nb(Cr) composite, so the source of oxygen would appear to be the Nb_3Al target. Hydration of the aluminum oxide surface film on Al segments of the target is a possible source. The formation of Al_2O_3 particles in Nb_3Al at an oxygen content of 750 wppm indicated an extreme sensitivity of this compound to oxygen.

The metal layers of both composites formed by bcc columnar growth. Nb_3Al intermetallic layers grew by columnar metastable bcc grain structure. The A15 Nb_3Al phase formed rapidly upon annealing at temperatures of 800°C and above. Cr_2Nb-Nb(Cr) microlaminates had the same metal layer structure as the Nb_3Al-Nb microlaminates, but the Cr_2Nb layer appeared to have been deposited as an amorphous structure which then precipitated metastable bcc precipitate particles during synthesis. The temperature of the composite during synthesis was estimated to have been between 400°C and 500°C. There was no cracking in the composite due to this structural transformation which was further evidence of the beneficial toughening effect of the Nb layers.

Transformation of the metastable bcc layer to the Cr_2Nb Laves crystal structure was transformation-rate limited at temperatures below 1200°C. This sluggish formation of the C15 Cr_2Nb Laves phase was in contrast to the rapid formation of the A15 Nb_3Al phase, although slow Laves phase transformation kinetics have also been observed in other intermetallic alloy studies [12, 16]. The grain structure of both Cr_2Nb and Nb_3Al intermetallic layers was very fine, partially stabilized by the presence of a second phase and partially stabilized by entrapped argon bubbles. Kinetically limited Cr_2Nb crystallization may also have contributed to the very fine grain structure of the intermetallic layer of that system after annealing at 1200°C/2hr. Kinetics cannot explain the fine grain structure of the Nb_3Al layer, however. More work on the crystallization kinetics, grain growth inhibitors and equilibrium structures may be needed to control the microstructure of the intermetallic layer.

Mechanical Properties

The limiting fracture toughness of the Cr_2Nb-Nb(Cr) microlaminates was determined by two techniques and for two different lamellar thicknesses to be about 20 $MPa\sqrt{m}$. The Nb_3Al-Nb fracture resistance curves suggest a limiting toughness of approximately 10 $MPa\sqrt{m}$. This lower toughness can account for the large differences in the fracture strengths of the 2 μm layer thickness Nb_3Al-Nb and Cr_2Nb-Nb(Cr) microlaminates. Preliminary evidence suggests that the Nb(Cr) phase in the 6 μm layer Cr_2Nb-Nb(Cr) microlaminate exhibits 3-5 times more extension to failure than the Nb phase in the 2 μm layer Nb_3Al-Nb microlaminate; this produces longer bridge lengths and greater toughening.

The large difference in fracture strength between Cr_2Nb-Nb(Cr) microlaminates with 2 and 6 μm layer thickness may be due to the difference in the intermetallic layer thickness. The fracture resistance curves of Cr_2Nb-Nb(Cr) microlaminates L17 and L60 suggest that the toughening effect of 50 vol.% Nb(Cr) is the same for 2 and 6 μm layer thicknesses. SEM fractographs in Figures 14(b) and (c) show that the failure mode of the metal layer is similar for the 2 and 6 μm layer thicknesses, so that it is reasonable that the fracture toughnesses are comparable. Assuming that the characteristic crack length of a microlaminate is limited by the thickness of the intermetallic lamellae and that linear elastic fracture mechanics applies (where the fracture stresses of linear elastic materials are inversely related to the square root of the largest defect in the sample, $\sqrt{a}$, and directly proportional to the fracture toughnesses K_{1c} of the materials).

$$\frac{\sigma^F_{L60}}{\sigma^F_{L17}} = \frac{K_{1C}^{L60}}{K_{1C}^{L17}} \frac{\sqrt{a_{L17}}}{\sqrt{a_{L60}}} = \frac{K_{1C}^{L60}}{K_{1C}^{L17}} \frac{\sqrt{2}}{\sqrt{6}} = 0.58 \frac{K_{1C}^{L60}}{K_{1C}^{L17}} \qquad (1)$$

The lamination with the 6 μm lamination spacing, L60, should have a fracture stress of 58% of the composite with 2 μm laminations for equal fracture toughnesses. This is reasonably close to the experimentally observed ratio of 65%.

CONCLUSIONS

- In-situ vapor phase synthesis by Magnetron® sputtering was used successfully to synthesize metal-intermetallic laminated composites with independent control over the composition, layer thickness and volume fraction of the layers.
- As-deposited Nb_3Al and Cr_2Nb layers had metastable crystal structures which reverted to the equilibrium structure upon annealing. No cracking was observed due to crystallographic transformation at 800 to 1400°C.
- Formation of the stable Cr_2Nb Laves phase structure from the metastable initial state was very sluggish, requiring 2 hr. at 1200°C to fully transform.
- Cr_2Nb-Nb(Cr) microlaminates with 2 μm layer thickness had a fracture strength of over 725 MPa at room temperature. Its limiting fracture toughness was determined to be about 20 MPa$\sqrt{m}$.
- The fracture toughness of the Nb_3Al-Nb microlaminate was 10 MPa$\sqrt{m}$ which partially accounted for its lower fracture strength relative to the Cr_2Nb-Nb(Cr) microlaminate.
- There was a difference in the fast fracture failure mode of the metal layers in the Nb_3Al-Nb and Cr_2Nb-Nb(Cr) microlaminates. The Nb layer in Nb_3Al-Nb microlaminate failed in fast fracture by chisel-point necking while the Nb(Cr) layer in Cr_2Nb-Nb(Cr) separated with a fluted ductile dimpling pattern. Under stable crack growth conditions, both types of metal layers failed by chisel-point necking with evidence of void growth and coalescence along the necking ridge.
- The 6 μm Nb(Cr) phase exhibited 3-5 times more extension to failure than the 2 μm Nb phase. While this could account for the greater toughening in the 6 μm layer Cr_2Nb-Nb(Cr) microlaminate, the differences in the stress-displacement behavior of Nb and Nb(Cr) layers and the relative contributions to toughening remain to be examined.
- Thicker intermetallic layer spacing did not affect fracture toughness of the Cr_2Nb-Nb microlaminates but it resulted in lower fracture strength. This reduction in fracture strength

could be rationalized with a linear-elastic fracture mechanics analysis using a defect size equal to the thickness of the intermetallic layer.

REFERENCES

1. Fleischer, R.L. and R.D. Field, "Development Potential of Advanced Intermetallic Materials, Final Report, USAF Contract F33615-86-C-5055", Report # WRDC-TR-90-4046, GE Corporate Research and Development, Schenectady, NY, 1990.

2. Fleischer, R.L., "Mechanical Properties of Diverse High-Temperature Compounds -- Thermal Variation of Microhardness and Crack Formation", Mat. Res. Soc. Symp. Proc., 133, 305-310, (1989).

3. Shah, D.M. and D.L. Anton, "Ternary Alloying of Refractory Intermetallics", Mat. Res. Soc. Symp. Proc., 213, 63-68, (1991).

4. Anton, D.L. and D.M. Shah, "High Temperature Properties of Refractory Intermetallics", Mat. Res. Soc. Symp. Proc., 213, 733-738, (1991).

5. Anton, D.L. and D.M. Shah, "Development Potential of Advanced Intermetallic Materials, Final Report, Final Report USAF Contract F33615-87-C-5214" Pratt and Whitney, West Palm Beach, FL, Report # WRDC-TR-90-4122, 1991.

6. Déve, H.E., *et al.*, "Ductile Reinforcement Toughening of Gamma-TiAl: Effects of Debonding and Ductility", Acta Metall. Mater, 38, 1491-1502, (1990).

7. Sigl, L.S., *et al.*, "On the Toughness of Brittle Materials Reinforced with a Ductile Phase", Acta Metall. Mater, 36, 945-953, (1988).

8. Cao, H.C. and A. Evans G,, "On Crack Extension in Ductile/Brittle Laminates", Acta Metall. Mater, 39, 2997-3005, (1991).

9. Anton, D.L. and D.M. Shah, "Ductile Phase Toughening of Brittle Intermetallics", Mat. Res. Soc. Symp. Proc., 194, 45-52, (1990).

10. Jackson, M.R., *et al.*, "Response of Nb-Ti Alloys to High Temperature Air Exposure". in Refractory Metals Extraction, Processing and Applications, Edited by K.C. Liddell, S. D.R., andR.G. Batista, TMS, Warrendale, PA, 1991, 335-346.

11. Massalski, T.B., Binary Alloy Phase Diagrams. ASM International, Metals Park, OH, 1986.

12. Thoma, J.D. and J.R. Perepezko, "An Experimental Evaluation of the Phase Relationships and Solubilities of the Chromium-Niobium System", Mat'ls. Sci. & Engrg., A156, 97-108, (1992).

13. Rowe, R.G. and D.W. Skelly, "The Synthesis and Evaluation of Nb_3Al-Nb Laminated Composites", Mat. Res. Soc. Symp. Proc., 273, 411-416, (1992).

14. Rooke, D.P. and D.J. Cartwright, Compendium of Stress Intensity Factors. Her Majesty's Stationery Office, London, 1976.

15. Bannister, M. and M.F. Ashby, "The Deformation and Fracture of Constrained Metal Sheets", Acta Metall. Mater., 39, 2575-2582, (1991).

16. Thoma, J.D., "Microstructural Development in Niobium Chromium(2)-Based Alloys", Ph.D. Dissertation, University of Wisconsin, Madison, Wisconsin, 1993.

ACKNOWLEDGMENTS

This work was partially funded by the U.S. Air Force, Wright Research and Development Center, Wright-Patterson AFB, OH under contract F33615-91-C-5613, Mr. T.F. Broderick, program monitor. The authors would like to acknowledge the contributions of Mr. R. Nardi and Ms. K.K. Denike in sputter deposition and processing of the microlaminated composites. We would like to acknowledge the help of Dr. M.F. Garbauskas for interpreting X-ray diffraction results and to thank Dr. M.R. Jackson for critical reading of the manuscript.

TENSILE AND STRESS-RUPTURE BEHAVIOR OF HAFNIUM CARBIDE DISPERSED MOLYBDENUM AND TUNGSTEN BASE ALLOY WIRES

H.M. YUN*† AND R.H. TITRAN**
*Cleveland State University, Cleveland, Ohio 44115
**National Aeronautics and Space Administration, Lewis Research Center,
21000 Brookpark Road, Cleveland, Ohio 44135

ABSTRACT

The tensile strain rate sensitivity and the stress-rupture strength of Mo-base and W-base alloy wires, 380 μm in diameter, were determined over the temperature range from 1200 to 1600 K. Three molybdenum alloy wires; Mo + 1.1 wt% hafnium carbide (MoHfC), Mo + 25 wt% W + 1.1 wt% hafnium carbide (MoHfC+25W) and Mo + 45 wt% W + 1.1 wt% hafnium carbide (MoHfC+45W), and a W + 0.4 wt% hafnium carbide (WHfC) tungsten alloy wire were evaluated.

The tensile strength of all wires studied was found to have a positive strain rate sensitivity. The strain rate dependency increased with increasing temperature and is associated with grain broadening of the initial fibrous structures. The hafnium carbide dispersed W-base and Mo-base alloys have superior tensile and stress-rupture properties than those without HfC. On a density compensated basis the MoHfC wires exhibit superior tensile and stress-rupture strengths to the WHfC wires up to approximately 1400 K. Addition of tungsten in the Mo-alloy wires was found to increase the long-term stress-rupture strength at temperatures above 1400 K.

INTRODUCTION

High temperature applications such as space power conversion have generated great interest in fiber reinforced metallic composites. Refractory metals and alloys reinforced with refractory metal alloy fibers have been shown to be applicable for extremely high temperature ranges [1]. The useful temperature depends upon the combination of fiber and matrix. The tungsten (W) fiber reinforced niobium alloy composite was reported to have high tensile and creep strength in the temperature range of 1400 to 1500 K [1]. The performance of a composite is usually dependent upon the fiber component. The major portion of the tensile and creep strength of the composite is associated with the properties of the fiber. The use of a strong and stiff fiber is desired for a high strength composite material.

Wires of the hafnium carbide dispersion strengthened W and W-Re alloys, ranging in diameter from 200 to 380 μm, have recently been shown to possess superior tensile and stress-rupture strengths, compared to the potassium bubble dispersed or the thoria dispersed W wires [2,3]. The fine hafnium carbide dispersoids were reported to be more effective than bubble or thoria dispersoids [3,4] in preserving the heavily unidirectionally elongated fibrous grain structure of the W alloy wires. The effectiveness of the hafnium carbide on the mechanical properties of other refractory metal base alloy wires, such as molybdenum (Mo), is of interest. Molybdenum (Mo) with its lower density than W appears to be attractive for making lower weight composites.

†NASA Resident Research Associate at Lewis Research Center.

Mat. Res. Soc. Symp. Proc. Vol. 322. ©1994 Materials Research Society

Houck [5,6] has studied the mechanical properties of Mo alloys, such as TZC (Mo + 1.25% Ti + 0.30% Zr + 0.15% C), TZM (Mo + 0.5% Ti + 0.08% Zr + 0.015% C), Mo + 0.5% Ti (all percentages in this report are in weight percent) and Mo + 0.5% Zr, and reported that the recrystallization temperature for these alloys varies from 1200 to 1700 K, depending on the alloying element. The TZC and TZM alloys possess a relatively high tensile strength, but the alloying elements do not appear stable at the higher testing temperatures. The stress-rupture strength of these alloys generally are much lower than the W-base alloys. The present study focussed on the determination of the tensile and stress-rupture properties of the hafnium carbide dispersed Mo-based alloy wires, and on the comparison with hafnium carbide dispersed W alloy wires. The study also evaluated the effect of HfC dispersoids in stabilizing the fibrous microstructures in the wires over the temperature range of 1200 to 1600 K.

EXPERIMENTAL PROCEDURE

Materials

The chemical compositions of the hafnium carbide dispersed Mo and W alloy wires examined in this study are given in Table I. MoHfC wires, Mo with hafnium carbide, were the HfC dispersed simple Mo-base alloys, and MoHfC+45W and MoHfC+25W wires were the HfC dispersed and alloyed with 49.5% W and 30.4% W, respectively. The Mo-base wires were fabricated by powder metallurgy techniques, the W-base WHfC wires were produced by vacuum arc-melting.

Hafnium carbide in the Mo alloys was formed by alloying of elemental Hf and C during sintering at high temperature. This Mo alloy wire (MoHfC+45W) is believed to have about 0.1% HfC and about 0.7% HfC for WHfC. The MoHfC wires also contained a small unintended amount (4%) of W, which can provide some solid-solution strengthening.

All wires were heavily drawn to their final nominal diameter of about 380 μm. Figure 1 shows the microstructures of the as-drawn wires. The grain structures are noted as infinitely long and of a very fine width, so-called fibrous grain structures. The grain width of the MoHfC wires is about 0.5 μm, and that of the WHfC wires about 0.3 μm. The size distribution of the dispersoids in the MoHfC wires was inhomogeneous, ranging from less than 0.1 to 1.0 μm, whereas dispersoids in the WHfC wires were finely distributed with an average size of less than about

TABLE I.—CHEMICAL COMPOSITION OF Mo AND W BASE ALLOY WIRES

Material	Chemical composition, wt% (at.%)					
	C	N	O	Hf	W	Mo
MoHfC	0.044 (0.36)	0.0026	0.016	1.2 (0.66)	4.4 (2.50)	Balance
MoHfC+25W	0.020 (0.19)	0.0023	0.0036	0.9 (0.56)	30.4 (19.0)	Balance
MoHfC+45W	0.009 6 (0.10)	0.0019	0.0038	0.8 (0.56)	49.5 (34.8)	Balance
WHfC	0.03 (0.45)	0.0009	0.0039	0.4 (0.41)	Balance	---------

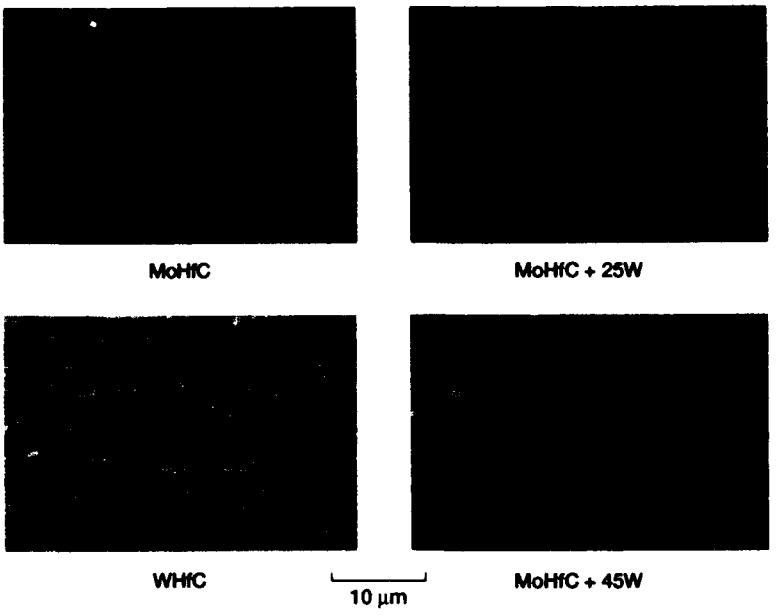


Figure 1.—As-drawn microstructures (SEM secondary electron images) of Mo and W base alloy wires.

0.1 μm. MoHfC+25W and MoHfC+45W wires appear to result in a finer grain width and a more inhomogeneous spacing of the dispersoids than the MoHfC wires.

Test Procedure

Tensile and stress-rupture tests were conducted in a vacuum of 10^{-5} Pa at temperatures ranging from 1200 to 1600 K. The furnace temperature was monitored with a platinum/platinum-13% rhodium thermocouple, and controlled within ±3 K during the test. The experimental details of the tensile and stress-rupture test procedures have been given previously [3,7]. The wire was cut to about 40 cm. lengths and then suspended through a vertically mounted resistance furnace. Tensile testing was at a constant cross-head speed and the load-time curves were recorded autographically. The proportional limit (PL), ultimate tensile strength (UTS) were determined from the load-time curves. For the stress-rupture test, the wire was loaded with an appropriate deadweight, which was supported by a retractable support during specimen heating. The stress-rupture strength (σ_t) was determined from the stress versus rupture time plots. The reduction of area (RA) of failed specimens was measured using an optical microscope.

Stress-rupture and tensile tests were performed on wires in the as-drawn condition. In addition tensile tests were performed on specimens electropolished [3] to produce a definite gauge section about 25.4 mm long and 280±10 μm in diameter.

RESULTS

Tensile Stress-Strain Rate Behavior

The effect of the strain rates at 1400 and 1600 K on the PL of the as-drawn and electropolished wires is shown in Fig. 2. Electropolishing provided a tensile specimen with a well defined 25.4 mm long gauge section. The PL of the electropolished wires appeared to be higher than that of the as-drawn wires, ~650 versus 480 MPa at 1400 K. The original 380 μm wire diameter was reduced to 280 μm. The strain rates were calculated based on the assumption that all deformation took place in the electropolished gauge section.

The decrease of the PL with decreasing strain rate was small or negligible within the high strain rate range of 3.3×10^{-4} to 3.3×10^{-2} sec^{-1}. However, it is noted that the drop of the PLs is quite large at the slower strain rates, 3.3×10^{-4} to 3.3×10^{-5} sec^{-1}. The drop of the PLs at the low strain rates is due to the onset of primary recrystallization at 1400 to 1600 K. The difference in the dependency of the strain rate between the MoHfC, MoHfC+25W and MoHfC+45W wires was negligible at 1400 K. At 1600 K the PL of MoHfC+45W wires is higher than that of the MoHfC wires over the strain rate range studied.

Stress-Rupture Properties

The stress-rupture properties of the as-drawn wires are shown in Fig. 3. Test temperature ranged from 1200 to 1477 K and the stress-rupture time from 0.1 to about 1000 hr. The error bar indicates a representative range of rupture time data at one stress. The 10- and 100-hr stress-rupture strengths, $\sigma_{t=10}$ and $\sigma_{t=100}$, determined from the stress-rupture curves, are summarized in Table II. The difference in the σ_t between the Mo-base alloy and the W-base alloy wires

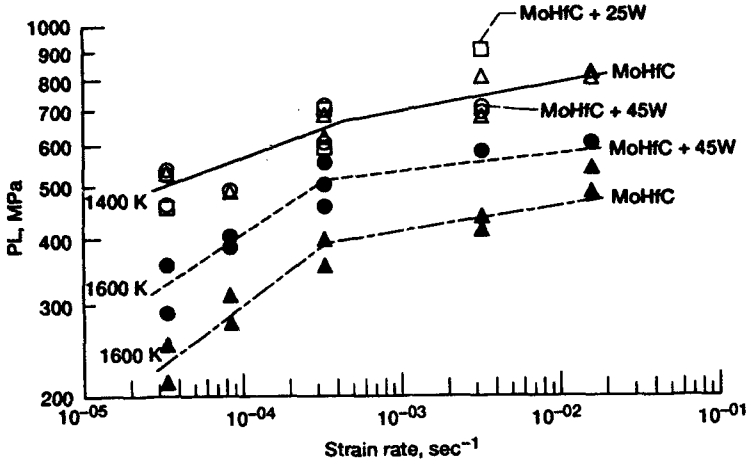


Figure 2.—Effect of the strain rate on the tensile strength of Mo-base alloy wire at 1400 and 1600 K.

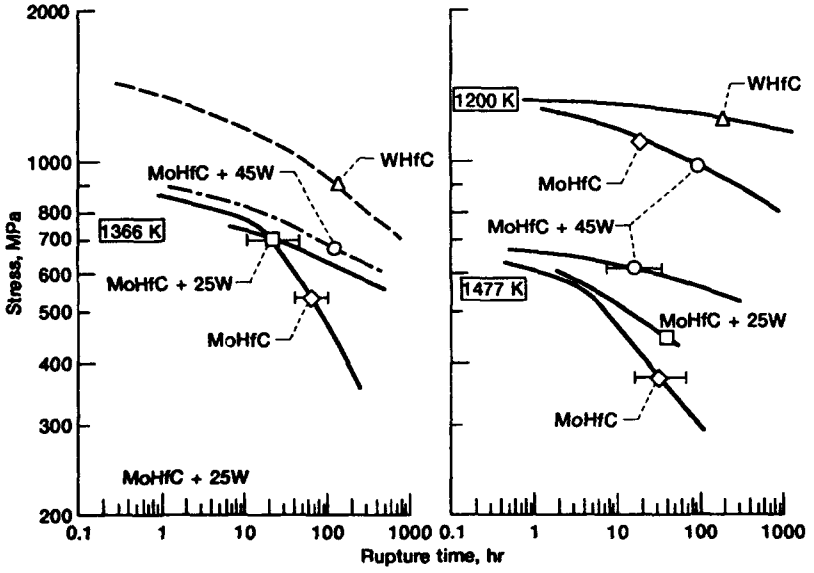


Figure 3.—Stress-rupture behavior of Mo- and W-base alloy wire at 1200, 1366 and 1477 K.

increased with increasing rupture time and testing temperatures. At 1200 K, the $\sigma_{t=10}$ (10-hr stress-rupture strength) and the $\sigma_{t=100}$ were, respectively, 1237 and 1038 MPa for MoHfC, and 1275 and 1221 MPa for WHfC. At 1366 K, the $\sigma_{t=100}$ of MoHfC was much lower than that of WHfC, i.e., 480 MPa versus 950 MPa.

It is noted that the difference in the σ_t between the simple MoHfC and the MoHfC+45W also increased with increasing temperature and time. At 1200 K, the $\sigma_{t=10}$ of MoHfC was comparable with that of MoHfC+45W (about 1237 MPa). From 1366 to 1477 K, the 100-hr stress-rupture strength of the MoHfC+45W wires was substantially higher than that of the MoHfC wires, whereas the 10-hr short-term strength of the MoHfC+45 wires was slightly higher than that of MoHfC wires. This suggests that the W containing Mo alloy wires may be a candidate composite fiber reinforcement wires for the long-term and high temperature applications, and the simple MoHfC wires may be suitable for short-term and low temperature application below 1400 K.

The relationship between the initial stress and the rupture time, t_R, is shown in Fig. 4 as a function of testing temperature for the MoHfC wires. At 1200 and 1600 K a unique slope existed for each temperature, and the stress-rupture strength value at 1200 K was clearly higher than that at 1600 K for all the rupture times. The slope at 1200 K was steeper than that at 1600 K. From 1366 to 1477 K, however, two slopes existed, one for rupture times above about 10 hr, and another one for the relative short-term rupture time of less than 10 hr. The two different slopes at 1366 and 1477 K arose because the long-term $\sigma_{t=100}$ of MoHfC wires at 1366 K was considerably higher than that at 1477 K, 500 and 300 MPa, respectively. The sharp drop of the stress rupture strength for the long-term rupture time is associated with the change in the fibrous grain structures, such as grain broadening.

The relation between the initial stress and the rupture time of the MoHfC was correlated by using the conventional power-law expression [8,9]:

$$t_R = A\sigma^{-p} \exp (Q/RT) \quad (1)$$

where t_R = rupture time (hr), A = constant, σ = applied stress (MPa), p = stress exponent for stress-rupture, T = testing temperature (K), R = gas constant (8.314 J/mol.K) and Q = apparent activation energy for stress-rupture (kJ/mol). The stress exponent, p, the slope of the curves in Fig. 4, is ~14, at 1200 K over the entire test time range, and at 1366 and 1477 K for the short-term tests. A high p value at low temperatures is indicative of a high sensitivity of the rupture time with the applied stress, the observed stress value for $\sigma_{t=10}$ is almost equivalent to $\sigma_{t=100}$ at

TABLE II.—10- AND 100-HR STRESS-RUPTURE STRENGTH OF Mo AND W BASE ALLOY WIRES

Wire	10-Hr stress-rupture strength at K, MPa					100-Hr stress-rupture strength at K, MPa				
	1200	1366	1400	1477	1600	1200	1366	1400	1477	1600
MoHfC	1237	728	564	464	[a]160	1038	480	350	310	[a]91
MoHfC+25W	-----	675	----	494	-----	-----	574	----	405	----
MoHfC+45W	1237	808	----	615	-----	1038	679	----	589	----
WHfC	1275	1176	----	----	-----	1221	950	----	[b]780	----

[a]Extrapolated from the measured short-term data.
[b]From Petrasek et al. [1].

1200 K. The long-term stress-rupture data at 1366 K displayed considerable scatter, however, the data appeared to correlate best with a stress exponent of about 5. The apparent activation energy, Q for the stress versus rupture-time was determined to be about 480 kJ/mol over the stress range of 400 to 500 MPa, for temperatures of 1366 to 1477 K, and for the long- term rupture time data of about 10 hr or larger. This value compares well with the steady-state creep value of 470 kJ/mol determined for recrystallized TZM Mo alloy at 1573 to 1673 K [10].

DISCUSSION

Strengthening by the Dispersoid Particles

The tensile and stress-rupture properties of the HfC dispersed Mo alloy wires appear to have comparable strengths to the WHfC wires at about 1200 K. However, for temperatures above 1200 K, the Mo-base alloy wires are weaker than the W-base alloy wires. The addition of W as an alloying element enhances the stability of the microstructure at high temperature and yields a higher strength MoHfC base alloy.

The short-term and/or low temperature tensile and stress-rupture strength results from the fibrous grain structures and Hall-Petch type grain boundary strengthening. The fine fiber grain contains more elastically stored energy [3,11], which results from the large amount of cold working employed in the wire drawing process, and contributes considerably to the wire's strength. For example, the high tensile strength of the heavily drawn Mo-33Re alloy was reported to be due to the highly developed, fine-scale cell structures with a high background dislocation density [12]. For the HfC dispersoid strengthened Mo alloy, the long-term and high temperature stress-rupture and tensile strengths, however, may be the combined effects of strengthening from the fine dispersoids, Orowan stress from the dispersoids, and/or the solid solution hardening from the strong and hard alloying element. The fine and closely distributed HfC dispersoids have been shown to effectively block dislocation motion and to affect the formation of the cell and wall structures [11].

Table III shows the increase in the tensile and stress-rupture strength of the hafnium carbide dispersed wires compared to the literature values of the unalloyed wires and recrystallized W or Mo sheets at 1366 K. The increase in the tensile strength of the hafnium carbide dispersed wires was about fivefold and sevenfold for the stress-rupture strength in comparison to W and Mo sheets, respectively. The increase in tensile strength due to the addition of HfC particles to Mo or W and the cold work was about 650 MPa, which is somewhat higher than earlier estimates: Previous work indicated about a 120 MPa increase for the 200 μm WHfC wires with a 1.55 vol% fraction of HfC [3].

Property Comparisons

The stress-rupture data for the wires indicated that in the higher temperature range the WHfC wires have a higher strength than the MoHfC wires and that the W addition to the MoHfC is an effective strengthener. The density compensated specific strength values, stress/density, i.e., MPa/(g/cm^3) or m, is an important criterion in choosing a candidate wire for fiber composite reinforcement. Figure 5 shows the comparison of the density compensated stress-rupture strength of the MoHfC, MoHfC+25W, MoHfC+45W and WHfC wires, including the 218, ST300, and

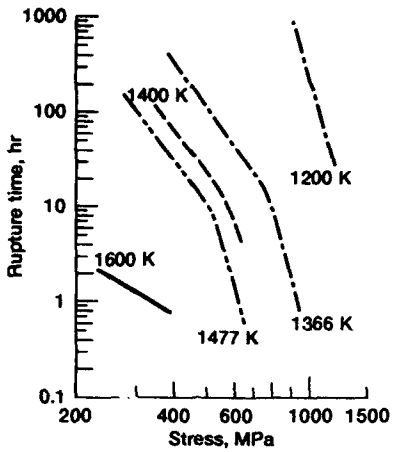


Figure 4.—Stress-rupture behavior of as-drawn MoHfC wires in the temperature range of 1200 to 1600 K.

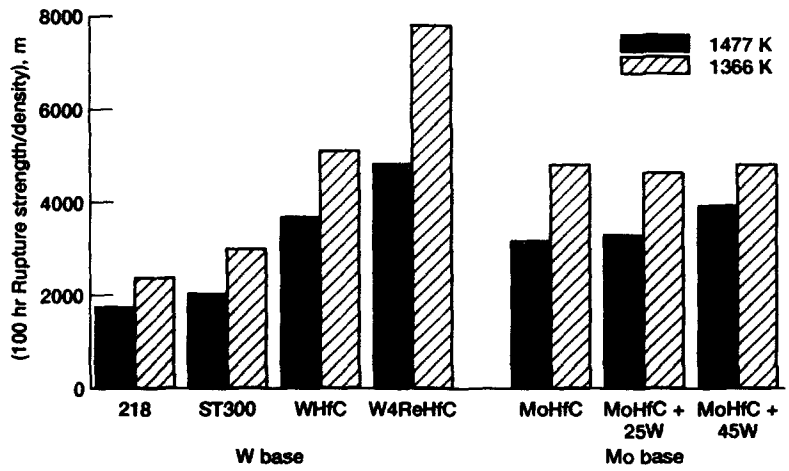


Figure 5.—Comparison of density compensated 100 hr-stress-rupture strength of candidate Mo- and W-base alloy wires for fiber reinforcements. The value of 218, ST300 and W4ReHfC wires came from reference [4].

TABLE III.—THE INCREASE IN THE TENSILE AND STRESS-RUPTURE STRENGTH OF THE HfC PARTICLE DISPERSED MoHfC ÅND WHfC WIRES IN COMPARISON TO THE UNALLOYED MOLY AND TUNGSTEN WIRES AT 1366 K

Material	Condition	Particle size, nm	Units, MPa	100-Hr stress-rupture strength, MPa	Young's modulus, GPa
MoHfC	Wire (380 μm)	150	970	480	-----
Mo	Wire (380 μm)	----	[a]320	[b]80	-----
Mo	Sheet (recrystallized)	----	[b]172	[b]57	[b]220
WHfC	Wire (380 μm)	35	1240	950	-----
W	Wire (380 μm)	----	[a]650	[a]460	-----
W	Sheet (recrystallized	----	[b]241	[b]145	[b]365

[a]Unpublished work by H.M. Yun.
[b]From reference [5].

W4ReHfC [13]. It is noted that the specific rupture strength of Mo-base wires is almost equivalent to that of the WHfC wires. The 100-hr specific rupture strength of the Mo-base alloy wires appeared to be lower at 1366 K than that of the W4ReHfC wires.

The present HfC dispersed Mo-base wires (MoHfC, MoHfC+25W and MoHfC+45W) also have a higher 100-hr specific rupture strength than the lamp grade 218 W or the thoria dispersed ST300 wire at 1366 or 1477 K. These results indicate that the MoHfC wire reinforced composites, such as Nb alloy matrix composites, may have a greater stress-rupture strength than similar composites reinforced with the 218 or ST300 W wire [1].

SUMMARY

Tensile and stress-rupture behavior of molybdenum (Mo) and tungsten (W) alloy wires, 380 μm diameter, have been studied in the temperature range of 1200 to 1600 K, and the results are summarized below:

(1) Long-term stress-rupture strength of the MoHfC wires was improved by W addition.

(2) The tensile strength of the MoHfC wires increased with increasing strain rates, and the strain rate dependency increased with increasing temperatures.

CONCLUSION

The hafnium carbide dispersed Mo-base alloy wires have a higher stress-rupture strength than the commercially available W-base alloy wires. The density compensated specific strengths of MoHfC wires is comparable to those of the strongest experimental W-base alloy wires. These Mo-base alloy wires, therefore, appear to be an attractive alternative candidate for metal matrix composite fiber reinforcements.

REFERENCES

1. D.W. Petrasek and R.H. Titran: NASA TM–100804, National Aeronautics and Space Administration, Washington, DC, 1988.

2. D.W. Petrasek: NASA TN D–6881, National Aeronautics and Space Administration, Washington, DC, 1972.

3. H.M. Yun: "Proc. of the Symposium on Refractory Metals—State of the Art," sponsored by TMS of AIME, Chicago, IL, Sept. 27–29, 1988, pp. 49–64.

4. D.W. Petrasek and R.A. Signorelli: NASA TN D–5139, National Aeronautics and Space Administration, Washington, DC, 1969.

5. T.E. Tietz and J.W. Wilson: Stanford University Press, Stanford, CA, 1965, pp. 156–205.

6. J.A. Houck: *Defense Metal Information Center Rept.* 140, OTS PB 151099, 1960.

7. D.L. McDanels and R.A. Signorelli: NASA TN D–3467, National Aeronautics and Space Administration, Washington, DC, 1966.

8. R. Warren and C.H. Anderson: "Proc. 10th Plansee Seminar, vol. 2, H.M. Ortner, ed., Metallwerk Plansee, Austria, 1981, pp. 243–246.

9. S.L. Robinson and O.D. Sherby: Acta Metall., 1969, vol. 17, pp. 109–125.

10. D. Agronov, E. Freund, and A. Rosen: High Temperature-High Pressure, 1986, vol. 18, pp. 151–159.

11. R. Ebeling and M.F. Ashby: Phil. Mag., 1966, vol. 13, pp. 805–834.

12. R.N. Wright, J.A. Brusso, and D.E. Mikkola: Mats. Sci. and Engr., 1988, A104, pp. 85–93.

13. D.W. Petrasek: NASA TN D–6881, National Aeronautics and Space Administration, Washington, DC, 1972.

MICROSTRUCTURAL EVOLUTION AND DENSIFICATION KINETICS DURING SINTERING OF OXIDE-DISPERSED TUNGSTEN ALLOYS

Li-Chyong Chen and Bernard P. Bewlay
GE Corporate Research and Development, Schenectady, NY 12301.

ABSTRACT

The present paper discusses the role of ceria and hafnia dispersions in tungsten alloys on the microstructural evolution and densification kinetics during sintering. Densification kinetics were measured using dilatometry, and microstructural changes were examined using scanning electron microscopy and Auger electron spectroscopy. Activation energies for sintering were obtained by analyzing the shift of the iso-density points as a function of linear heating rate. Sintering of both tungsten and ceria-dispersed tungsten were found to be controlled by grain boundary diffusion, with apparent activation energies of 318±21 and 385±15 kJ/mole, respectively. However, densification of hafnia-dispersed tungsten is not controlled by a single mechanism. Under different conditions hafnia can enhance or retard densification; the mechanisms associated with this behavior are discussed. In particular, the relationships between sintering behavior and the tungsten-ceria and tungsten-hafnia interfaces are examined. Comparison with conventional oxide dispersoids, such as thoria, will also be made.

INTRODUCTION

Multiphase refractory alloys have improved high temperature mechanical properties, and one of the earliest examples is thoria-dispersed W [1]. Further development of dispersion-strengthened W based alloys during the sixties was described by Sell et al. [2]. More recently, ceria, lanthana, yttria, and zirconia additions to W have been evaluated [3-6]. Since the oxide-dispersed W is intended for applications at temperatures above 2000 °C, the chemical stability of the dispersed particle and its resistance to coarsening are critical. For improved performance and manufacturability, high density and a fine-grain microstructure are required. Sintering is critical since it controls density and microstructure. The present paper describes the effect of ceria and hafnia dispersions on sintering of tungsten.

Chen *et al.* [7] observed that the W-ceria interface was characterized by a low contact angle ("wetting"), while the W-hafnia interface was characterized by a high contact angle ("non-wetting"). Relationships between the dispersoid-matrix interface and sintering behavior have been investigated by a number of authors in the past. For example, Kuczynski and Lavendel [8] proposed a model for the effect of oxide particles upon sintering of metallic compacts, and concluded that non-wetted particles retarded sintering more than wetted particles. While some success was obtained in predicting the density versus volume fraction of oxide, the prediction of a weaker retardation on sintering by more wetted particles was controversial. Tikkanen, *et al.* [9] observed that the more wetted oxide had a greater effect in the sintering retardation. The discrepancy between the model of Kuczynski and Lavendel and experimental observations by Tikkanen, *et al.* is due, in part, to the fact that in the Kuczynski and Lavendel model the particles were immobile and had to be covered by the metal if the interface was to advance. Johnson [10] pointed out that while non-wetted particles provide greater restraint forces than wetted particles for advancing interfaces, they provide less restraint for receding interfaces than wetted particles. Since sintering involves both advancing and receding interfaces, it was suggested that the more wetted particles will be more effective in overall sintering retardation. The present study investigated the conditions under which ceria or hafnia can enhance or retard densification; the mechanisms associated with these behaviors are discussed.

Mat. Res. Soc. Symp. Proc. Vol. 322. ©1994 Materials Research Society

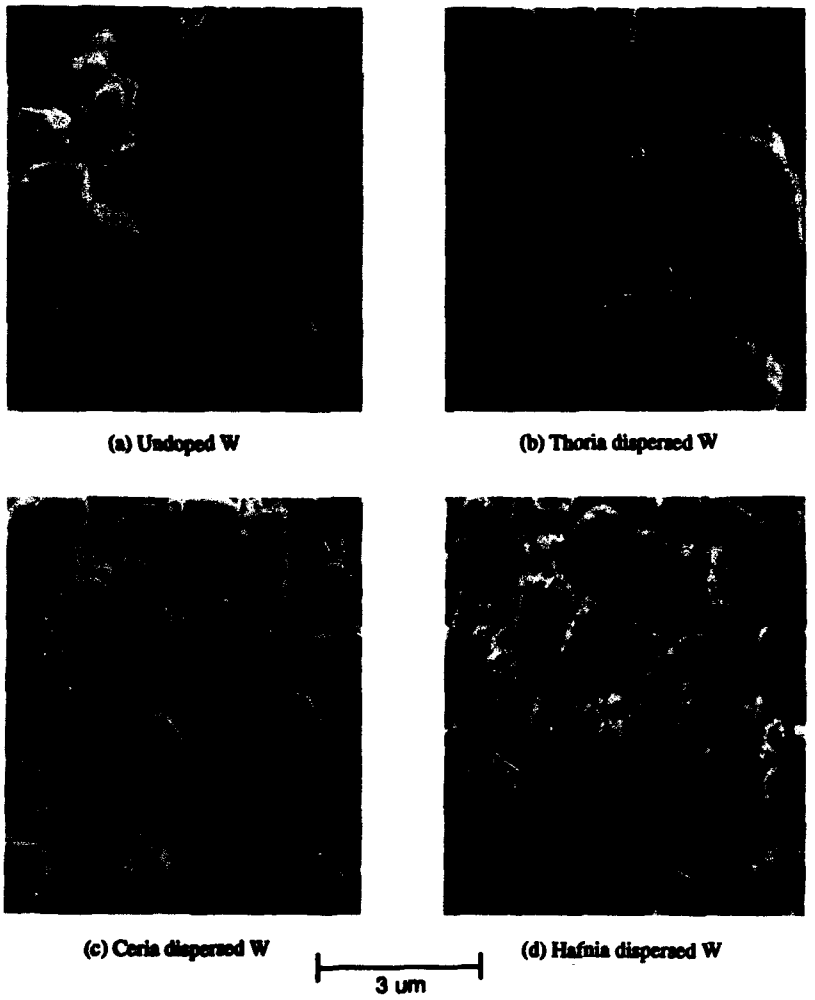


Figure 1. SEM micrographs of pressed powder compacts for (a) undoped, (b) thoria-dispersed, (c) ceria-dispersed, and (d) hafnia-dispersed W.

EXPERIMENTS

Tungsten containing 1 wt% (equivalent to 2.67 vol%) ceria and 1 wt% (equivalent to 1.98 vol%) hafnia were processed using a conventional powder metallurgy route [11]. In the present paper, C and H are used to refer to ceria and hafnia additions. For example, W with 1 wt% ceria is referred to as W-1C. Tungsten powder size distributions were determined by image analyses. Cold isostatic pressing was used to press cylindrical rods from the powder. A dilatometer manufactured by Theta Industries was used for the shrinkage measurements. Linear heating rates from 2 to 20 °C/min between 1000-1750 °C were employed (there was little sintering below 1000 °C). Dilatometry was performed in hydrogen (Dew point -77 °C) at a flow rate of 0.05 liter/min. A W mesh muffle furnace was also used for separate sintering treatments at temperatures above 1700 °C. During sintering, hydrogen (Dew point -77 °C) was flowing at a rate of 0.3 liter/min.

Scanning electron microscopy (SEM) and Auger electron spectroscopy (AES) were used to examine ingot microstructures and interfaces compositions. The microstructure evolution, in particular, the W grain size and the dispersed oxide particle size, was monitored at various stages.

RESULTS AND DISCUSSION

SEM micrographs of pressed undoped W powder compacts and W powder compacts containing thoria, ceria, and hafnia, respectively, are shown in Figure 1. Extremely fine (20-50 nm) hafnia and thoria particles were observed on the micron-sized W powder surface. In contrast, ceria particles were not observed in the W-1C compact. The ceria particles appeared to "wet" the W powder surface, as indicated from AES analyses [7].

The dilatometric traces at a linear heating rate of 3 °C/min for W.1, W.2, W-1C.1, and W-1H.1 are shown in Figure 2. The last number of sample identification (.x) was used to distinguish samples with the same composition but different processing parameters such as initial powder size or compacting pressure. W.1, W-1C.1, and W-1H.1 were pressed at 172 MPa, and W.2 was pressed at 310 MPa. Table I summarizes the initial average W powder size, d, together with its standard deviation, and the as-pressed fractional density, ρ_o/ρ_{th}, for these four samples.

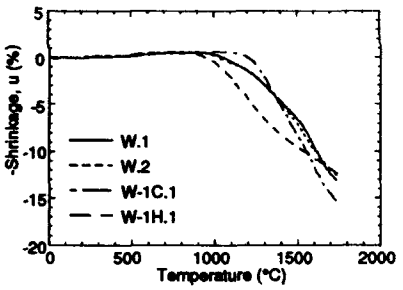


Figure 2. Dilatometric traces at a heating rate of 3 °C/min for W.1, W.2, W-1C.1, and W-1H.1.

Table I. Dilatometric shrinkages for W.1, W.2, W-1C.1, and W-1H.1

Material	ρ_o/ρ_{th}	d (μm)	@ 3 °C/min ($\%\Delta l/l_o$, ρ/ρ_{th})	@ 5 °C/min ($\%\Delta l/l_o$, ρ/ρ_{th})	@ 10 °C/min ($\%\Delta l/l_o$, ρ/ρ_{th})
W.2	0.55	2.1±0.6	13.4±0.5 (0.85)	12.7±0.6 (0.83)	11.3±0.3 (0.79)
W-1C.1	0.54	2.0±0.6	17.0±0.5 (0.94)	15.9±0.4 (0.91)	14.4±0.6 (0.86)
W.1	0.50	2.1±0.6	14.7±0.3 (0.81)	13.5±0.2 (0.77)	-
W-1H.1	0.47	1.9±0.5	13.4±0.5 (0.75)	13.6±0.3 (0.76)	13.1±0.4 (0.75)

The dilatometric traces for W.1 and W.2 were almost indistinguishable. Additions of ceria and hafnia influenced the densification process so that the shrinkage versus temperature curve had

a characteristic shape for each material. The dilatometric traces at higher heating rates shifted to higher temperatures while retaining a similar shape that is distinctive to each type of material. Final shrinkages, $\Delta l/l_o$ expressed in %, after completion of dilatometry runs at three different heating rates are also listed in Table I. Final fractional densities, ρ/ρ_{th}, are shown in parentheses. In all cases the shrinkage for W-1C.1 was much more pronounced than that for W.2. While the shrinkages for W.1, W.2, and W-1C.1 strongly depended upon the heating rate, the shrinkage for W-1H.1 was less sensitive to the heating rate. Dilatometry measurements were also performed using finer W and hafnia-dispersed W powders. The results are shown in Table II. Typical uncertainty of the shrinkage value was approximately ±0.5%. Like W-1H.1, the difference in the final shrinkage for W-1H.2 at different heating rates was negligible.

Table II. Dilatometric shrinkages for W.3, and W-1H.2

Material	ρ_o/ρ_{th}	d (μm)	@ 2 °C/min ($\%\Delta l/l_o$, ρ/ρ_{th})	@ 5 °C/min ($\%\Delta l/l_o$, ρ/ρ_{th})	@ 10 °C/min ($\%\Delta l/l_o$, ρ/ρ_{th})	@ 20 °C/min ($\%\Delta l/l_o$, ρ/ρ_{th})
W.3	0.41	1.2±0.5	22.9 (0.89)	22.1 (0.87)	21.8 (0.86)	21.2 (0.84)
W-1H.2	0.42	0.9±0.3	21.7 (0.87)	21.8 (0.88)	21.9 (0.88)	21.9 (0.88)

From the raw dilatometer traces, such as those shown in Figure 2, the densification rate of W can be derived. Positive dimensional change below 1000 °C was due to thermal expansion as described elsewhere [12]. The activation energy, Q, for the densification rate was determined by plotting $\ln(T d\rho/dt)$ versus $1/T$ for each ρ. Figure 3 shows the results for W.3. The slope of a straight line fit through the iso-density points in the plot gives an activation energy at that specific ρ [12]. For W.3, the average apparent activation energy derived for densities in the range of 0.45-0.8 was 318±21 kJ/mole. For W-1C.1, similar analyses gave an apparent activation energy of 385±15 kJ/mole. Unlike W and ceria-dispersed W, hafnia-dispersed W did not give a constant activation energy. The activation energy varied from 581 kJ/mole to 1195 kJ/mole for W-1H.2 (Figure 4). For W-1H.1 the activation energy varied from 279 kJ/mole to 844 kJ/mole. The activation energies for the sintering of W obtained from the present work and from literature are listed in Table III. The variations in the reported activation energies were partly because different rate equations were used by various authors. The present W results agree with those of Charles and Prochazka [13].

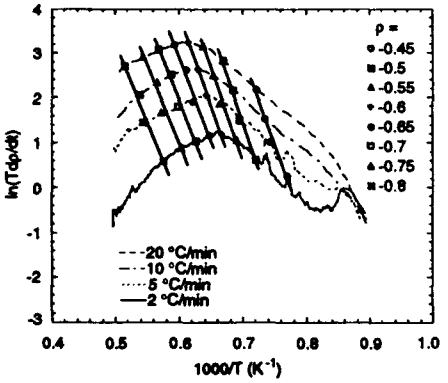


Figure 3. A plot of $\ln(Td\rho/dt)$ versus $1/T$ for W.3 taken at heating rates of 2, 5, 10, and 20 °C/min.

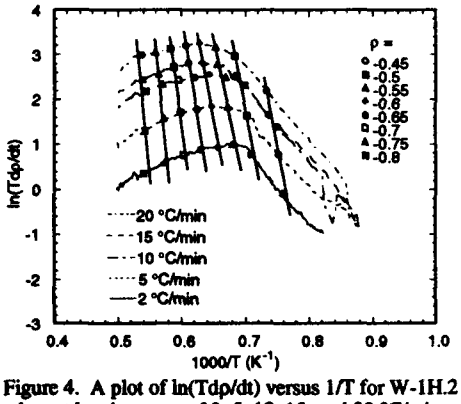


Figure 4. A plot of $\ln(Td\rho/dt)$ versus $1/T$ for W-1H.2 taken at heating rates of 2, 5, 10, 15, and 20 °C/min.

Table III. Activation energies for sintering of W

Material	Powder size (μm)	Temperature range (°C)	Activation energy (kJ/mole)	Reference
W	1.2; 2.1	1000 - 1750	318 ± 21; 290 ± 25	this work
W-1C	2.0	1000 - 1750	385 ± 15	this work
W-1H	0.9; 1.9	1000 - 1750	581 - 1195; 279 - 844	this work
W	0.6 - 3	1000 - 1800	314 - 335	[13]
W	3	1100 - 1500	428 ± 8	[14]
W	0.5	1100 - 1600	370	[15]
W	0.45 -0.88	1370 - 1750	466	[16]

Literature data of the activation energies for lattice diffusion, grain boundary diffusion, and surface diffusion in pure W are 507-640 kJ/mole [17], 385 kJ/mole [18], and 268-327 kJ/mole [19], respectively. The present activation energies for W and W-1C indicate that densification was controlled by grain boundary diffusion. A higher activation energy for ceria-dispersed W suggests stronger bonding at W-ceria interfaces (i.e. a lower interfacial energy) since grain boundary diffusion requires bond breaking. The W-ceria interfacial energy was estimated as 0.941 J/m^2 [7], which is lower than the W-W grain boundary energy of 1.08 J/m^2 [20]. A low W-ceria interfacial energy and a high W surface energy of 2.8 J/m^2 [20] suggested wetting of ceria on W, consistent with AES observations.

Final densities of W-1C.1 and W-1H.1 after sintering at some selected high temperatures are listed in Table IV. It is evident that the sintered density of W-1H.1 was lower than that of W-1C.1 when sintered at lower temperatures, while the difference was not significant at higher temperatures. Grain size measurements revealed that grain growth was negligible until the fractional density exceeded 0.8 for undoped W. If ceria or hafnia were added, the transition from insignificant grain growth to rapid grain growth occurred at a fractional density of 0.95 (Figure 5).

Table IV. Sintered density, ρ in g/cm^3 and (ρ/ρ_{th}), for W-1C.1 and W-1H.1

Material	1900 °C, 5 min	2100 °C, 5 min	2300 °C, 5 min	2300 °C, 120 min
W-1C.1	15.6 (0.82)	17.4 (0.92)	18.2 (0.96)	18.6 (0.98)
W-1H.1	13.8 (0.72)	16.8 (0.88)	18.1 (0.95)	18.4 (0.96)

Typical SEM micrographs of sintered W and thoria-, ceria-, and hafnia-dispersed W ingots with densities above 0.95 are shown in Figure 6. In comparison to undoped W, additions of ceria, hafnia, and thoria were effective in retarding grain growth and achieving a higher density. However, the oxide particle size evolved quite differently. Both thoria and ceria particles grew to 1-2 μm after sintering at 2300 °C, while the majority of hafnia particles were ~ 100 nm. The lower resistance to coarsening for ceria particles can have a detrimental effect.

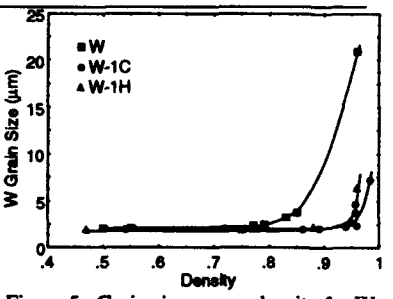


Figure 5. Grain size versus density for W, W-1C, and W-1H.

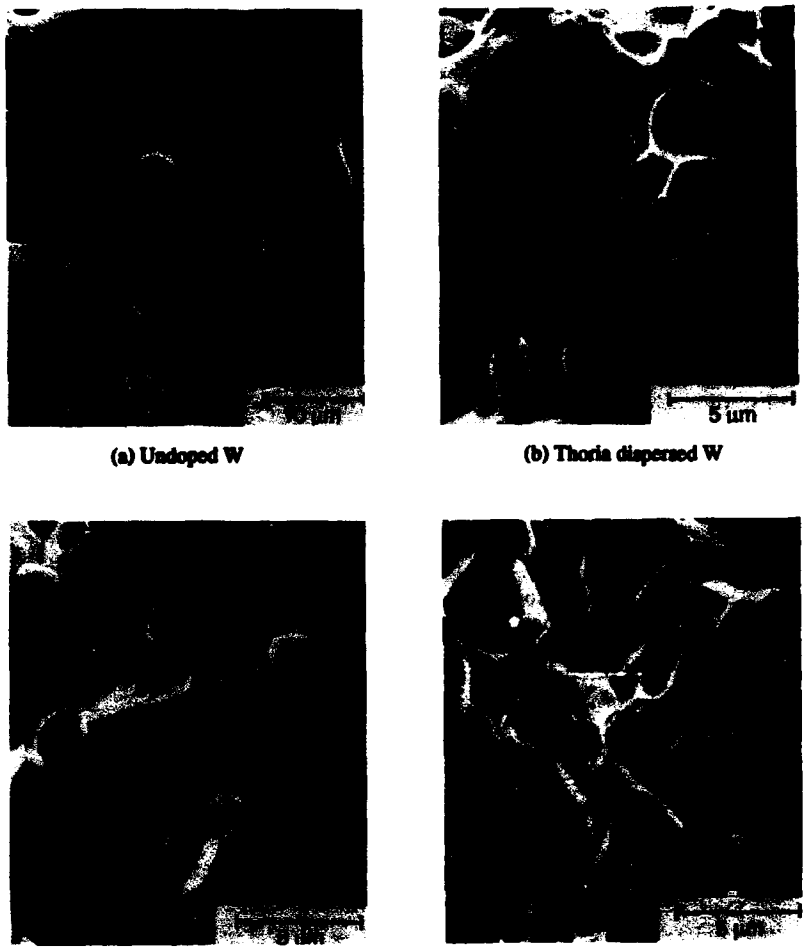


Figure 6. SEM micrographs of well-sintered ingots for (a) undoped, (b) thoria-dispersed, (c) ceria-dispersed, and (d) hafnia-dispersed W.

CONCLUSION

The effects of ceria and hafnia additions on sintering of W were investigated. Density changes and microstructural evolution including W grain and oxide particle size were monitored. A "crossover" in the behavior of densification between W-1C and W-1H was observed: Ceria retarded W densification more than hafnia during the early stages of sintering, and the opposite occurred as the sintering proceeded. During the last stage of sintering (in which W grain growth and coarsening of particles started), particles such as hafnia with higher resistance to coarsening became more effective in retarding W grain growth. The last point provides the explanation for a more rapid elimination of porosity during sintering of hafnia-dispersed W compacts at high temperatures. Dilatometric analyses gave an apparent activation energy for the densification rate of W and W-1C of 318±21 and 385±15 kJ/mole, respectively, suggesting that densification of W and W-1C was controlled by grain boundary diffusion. W-1H gave an activation energy that varied from 279 to 1195 kJ/mole. While the higher activation energy of sintering in W-1C in comparison to W can be attributed to a lower W-ceria interface energy, the origins of anomalous high values of activation energy of sintering in W-1H are unknown.

ACKNOWLEDGEMENTS

The authors are very grateful to M. Curran, K. Denike, and L. Rogers, J. McKiever, E. Whittemore, J. Grande and K. Lou for sample preparations and measurements. L. C. Chen is also indebted to R. Charles, F. Klug, S. Prochazka, A. Taub, and H. Lipsitt for valuable discussions.

REFERENCES

1. W. D. Coolidge, *Proc. Am. Inst. Elec. Eng.*, 961 (1910).
2. H. G. Sell, W. R. Morcom, G. W. King, and N. F. Cerulli, AFML-TR-65-407, Part I (1965), and Part II (1966).
3. V. V. Bukhanovskii, V. K. Kharchenko, V. S. Kravchenko, A. B. Ol'shanskii, S. A. Golovin, and V. N. Nikol'skii, *Soviet Powder Metallurgy and Metal Ceramics* **24**, 652 (1985).
4. E. Barwa and R. Schwab, *Schweissen Schneiden* **40**(1), 24 (1988).
5. F. Matsuda, M. Ushio, and T. Kumagai, *Weld. Int.* **3**(6), 497 (1989); *Q. J. Jpn, Weld. Soc.* **6**(2), 3(1988); *Yosetsu Gakkai Ronbunshu* **6**(2), 205(1988); *Trans. JWRI* **16**(2), 247(1987); *Trans. JWRI* **15**(1), 13 (1986).
6. M. Ushio, A. A. Sadek, and F. Matsuda, *Plasma Chem. Plasma Process* **11**, 81 (1991).
7. L. C. Chen, K. A. Lou, and B. P. Bewlay, *Proceedings of the Third Int. Conference on Powder Metallurgy in Aerospace, Defense and Demanding Applications*, F. H. Froes, ed., 111 (1993).
8. G. C. Kuczynski and H. W. Lavendel, *Int. J. of Powder Metallurgy* **5** [4], 19 (1969).
9. M. H. Tikkanen, B. O. Rosell, and O. Wiberg, *Powder Met.* **10**, 49 (1962).
10. D. L. Johnson, *J. Mater. Sci.* **11**, 2312 (1976).
11. J. L. Walter and A. U. Seybolt, *Trans. TMS-AIME* **245**, 1093 (1969).
12. L. C. Chen, *Int. J. Refractory Metals & Hard Mater.* (in press).
13. R. J. Charles and S. Prochazka, *J. Mater. and Engin. Sci.* (in press).
14. N. C. Kothari, *J. Less Common Metals* **5**, 140 (1963).
15. N. C. Kothari, *Physics of Sintering*, **3**, 85 (1971).
16. T. Vasilos and J. T. Smith, *J. Appl. Phys.* **35** [1], 215 (1964).
17. V. P. Vasil'ev and S. C. Chernomorchenko, *Zavodsk. Lab.* **22**, 688 (1956); W. Danneberg, *Metall.* **15**, 977 (1961); R. L. Andelin, J. D. Knight and M. Kahn, *Trans.-AIME* **233**, 19 (1965).
18. K. G. Kreider and G. Bruggeman, *Trans.-AIME* **239**, 1222 (1967).
19. J. P. Barbour, *et al.*, *Phys. Rev.* **117**, 1452 (1960); B. C. Allen, *Trans.-AIME* **227**, 1175 (1963); B. C. Allen, *Trans.-AIME* **236**, 915 (1966); D. M. Moon and R. C. Koo, *Met. Trans.* **2**, 2115 (1971).
20. B. C. Allen, *J. Less-Common Metals* **29**, 263 (1972).

MICROSTRUCTURES AND MECHANICAL BEHAVIOR OF Nb-Ti BASE BETA + SILICIDE ALLOYS

P. R. SUBRAMANIAN*, M. G. MENDIRATTA*, and D. M. DIMIDUK**
*Materials Research Division, UES, Inc., 4401 Dayton-Xenia Road, Dayton, OH 45432.
**Wright Laboratory, WL/MLLM, Wright-Patterson AFB, OH 45433.

ABSTRACT

Studies on Nb/Nb_5Si_3 based *in-situ* composites have demonstrated an acceptable balance of low-temperature damage tolerance and high-temperature strength/creep resistance. However, catastrophic oxidation and embrittlement of these materials limit their usefulness in structural applications. Alloying studies were initiated at Wright Laboratory with the aim of obtaining incremental improvement in the overall oxidation response of the Nb/Nb_5Si_3 system, while seeking microstructurally similar systems. The results showed that reduced metal recession rates and oxygen embrittlement can be obtained by Ti and Al additions to Nb-Si base alloys. This paper focuses on the effect of Ti and Al alloying additions to Nb-Si base alloys on phase equilibria, microstructures, temperature dependence of strength, low-temperature toughness, and environmental resistance.

INTRODUCTION

Advanced intermetallic materials, such as refractory silicides, typically exhibit high melting temperatures, high stiffness, moderately low densities, and good strength retention at elevated temperatures, thereby offering the potential for applications in the 1000-1600°C temperature range. However, these attractive characteristics are accompanied by a lack of damage tolerance manifested by extremely low fracture toughness at low temperatures. This attribute alone dictates that the advanced intermetallics in monolithic form have limited prospects for providing the required balance of properties for use at very high operating temperatures. Multiphase intermetallic systems, on the other hand, may provide one solution to the intrinsically poor damage tolerance of the monolithic intermetallics. One of the alloy development approaches that holds promise involves distributing a ductile, refractory phase in a brittle intermetallic matrix. In such a system, plastic energy dissipation by the ductile phase can be exploited for improving the overall fracture resistance of the system, while the intermetallic matrix yields high-temperature strength and creep resistance.

The overall objectives of our research program on advanced intermetallic materials are as follows: a) Investigate fundamentals of mechanical behavior within multiphase intermetallic systems, focusing on the balance between low-temperature damage tolerance and high-temperature strength and creep resistance of alloy systems, (b) Study microstructural evolution and/or processing influences on the balance in mechanical properties, and (c) Improve environmental resistance through alloying, and evaluate structural properties of systems with improved environmental resistance.

Detailed studies [1,2] on a two-phase Nb-Nb_5Si_3 alloy system have demonstrated that substantial improvements in damage tolerance can be obtained via ductile phase toughening, but without sacrificing the high-temperature strength. However, it is well-recognized that all Nb-base alloys suffer from catastrophic oxidation and oxygen penetration embrittlement upon exposure to air at temperatures above 500°C. Typically, Nb-base alloys oxidize mainly by anionic diffusion, with the rapid formation of stratified and porous layers which spall off easily. Nb-Nb_5Si_3 alloys are no exceptions to this behavior, and suffer from two problems: (a) High recession rates, spalling and general structural disintegration of the alloy, and (b) fast diffusion of oxygen through the oxide layers, followed by dissolution of oxygen in the Nb phase, resulting in substantial hardening and embrittlement of the Nb phase in the alloy. It should be realized that the oxidation problem in these alloys cannot be solved completely in that the alloys never exhibit parabolic rate

Mat. Res. Soc. Symp. Proc. Vol. 322. ©1994 Materials Research Society

constants; for eventual application of these alloys, coatings will have to be developed. The database generated by several past research efforts on Nb-base alloys formed the basis for initial alloying studies in the Nb-Si system. The general philosophy of this alloying scheme was to seek incremental improvements in the overall oxidation behavior of the Nb-Nb_5Si_3 system, while reducing the oxygen solubility in the (Nb) phase. The preliminary microstructural and oxidation screening studies were conducted on (a) ternary Nb-(10-20)Si base alloys with Mo, Ti, W, and V additions, and (b) Nb-Ti base alloys with ternary Si and quaternary Al, Zr, and Ru additions. The screening results showed that reduced metal recession rates and oxygen embrittlement can be obtained by Ti and Al additions to Nb-Si base alloys. In this paper, we report on the effect of the Ti and Al alloying additions to Nb-Si base alloys on phase equilibria, low-temperature toughness, high-temperature strength, and environmental resistance.

EXPERIMENTAL

For phase relationship investigations, selected alloys in the Nb-Ti-Si ternary and Nb-Ti-Si-Al quaternary systems were prepared in the form of ~250 g cigar-shaped castings, by arc-melting the constituent elements in a water-cooled copper hearth, using a non-consumable tungsten electrode. The arc-melted "cigars" were wrapped in Ta foil and heat-treated at 1500°C for 100 h in flowing argon, which was first gettered over Ti chips heated to 800°C. Backscattered scanning electron microscopy (SEM) and electron probe microanalysis (EPMA) were conducted on the heat-treated alloys to characterize the microstructure and composition of the equilibrium phases. The identity of the phases was verified by X-ray diffraction (XRD). The oxidation behavior of the selected alloys was evaluated by exposing ~5 mm thick coupons of the alloys in an air furnace at 1200°C for 24-100 hours. This test furnishes qualitative information on the oxidation resistance of the alloys, and aids in screening out alloys which show little or no protection from oxidation. Cross-sectional microstructural analyses were performed on the oxidized samples to measure the adherent scale thickness and the extent of metal loss or recession. The microstructural analysis was complemented by Vickers microhardness depth profiling to evaluate the extent of oxygen penetration and embrittlement in the beta phase. This allows us to determine qualitatively the extent of retention of plasticity in the beta phase after oxidation.

For mechanical behavior characterization, two alloys with nominal compositions 42.5Nb-42.5Ti-15Si and 40Nb-40Ti-15Si-5Al were procured in the form of large castings and then hot-extruded (1482°C; 10:1 extrusion ratio) in Mo cans. Specimens from the castings were annealed at 1200 and 1500°C for 100 h in flowing argon, prior to microstructural characterization. Smooth bend bars (2.86 cm long x 0.64 cm wide x 0.32 cm thick) and single-edge notched bend bars (2.86 cm long x 0.64 cm wide x 0.64 cm thick; EDM notch: 0.25 cm deep, 0.02 cm root radius) were obtained from the extruded specimens by electrical-discharge machining, wrapped in Ta foil, and then heated in flowing argon for 100 h at 1500°C. The smooth bend bars were tested in a vacuum of ~10^{-4} Pa at selected temperatures between ambient and 1200°C under four-point loading, in order to obtain bend strengths as a function of temperature. The single-edge notched bend bars were tested under three-point loading conditions to determine room-temperature notch toughness, K_Q.

Following mechanical testing, SEM examinations were conducted on the fracture surfaces and lateral surfaces of the bend specimens to characterize the fracture mechanisms. It is of particular interest to determine the crack propagation modes in the matrix as well as the reinforcement, in order to establish the operative toughening mechanism(s).

RESULTS AND DISCUSSION

Phase Relations and Microstructures

Nb-Ti-Si Alloys: Table I lists the nominal alloy compositions as well as the compositions of the equilibrium phases present after heat-treatment for the Nb-Ti-Si alloys. In the Nb-Ti-Si alloys,

Table I. Nb-Ti-Si Alloy Compositions and Phase Analysis.

Alloy Composition (at.%)	Phases	Phase Composition (at.%) after 1500°C/100 h Heat-Treatment Nb	Ti	Si
80Nb-10Ti-10Si	Beta	88.8	10.5	0.7
	$(Nb,Ti)_3Si$	62.7	12.2	25.1
	$(Nb,Ti)_5Si_3$	50.6	11.8	37.6
75Nb-15Ti-10Si	Beta	83.9	15.2	0.9
	$(Nb,Ti)_3Si$	57.7	17.0	25.3
42.5Nb-47.5Ti-10Si	Beta	47.6	51.3	1.1
	$(Ti,Nb)_3Si$	33.6	42.9	23.5
40Nb-45Ti-15Si	Beta	46.8	51.7	1.5
	$(Ti,Nb)_3Si$	34.6	42.2	23.2
37.5Nb-42.5Ti-20Si	Beta	48.3	50.2	1.5
	$(Ti,Nb)_3Si$	36.2	40.2	23.6
42.5Nb-42.5Ti-15Si	Beta	53	46.5	0.5
	$(Ti,Nb)_3Si$	35.5	39.7	24.8

the equilibrium phases were beta (Nb,Ti), with 0.5-1.5 at.% Si in solution, and $(Ti,Nb)_3Si$. In the binary Nb-Si and Ti-Si systems, the phases Nb_3Si and Ti_3Si exist with a similar crystal structure (Ti_3P-type), although Nb_3Si is a high-temperature phase, which is stable only between ~1765 and 1975°C [3], while Ti_3Si is a stable phase between ambient and 1170°C [3]. It appears that the $(Ti,Nb)_3Si$ phase observed in the Nb-Ti-Si alloys may be Ti_3Si stabilized at 1500°C by Nb additions. Figure 1 shows the Nb+Ti-rich section of the Nb-Ti-Si ternary phase diagram at 1500°C. As a representative example, a backscattered SEM micrograph of the alloy Nb-42.5Ti-15Si in the cast + 1500°C/100 h heat-treated condition is shown in Fig. 2(a). Figures 2(b) and (c) show SEM micrographs of the same alloy in the as-extruded condition, and after heat-treatment of the extruded alloy at 1200°C/100 h, respectively. As seen in Fig. 2(b), hot-extrusion of the alloy has resulted in dynamic recrystallization of both the beta and $(Ti,Nb)_3Si$ phases.

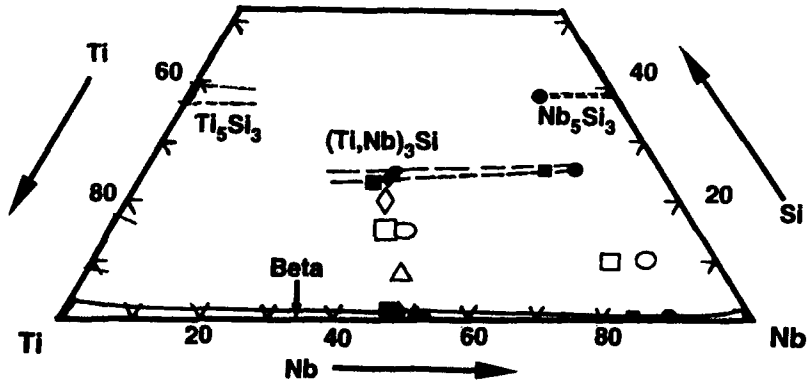


Figure 1. Nb+Ti-Rich Section of the Nb-Ti-Si Phase Diagram at 1500°C.
Open Symbols: Nominal Bulk Compositions; Filled Symbols: Phase Compositions.

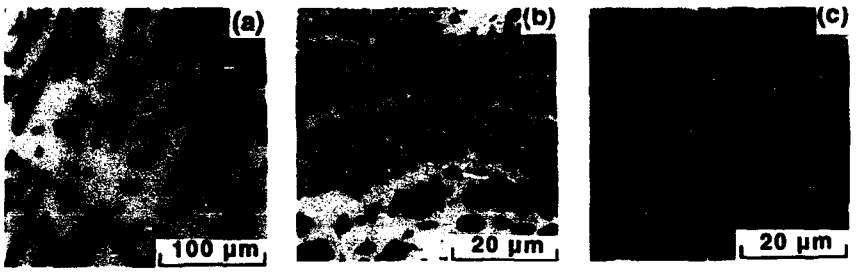


Figure 2. Backscattered SEM Micrographs of the Alloy Nb-42.5Ti-15Si: (a) As-Cast + 1500°C/100 h, (b) As-Extruded (1482°C; 10:1 Extrusion Ratio), and (c) Extruded + 1200°C/100 h. Light Phase: Beta; Dark Phase: $(Ti,Nb)_3Si$.

Nb-Ti-Si-Al Alloys: Alloys with several Nb/Ti ratios, specifically Nb/Ti = 7.5, 4.7, 1.0, 1.125, and 1.27, were evaluated for phase equilibria. Table II lists the phases present and their compositions in cast+heat-treated Nb-Ti-Si-Al alloys with Nb:Ti ratio = 1.0. In these alloys, the

Table II. Alloy Compositions and Phase Analysis for Nb-Ti-Si-Al Alloys With Nb/Ti=1.0.

Alloy Composition (at.%)	Phases*	Phase Composition (at.%) after 1500°C/100 h Heat-Treatment Nb	Ti	Si	Al
40Nb-40Ti-15Si-5Al	$(Nb,Ti)_5(Si,Al)_3$	33.0	29.8	33.8	3.4
	$(Nb,Ti)_3Si$	39.9	35.0	24.9	0.2
	Beta	50.0	40.6	1.6	7.8
38Nb-38Ti-19Si-5Al	$(Nb,Ti)_5(Si,Al)_3$	34.8	29.6	31.9	3.7
	$(Ti,Nb)_5(Si,Al)_3$	24.6	39.6	33.0	2.8
	Beta	45.6	44.4	1.5	8.4
36.5Nb-36.5Ti-19Si-8Al	$(Nb,Ti)_5(Si,Al)_3$	34.8	27.9	32.8	4.5
	$(Ti,Nb)_5(Si,Al)_3$	22.9	39.8	33.9	3.4
	Beta	43.7	44.3	0.7	11.3
35Nb-35Ti-20Si-10Al	$(Nb,Ti)_5(Si,Al)_3$	35.5	27.7	31.8	5.0
	$(Ti,Nb)_5(Si,Al)_3$	24.8	38.1	31.8	5.3
	Beta	38.9	44.5	0.8	15.8
32.5Nb-32.5Ti-25Si-10Al	$(Nb,Ti)_5(Si,Al)_3$	31.4	31.9	27.6	9.1
	$(Ti,Nb)_5(Si,Al)_3$	23.1	40.1	29.7	7.1
	Beta	~39	~41	<1	~20
	Orthorhombic?	~16	~60	<1	~23
30Nb-30Ti-30Si-10Al	$(Nb,Ti)_5(Si,Al)_3$	27.0	36.6	26.7	9.7
	$(Ti,Nb)_5(Si,Al)_3$	20.2	42.8	30.3	6.7
	Beta	34.0	45.9	0.6	19.5
	Orthorhombic?	15.7	60.0	0.8	23.5
30Nb-30Ti-20Si-20Al	$(Nb,Ti)_5(Si,Al)_3$	33.1	29.1	29.4	13.4
	$(Ti,Nb)_5(Si,Al)_3$	24.8	38.2	27.5	9.5
	γ-TiAl ?	16.1	30.2	0.4	53.3

Si concentration of the alloys ranged from 15 to 30 at.%, while the Al concentration was varied from 5 to 20 at.%. For Nb/Ti>1, the Si and Al concentrations were fixed at 22 and 10 at.%, respectively, and phase relationships were evaluated at 1200 as well as 1500°C. Additionally, two Nb-rich alloys with 10-15 at.% Ti, 10 at.% Si, and 5 at.% Al were evaluated. Table III summarizes the composition data for alloys with Nb:Ti ratios greater than 1.0. The primary objective was

* $(Nb,Ti)_5(Si,Al)_3$: $D8_l$-type Nb_5Si_3-base alloy; $(Ti,Nb)_5(Si,Al)_3$: $D8_8$-type Ti_5Si_3-base alloy.

Table III. Alloy Compositions and Phase Analysis for Nb-Ti-Si-Al Alloys with Nb/Ti>1.0.

Nb/Ti Ratio	Alloy Compositions (at.%)	T (°C)	Phases	Phase Composition (at.%) Nb	Ti	Si	Al
1.125	36Nb-32Ti-22Si-10Al	1500	$(Nb,Ti)_5(Si,Al)_3$	34.6	28.8	29.3	7.3
			$(Ti,Nb)_5(Si,Al)_3$	27.3	36.3	30.5	5.9
			Beta	41.9	41.8	0.6	15.6
		1200	$(Nb,Ti)_5(Si,Al)_3$	34.8	28.1	30.4	6.7
			$(Ti,Nb)_5(Si,Al)_3$	26.9	36.2	30.9	6.0
			$(Nb,Ti)_3Al$	50.8	28.5	3.3	17.4
			Beta	42.4	41.4	0.6	15.6
1.27	38Nb-30Ti-22Si-10Al	1500	$(Nb,Ti)_5(Si,Al)_3$	36.8	26.1	30.3	6.8
			$(Ti,Nb)_5(Si,Al)_3$	28.1	34.7	30.9	6.3
			Beta	43.3	40.3	0.6	15.8
		1200	$(Nb,Ti)_5(Si,Al)_3$	34.9	28.3	28.4	8.4
			$(Ti,Nb)_5(Si,Al)_3$	24.2	38.7	30.7	6.4
			$(Nb,Ti)_3Al$	50.8	28.1	3.7	17.4
			Beta	43.4	41.4	0.6	14.6
4.7	70Nb-15Ti-10Si-5Al	1500	$(Nb,Ti)_5(Si,Al)_3$	48.5	13.7	34.5	3.3
			Beta	75.5	15.8	1.0	7.7
7.5	75Nb-10Ti-10Si-5Al	1500	$(Nb,Ti)_5(Si,Al)_3$	52.1	10.4	33.6	3.9
			Beta	81.4	10.8	0.8	7.0
			Unknown	71.8	9.2	6.6	12.4

to investigate high-temperature phase stability and microstructures over a range of compositions within the beta (Nb,Ti)-Nb_5Si_3-Ti_5Si_3 phase field. As seen in Table II, in most cases, the phases observed were $(Nb,Ti)_5(Si,Al)_3$, $(Ti,Nb)_5(Si,Al)_3$, and beta (Nb,Ti,Al). As an example, Fig. 3 shows the SEM microstructure from a cast+heat-treated Nb-38Ti-19Si-5Al alloy. The beta phase had Si solubilities ranging from 0.6-1.6 at.% Si depending upon bulk alloy composition. For Nb/Ti=1.0, alloys containing ≥25 at.% Si showed the formation of needle-like precipitates (Fig. 4) within the beta phase having an average composition ~16Nb-60Ti-1Si-23Al, which presumably corresponds to the orthorhombic Ti_2AlNb phase [4]. Further, the beta phase is no longer present

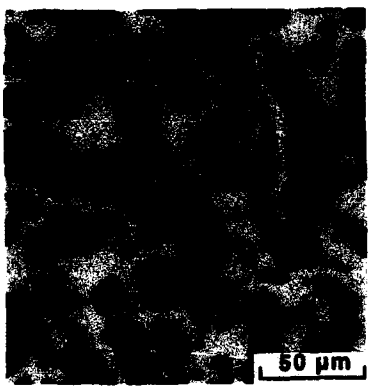


Figure 3. Backscattered SEM Micrograph of Cast + 1500°C/100 h Heat-Treated 38Nb-38Ti-19Si-5Al Alloy.

Gray Phase: $(Nb,Ti)_5(Si,Al)_3$
Black Phase: $(Ti,Nb)_5(Si,Al)_3$
White Phase: Beta

at an Al concentration of 20 at.% in alloys with Nb/Ti=1.0. Hence, in order to have beta as one of the phases, which is a requirement for low-temperature toughness, the Al concentration cannot be increased much beyond 10%. At 1200°C, the A15-type $(Nb,Ti)_3Al$ phase was observed to form within the beta phase as needle-shaped precipitates in alloys with Nb/Ti=1.125 and 1.27 (e.g., see Fig. 5).

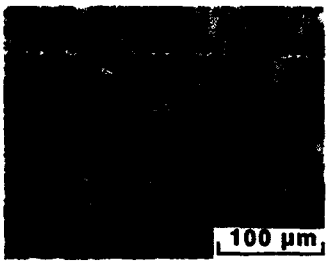


Figure 4. Backscattered SEM Micrograph of Cast + 1500°C/100 h Heat-Treated 32.5Nb-32.5Ti-25Si-10Al Alloy Showing the Formation of Precipitates Within the Beta Phase.

Gray Phase: $(Nb,Ti)_5(Si,Al)_3$
Black Phase: $(Ti,Nb)_5(Si,Al)_3$
White Phase: Beta
Precipitates: Orthorhombic Ti_2AlNb?

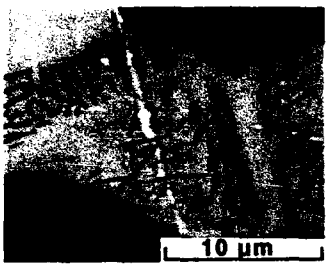


Figure 5. Backscattered SEM Micrograph of Cast + 1200°C/100 h Heat-Treated 38Nb-30Ti-25Si-10Al Alloy Showing the Formation of Needle-like Precipitates of the A15-type $(Nb,Ti)_3Al$ Phase Within Beta.

Gray Phase: $(Nb,Ti)_5(Si,Al)_3$
White Phase: Beta
Precipitates: $(Nb,Ti)_3Al$

Figure 6 shows the SEM micrographs of the ingot with the composition Nb-40Ti-15Si-5Al in the (a) as-cast state and (b) as-extruded condition, and (c) after extrusion, followed by heat-treatment at 1500°C/100 h. In the as-cast state, the phases observed in this alloy were $(Nb,Ti)_5(Si,Al)_3$, $(Ti,Nb)_5(Si,Al)_3$, and beta (Nb,Ti,Al), as well as an eutectic-type phase with average composition 28Nb-50Ti-18Si-4Al. Upon extrusion and heat-treatment at 1500°C/100 h, the phase-field appeared to have shifted in this alloy, resulting in a three-phase equilibrium between beta (Nb,Ti,Al), $(Nb,Ti)_5(Si,Al)_3$, and $(Nb,Ti)_3Si$. This $(Nb,Ti)_3Si$ phase was not observed in any of the other Nb-Ti-Si-Al alloys. Based on the observed phases, a schematic quaternary Nb-Ti-Si-Al phase diagram, highlighting only the regions of interest in this study, is shown in Fig. 7.

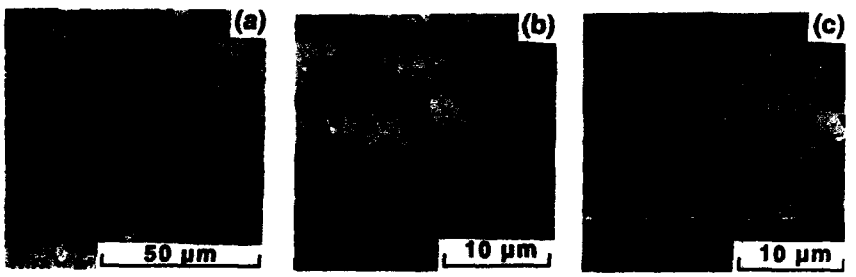


Figure 6. Backscattered SEM Micrographs of the alloy Nb-40Ti-15Si-5Al: (a) As-Cast + 1500°C/100 h (b) As-Extruded (1482°C; 10:1 Extrusion Ratio), and (c) As-Extruded + 1500°C/100 h.

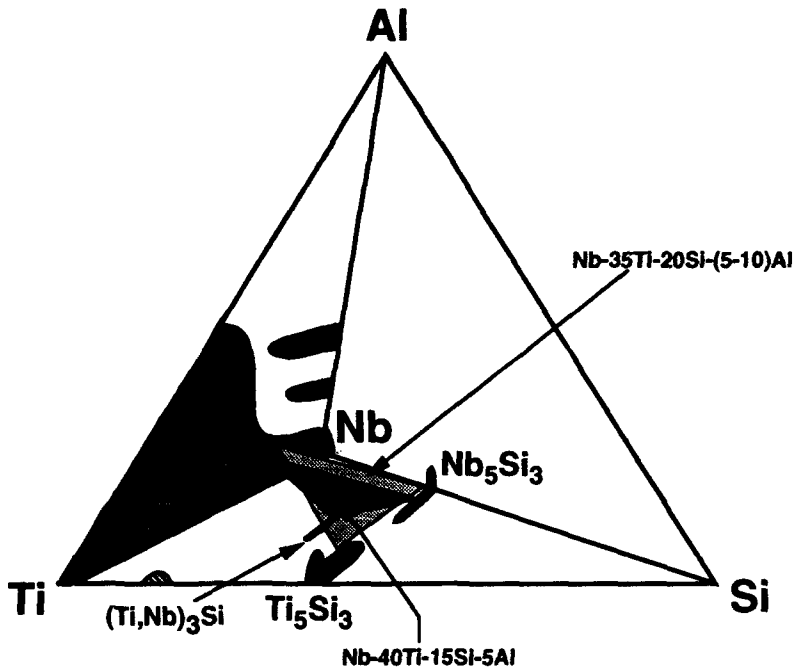


Figure 7. Schematic Quaternary Nb-Ti-Si-Al Phase Diagram at 1500°C, Showing Regions of Interest in this Study.

Oxidation Screening

A cross-section SEM micrograph of the oxidized specimen of a selected Nb-Ti-Si-Al alloy is shown in Fig. 8. In addition to a surface oxide scale, a region with internal oxidation of the beta phase was observed in all of the alloys. Further, there exists a region below the internal oxidation region, within which the beta phase contains dissolved oxygen. Figure 9(a) compares the recession data after a 1200°C/24 h static air exposure for selected Nb-Ti-Si and Nb-Ti-Si-Al alloys, along with data for the baseline Nb-Nb_5Si_3 alloy and a commercial Nb-base alloy (B66), while Fig. 9(b) shows the oxygen penetration depths in the beta-phase constituent of the alloys after the 1200°C exposure. As seen in Fig. 9(a), the addition of Ti to Nb-Si dramatically reduces the metal loss or recession rate. A further reduction in recession rate was observed with Al additions. A goal for an environmentally stable, high-temperature structural alloy system is also shown in Fig. 9(a). This specifies the maximum use temperature for an alloy system as the temperature below which a recession rate of <0.1 mil/h is obtained in an oxidizing atmosphere. The oxidation resistance of the alloys examined thus far is still inadequate for structural applications at 1200°C, although substantial improvements have been demonstrated over the baseline Nb-Si system. The dissolution of oxygen within the beta phase results in hardening and embrittlement of the beta phase. The implications of the oxygen dissolution are not well-understood, in that while it is expected to have a deleterious effect on the overall toughness of the alloy system, the tolerance for dissolved oxygen has not been quantitatively established.

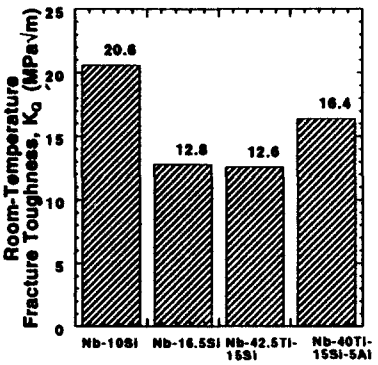


Figure 11. Comparison of Ambient Temperature Fracture Toughness Data for Alloys Nb-42.5Ti-15Si and Nb-40Ti-15Si-5Al with Data for Nb-Si Alloys [1,7].

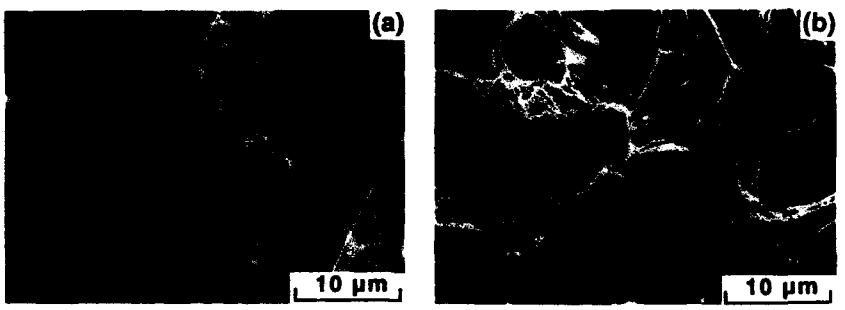


Figure 12. SEM Fractographs for (a) Alloy Nb-42.5Ti-15Si and (b) Alloy Nb-40Ti-15Si-5Al Fractured at Room-Temperature Under Three-Point Loading Conditions.

the case of the Nb-Ti-Si-Al alloy, the small size (~4-5 μm) of the beta particles may not have contributed significantly to toughening. These results demonstrate the need for further optimization of microstructure through alloying and/or processing modifications. If ductile-phase bridging is assumed to be a primary mode of toughening, then the composite toughness of the alloys can be obtained using the following equation [8,9]:

$$K_c = \sqrt{\left(\frac{E_c(1-f)K_m^2}{E_m}\right) + \chi f E_c \sigma_o a_o} \qquad (1)$$

where E_c and E_m are the elastic moduli of the composite and the intermetallic matrix, respectively, K_m is the matrix toughness, and f, σ_o, and $2a_o$ are the volume fraction, yield strength, and the size of the ductile phase, respectively. Table IV summarizes these parameters for the Nb-Ti-Si and Nb-Ti-Si-Al alloys. The parameter χ is the normalized work of rupture of the ductile phase and is strongly influenced by the constraint imposed upon the ductile phase by the surrounding elastic

intermetallic matrix. Previous work [1,7] on wrought Nb-Nb_5Si_3 alloys have shown that the toughness increment in these alloys due to ductile-phase bridging can be predicted reasonably well by using χ = 1.6-1.75. Using a value of χ = 1.6 in Eq. (1), the toughness of the Nb-Ti-Si and Nb-Ti-Si-Al alloys were calculated as 17.8 MPa$\sqrt{m}$ and 16.5 MPa$\sqrt{m}$, respectively. These results compare fairly well with the experimental data, considering the assumptions used in the calculations. This suggests that the toughening mechanisms in the ternary and quaternary Nb-Ti-Si-(Al) alloys are, at least, in qualitative agreement with theories on ductile-phase toughening of brittle intermetallic matrices.

Table IV. Parameters Used for the Calculation of Fracture Toughness of Nb-42.5Ti-15Si and Nb-40Ti-15Si-5Al Alloys Based on Equation (1).

Parameter	Alloy Nb-42.5Ti-15Si	Alloy Nb-40Ti-15Si-5Al	Comments
f	0.34	0.41	---
$2a_o$	7.9 μm	4.2 μm	---
σ_o	552 MPa*	~730 MPa§	See below
K_m	3 MPa$\sqrt{m}$	3 MPa$\sqrt{m}$	Obtained from [10]
E_m	338 GPa	338 GPa	Measured by ultrasonic method
E_c	263 GPa	247.4 GPa	**
Calculated K_c	17.8 MPa$\sqrt{m}$	16.5 MPa$\sqrt{m}$	---
Experimental K_c	12.6 MPa$\sqrt{m}$	16.4 MPa$\sqrt{m}$	---

* Estimated from hardness value of 230 DPH using the relation: σ_o = 0.8 x 3 (DPH) [11].
§ Obtained from data for beta Nb-Ti-Al alloys from [6].
** Calculated using rule-of-mixtures and a modulus of ~117 GPa for the beta phase [6].

SUMMARY AND FUTURE WORK

Alloying studies of the Nb-Si base alloys have shown that marked improvements in oxidation resistance could be obtained through Ti and Al additions. Phase equilibria investigations of the ternary Nb-Si-Ti and quaternary Nb-Si-Ti-Al systems have shown that the equilibrium phase fields can be varied substantially through minor modifications in chemistry. This, in turn, leads to microstructural changes, which may be controllable through further alloying modifications. Initial mechanical evaluations on thermo-mechanically processed alloys showed room-temperature toughness and high-temperature strength values which are somewhat inferior to the base Nb/Nb_5Si_3 alloy. However, comparisons are not being made on microstructurally equivalent systems, and the effect of chemistry on constituent properties are not yet quantified. It is clear that detailed evaluations of the microstructural and chemistry dependence of toughness, tensile strength, and creep resistance are required for a more thorough understanding of this class of materials. Future work on these systems will focus on the following deficiencies:

(a) Lack of strength in the ductile phase at high temperatures. This may be remedied by solid-solution strengthening of the ductile phase. Alloying additions capable of increasing the strength/creep resistance of the ductile constituent in the two-phase alloys include Mo, W, Ta, Re, and Hf. Mo and W, especially, are potent solid-solution strengtheners in Nb-base alloys, and in this case, may not compromise the ductility of the beta phase.

(b) Inadequate oxidation resistance of the two-phase alloys. The oxidation resistance may be enhanced through further alloying efforts, specifically, to decrease the extent of oxygen penetration, as well as the recession rate, while increasing the temperature capability of the systems. These improvements may still be inadequate for structural applications in uncoated form. It should be emphasized that the goal of these alloying efforts is to seek incremental improvements in environmental resistance so that when used in conjunction with oxidation-protective coatings, the alloys will have sufficient environmental tolerance to forestall short-life catastrophic failure.

Best Available Copy

facilitated fracture monitoring via Scanning Electron Microscopy (SEM) techniques or post-test examination of damage accumulation during crack growth.

Mechanical tests on the smaller notched three point bend composite specimens were conducted at a load point displacement (LPD) rate of 1 μm·sec^{-1} on a JEOL 840A Scanning Electron Microscope equipped with an Oxford Instruments Deformation Stage. During testing, the polished sample surfaces were oriented perpendicular to the electron beam so that surface cracking events extending from the notch root could be monitored. Computer aided data acquisition was used to record load versus time traces for all tests and later converted to load-load point displacement (LPD) traces. The loads (P_Q) at which initial and subsequent cracking events were observed were used in the following ASTM E-399 equation [14] to determine the initiation toughness and construct the resistance(R)-curves (K versus Δa):

$$K_Q = \left(\frac{P_Q S}{B W^{3/2}}\right) \cdot f\left(\frac{a}{W}\right)$$

where loading span [S], specimen thickness [B], specimen width [W], load corresponding to fracture events [P_Q], and geometrical factor [f(a/W)] are utilized to determine stress intensity in units of [MPa√m]. Post-failure analysis consisted of SEM examination of the fracture surfaces in regions of the rising R-curve in order to observe the fracture behavior of the Nb(ss-Si).

Environmental exposure of samples to air, N_2, O_2 and H_2 was conducted in either a tube furnace or a Cahn Microbalance 3000 under 1 atm pressure of gases. Heat treatment schedules were kept the same at 873 K for 4 h except for additional exposures to H_2 at 473 K and 673 K. Samples were exposed at 873 K, as this temperature is close to the temperature that gives maximum weight gain for niobium in an oxygen environment [15]. Vickers microhardness indentations at 10 g for 15 sec were additionally made on the unexposed and exposed samples to try to detect differences in mechanical response (e.g., yield strengths).

RESULTS AND DISCUSSION

MICROSTRUCTURES

The typical microstructures of the extruded and heat treated materials have been shown elsewhere [4,10,16]. The microstructures consist of large niobium particles (primary niobium) and Nb_5Si_3 which have been elongated in the direction of extrusion. In the Nb-10 at.% Si, the larger primary niobium (Nb_p) occupies 51.3±4 vol.%, and has an average width of 17.0± 1.2 μm and aspect ratio of 5:1 to 10:1 along the extrusion direction. In the Nb-8.8 at.% Si, the Nb_5Si_3 occupies about 20 vol.%. The as-processed materials had relatively low interstitial contents in the range of 230 ppm for oxygen and 50 ppm for nitrogen.

IN SITU TESTING

Figures 1 shows the typical K-Δa plots for the Nb-10 at.% Si materials. Crack initiation in the composites occurred on the surface of the bend bars over a range from 5 to 20 MPa√m depending on the location of the notch tip with respect to the phases in the microstructure. When the notch tip was placed into or just next to a Nb_p phase, the higher values of applied stress intensity were required to initiate cracks in the Nb_5Si_3 on the other side of the Nb_p. In the other extreme, with the notch tip in the Nb_5Si_3, the lower stress intensities (i.e., 5 to 10 MPa√m) were sufficient to initiate cracking. Crack initiation was followed by the development of a microcracking "damage zone" and ligament bridge formation requiring higher applied stress intensities to propagate cracks. As a result, a steep rise in the R-curve was noted. The average steady state peak stress intensity value of 28 MPa√m was found at 380 μm crack extension.

The typical view of the bridging ligaments and the microcrack damage zone leading to the R-curve behavior is pictured in Figure 2. The microcracking of Nb_5Si_3 (darker contrast phase) and plasticity of the Nb_p (lighter contrast) are clearly visible. The microcrack "damage zone" in the Nb_5Si_3 extends over 300 to 400 μm ahead of the contiguous crack. The fracture surfaces in the regions of the rising R-curves typically appeared like those shown in Figure 3. Extensive plastic stretching and dimpled fracture of the Nb_p as well as some interfacial debonding are evident. The plasticity exhibited by the niobium phases has contributed to the high toughness of these materials.

EXPOSURE TO AIR

Figure 4 and 5 show the results of the *in situ* bend testing after exposure to air at 873 K for 4 h and removal of the white oxide scale from the surface and polishing to a 1 μm finish. These results are clearly different from those found in the unexposed materials as shown earlier in Figures 2 and 3. Although cracks are observed to initiate at approximately the same values and grow in a stable manner, the rise in the R-curve is significantly more shallow than for unexposed material, and the sample catastrophically fractured at 19 MPa√m, at about one-half the stress intensity measured prior to air exposure. In Figure 5, a crack propagating from the notch is shown. In contrast to that

Best Available Copy

observed in Figure 2, the crack is planar (i.e., minimal damage zone) and the niobium is clearly behaving in a macroscopically brittle fashion, although some deformation is evident at the crack tip.

It is clear that exposure to air has significantly reduced the toughness of the Nb-8.8 at.% Si composite, although the resulting toughness is still significantly in excess of the monolithic silicide (i.e., > 1 to 3 MPa$\sqrt{m}$). The niobium has been embrittled, at least at the surface of the sample, causing fracture before significant macroscopic deformation can take place. The degree of toughening dictated by the ductile-phase toughening phenomenon is clearly affected by changes in the stress-strain response of the niobium. In the unexposed case, the niobium can deform extensively without fracture. However, lower toughness is obtained after air exposure as fracture precedes significant deformation.

NITROGEN EXPOSURE

Both composite types were exposed in their as-notched condition to N_2 at 873 K for 4 h and subsequently tested at room temperature on the SEM deformation stage. Samples did not exhibit visible scaling or measurable weight gain during exposure. When tested, peak toughnesses were slightly higher (≈10%) than those found in the unexposed cases. Unlike the results after air exposure, fracture propagated with visible plasticity of the niobium and a microcrack process zone. Fracture surfaces were similar to those observed in the as-processed unexposed material. Vickers hardness indentations were made in niobium particles on the sample surfaces and in the bulk. Hardness values of the niobium on the surface were 265±22.8 kg·mm^{-2}, while those in the bulk were 167±17.4 kg·mm^{-2}. The unexposed values were 163.6±16.9 kg·mm^{-2}. The surface was significantly hardened by nitrogen, while the bulk remained unaffected.

From these results and observations of plasticity in the notch tip regions, it is reasonable to suggest that the nitrogen has increased the yield strength without causing brittle fracture of the niobium, providing for a greater degree of toughening. The effect of solid solution strengthening of niobium with nitrogen through increasing frictional stresses have been observed previously [17,18]. The results indicate that nitrogen at these levels does not contribute to embrittlement of the composites or a drop in toughness observed in the specimens given an air exposure at 873 K.

OXYGEN EXPOSURE

Samples were exposed to pure O_2 at 873 K for 0.5 h in either the notched or unnotched conditions, producing a surface oxide that was removed by polishing. Toughness tests indicated a lack of macroscopic ductility in the niobium accompanied by a drop in toughness from 24 MPa$\sqrt{m}$ to 20 MPa$\sqrt{m}$ for the Nb-10 at.% Si sample. Fracture surfaces shown in Figure 6 showed that the niobium in the center of the sample deformed in a ductile manner, as observed in the unexposed cases. However, in areas within ≈30 μm of the surface, the Nb_p fractured in a brittle transgranular fashion, as shown in the schematic in Figure 7. A ring of transgranular fracture along the exposed surfaces of the specimen was exhibited, while microhardness indentations in these regions indicated that the niobium was hardened to 255±37 kg·mm^{-2} by oxygen dissolution to a depth roughly corresponding to the depth of the brittle fracture. The presence of O in pure Nb has been documented by several authors to increase the yield strength [19-21]. The hardnesses in the bulk of the specimen remained unchanged and these areas fractured in a ductile manner.

To determine whether the decrease in toughness and stable crack growth resulted from this affected surface layer, an unnotched sample was exposed to 1 atm O_2 at a temperature of 873 K for 0.5 h. Fifty micrometers were then removed from each face and the specimen was then notched to the standard depth. The toughness of this specimen was nearly identical to that exhibited by the unexposed specimen, and the fracture was ductile. Thus, the effect of the oxidation was found to be only on the exposed surface, and removal of the embrittled layer restored the original properties.

Oxygen in pure Nb has been observed to increase the ductile-to-brittle transition depending on its content [20]. In charpy impact, the transition temperature increased from 123 K to 233 K by increasing the oxygen content from 100 ppm to 400 ppm as well as other impurities. Notch sensitivity ratios on these materials were in the range of 1.5 at 298 K. In a study encompassing a wider range of temperatures, Nb containing 480 ppm or 1320 ppm oxygen became notch sensitive at about 77 K (more severe drop for the higher interstitial containing materials), where the pure Nb had not. It is clear that the oxygen can increase the yield strength and aid in the brittle-to-ductile transition.

HYDROGEN EXPOSURE

Samples of Nb-8.8 at.% Si were exposed to 1 atm of H_2 at different temperatures between 473 K and 873 K for 4 h and tested in the SEM bend stage. The results of the toughness tests and observations are presented in Table 1. After charging at 673 K and above, fracture was often catastrophic, and the toughnesses were substantially decreased. The decrease in fracture resistance was accompanied by a change in fracture mode from ductile tearing to cleavage over the entire fracture surface as shown in Figure 8. Figure 9 shows a crack that initiated from a notch during *in situ* testing and

Best Available Copy

Best Available Copy



Figure 6: The fracture surface of the Nb-10 at.% Si samples exposed to oxygen for 0.5 h at 873 K. A surface layer has been embrittled by the oxidation (white arrow), however, interior Nb_p phases (dark arrow) remain ductile.

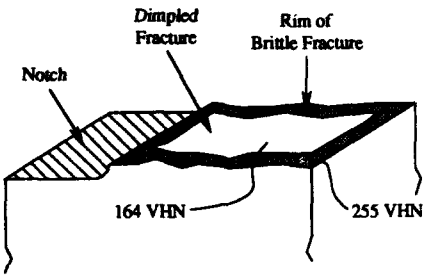


Figure 7: A schematic summarizing the fracture surface details and the hardnesses of the niobium in various positions on the oxidized samples.



Figure 8: The fracture surfaces of the hydrogen-embrittled Nb-10 at.% Si.

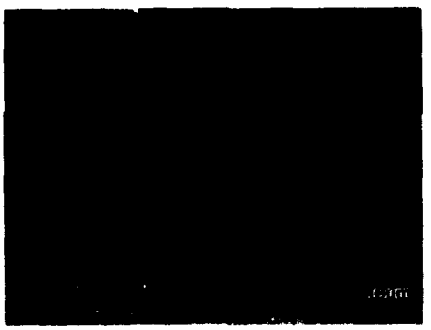


Figure 9: A view of a crack initiated from a notch in a hydrogen-embrittled sample.

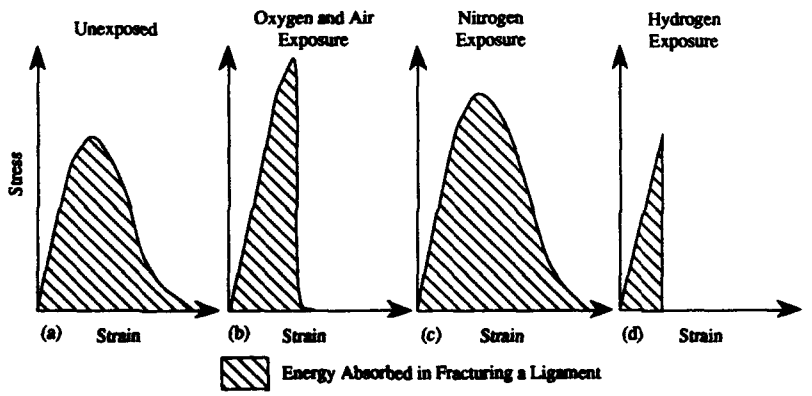


Figure 10: A schematic comparing the envisioned stress-strain diagrams for the unexposed and embrittled samples.

REFERENCES

[1] R.L. Fleischer, *J. Mater. Sci.*, **22**, 2281 (1987).
[2] T.B. Massalski, *Binary Alloy Phase Diagrams, Vols. 1 and 2.* ASM International, Materials Park, OH (1986).
[3] G. Stauthoff, *Z. Metallknde*, **77**, 654 (1986).
[4] M.G. Mendiratta, J.J. Lewandowski and D.M. Dimiduk, *Metall Trans.*, **22A**, 1573, (1991).
[5] P.R. Subramanian and M.G. Mendiratta, UES, Inc., DaytonOH, unpublished results (1992).
[6] R.M. Nekkanti and D.M. Dimiduk, *Intermetallic Matrix Composites. Materials Research Society Proceedings*, Materials Research Society, Pittsburgh, PA, **194** (1990), p. 175.
[7] J. Kajuch, J. Rigney and J.J. Lewandowski, *Mater. Sci. Eng.*, **A155**, 59 (1992).
[8] M.G. Mendiratta and D.M. Dimiduk, *Scripta Metall.*, **25**, 237 (1991).
[9] J.D. Rigney, Ph.D. Dissetation, Department of Materials Science and Engineering,Case Western Reserve University, Cleveland, OH (1993).
[10] J.D. Rigney and J.J. Lewandowski, *Advanced Composite Materials*, American Ceramic Society, Westerville, OH (1990), p. 519.
[11] V.D. Krstic, *Phil. Mag. A*, **48**, 695 (1983).
[12] B. Budianski, J.C. Amazigo and A.G. Evans, *J. Mech. Phys. Solids*, **36**, 167 (1988).
[13] P.A. Mataga, *Acta Metall.*, **37**, 3349 (1989).
[14] "Standard Test Method for Plane Strain Fracture Toughness of Metallic Materials," ASTM Standard E 399-83 in Annual Book of ASTM Standards, Vol. 03.01, American Society for Testing and Materials, Philadelphia, PA (1988), p. 480.
[15] D.W. Bridges and W.M. Fassel, Jr., *J. Electrochem. Soc.*, **103**, 326 (1956).
[16] J.D. Rigney, P.M. Singh and J.J. Lewandowski, *J. Metals*, **44**, 36 (1992).
[17] P.R.V. Evans, *J. Less-Common Metals*, **4**, 78 (1962).
[18] Z.C. Szkopiak, *J. Less-Common Metals*, **21**, 383 (1970).
[19] A.L. Mincher and W.F. Sheeley, *Trans. Metall. Soc. AIME*, **221**, 517 (1961).
[20] A.G. Imgram, E.S. Bartlett and H.R. Ogden, *Trans. Metall. Soc. AIME*, **227**, 131 (1963).
[21] W.F. Sheeley, *J. Less-Common Metals*, **4**, 487 (1962).
[22] B.A. Wilcox and R.A. Huggins, *J. Less-Common Metals*, **2**, 292 (1960).
[23] H.K. Birnbaum, "Hydrogen Effects on the Fracture of BCC Metals," Office of Naval Research Technical Report , Univ. of Illinois at Urbana-Champaign, Dept. of Metallurgy and Mining Engineering (1981).

511 Best Available Copy

into the melt and withdrawn at 5 mm/min to produce a casting ~10 mm in diameter and ~100 mm in length. The IM casting was prepared similarly to the DS casting but was allowed to re-solidify within the crucible. All of the alloys were melted in high-purity argon atmospheres to minimize interstitial concentrations.

Chemical compositions for all of the castings were determined by spectrographic and LECO inert gas fusion methods and are listed in Table I. Interstitial concentrations were sensitive to both the V melting stock and the casting method. The degassed V sheet used in AM-1 produced a high O, N, and low H casting while the V chips in AM-2 produced a moderate O, N, and high H casting. The cold crucible techniques used for both the DS and IM castings produced relatively low O, N, and H concentrations.

Table I. Chemical compositions (by wt.)

Casting Method	Casting ID#	Si (%)	V (%)	O (ppm)	N (ppm)	H (ppm)
Arc Melt	AM-1	7.66	92.2	410	870	4
Arc Melt	AM-2	7.3	92.6	260	280	72
Directional Solidification	DS	7.3	92.6	130	58	22
Induction Melt	IM	7.25	92.7	200	30	9

Fracture toughness measurements were performed in three-point bending using single-edge-notched specimens with dimensions of approximately 3.5x7x30 mm. The specimens were tested at a span of 28 mm and a displacement rate of 0.02 mm/s. All specimens were fabricated and notched by electro-discharge machining (EDM) with a notch opening width of 0.3 mm and (a/w) of 0.45. Pre-cracking was performed under continuous loading and crack resistance data were measured by unloading immediately after each crack extension. Crack lengths were measured optically from metallographically polished specimen surfaces. The DS casting was tested in two orientations; with the direction of crack propagation either transverse or longitudinal to the DS direction. Because of the limited DS casting diameter, longitudinal DS specimens could not be machined directly into standard specimen dimensions. Instead, 8 mm sections of the casting were cut with the desired longitudinal crack orientation and brazed to two end pieces of eutectic material to produce specimens of the same dimensions as above. Brazing was performed in vacuum at a peak temperature of 965°C using a Ni-Au eutectic foil with a thickness of 0.05 mm. After brazing, the specimens were ground to final dimension and EDM notched.

Fracture profiles were prepared by electroplating 0.5 mm of Ni onto the fracture surfaces prior to sectioning and metallographic preparation. Backscattered electron imaging was used in the SEM, and phase interference contrast in the optical microscope, for improved contrast between the V(Si) and V_3Si phases.

RESULTS

The microstructures in each of the V-V_3Si castings consisted of eutectics between discontinuous V_3Si rods and a V(Si) matrix. The V_3Si volume fraction was measured for the DS casting as 0.48 using optical image analysis and the V(Si) and V_3Si compositions were measured as 4.5 and 20.1 at.% Si by electron probe microanalysis. Metallographic cross sections of the V_3Si rods revealed some degree of faceting, with equiaxed dimensions that varied in alignment and thickness along the rod lengths. Rod length-to-diameter ratios of up to 20:1 were present in all of the castings. In the AM and IM castings, the solidification structure was cellular, with cell diameters of 75 to 100 μm and lengths of 150 to 200 μm, as shown in Figure 1. The rod orientations were related within each cell core, but varied from cell to cell. The eutectic was coarser within the intercellular regions. The DS castings also possessed the cellular structure but the cells were highly elongated with cell diameters of 100 to 200 μm and lengths of at least 1.5 to 2 mm. The V_3Si rod lengths exhibited strong alignment with the DS growth direction within the cell cores, but the orientation varied within the intercellular regions, as shown in Figure 2. The rod diameters were larger in the DS casting than either the AM or IM castings. Typical rod diameters within the cell cores were between 1 and 1.5 μm in the AM and IM castings, and 1.5 to 3 μm in the DS casting. For all of the castings, the intercellular rods were up to 4 μm in diameter. The

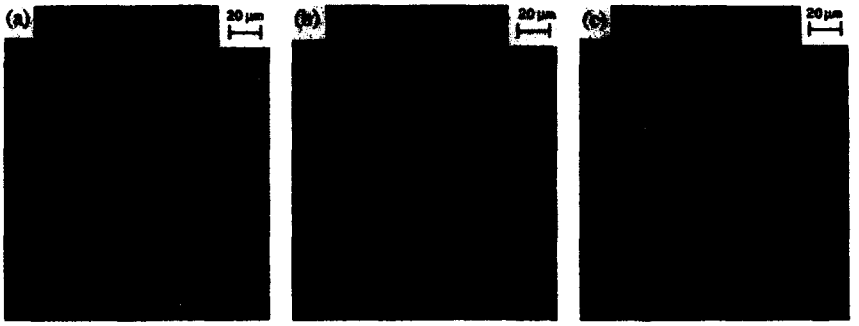


Figure 1. Typical microstructures for AM-1 (a), AM-2 (b), and IM (c) castings.

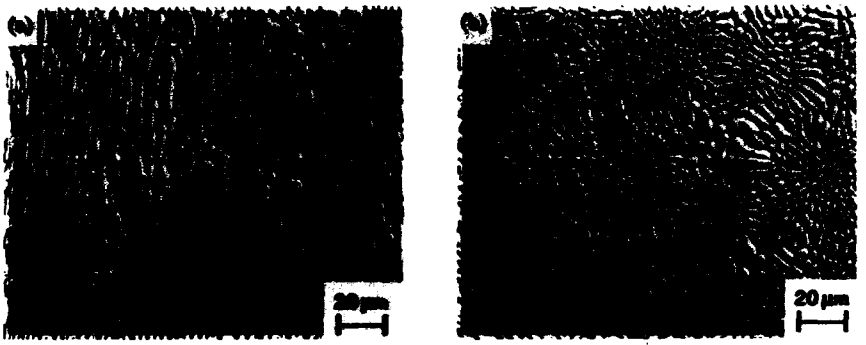


Figure 2. Typical microstructures for the directionally solidified casting in the longitudinal direction (a) and transverse direction (b).

V(Si) ligament dimensions increased with increasing rod diameter, as expected. In addition to the microstructural coarsening within the intercellular regions, occasional V_3Si dendrites were also present. These accounted for less than 1% of the casting volume except for the casting AM-1 (7.66Si), which contained approximately 2%. The AM-1 microstructure shown in Figure 1 represents the maximum amount of primary V_3Si observed.

As plotted in Figure 3, the toughness of castings AM-1 and AM-2 were similar, with average values of 10.4 and 10.6 MPa$\sqrt{m}$, respectively, . The toughness of the DS casting increased from an average of 14.4 MPa$\sqrt{m}$ for longitudinal crack propagation (DS-L) to 18.5 MPa$\sqrt{m}$ for crack propagation transverse to the crystal growth direction (DS-T). The highest average fracture toughness, 20.4 MPa$\sqrt{m}$, was measured in the IM casting. Fracture resistance data, plotted in Figure 3a, shows the absence of any significant changes in toughness with crack propagation. The data appear evenly scattered about the average values and indicate the absence of bridging zone development with increasing crack length.

The fracture surfaces of the AM, IM, and DS castings contained mixtures of large cleavage facets and fine micro-roughened zones, as shown in Figure 4. The size of the macroscopic cleavage facets and the cleavage area fraction were both highest in the AM castings, and decreased significantly for the DS and IM castings. Macroscopic cleavage zones typically consisted of a large number of facets corresponding to individual V_3Si rods connected by smooth or stepped regions corresponding to the intervening V(Si) ligaments. The extent of V(Si) stretching in these regions was minor, as shown in Figure 5 for the AM-2 casting. Conversely, the micro-roughened zones consisted of V_3Si rods containing secondary cracks and V(Si) ligaments which display considerable plastic extension. The bright contrast at the center of the stretched ligaments clearly

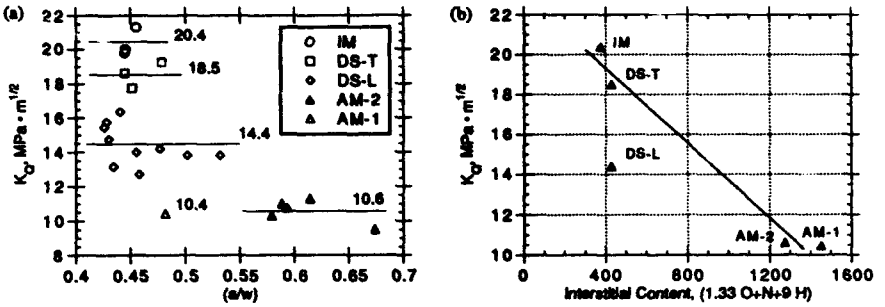


Figure 3. Fracture resistance data and average fracture toughness values for each casting (a), and fracture toughness vs. effective interstitial content (b).

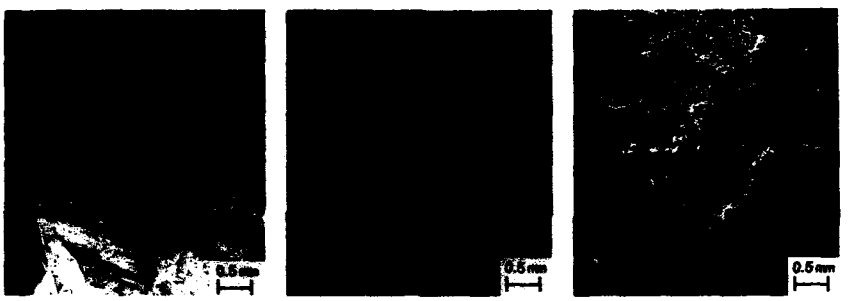


Figure 4. Fracture surfaces of, left to right, AM-2, DS-T, and IM castings.

outline each of the V_3Si rods. Similar features and contrast were observed in the IM casting.

Profiles of the fracture surfaces were prepared to quantify the magnitude of V(Si) plastic extensions beyond the V_3Si facets. However, unlike the apparently large plastic extensions viewed by SEM fractography, the presence of clearly visible V(Si) extensions was uncommon. The maximum plastic extensions measured were 0.33 to 0.66 μm for AM-2 , and 0.8 to 1.0 μm for the DS-T specimens.

DISCUSSION

The fracture toughness increased by a large increment for all of the eutectic composites relative to the toughness of monolithic V_3Si (< 1.3 MPa√m [10]) with values from 10.4 to 20.4 MPa√m. Decreases in Si content from 7.66 (AM-1) to 7.3 wt.% (AM-2) reduced the quantity of primary V_3Si dendrites but had no significant effect on the fracture toughness, which only increased from 10.4 to 10.6 MPa√m. While the DS casting contained a coarser eutectic microstructure (indicative of the reduced thermal gradient and solidification rate during casting), the scale of the microstructure was similar for both the AM and IM castings, and therefore is unable to solely account for the toughness variations. The DS casting also contained a highly directional microstructure, with cells and rods strongly aligned in the growth direction within the cell cores.

The interstitial concentrations were affected by the synthesis methods, as shown in Table I, decreasing from the highest levels in the AM castings to much lower levels in the IM and DS castings. The influence of interstitial concentration on the Charpy impact toughness of pure V has been well documented [11], and the sensitivity to individual interstitial elements at room temperature was found to vary for N, O, and H in the ratio of 1 to 1.33 to 9, respectively. Assuming that this same ratio of interstitial sensitivities applies to the V(Si) ligaments, an effective

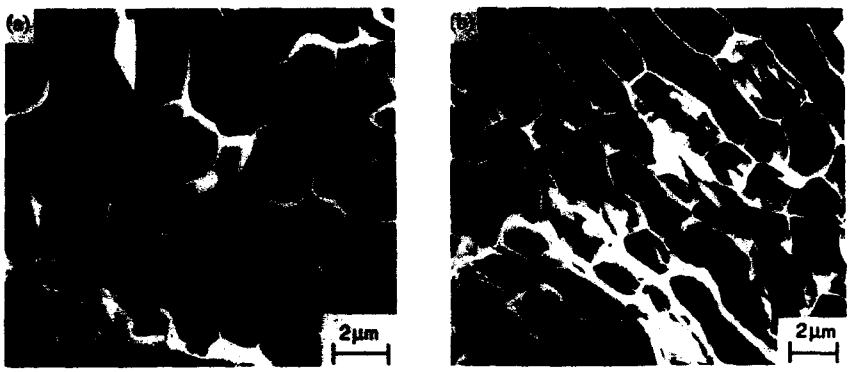


Figure 5. SEM fractographs of the cleavage region (a), and micro-roughened region (b) for AM-2.

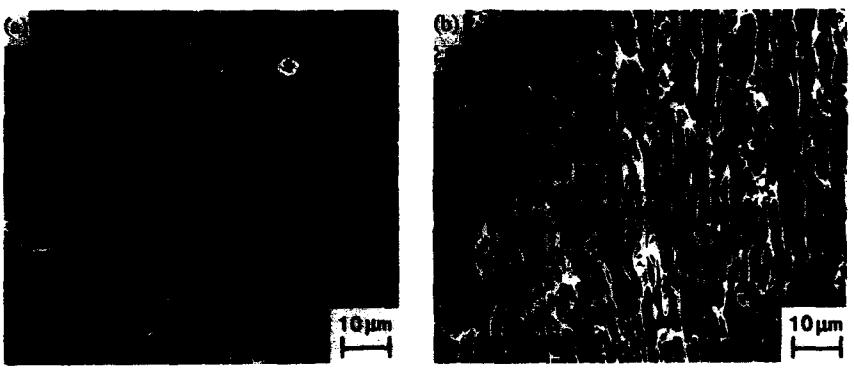


Figure 6. SEM fractographs of transverse (a) and longitudinal (b) crack growth orientations.

interstitial content was calculated for each casting and plotted vs. fracture toughness in Figure 3b. A linear fit to the data, for reference, reveals a good correlation for all of the test specimens with random or transverse rod orientations with respect to the crack propagation direction. Further increases in purity would be expected to provide additional toughening but the data are insufficient to predict a linear or exponential increase.

To determine the source of decreased toughness with longitudinal vs. transverse crack growth in the DS castings, one must consider the mechanism responsible for the eutectic toughening. The predominant toughening model used by others to describe both in-situ and artificial composite toughening by dispersion of a ductile phase is one of crack bridging [1,3,12-14]. In these models, the toughness should increase with increased ductile-phase stretching and with increasing crack length as the bridging zone is extended. In this study, the maximum ductile-phase extension measured is less than 1 μm, typically less than 0.33 μm, and only small bridging zones can be expected. The absence of toughness increases with crack propagation, shown in Figure 3a, is consistent with this behavior. Furthermore, the toughness dependence on the ductile phase fraction in AM V-V_3Si composites [10], suggests that a rule-of-mixtures model for the composite toughness may be more appropriate. In this case, the V(Si) phase largely determines the composite toughness due to the low toughness of the V_3Si. Increased composite toughness is expected from reduced interstitial concentrations which further increase the toughening contribution of the V(Si). The mechanism responsible for the decrease in toughness for crack propagation longitudinal (DS-

L) vs. transverse (DS-T) to the growth direction is under investigation, but may result from increased constraint in the V(Si) for the DS-L specimen. This behavior is predicted for cracks propagating parallel to the fiber (rod) direction [15] and would reduce the plastic energy dissipated during fracture.

CONCLUSIONS

The room temperature fracture toughness of V_3Si (< 1.3 MPa$\sqrt{m}$) can be increased by in-situ ductile-phase toughening with V. A toughness of over 20 MPa$\sqrt{m}$ has been measured for eutectic composites containing nearly equal volume fractions of V_3Si and V(Si) solid solution.

The toughness of V-V_3Si in-situ eutectic composites is sensitive to the method of synthesis. Measured toughness values range from 10 MPa$\sqrt{m}$ for AM material to over 20 MPa$\sqrt{m}$ for IM alloys. The sensitivity of fracture toughness to synthesis method is due to the resulting differences in interstitial impurity contents and the directionality of the microstructure with respect to the direction of crack propagation. A decrease in toughness was observed in DS material oriented with the direction of crack propagation parallel to the axis of the V_3Si rods, or growth direction.

Little ductile-phase extension was observed in fractured composites, and no increase in toughness with increasing crack length ("R-curve behavior") was observed. These results suggest that fracture toughness models based on crack bridging may be unsuccessful in simulating the behavior of V-V_3Si composites.

The fracture toughness decreases with increasing "effective" interstitial impurity content ([N]+1.33[O]+9[H]) for composites with a random or transverse orientation of the crack with respect to the axis of the V_3Si rods. Fracture toughness is predicted to increase above 20 MPa$\sqrt{m}$ for effective interstitial impurity concentrations below approximately 300 ppm.

ACKNOWLEDGMENTS

Work by two of the authors (MJS and GAH) was performed under the auspices of the U. S. DOE for the Lawrence Livermore National Laboratory under contract W-7405-Eng-48.

REFERENCES

1. L. S. Sigl, P. A. Mataga, B. J. Dalgleish, R. M. McMeeking, and A. G. Evans, Acta Metall. **36**, 945 (1988).
2. H. E. Deve, A. G. Evans, G. R. Odette, R. Mehrabian, M. L. Emiliani, and R. J. Hecht, Acta Metall. **38**, 1491 (1990).
3. L. Xiao and R. Abbaschian, Met. Trans. 23A, 2863 (1992).
4. W. O. Soboyejo, K. T. Rao, S.M.L. Sastry, and R.O. Ritchie, Met. Trans 24A, 585 (1993).
5. J.J. Lewandowski, D. Dimiduk, W. Kerr, and M. G. Mendiratta, in High Temperature/High Performance Composites, edited by F. D. Lemkey et. al. (Mater. Res. Soc. Symp. Proc. **120**, Reno, NV, 1988), pp 103-109.
6. D. L. Anton and D. M. Shah, in Intermetallic Matrix Composites, edited by D. L. Anton et. al. (Mater. Res. Soc. Symp. Proc. **194**, Pittsburg, PA, 1988), pp. 45-52.
7. M. G. Mendiratta, J. J. Lewandowski, and D. M. Dimiduk, Met. Trans. 22A, 1573 (1991).
8. J. F. Smith, Bull. of Alloy Phase Diagrams 6, 266 (1985).
9. K-M. Chang, B. P. Bewlay, J. A. Sutliff, and M. R. Jackson, J. of Metals 44, 59 (1992).
10. M. J. Strum, G. A. Henshall, in High Temperature Ordered Intermetallic Alloys V, edited by I. Baker et. al. (Mater. Res. Soc. Symp. Proc. **288**, Boston, MA), pp. 1093-1098.
11. B. A. Loomis and O. N. Carlson in Reactive Metals, edited by W. R. Clough (Interscience Publ, New York, 1958), p. 227.
12. M. F. Ashby, F. J. Blunt, and M. Bannister, Acta Metall. 37, 1847 (1989).
13. B. Budiansky, J. C. Amizago, and A. G. Evans, J. Mech. Phys. Solds 36, 167 (1988).
14. K. S. Ravichandran, Acta Metall. 40, 3349 (1989).
15. R. C. Wetherhold and L. K. Jain, Mater. Sci and Engr. A165, 91 (1993).

PART VIII

Applications of Refractory Alloys

PROCESSING, PROPERTIES AND APPLICATIONS OF HIGH-TEMPERATURE NIOBIUM ALLOYS

C. CRAIG WOJCIK
Teledyne Wah Chang Albany, P.O. Box 460, Albany, OR 97321

ABSTRACT

Niobium alloys are used in a variety of high-temperature applications ranging from light bulbs to rocket engines and nuclear reactors. The unique physical and chemical properties of these alloys have often dictated that only niobium alloys could fulfill certain application requirements. Compared to other refractory metals, niobium alloys have low density and are very ductile even at cryogenic temperatures. Most niobium alloys are also very resistant to corrosion by acids and liquid alkali metals; however, oxidation resistance at high temperatures is usually catastrophic unless protective coatings are used.

An overview of the commercial high-temperature alloys is presented. Some of the unique properties of these alloys, which require unusual processing methods and equipment, are highlighted. Important physical properties of these alloys are discussed with reference to specific applications. The needs and design restraints of these applications provide valuable insights for those developing other high-temperature materials.

INTRODUCTION

To put niobium alloys into proper perspective, it should be noted that approximately 75% of all niobium metal is used as minor alloying additions in low-alloy steel. Another 20-25% is used as alloy additions in nickel-base superalloys and heat-resisting steels. Only 1-2% of all niobium is used in the form of niobium-base alloys and pure niobium metal. Superconducting niobium-titanium alloy accounts for over one-half of all niobium alloys produced. The total usage of high-temperature niobium alloys is less than 100,000 Kg/year. All the high-temperature niobium alloys in use today were developed in the 1960s [1-3] during the intensive nuclear and aerospace materials development efforts. Compared to other refractory metals and the hundreds of refractory alloys investigated in the 1960s-1970s, commercial niobium alloys are relatively low-density, and low-strength but, most importantly, extremely fabricable. Even though niobium alloys have useful strength hundreds of degrees above nickel-base superalloys, their use has been very limited due to oxidation and long-term creep behavior.

CURRENT PRODUCTION METHODS

Originally, niobium metal was produced by powder metallurgy methods which involved high temperature vacuum sintering and carbon reduction. In the early 1960s, however, aluminothermic reduction and electron beam purification became the standard practices. In aluminothermic reduction Nb_2O_5 and aluminum powders are blended together and then reacted exothermically to form crude niobium metal and Al_2O_3 slag. The crude niobium metal typically

Mat. Res. Soc. Symp. Proc. Vol. 322. ©1994 Materials Research Society

contains several percent impurities including aluminum and oxygen. These impurities have a much higher vapor pressure than niobium metal at elevated temperature. Because of this vapor pressure difference purification is performed commercially by electron beam melting. After several electron beam melts niobium is typically 99.95% pure. Other naturally occurring impurities with low vapor pressure such as tantalum and tungsten can not be removed by electron beam melting so they must first be removed by other liquid extraction methods prior to aluminothermic reduction. When the electron beam process was first developed, it produced such a reduced level of impurities, and lower level of strength, that it opened the pathway for alloy development in the early 1960s. The same process is used today for production of pure metal, however, major advances have been made in equipment. Typical production electron beam furnaces are now 500-2000 KW of beam power [4] and are capable of purifying ingots 300-500 mm in diameter, and over two meters long. Drip melting is the standard electron beam method now being used; however, with the advent of more modern and higher power furnaces, hearth melting may soon become practical. Niobium alloys are made by subsequent vacuum arc remelting with the appropriate elemental additions. The most common alloy additions are zirconium, titanium, hafnium, and tantalum, which readily go into solution during arc melting. Currently all commercial suppliers cast ingots into simple shaped round copper molds rather than shapes to fit specific products, i.e., rectangular castings for rolling to plates or hollow cylinders to produce tubes.

Fabrication of the common alloys is generally accomplished by high- temperature extrusion or forging near the alloy recrystallization temperature, which is typically 1000-1300°C. All the commercial alloys oxidize readily at these temperatures so after hot working a heavy oxide scale must be removed by grinding, chemical milling or machining. Secondary fabrication is performed by warm working and ultimately cold working to final shapes with appropriate stops for recrystallization annealing, which is performed under high vacuum. Most commercial alloys are ductile enough to be processed into various mill products such as sheet, foil, rod, wire and tubing, often with cold reductions in excess of 50%.

Niobium alloy mill products can subsequently be fabricated into various complex shapes by almost all of the common metal-forming processes such as closed die forging, spinning, hydroforming, welding, etc. The relatively low density of niobium alloys, combined with their ease of fabrication, frequently favors the use of niobium alloys as compared to other refractory metals such as molybdenum or tantalum.

PROPERTIES OF COMMERCIAL ALLOYS

The most common high-temperature niobium alloys are listed in Table 1. All these alloys are hardened primarily by solid solution-strengthening however, second-phase particles are observed in the microstructure of these alloys. The composition of these particles vary but they are generally associated with impurities such as oxides, nitrides, and carbides. Often the size and distribution of second phases can have a strong influence on mechanical properties and recrystallization behavior [5]. A variation of the Nb-1Zr alloy, commonly known as PWC-11, contains an intentional addition of 0.1 weight percent carbon specifically to form carbide precipitates which significantly improve high-temperature creep properties. One of the other alloys listed, WC-3009, normally contains ~0.10 weight percent oxygen which is approximately five times more oxygen than other niobium alloys. This high level of oxygen, which is introduced

by powder processing, is not deleterious to mechanical properties because the oxygen combines with hafnium in the alloy to form stable hafnium oxide precipitates. The WC-3009 alloy is unique in that it exhibits an oxidation rate less than one tenth that of most other niobium alloys [3]. When this alloy was developed it was speculated that such an alloy could survive a short aerothermal mission even in the event of a protective coating failure.

Alloys which contain second-phase particles that have formed a continuous boundary between grains can exhibit drastically reduced tensile elongation [6]. This undesirable condition is usually caused by contamination or improper heat treatment. In general, niobium alloys are much less tolerant of impurity pickup than other reactive metals such as titanium and zirconium alloys. Copper, which can accidently be introduced in welding operations, is particularly diasatrous to mechanical properties. The total interstitial oxygen, hydrogen, carbon, and nitrogen content of niobium alloys is typically one-fifth to one-tenth that of titanium or zirconium alloys.

Table I - Commercially Available Niobium Alloys
for High Temperature Use

ALLOY	COMPOSITION (weight %)	DENSITY (gm/cm3)
C-103	Nb-10Hf-1Ti	8.85
Nb-1Zr	Nb-1Zr	8.57
PWC-11	Nb-1Zr-0.1C	8.57
WC-3009	Nb-30Hf-9W	10.1
FS-85	Nb-28Ta-10W-1Zr	10.6

Tensile properties of the common alloys at 20°C are given in Table II. All the commercial alloys are quite ductile at room temperature. The highest tensile strength at room temperature and elevated temperature, Figure 1, is exhibited by the WC-3009 alloy. Creep stresses for 1% strain in 100 and 1000 hours are summarized in Figures 2 and 3. Even though WC-3009 alloy clearly exhibits the highest tensile strength, FS-85 has superior creep strength, probably due to its higher melting point from the alloys high concentration of tantalum and tungsten.

Table II - Typical Room Temperature Tensile Properties
of Niobium Alloys

ALLOY	YIELD STRENGTH (MPa)	ULTIMATE (MPa)	ELONGATION %
C-103	296	420	26
Nb-1Zr	150	275	40
PWC-11	175	320	26
WC-3009	752	862	24
FS-85	462	570	23

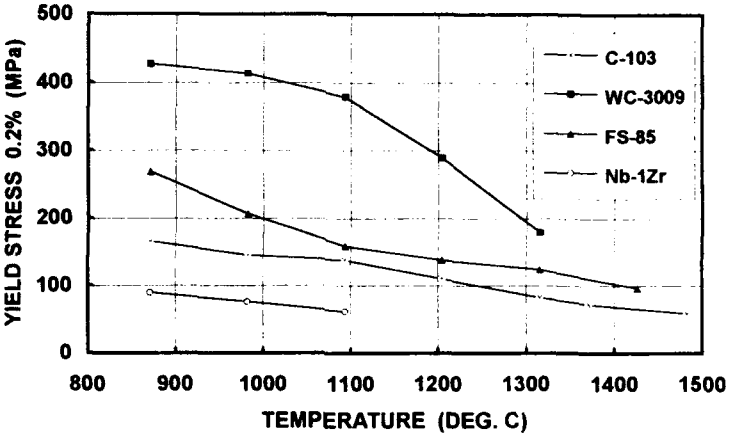


Figure 1 - Tensile Yield Strength vs. Temperature
for Common Niobium Alloys

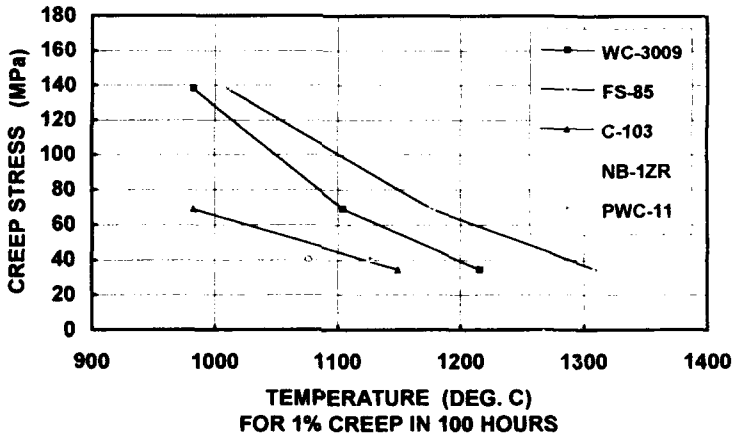


Figure 2 - Stress to Produce 1% Creep after 100 Hours [6-9]

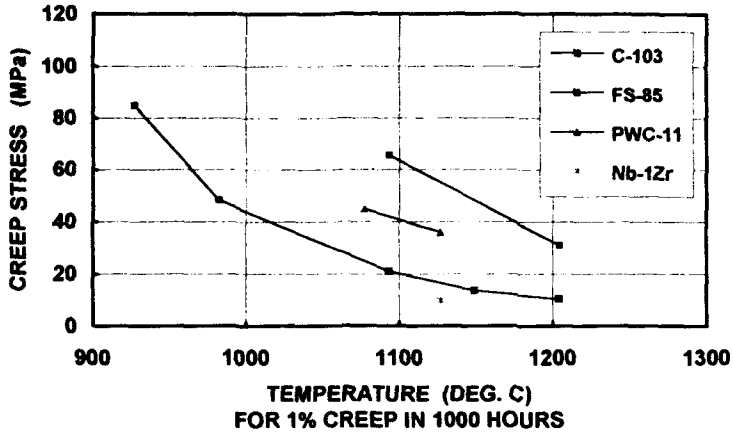


Figure 3 - Stress to Produce 1% Creep after 1000 Hours [6-9]

Elastic modulus, thermal conductivity, and total hemispherical emissivity are listed in Tables III - V. The emissivity data are for smooth and non-oxidized surfaces which exhibit much lower emissivity values than oxidized material. Also shown in Table V is an emissivity value of 0.7-0.82 for silicide coated C-103. This value is for a common Si-20%Fe-20%Cr coating applied by the slurry coat and fusion method. Thermal expansion data are shown in Figure 4.

Table III - Elastic Modulus for Common Niobium Alloys

ALLOY	ELASTIC MODULUS	
	20°C	**1200°C**
C-103	90GPa	64GPa
Nb-1Zr	80	28
WC-3009	123	
FS-85	140	110

Table IV - Thermal Conductivity of Niobium Alloys

ALLOY	**800°C**	**1200°C**
C-103	37.4W/m°C	42.4W/m°C
FS-85	52.8	56.7
Nb-1Zr	59.0	63.1

Table V - Total Hemispherical Emissivity
for Common Niobium Alloys

ALLOY	TOTAL EMISSIVITY	
	800°C	1200°C
C-103	0.28	0.40
Nb-1Zr	0.14	0.18
C-103(silicide coated)	0.70-0.82	

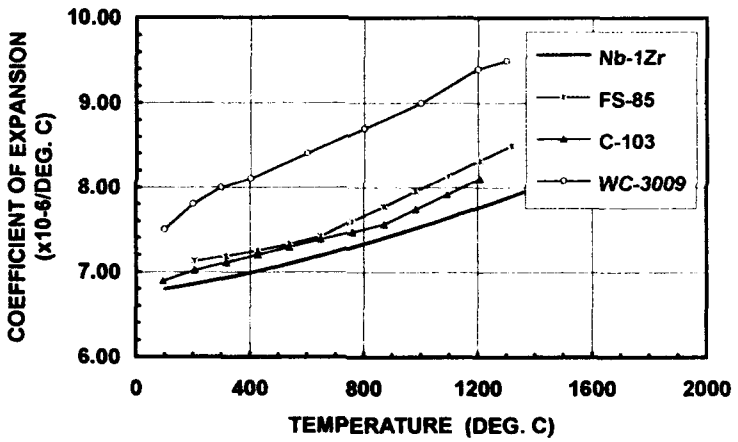


Figure 4 - Thermal Expansion Coefficient for Various Niobium Alloys
at Elevated Temperature

RECENT ADVANCES IN NIOBIUM ALLOYS

As mentioned previously, limited alloy development work has been devoted to niobium alloys since the early 1970s. Considerable effort, however, has been devoted to exploring methods to decrease the cost of niobium alloys and produce net shapes. In the last twenty years there have been numerous attempts to manufacture niobium alloy parts by investment casting. While it has been shown that casting is possible even for niobium alloys with melting temperatures over 2400°C the "as cast" microstructure is typically less ductile than normal wrought microstructures. The economic aspects of producing niobium alloy castings has also been

severely hindered by the loss of metal in the form of gates, skull, and risers which are more costly per Kg than titanium or other commonly cast materials. Considerable research has also been devoted to powder metallurgy process development. The most common aerospace alloy, C-103, and a high-strength alloy, Nb-30Hf-9W, were evaluated after preparation by a wide variety of powder metallurgy processes including rapid solidification methods [6]. The most difficult aspect of processing niobium alloys by powder methods is preparation of the alloys into powder. These difficulties arise from the high melting temperature and reactive properties of the alloys which contain elements such as hafnium, titanium, and zirconium. Consequently, powder can be manufactured only by the hydride-dehydride process or atomization in a crucible free process such as centrifugal atomization using either an electron beam or plasma torch as a heat source. In summary, it was demonstrated that net shapes could not be produced economically due to the high production cost of centrifugally atomized powder (PREP and EBA processes). An unexpected result of this research, was that the least pure and most economical powder, produced by the hydride-dehydride process (Table VI) could be used to produce hot working preforms of a high-strength alloy, Nb-30Hf-9W. After hot working, it was determined that the increased fraction of hafnium oxides associated with hydride-dehydride type powder does not degrade high-temperature tensile or creep properties. Powder metallurgy methods are now used to produce commercial quantities of this alloy.

Table VI- Chemical Analysis of P/M Nb-30Hf-9W After Hot Isostatic Pressing to Full Density

POWDER TYPE	ALLOY COMPOSITION					
	Hf	W	O	N	C	H
			ppm	ppm	ppm	ppm
Electron Beam Atomized (EBA)	29.5	9.2	85	40	100	<5
Hydride-Dehydride (HDH)	29.5	9.2	910	100	180	<5
Plasma Rotating Electrode (PREP)	30.1	9.5	130	94	100	<5

APPLICATIONS OF HIGH-TEMPERATURE NIOBIUM ALLOYS

The most common application for niobium alloys is in sodium vapor lamps, as shown in Figure 5. In this product, Nb-1%Zr alloy is used because of its excellent formability, weldability, and long life in a sodium vapor environment. The small tubular pieces of Nb-1Zr in these lamps have been made from seamless tubing, and more recently from sheet which is deep drawn into tubes. These bulbs are used throughout the world for highway lighting, etc., because of their high electrical efficiency and long life, which is typically in excess of 25,000 hours. The high carbon version of this alloy, PWC-11, is now being considered for use in sodium cooled space nuclear reactors (SP-100 Program). The creep rate of PWC alloy is approximately five times slower than Nb-1Zr at 1100°C due to the effects of carbide precipitates [9]. PWC-11 alloy also has excellent fabrication, diffusion bonding, and welding characteristics which will be critical to the success of this complex reactor.

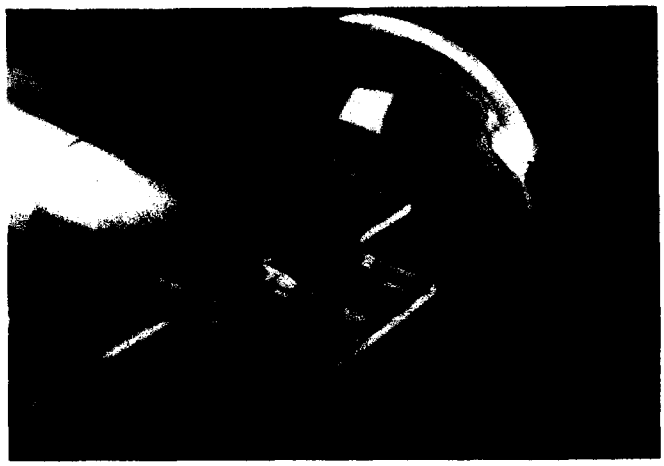


Figure 5 -Sodium Vapor Lamp Showing
Internal Nb-1Zr Alloy Parts

For aerospace applications at 1100-1500°C, C-103 alloy has been the workhorse of the niobium industry because of its higher strength. Excellent cold forming and welding characteristics of this alloy enable fabricators to construct very complex shapes such as thrust cones, high-temperature valves, etc., Figure 6. Closed die forgings are also easily produced, Figure 7. Most of these applications in propulsion systems operate for relatively short times at temperatures between 1200-1400°C. Often the operating environment is less oxidizing than normal atmosphere. Since C-103 has virtually no oxidation resistance, silicide coatings are used extensively. These coatings, as shown in Figure 8, contain elements such as Cr, Hf, Fe, and Ni, in addition to silicon. After the elemental coating is applied by spraying or dipping, it is fused at high temperature to form the various reaction products. These coatings normally contain a high density of microcracks that form due to differences in expansion coefficients of the different intermetallic layers. Surprisingly, these cracks do not propagate catastrophically during high temperature service.



Figure 6 - Rocket Thrust Cone Fabricated from C-103 Alloy,
Prior to Application of Protective Silicide Coating



Figure 7 - Closed Die Forgings Fabricated from C-103 Alloy



Figure 8 - Micrograph of Typical Si-20Cr-20Fe Silicide Coating Showing the Multiple Reaction Layers that Form During the Fusion Reaction

Another very successful application for coated C-103 is thrust augmenter flaps used in one of the Pratt & Whitney turbine engines. As shown in Figure 9, these flaps are used at the flow constriction tail end of the engine to form a high temperature liner for the afterburner section. These flaps typically reach 1200-1300°C and last for ~100 hours of afterburner time.

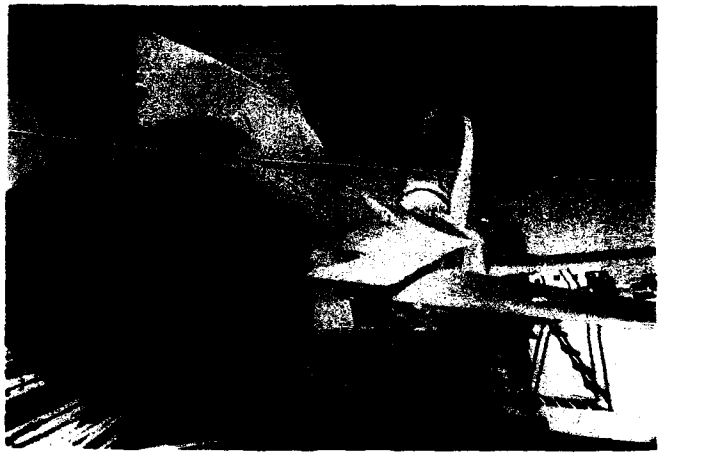


Figure 9 -Thrust Augmenter Flap Fabricated from C-103 and Silicide Coated to Resist Intense Heat in Afterburner.

Several years ago one of the most intriguing applications being evaluated for the NASP (National Aerospace Plane) was niobium alloy heat pipes. A heat pipe can be visualized simply as a "superconductor of heat". Without having any moving parts, a heat pipe functions as an evaporator and condenser of liquid metal, such as lithium, to carry heat away from a heat source to a heat sink. Using this concept, a heat pipe can transport extreme heat away from hot spots such as hypersonic leading edges. A C-103 alloy heat pipe in operation is shown in Figure 10. In this figure the heat pipe, which is silicide coated, is being heated at its midpoint by a standard oxygen/mapp gas cutting torch. Under these test conditions a normal piece of silicide coated C-103 would reach 1800-1900°C in seconds and then begin burning. The heat pipe, however, resists overheating by absorbing the heat flux and then using this energy to convert liquid lithium into lithium vapor inside the sealed heat pipe. The lithium metal vapor is transported to the cooler ends of the pipes where it condenses into the porous metal wick and a 1.0 mm diameter artery which returns the liquid lithium back to the heat source by capillary action. A typical 500 gram niobium heat pipe can dissipate over 10 kilowatts of heat and operate isothermally at 1250-1350°C. Niobium alloy heat pipes were successfully manufactured into hypersonic leading edges and nose cones. These devices were also successfully tested in combustion torches, high velocity jet fuel burners[10], tungsten quartz lamps, and even electric welding arcs at heat fluxes well over 1000 watts/cm^2 [11].

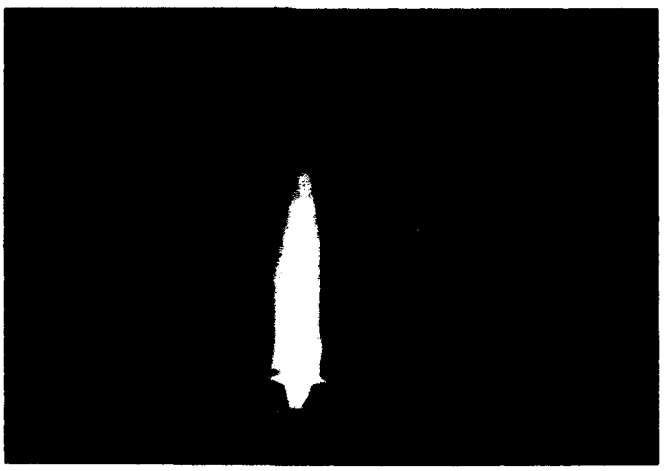


Figure 10 - Niobium Alloy Heat Pipe Which Was Used in a Leading Edge Designed to Resist Hypersonic Aerothermal Heating

CONCLUSION

In summary, we have briefly described the properties and uses of commercial high-temperature niobium alloys. Applications for these alloys are increasingly being challenged by other improved alloys and new nonmetallic materials. Frequently, however, users are finding that these newer materials cannot be easily fabricated into the desired shapes required. In other instances, users of high-temperature materials are rediscovering that advanced nonmetallic and composite materials may be more limited by their low thermal conductivity than metal alloy systems. As designers continue to develop experience with other less ductile high-temperature materials, it is most likely that the higher strength and less fabricable niobium alloys will also be reevaluated, especially if improved protective coatings are developed.

REFERENCES

1. R.G. Frank, "Recent Advances in Columbium Alloys", *Refractory Metal Alloys* (Plenum Press, 1968), pp. 325-365.

2. J.A. Cornie,. "Development of Precipitation Strengthened Columbium Base Alloys," AFML-TR-71-5, (December, 1971).

3. T.K. Roche and D.L. Graham, "Development of Oxidation Resistant, High Strength, Columbium Alloys," AFML-TR-69-344, (January, 1970).

4. R. Bakish, Conference Proceedings, "Electron Beam Melting and Refining State of the Art 1985," Library of Congress, ISSN 0740-8706, (November 1985).

5. R.M. Bonesteel, D.J. Rowcliffe and T.E. Tietz, "Mechanical Properties and Structure of Internally Oxidized Niobium-1% Zirconium Alloy," *TransTIM* Vol. 9 Supplement, (1968).

6. C. C. Wojcik, "Evaluation of Powder Metallurgy Processed Nb-30HF-9W," MPIF, *1988 International Powder Metallurgy Conference Proceedings*, Vol. 19, pp. 187-200.

7. R. Titran and W. Klopp, "Long Time Creep Behavior of the Niobium Alloy C-103," NASA TP-1727, (1980).

8. R. Titran and R. Hall, "High Temperature Creep Behavior of a Columbium Alloy, FS-85," NASA TN-D-2885, (1965).

9. R. Titran, "Long-Time Creep Behavior of Nb-1Zr Alloy Containing Carbon,"NASA TM-100142, (1986)

10. C. Wojcik and K. Jordan, Unpublished research ,1992

11. C. Wojcik and L. Clark, "Design, Analysis, and Testing of Refractory Metal Heat Pipes Using Lithium as the Working Fluid," *AIAA Thermophysics Conference*, (June, 1991)

APPLICATION OF TUNGSTEN ALLOYS IN THE LIGHTING INDUSTRY

L. BARTHA

Research Institute for Technical Physics
of the Hungarian Academy of Sciences
Budapest, Hungary

INTRODUCTION

The properties of W alloys are determined by the extremely high melting point of the W. The alloys can be prepared mainly by powder metallurgical processing. Their equilibrium concentration is limited by the partial pressure of the alloying component at the temperature of preparation or application and is generally low.

There are intermetallic alloys with metal concentrations comparable to the W, like heavy metals, W-Cu and W-Ag alloys for electric contacts etc, but they have no lighting applications. There are alloys with other refractory metals like W-Mo or W-Re, with mutual solubility of the components, with properties proportional to the concentration. They might have some limited lighting applications.

The most important group of W-alloys for lighting is the doped W. They have non-metallic or at least not dissolved alloying components with low concentration. The properties change much as compared to the concentrations. Dopants are present either as soft or as hard dispersed second phase particles. The best known examples are the K-doped and the thoriated W.

The main applications of W alloys in lighting are as
(a) filaments (coils) in incandescent lamps
(b) electron emitting cathodes in gas discharge lamps
(c) heaters to evaporate metals for reflecting coatings
(d) electric leads.

DISCUSSION

(a) Filaments (Coils) in Incandescent Lamps

Incandescent filaments are certainly the oldest and most important lighting application of W alloys. This has founded the modern lighting and helped to develop mass production of miniature parts.

Three basic types of alloys are used:
- KAS doped, soft phase (bubble) strengthened W
- ThO_2 doped, hard phase strengthened W
- Re containing solid solution.

The overwhelming majority of W filaments is made of KAS-doped W, containing usually less then 100 ppm K. This material consumes 4-5% of the yearly world-wide W production.

The requirements of the W filament can be described as creep resistance at elevated temperature, stability against mechanical and thermal shocks in a chemically more or less active atmosphere. Reproducibility in an amount of some billion pieces/year on a reasonable price.

Fig.1 shows the typical creep characteristics of the pure and of the K-doped W filament.

Mat. Res. Soc. Symp. Proc. Vol. 322. ©1994 Materials Research Society

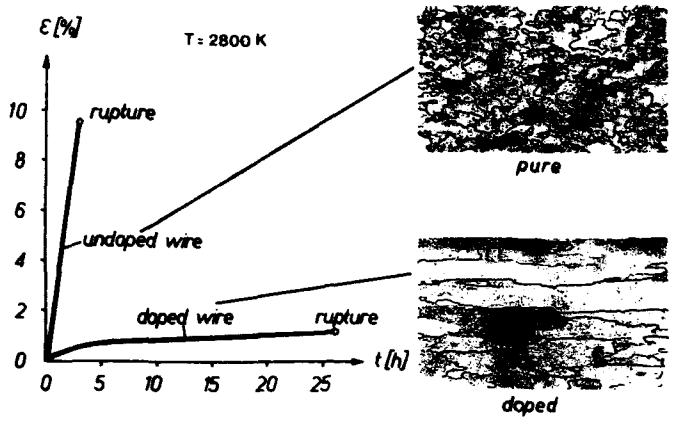


Fig. 1. Creep curves and grain structures of pure (a) and K-doped (b) tungsten wires [1].

The curve (b) of the K-doped wire corresponds to a lamp grade material in which as a result of doping characteristic, axially elongated, recrystallized grain structure developes.

At KAS doping W-blue oxide, a decomposition product of ammonium paratungstate is mixed with K, Al and Si salts and this mixture will be reduced to metal grains. During the reduction inclusions, which were characterized as K, Al Silicates will be incorporated into the metal grains. Fig.2 shows pure and doped W particles.

The presence of inclusions can be proven also in the sintered ingots, where a great number of very small pores are detected, which cannot survive the sintering if they are empty, as in case of pure W.

An unsolved question of KAS doping is the incorporation mechanism during reduction.

Millner [3] had the idea that K-containing transitional compounds like W-oxidebronzes or ß-W will be covered by volatile W-oxides during a gas-phase transport and deposition.

Zeiler et al. [4] described recently the trapping of dope particles by small W grains when sintered together.

Neugebauer [5] suggested a chemical incorporation occurring in several steps in the course of the reduction, as an interaction between solid and molten compounds, including also gas phase transport.

Bewley [6] described the transformation of the dope inclusions into K-bubbles in the course of thermomechanical treatment.

Some contradictions of the different models allowes us to assume the lack of full understanding. Research should be done because of the scientific and technical importance of this field.

The K-doped W makes the largest amount of W filaments. There are some special lamps, mainly shock or vibration resistant ones, containing ThO_2 particles as hard phases. Their strengthening mechanism is not clarified well enough. Their production declines because of the radiation danger of the Th.

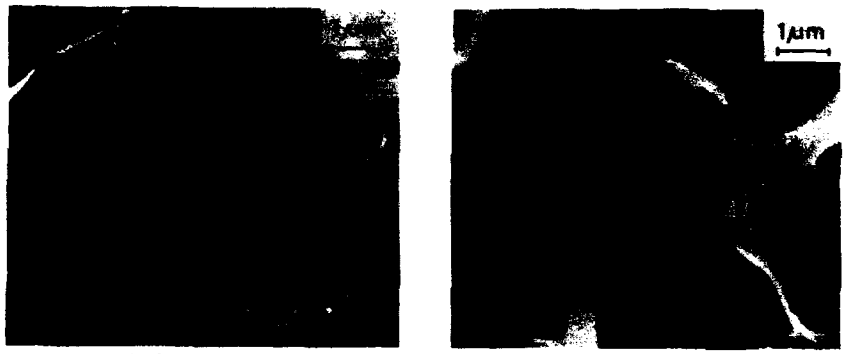
The K-doping occures sometimes in Re containing W alloy, also increasing shock resistance of the filament. There are difficulties of homogenization, which causes problems in wire drawing. Splitting is a typical failure. The amount of lamps made with such wires is negligible.

Having these different types of alloys, we should see the mechanisms how they act.

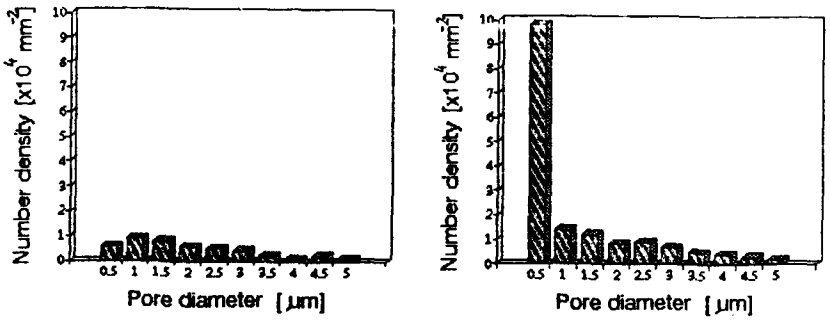
The KAS doped W contains K-filled bubbles, arranged in rows parallel to the wire axis. (Fig.3.)



.Fig.2. (A) Pure (a) and doped (b) W powder particles.



(B) Grain structure and porosity of pure (a) and doped (b) sintered ingots.



(C) Pore size distribution in sintered ingot of pure (a) and doped (b) W. [2]

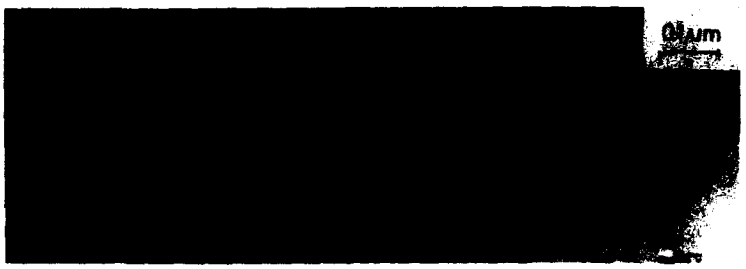


Fig.3. (A) K-bubble rows in doped W-wire.



(B) Partly spheroidised K-bubbles.



(C) Grain boundaries in W pinned by K-bubbles [7].

The increased creep resistance of such materials is based on at least two effects:
- The interlocking grain structure hinders boundary sliding.
- The bubbles pin the boundaries, decreasing grain boundary migration.

ThO_2 particles also arranged in rows might restrict the motion of dislocations, similar to K-bubbles.

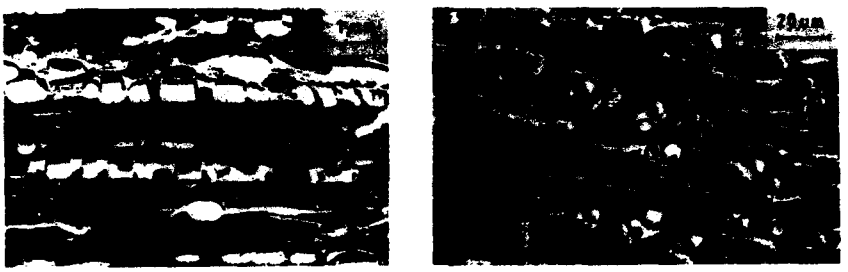


Fig.4. (A) ThO_2 particles rows in thoriated W filament [8]. (B) Dispersed ThO_2 particles in sintered W.

In case of Re-W alloys the Re hardens the matrix in which the effect of K-bubbles might be more expressed.

(b) Electron Emitting Cathodes in Gas Discharge Lamps

The cathods of gas discharge lamps emit electrons to ionize the gas filling of the lamps. The electron emission depends on the work function of the cathode surface. The work function of W is high - ≈ 4,5 eV - and can be decreased by a Th layer, which can be formed using thoriated W. A typical thoriated cathode contains 0,5-1% ThO_2 dispersed in small particles as seen in Fig.4. It has to be activated by high temperature annealing over 2700 K, when ThO_2 decomposes. Deliberated Th atoms dissolve into the W matrix and diffuse towards the surface. They arrive onto the surface at discrete sites where enhanced diffusion occures. At a proper temperature they spread on the surface and form a thin layer coating which results in a considerably lower work function. The existence of the layer is not stable over 2000 K because of evaporation. EEM pictures of a thoriated W surface show the behaviour at 2200 K. The twinkling spots are ends of pathes where Th arrives to the surface and emit intensively electrons, but evaporate in a short time. (Fig.5.)



Fig.5. Low work function spots on the surface of thoriated W at 2200 K.

An optimal temperature for diffusion and for constant electron emission has to be applied. There is a tendency to substitute Th with other materials which might supply the surface with emission increasing coating. Intensive research should be done to find the proper atoms.

In many cases tungsten serves in cathodes only as a support and heater, when coated with pastes containing work function decreasing components.

(c) Heaters to Evaporate Metals for Reflecting Coatings

In some special purpose lamps envelopes are covered with metal coating - mainly Al - to form light reflecting mirrors. The evaporation occures in vacuum and W coils are used for rapid heating of the Al. The lifetime of the W coils is limited by an interaction of the Al and W along the grain boundaries. A chemically activated recrystallization takes place which destroys the heater. As the process is concentrated mainly to the grain boundaries, coils made from very large grained filaments could be the solution of the problem. Research is done in order to increase grain size.

(d) Electric Leads

Light sources are built into envelopes made from soft or hard glasses, quarz or ceramics. The thermal expansion of these materials varies. The expansion of the lead wires should fit properly, otherwise failures occur.

Recently W-Mo alloys were applied, the expansion of which can be fitted by varying the concentration. As W and Mo have unlimited solubility, the expansion values change continuously between the two limits.

CONCLUSIONS

Three, basically different kinds of W alloys - solid solutions, hard and soft phase dispersions - are applied in the lighting industry. Alloying and doping should be differentiated. The most important material is the KAS doped filament.

There are four types of applications:
- incandescent filaments
- electron emitting cathodes
- heaters
- electric leads.

Research should be done to solve many questions, like to
- clarify the KAS dopant incorporation into W grains
- substitute ThO_2 with other materials in cathodes
- reduce the destroying effect of Al on grain boundaries of W.

REFERENCES

1. O. Horacsek, L. Bartha, High Temperatures, High Pressures, **6**, 371-381 (1974).
2. O. Horacsek, in Metallurgy of Doped Non-Sag Tungsten, edited by E. Pink, L. Bartha (Elsevier Appl. Sci. 1989), pp. 175-187.
3. T. Millner, Acta Techn. Acad. Sci. Hung. **7**, 269-289 (1971).
4. B. Zeiler, W.D. Schubert, B. Lux, Refr. Met. and Hard Materials, **10**, 91-105 (1991).
5. J. Neugebauer, L. Bartha, I. Mészáros, Plansee Proc. **1**, 312-320 (1993).
6. B.P. Bewley, N. Lewis, K.A. Lou, Metallurgical Transactions **A, 23A,** 121-133 (199).
7. Courtesy of C. Briant, G.E.Co., R&D Center.
8. G.D. Rieck, Tungsten and its Compounds (Pergamon Press, 1967).

POTASSIUM IN GRAIN BOUNDARIES OF TUNGSTEN

MILAN R. VUKCEVICH
GE Lighting #5430, Nela Park, Cleveland, Ohio 44112

ABSTRACT

Most of the recent work on the role of potassium in tungsten wire deals with the origin of bubbles and their effect on the recrystallization process. Two very important areas are neglected: the effect of potassium strings on the mechanical properties of wire during manufacturing, and the differences in distribution of bubbles in the grain boundaries vs. the bulk. Although other advances in our understanding of potassium in tungsten are reviewed, the main attention is on these two neglected areas. Derived are expressions for the yield point of the fibrous wire structure, and for the increased concentration of bubbles in the transverse boundaries. The theory and experiments are in good agreement.

1. INTRODUCTION

In tungsten wire for high temperatures applications, such as filaments in incandescent and halogen lamps, potassium is present in the form of numerous tiny bubbles which are aligned in strings parallel to the wire axis. Potassium bubbles direct the recrystallization process, and help create a microstructure of elongated grains with rugged transverse grain boundaries. This structure resist sag at filament temperatures which often exceed 3000K.

Because of the significance of potassium for the quality of the final product, most of the work on tungsten wire has centered on the origin of potassium bubbles [1-3] and on their effect on recrystallization [4,5]. What is often neglected is that potassium is extremely important during the manufacture of wires: it determines the mechanical properties of tungsten, and distorts the quantitative results of metallographic tests on interim and finished products. These two seemingly unrelated effects are due to interactions of potassium with grain boundaries of tungsten, and are the main subject of this paper. We will touch upon the origin of potassium strings and bubbles only briefly, to provide the necessary background.

2. POTASSIUM PORES IN THE INGOT

Potassium is incorporated into grains of tungsten powder, and during sintering, it spreads through the connected pores. It has a significant effect on the mechanism of sintering and on the density of ingots [6]. In a recent work on the characterization of voids [7], the following expression was derived for the volume concentration of the potassium pores in sintered tungsten ingots:

Mat. Res. Soc. Symp. Proc. Vol. 322. ©1994 Materials Research Society

$$N_p = \frac{R\ C_k\ \rho\ T_s}{8\ \pi\ M_k\ \gamma\ \langle r \rangle^2}\ , \qquad (1)$$

Here, C_k is the weight fraction and M_k the atomic weight of potassium, ρ is the density and γ the surface energy of tungsten. Also, R is the gas constant, T_s the sintering temperature, and $\langle r \rangle$ the average bubble radius.

These pores are approximately 1.0 micron in radius, and they are the precursors of smaller bubbles in tungsten wires. The ingot pores are elongated into strings during rolling, swaging, and wire drawing. Their aspect ratio (A), follows the deformation of the tungsten matrix [1,3]:

$$A_n = A_{n-1}\ (\ 1\ -\ R_n\ )^{-3/2}\ , \qquad (2)$$

where R_n is the reduction in area of the tungsten piece produced in the step n in the sequence of metal-forming operations.

3. POTASSIUM STRINGS AND THE FIBROUS STRUCTURE

While metal forming operations change potassium pores into strings, they simultaneously change the microstructure of tungsten: from random equiaxed grains into fibers and subgrains with the $\langle 110 \rangle$ -axis oriented in the drawing direction. At medium strains, the cells are ribbon shaped, but they start and end with circular transverse sections. This unusual grain shape was explained by Hosford [8]: in the $\langle 110 \rangle$ bcc wire texture, only two of the four $\langle 111 \rangle$ -slip directions are parallel to the drawing direction and can contribute to the extension of grains. This leads to the plain-strain conditions and ribbon-shaped grains. As shown on iron by Langford and Cohen [9], dynamic recovery in later stages of deformation tends to produce circular cylindrical grains.

During most of the metal forming, tungsten has the fibrous structure. Typically, there are fifty rolling, swaging and drawing steps leading from an ingot 2.0 centimeters in diameter to the 0.006 centimeters wire for incandescent lamps of 100 watts. In potassium doped tungsten, walls of fiber grains and cells tend to become stabilized at potassium strings. Annealing broadens the fibers mostly by annihilating cell walls which are not anchored by the strings.

From the absence of dislocations within the cells, it was concluded [9] that the plastic deformation is caused mainly by the newly created dislocation loops, which originate and disappear at walls of cells and boundaries. From the geometry of the structure, Figure 1(b), it follows that a single loop with Burger's vector **b**, after traversing the entire glide plane in a cell of length **l**, will produce a plastic strain increment:

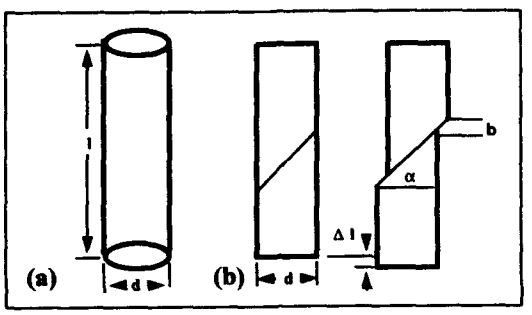


Figure 1. (a) Orientation of a cell and a glide plane in the Hosford bcc structure. (b) Strain produced by a completely spread dislocation loop.

$$\Delta\epsilon = \frac{\Delta l}{l} = \cos\alpha \, \frac{b}{l} = \sqrt{\frac{2}{3}} \, \frac{b}{l} \, . \tag{3}$$

Following Langford and Cohen [9], we assume that the total work in creating a dislocation loop ($\sigma_y \Delta\epsilon$), is equal to the energy to move the dislocation across the glide plane ($\sigma_{y,o}$ $\Delta\epsilon$), plus the energy of the newly created loop:

$$\sigma_y \, \Delta\epsilon = \sigma_{y,o} \, \Delta\epsilon + \frac{P_g \, W}{A \, l} \, , \tag{4}$$

where W is the dislocation energy, and, as in Figure 1, P_g is the perimeter of the elliptic glide plane, A is the cross section of the subgrain, and L is its length.

By simple trigonometry, the perimeter of the glide plane is related to the perimeter of the subgrain P:

$$\frac{P_g}{P} = \frac{1}{2} \left(1 + \frac{|110| \, |011|}{(110) \cdot (011)} \right) = 1.5 \, , \tag{5}$$

and

$$\frac{P}{A} = \frac{4}{d} \, . \tag{6}$$

Combining Equations (1) to (5), we obtain an expression for the yield stress:

$$\sigma_y = \sigma_{y,o} + 6\sqrt{\frac{3}{2}}\,\frac{W}{b\,d}\,, \tag{7}$$

The appropriate formula for the energy of a dislocation loop is given by Friedel [10]:

$$W = \frac{G\,b^2}{4\,\pi\,K}\,\ln\left(\frac{d}{b}\right)\,. \tag{8}$$

Here, K depends on geometry and the Poisson ratio ν:

$$\frac{1}{K} = \cos^2\Psi + \frac{\sin^2\Psi}{1-\nu}\,, \tag{9}$$

where Ψ is the angle between Burgers vector and the glide plane. Averaging by integration between 0 and $\pi/2$, yields

$$\left\langle\frac{1}{K}\right\rangle = \frac{2}{\pi}\int_o^{\pi/2} d\left(\frac{1}{K}\right) = \frac{2-\nu}{2\,(1-\nu)}\,. \tag{10}$$

Therefore, the yield stress for the Hosford structure may be written as:

$$\sigma_y = \sigma_{y,o} + 3\sqrt{\frac{3}{2}}\,\frac{G\,(2-\nu)}{1-\nu}\,\frac{b}{d}\,\ln\left(\frac{d}{b}\right)\,. \tag{11}$$

The numerical value of the friction stress $\sigma_{y,o}$ has been measured on single crystals of tungsten [11]. For the same orientation as in the Hosford texture, we have:

$$\sigma_{y,o} \sim \sigma_{\langle 110\rangle} = 3.48\times10^9 \quad (dyne/cm^2)\,. \tag{12}$$

Also, for tungsten, $G=1.6\times10^{12}$ (dyne/cm^2), and $\nu=0.3$, and Equation (11) becomes:

$$\sigma_y = 3.48\times10^9 + 1.17\times10^{12}\ \frac{b}{d}\ \ln\left(\frac{d}{b}\right)\ \ (dyne/cm^2)\,. \qquad (13)$$

As shown in Figure 2, this formula agrees well with the experimental results on wire made of both, potassium doped and undoped tungsten [12].

However, when samples are annealed, there is a significant difference between the two types of tungsten. Unobstructed by potassium strings, fibrous grains and cells of undoped tungsten broaden faster than in doped tungsten, and the yield point decreases to a lower level under the same annealing conditions [12].

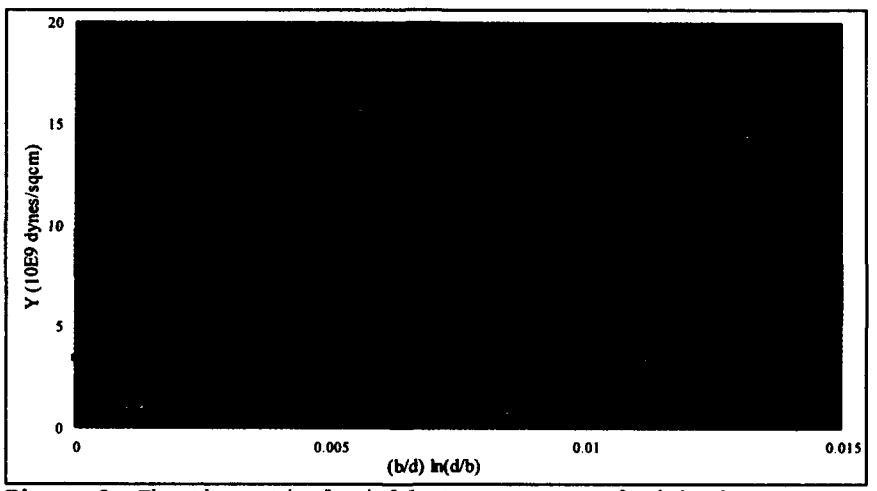


Figure 2. The theoretical yield stress compared with the experimental 0.1% proof stress of doped and undoped tungsten wires.

Another effect of potassium strings can be detected by observing how the yield point of annealed and as-drawn wires, increases upon subsequent processing. When wire of doped tungsten is annealed, the rate of yield point increase with deformation is, at first, slower than the rate observed in the wire which has not been annealed. This is most likely due to the stability of the boundaries which contain potassium strings. The annealing removes cell walls which are not potassium pinned, and the yield stress increases at a slower rate until new unpinned cell walls are created.

4. POTASSIUM BUBBLES AND GRAIN BOUNDARIES

The potassium strings are thermodynamically unstable [1-3,13,14]. When fibrous wire is heated above approximately 1100K, potassium strings will transform within minutes. If their aspect ratio is larger than the critical value

$$A_c = 2\sqrt{2\pi} = 8.89 \quad , \tag{14}$$

they will break into small bubbles. This will occur after the threshold time [1,12]:

$$\tau = \frac{4\, r_o^4\, k\, T}{D_s\, \gamma\, \Omega^{4/3}} \quad , \tag{15}$$

where r_o is the initial cylinder radius, γ the surface energy, Ω the volume per atom, D_s the surface diffusion coefficient, and k the Boltzmann constant.

Upon the breakup of the strings, the new bubbles have diameters (D_b) somewhat larger than the parent cylinders (D_c):

$$D_b = \sqrt{\frac{3}{4}\sqrt{2}\,\pi}\, D_c = 1.825\, D_c \quad , \tag{16}$$

and are separated by the distance

$$X = \frac{4}{3}\,\frac{D_b^2}{D_c} \quad . \tag{17}$$

If the aspect ratio is smaller than the critical value, the potassium strings will start spheroidizing, and their aspect ratio will decrease according to [1]:

$$\begin{aligned} &\frac{3}{2}\left(A_t^{2/3} - A_o^{2/3}\right) + \\ &2\sqrt{3}\tan^{-1}\left[\frac{2\sqrt{3}\left(A_t^{1/3} - A_o^{1/3}\right)}{3 + \left(2\,A_t^{1/3} + 1\right)\left(2\,A_o^{1/3} + 1\right)}\right] + \\ &\ln\left[\frac{\left(1 - A_t^{1/3}\right)^2\left(1 + A_o^{1/3} + A_o^{2/3}\right)}{\left(1 - A_o^{1/3}\right)^2\left(1 + A_t^{1/3} + A_t^{2/3}\right)}\right] = -\,C\,t \quad , \end{aligned} \tag{18}$$

where A_o and A_t are, respectively, the original aspect ratio and the aspect ratio after t-seconds. The constant at the end of this cumbersome formula is related to the breakup time in Equation (15):

$$C = \frac{12}{A_o^{4/3}\,\tau} \quad . \tag{19}$$

The last six equations, and Equations (1) and (2), are the basis of our structure modeling program, which was originally used to help redesign the manufacturing process, and is now used in conjunction with the metallographic tests of the interim and the final product.

In view of the significance of potassium bubbles to production and the use of tungsten wire for incandescent filaments, it is necessary to have a simple and fast quality test for size and distribution of stringers and bubbles. A popular method is to immerse the tungsten wire in liquid nitrogen, break it or split it, and examine the fracture surface. To observe strings or bubbles in the split longitudinal section is tedious: the roughness of the fibrous structure hides smaller potassium aggregates [2]. The fastest method is to recrystallize the wire, cool it in liquid nitrogen, break it along the transverse boundaries, and count the number and size of bubbles. The common assumption is that the volume concentration of bubbles (N_v) is related to the surface concentration (N_s) by the well-known metallographic formula:

$$N_s = 2\,r\,N_v \quad (bubbles/cm^2) \quad , \tag{20}$$

where **r** is the bubble radius.

However, this is true only in the case of planar surfaces. To lower the energy, transverse grain boundaries bend out of plane to incorporate a larger number of bubbles than present in a transverse plane. This is illustrated in Figure 3. The process of incorporation of bubbles by bending the boundary is opposed by the boundary surface tension. The equilibrium configuration was calculated by Nes, Ryum and Hunderi [8], and referring to Figure 3, their result may be expressed as

$$Y = r\left(3 + \sqrt{2} + \ln\left(\frac{\sqrt{2}\,X}{2\,r}\right) \right) , \tag{21}$$

where Y is the effective thickness of the boundary and X is the average distance between the boundary bubbles.

This is the quantity which should be used instead of **2r** in Equation (20) to correlate the grain boundary to the volume concentration of bubbles:

$$N_{gb} = Y\,N_v \quad . \tag{22}$$

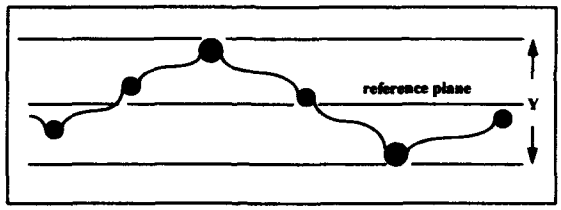


Figure 3. Potassium bubbles in a transverse boundary which is bent out of the reference plane.

Assuming a simple relation:

$$X \sim \frac{1}{\sqrt{N_s}} , \tag{23}$$

and using Equation (21), we can rearrange Equation (22) to read:

$$\frac{N_{gb}}{N_s} = \frac{1}{2}\left(3 + \sqrt{2} + \frac{1}{2} \ln\left(\frac{1}{2\, N_s\, r^2} \right) \right) . \tag{24}$$

A typical numerical example is $N_s \sim 10^8$ (1/cm^2) and $r \sim 2\text{x}10^{-6}$ (cm), which yields the ratio of grain boundary bubbles to the bubbles in a plane of approximately 4.0. This is in agreement with our observations [15], and it also explains why the number of bubbles observed in the fractured transverse boundaries is between 3 and 5 times larger than calculated from the model based on Equations (2) and (14) to (19) [1].

CONCLUSIONS

Potassium in doped tungsten is very important even before bubbles are formed. The mechanical properties and the response to annealing depend on the potassium strings which stabilize the longitudinal boundaries of the fibrous texture.

After recrystallization starts, and the potassium strings break up, the transverse boundaries bend out of planes to incorporate a larger number of bubbles. Besides the obvious effect on the pinning of boundaries, this bending also distorts the results of quantitative metallography. A formula has been developed which allows the easily-measured bubble densities in the fractured transverse boundaries to be used to calculate the correct volume densities.

ACKNOWLEDGEMENTS

I benefited greatly from many inspiring and informative discussions with my GE colleagues, Bob Arena, Barnard Bewley, Clyde Briant, Dan Hennessy, Istvan Meszaros and Attila Nagy. I can only hope that my interpretations of their inputs are equally useful.

REFERENCES

1. M.R. Vukcevich, Proc Fifth Int. Tungsten Symposium - Budapest, (MPR Publishing, Bellstone 1990), p. 157.
2. C.L. Briant, Proc Fifth Int. Tungsten Symposium - Budapest, (MPR Publishing, Bellstone 1990), p. 169.
3. M.R. Vukcevich, C.L Briant and J.W. Pugh, GEL Report, Cleveland (1993), (to be published)
4. J. Csako, Cs.L. Toth, I. Meszaros, J. Neugebauer, and O. Horacsek, Proc Fifth Int.Tungsten Symposium - Budapest, (MPR Publishing, Bellstone 1990), p. 132.
5. D.P. Snow, The Metallurgy of Doped/Non-Sag Tungsten, E. Pink and L. Bartha, Editors, (Elsvier Applied Science, 1989), p. 189.
6. B.P. Bewley,Proc Fifth Int. Tungsten Symposium - Budapest, (MPR Publishing, Bellstone 1990), p. 227.
7. J.L. Walter, K. Lou and M.R. Vukcevich, Proc. 12th Int. Plansee Conf., **1**, 493 (1989).
8. W.F. Hosford, Trans. AIME, **230**, 12 (1964).
9. G. Langford and Morris Cohen, Trans. ASM, **62**, 623 (1969).
10. J. Friedel, Dislocations, (Pergamon Press 1964), p. 21.
11. D. Hull, P. Beardmore and A.P. Valentine, Wright-Patterson Air Force Base Report AFML-TR-66-369, February 1967), pp. 3-26.
12. J. Tavernelli, C. Johnson and R.F. Hehemann, GEL Report, Cleveland (1974).
13. F.A. Nichols and W.W. Mulins, Trans AIME, **233**, 1840 (1965); JAP, **36**,1826 (1965).
14. D.M. Moon and R.C. Koo, Met. Trans, **2**, 2115 (1971).
15. M.R. Vukcevich, J. Johnson and W.A. Lasch, (to be published).

CREEP CHARACTERISTICS OF TUNGSTEN WIRES

WEGO WANG
U.S. Army Research Laboratory, Materials Directorate, Watertown, MA 02172-0001

ABSTRACT

In this study heavily-drawn tungsten wires were tested for creep at a constant load of 115 MPa in a 10^{-3} torr nitrogen atmosphere. These fine wires had an elongated rectangular grain morphology with small average grain sizes, 1.6 to 2.2 μm. The typical test sample wire was about 2.54 m long and 130 μm in diameter. The test wire was heated to the test temperature by self-resistance. The creep elongation was monitored by a transducer. Steady state creep rates were determined from the creep curves for four specimens that were tested at 1673, 1553, 1453, and 1273K, respectively. Diffusional creep is the predominant deformation mode. The experimental data were analyzed and compared with several creep theories: Ashby's combined, Coble's grain boundary and Nabarro's lattice diffusional creep models. The effects of recrystallization, grain aspect ratio, grain growth, impurity contents, nitrification and oxygen contamination on creep behavior are discussed in detail. However, their influences on creep kinetics are minimized in this study by carefully controlled experimental conditions. At a stress of 115 MPa, the grain boundary diffusional creep model successfully predicts the creep behavior at temperatures below 1453K. The instantaneous creep rate is inversely proportional to the cube of grain size at 1453K. The lattice diffusional creep model becomes predominant when the test temperature rises to 1553K. It is concluded that the creep behavior is controlled by grain boundary diffusion at a temperature below 1453K, and lattice diffusion above this temperature. Diffusion controlled creep and grain boundary sliding with diffusional accommodation are coupled in tungsten wires.

INTRODUCTION

In this study fine tungsten wires were purchased from the Westinghouse Electric Corporation. These wires (HRL9-E2) were unstraightened, electropolished and doped with 60 to 100 ppm potassium. They were tested for creep at a constant load in a 10^{-3} torr nitrogen gas atmosphere. Diffusional creep tends to be the predominant mode. There are two major diffusional creep mechanisms, each differentiated by their diffusional paths. At medium temperatures and stresses, the major diffusional path for coarsely-grained materials is through the lattice (i.e., grain interior) and the minimum creep rate, $\dot{\varepsilon}$, can be mathematically described as [1]:

$$\dot{\varepsilon} = 14\Omega D_l \sigma / kTd^2 \qquad (1)$$

where Ω is the atomic volume, D_l the lattice diffusivity, σ the applied stress, k the Boltzmann's constant, T the absolute temperature and d the grain size. This model indicates that the creep rate is inversely proportional to the square of grain size. At lower stresses, the grain boundary becomes the predominant diffusion path for fine-grained structures and the controlling mechanism for creep will switch to grain boundary diffusion. The minimum creep rate, $\dot{\varepsilon}$, can be calculated as [1]:

$$\dot{\varepsilon} = 14\pi\Omega\delta D_b \sigma / kTd^3 \qquad (2)$$

Mat. Res. Soc. Symp. Proc. Vol. 322. ©1994 Materials Research Society

where δ is the grain boundary width and D_b the grain boundary diffusivity. This grain boundary diffusional creep model predicts that the creep rate is inversely proportional to the cube of grain size. This was observed in a recent study on a 100 μm diameter tungsten wire [2]. The strong grain size dependence makes the contribution of grain boundary diffusion more important in fine-grained materials. In both models, a spherical grain shape is assumed and the compatibility problem is neglected. More recent studies have extended the theory to include considerations of grain boundary sliding, grain aspect ratio and grain growth. In fact, if creep occurs by diffusional processes, some grain boundary sliding is required in order to maintain material coherency; on the other hand, if creep results primarily from grain boundary sliding, diffusional processes are required for accommodation. The grains in heavily-drawn fine tungsten wires are roughly of rectangular shape. They have an average height H, width W, and aspect ratio R = H/W with a nominal grain size $d = (HW)^{1/2}$. The height H is measured in the direction of stress. Raj and Ashby [3] suggested the steady state creep rate for an elongated grain system as:

$$\dot{\varepsilon} = (16\sigma\Omega/3kTd^2)(D_l/R + \delta D_b/dR^{1/2}) \qquad (3)$$

if $H >> W$.

This equation takes both lattice and grain boundary diffusion effects into account and indicates that lattice diffusional creep will dominate for larger grain size materials, while grain boundary diffusional creep is predominant for small grain size materials.

EXPERIMENTAL

For creep testing at high temperatures the as-drawn tungsten wires were mounted in a 2.74 m long, 51 mm diameter copper tube built on a 0.028 cubic meter metal box. Three windows are available for sample sighting and temperature measurement using an optical pyrometer. The test wire is first statically loaded and then heated by self-resistance. The creep elongation is monitored by a transducer. An EMF suppression unit is connected between the transducer and the recorder to adjust sensitivity. The whole system is first evacuated by a mechanical pump and followed by a diffusion pump to 10^{-4} torr. Nitrogen gas is then flowing into this system, and maintained at 10^{-3} torr during the testing period.

The room-temperature yield strength of tungsten wire is 414 MPa. A constant nominal static stress of 115 MPa is applied to the specimen at various temperatures ranging from 1273 to 1673K. The measured creep rate is of the order of 10^{-9}/sec for the 2.54 m long, 130 μm diameter tungsten wires. The displacement vs. time data were recorded. The creep rates are compared with various theoretical predictions.

RESULTS

Steady creep rates are determined from the creep curves for four specimens that have been tested at 1673, 1553, 1453 and 1273K, respectively. At 1673K steady state creep is reached in about one and one-half hours, and the creep rate is 2.2×10^{-8}/sec. The thermal expansion effect has been compensated for by choosing the initial length as the length after 800 seconds of heating under the testing load. At 1553K, steady state creep occurs at about 5 hours and the rate is

3.5×10^{-9}/sec. The steady state creep rate continues to decrease when the testing temperature decreases. At 1453K the rate is 3.2×10^{-9}/sec and at 1273K the rate is 0.57×10^{-9}/sec.

To compare the experimental data with the theoretical predictions, the diffusion coefficients are first determined. Vasilos and Smith [4] calculated the grain boundary diffusivity in tungsten as

$$D_b = 3 \times 10^{-4} \exp(-110.7 \text{ kcal/mole/RT}) \text{cm}^2/\text{sec} \quad (4)$$

between 1573 and 2033K. Kreider and Bruggeman [5] calculated the grain boundary diffusivity as:

$$D_b = 3.33 \exp(-92 \text{ kcal/mole/RT}) \text{cm}^2/\text{sec} \quad (5)$$

between 1673 and 2473K. It was pointed out [6] that Eq. (4) might not take into account all the rate-controlling factors and Eq. (5) should be more accurate. The author used Eq. (5) in his calculation for D_b, except at 1273K, where Eq. (4) is applied. The lattice diffusivities are calculated following Robinson and Sherby's suggestion [6] for temperatures above 2473K:

$$D_l = 5.6 \exp(-140 \text{ kcal/mole/RT}) \text{cm}^2/\text{sec} \quad (6)$$

and for temperatures between 1473 and 2473K:

$$D_l = 10^{-4} \exp(-90 \text{ kcal/mole/RT}) \text{cm}^2/\text{sec}. \quad (7)$$

The experimental data are plotted in Figure 1 along with the predictions from Ashby's combined creep model Eq. (3), grain boundary diffusional creep model Eq. (2) and lattice diffusional creep model Eq. (1). The heavily-drawn fine tungsten wires have a rectangular grain morphology as shown in Figure 2. Pre-test tungsten wires have grain size dimensions H = 5 μm, W = 0.5 μm, R = H/W=10, and $d = (HW)^{1/2} = 1.6$ μm, with an experimental error ±0.001 μm. The average grain size was measured between any time interval, then a relationship between instantaneous creep rate and grain size was established as shown in Figure 3. From Figure 3 we find that creep rate is inversely proportional to the cube of grain size within the limits of experimental error at 1453K, demonstrating that grain boundary diffusion is predominant at this temperature.

DISCUSSION

In an earlier study [7] on creep of tungsten wires from 2400 to 2800K, recrystallized wires showed much better creep resistance than as-drawn wires. It was suggested that the inferiority of creep resistance in the as-drawn wires was attributable to: 1. creep that occurred early in the test while the sample was undergoing recrystallization, 2. grain boundary sliding and cavitation due to the fine-grained as-drawn structure, and 3. void formation occurring prior to recrystallization that accelerates creep following recrystallization. In summary, the inferior creep properties of as-drawn wires primarily results from "defects" initiated prior to or during recrystallization and these

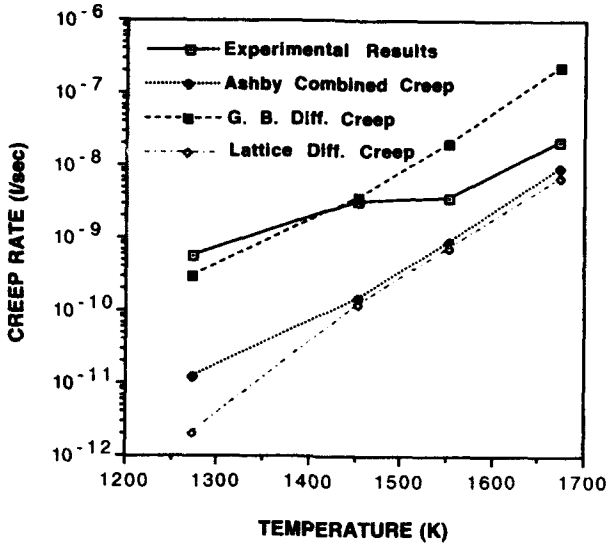


Fig. 1. The temperature - creep rate correlation.

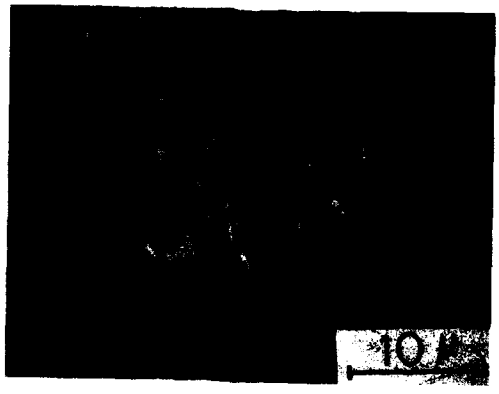


Fig. 2. Rectangular grain morphology observed in the tungsten wire.

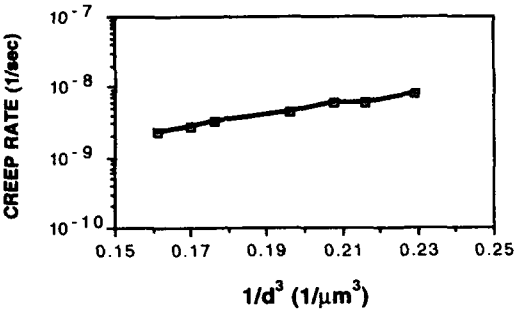


Fig. 3. Relationship between creep rate and grain size at 1453K.

"defects" grow after recrystallization. In this experiment we neglect the recrystallization effect because all testing temperatures are below the recrystallization temperature 1838K [8] and little recrystallization was observed during the test. The grain growth effect is compensated for by taking the average grain size. Experimental data show that at low temperatures, below 1453K, grain boundary diffusional creep is consistent with the experimental results; at higher temperatures, above 1453K, lattice diffusion becomes more significant, and at 1673K the Ashby combined and lattice diffusional creep models fit the creep behavior better. Over the whole experimental temperature region, the combined creep model fits better than a simple lattice diffusional creep model, because it factors in both the grain boundary and lattice diffusion contributions, and uses a rectangular grain shape.

The fracture modes of tungsten wires under creep are usually transgranular at higher stresses and intergranular at lower stresses. Despite the difference in fracture appearance with stress, no direct correlation between macro-fracture modes and creep failure kinetics (creep rate, grain size, stress and temperature dependence) was found. This results from the fact that creep failure kinetics depends on the creep rate controlling mechanism, e.g. grain boundary or lattice diffusion, grain boundary sliding and dislocation climb or glide. It is micro-process and rate sensitive. However, fracture modes observed with SEM result from macro-processes, e.g. cavitation and necking. There is little dependence of these macro-processes on testing rate.

Creep strain resulting from void formation by diffusion could be significant. However, this effect is relatively small in this study due to the compatibility restraint associated with the elongated fine grain structure [9]. The impurity contents in specimens are Al 50 ppm, Mo 25 ppm, Ni 20 ppm, O_2 170 ppm (pre-test) and 210 ppm (1673K, 67 hours), all measured by weight. At 10^{-3} torr nitrogen gas atmosphere the nitriding temperature is 1773K [8], therefore nitriding is not expected during the experiment. The oxygen pickup was only 40 ppm during testing at 1673K for 67 hours. It is considered that the effect of this small amount of oxygen contamination on the creep rate is negligible.

The effects of grain aspect ratio on creep behavior and other mechanical properties have been recognized for a variety of alloys. A super-α_2 (Ti-25Al-10Nb-3V-1Mo) alloy showed a 60% longer stress rupture life tested at 922K and 380 MPa when the α_2 grain aspect ratio was increased from 5 to 10 [10]. A similar effect of grain aspect ratio on creep behavior of tungsten wire was also reported [7]. At a grain aspect ratio less than 11, the creep mechanism is dominated by diffusion and grain boundary sliding; the creep failure time increases rapidly with increasing grain aspect ratio. However, at higher aspect ratio, the creep is governed by a dislocation-bubble dispersion strength mechanism and independent of grain aspect ratio.

CONCLUSIONS

For tungsten wires with small grain size, 1.6 to 2.2 μm, under low stress σ = 115 MPa, the grain boundary diffusional creep model successfully predicts the creep behavior below 1453K. The steady state creep rate is inversely proportional to the cube of grain size at 1453K. Lattice diffusional creep becomes significant when the temperature rises above 1553K. It is concluded that 1453K should be a diffusion mechanism transition temperature; below this temperature creep behavior is controlled by grain boundary diffusion, above it lattice diffusion is predominant.

The average grain aspect ratio of the tungsten wires used in this study is 10, and the conclusion in this study is in general agreement with the earlier study [7] that the creep of tungsten wires with a low grain aspect ratio is diffusionally controlled. Figure 1 shows that grain boundary diffusional creep is the maximum limit of the combined creep for the samples with elongated grains. The better fitting between the experimental results and the combined creep model, compared with the lattice diffusional creep model at higher temperatures, also verifies that diffusion controlled creep and grain boundary sliding with diffusional accommodation are coupled in tungsten wires.

ACKNOWLEDGMENTS

The author wishes to thank the NSF for financial support for this study that was completed before the author joined the U.S. Army Research Laboratory. The author would also like to express his appreciation to the late Dr. R. Coble for valuable advice and to Dr. J. Montgomery and Mr. R. Dowding for their comments on the manuscript.

REFERENCES

1. W.D. Kingery, H.K. Bowen and D.R. Uhlmann, Introduction to Ceramics (John Wiley, New York, 1976), p. 742.
2. K. Tanoue, E. Masaoka and H. Matsuda, in Proceedings of the First International Conference on the Metallurgy and Materials Science of Tungsten, Titanium, Rare Earths and Antimony, edited by C. Fu, J. Li and S. Li (International Academic Publishers, New York, 1989), pp. 730- 735.
3. R. Raj and M.F. Ashby, Met. Trans. **2**, 1113 (1971).
4. T. Vasilos and J.T. Smith, J. Appl. Phys. **35**, 215 (1964).
5. K.G. Kreider and G. Bruggeman, AIME Trans. **239**, 1222 (1967).
6. S.L. Robinson and O.D. Sherby, Acta Met. **17**, 109 (1969).
7. P.K. Wright, Met. Trans. **9A**, 955 (1978).
8. C.A. Hamper, Rare Metals Handbook, 2nd ed. (Reinhold Publishing Co., London, 1961), p. 589.
9. O. Horacsek, in The Metallurgy of Doped/Non-Sag Tungsten, edited by E. Pink and L. Bartha (Elsevier Appl. Sci., New York, 1989), pp. 251-265.
10. W. Wang, M.R. Scanlon and M.G.H. Wells in High-Temperature Ordered Intermetallic Alloys IV, edited by L.A. Johnson, D.P. Pope, and J.O. Stiegler (Mater. Res. Soc. Proc. **213**, Boston, MA 1991) pp. 931-936.

SINTERING BEHAVIOR OF Ba_2CaWO_6-DOPED-TUNGSTEN

J.A. RUUD AND B.P. BEWLAY
General Electric Company, Corporate Research and Development Center, Schenectady, NY 12301

ABSTRACT

The sintering behavior of Ba_2CaWO_6 co-sintered with W powder was investigated. Measurements of density and mass loss of sintered compacts showed that the Ba_2CaWO_6-doped-W had a lower density than undoped W and that there was little volatilization of Ba_2CaWO_6 at temperatures below 1750 °C. The activation energies for densification of Ba_2CaWO_6-doped-W and undoped W were both measured to be 389 kJ/mol, which indicates the same densification mechanism, grain boundary diffusion, operated for both materials. The reduced densification kinetics of the Ba_2CaWO_6-doped-W was probably due to increased coarsening in the early stages of sintering.

INTRODUCTION

Refractory metal powders are often combined with a small addition of an element or a compound and then sintered. The addition can be included to increase the sintering rate, or it can included for enhancement of the chemical, mechanical or thermionic properties. There are many examples of the last type of addition which have important technological applications. Examples of devices which use bodies of W co-sintered with an emission material include vacuum tube cathodes [1], low pressure discharge electrodes [2], high pressure discharge electrodes [3,4], and arc welding electrodes [5]. The choice of emission material is determined in part by the operating temperature of the sintered body. Vacuum tube cathodes, which operate at temperatures between 1000 °C - 1250 °C, have been fabricated from porous sintered W-Mo compacts with barium calcium aluminate [1] and from porous sintered W with barium calcium tungstate [6]. Rods made from co-sintered W and a solid solution of BaO:SrO:CaO have been patented for use as electrodes for low pressure discharges such as fluorescent lamps [2], which have electrode temperatures of 1150 °C - 1250 °C. Co-sintered, porous bodies of W and barium calcium tungstate [7], Y_2O_3 [8], and Dy_2O_3 [9] have been studied for use as electrodes operating at temperatures between 1500 °C - 2100 °C in high pressure discharges, such as high pressure mercury lamps, high pressure sodium lamps, and metal halide lamps. Arc welding electrodes, which operate in the temperature range 2500 °C - 3200 °C, have been fabricated by co-sintering W with additions of ThO_2, Y_2O_3, ZrO_2, CeO_2, or La_2O_3 [5] and also subsequent thermomechanical processing.

There is little published data on the sintering behavior of emission materials with W. The sintering behavior of hafnia and ceria with W has been studied recently[10]. The addition of ceria to W compacts did not change the densification mechanism from that of undoped W, but compacts with hafnia sintered by a combination of densification mechanisms. The aim of the present study was to investigate the feasibility of co-sintering a Ba-containing emission oxide with W. Generally, temperatures of 1850 °C and above are required to sinter W to a density which provides acceptable electrical and mechanical properties [11]. A relative measure of the thermal stability of selected emission materials is given in Table I, where the decomposition temperature refers to the lowest temperature at which decomposition products can be detected by mass spectrometry or thermionic emission. Table I shows that most of the commercially available emission oxides decompose and volatilize at temperatures below

Mat. Res. Soc. Symp. Proc. Vol. 322. ©1994 Materials Research Society

Table I. Thermal Stability of Selected Emission Materials

Material	Decomposition Temperature (°C)	Reference
ThO_2 / Ba_2CaWO_6 / $BaThO_3$	1335	[12]
Ba_3WO_6	1370	[13]
$Ba_3Y_2(W_{0.2}M_{0.8})O_9$	1415	[12]
$Ba_3Y_2(W_{0.8}M_{0.2})O_9$	1420	[12]
Ba_2CaWO_6	1420	[12]
$Ba_{1.8}Sr_{0.2}CaWO_6$	1430	[13]
$Ba_3Y_2WO_9$	1470	[12]

1500 °C. Thus, the aim of the present investigation was to identify conditions under which W can be co-sintered with a Ba-containing emission oxide, such that adequate density is obtained in the sintered part and sufficient emission oxide is retained. Ba_2CaWO_6 was selected as the emission material for this sintering study because it is one of the most stable Ba-containing emission materials.

EXPERIMENTAL

The densification and mass loss of Ba_2CaWO_6-doped-W compacts and undoped W compacts were measured for compacts sintered at temperatures between 1250 to 2000 °C for 10 minutes in dry H_2 (dew point less than -60 °C). The W-Ba_2CaWO_6 compacts were prepared by blending 0.5 μm W powder (Johnson Matthey) with 2.5 at% Ba_2CaWO_6 (7.7 wt % or 20 vol%) and compacting using cold isostatic pressing at 345 MPa. A green density of about 45% of theoretical density was achieved. The undoped W compacts were prepared in an identical manner. In addition, mass loss was measured for loose Ba_2CaWO_6 powder in Mo pans. There were, then, three different samples in each sintering treatment. Density was determined by measuring the volume and mass of the pressed ingots both before and after sintering. Comparison of the density and mass loss measurements of doped and undoped W compacts allowed the determination of the effect of Ba_2CaWO_6 doping on the sintering of W.

RESULTS AND DISCUSSION

The relative densities of compacts sintered 10 minutes in dry H_2 are shown in Figure 1 as a function of sintering temperature. The addition of Ba_2CaWO_6 to W dramatically decreased the sintered density. The highest fraction of theoretical density measured for W compacts was just below 90% while the highest density Ba_2CaWO_6 - doped- W compact was 70%.

The mass loss during sintering was measured for the three samples and is plotted against sintering temperature in Figure 2. The mass loss of W samples was about 1.6%, independent of temperature; this was probably due to reduction of tungsten oxide on the surface of the particles during sintering in H_2. Appreciable mass loss of the Ba_2CaWO_6 in both powder form and, when combined with W, occurred at sintering temperatures above 1750 °C.

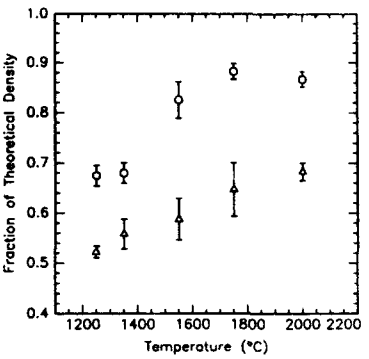


Figure 1. Fraction of theoretical density versus temperature for Ba_2CaWO_6-doped-W (triangles) and undoped W (circles) compacts sintered for 10 minutes in dry H_2.

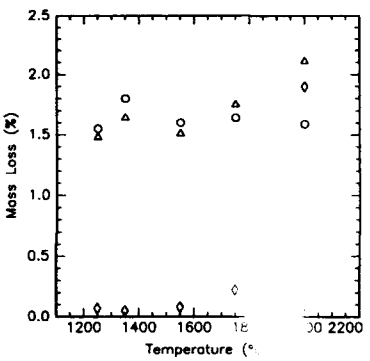


Figure 2. Mass loss versus temperature for W compacts (circles), W-Ba_2CaWO_6 compacts (triangles) and loose Ba_2CaWO_6 powder (diamonds) for samples sintered 10 minutes in dry H_2.

These results show that the onset of vaporization of Ba_2CaWO_6 in H_2 occurs at a much higher temperature than previously reported for vaporization in vacuum [12].

Examination of fracture surfaces of compacts using scanning electron microscopy showed no evidence of macroscopic Ba_2CaWO_6 particles in the compacts after pressing or after sintering. However, Auger electron spectroscopy detected Ba and Ca on the fracture surfaces of the sintered ingots, which suggests that the Ba_2CaWO_6 existed as a surface layer on the W particles. The microstructure of the doped W ingots showed spheroidization of the grains, whereas the undoped W ingots had faceted grains. X-ray diffraction showed only Ba_2CaWO_6 and W, and no other phases, in the sintered compacts indicating that there was no significant Ba_2CaWO_6 decomposition or reaction between Ba_2CaWO_6 and W at these sintering temperatures and times.

W grain size is plotted versus fraction of theoretical density in Figure 3. The grain size increased with increasing fraction of theoretical density for both W and Ba_2CaWO_6-doped-W, but the Ba_2CaWO_6-doped-W compacts showed substantially more grain growth at lower fraction of theoretical density than the undoped W. The behavior of the undoped W compacts is similar to that reported by Cameron and Raj [14] for sintered Al_2O_3. They found that the Al_2O_3 grain size was essentially constant below a fraction of theoretical density of about 92%, and above that the grain size increased rapidly with the fraction of theoretical density.

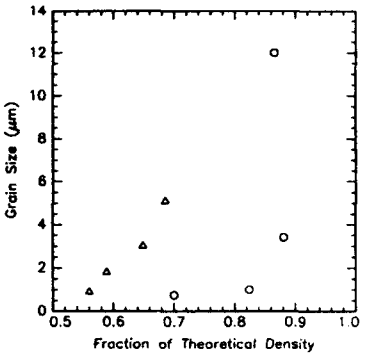


Figure 3. Grain size versus fraction of theoretical density for undoped W compacts (circles) and W-Ba_2CaWO_6 compacts (triangles).

Cameron and Raj performed surface area measurements and correlated the onset of grain growth with the removal of interconnected porosity. They surmised that the interconnected pores, which existed as approximately cylindrical pores along the grain edges, served to inhibit the motion of grain boundaries. In the present case, it is significant that appreciable grain growth occurred in the doped W compacts at lower fractions of theoretical density than in undoped W. This suggests that a grain coarsening mechanism occurred in the doped W compacts that did not occur in the undoped W compacts.

Six mechanisms have been identified for neck growth between particles during sintering [15]. Three mechanisms result in densification of the compact, and three mechanisms produce neck growth without densification. The reduced sintering kinetics of the Ba_2CaWO_6-doped-W may be due to the fact that the Ba_2CaWO_6-doped-W densifies by a mechanism that is slower than the densification mechanism for W or the mechanisms for neck growth without densification may be enhanced in Ba_2CaWO_6-doped-W . In the latter case, Ba_2CaWO_6-doped-W may coarsen more rapidly in the early stages of sintering, perhaps due to the vaporization of the emission material, and it is the coarsening that reduces the densification. In order to determine the densification mechanism of Ba_2CaWO_6-doped-W, the activation energy for densification was measured. 1.8 μm W powder was blended with 2.5 at% Ba_2CaWO_6 and compacted using die pressing at 240 MPa to a relative density of 55%. Samples of the doped and undoped W were sintered in dry H_2 for 10, 30, 100, and 300 minutes at temperatures between 1500 °C and 1700 °C. The diffusion coefficient for the densification process, D, is given by the following equation [16,17]:

$$D = \frac{\frac{dP}{dt}(G_T^3 - G_0^3)kT}{N\gamma\Omega} \qquad (1)$$

where dP/dt is the isothermal rate of pore volume change, G_T is the grain size after sintering, G_0 is the initial grain size, k is the Boltzman constant, T is the sintering temperature, N is a numerical constant, γ is the surface energy, and Ω is the atomic volume. Density and grain size were measured as a function of sintering time and temperature, and the rate of pore volume change was determined from the slope of a plot of densification versus time.

The grain size after sintering for 300 minutes at different temperatures is given in Table II. The Ba_2CaWO_6-doped-W samples always had a larger grain size than the undoped W samples. Diffusion coefficients were calculated from Equation 1 for both W and W-Ba_2CaWO_6, and the results are plotted along with data for W from the literature in Figure 4. The data for W agreed well with the results of Vasilos and Smith [16], and the diffusion coefficients for W-Ba_2CaWO_6 were slightly smaller than those for W. The activation energies for densification of W and W-Ba_2CaWO_6 are given in Table III, along with values for W from the literature. The activation energies for densification of W and W-Ba_2CaWO_6 are the same and agree well with the activation energy for grain boundary diffusion in W, 381 kJ/mol [20]. Since the densification mechanism for sintering of W and W-Ba_2CaWO_6 are the same, the slower densification kinetics of W-Ba_2CaWO_6 are most likely due to increased coarsening of W-Ba_2CaWO_6 in the early stages of sintering.

Table II. Grain size of Ba_2CaWO_6 / W and W compacts after sintering for 300 minutes at different temperatures.

	Grain size after sintering for 300 min (μm)	
Temperature (°C)	W	2.5 at% Ba_2CaWO_6 / W
1500	2.67	3.90
1600	3.18	4.55
1700	5.16	6.17

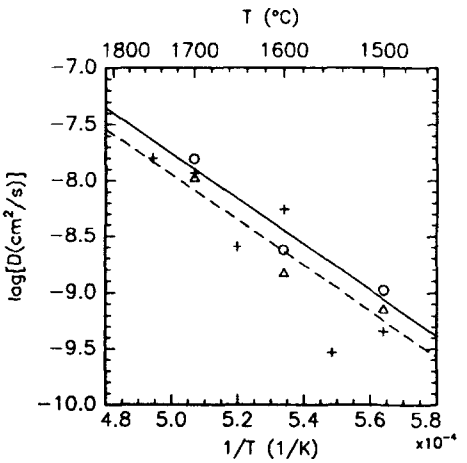


Figure 4. Logarithm of the diffusion coefficient versus inverse temperature for W (circles) and W-Ba_2CaWO_6 (triangles). Also included are the data for W (crosses) from Vasilos and Smith [16]. The solid line is a least squares fit to the three circles, and the dashed line is a least squares fit to the three triangles.

Table III. Activation energies for densification for W and W-Ba_2CaWO_6

	W This work	W-Ba_2CaWO_6 This work	W Ref. 16	W Ref. 18	W Ref. 19
Activation Energy (kJ/mol)	389	389	465	419	377

CONCLUSION

The addition of 2.5 at% Ba_2CaWO_6 to W dramatically decreased the sintering kinetics compared with undoped W. Measurement of the activation energy for densification showed that the doped and undoped W densified by the same densification mechanism, grain boundary diffusion. The decreased densification of the Ba_2CaWO_6-doped-W was probably due to increased coarsening. Ba_2CaWO_6-doped-W can be sintered to about 65% of theoretical density without significant emission material volatilization.

ACKNOWLEDGMENTS

The authors thank M.J. Curran and M.C. Hill for the heat treatments, K. Lou for Auger electron spectroscopy measurements, and D. Marsh for the x-ray diffraction.

REFERENCES

1. R.C. Hughes and P.P. Coppola, Philips Technical Review **19**, 179 (1957).
2. E. Goldburt and W. Hellebrekers, European Patent No. EP 0489463A2 (1991).
3. T. Iida, K. Iitoyo, and H Ito, Japanese Patent No. 52-39976 (1977).
4. K. Ishima, H. Ono, and H. Fukunaga, Japanese Patent No. 58-18863 (1983).
5. A.A. Sadek, M. Ushio, and F. Matsuda, Met. Trans. A **21A**, 3221 (1990).
6. A.I. Mel'nikov, A.V. Morozov, B.N. Popov, and A.A. Maklakov, Izvest. Akad. Nauk S.S.S.R, Ser. Fiz. **22**, 613 (1958).
7. Y. Mihashi, H. Ito, T. Iida, and K. Iitoyo, Nippon Tungsten Review **9**, 14 (1976).
8. M. Koitabashi and K. Sano, Mitsubishi Denki Laboratory Reports **14**, 53 (1973).
9. K. Watanabe and K. Awazu, Mitsubishi Denki Laboratory Reports **14**, 45 (1973).
10. L.C. Chen, K.A. Lou, and B.P. Bewlay, Proceedings of the Third Int. Conference on Powder Metallurgy in Aerospace, Defense and Demanding Applications, F.H. Froes, ed., 111 (1993).
11. C.J. Smithells, Tungsten (Chapman and Hall, Ltd., London, 1952).
12. C. Hirayama and R.S. Bhalla, Journal of the Illuminating Engineering Society **9**, 240 (1980).
13. K. Watanabe, M. Saito, and M. Tsuchihashi, Journal of Light and Visual Environment **1**, 13 (1977).
14. C.P. Cameron and R. Raj, J. Am. Ceram. Soc. **71**, 1031 (1988).
15. F.B. Swinkels and M.F. Ashby, Acta Metall. **29**, 259 (1981).
16. T. Vasilos and J.T. Smith, J. Appl. Phys. **35**, 215 (1964).
17. R.L. Coble, J. Appl. Phys. **32**, 793 (1964).
18. N.C. Kothari, J. Less Common Metals **5**, 140 (1963).
19. H.W. Hayden and J.H. Brophy, J. Less Common Metals **6**, 214 (1964).
20. K.G. Kreider and G. Bruggerman, Trans. AIME **239**, 122 (1967).

VARIOUS PROPERTIES OF SPUTTERED Ta_xAl_{1-x} FILMS

V.J.Minkiewicz,J.O.Moore,G.Keller,S.J.Woodman,D.Dobbertin,R.Savoy, and J.M.Eldridge, Almaden IBM Research Center,San Jose, Ca.

ABSTRACT

Films of Ta_xAl_{1-x} have been prepared by diode sputtering from a target consisting of an Al mask placed on the face of a Ta target. The Ta target was 8" in diameter while the Al mask was 0.125" thick and machined with a grid-like shape. Films were deposited for a range of pressure, at a power of 300 watts, onto oxidized 100 mm diameter Si substrates that were placed on a planetary table beneath the target. The Al/Ta area ratio of the composite target was determined on the basis of the relative sputtering rates for these metals with the intent of producing a film composition with x = 0.5. The film composition was found to vary with argon pressure, going from 24 at.% Al at 4 mtorr to 72 at.% Al at 30 mtorr. This finding was quite unexpected. This result made it possible to deposit a wide range of film compositions from one composite target. The electrical resistivity has a broad maximum of ≈ 240 micro-ohm/cm between x = 0.3 and 0.6. These results compliment and extend the earlier observations by Steidel [1] The as-deposited stress of the films varied from -400 to +150 MPa as x was decreased from 0.76 to 0.28. The temperature dependence of the film stress is hysteretic on the first cycle to 475 C. After the first cycle the films are driven more into tension by as much as 500 Mpa. The oxidation characteristics of one composition $Ta_{0.66}Al_{0.34}$ were characterized in some detail using a combination of electrical resistance, AES and XPS measurements. The results show that such films oxidize at temperatures in the 300 to 600C range via a diffusion-controlled process with an activation energy of 0.98 eV. Such films are substantially more oxidation-resistant than either α-or β-tantalum.

INTRODUCTION

The materials that are used to fabricate the thin film resistors in bubble-jet transducers play a key role in determining their reliability and lifetime. The most popular resistor materials that are currently in use are sputtered Ta_xAl_{1-x}, heavily doped silicon, and sputtered HfB_2. These thin films, that are typically 0.08 microns thick, are expected to survive billions of temperature cycles to 400 C at heating rates of 10^8 C/sec. In view of these rather severe requirements, it would be prudent to characterize the materials properties of these thin film systems. The materials properties of Ta_xAl_{1-x} and HfB_2 are generally not as well documented as heavily doped silicon. In this paper we will concentrate on sputtered films in the Ta_xAl_{1-x} system. We have studied the resistivity of the films as a function of their composition, their as-deposited stress and it's temperature dependence, the stability of their microstructure as a function of temperature, and the oxidation kinetics of a film for x = 0.66.

Sputtered films of Ta_xAl_{1-x} have been studied by Steidel [1] and by Duckworth [2]. Both studies show that the system is complex because the metals are insoluble in solid form, which leads to a host of intermetallic compounds. Steidel also emphasizes that the sputtering gas ambient has a crucial effect on the resulting films because they can be based on either the α or the β phase of Ta. The materials properties of the films he deposited greatly depended on whether the sputtering system was pumped by a turbomolecular or oil-diffusion pump. Duckworth deposited films in four different sputtering systems, and he also notes that the sputtering process was complicated by the two forms of Ta. Electron diffraction from some of his films show that they are mainly small crystals of Al, Ta_3Al,

Mat. Res. Soc. Symp. Proc. Vol. 322. ©1994 Materials Research Society

Ta_2Al, and β-Ta in a mainly amorphous phase. Our data cover a large range in composition. It presents a more comprehensive and somewhat different picture of the dependence of resistivity on film composition.

EXPERIMENT

The experiments were done in a three target Innotec VS24C sputtering system. It is a cryopumped system with a base pressure of 10^{-7} torr. The substrates were 100 mm diameter silicon wafers that had 2 microns of thermal oxide on both sides. The wafers rest on "platters" that spin on a rotating planetary substrate table. There are six platters on the table. The combination of both the spinning and rotating degrees of freedom produced films with excellent composition and thickness uniformity. The standard deviation of the sheet resistance for four wafers in a typical deposition was 0.2 % rms. The composition of the films was measured by Electron Microprobe Spectroscopy. The stress in the films was measured by a commercial Flexus instrument, which is a technique that measures wafer bow using a split laser beam. The Flexus instrument can cycle a wafer to 475 C with predetermined heating and cooling rates. The stress can be measured in-situ during a temperature cycle. The film thickness for the depositions was $\simeq$ 0.22 microns. The films were deposited at 300 watts target power. Two targets were used in the experiments, a specially made composite target and a hot pressed target. The hot-pressed target was used to deposit the films that were used for the oxidation studies. These films had the composition $Ta_{0.66}Al_{0.34}$.

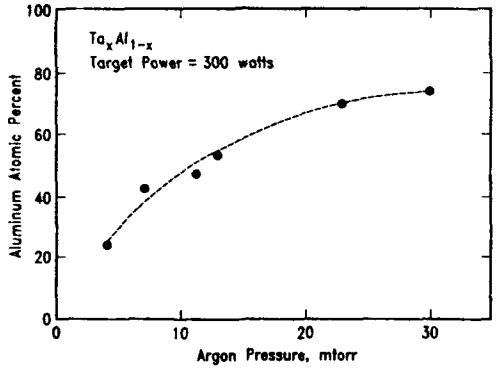


Figure 1. The figure illustrates the composition range over which films can be deposited from a single Ta target covered with an Al mask.

RESISTIVITY AND STRESS

The resistivity, stress, and temperature stability studies were done on films that were deposited from a Ta target covered with an Al mask that was designed to produce films with $x = 0.5$. Experiments showed that the composition of the films deposited from this target could be controlled over a wide range. Fig.[1] shows the dependence of the film composition on the argon pressure. The results shown in the figure are very surprising in that the target was designed to produce films with $x = 0.5$. One could argue that the Al content of films deposited from this composite target could be larger than 0.5. At the higher sputtering gas pressures, where the dark space is smaller, the dark space could conform to

the Al mask, which would increase the Al sputtering from the side walls of the mask, and thereby increase the Al content of the films. However, films with Al compositions less than $x = 0.5$ that are deposited from this target are more difficult to understand. If the variation in the dark space with pressure is the only mechanism that is responsible for this behavior, the Al composition of the films should asymptotically approach 0.5. The reason why the composition of the films can vary over a wide range is obviously more complicated, and is not understood at present.

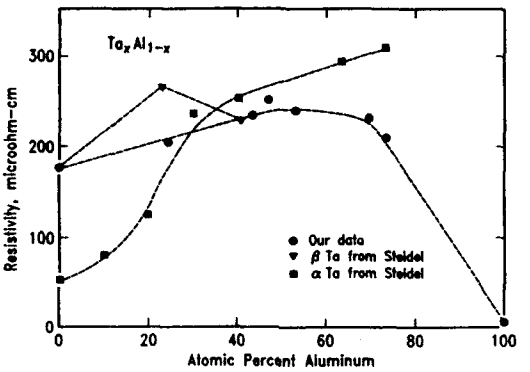


Figure 2. The resistivity of Ta_xAl_{1-x} films is plotted as a function of composition. For comparison, the figure also contains the data from Steidel [1].

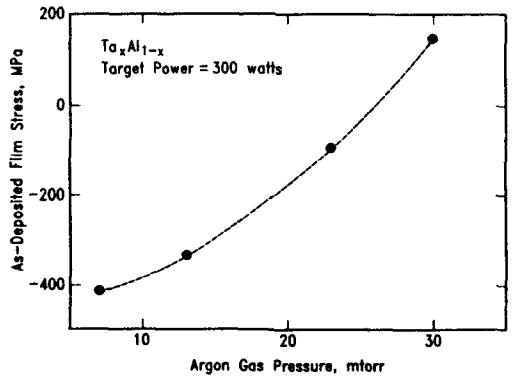


Figure 3. The figure shows the dependence of the as-deposited stress on argon gas pressure or equivalently on composition (see Fig. [1]).

The electrical resistivity as a function of film composition is shown in Fig. [2]. We should point out that our sputtering system is a clean cryopumped system that deposits β-Ta films for $x = 1.0$. The difference between our data and Steidel's results for α-Ta is probably due

to the structural difference between α-and β-Ta, and other effects such as grain structure. The most important feature of the data is that it shows that the resistivity of the Ta_xAl_{1-x} system has a very broad maximum between x = 0.3 and 0.6. This is especially important in manufacturing bubble-jet devices because the resistivity of the heater material, which is a critical material parameter in this technology, is relatively independent of the composition of sputtering target in this range.

The as-deposited stress in the films is shown in Fig. [3] as a function of sputtering gas pressure. The Ta rich films are in compression while the Al rich films are in tension. One reason for this effect could be that the thermal induced stress component of the Al rich films is large enough to drive them into tension on cooling from the deposition temperature. In other words, the Al rich films simply have a larger coefficient of expansion than the Ta rich films [3].

An example of the temperature dependence of the stress of a film , during the first cycle to 475 C, is shown in Fig. [4]. After the first cycle, the room temperature stress does not change after further temperature cycles. The hysteric change in film stress after the first temperature cycle is often observed in other metal systems, and reflects as-deposited film stress annealing by a variety of mechanisms [4].

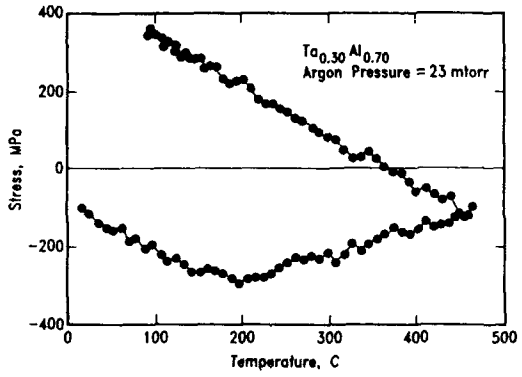


Figure 4. The film stress is hysteretic after the first temperature cycle to 475 C. Afterwards, the stress follows the expected linear relation expected from difference between the thermal expansion coefficients between the film and the substrate.

OXIDATION CHARACTERISTICS

The oxidation characteristics of one particular composition $Ta_{0.66}Al_{0.34}$ (Ta_2Al) were investigated in some detail using electrical resistance, AES and XPS measurements. The reason why this composition was chosen is because the films would be representative of the kind that would be used in bubble-jet devices (see Fig. [2]).

Films were oxidized in air at temperatures ranging from 300 to 600C for times up to about 250 minutes. The most oxidized Ta_2Al films experienced resistance increases in excess of 400 ohms/cm^2. Metal loss (δd_t) at time t can be estimated directly from:

$$\delta d_t = R_o d_o (1/R_o - 1/R_t) \qquad (1)$$

where: d_o and R_o are the initial film thickness and sheet resistance, respectively, and R_t is the resistance after oxidation. This relationship assumes: the oxide layer formed is insulating and grows with a planar inner interface; and, the resistivity of the underlying metal compound remains constant. Thus effects of oxygen penetration into the underlying metal via grain boundary diffusion are neglected. Metal losses calculated from this expression are shown to increase linearly with time$^{1/2}$ in Fig. [5]. This time dependence is consistent with a diffusion-controlled oxidation process. The slopes of the lines in Fig. [5] are plotted against the reciprocal oxidation temperatures in Fig. [6] and demonstrate a good fit to an Arrhenius function with an activation energy of 0.98 eV/mole. The relatively large activation energy and the $t^{1/2}$ rate dependence for oxidation are consistent with the notion that the process is limited by diffusion of an oxygen species through the growing oxide layer. Included also are metal thickness loss rates determined from AES depth profiling of oxidized Ta_2Al films. The metal thickness losses were estimated from the AES-determined oxide thicknesses by dividing by a factor, R = 2.24. This number represents the molar volume ratio of oxide formed divided by Ta_2Al consumed, assuming the following reaction occurs more or less to completion:

$$2\,Ta_2Al + 13/2\,O_2 = 2\,Ta_2O_5 + Al_2O_3 \quad R = 2.24 \qquad (2)$$

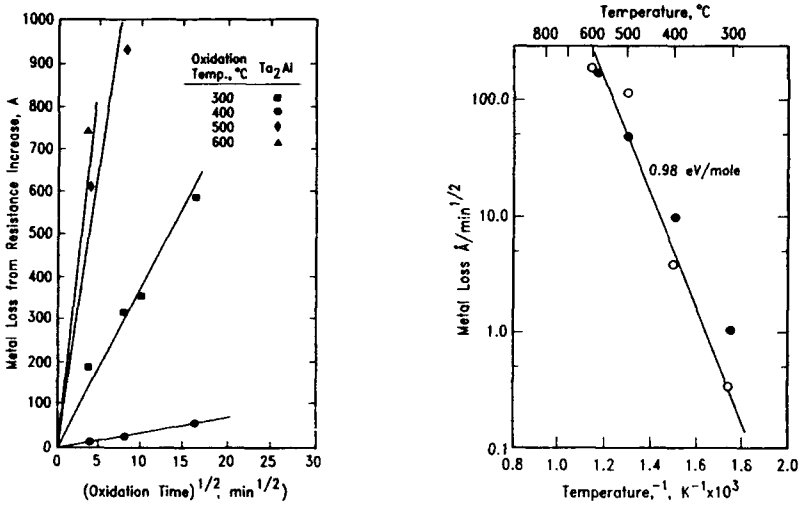


Figure 5. The figure on the left shows the metal loss, or alternatively oxide thickness, of Ta_2Al films plotted as a function of $t^{1/2}$. The straight line dependence is consistent with a diffusion controlled process.

Figure 6. The figure on the right is an Arrhenius plot of the oxide growth process from both the metal loss (see Fig. [5]) and AES depth profile experiments. The activation energy for the growth process is 0.98 eV/mole. The open and closed data points represent the metal loss and AES experimental results, respectively.

The results obtained from the resistance increase and AES measurements are in good agreement, especially considering the simplifying assumptions that were made and the fact that the two techniques differ so markedly. For example, the AES depth profiles of the oxidized Ta_2Al films revealed that oxidation also increased the oxygen content of the underlying metallic layer. Moreover the apparent oxygen concentration in the underlying metal increased monotonically with increasing thickness of the surface oxide layer. Apparently the effect of the oxygen on the resistivity of the underlying metal was not very significant.

Some evidence for preferential oxidation of aluminum was observed by XPS measurements. Such measurements also suggested that some aluminum may remain in metallic form (more or less) as part of a second phase in a Ta_2O_5 matrix. However these features were not investigated in sufficient detail to bear further comment here.

TEMPERATURE STABILITY

In addition to the resistivity, stress, and oxidation experiments, we have also studied the stability of the microstructure of the films. We performed in-situ Transmission Electron Microscopy (TEM) on films with $x = 0.3$ and $x = 0.7$. They are films with compositions on the endpoints of the resistivity plateau. The films were studied in-situ during a 2 hr heating excursion from room temperature to 1200 C. The microstructure was monitored both with photographs and electron diffraction.The as-deposited films are amorphous. The film with $x = 0.3$ stays amorphous to $\simeq$650 C, at which temperature, it basically transforms to the bcc $TaAl_3$ phase. The film for $x = 0.7$ stays amorphous up to 1200 C, with no obvious change in it's microstructure. These observations are consistent with the phase diagram of Ta_xAl_{1-x} [5].

CONCLUSIONS

The data presented in this paper present additional evidence that films in the Ta_xAl_{1-x} system, with the proper composition, are obviously very good candidates for thin film resistors. In fact, most bubble-jet transducers in the market place have Ta_xAl_{1-x} heaters [6]. The resistivity of the films near $x = 0.5$ are at a broad maximum as a function of composition, which would make the resistance of the heaters relatively insensitive to composition. The sputtered films are amorphous, and are stable to high temperatures. The TEM results for the Ta rich film show that the microstructure of the film is stable to 1200 C. The peak temperature that the heaters in these devices experience is $\simeq$400 C. The oxidation studies show that films in this range are substantially more oxidation resistant than either α-or- β Ta. The results suggest that films in the Ta_xAl_{1-x} system,in this composition range, would have excellent long term reliability.

ACKNOWLEDGEMENTS

We would like to thank F.C.Lee for many useful discussions and encouragement.

REFERENCES

1.C.A.Steidel,J.Vac.Sci.Tech.,vol.6 (4),694,(1969)
2.R.G.Duckworth,Thin Solid Films,vol.26,77,(1975)
3.R.C.Weast,Handbook of Chemistry and Physics,55th ed.(CRC Press,Cleveland,Ohio,1974) p. D-152.
4.D.S.Gardner,P.A.Flinn, IEEE Trans.on Electronic Devices,vol.,35,2160, 1988.
5.H.Kimura,O.Nakano,T.Ohkoshi, J.Japan Inst. Light Metals,vol. 23, No.3,106,1973.
6.E.V.Bhashar,J.S.Aden,Hewlett-Packard Jour.,vol.36,27,(1985).

Author Index

Abbaschian, R., 87
Agarwal, Gaurav, 297
Aindow, M., 453
Alman, D.E., 59, 255
Anton, D., 423
Asaro, R.J., 49

Bailey, D.E., 139
Bartha, L., 531
Basu, Ajoy, 41, 215
Beatrice, P., 243
Bewlay, Bernard P., 49, 483, 511, 553
Bingert, S.R., 407
Bose, A., 431
Briant, C.L., 205
Buckman Jr., R.W., 329
Butt, Darryl P., 197

Castro, R.G., 81
Chang, H., 175, 223
Chen, Li-Chyong, 483
Chen, S.P., 229
Chen, S.R., 407
Chin, S., 423
Czarnik, C.M., 175, 185

Davidson, D.L., 431
Deevi, Seetharama C., 119
Dimiduk, D.M., 491
Disam, J., 113
Dobbertin, D., 559
Doty, H., 87

Eldridge, J.M., 559

Feng, C.R., 157
Fraser, H.L., 387, 437
French, Jonathan D., 203

Garrett, J.D., 185
German, Randall W., 341
Ghosh, Amit K., 41, 215
Giamei, A.F., 423
Gibala, R., 175, 185, 223, 261
Gonsalves, Kenneth E., 149
Govindarajan, S., 113
Gray III, G.T., 407

Hampden-Smith, M.J., 127
Hardwick, D.A., 209
Heathcote, J., 461
Heilmann, J.R., 81
Henshall, G.A., 511
Herman, H., 71
Heuer, A.H., 21
Hillig, W.B., 59
Hirvonen, J-P., 27, 279
Holmes, J.W., 261
Hou, D.-H., 387, 437

Hughes, John R., 363
Huntley, Mark, 353

Idasetima, J.S., 107
Ikarashi, Yukinori, 235
Ishizaki, Kozo, 235

Jackson, M.R., 511
Jacubinas, Richard M., 133
Jayashankar, S., 33, 291
Jerina, K.L., 191
Jervis, T.R., 27, 279

Kad, B.K., 49
Kaner, Richard B., 133
Kattelus, H., 279
Kaufman, M.J., 33, 291
Keller, G., 559
Korzekwa, David A., 197
Kreider, Kenneth G., 285
Kumar, P., 413
Kung, H., 27, 197, 279
Kurokawa, K., 243
Kush, M.T., 261

Lappalainen, R., 279
Larsen, M., 461
Lavernia, E.J., 139
Lawrynowicz, D.E., 139
LeSar, R., 229
Lewandowski, John J., 21, 503
Lin, Wen-Yi, 267, 297
Livingston, James D., 395
Loretto, M.H., 453
Lucas, G., 461
Luo, Ping, 149

Maloy, Stuart A., 21, 197
Martin, P.L., 209
Mendiratta, M.G., 491
Michaluk, C.A., 413
Minkiewicz, V.J., 559
Mishra, B., 113
Mitchell, T.E., 21, 27
Monroe, K., 113
Moore, J.J., 113
Moore, J.O., 559
Mosheim, C.E., 413

Nakano, T., 9
Nakashima, T., 9
Nastasi, M., 27, 185, 279
Nieh, T.G., 315
Nutt, S., 139

Odette, G.R., 461
Olson, D.L., 113

Patibandla, N., 59

Petrovic, John J., 3, 21, 107, 197, 203
Pope, David P., 353

Ramakrishnan, M.R., 59
Ramberg, C.E., 243
Riddle, S.E., 33, 291
Rigney, Joseph D., 503
Rollett, A.D., 229
Romanow, William, 353
Rowe, R.G., 461
Rudd, J.A., 553

Sadananda, K., 157
Sampath, S., 71
Sastry, S.M.L., 191
Savoy, R., 559
Segall, A.E., 81
Shah, Dilip M., 353
Shelleman, D.L., 81
Shyue, J., 437
Sickinger, A., 139
Singh, Preet M., 503
Skelly, D.W., 461
Smith, L.S., 453
Somerday, M., 87
Speyer, Robert F., 267, 273, 297
Srinivasan, R., 377
Stoloff, N.S., 59, 255
Strum, M.J., 511
Strutt, Peter R., 149
Subramanian, P.R., 491
Sundaram, S. Kamakshi, 273
Suni, I., 279
Suryanarayanan, R., 191
Sutliff, J.A., 511

Thirukkonda, M., 377
Titran, R.H., 443, 473
Torri, P., 279

Umakoshi, Y., 9
Uz, Mehmet, 443

Vasudevan, A.K., 3
Vecchio, K.S., 49
Vukcevich, Milan R., 537

Wadsworth, J., 315
Wang, L.-M., 127
Wang, Wego, 547
Weiss, I., 377
Wiederhorn, Sheldon M., 203
Wojcik, C. Craig, 519
Wolfenstine, J., 139
Woodman, S.J., 559
Worrell, W.L., 243
Wright, S.I., 407

Yanagisawa, E., 9
Yang, S.S., 437
Yun, H.M., 473

Zeng, D., 127

Subject Index

aluminides, 87, 157, 243, 395, 559

bubble strengthening, 531, 537

cathodic protection, 273
chromides, 395, 461
coatings
  silicides, 3, 243, 267
  ZrO_2 on $MoSi_2$, 185
combustion synthesis, 113, 119
$CoSi_2$, 9
Coolidge process, 305, 341
composites
  ceramic matrix, 3
  combustion synthesis, 113, 119
  creep, 157, 197, 203
  ductile phase toughening, 305, 461, 491, 503, 511
  hipping, 191
  in-situ, 353, 491, 503, 511
  microlaminates, 461
  $MoSi_2$
    Al_2O_3, 87, 461
    Mo, 297
    Nb, 191, 255
    SiC, 27, 33, 59, 71, 87, 113, 139, 197, 203, 291
    TiB_2, 71
    TiC, 261
    ZrO_2, 229
  Nb
    -base, 315, 461, 491
    -Si, 377
  $NbAl_3$-Nb, 87, 461
  Nb-Cr_2Nb, 461
  oxidation, 71, 255
  plasma spray, 139
  processing, 59, 353
  silicide matrix, 3, 305, 315
  synthesis, 59, 127
  thermal fatigue, 261
  transformation toughening, 229
  tungsten fibers in, 315
  V-V_3Si, 511
containerless processing, 353
corrosion, 273
creep, 9, 139, 157, 191, 197, 203, 443, 473, 531, 547
$CrSi_2$
  deformation, 9
  dislocation structures in, 9
  properties, 255

densification, 483, 553
directional solidification, 353
ductile phase toughening, 305, 461, 491, 503, 511
dynamic recrystallization, 209

extrusion, 377

fabrication
  Mo, 305
  Nb alloys, 305, 519
  Ta alloys, 305, 329
  W alloys, 305
fiber morphology, 255
film softening, 175, 185
functionally graded materials, 113, 497

grain
  boundary sliding, 547
  size effects, 157, 209

hot
  isostatic pressing (hipping), 191, 261
  pressing, 113, 157, 261, 431
hydrogen embrittlement, 503

intermetallic compounds, 305, 315, 413, 437, 461
  deformation, 395, 453
  composites containing, 461, 491, 503, 511
  Laves phases, 395
  mechanical properties, 305, 315, 387, 395
  precipitation of, 413
  preparation, 353

Laves phases, 395
lighting industry, 483, 531, 537, 553
liquid phase sintering, 341

mechanical alloying, 33
melting practices, 363
microlaminates, 461
molybdenum (see also $MoSi_2$ and other specific Mo alloys and compounds)
  alloys of, 305, 315, 473
  corrosion, 273
  creep, 157, 473
  general properties, 305, 315
  HfC in, 473
  mechanical properties, 305, 363
  melting practices, 363
  wires, 473
Mo-HfC, 473
Mo-Si-N, 279
$MoSi_2$
  alloying effects, 423, 431
  combustion synthesis, 113, 119
  corrosion, 71, 273
  creep, 9, 157, 191, 215
  deformation, 9, 21, 71, 175, 209, 223, 315, 423
  dislocation structure, 9, 21, 49, 223
  film softening, 175, 185
  grain
    growth, 41
    size, 215
  hot isostatic pressing, 191, 261
  mechanical properties, 21, 71, 191

$MoSi_2$ (continued)
oxidation, 107, 243, 267, 423
plasma spray, 71, 81
processing, 59
reactive hot compactions, 87
sintering, 59, 107
stacking faults in, 49
strain rate effects, 21
synthesis, 59, 133
thermal fatigue, 261
thermoelectric properties, 285
$MoSi_2$-
Mo, 297
Nb, 191, 255
Rh, 431
SiC,
combustion synthesis, 113, 119
creep, 139, 157, 191, 197, 203, 215
grain
growth, 41
size, 215
hardness, 33
hot
isostatic pressing, 191
reactive compaction, 87
mechanical alloying, 33, 291
nanolayer composites, 27
reactions, 27, 33
plasma spray, 33, 71
preparation, 59, 127
volume fraction of SiC, effect of, 33
TiC, 261
Mo-W alloys, 363

niobium (see also specific Nb alloys and compounds)
alloys, 305, 315, 443
applications, 519
creep, 519
composites of, 377, 461, 491, 503
general properties, 305, 315, 519
intermetallic compounds of, 387
mechanical properties, 305, 363, 519
melting practices, 363, 519
oxidation, 305, 315
Nb-15Al-Ti, 387, 437
Nb-Nb_5Si_3, 491, 503
Nb-$NbCr_2$, 461
Nb-Si composites, 377, 491, 503
Nb-Zr, 443
Nb_3Al, 87, 453, 461
Nb_3Si, 377
$NbCr_2$, 395
$NbSi_2$, 133
NiAl, 87, 157, 243
nitrogen hardening, 503

optical imaging floating zone technique, 353
ordering, 437

oxidation
combustion products, 267
$MoSi_2$, 71, 243, 267, 423
-Nb, 255, 423
-Rh, 431
-SiC, 71
-TiB_2, 71
refractory metals, 305, 315
Ta-Al, 559
oxides
dispersion alloys, 483
energy of formation, 243
vapor pressure of, 243
oxygen embrittlement, 491, 503

particle strengthening, 473
phase transformations, 49, 395, 423, 437, 443
plasma spray forming, 71, 81, 139
potassium bubbles in tungsten, 531, 537
powder
injection molding, 341
metallurgy, 341
prestraining, 223

reaction synthesis, 209
reactive
hot compaction, 87
powder sintering, 59
refractory alloys and metals (see specific metal)
rhenium
additions to $MoSi_2$, 431
alloying additions to Mo and W, 305
physical properties, 315

silicides (see also $MoSi_2$ and other specific compositions)
alloying, 235, 431
applications, 3
composites, 27, 33, 503
creep, 157
intermetallic compounds of, 395, 503
joining, 3
melting points, 243
theoretical studies, 235
thermoelectric properties, 285
synthesis, 133
tantalum in, 413
Si_3Zr_5, 235
sintering
$MoSi_2$, 107
refractory metals, 341
tungsten, 483, 531, 537, 553
solid state metathesis, 133
spring network model, 229
sputtering, 27, 279, 285, 461, 559
stacking faults, 49
synchroshear, 395

tantalum (see also specific Ta alloys and compounds)
alloys, 305, 315, 329, 407, 413, 559
fabrication, 329, 413
general properties, 305, 315

tantalum (continued)
mechanical properties, 329, 363
melting practices, 363
sheet product, 329
silicides in, 413
texture, 407
thin films, 559
Ta-Al, 559
$TaSi_2$
deformation, 9
properties, 243
synthesis, 133
thin films, 285
Ta-W alloys, 305, 407
thermal fatigue, 261
thermocouples, 285, 305
thin films, 279, 387, 461, 559
Ti_5Si_3
deformation, 9
properties, 243
$TiSi_2$, 285
transformation toughening, 229, 395

tungsten (see also specific W-alloys)
alloys of, 305, 315, 473, 483
applications, 305, 531
Ba_2CaWO_6 in, 553
ceria in, 483
creep, 157, 473, 531, 547
fibers in composites, 315
general properties, 305, 315, 531
HfC in, 305, 315, 473
HfO_2 in, 483
potassium doping of, 531, 537
powder metallurgy of, 341, 531, 537
sintering, 483, 531, 537, 553
wires, 473, 531, 537, 547
twinning, 395

V-V_3Si, 511
vapor infiltration, 59

W-Ba_2CaWO_6, 553
W-HfC, 473
W-Re alloys, 305, 315, 531
wire drawing, 53, 473, 537, 547
WSi_2, 133, 285